Petroleum and Coal

Article **Open Access**

THE EFFECT OF SO_2 ON Cu-SSZ-13 SYNTHESIZED BY SiO_2 AEROSOL IN SELECTIVE CATALYTIC REDUCTION OF NO WITH NH_3

*Hao Fan, Rui Wang**

School of Environmental Science and Engineering, Shandong University, No. 27 Shanda South Road, Jinan 250199, China

Received March 17, 2018; Accepted May 11, 2018

Abstract

Cu-SSZ-13 was successfully synthesized by a one-pot method with silica aerosol acting as the silicon source. The physicochemical properties of obtained samples were characterized by X-ray diffraction, thermogravimetric and differential scanning calorimetry, and NH_3-temperature programmed desorption. The effects of deionized water usage during catalyst preparation on catalyst activity were investigated in detail. Among all catalysts, Cu-SSZ-13-25 possessed best NO conversion up to 85% at 250-450 °C, and the denitration efficiency at 300 °C could be stabilized at about 90%. Furthermore, the NH_3-SCR activity of Cu-SSZ-13-25 reduced to 62% in the presence of water vapor and bounced back to 88% with the removal of H_2O (g). The SO_2 in flue gas reduced the desorption rate of ammonia on the catalyst surface, resulting in the activity of Cu-SSZ-13-25 down to 47%.

***Keywords**: Cu-SSZ-13; SiO_2 aerosol; Selective Catalytic Reduction; NH_3-TPD; SO_2 poisoning.*

1. Introduction

NO may cause a series of non-negligible environmental problems such as photochemical smog and acid rain[1-2]. In the previous decade, selective catalytic reduction of NO using NH_3 as a reducing agent (NH_3-SCR) has been a commonly used method to effectively reduce NO emission[3]. At present, V_2O_5/TiO_2 series catalysts are widely used in industrial denitration which can remove 90% NO at 300-400°C [4]. However, the above-mentioned catalyst is restricted by the volatilization of vanadium in the catalyst at high temperature[5]. Thus, further development of high efficiency and eco-friendly SCR catalyst remains to be a challenge.

Alternatively, the molecular sieve catalysts especially zeolite-supported metal catalysts have obtained a lot of attentions due to their good specific surface area and stable space structure [6]. Song *et al.* [7]analyzed the effect of copper precursors of Cu/ZSM-5 catalysts on the SCR catalytic activity and verified copper nitrate was the optimized one to remove 90% NO_x at 225–405 °C. Another prominent molecular sieve catalyst is Cu-SSZ-13 because of its regular microporous structure and excellent resistance to hydrothermal aging [8]. Mn-Ce/Cu-SSZ-13 catalyst [9] was synthesized with favorable activity from 125°C to 450 °C up to 90% NO conversion. Nevertheless, the template of Cu-SSZ-13 N,N,N-trimethyl-1-adamantammonium hydroxide (TMAdaOH) and silica sol used as silicon source was expensive leading to high cost in catalyst synthesis [10]. In order to reduce the cost, Xie *et al.* [11] reported a one-pot synthesis method using copper–tetraethylenepentamine (Cu–TEPA) as both template and copper source. This method significantly reduced the synthesis cost which is good for commercialization. However, perfect alternatives to silica sol have not been found. A possible cheaper silicon source is silica aerosol with the advantages of small silicon particles (about 50 nm) and benign dispersion in water.

In this study, a series of Cu-SSZ-13 were synthesized by one-pot method where Cu–TEPA used as template and silica aerosol acting as silicon source. The effects of deionized water usage during catalyst preparation on catalyst activity were investigated in detail. The sample

with the best activity was selected to investigate the influence of poisoning caused by water vapor and SO_2 in flue gas. And physicochemical properties of samples were characterized by X-ray diffraction (XRD), Thermogravimetric and differential scanning calorimetry (TG-DSC), and NH_3-temperature programmed desorption (NH_3-TPD).

2. Materials and methods

2.1 Materials

In this work, all reagents and solvents used were A.R. grade without further purification. $CuSO_4 \cdot 5H_2O$ was purchased from Liqiang (Guangzhou) Chemical Co. Ltd. $NaAlO_2$ were received from the Xiya Reagent Co. Ltd. Tetraethylenepentamine(TEPA) was supplied by Damao (Tianjin) Chemical Co. Ltd. Silica aerosol was produced by Tianjin Kemiou Chemical Reagent Co. Ltd. the NaOH was purchased from Tianjin Guangcheng Chemical Reagent Co. Ltd.

2.2. Catalysts preparation

The Cu–SSZ-13 samples were prepared using the one-pot method. In a typical synthesis, 0.51 g $NaAlO_2$ and 0.5 g NaOH were dissolved in 4.72 g of deionized water by ultrasound for 10 minutes. Then 1.149 g $CuSO_4 \cdot 5H_2O$ was added to the solution and stirred for 30 minutes. Next, 1.07 g TEPA was dropped into the mixture followed by intense stirring for 1h. Finally, 2.63 g silica aerosol and x g deionized water (x=13, 17, 25, 35, 50) were added and stirred for 3h. The resulting solution was transferred into Teflon-lined autoclaves and heated at a temperature of 140°C for 6d. The product was collected by vacuum filtration, washed by deionized water for several times and dried at 100°C for 12h, named as Cu-SSZ-13-x. Before NH_3-SCR activity tests, 1 g Cu-SSZ-13-x was added into 100 ml NH_4NO_3 solution (1 mol·L^{-1}) and stirred for 12h to remove excess copper ions. Then, the samples dried at100°C for 12h and calcinated at 550°C for 8h (heating rate was kept at 5°C·min^{-1}).

2.3. Catalyst characterization

The XRD pattern of sample is conducted with a Bruker D8 Advanced diffractometer with a Cu target Kα-ray and Nickel filter was utilized to ensure the incoming x-rays are monochromatic. In addition, the scanning angle is from 5 to 50° of 2θ at a scanning rate of 2.8° per minute. Thermogravimetric (TG) and differential scanning calorimetry (DSC) analysis of obtained samples were carried out with a SDT Q600 Universal V4.1D TA instrument under a flow of N_2 from 100°C to 700°C with a heating rate of 10°C·min^{-1}. NH_3-TPD was finished by a thermal conductivity detector (TCD) at a heating rate of 8°C·min^{-1}, and the total carrier gas flow is 100 ml·min^{-1}.

2.4. NH_3-SCR activity

The NH_3-SCR activity measurements were carried out in a fixed bed reactor placed in the center of a tubular furnace. The catalyst was positioned in the quartz tube between two layers of quartz wool. The typical reaction conditions were regulated by mass controllers as following: 600 parts per million by volume (ppmv) NO, 700 ppmv NH_3, 6% O_2 and N_2 was the equilibrium gas. In typical conditions, 0.13 g sample was used in each run. The total flow rate was 100 ml·min^{-1} corresponding to a space velocity (GHSV) of 15000 h^{-1}. The NO_x conversion rate can be expressed as $(C_0\text{-}C)/C_0 \times 100\%$, where C_0 stands for the concentration of NO_x in the feed gas and C stands for the concentration of NO_x in the outlet gas.

3. Results and discussion

3.1. Characterizations

XRD pattern of Cu-SSZ-13-25 was shown in Fig. 1, it can obviously find the characteristic peaks of CHA molecular sieves [12] (2θ=9.5°, 12.9°, 16.2°, 20.8°) illustrating that Cu-SSZ-13 was successfully synthesized with silica aerosol. However, the intensity of peaks is weaker than Cu-SSZ-13 synthesized by silica sol. It has been reported that the interaction between

the templating agent and inorganic species is the key to the formation of a stable hybrid mesostructured. Different silicon sources have diverse effects on the structure and species of the silicate ions in the crystallization solution [13]. The poor dispersion of silica aerosol in water resulted in a decrease of silicate ions in crystallization solution which is the main reason for the weaker crystallinity of the catalyst.

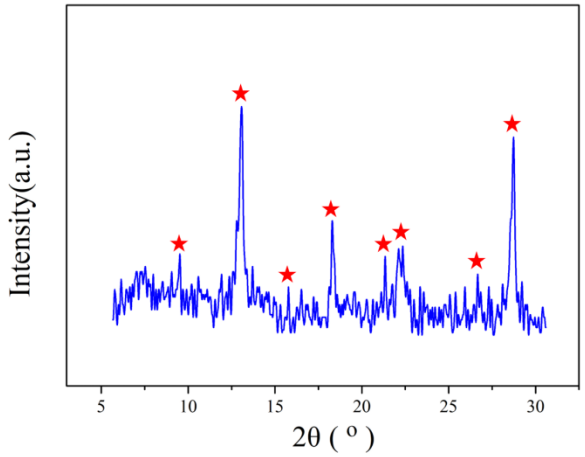

Fig. 1. XRD pattern of Cu-SSZ-13-25 sample

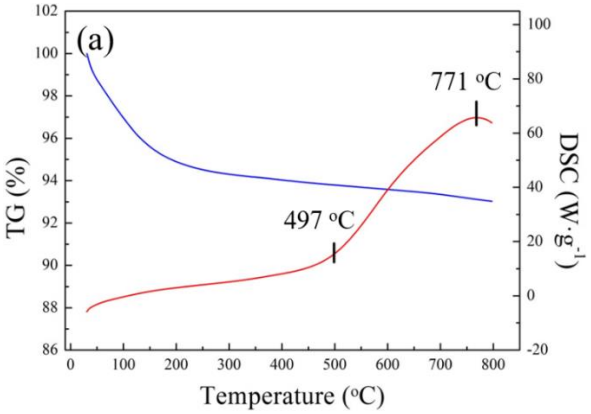

Fig. 2. TGA-DSC curves of Cu-SSZ-13-25 sample

In order to study the thermal stability of the catalyst, TG-DSC analysis of Cu-SSZ-13-25 was done, as shown in Fig. 2. It was obvious that the mass fraction of the sample dropped to 94% at a temperature below 200ºC due to moisture evaporation from the sample. Then, the mass fraction went down steadily and slowly indicating that the catalyst had good thermal stability. Furthermore, there are two endothermic peaks located at 497ºC and 771ºC, which could be attributed to the decomposition of residual TEPA calcination and the oxidation of the Cu species, respectively.

3.2. SCR activity

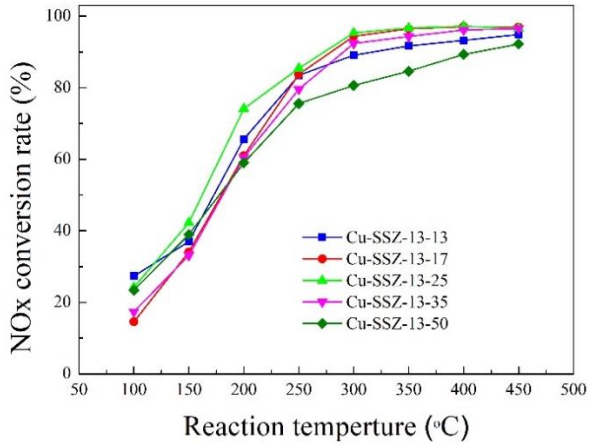

Fig. 3. The effects of deionized water usage during catalyst preparation on catalyst activity

It is undoubted that the amount of deionized water and NaOH used in catalyst preparation has a great influence on the structure and activity of Cu-SSZ-13, and moderate Na^+ content can improve both the low-temperature activity and the hydrothermal stability [14]. Xie *et al.* [15] testified that higher Na^+ contents brought in poorer hydrothermal stability because excess Na^+ ions in the catalysts decreased the stability of Cu species seriously.

In this study, deionized water usage was changed in order to improve the dispersion of silica aerosol in crystallization solution leading to the change of Na^+ concentration. Hence, the effects of deionized water usage during catalyst preparation on catalyst activity was nonnegligible. As shown in Fig. 3, the tendency of the catalytic activity of each sample was similar, among them, Cu-SSZ-13-25 possessed the best NO conversion up to 85% at 250-450ºC, and the denitration efficiency at 300ºC can be stabilized at about 90%. Comprehensively, Cu-SSZ-13-50 has the lowest catalytic efficiency due to the increase of deionized water usage decreased the Na^+ concentration in

the crystallization solution leading to the insufficient crystallinity of sample [15]. In summary, Cu-SSZ-13-25 is the optimal catalyst.

3.3. Effect of SO_2 and water vapor

In the life test, the conversion of NO could be stabilized at 95% in 10 minutes, and there is no significant fluctuation in the test. However, in the presence of water vapor, the activity of Cu-SSZ-13-25 decreased rapidly within half an hour, then stabilized at about 62% after an hour. After removing $H_2O(g)$, the NO conversion recovered to 88% within half an hour, furthermore, as the reaction continues, the activity of the sample is returned to the initial state after two hours.

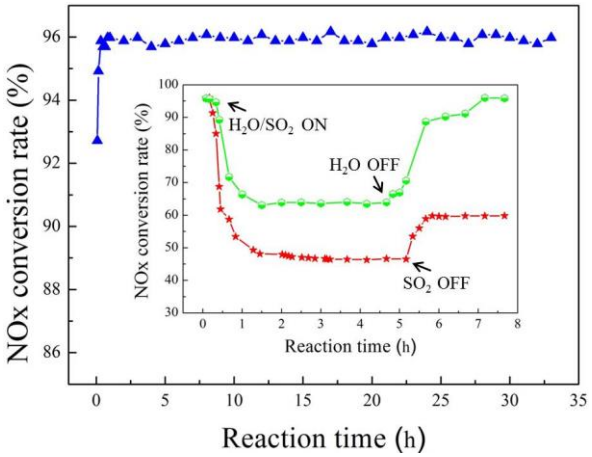

Fig. 4. The life test and the effect of SO_2 and water vapor on the SCR activities of the Cu-SSZ-13-25 catalyst. All Reaction was conducted at 300 °C

In the denitrification reaction with SO_2 in the flue gas, low temperature deactivation is primarily caused by the formation of ammonium sulfate species or competitive adsorption between SO_2 and NO_x. what is more, the formation of metal sulfate species is considered to be a key step in the standard SCR reaction [16]. As shown in Fig. 4, after the introduction of SO_2, the NO conversion was significantly reduced to about 47% after one hour, and then it was basically stable. With the removal of SO_2, the activity of Cu-SSZ-13-25 recovered rapidly to 60%. Therefore, the activity of the catalyst is not sufficient to meet the needs of industrial applications. Further work is needed to improve the resistance to SO_2 of Cu-SSZ-13 synthesized by silica aerosol.

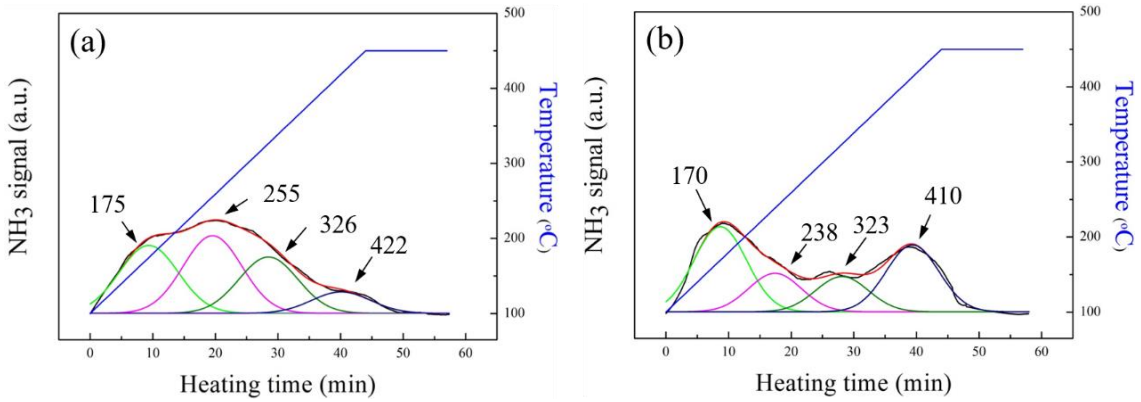

Fig. 5. NH_3-TPD profiles of (a) Cu-SSZ-13-25, (b) Cu-SSZ-13-25 after SO_2 and water vapor poisoning experiment.

NH_3-TPD results (Fig. 5) demonstrated the change of the surface acid amount of Cu-SSZ-13-25 before and after SO_2 and water vapor poisoning experiment. As shown in Fig. 5(a), The peaks position of Cu-SSZ-13-25 was mainly concentrated in the low temperature, where the peak at 175°C was attributed to weak acid sites and peaks at 255°C, and 326°C are assigned to mid-strong acid sites [17]. The peaks position of Cu-SSZ-13-25 after SO_2 and water vapor poisoning experiment did not change significantly, but the peak intensity of mid-strong acid sites obviously reduced, indicating that the poisoning effect of SO_2 was mainly concentrated on the medium-strong acid sites. However, the intensity of the peak at 410 °C was increased, verifying that the active sites were converted to strong acid sites after the introduction of SO_2

in the flue gas, which was more difficult to desorb in NH_3-SCR reaction at 300°C. Therefore, the presence of SO_2 reduced the desorption rate of ammonia on the catalyst surface, resulting in a decrease in the activity of Cu-SSZ-13-25.

4. Conclusions

Cu-SSZ-13-x was successfully synthesized by a one-pot method with silica aerosol acting as the silicon source. However, the crystallinity of Cu-SSZ-13-x is weaker than Cu-SSZ-13 synthesized by silica sol due to the poor dispersion of silica aerosol in water. In all catalysts, Cu-SSZ-13-25 possessed best NO conversion up to 85% at 250-450°C, and the denitration efficiency at 300°C can be stabilized at about 90%. Furthermore, the NH_3-SCR activity of Cu-SSZ-13-25 reduced to 62% in the presence of water vapor and bounced back to 88% with the removal of H_2O. SO_2 reduced the desorption rate of ammonia on the catalyst surface, resulting in the activity of Cu-SSZ-13-25 down to 47%. Further work is needed to improve the resistance to SO_2 of Cu-SSZ-13 synthesized by silica aerosol.

Acknowledgements

This work was financially supported by the Ministry of Education of China under New Century Excellent Talents program (NCET-05-0584), Natural Science Foundation of China (20776080, 20911120088), and Scientific & Technological Development Program of Shandong Province (2008GG10006005).

References

[1] Günter T, Pesek J, Schäfer K, Bertótiné Abai A, Casapu M, Deutschmann O, Grunwaldt J.-D. Cu-SSZ-13 as pre-turbine NOx-removal-catalyst: Impact of pressure and catalyst poisons. Appl. Catal. B, 2016; 198: 548-557.

[2] Zhang RR, Li YH, Zhen TL. Ammonia selective catalytic reduction of NO over Fe/Cu-SSZ-13. Rsc Adv., 2014; 4: 52130-52139.

[3] Han S, Cheng J, Zheng CK, Ye Q, Cheng SY, Kang TF, Dai HX. Effect of Si/Al ratio on catalytic performance of hydrothermally aged Cu-SSZ-13 for the NH_3 -SCR of NO in simulated diesel exhaust. Appl. Surf. Sci., 2017; 419: 382-392.

[4] Chen L, Li JH, Ge MF. Promotional effect of Ce-doped V_2O_5-WO_3/TiO_2 with low vanadium loadings for selective catalytic reduction of NOx by NH_3. J. Phys. Chem. C, 2009; 113: 21177-21184.

[5] Shi A, Wang XQ, Yu T, Shen MQ. The effect of zirconia additive on the activity and structure stability of V_2O_5/WO_3-TiO_2 ammonia SCR catalysts. Appl. Catal. B, 2011; 106: 359-369.

[6] Martín N, Paris C, Vennestrøm PNR, Thøgersen JR, Moliner M, Corma A. Cage-based small-pore catalysts for NH_3 -SCR prepared by combining bulky organic structure directing agents with modified zeolites as reagents. Appl. Catal. B, 2017; 217: 125-136.

[7] Song ZX, Zhang QL, Ning P, Liu X, Zhang JH, Wang YC, Xu L. S, Huang ZZ. Effect of copper precursors on the catalytic activity of Cu/ZSM-5 catalysts for selective catalytic reduction of NO by NH_3. Res. Chem. Intermediat., 2016; 42: 7429-7445.

[8] Kim YJ, Lee JK, Min KM, Hong SB, Nam I-S, Cho BK. Hydrothermal stability of Cu-SSZ-13 for reducing NOx by NH3. J. Catal., 2014; 311: 447-457.

[9] Liu Q. L, Fu ZC, Ma L, Niu HJY, Liu CX, Li JH, Zhang ZY. MnOx -CeO2 supported on Cu-SSZ-13: A novel SCR catalyst in a wide temperature range. Appl. Catal. A, 2017; 547: 146-154.

[10] Chen B, Xu R, Zhang R, Liu N. Economical way to synthesize SSZ-13 with abundant ion-exchanged Cu+ for an extraordinary performance in selective catalytic reduction (SCR) of NOx by ammonia. Environ. Sci. Technol., 2014; 48: 13909-13916.

[11] Xie L, Liu F, Ren L, Shi X, Xiao FS, He H. Excellent performance of one-pot synthesized Cu-SSZ-13 catalyst for the selective catalytic reduction of NOx with NH_3. Environ. Sci. Technol., 2014; 48: 566-572.

[12] Zhang T, Li JM, Liu J, Wang DX, Zhao Z, Cheng K, Li JH. High activity and wide temperature window of Fe-Cu-SSZ-13 in the selective catalytic reduction of NO with ammonia. AIChE Journal, 2015; 61: 3825-3837.

[13] Kresge CT, Leonowicz ME, Roth WJ, Vartuli JC, Beck JS. Ordered mesoporous molecular-sleves synthesied by a liquid-crystal template mechaniem. Nature, 1992; 359: 710-712.

[14] Zhao ZC, Yu R, Zhao RR, Shi C, Gies H, Xiao F-S, De Vos D, Yokoi T, Bao XH, Kolb U, Feyen M, McGuire R, Maurer S, Moini A, Müller U, Zhang WP. Cu-exchanged Al-rich SSZ-13 zeolite from organotemplate-free synthesis as NH3 -SCR catalyst: Effects of Na+ ions on the activity and hydrothermal stability. Appl. Catal. B, 2017; 217: 421-428.
[15] Xie LJ, Liu FD, Shi XY, Xiao FS, He H. Effects of post-treatment method and Na co-cation on the hydrothermal stability of Cu–SSZ-13 catalyst for the selective catalytic reduction of NOx with NH_3. Appl. Catal. B, 2015; 179: 206-212.
[16] Zhang L, Wang D, Liu Y, Kamasamudram K, Li JH, Epling W. SO_2 poisoning impact on the NH3-SCR reaction over a commercial Cu-SAPO-34 SCR catalyst. Appl. Catal. B, 2014; 156-157: 371-377.
[17] Ren ZY, Fan H, Wang R. A novel ring-like Fe_2O_3-based catalyst: Tungstophosphoric acid modification, NH_3 -SCR activity and tolerance to H_2O and SO_2. Catal. Commun., 2017; 100: 71-75.

To whom correspondence should be addressed: prof. Rui Wang, School of Environmental Science and Engineering, Shandong University, No. 27 Shanda South Road, Jinan 250199, China, ree_wong@hotmail.com

Petroleum and Coal

Article **Open Access**

ESTIMATION OF GLOBAL WARMING AGENT FROM ROAD TRANSPORT SYSTEM IN NIGERIA

T. T. Adepoju[1], O. A. Adesina[2], B. S. Fakinle[3], O. B .Okedere[4], J. A. Sonibare[2]

[1] *Environmental Engineering Research Laboratory Department of Chemical Engineering Obafemi Awolowo University*
[2] *Department of Chemical & Petroleum Engineering, Afe-Babalola University, Ado-Ekiti, Nigeria*
[3] *Department of Chemical Engineering, Landmark University Omu-Aran, Nigeria*
[4] *Faculty of Engineering, Osun State University, Osogbo, Nigeria*

Received March 8, 2018; Accepted April 27, 2018

Abstract

World attention has been drawn to the climate change as a result of global warming. Carbon dioxide (CO_2) is a greenhouse gas contributing 9-26 % to global warming. Hence this study focused on estimating CO_2 emission from road transport system in Nigeria from 2004 – 2007. Inventory of all the automobile on the roads of the selected states in Nigeria was taken for the years under review. CO_2 emission from this automobile was estimated using emission factor approach. The result showed Lagos state contributed highest total emission of CO_2 with 116007706.2 ton/annum in the years under review while Cross River State contributed the lowest emission of 1170712.9 ton/annum. Also, motor cars contributed the highest emission of CO_2 of 6720036.462 ton/annum to the ambient environment in the years under review while Lorries contributed lowest emission of 927541.18 ton/annum. The work provides an insight into the contribution of road transport system into the ambient level of CO_2. The result from this work will help to put in proper legislation in reducing the emission of these pollutants.

Keywords: *vehicular emission; carbon dioxide; pollution.*

1. Introduction

There is an unprecedented increase in surface temperature on the earth and this has been attributed to an anthropogenic increase in the rate of emission of greenhouse gasses [1-3]. Among the six greenhouses gases, CO_2 a has been identified as a major culprit for global warming contributing 9-26 % [1,4]. The effects of this temperature rise on human beings and the environment have been extensively reported [5]. Developing countries such as Nigeria has had her share of the effect of global warming, the devastating effects of recent flooding in some part of the of the country and the various prolonged droughts and heat meningitis experienced in some parts of the Northern region of in the are typical effects of global warming [6].

The vast majority of CO_2 emissions come from fossil fuel combustion (coal, natural gas, and petroleum), with small amounts from the nonfuel use of energy inputs, and emissions from electricity generation using non-biogenic municipal solid waste and geothermal energy. Other sources include emissions from industrial processes, such as cement and limestone production [7]. In Nigeria vehicular emission is an important source of carbon dioxide emissions contributing around 20% of Western Europe's CO_2 emissions as at the year 2000 [8]. Nonetheless, CO_2 emissions from vehicles are projected to continue to increase, so proportionally their role may become more significant.

It has been reported that between 1956-2005, the average earth's temperature rose significantly by 13°C per decade which doubled the rate for the 100 years from 1906 to 2005 [6]. Temperatures in colder areas, like the Arctic, also rose twice as fast as the average. This has led to the ice caps melting at a rate of 2.7% per decade since 1978. It also caused sea level

to rise at an average rate of 3.11mm per year between the periods 1993-2003, nearly double the rate between the periods 1961-2003 [7].

There has been an enormous growth in road traffic activity and the use of automobiles in Nigeria. The result of this trend is that air quality in some towns and cities in Nigeria is now dominated by emissions from road vehicles [9]. Global environmental impact due to the burning of associated or solution gas, which produces carbon dioxide (CO_2) and methane (CH_4) is worrisome. One of the sinks for these gasses is the stratosphere, where shortwave UV radiation photo dissociates the molecules, releasing chlorine (Cl) atoms. These Cl atoms are projected to reduce the steady-state stratospheric ozone concentration, in turn increasing the penetration of harmful UV radiation which causes global warming.

There are many methods for estimating emission of air pollutants to the ambient air; these include: direct measurement, mass balance, fuel analysis and emission factors. Among these techniques, emission factor method is a simplified technique for estimation of pollutant emission associated with an activity and has been widely used to quantify the number of pollutants released from an activity [9-11]. It is a representative value that attempts to relate the quantity of a pollutant that is released to the atmosphere with the activity associated with the release of that pollutant [12]. Hence this study is focusing on estimation the total emission of CO_2 from road transport system in Nigeria for the years under review; this is with the view of determining the contribution of the vehicular emission to the ambient level of CO_2 in the country.

2. Methodology

2.1. Study area

This study area is Nigeria with a population over 176 million according to World Bank estimation. Nigeria is situated on the West coast of Africa, lies on latitudes 4° north of the Equator and latitudes 3° and 14° on the east of the Greenwich Meridian. Shares boundaries with The Republics of Benin and Niger in the West, Cameroon in the East, Niger and Chad in the North and the Gulf of Guinea in the South.

2.2. Estimation of CO_2

An emission factor approach was used for emission calculation. The national vehicle statistics were collected from the Central Bank of Nigeria (CBN) and the National Bureau of Statistics of Nigeria (NBS) "Annual Abstract of 2010". Estimation of transport-related emissions was based on equation (1)

$$E = e * a \quad (1)$$

where "E" is the emission rate; "e" is the emission factor per unit of activity; and "a" is the amount of transport activity.

This equation was applied to each vehicle category since the emission factors, and the activity is different. The emission factor, e, is usually expressed in g/kg of fuel and primarily related to driving conditions and vehicle type. The activity, a, is the kg of fuel consumed for travelling a distance of 100km/hr by vehicle over the time unit, in km. Summarized in table 1 are the emission factors used for each of the vehicle types. This was done with the assumption that: the vehicles move at 100km/hr on highways.

Table 1. Emission factors of vehicle categories

Emission source	Uncontrolled fuel economy, L/100 km	CO_2	NOx g/kg fuel	CH4
Cars	11.2	3 183	0.059	0.83
Buses	13.6	3 183	0.059	0.783
Lories	22.5	3 183	0.036	0.653
Motorcycles	2.4	3 138	0.056	5.55

Source: Emission Inventory Guidebook 1 September 1999

3. Results and discussion

This study determined the CO_2 level as one of the global warming agents from fuel consumption by road transportation system in Nigeria. This was with the view to providing information on the current contribution of road transport in Nigeria to her national emission levels.

These emissions calculations are presented as annual emissions with units of ton/year which are presented in Table 2-5.

Table 2. Carbon dioxide (CO_2) from Nigeria roads in 2004 (ton/annum)

States	Cars	Buses	Lorries	Motorcycles
Abia	782 411.4	729 423.1	81 339.5	-
Akwa Ibom	1 057 137.0	66 942.5	17 003.2	1 468 045
Bayelsa	104 414.3	49 998.5	16 084.09	22 058.2
Cross River	195 370.8	-	-	188 965.0
Ebonyi	504 437.2	120 274.3	117 643.6	478 123.2
Edo	1 058 065	249 992.7	496 309	59 606.1
Gombe	27 147.73	21 388.26	9 190.907	13 823.1
Imo	402 111.2	168 883.9	28 032.27	367 685.3
Kaduna	768 489.4	281 380.6	-	318 863.2
Katsina	336 214.1	68 053.6	75 824.9	317 196.6
Kebbi	706 304.9	794 421.2	1 479 276.0	797 427.6
Kwara	712 105.7	393 599.6	108452.7	213 131.0
Lagos	1 3417 473.0	1 803 836.0	877 731.6	566 110.9
Niger	433 435.5	407 765.8	98 342.7	104 212.6
Osun	532 049.0	11 3330.0	19 300.9	81 762.3
Oyo	136 202.7	19 443.9	39 061.4	19 607.3
Plateau	218 109.9	137 773.7	8 731.4	103 624.4
Sokoto	1 081 500.0	369 711.4	488 037.2	714 684.9
Yobe	313 243.0	61 387.1	45 035.4	469 594.1
Zamfara	144 787.9	101 663.7	141 080.4	184 602.4

Table 3. Carbon dioxide (CO_2) from Nigeria roads in 2005 (ton/annum)

States	Cars	Buses	Lorries	Motorcycles
Abia	577 527.2	545 539.6	62 498.2	1 802 545.2
Akwa Ibom	1 153 198.0	73 331.2	52 388.2	1 084 478.0
Bayelsa	157 781.7	83 330.9	26 653.6	34 312.7
Cross River	240 617.0	-	-	169 259.7
Ebonyi	224 374.8	57 498.3	50 090.4	116 614.2
Edo	1 142 757.0	284 713.9	522 043.5	66 370.6
Gombe	36 661.0	27 499.2	22 058.2	11 715.3
Imo	332 269.6	147 773.4	20 679.5	428 222.7
Kaduna	768 721.5	111 663.4	-	53 135.7
Katsina	372 179.1	165 828.5	79 501.4	293 177.7
Kebbi	2 220 545.0	1 811 891.0	1 630 926.0	831 887.4
Kwara	1 266 198.0	699 423.9	193 009.0	574 983.1
Lagos	16 357 316.0	1 986 053.0	906 223.4	393 223.8
Niger	512 790.4	484 985.8	138 782.7	121 172.9
Osun	778 466.8	217 215.9	25 274.9	216 072.1
Oyo	390 045.5	81 942.0	24 815.5	127 251.2
Plateau	1 121 178.0	53 609.5	14 705.5	152 985.7
Sokoto	282 382.7	71 664.6	58 821.8	188 916.0
Yobe	375 427.5	114 996.6	36 763.6	500 475.5
Zamfara	144 787.9	101 663.7	141 080.4	184 602.4

Table 4. Carbon dioxide (CO_2) from Nigeria roads in 2006 (ton/annum)

States	Cars	Buses	Lorries	Motorcycles
Abia	688 902.5	520 262.5	99 721.3	583 071.1
Akwa Ibom	456 406.6	57 498.3	12 867.3	535 033.3
Bayelsa	185 625.5	138 884.8	38 142.3	59 066.9
Cross River	57 543.9	-	-	225 679.7
Ebonyi	73 322.1	47 776.3	7 812.27	219 601.4
Edo	1 403 792.6	291 658.1	206 795.4	59 066.9
Gombe	38 749.3	2 162 158.8	24 355.9	31 763.8
Imo	90 956.5	30 832.4	9 650.5	150 730.9
Kaduna	253 842.8	38 054.4	-	8 627.2
Katsina	230 639.7	91 663.9	29 410.9	118 231.8
Kebbi	914 437.5	1 066 079.9	487 577.6	790 614.1
Kwara	795 173.1	439 431.6	121 319.9	236 953.8
Lagos	27 402 728.1	4 104 046.4	2 194 329.1	580 669.3
Niger	542 954.5	551 928.3	154 866.8	125 290.4
Osun	668 483.7	217 771.4	5 054.9	249 992.7
Oyo	287 951.5	76 664.4	14 245.9	81 909.4
Plateau	1 222 575.8	587 482.8	10 569.5	266 560.8
Sokoto	157 317.6	60 831.5	39 520.9	101 026.5
Yobe	417 889.3	104 163.6	41 818.6	678 901.7
Zamfara	181 912.9	32 776.8	34 006.4	211 072.2

Table 5. Carbon dioxide (CO_2) from Nigeria roads in 2007 (ton/annum)

States	Cars	Buses	Lorries	Motorcycles
Abia	1 318 172.9	802 754.2	258 264.5	2 291 256.4
Akwa Ibom	338 534.5	40 554.37	21 139.1	878 552.7
Bayelsa	464 063.7	194 438.7	46 873.6	95 781.5
Cross River	93 276.8	-	-	-
Ebonyi	45 942.3	22 221.57	36 763.6	85 634.7
Edo	1 358 546.4	412 487.9	103 397.7	46 469.2
Gombe	48 958.7	31 943.51	31 249.1	5 588.1
Imo	12 761.8	46 943.07	6 433.6	165 828.5
Kaduna	428 562.8	1 771 059	-	312 539.9
Katsina	489 587.1	35 554.51	103 857.2	197 494.2
Kebbi	922 558.6	1 353 294	607 059.4	713 753.6
Kwara	616 044.5	340 545.6	93 747.3	187 494.5
Lagos	36 396 050.1	4 788 749	3 306 429.0	926 737.5
Niger	603 282.8	479 708.2	238 963.6	157 642.4
Osun	766 401.1	246 381.7	3 676.4	432 242.2
Oyo	463 831.645	144 995.7	39 520.9	110 290.9
Plateau	1 380 821.47	835 808.8	9 650.5	358 567.9
Sokoto	5420 26.375	108 052.4	2 757.3	305 383.2
Yobe	446 661.289	133 607.2	51 469.1	698 999.1
Zamfara	207 204.432	59 720.47	49 630.9	374 204.7

The emission of carbon dioxide (CO_2) from cars in all the states in 2004 were estimated to be 71 550-16 665 152 ton/annum with the highest emission in Lagos while the lowest estimated emission was in Gombe state. In the year 2005 estimated emission from all the states were ranged from 97 933.7-19 642 816 ton/annum, Lagos state has the highest emission and Gombe state with the lowest emission. Estimated emission ranged from 282 170.3-34 281 773 ton/annum in the year 2006 with lowest and highest concentration in Imo state and Lagos state, respectively. Estimated emission in the year 2007 ranged from 17 739.4- 45 417 966 ton/ annum, with the highest concentration in Lagos state and lowest in Gombe state. The result showed that Lagos state contributed the highest emission to the Nigerian tropospheric CO_2, this is connected with a large number of the automobile in the road of the state. Also, major Petroleum depot is located in Lagos which make it a hotspot for petroleum takers that convey the petroleum product to other parts of the country. Due to the number of the petroleum taker and longer time they spend on the road as a result of the holdup usually, experience in the metropolis a large

amount of CO_2 could be emitted from the exhaust of this vehicle which could cause a considerably increase in the ambient concentration of CO_2. Figure 1 shows the total emission of CO_2 from each state under review. The trend observed showed virtually in all the state a progressively increase in the total emission of CO_2 from the year 2004 to 2007 and this is connected with increasing in the number of the automobile in the roads of the states in view. However, some state estimated CO_2 decreases progressively in these years considered this could be attributed to some factors such as government policies on petroleum products. It has shown that whenever petroleum price is increased by the government low income earner are tend to dispose of their automobile thereby reduce the number of the automobile in this state and in turn reduce the emission of CO_2 at the particular year. Figure 2 shows the emission of CO_2 from the various automobile in Nigeria road; the result showed the motor cars contributed the highest emission of CO_2 to the ambient environment in the years under review this could be as a result of a large number of cars on the roads of the states under review. Buses contributed second highest followed by motorcycles and lorries. The trend also showed a progressive increase in the emission from virtually all the automobile from 2004 to 2007 this could be as result of a progressive increase in the number of this automobile as the year progressed.

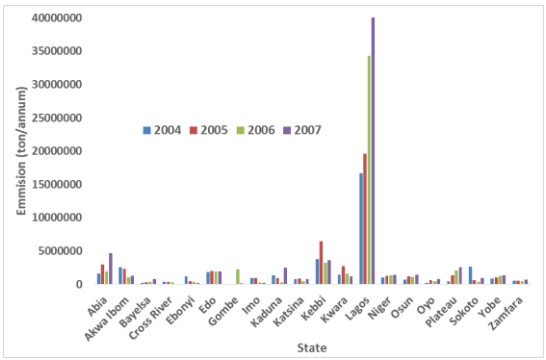

Figure 2. CO_2 Emission from each State of Nigeria

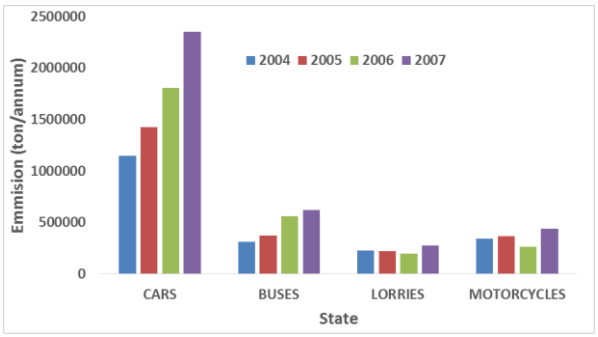

Figure 2. CO_2 from all automobile on the road in Nigeria

4. Conclusion

The work focused on estimation of emission rate of CO_2 from road transport system in the some selected state of Nigeria between the years 2004 to 2007. The result showed the emission CO_2 is a function of the population of the automobile in the road. Lagos state contributed highest total emission rate of CO_2 with 11 6007 706.2 ton/annum in the years under review while Cross river State contributed the lowest emission of 1 170 712.9 ton/annum. Also, motor cars contributed the highest emission of CO_2 of 6 720 036.462 ton/annum to the ambient environment in the years under review while lorries contributed lowest of 927 541.18 ton/annum. The work provides an insight into the contribution of road transport system into the ambient level of CO_2 and as such help in putting in place an appropriate mitigation measure for this emission.

References

[1] Hansen J, Sato M, Ruedy R, Lo K, Lea DW, and Medina-Elizade M. Global temperature change. PNAS, 2006; 103(39): 14288-14293.

[2] Kaufmann RK, Kauppi H, and Stock JH. Emissions, concentrations, and temperature: a time series analysis", Climate Change, 2016; 77(3-4): 249-278.

[3] Roshan GR, Ranjbar F, and Orosa JA. (2010) Simulation of global warming effect on outdoor thermal comfort conditions. International Journal of Environmental Science and Technology, 2010; 7(3): 571-580.

[4] Xiaoli C, Ziyang L, Shimaoka T, Nakayama H, Ying Z, Xiaoyan C, Komiya T, Ishizaki T, and Youcai Z. Characteristics of environmental factors and their effects on CH_4 and CO_2 emissions from a closed landfill: an ecological case study of Shanghai", Waste Management, 2010; 30(3): 446-451.

[5] Calabro PS. Greenhouse gas emission from municipal waste management. The role of separate collection. Waste Management, 2009; 29: 2178-2187.

[6] Kigho PE. Global warming and its implication on the economy: the Nigerian perspective. Journal of Research in Peace, Gender and Development. 2013; 3(4): 54-57.

[7] IPCC Climate Change.The Impact of Global Warming on the Economy. IPCC Report 2007.

[9] Okedere OB, Sonibare JA, Ajala OE, Adesina OA, Elehinafe F. Estimation of sulphur dioxide emission from consumption of premium motor spirit and automotive gas oil in Nigeria. Cogent Environmental Science., 2017; 3: 1330456.
[10] Sonibare JA, and Akeredolu FA. Contribution of Volatile Organic Compounds to Nigeria's airshed by Petroleum Refineries. Petroleum Science and Technology, 2007; 25: 503-516.
[11] Sonibare JA. Air pollution implications of Nigeria's present strategy on improved electricity generation. Energy Policy, 2010; 38 : 5783–5789
[12] Rolander TA. The emission inventory and its role in modelling air quality and the subsequent implementation strategy. Paper No. 71-AP-20 presented at the pacific North-west international section of the Air Pollution Control Association Annual Meeting 1971, Calgary, Canada

To whom correspondence should be addressed: Dr. O. A. Adesina, Department of Chemical & Petroleum Engineering, Afe-Babalola University, Ado-Ekiti, Nigeria, adesinaolusola50@yahoo.com

Petroleum and Coal

Article **Open Access**

THE USE OF LORENZ COEFFICIENT IN THE RESERVOIR HETEROGENEITY STUDY OF A FIELD IN THE COASTAL SWAMP, NIGER DELTA, NIGERIA

O. A. Anyiam, A. W. Mode, B. C. Okpala and C. G. Okeugo*

Department of Geology, University of Nigeria, Nsukka

Received March 9, 2018; Accepted April 27, 2018

Abstract

This study presents a quantitative method for the characterization of static measure of the heterogeneity of reservoirs of a field in the Coastal Swamp Depobelt, Niger Delta, using Lorenz coefficient (LC). The understanding of reservoir heterogeneity and fluid flow channels enables proper prediction of hydrocarbon recovery from the field. Lorenz curve was obtained using the petrophysical model to generate the permeability-porosity and normalization of the flow capacity (kh) and storage capacity (φh). Then, the Lorenz coefficient was calculated as the area between the curve and the diagonal, and it was used quantitatively to identify levels of heterogeneity in the reservoirs. The results show good porosity of 0.21-0.32v/v and permeability of 4,381.66-94,084.98mD. There is significant spatial heterogeneity in the reservoirs with a Lorenz coefficient (LC) of between 0.6464 and 0.9400 for Res 1-A, 2-A, 3-A and 3- of all the 3 wells and fairly heterogeneous reservoir areas with Lorenz coefficient of between 0.3770 and 0.2430 in Res 1-B, C, D for well-1, Res 2-B, C, D, for well-2 and Res 3-B, C for well-3. The Lorenz coefficients show that most of the reservoirs are fairly heterogeneous, hence, enhances the overall hydrocarbon recovery potential of the reservoirs. The findings from this study have important implications for the variability of fluid flow and possible management decision on the hydrocarbon recovery of the field.

Keywords*: Reservoir heterogeneity; flow and storage capacity; Lorenz coefficient.*

1. Introduction

Reservoir heterogeneity has long been recognized as an important factor governing reservoir performance [1]. In many cases, the predicted performance of a reservoir is so completely dominated by irregularities in the physical properties of the formation that the assumption of a particular form for the variation can reduce the solution of the problem to mere exercise [2]. The property normally considered when referring to heterogeneity is that which controls flow (i.e., porosity, permeability). Several kinds of literature existed both theoretical and field studies on the impact of this heterogeneity on reservoir quality [3-7]. Most of the described techniques are required to assess and mitigate its effect on reservoirs. The theoretical studies, however, enable awareness of the adverse effect of heterogeneity and also provide some techniques for applying the result obtained to situations of immediate interest notwithstanding the fact that each reservoir is uniquely heterogeneous. The uniqueness of each reservoir, however, does not necessarily prevent the heterogeneity studies either but the essence of such (e.g., this study) will be to identify the features which impact the performance and quantitatively define their levels. This study, however, focuses on the static measure of heterogeneity for the reservoirs of a field in the Coastal Swamp, Niger Delta (Fig. 1), using the Lorenz coefficient. Obtaining the Lorenz coefficient involves the use of a mathematical model of reservoir properties (porosity-permeability), determined from well logs to evaluate the degree of heterogeneity in a pay-zone section and to identify its possible effect on hydrocarbon recovery. The research will serve as a guide in reservoir management decision when the degree of heterogeneity is known for a particular reservoir in the field.

2. Geological setting and stratigraphy

The Niger Delta clastic wedge spans a 75,000 km^2 in southern Nigeria and is located at the apex of Gulf of Guinea, offshore Nigeria (Fig. 1).

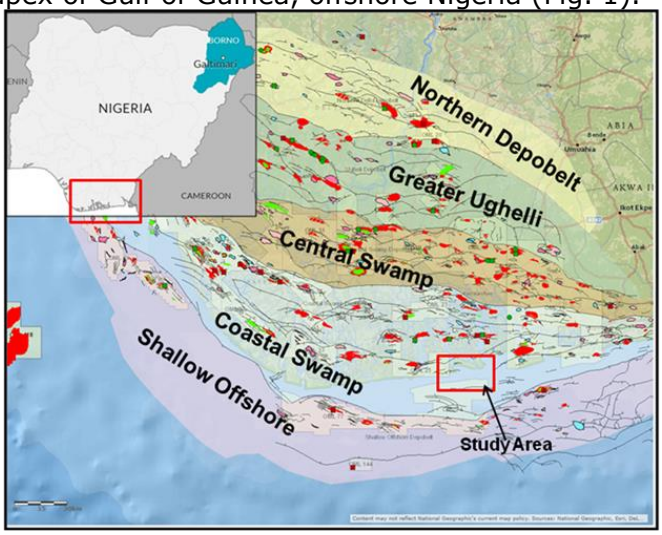

Fig.1. Map of Nigeria showing the location of the sty area in the Niger Delta *(Modified from Ejedawe [18])*

It lies between latitudes 3° and 6°N and longitudes 5° E and 8°E. It is made up of an overall regressive clastic sequence that reaches a maximum thickness of 30,000 to 40,000ft (9000 to 12,000m) [8]. Stacher [9] developed a hydrocarbon habitat model for the Niger Delta based on sequence stratigraphic method. The Tertiary deltaic complex was divided into three major facies units based on the dominant environmental influences [10]. These sedimentary environments are the continental environment, the transitional environment, and marine environment. In an advancing delta, such as the Niger Delta, sediments of the three environments mentioned above become stratigraphically superimposed and its stratigraphic sequence is represented by marine shales. The middle part of the sequence is represented by interbedded shallow marine and fluvial sands, silts, and clays which are typical of a parallic setting. The sequence is capped by a section of massive continental sands.

The three main lithostratigraphic units in the subsurface of the Niger Delta are known as the Akata, Agbada and Benin formations (Fig. 2) decrease in age basin ward, thereby reflecting the overall regression of depositional environments within the Niger Delta.

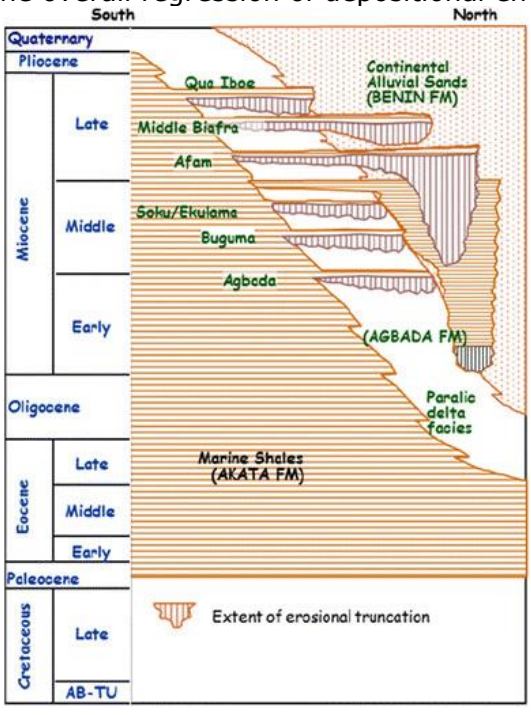

Fig. 2: Regional stratigraphy of the Niger Delta showing different formations *(after Ozumba [19])*

The Akata Formation is interpreted to be deep water low stand deposits by Stacher [9]. It is estimated to be 21,000 ft thick in the central part of the clastic wedge [11]. Marine planktonic foraminifera make up to 50% of the microfauna assemblage and suggest shallow marine shelf deposition that ranges from Paleocene to Recent [11]. The onshore equivalent of this formation is exposed as the Imo shale. The formation also crops offshore in diapirs along the continental slope where deeply buried marine shales are typically over pressured. Agbada Formation overlies the Akata and it occurs throughout the Niger Delta clastic wedge with a maximum thickness of about 13,000 ft. The lithologies consist of alternating sands, silts and shales arranged within ten to hundred feet successions defined by progressive upward change in grain size and bed thickness. The strata are generally interpreted to have formed in fluvial-deltaic environments and ranges in age from Eocene to Pleistocene. The Benin Formation is the top part of the Niger Delta clastic wedge, from the Benin-Onitsha area

in the north to beyond the coast line [10]. The top of the Formation is recent, sub aerially exposed delta top surface and its base extends to a depth of 4,600 ft. The base is defined by the youngest marine shale. Shallow parts of the formation are composed entirely of non-marine sand deposited in alluvial or upper coastal plain environments during progradation of the delta [11]. Although lack of preserved fauna inhibits accurate age dating, the age of the formation is estimated to range from Oligocene to Recent [10].

3. Materials and methods

In this study, a suite of well logs from three wells (Fig. 3), of a field in the Coastal Swamp, Niger Delta was analyzed using PETREL and Mat lab software.

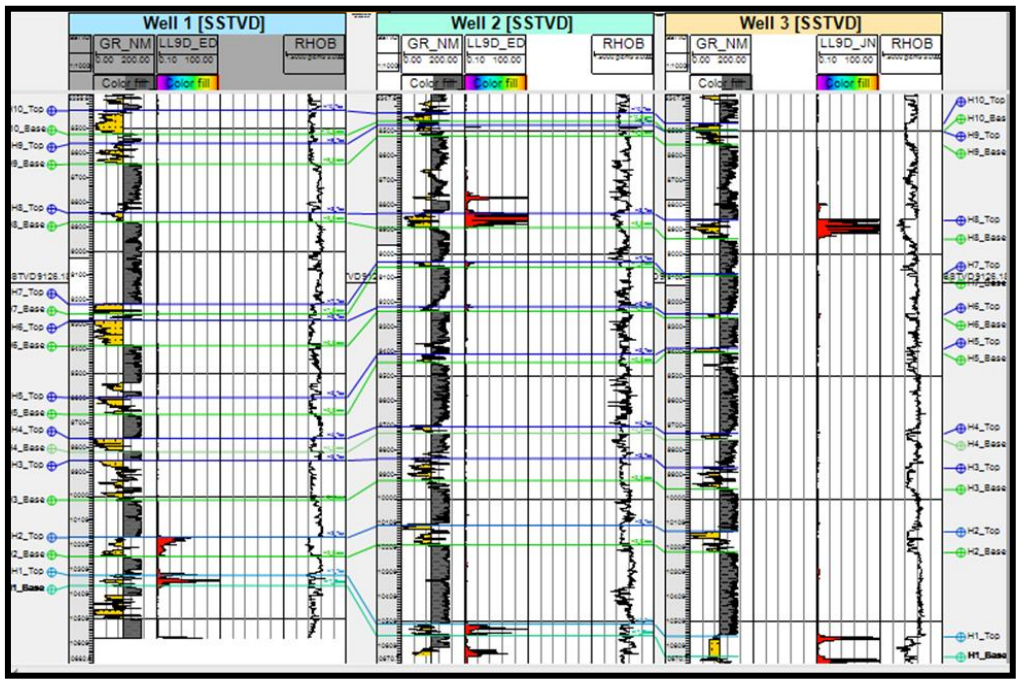

Fig. 3. Correlation panel for Wells 1, 2 and 3 in a dip section

The petrophysical characteristic of the reservoir was evaluated using the suite of well logs (i.e., neutron, density, gamma ray, resistivity, etc.) to calculate the porosity and permeability [12], which are the major parameters required to assess the quality of the reservoir and its heterogeneity. The stile plot is one of the most commonly used techniques for measuring the static heterogeneity. To achieve this, the product of the representative thickness (h) and the permeability (k) was arranged in descending order alongside the corresponding product of representative porosity (ϕ) and thickness (h) for a reservoir. The cumulative of the product (kh) was normalized (between 0 & 1) known as a fraction of the total flow capacity (F). A similar normalization was performed on the cumulative values of ϕh and the result is known as a fraction of total storage capacity(C). A plot of F against C gives the Lorenz curve.

$$F = \sum_{i=1}^{n} kh \Big/ \sum_{i=1}^{N} kh \qquad (1)$$

$$C = \sum_{i=1}^{n} \emptyset h \Big/ \sum_{i=1}^{N} \emptyset h \qquad (2), \text{ where } 1 \le n \le N$$

The curve was made to pass through (0, 0) and (1, 1). The Lorenz coefficient was then calculated using 2 multiplied by the area between the curve and the diagonal. This area was computed by integrating the curve.

4. Results and discussion

4.1. Well-1(5,500 -10,500ft)

The results show that four reservoirs (1-A to 1-D) were delineated from well-1. Reservoir 1-A has a gross thickness of 1459ft between 5385.5ft to 6844.5ft, with a net thickness of 1082ft (Table 1).

Table 1. Average petrophysical properties and Lorenz coefficient evaluated for Well-1 Reservoir

Res. No.	Depth interval (ft)		Net Thick-ness, (ft)	IGR (API)	Vsh (v/v)	Φ_e	Sw (v/v)	Sh (v/v)	K (mD)	Lorenz coefficient (LC)
	Top	Base								
1-A	5385.50	6844.5	990.00	0.23	0.13	0.25	0.10	0.89	18880.53	0.6286
1-B	7272.50	7776.0	404.50	0.30	0.14	0.23	0.26	0.74	7627.83	0.3532
1-C	7942.00	8566.0	376.50	0.36	0.20	0.21	0.29	0.71	6443.27	0.3498
1-D	9328.50	9431.0	102.50	0.18	0.06	0.26	0.30	0.70	7823.27	0.2491

The average volume of shale (Vsh) of the reservoir is 0.13v/v decimal indicating dirty sand zone [13]. Its average effective porosity (ϕ_e) is 0.244v/v which indicates a good reservoir for hydrocarbon accumulation [14]. The reservoir is predominantly (~90%) hydrocarbon saturated and 10% water saturated. An average permeability value of 18880.53mD suggests excellent connectivity for fluid to flow in the reservoir. The Lorenz coefficient value was estimated to be 0.6286 (Table 1), which shows high heterogeneous reservoir. Also, an observed modified Lorenz plot (MLP) shows substantial separation between the storage and flow capacities (Fig.4a & b), which indicates that all pores are not contributing to flow within the reservoir interval.

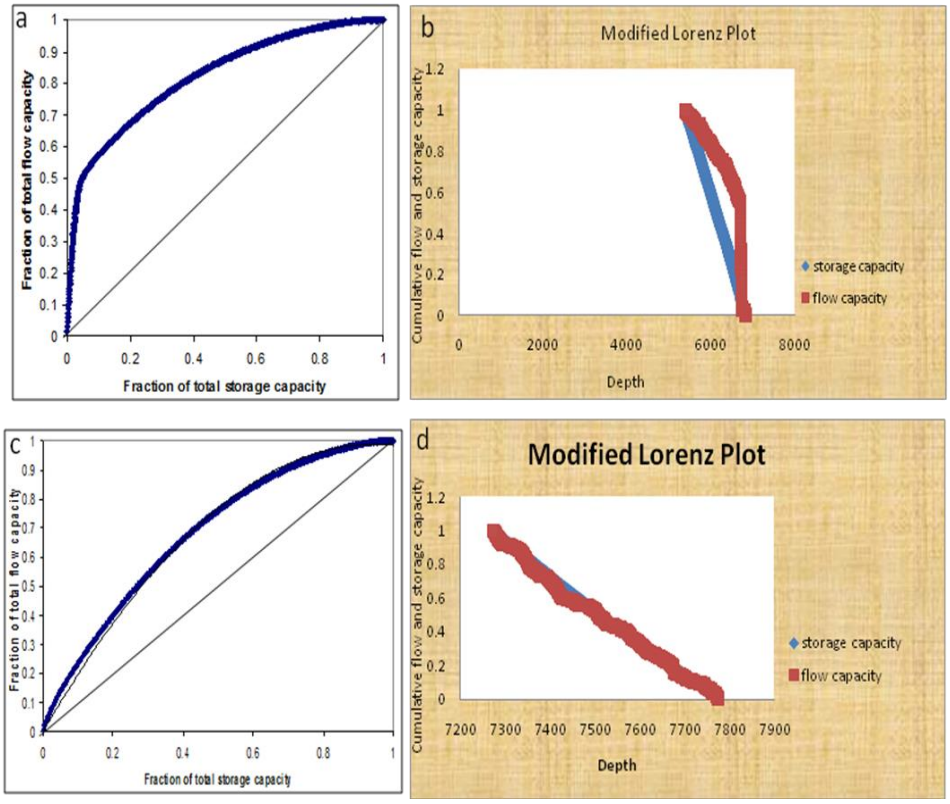

Fig. 4. Lorenz plot and modified Lorenz plots for Well 1: Reservoir 1-A interval (5385.5-6844.5ft) – (a) Lorenz plot (b) modified Lorenz plot; Reservoir 1-B interval (7272.5-7776.0ft) – (a) Lorenz plot (b) modified Lorenz plot

The high heterogeneity of this reservoir has great potential to affect hydrocarbon recovery, possibly causing production of water before the predicted time. Reservoir 1-B has a net thickness of 404.5ft (7272.5-7776.0ft) with an average shale volume (Vsh) of 0.142v/v (Table 1). Although the sand is shaly, it is also within the acceptable limit of clay in the reservoir [13]. Its average effective porosity of 0.23v/v decimal and average permeability of 7627.83mD suggests good pore volume with excellent fluid flow system. The reservoir is dominantly hydrocarbon saturated with little water (~26%) saturation. Estimated Lorenz coefficient of 0.3532 shows that the reservoir is slightly heterogeneous and can easily be ignored. Additionally, a quick look at the MLP indicates an overlap between the flow and storage capacity (Fig.4c & d), which shows that all the pores are contributing equally to flow within the reservoir interval [15]. Reservoir 1-C has net thickness of 376.5ft (7942-8566ft) with an average shale volume (Vsh) of 0.2v/v decimal (Table 1), which is above the limit of 15% that can affect the water saturation value. The average effective porosity and permeability are 0.21v/v and 6443.27mD indicate good reservoir. Average hydrocarbon and water saturations are 71% and 29% respectively indicates shows that the reservoir is predominantly hydrocarbon. Its Lorenz coefficient value of 0.3498 suggests that the reservoir is slightly heterogeneous.

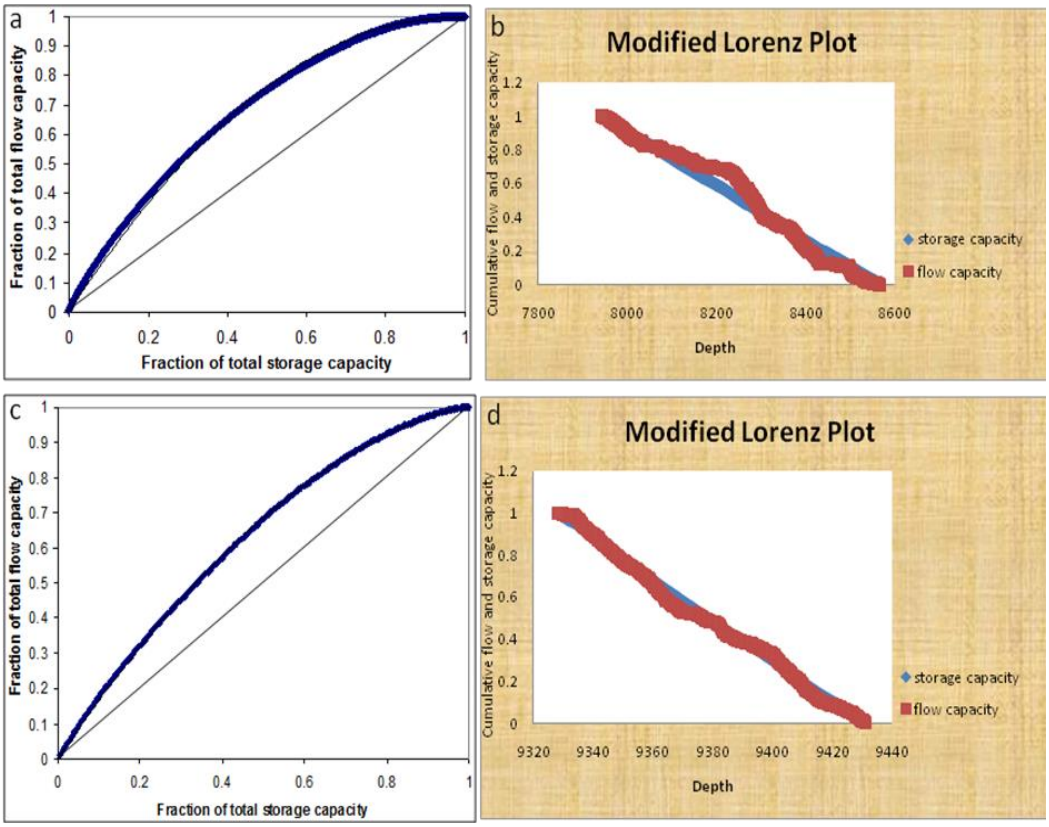

Fig. 5. Lorenz plot and modified Lorenz plots for Well 1: Reservoir 1-C interval (7942.0-8566.0ft) – (a) Lorenz plot (b) modified Lorenz plot; Reservoir 1-D interval (9328.5-9431.0ft) – (a) Lorenz plot (b) modified Lorenz plot

4.2. WELL-2 (5,500 -11,000ft)

In this well, four reservoirs (2A-2D) were delineated (Table 2). Reservoir 2-A is 506ft net thick (5895-6472ft) with an average shale volume (Vsh) of 0.2v/v indicating shaly-sandstone. The average effective porosity and permeability of 0.32v/v and 9408.9mD respectively are quite high and excellent despite the high volume of shale.

Table 2. Average petrophysical properties and Lorenz coefficient evaluated for Well-2 Reservoir

Res. No.	Depth interval (ft)		Net Thick-ness, (ft)	IGR (API)	Vsh (v/v)	Φ_e	Sw (v/v)	Sh (v/v)	K (mD)	Lorenz coefficient (LC)
	Top	Base								
2-A	5895.0	6472.0	577	0.22	0.11	0.32	0.15	0.85	94084.98	0.7245
2-B	6729.0	7009.0	280	0.33	0.16	0.21	0.31	0.69	4508.89	0.3472
2-C	7134.5	7482.0	348	0.35	0.18	0.21	0.34	0.66	5347.38	0.3499
2-D	7944.0	8055.5	112.5	0.29	0.14	0.22	0.36	0.65	4381.66	0.2984

This suggests that the clay type/form is not those that can reduce pore volume but might create baffles that can reduce both vertical and horizontal flows [17]. The Lorenz coefficient value of 0.7245 for the reservoir indicates highly heterogeneous sand (Fig. 6a & b).

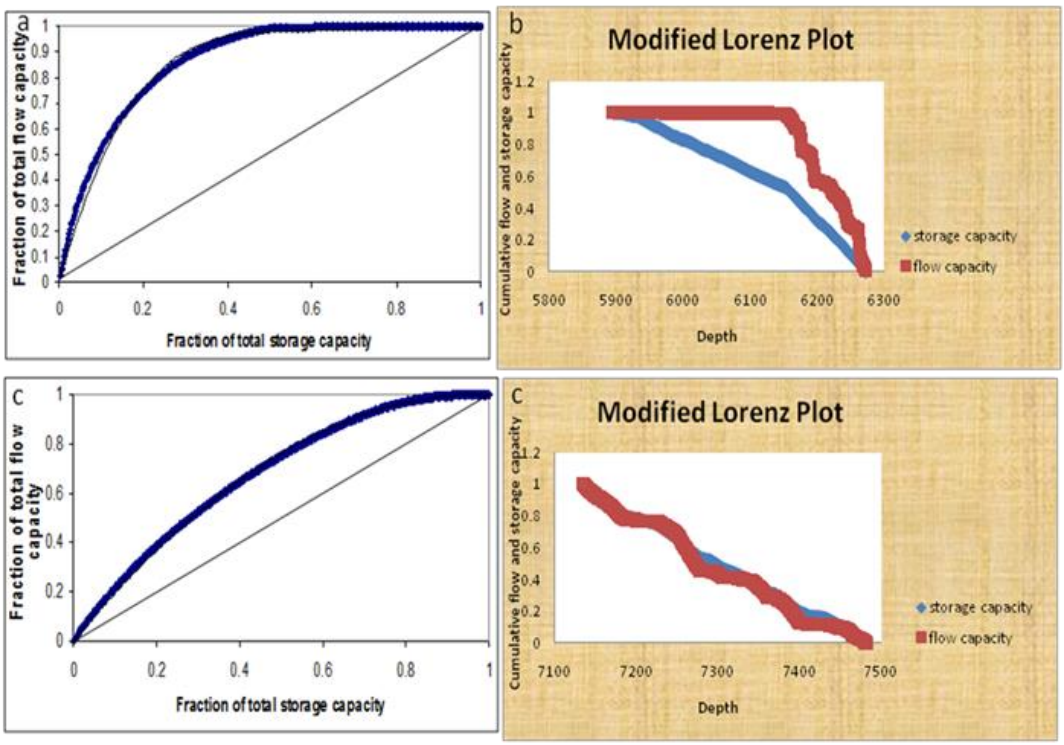

Fig. 6. Lorenz plot and modified Lorenz plots for Well 2: Reservoir 2-A interval (5895.0-6472.0ft) – (a) Lorenz plot (b) modified Lorenz plot; Reservoir 2-C interval (7134.5-7482.0ft) – (a) Lorenz plot (b) modified Lorenz plot

Similarly, the modified Lorenz plot (MLP) shows strong separation between the storage and flow capacity. These results apparently show that the pores are not uniformly contributing to the flow system [15], hence has a high effect on hydrocarbon recovery over time. Average hydro-carbons and water saturations are 85% and 15% respectively which shows that the reservoir is dominantly hydrocarbon saturated. The net thickness of reservoir 2-B is 205ft which occurs at a depth interval of 6729-7000ft (Table 2). The volume of shale (Vsh) is 0.16v/v which is a little above the limit of 15% that can affect the water saturation value [13]. The reservoir also has an effective porosity of 0.21v/v and permeability of 508.89mD, which indicates good reservoir quality for hydrocarbon accumulation and production. Hydrocarbon and water saturation of 69% and 31% respectively were computed for the reservoir. Lorenz coefficient value was also calculated to be 0.3472, an indication that the reservoir is slightly heterogeneous with the minute rate of spreading.

Reservoir 2-C was delineated between 7134.5ft and 7482ft with a net thickness of 227ft (Table 1). The average volume of shale (Vsh) is 0.179v/v indicating a sand shaly zone. The average effective porosity of 0.21v/v shows good reservoir quality (Table 2). Also, the

permeability obtained for the interval is 5347.38mD, which shows an excellent reservoir for hydrocarbon production. The reservoir is relatively hydrocarbon filled with a saturation of 0.66v/v. Its Lorenz coefficient value of 0.3499 indicates a low level of heterogeneity (Fig. 6c &d). The deepest reservoir (2-D) has a net thickness of 88.5ft (7944-8055ft) with shale volume (Vsh) of 0.14v/v. The average effective porosity and permeability are 0.22v/v and 4382.66mD respectively (Table 2); with hydrocarbon saturation of 0.65v/v (65%). The reservoir is slightly heterogeneous with Lorenz coefficient value of 0.298. The MLP shows overlapping between the flow and storage (Fig. 7a & b); capacity indicating that all the pores are contributing equally to flow with an encouraging prospect that will enhance smooth hydrocarbon recovery.

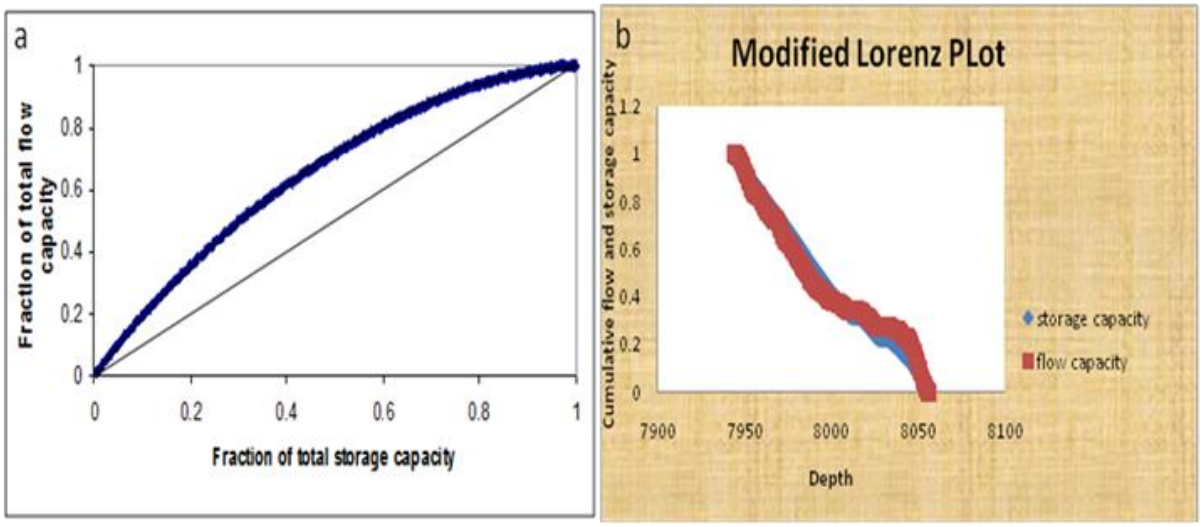

Fig. 7. Lorenz plot and modified Lorenz plots for Well 2: Reservoir 2-D interval (7944.0-8055.5ft) – (a) Lorenz plot (b) modified Lorenz plot

4.3. WELL-3 (5500 -11,000ft)

In this well, four reservoir units were also delineated from Reservoir 3-A down to 3-D (Table 3). Reservoir 3-A occurs at depth 7061-7620ft with a gross and net thickness of 559.5ft and 483.5ft respectively. The average shale volume (Vsh) content is 0.16v/v, having an effective porosity of 0.26v/v. Also, the estimated permeability for this unit is 21799.17mD. The porosity-permeability values are good despite the marginally high value of the shale volume. Also, the Lorenz coefficient value of 0.6464 shows a high degree of reservoir heterogeneity; indicating high variability of flow performance. Also, the modified Lorenz plot (MLP) shows separation between storage and flow capacity (Fig. 8a & b), which is a confirmation that the reservoir is highly heterogeneous, hence, all the pores are not contributing to flow.

Table 3. Average petrophysical properties and Lorenz coefficient evaluated for Well-3 Reservoir

Res. No.	Depth interval (ft)		Net Thick-ness, (ft)	IGR (API)	Vsh (v/v)	Φ_e	Sw (v/v)	Sh (v/v)	K (mD)	Lorenz coefficient (LC)
	Top	Base								
3-A	7061.0	7620.0	559.5	0.419	0.16	0.26	0.31	0.69	21799.17	0.6464
3-B	7698.5	7995.0	296.5	0.221	0.10	0.24	0.35	0.65	6077.31	0.3039
3-C	8519.0	8607.0	88.0	0.410	0.21	0.22	0.34	0.66	7456.62	0.3369
3-D	8913.0	8988.5	75.5	0.415	0.20	0.24	0.05	0.95	27263.86	0.5103

Nevertheless, the reservoir has substantial hydrocarbon saturation of 69% with minimal water. The second reservoir unit (3-B) has net thickness of 256.5ft with an average shale volume (Vsh) of 0.1v/v which is within the negligible value that could affect water saturation. The reservoir has an average porosity is 0.24v/v and permeability of about 6077.31mD, which indicates good quality reservoir that can contain and transmit fluids homogenously. The

reservoir's good quality is also confirmed by the Lorenz coefficient of 0.3039 (Fig. 8c & d), which indicates low level of reservoir heterogeneity.

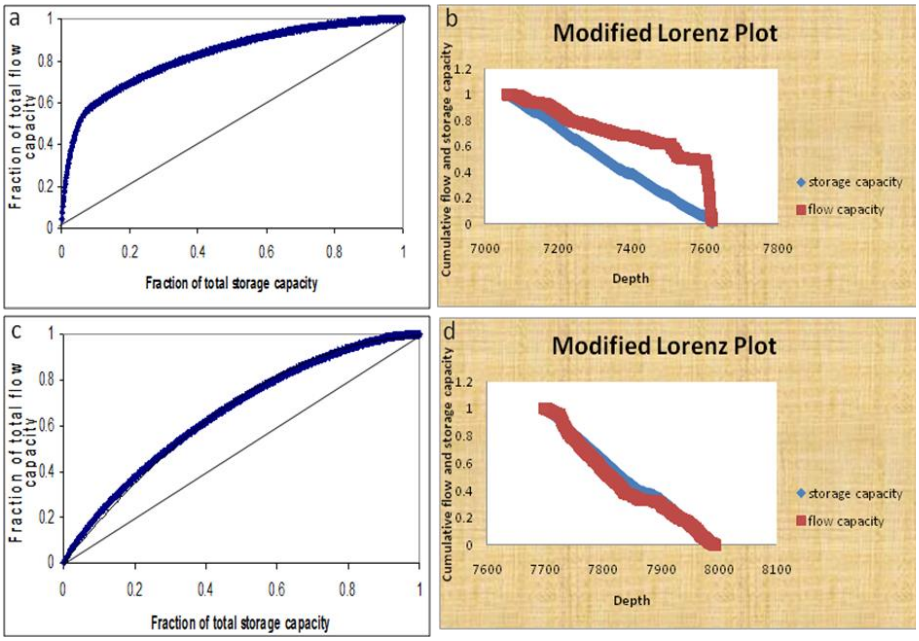

Fig. 8. Lorenz plot and modified Lorenz plots for Well 3: Reservoir 3-A interval (7061-7620ft) – (a) Lorenz plot (b) modified Lorenz plot; Reservoir 3-B interval (7698.5-7995.0ft) – (a) Lorenz plot (b) modified Lorenz plot

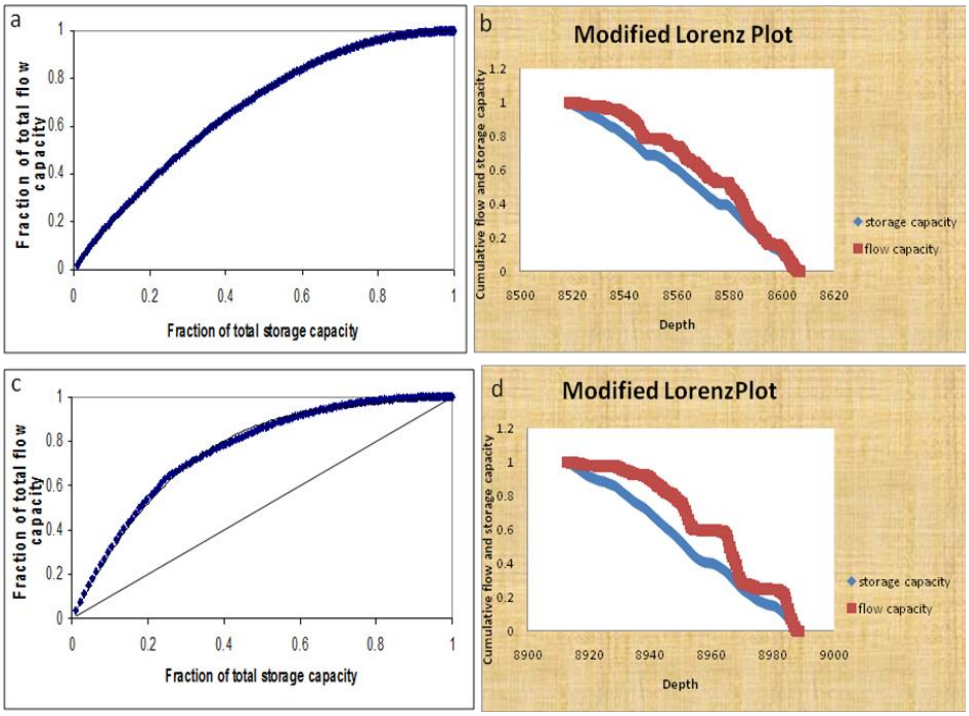

Fig. 9. Lorenz plot and modified Lorenz plots for Well 3: Reservoir 3-C interval (8519.0-8607.0ft) – (a) Lorenz plot (b) modified Lorenz plot; Reservoir 3-D interval (8913.0-8988.5ft) – (a) Lorenz plot (b) modified Lorenz plot

Reservoir 3-B is mainly hydrocarbon filled with an estimated hydrocarbon saturation of 65% against 30% water saturation. Also, the Reservoir 3-C has a net thickness of 61ft and an average shale volume (Vsh) of 0.21v/v indicating a shaly sand zone. Reservoir quality of the unit is relatively good with its porosity-permeability values as 0.22v/v and 7456.62mD (Table 3). Lorenz coefficient value 0.3369 shows the reservoir to be slightly heterogeneous and can be ignored because its effect on reservoir performance is minimal. The modified Lorenz plot (MLP) also shows slight separation between the storage and flow capacities (Fig. 9a & b), which confirms that the pores are relatively contributing to the flow. An average hydrocarbon saturation of 66% shows that the reservoir is dominantly hydrocarbon saturated (Table 3). The deepest reservoir in well-3 (3-D) has net thickness of 47.5ftwith an average shale volume (Vsh) of 0.21v/v and average effective porosity of 0.24v/v. It also has an excellent permeability of 27263.86mD and is dominantly hydrocarbon filled with 95% hydrocarbon saturation. The Lorenz coefficient value calculated is 0.5103 (Table 3), which indicates a relatively high level of reservoir heterogeneity. On the other hand, the modified Lorenz plot (MLP) shows separation of the storage and flow capacities (Fig. 9c & d), which indicates relatively high variability of the flow performance, thereby, increasing the risk of water production before the predicted time.

5. Conclusions

The degree of static reservoir heterogeneity of three oil wells has been effectively studied using the Lorenz coefficient derived from Lorenz and Modified Lorenz Plots. The results indicate that the reservoirs' heterogeneity ranges from significant to fair. Significant heterogeneity occurs in the reservoir (1-A, 2-A, 3-A, and 3-D) of all the three wells. The rest of the reservoirs studied are fairly heterogeneous; which including Res1-B, C, D for well-1, Res 2-B, C, D, for well-2 and Res 3-B, C for well-3. It implies that the reservoirs with a high degree of heterogeneity have a greater number of baffle zones with non-homogeneous pore contributions, giving rise to a steady shallow decline in production. On the other hand, those with a fair level of heterogeneity have a greater number of speed zones (flow units) that constitute greater contribution from the numerous pores which are associated with ling time dominance with production. Thus, hydrocarbons production over a long time can be steadily sustained from these baffles, which usually have shallow production decline as compared to the speed zones with a sharp decline. This study guides in the accurate design of reservoir simulation, apart from capturing the reservoir heterogeneity, which is a major factor that affects oil recovery.

References

[1] Dawe RA. Miscible Displacement in heterogeneous porous Media, Proceedings of the sixth Caribbean Congress of fluid dynamics Trinidad, West Indies January 21-23. 2004.

[2] Warren, J.E. and Price, H.S., 1961. Flow in Heterogeneous porous media, SPE Journal, p.153-169.

[3] Tyler N and Finley RJ. 1991. Architecture controls on the recovery of hydrocarbon from sandstone reservoir, Chemical Geology, 1991; 27: 11-28.

[4] Dawe RA. Reservoir Engineering in Dawe R.A editor Modern Petroleum Technology, upstream volume., Institute of Petroleum 2000, Chichesler: John Wiley and Sons lnc. p.207-282.

[5] Singhal AK and Springer SJ. Characterization and role of reservoir heterogeneity in the performance of infill well in water flood and miscible projects. PETSOC paper 2004265 presented at the petroleum society's 5th Canadian International Petroleum Conference 2004, Calgary, Alberta, Canada.

[6] Malureanu II. The analysis of reservoir heterogeneity from well logs data. Proceedings of the XIX CBGA Congress 2010, Thessaloniki, Greece v.99, p.149-154.

[7] Mode AW, Anyiam OA, and Onwuchekwa CN. 2014. Flow Unit Characterization:-Key to delineating Reservoir Performance in ''Aqua-Field'', Niger Delta, Nigeria. Journal of the Geological Society of India. 2014; 84(6): 701-708

[8] Evamy BD, Haremboure R, Kammerling W, Knaap A, Moolloy FA, and Rowlands PH. Hydro-carbon habitat of tertiary Niger Delta: AAPG Bulletin, 1978; 62: 1-39.

[9] Stacher P. Present understanding of the Niger Delta hydrocarbon habitat. In: M.N Oti and G. Postmaeds, Geology of Deltas: Rotterdam 1995, A.A Balkema, p.257-267.
[10] Short KC, and Stauble AJ. 1967. Outline of Geology of Niger Delta. AAPG Bulletin, 1967; 51: 761-779.
[11] Doust H, and Omatsola E. 1989. Niger Delta: AAPG Memoir, 1989; 48: 201-238.
[12] Asquith GB and Gibson CR. Basic Well Log analysis for Geologists AAPG methods in exploration Series. American Assoc. Petrol. Geol. 1982, Oklahoma. 216p.
[13] Hilchie DW. Applied Openhole Log Interpretation. D.W Hilchie Inc: Goldon, Colorado 1978, p.161.
[14] Dresser A. Well logging and interpretation techniques the course for home study. (3rd Edition 1982) Dresser Atlas Industries Inc.: 211.
[15] Gunter GW, Finneran JM, Hartmann DJ, and Miller JD. Early Determination of Reservoir Flow Units Using an Integrated Petrophysical Method. SPE paper presented at the 1997 SPE Annual Technical Conference and Exhibition, San Antonio, Texas, p.5-8.
[16] Maglio-Johnson T. Petrophysical definition of flow units in deep-water sandstone, Lewis Shale, Wyoming (abs.). American Association of Petroleum Geologists Bulletin, 2000; 84(11): 867.
[17] Anyiam OA, Andrew PJ, and Okwara IC. 2017. Assessment of the heterogeneity and petro-physical evaluation of reservoirs in the ''Akbar Field'' Niger Delta, Nigeria. Journal of Petroleum Exploration and Production Technology, 2017; 7(4): 1035-1050.
[18] Ejedawe JE. 1981; Patterns of incidence of oil reservoir in Niger Delta Basin; AAPG, 1981; 65: 1574-1585.
[19] Ozumba B. Geology of the Niger Delta: An overview of Geophysics processes. An SPDC pre-sentation for geologists in Nigeria 2013.

To whom correspondence should be addressed Dr. Okwudiri A. Anyiam, Department of Geology, University of Nigeria, Nsukka, okwudiri.anyiam@unn.edu.ng

Petroleum and Coal

Article **Open Access**

Experimental Study and Dynamic Pore Scale Modelling of Asphaltene Precipitation in Porous Media

Abbas Khaksar Manshad[1,4], Ali Nikooey[2], Siavash Ashoori[2], Amir H. Mohammadi[3*], Rasoul Hassanalizadeh[3], Jagar A. Ali[4]*

[1] *Department of Petroleum Engineering, Abadan Faculty of Petroleum Engineering, Petroleum University of Technology (PUT), Abadan, Iran*
[2] *Department of Petroleum Engineering, Ahwaz Faculty of Petroleum Engineering, Petroleum University of Technology (PUT), Ahwaz, Iran*
[3] *Discipline of Chemical Engineering, School of Engineering, University of KwaZulu-Natal, Howard College Campus, King George V Avenue, Durban 4041, South Africa*
4 Department of Petroleum Engineering, Faculty of Engineering, Soran University, Soran, Kurdistan Region-Iraq

Received February 7, 2018; Accepted April 23, 2018

Abstract

Asphaltene precipitation in the porous environment is one of the important problems that redeuces the oil reservoir's productivity. In this work, we re-visited several experimental works which have been designed and performed to obtain the permeability declination in a slim tube. By using a slim tube packed with glass beds as a synthetic porous medium and under different conditions this modeling has been performed. At different temperatures, various injection rates and oil to solvent volume ratios studied under different flood test experiment. In this study, single phase flow of oil in the slim tube using a dynamic pore scale network model was simulated, and a mathematical model was developed for matching an experimental data. The results obtained from various simulations of network model were compared to those data which have been achieved experimentally. The current model is based on the theory of deep bed filtration as well as an introduction of the relationship of initial and damaged permeability as a function of porosity change which was caused by deposition of asphaltene on the experimental setup. To simulate the porous medium under the experimental condition in order to estimate the value of the inclination of permeability. There is a good agreement between obtained experimental data and model results which shows the quality of the model.

Keywords: *Asphaltene precipitation; Slim-tube; Permeability reduction; Porosity; Network model.*

1. Introduction

Asphaltene precipitation and deposition can be decreased by means of different processes (mechanical, electrical or chemical) which are capable of elimination or decreasing colloidal particles leading to asphaltene deposition [1]. There are plenty of experimental efforts regarding asphaltene precipitation and deposition. Developed models with respect to asphaltene precipitation prediction can be categorized into two main groups of scaling rules and thermodynamic studies [1].

Network based models consider the connectivity to represent the macroscopic level of the porous medium with acceptable results. Consequently, to calculate the macroscopic properties of the network, Percolation theory needs to be employed [2].

The earliest works on this subject [3-4] determined algorithms in 2D or 3D networks of the porous medium. The models are capable of simulating the porosimetric curves, which apply the theory of percolation to calculate the absolute permeability.

There are available literature works [5] that include phase saturation calculation and relative permeability in the multiphase flow. The established algorithm cannot satisfy the relative permeability and saturation as it does for absolute permeability.

Leontaritis [6] developed an asphaltene near-well formation damage model to investigate the degree of formation damage resulted from deposition of asphaltene considering the time and the effect of asphaltene deposition on hydraulic of near wellbore region as well as wellbore itself.

Pore scale network model developed by Blunt *et al.* [7] is suitable for asphaltene precipitation simulation of two-phase flow. They used the experimental data obtained for the relative permeability of oil and water. In addition, it consists of some results for capillary pressure obtaining from network model. They treated the mentioned data with a BOAST simulator (a simulator of black oil in three phase, three-dimensional environment) which is developed and released by US energy department.

Current work includes a network model employed which aims to simulate asphaltene deposition effect on absolute permeability at the micro scale. In this model, flow through the pore bodies is assumed laminar. It represents a linear response between flow and pressure drop from a pore to the throat. Accumulation of the fluid inside a single element is neglected which shows the inability of the model to capture all of the effects including unusual behavior in higher Reynolds numbers. The driving force to move the fluid from pore to throat is considered to be the pressure difference between the throat and pore centers.

1.1. Asphaltene precipitation fundamentals in a porous environment

The three main sources of colloidal particles in crude oil, which can initiate the asphaltene deposition, are as follows:

1. Contamination of the system during injection of the fluids to the reservoir, work over and the methods which are prevalent in recovery interests.
2. Incompatible materials injected into the reservoir, can interact with rock and mobilize the forming particles.
3. Chemical reactions, as well as organic and inorganic precipitation, can produce particulates.

Four initial mechanisms to migrate the several fine particles along with the flow of the fluid are as follows: [8-9]: penetration, adsorption, precipitation and sedimentation,and Fluid forces.

Asphaltene deposition near to the wellbore can be caused by different parameters including filtrate with high pH and injecting the fluid with low surface tension (e.g., diesel, light alkanes C5-C6 and gas condensates) to the reservoir [10]. During the acidizing process, low pH acids can form which would probably help forming asphaltenic or paraffinic sludge [10].

During petroleum production process, organic deposits can form in the different parts of the plant including reservoir, pipelines, and well. Asphaltene, wax, and resins are the typical and primary sources for the sediments. For the organic sediments, the upper section of the producing well is favorite parts to start deposition. As the asphaltene forms, pressure would drop to below asphaltene fluctuation point, and this will guide the deposition process toward the next parts of the well. This gradual progress would continue until the organic sediments reach to the wellbore and start to form in that zone [11]. Especially, in the reservoirs, which contain large specific area clays (e.g., kaolinite) the initial adsorption and retaining of the polar resins and asphaltenes are very quick [11]. Consequently, molecular deposits (multi-layer arrangement) will sediment close to the surface area of the pores [12.] Regardless of the large aggregate size of the formed asphaltene from suspended sediments in the oil phase, it is impossible for them to pass the pore and they will trap inside the throat [11]. Plugging in the pore throat intense problem on permeability as it closes the passages between the throats. The blockage will intensify the in-situ cake growth under very small remaining flow in to the jammed zone.

Because of deformability and stickiness of the deposits, they normally make sealing on flow constrictions. However the pore space is not completely blocked, it leads to diminishing the flow path conductivity [13-16]. Leontarities [6] emphasizes the asphaltene deposition as the ini-

tial cause of the organic damage. The organic deposition will probably widen the rage of its effect by growing toward the wellbore which more noticeable during the miscible recovery. The deposition initiated from wax deposition does not extend more than 0 to 1 feet, which occurs from pressure loss and cooling the oil during the production of oil.

Minssieux [11] illustrated the same behavior of permeability reduction caused by colloidal particle immigration while there is a running injection of the brine. He conducted several experiments on different porous media, which led to the aforementioned results. Therefore, to study and interpret the obtained results from the tests, a different model was employed to investigate the data. Because of the lack proper experimental data in this regard, it is necessary to conduct experimental studies using different particulates including water and polymers to investigate the mechanism in association with asphaltene deposition in the porous environment.

1.2. The physics of permeability damage

Roque *et al.* [17] conducted comprehensive experiments on Quartzite porous stone and prior to measurements characterized the sample very well. With an aim to investigate the effect of different parameters including operating parameters, flow rate, concentration and particle size on the permeability of the porous medium was investigated. The obtained result shows the importance of those parameters especially due to the deep condition that precipitation needs to be considered. The results are briefly provided in Figures 1 and 2. In Figure 2, the dashed line shows the effect of initial concentration on the concentration of the particles. The solid lines represent the effect of permeability ratio on sedimentations. Experiments have shown that in sole phases, the particle retention is independent of its total effect on permeability. Considering permeability declination and deposition mechanism, the most important parameters are of the particle location as well as deposition kinetics. Further investigations have shown that the reduction of the permeability is highly dependent on the mechanism of the specific particle deposition.

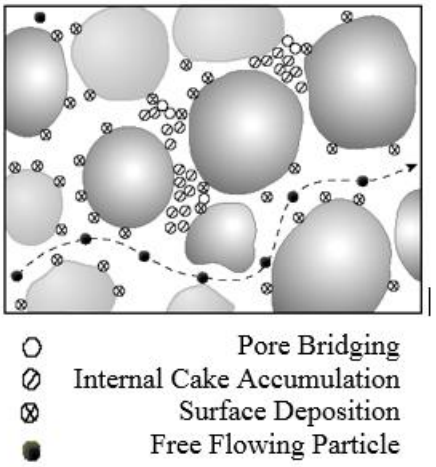

Fig. 1. Inter-pack damage mechanisms [17]

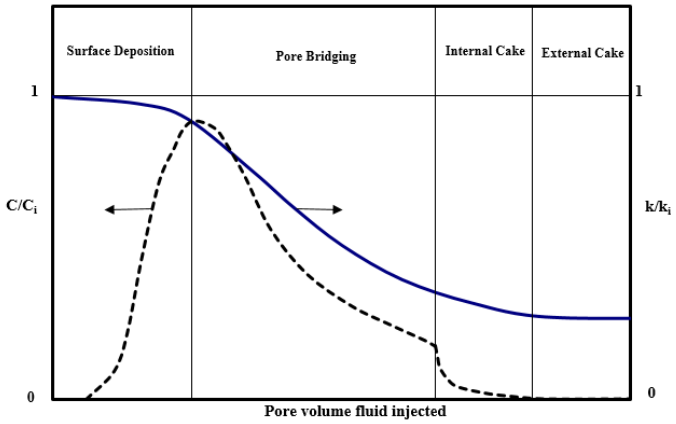

Figure 2. Phases of fines damage process and relative effects on permeability [17]

1.2.1. Particle surface precipitation

In surface precipitation, the deposition site is surface of the grain/pore. The difference of the electrostatic charge between the surface of the pore and particle, the texture of the pore surface and chemical properties and concentration of the pore play the main roles on the kinetics of the deposition process on the surface of the pore. Reduction of the permeability would be significant only if the deposition on the surface of the pore initiates on the throat of the pore.

Therefore, the effect of throat sediments fractions is more important than their quantity on permeability reduction. If the suspensions flow rate is stable, the surface deposition will become strictly mono layer due to strong repulsion between almost static particles. For this phase, the monolayer deposition would occur if the opposing energy of aggregation is high. Due to the results of experiments as well as theoretical sources, it can be concluded that the deposition on the surface has a minor effect on permeability reduction which is denoted in Figures 1 and 2. Small size particles (e.g., clay-size and colloidal) are the favorite species to follow the surface precipitation mechanism as the large particles are not available [18].

1.2.2. Bridging of pore throat

Bridging of pore throat is an issue as the particle makes bridge while attempting to pass the pore throat (shown in Figure 2). Bridging would be in either way of two particles (deposition of a flowing particle on a previously deposited particle) or three particle bridging (bridging of a flowing particle on two formerly deposited particles). Another condition, which can initiate the blockage, is a larger particle diameter in comparison with pore diameter. Obviously, it would possibly bridge with the mechanism of one particle bridging. Forming the bridge would block the pore throat leading to accumulation of the new arriving particles. It would decrease the flow rate in the result. The most significant permeability reduction belongs to this phase (as shown in Figure 2).

1.2.3. Internal cake formation

After bridging the throat to the critical state, it is not functioning in the network of the pores in the depth of damage. Thereafter, accumulation would intensify inside the pore throat and will infect the bodies of the connected pores to the flowing particles leading to initiation of the filter cake within the zone (as shown in Figure 1). The system permeability is controlled by the permeability of the damaged region and its depth. A rapid decrease in particle concentration of the downstream is an indicator of internal cake formation (denoted in Figure 2). Small particle distribution and concentration are the main factors influencing the amount of the damage on permeability.

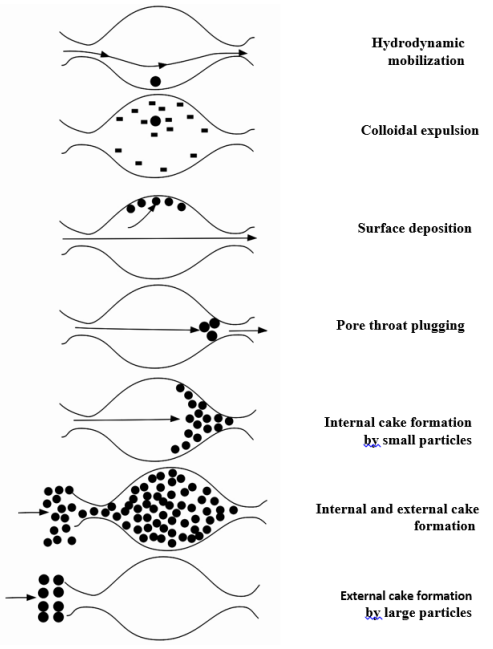

Fig. 3. Varions particulate processes [23]

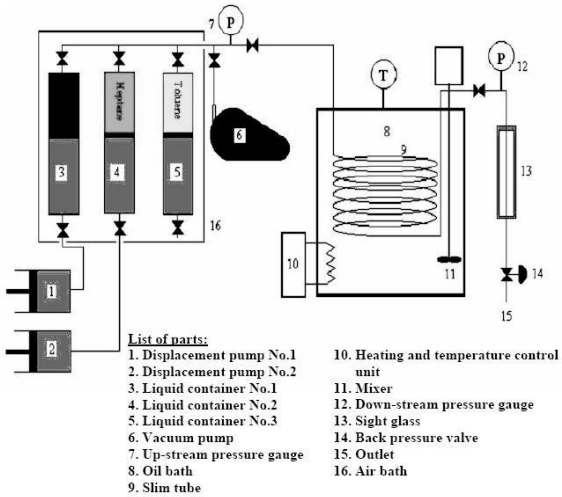

Fig. 4. A schematic diagram of the experimental setup

1.2.4. Formation of the external cake

Right after internal cake formation, the accumulation would move into the upstream and initiate the external cake formation (illustrated in Figures 2 and 3). Figure 3 shows the process of several particulates schematically.

2. Experimental section [22]

2.1. Materials and apparatus

By conduction of several experiments on synthetic porous medium, this phenomenon was studied. The main effort was to simulate the reservoir condition which includes high temperatures and pressures. The equipment is shown in Figure 4. It is made of a slim tube, situated inside an oil bath, a pump to evacuate the cell, and a pump to pump the liquid, a vessel to transfer the fluid, a transparent slim tube to monitor the behavior of the stream which is equipped to a jacket. The experimental equipment consists of a slim tube placed inside an isothermal oil bath, vacuum and liquid pumps, fluid transfer vessels; transparent capillary with a heating jacket that eases the monitoring while the fluid passes the tube, a regulator for the pressure, an oil collection flask, fittings, pipes and pressure gauges.

The mentioned tube is similar to the Ruska tube, which is suitable for determination of the quantity of the damage on permeability. It is a narrow tube made of stainless steel wrapped with a coil. External and internal diameters are 7.9 and 6.2 mm, respectively and coiling diameter is 200 mm. The tube is 18.3 meters long, which is packed using round glass packing.

The approximate porosity of the medium is 27%, and the absolute permeability is 4.93×10^{-12} m^2 (equivalent to five Darcies). The approximate pore volume of the system is 150 cm^3.

The isothermal bath with a volume of 60 liters, is controlled by a temperature controller which is adjustable either using a computer or manually. It can reach to 175°C. There is a designed duct to hold the circulating mixer and heating element to help to mix the fluid thoroughly and the equipment free from the bath with a space between them. The bath is equipped with an adjustable outlet, and inlet valves of the slim tube are connected to the top side of the bath. The tube is placed in a way that the whole tube is submerged into the bath to have a uniform temperature distribution. Downstream of the tube is connected to the transparent capillary that can hold up to higher pressures. It is equipped with a heating jacket to facilitate the monitoring of either one or two phase flow passing the tube.

Two pressure gauges are located in down and upstream sides of the tube to observe the pressure. To control the pressure, a backpressure regulator is placed, and thereafter the oil can be flashed to the atmospheric pressure. The pressure of the upstream can be monitored by employing a pressure gauge (the same regulator is connected to the downstream side).

The pumps are made of the cylinder-piston frame which can contain 500 cm^3. Its flow rate range can be varied between 1 to 2000 cm^3/hr. The pump has two cylinder and piston configuration (capacity of each cylinder is 500 cm^3). It operates up to 70 MPa which can work in either way of manual or computer adjustment.

The material is a crude oil sample from an oil field in the southern part of Iran. It was kept in laboratory condition for quite an appropriate period of time (3 months) to get rid of volatile components and reach a stable composition. Specifications of the sample are provided in table 1. Its gravity index is 20°API (heavy oil) with asphaltene content of 11-weight percentage. To eliminate the possible impurity produced together with crude oil such as sand and clay, it is filtered using Wattman number 42 standard filtrate. As a precipitant, n-heptane was used in the experimentals, and the measurement method to capture the deposited quantity was the gravi-metric method.

2.2. Experimental method

There are two main experimental methods, which include:

2.2.1. Preliminary activities

These series of activities consist of washing, drying and evacuating the tube, filing the vessel with fluid to transfer it, measurement of the pore volume, system behavior investigation, and measurement of the permeability and eventually applying the Carman-Kozny equation with respect to porosity calculations.

Table 1. Composition and characteristics of the crude oil [1, 21, 22]

Component	Mole fraction	Property	Value
H_2S	0.192	Reservoir Oil MW (g/gmol)	156.67
Nitrogen	0	Test temperature (F)	225
CO_2	2.204	MW C_{7+} (g/gmol)	316.49
Methane	26.945	SG C_{7+}	0.9272
Ethane	8.008	Density of reservoir fluid @ Pb (g/cc)	0.7646
Propane	6.426	Bubble point pressure (psia)	1890
i-Butane	1.134	Asphaltene content in stock tank oil, wt%	11
n-Butane	3.682		
i-Pentane	1.742		
n-Pentane	2.233		
Hexanes	4.202		
$Heptanes_+$	43.212		

2.2.2. Flooding experiments

The effect of the different parameters such as injection rate, temperature, permeability reduction and oil ratio was investigated by conducting series of experiments (flooding experiments). The precipitant was n-heptane in all of the flooding experiments in a porous medium. One of the objectives of the measurements was designed based on using Darcy's equation which requires low Reynolds number. Therefore, the rate of injection was taken equivalent to the Reynolds number of unity into the porous medium.

The preliminary activities were undertaken with the aim of concluding the operational conditions of the porous medium for the flooding tests. The flooding test can be done following the steps of:

1. Filling the vessel of the fluid transfer with the oil (filtered oil) and same for the other vessel with n-heptane.
2. To connect the top valves of the vessels to each other using a T-junction connection.
3. Connecting the pumps to both vessels at the desired flow rate and running the vacuum to evacuate the vessels from unwanted impurities such as air and moisture.
4. Connecting the T-junction (free port) to the evacuated porous medium's inlet. Note that the valve should be closed.
5. Introducing the fluids and mixing them should start. Activating the pump while the the valve of the porous medium is opened (note that it should be simultaneously). After his point, time for any action needs to be recorded.
6. Recording the entrance valve pressure after the proper fixed amount of time (for example 2 minutes). Passing the mixture through the porous environment. The injection should be continued up until the time that the filled volume reaches to 150 cm^3 (one pore volume). The indication of the filled pore volume is pressure rising. This is the point that the outlet valve needs to be opened and consequently, inlet pressure starts to decrease, and in a very short time, it reaches to equilibrium condition (steady state). Asphaltene starts to deposit, and it increases the pressure of the medium. A sample of 10 cm^3 is taken as soon as the level of the mixture increases to the out let valve (time step of 10 minutes). After passing the 600 cm^3 from the tube (equivalent to four pore volume), the sampling would need to stop. The highest allowed pressure to minimize the safety problems is 28 MPa.
7. Step 6 shows the quantity of the deposited asphaltene.

To calculate the pore volume or permeability versus time, it is demanded to use Darcy's law to treat measured data from step 6. The permeability dependence on different parameters can be investigated by following this approach which can determine the level of the damage which is resulted from asphaltene deposition. It is possible to calculate the time dependent concentration of the asphaltene in the final product using data from the latest step (step 7). The operational conditions for the experiments are listed in tables 2 and 3.

Table 2. Input parameters (test conditions) [1, 21, 22]

Parameters	Test #1	Test #2	Test #3	Test #4	Test #5	Test #6
Flow rate, (cm^3/hr)	60	30	30	60	90	30
Concentration of n-C_7 in the mixture, (%)	40	40	60	50	40	50
Concentration of asphaltene in the mixture, (vol./vol.)	0.001811	0.001811	0.003066	0.002462	0.001811	0.002462
Mixture density, (g/cm^3)	0.808	0.808	0.77	0.79	0.808	0.79
Asphaltene density, (g/cm^3)	1.1	1.1	1.1	1.1	1.1	1.1
Mixture viscosity, (cP)	1.1	1.1	0.59	0.71	1.1	0.71
Total length of porous medium, (cm)	1828.8	1828.8	1828.8	1828.8	1828.8	1828.8
Cross-section area of porous medium, (cm^2)	0.30	0.30	0.30	0.30	0.30	0.30
Temperature, (°C)	90	90	90	90	90	90

Table 3. Selected Oil and asphaltene properties [1, 21, 22]

Property	Value	Property	Value
Flow Rate	60 cm^3/hr	Asphaltene concentration, (vol/vol)	0.0024
Viscosity	0.79 cP	Oil density	0.79 g/cm^3
Temperature	90°C		

3. Methodology

3.1. Network and pore geometry

Representation of the porous medium includes a lattice of throats and pores which is arranged rectangularly as the solid blocks are connected to a layer of pores. Circular shape in the cross sectional view are indications of throats and pores. Each pore includes different branches showing the connected throats and their extensive effect on the network. Weibull [19] showed that the distribution of the pore radius lays within a random interval and which be calculated using the following equation:

$$R_r = (R_{t\max} - R_{t\min}) \times \left[-\alpha \ln\left(z\left(1 - e^{\frac{-1}{\alpha}}\right) + e^{\frac{-1}{\alpha}} \right) \right]^{\beta} + R_{t\min} \quad (1)$$

where R_t and z denote throat radius and a positive random number smaller than unity, respectively. Other parameters (α and β) are the statistical constant. The pore radius should not be smaller than largest radius of the throats which can be calculated as follows:

$$R_p = \max\{R_{ti} \mid i = 1,\ldots,n\} \times f \quad (2)$$

where n and *f* (*f* ≥1) denote the throat number and aspect ratio, respectively. The aspect ratio shows the pore radius ratio to the largest throat radius. The topological shape of the lattice is considered to be rectangular which gives a freedom to the throat and pore length to vary. In equation 2, if we replace the l parameter with R, it can change its application from the calculation of pore to the throat length. The network model randomness cab is quantified using equation 1 which defines the index of heterogeneity. Obviously, as the heterogeneity of the system increases, the system would become more heterogenic with a larger index.

$$H_i = \frac{\bar{R} \times \beta \times (f_{max} - f_{min})}{R_{max} - R_{min}} \quad (3)$$

where $\bar{R}$ denotes the average throat/pore radius.

3.2. Passing the fluid from network

Flowing fluid fills the whole cross-section of the element. The resistance of the fluid hydraulic (ω) has a general form which can be calculated as follow:

$$\omega = \mu_f \int_{x_1}^{x_2} \frac{dx}{g(x)} \quad (4)$$

where *g(x)* and μ_f denote conductance fluid per length and viscosity of the fluid, respectively. Poiseuille's law shows the calculation if *g(x)* is considered for a cylindrical flow:

$$g = \frac{\pi}{8} R^4 \quad (5)$$

3.3. Distribution of fluid pressure

In the equation of volume conversion, hydraulic resistance (equivalent) is taken into account. Using this concept, the flow rate of the oil between neighboring throat and pore centers can be calculated by the equation 6:

$$q = \frac{P_p - P_t}{\omega_e} \quad (6)$$

where, indices of p and t are denoting pore and throat, respectively. ω_e denotes hydraulic resistance (hydraulic). A network with a number of throats and b number of pores is considered then conservation of volume for throats and pores is applied.

The conservation of volume is included with equation 6 (equation of flow). This leads to a list of equation systems with a + b unknowns (pressure at pore/throat center) that are illustrated in the Equation 7 and 8 for pores and throats respectively:

$$\sum_{i=1}^{n} q_{ij} = \sum_{i=1}^{n} \frac{P_p^j - P_t^i}{\omega_e^{ij}} = 0 \quad (7)$$

$$\frac{P_p^2 - P_t^i}{\omega_e^{i1}} + \frac{P_p^2 - P_t^i}{\omega_e^{i2}} = 0 \quad (8)$$

where indices j and i indicate throats and pores respectively. 1 and 2 show two connected pores to a throat.

According to Equations 7 and 8 for any network with a + b members (throat/pore), a system of linear equations with a+b unknowns is obtained. Solving the mentioned system including proper boundary condition determines pressure distribution for the network. Network absolute permeability can be calculated based on Darcy's low for single-phase flow; it is assumed that fluid viscosity does not change due to asphaltene precipitation during the process. Having pressure distribution through the network gives the ability to calculate the thermodynamic state of the fluid as well as probability and quantity of deposited asphaltene with respect to the introduced scale in the next section.

3.4. Asphaltene precipitation model

Because of the complexity of the thermodynamics model with a required number of fitted parameters from experimental data, the available parameters are lacking the power to extend the predictions to some unmeasured operational conditions [20]. Therefore, the scale equation is included to predict the asphaltene deposition conditions of the investigated sample [20]. The model includes different parameters such as the pressure of the oil, initial content of the asphaltene inside the oil, bubble point, temperature, pressure and eventually the critical

properties. Properties of the tested asphaltene and oil are provided in Tables 2 and 3. This scaling equation was coupled with previously described network model to predict the amount of deposited asphaltene in each pore or throat.

3.5. Simulation of the precipitation process

Asphaltene deposition is highly dependent on pressure fluctuation of the pore as it is the driving force for flowing the oil in between throat and pore. Changing the condition during this fluctuations would possibly initiate the deposition (basic assumption for scaling rule). Time dependent asphaltene content of the pore and throat can be calculated by equation 8 and following material balance:

$$V_{a,prec} = \frac{\rho_o x v_a}{MW} x f_{a,SE} x V_{p/t} \quad (9)$$

where $V_{a,prec}$, ρ_o, v_a, Mw_a, $f_{a,SE}$ and $V_{p/t}$ denote the deposited asphaltene volume, oil density, molar volume of the asphaltene sample, molecular weight, mass based fraction of the deposit and volume of the throat/pore, respectively.

At each time step the change in radius of each pore or throat is computed according to the following equation:

$$dR_i = \frac{V_{a,prec}^i}{2\pi R_i L_i} \quad (10)$$

where dR_i is a reduction in radius of element i due to asphaltene precipitation, $V_{a,prec}^i$ is the volume of deposited asphaltene in element i, R_i is the radius of element i and L_i is its length.

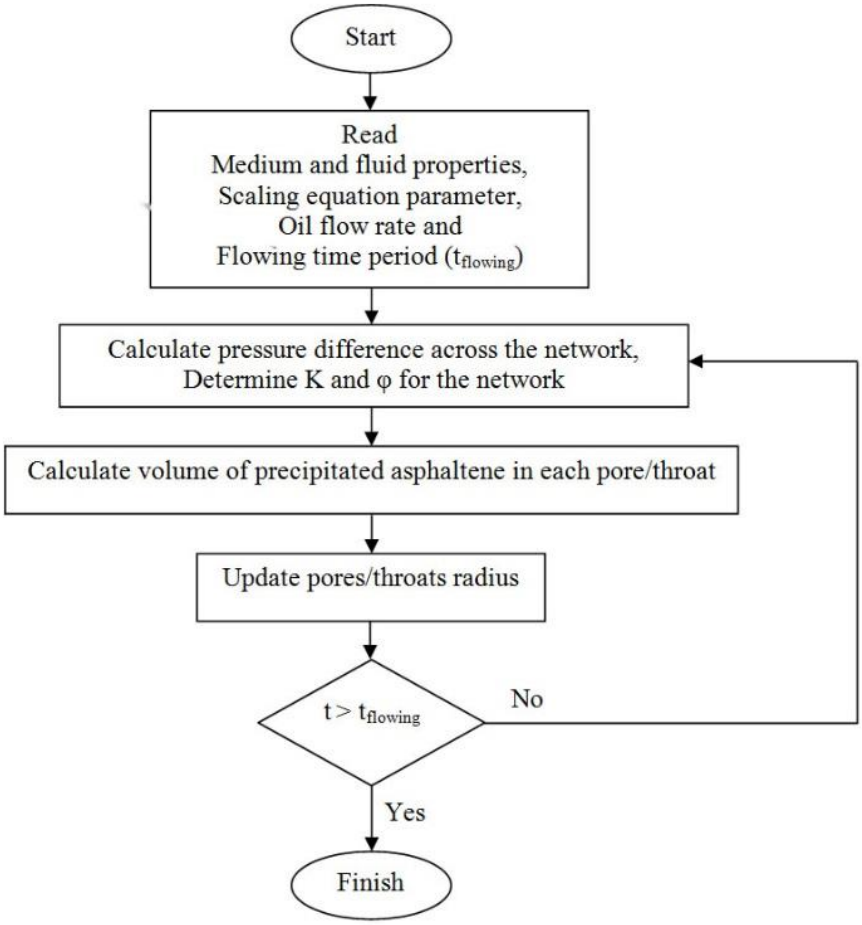

Figure 5. Algorithm for simulation of asphaltene precipitation in network model

The flow chart of the developed computer program is provided in figure 5, which simplifies the discussed mathematical computations. This program was used to simulate the asphaltene precipitation phenomenon in porous medium duo to fluid (asphaltenic crude oil) flow. The network model used this simulation shows only a very small part of the tube; hence, we can neglect the effect of temperature change and assume the process to be in an isothermal condition. To have the similar opportunity of precipitation in both slim tube and network model it is assumed that the network model is entrance part of slim tube consequently a number of filling of the network model with oil is calculated according to the slim tube and network model dimensions and their average porosity:

$$N_f = \frac{V_{BS}\varphi_S}{V_{BN}\varphi_N} \quad (11)$$

where N_f is a number of completely filling of the network model with oil, V_{BS} and V_{BN} are the bulk volume of the slim tube and network respectively, in addition, φ_S and φ_N are porosity of average porosity of slim tube and network, respectively.

3.6. The sensitivity of the network permeability

The morphology defining parameters for the network model are as follows (from the most important to the least important). Distribution of the diameter of pore/throat, length of the throat (pore), an average of the pore coordination number and pore number (throat). At a different range of the length, radius, and number of pores, a one-phase flow is simulated with a network model. Looking at results, one can conclude that the permeability within the range of 10-700 pores is unstable. In the constant condition for the rest of the parameters, results have shown that after 700 number of pores, the system becomes stable and it is less sensitive to the parameter which is shown in figure 6. Hence, the included lattice is made of 24×32 dimensions of pores, which rectifies the limitation.

4. Permeability and porosity reduction due to asphaltene precipitation

In this study, asphaltene precipitation was simulated during oil flow using the pore scale network model with the rate of 60 cc/hr. The oil asphaltene content was 0.0024 (volume/volume) based on the experiment that was performed on the slim tube. Permeability was less sensitive to the change of porosity in comparison with precipitation. The asphaltene precipitation decreases path connectivity for fluid flow. However the deposit volume occupies a small part of the medium, and it doesn't decrease the porosity significantly. This fact is in a good agreement with results of experiment (see Figure 7 and 8). Figures 4 and 5 show normalized permeability and normalized porosity with respect to their initial values for both model and experiment. Some parameters of network model were changed to reach the best match between the network model prediction and experiment results. These parameters values are shown in Table 4. According to Figures 6 and 4, network model could predict porosity reduction more reliably than the estimation of permeability reduction. It might be the result of different heterogeneities of the slim tube and network model. The flow was simulated using three different indices of heterogeneity (H_i) inside the network.

Table 4. Network parameters used in the simulations

Parameter	Value	Parameter	Value
R_{tmin}-R_{tmax}	3-20 μm	A	0.8
l_{min}-l_{max}	10-100 μm	B	1.6
f_{min} -f_{max}	2-2.2		

The more the heterogeneity, the higher the probability to deposit asphaltene (shown in Figure 9). For the presented results *f* and β were varying in equation 3 and the size of the throat radius was constant. As the number of the parameters rises, consequently the complexity of the model increases. Therefore in such simulations permeability alteration is a sensitive function of associated pore volume parameters like pore size distribution and

coordination number. During the described process, pore size distribution changes as a result of decreasing pore/throat radius due to asphaltene precipitation (see Figure 10).

5. Results and discussion

In this study, a pore scale network simulator was used to calculate the change of the porosity and permeability of a 2D porous medium (hypothetical) resulting from asphaltene precipitation. The result were compared to the results of an experiment that was carried out on the slim tube. Initially based on the simplified Navier-Stokes equation pressure distribution through the network is calculated. Thereafter, to predict the fraction of precipitated asphaltene of every pore or throat, a scaling equation is employed with respect to the pressure fluctuations. Finally, distribution of the pore size, porosity, element size reduction and permeability is determined consequently by a material balance for each throat or pore. The pore scale network model predicts the porosity reduction more acceptable than permeability changes. This fact is the result of medium heterogeneity. In fact, the slim tube that was used in the experiments is more heterogeneous than the network model of this study. Simulations show more heterogeneous networks are more sensitive to asphaltene precipitation. Authors recommend that a thermodynamic model which includes the colloidal nature of asphaltene particle is used in such simulation. It should be mentioned that coupling network model with a thermodynamic model is more complex than the model used in this study.

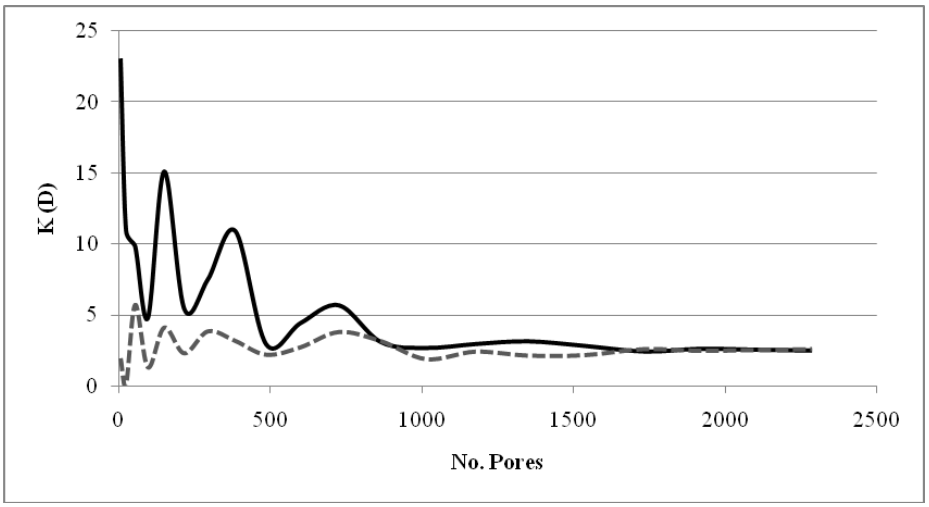

Figure 6. Effect of number of pores on absolute permeability.

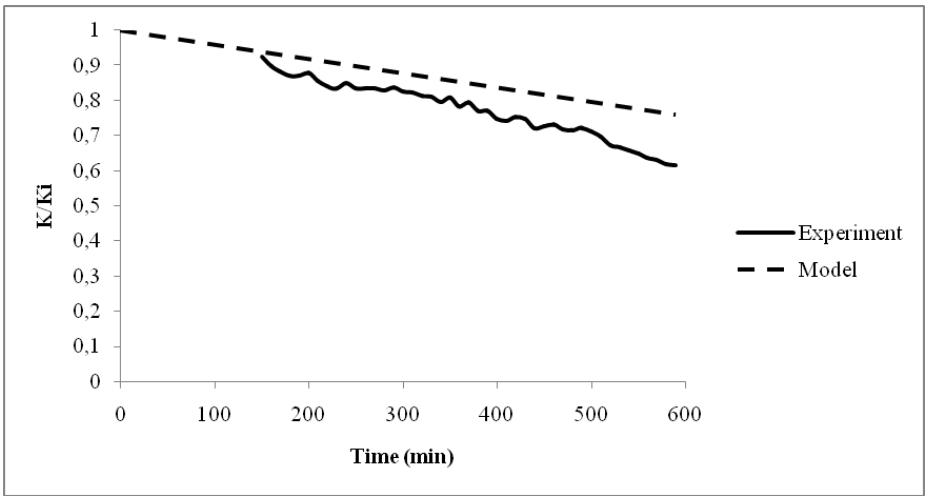

Figure 7. Permeability reduction due to asphaltene precipitation.

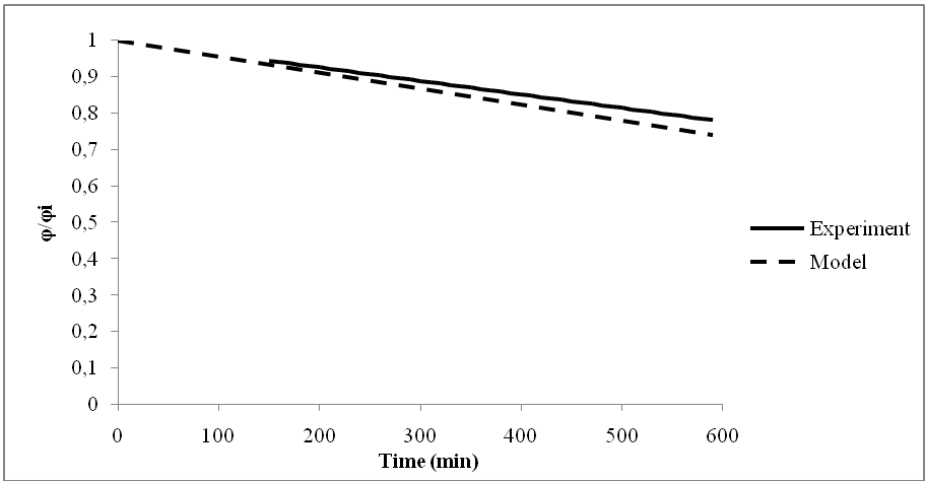

Figure 8. Porosity reduction due to asphaltene precipitation.

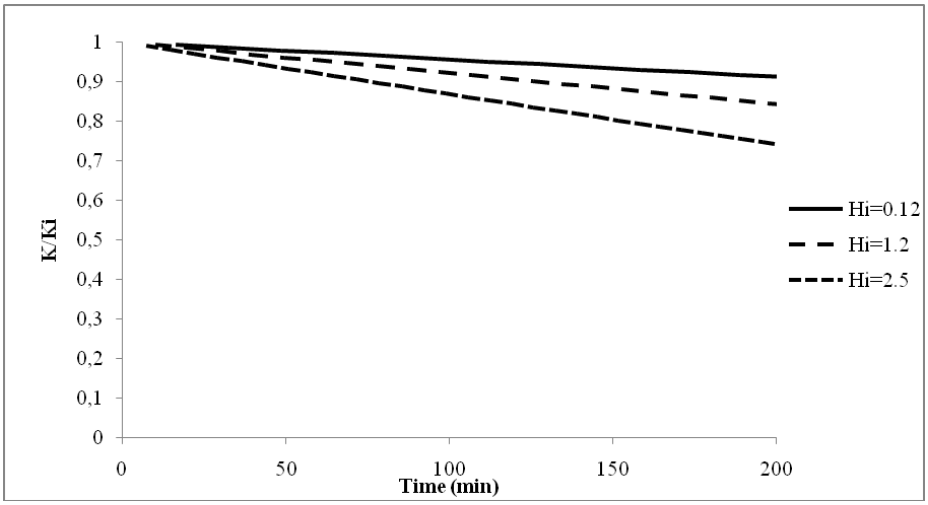

Figure 9. Effect of heterogeneity on permeability reduction.

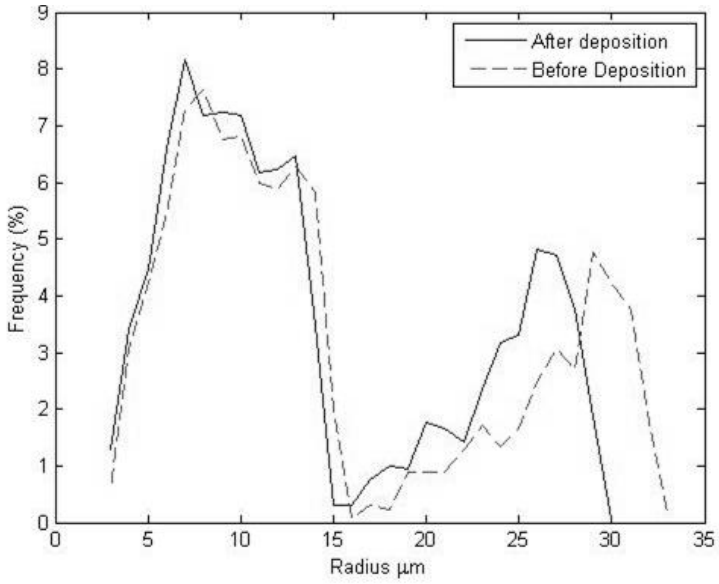

Figure 10. Pore size distribution change due to asphaltene precipitation.

6. Conclusions

In this work, asphaltene precipitation in granular porous media was simulated in pore scale using a network modeling method. The numerical results of pore-scale network modeling for the permeability reduction versus time were developed for the evolution of the permeability of a slim tube during precipitation of asphaltene. The main outcomes of this study can be expressed as below.

- ✓ For enough long slim tubes, the model can be simplified to the form which fits well with the laboratory experiments. The proposed models describe the permeability change with no need to know the changes of porosity.
- ✓ The developed model was coded on the computer. The developed model can simulate the porous medium under the experimental condition to investigate decreasing the permeability. It shows a good correlative agreement with experimental data which indicates the quality of the model.
- ✓ In addition, the change in the distribution of pore size resulting from asphaltene deposition can be calculated.

References

[1] Manshad AK, Edalat M. Application of continuous polydisperse molecular thermodynamics for modeling asphaltene precipitation in crude oil systems. Energy & Fuels, 2008; 22(4): 2678-2686.

[2] Monteagudo JE, Lage PL, Rajagopal K. Towards a polydisperse molecular thermodynamic model for asphaltene precipitation in live-oil. Fluid Phase Equilibria, 2001; 187: 443-471.

[3] Dullien FA. New network permeability model of porous media, AIChE Journal, 1975; 21(2): 299-307.

[4] Chatzis I, Dullien FA. Modelling Pore Structure By 2-D And 3-D Networks with Application To Sandstones, Journal of Canadian Petroleum Technology, 1977; 16(1).

[5] Fenwick D, Blunt M. Use of network modeling to predict saturation paths, relative permeabilities and oil recovery for three phase flow in porous media. in: SPE Annual Technical Conference, 1997, pp. 383-396.

[6] Leontaritis K, SPE Formation Damage Control Conference, Lafayette, Louisiana, (1998).

[7] Blunt MJ, Jackson MD, Piri M, Valvatne PH. Detailed physics, predictive capabilities and macroscopic consequences for pore-network models of multiphase flow, Advances in Water Resources, 2002;25: 1069-1089.

[8] Wojtanowicz A, Krilov Z, Langlinais J. Study on the effect of pore blocking mechanisms on formation damage. in: SPE Production Operations Symposium, Society of Petroleum Engineers, 1987.

[9] Wojtanowicz A, Krilov Z, Langlinais J. Experimental determination of formation damage pore blocking mechanisms, Journal of energy resources technology, 1988; 110(1): 34-42.

[10] Amaerule JO, Kersey DG, Norman DK, Shannon PM. Advances in formation damage assessment and control strategies, in: Annual Technical Meeting, Petroleum Society of Canada, 1988.

[11] Minssieux L. Core damage from crude asphaltene deposition. in: International Symposium on Oilfield Chemistry, Society of Petroleum Engineers, 1997.

[12] Acevedo S, Ranaudo MA, Escobar G, Gutiérrez L, Ortega P. Adsorption of asphaltenes and resins on organic and inorganic substrates and their correlation with precipitation problems in production well tubing. Fuel, 1995; 74(4): 595-598.

[13] Civan F. A multi-phase mud filtrate invasion, and wellbore filter cake formation model, in: International Petroleum Conference and Exhibition of Mexico, Society of Petroleum Engineers, 1994.

[14] Civan F. Modeling, and simulation of formation damage by organic deposition. in: First international symposium in colloid chemistry in oil production: Asphaltenes and wax deposition, JSCOP, 1995; 26-29.

[15] Civan F. Mechanism of Clay Swelling from Reservoir Formation Damage-Fundamentals. Modeling, Assessment and Mitigation. (2000).

[16] Civan F, Knapp R. Effect of clay swelling and fines migration on formation permeability. in: SPE Production Operations Symposium, Society of Petroleum Engineers, 1987.

[17] Roque C, Chauveteau G, Renard M, Thibault G, Bouteca M, Rochon J. Mechanisms of formation damage by retention of particles suspended in injection water. in: SPE European Formation Damage Conference, Society of Petroleum Engineers, 1995.

[18] Blauch M, Weaver J, Parker M, Todd B, Glover M. New insights into proppant-pack damage due to infiltration of formation fines. in: SPE Annual Technical Conference and Exhibition, Society of Petroleum Engineers, 1999.
[19] Weibull W. Wide applicability. Journal of applied mechanics, 1951; 103: 293-297.
[20] Soltani Soulgani B, Rashtchian D, Tohidi B, Jamialahmadi M. Integrated modelling methods for Asphaltene deposition in wellstring. Journal of the Japan Petroleum Institute, 2009; 52: 322-331.
[21] Manshad AK, Manshad MK, Ashoori S. The application of an artificial neural network (ANN) and a genetic programming neural network (GPNN) for the modeling of experimental data of slim tube permeability reduction by asphaltene precipitation in Iranian crude oil reservoirs. Petroleum Science and Technology, 2012; 30: 2450-2459.
[22] Ashoori S, Manshad AK, Alizadeh N, Masoomi M, Tabatabaei S. Simulationand Experimental Investigation of the Permeability Reduction due to Asphaltene Deposition in Porous Media. Iranian Journal of Chemical Engineering, 2010; 7(3).
[23] Civan F. Reservoir Formation Damage-Fundamentals, Modeling, Assessment, and Migration, Gulf Pub, Co., 2000, Houston, TX, 742p.

To whom correspondence should be addressed: Prof. Amir H Mohammadi, Discipline of Chemical Engineering, School of Engineering, University of KwaZulu-Natal, Howard College Campus, Durban 4041, South Africa, E-mail: amir_h_mohammadi@yahoo.com and Dr. Abbas Khaksar Manshad, Department of Petroleum Engineering, Abadan Faculty of Petroleum Engineering, Petroleum University of Technology (PUT), Abadan, Iran, khaksar@pur.ac.ir

Petroleum and Coal

Article **Open Access**

THE POSSIBILITY OF REDUCING THE CARCINOGENICITY OF COAL TAR ELECTRODE PITCHES

Fedor F. Cheshko, Alexandr L. Borisenko, Alla Yu. Martynova, Vladimir M. Shmalko, Oleg I. Zelenskii

Ukrainian State Coal-Chemistry Institute, 61023, Kharkov, 7 Vesnina Str., Ukraine

Received March 13, 2018; Accepted April 27, 2018

Abstract

The technological value of the coal tar electrode pitch is largely determined by the high content of condensed polyaromatic compounds in its composition. An attempt to change the chemical composition of the coal tar electrode pitch in order to reduce the content of carcinogenic polyaromatical hydrocarbons (PAH) will bring it closer to oil binders that are significantly inferior in their technological properties, or inform them of the new properties that are not desirable from the consumer's point of view. Involving carcinogenic PAH in the process of chemical transformations the products of which are not determined by analytical methods as indicators of cancer risk, will not necessarily lead to a decrease in the carcinogenic risk of coal tar pitch as a physicochemical system.

Keywords: *coal tar pitch; carcinogenity; polyaromatical hydrocarbons; benz(a)pyrene.*

1. Introduction

As known, the coal-tar electrode pitches namely the product of coal tar processing, are used in the production of a wide range of conductive materials as well as structural elements. For example, these are anodes and anode masses for the production of aluminum, graphitized electrodes for the electrowelding of steel, materials for sliding contacts, *etc.* The main purpose of the pitch in such industries is to act as a binder for carbon fillers which are mainly electrode cokes based on the same coal tar pitch, as well as oil and shale tar. The indispensable processing stages, which are mixtures of filler and binder, are high, and in some cases–very-high-temperature processing (up to 1500-2500°C) [1]. As a result, a fairly uniform material with high carbon content, a low electrical resistivity, and a number of other specific properties are formed. When making electrodes, the pressed blank is subjected to preliminary heating, then the resulting porous solid body of the future product is impregnated with a special pitch for filling the pores, increasing the density and mechanical strength on further thermal and mechanical treatment.

The normative properties of electrode binders and impregnating pitches are determined by the requirements for qualitative parameters of the final electrode product and the features of the technology of its production at specific enterprises. The pitch, used as an electrode binder, should have optimal binding properties and cake well with carbonaceous fillers, firmly binding their grains and providing a high yield of the coke residue. The main requirements for impregnating electrode pitches are low viscosity at the impregnation temperature and the ability to penetrate into the pores of the impregnating material. In addition, impregnating pitches, as well as electrode binders, should create a strong adhesion contact with the surface of the work material, and while carbonizing, they should ensure the highest possible yield of the coke residue. To improve the technological properties of electrode binders (mainly) and impregnating materials, the initial pitches obtained directly at the rectification stage of the coal tar as a non-boiling residue are subjected to the subsequent treatment at temperatures from 250 to 400°C with the use of special technological methods intensifying the polyme-

rization and polycondensation reactions in the pitch melt. As such methods in different countries, different manufacturers produce thermooxidation with air oxygen, vacuum heat treatment, thermal soak under upacting pressure, modifying chemical-active additives, *etc.* [1-3].

Another property of the coal pitch that does not relate to specific technological indicators, but which is of great importance for the staff's health and life of manufacturing and processing enterprises, is carcinogenic activity. The biological index of carcinogenicity of various coal tar pitches (Aibolla index)[1] ranges from 20 to 45. It is massively higher than that of similar petroleum products. There are also numerous medical and statistical data that irrefutably prove the causal relationship of the systematic (professional) impact of the coal tar pitches and resins with the contraction of an oncology disease of a number of human organs [4-7].

The carcinogenicity of the coal tar materials that is resins and derived from them is related to the presence of polycyclic aromatic hydrocarbons (PAH) in their composition. However, not all representatives of this class of substances are equally oncologically dangerous.

There is no consensus on the carcinogenic hazards of the various components of the coal tar pitches. Few of them are produced in pure form on a scale that is sufficient for representative statistical generalizations concerning the oncological impact on production personnel. At the same time, it is well known that the same substances with respect to different biological organisms can exhibit different carcinogenic activity – from very strong to zero. Although nowadays the lines of laboratory animals that are genetically close to a person have been produced, it is undoubtedly impossible to achieve a one hundred percent identity. This is the reason for some discrepancies in the literary sources regarding the classification of substances that are cancerous for people.

Thus, according to the authors [8-9], among the high-molecular PAH, the most dangerous one is benzo(a)pyrene (BaP, $C_{20}H_{12}$, five conjugated rings in the molecule). In addition to BaP, a number of PAH are also classified as carcinogens. Among them, benz(a)anthracene, benzo(b)fluoranthene, benzo(k)fluoranthene, chrysene, dibenz(a,h)anthracene and indeno (1,2,3-cd)pyrene. PAH, known for its carcinogenic and mutagenic properties, also includes benz(j)fluoranthene, benz(ghi)perylene, coronene, ovalene, *etc.*

Currently, more than 500 carcinogenic PAH have been identified. Since it is not feasible to carry out individual sanitary monitoring of the content of such substances quantities in different environments, for this purpose various national and international environmental organizations identify a number of priority groups.

For example, 16 PAH, including BAP, is designated by the US Environmental Protection Agency to represent the results of test measurements; 4 PAH-BaP, benz(c)fluoranthene, benz(k)fluoranthene, indeno(123-cd)pyrene are used as indicators for emission inventories under UNECE Protocol[2]. In order to analyze the carcinogenicity of the exhaust gases of internal combustion engines, a priority group has been singled out. This group includes BaP and 11 PAH: benz(v)fluoranthene, benz(a)anthracene, chrysene, benz(g,h,i)perylene, fluoranthene, pyrene, benz(e)pyrene, perylene, indenoprene, diben(a,h)anthracene and coronene [10].

It should be noted that the level of BaP content (which is included in all the above and many other categories) has been used for a long time as a universal indicator of the carcinogenicity of the material. Thus, according to the Document of EC Commission No. 208/2005 / EEC[3], the content of benzo (a) pyrene can be used as an indicator of the presence and danger of carcinogenic polycyclic aromatic hydrocarbons, even in food products.

[1] The index of carcinogenicity (Aibolla) Ikants is determined by the results of biological tests on living organisms. Ikants = (A / L) × 100; where A is the number (%) of the test specimens in which malignant tumors were detected as a result of the tests; L - duration (days) of the latent period [4].

[2] The Protocol on Persistent Organic Pollutants to the 1979 Convention on Long-range Transboundary Air Pollution of the United Nations Economic Commission for Europe.

[3] COMMISSION REGULATION (EC) No 208/2005 of 4 February 2005 No 466/2001 as regards polycyclic aromatic hydrocarbons.

Thus, the BaP to the present time is a kind of indicator of the presence in materials, atmospheric emissions, sewage and other media of carcinogenic PAH.

2. Experimental

Below (Tables 1-3) we give the obtained data on the content in the various coal tar peaks of the BaP (1995, Table 1), as well as carcinogenic PAH (2016, Tables 2, 3).

Table 1. The content of BaP in various coal tar pitches of industrial origin (1995)

Indicators	Initial pitches			Medium temperature pitches			High temperature pitches	
	1	2	3	4	5	6	7	8
Softening point according to K&S, %	50.5	56.0	60.0	67.5	68.0	86.5	149.0	250.0
The content of the BaP, %	1.60	2.25	2.30	2.15	1.48	2.10	1.83	1.52

The results obtained by us are well correlated with the literature data of the corresponding periods, for example, Table. 1 – with the data of the works [7, 11], and the data of Table 2 – with the data [12].

Table 2. The content of priority PAH, %, in industrial samples of the coal tar electrode pitch (2016)

Component name	Electrode pitches						High temperature pitches		
	Model number								
	1	2	3	4	5	6	1	2	3
Naphthalene	0.05	0.227	0.493	0.256	n.a.	0.229	1.509	0.099	0.147
2- Methylnaphthalene	0.03	0.065	0.121	0.072	n.a.	0.006	0.400	0.002	0.036
2,3 Dimethylnaphthalene	n.a.	0.026	0.029	0.025	n.a.	0.005	0.054	0.008	0.018
Ascenaphthylene	n.a.	0.004	0.008	0.004	n.a.	0.002	0.026	0.001	0.002
Acenaphthene	0.27	0.335	0.544	0.336	0.12	0.032	0.809	0.010	0.180
Fluorene	0.13	0.191	0.349	0.211	0.03	0.066	0.572	0.057	0.136
Fenatren	1.17	1.025	1.750	1.078	0.63	1.562	1.676	0.076	0.865
Anthracene	0.36	0.206	0.507	0.293	0.26	0.464	0.518	0.022	0.167
Fluoranthene	1.86	1.581	2.213	1.674	1.27	2.110	2.044	0.638	1.609
Pyrene	1.81	1.562	2.023	1.575	1.31	2.001	1.880	0.703	1.561
Benz (a) fluorene	0.50	0.495	0.424	0.419	0.35	0.444	0.409	0.280	0.524
Benz (b) fluorene	0.40	0.340	0.386	0.336	0.25	0.500	0.387	0.249	0.348
Benz (a) anthracene	1.18	0.886	1.191	1.073	0.74	1.175	1.194	0.738	0.919
Chrysene	1.42	1.177	1.305	1.192	1.32	1.325	1.170	1.063	1.274
Benz (b) fluoranthene	1.67	1.452	1.416	1.367	1.33	0.518	1.357	1.013	1.528
Benz (k) fluoranthene	0.73	0.501	0.526	0.501	0.71	1.334	0.508	0.296	0.497
Benz (e) pyrene	1.05	0.797	0.818	0.791	0.86	0.757	0.757	0.697	0.800
Benz (a) pyrene	**1.62**	**1.001**	**1.166**	**1.114**	**1.30**	**1.146**	**1.122**	**0.976**	**1.019**
Perilen	0.81	0.360	0.388	0.365	0.70	0.375	0.377	0.323	0.371
Indeno (1,2,3-c, d) pyrene	1.93	0.512	0.495	0.505	1.47	0.217	0.445	0.207	0.496
Dibenz (a, h) anthracene	0.47	0.264	0.260	0.271	0.23	0.920	0.231	0.816	0.260
Benz (g.h.i) perylene	1.75	0.727	0.572	0.728	1.27	0.763	0.487	0.659	0.698

n.a.-not available

A certain decrease in the content of the electrode coal tar pitches of BaP, noted over the past twenty years, is probably due to the general trends in the change of the raw material base and technological equipment for coking coal. Thus, a decrease in the content of coal gas in coal batches and the increase in the share of heavy-duty furnaces (including new ones or those that have undergone rearrangement) in the total volume of coke production led to a decrease in the degree of pyrolysis of the coal tar.

Nevertheless, despite the marked tendency, the level of carcinogenic activity of the pitches produced from the coal tar continues to be very high. This forces producers and consumers of raw materials for electrode products to look for the alternative types of binding and impregnating materials. However, the main driving force of such searches is the ratio of production and consumption of the coal tar pitches in the world.

Thus, the authors of the work [13] noted that in the pre-crisis period in most regions of the world, the production of coal-bearing electrode pitches was significantly lower than the demand. The greatest deficit was observed in the countries with a developed aluminum industry, which is the dominant consumer of coal tar pitches. The production of this kind of electrode raw materials is limited by the level of coke production.

It can be concluded that the tendencies of the world markets for pitch, aluminum, and metallurgical coke promise, at least in the near and medium term, the preservation of the deficit of electrode pitches. One way of making good this deficit can be the production of electrode binding and impregnating materials on an alternative basis. Taking into account the number of resources, the development consumption of such raw materials in related sectors (manufacture of electrode fillers, carbon fibers, carbon black, *etc.*), as well as the relative proximity to the coal tar according to the physico-chemical properties,oil stock attracts the most attention in this regard.

A petroleum pitch is produced from heavy oil residues, pyrolysis resins, cracked residues, *etc.* [14]. The use of such raw materials has also ecological and sanitary reasons: as it has already mentioned above, oil pitches are characterized by a much lower content of carcinogenic substances. In particular, the concentration of benzo(a)pyrene, according to the results of the studies, is 0.04-0.15 % in the pitches from cracked residues, and 0.3-0.8 % in pyrolytic pitches [14, 15].

However, the differences in the chemical composition of coal and petroleum pitches are an advantage of the latter only from the point of view of the relative ecological safety. In terms of technological properties, the situation is the opposite. At the same softening temperature, the coal tar pitches are characterized by a much higher content of high molecular components (substances which are insoluble in toluene, TI) than petroleum. For example, for vacuum-distilled cracked pitches, the content of such components is 5-16 times lower than in the coal tar pitch with a similar softening point value. Specifically, because petroleum pitches contain less polycondensed aromatic compounds, they have a lower C/H ratio and, consequently, a much lower yield of the coke residue compared to coal analogues. For even a partial leveling of these negative differences, it is necessary to increase the softening point of the petroleum pitches. However, this leads to an increase in viscosity and a decrease in the wetting power with respect to the filler [14-17].

There are known efforts to improve the properties of oil pitches by adding dust of petroleum coke, soot, and other high-carbon components in them [15, 18]. However, the increase in the coke residue due to only solid disperse additives without the presence of intermediate fusible carbonaceous components in the pitch can not contribute to the improvement of the entire complex of properties of the electrode material, both binding and impregnating ones.

For these above mentioned technological drawbacks, at present oil pitches find an extremely limited industrial application in the USA and Canada (about 10-12 % of the total amount of pitch used), traditionally experiencing a critical deficit of coal electrode binders. At the same time, it is proved that the oil pitch, due to the high yield of volatile substances, the low content of coke-forming components, the increased softening temperature, and high viscosity, is not able to replace coal analogues adequately. Therefore, it is considered expedient to use a petroleum pitch only in a mixture with coal tar. The approximate composition of such a compound is 15 % oil and 85 % the coal tar pitch [14, 19].

All the above mentioned information prompted and encourages various researchers to find the ways to reduce the carcinogenic activity of the coal tar pitch. The most common in this regard are the attempts to reduce the content of carcinogenic PAH, and most notably BaP through the chemical pitch treatment.

For example, it is known, that during the heat treatment of the initial pitch, which is necessary to impart the required technological properties, the addition of various chemically active additives can contribute to both intensification and inhibition of the processes that lead to the formation of additional quantities of BaP; it is also possible to achieve a significant reduction in its concentration in the processed pitch melting in comparison with the raw

material. Table 3 shows the conditions and results of our research in this field. The original pitch was subjected to the treatment with the following parameters: softening point – 50.5 °C; the mass fraction of substances that are insoluble in toluene – 25.4 %; the mass fraction of substances that are insoluble in quinoline – 8.8 %; the content of the BaP – 1.6 %. The heat treatment was carried out in a laboratory cube-reactor until electrode pitches with similar softening temperatures were obtained.

Table 3. The conditions and results of heat treatment of the pitch including chemically active additives

Processing parameters and pitch quality indicators	Additive		
	Benzoyl peroxide	Sulfanilic acid	
Experiment Number	1	2	3
The content of the additive,% of the mass of pitch loading	1	5	5
Liquid phase temperature, °C	330	290	330
Steam phase temperature, °C	300	250	300
Pitch quality indicators			
Softening point accordint to K&S, %	91	90	92
Mass fraction of substances insoluble in quinoline (QI), %	18.9	9.3	16.2
Mass fraction of substances insoluble in toluene (TI), %	37.0	41.9	42.1
Mass fraction of substances insoluble in toluene, but soluble in quinoline (β-resins), %	18.1	32.6	25.9
Mass fraction of substances soluble in toluene (TS), %	63.0	58.1	57.9
Volatile matter yield at 850 °C, %	53.9	52.0	52.7
The content of BaP, %	2.55	0.44	2.50

3. Result and discussion

According to the results of our earlier studies [20], benzoyl peroxide ($H_2N–C_6H_4–SO_3H$) under experiment No. 1, and sulfanilic acid ($(C_6H_5CO_2)_2$) under experiment No. 3 intensify the course of the radical polymerization processes, which, judging from the data in Table 3, lead to a significant (more than one and a half times) increase of the content BaP in the pitch. In contrast, sulfanilic acid under the conditions of experiment No. 2 intensifies the course of the reactions of increasing the molecular weight by the ionic mechanism, in which, apparently, BaP is not a product but a reagent, that leads to a decrease in its concentration in the final pitch 3.6 times compared with the initial one. In this case, the initiation of the primary course of ionic polymerization during the heat treatment of the initial pitch does not lead to a deterioration in the technological properties of the electrode pitch (see Table 3). If the BaP content was indeed a sufficient indicator of carcinogenic activity, the problem could be considered solved.

The same applies to another method of decreasing the carcinogenicity of coal tar pitch, which has been attracting researchers' attention for a long time [7, 12] – to the oxidation of coal raw materials.

Thus, according to the author of the paper [21], thermal oxidation with oxygen, ozone, and other oxidizing agents is an effective way to reduce the carcinogenic activity of coal tar pitches. For example, the low-temperature (up to 300 °C) thermal oxidation of the raw feedstock (especially the air with an additive 0.3-1.6 % ozone) makes it possible to reduce the content BaP in the electrode coal tar pitch to a level of 0.2-0.3 %, which is 10-15 times lower than in the ordinary industrial samples. It is commensurate with the content of BaP in petroleum pitches. A similar result was obtained by other investigators [22] during the thermal oxidation of a low-temperature pitch with the air at 265 °C for 1.5-2.0 hours. BaP level in such a pitch was 0.24 %. Similarly, the analysis of industrial samples of coal tar pitches [23] showed that

vacuum-distilled pitch contains 1.5 times more carcinogenic PAH than those obtained under the thermal oxidation with air oxygen.

From the point of view of the technological (consumer) properties of the thermooxidized pitches, it is appropriate to recall that the thermooxidative treatment of coal tar initial pitches did not become widespread due to a rather narrow range of raw material quality indicators (coal tar, initial pitch), suitable for obtaining high quality electrode binders for this technology [3]. In addition, according to the available data, some consumers put forward a requirement that the pitch cannot be oxidized by oxygen (including the air) during heat treatment. The most common opinion is that oxidation worsens graphitization because, during oxidation, strong cross-links are formed between the condensed layers in the form of oxygen bridges. In this connection, it is believed that the presence of more than 7 % oxygen in the feed leads to complete suppression of the mesophase processes and to the production of non-graphitized coke [3, 24]. However, the very fact of a decrease in the concentration of BaP and other specific carcinogenic PAH in the pitch as a result of chemical (especially oxidative) treatment is by no means evidence of a decrease in the overall oncological danger of the pitch as a physicochemical system.

PAH and their derivatives (except for epoxides), like some other chemical compounds (for example, aromatic amines), refer to genotoxic carcinogens of indirect action. Such substances are not carcinogenic in the original form, but, having relatively low reactivity, accumulate in the body, where in the process of metabolism they undergo enzymatic activation with the formation of highly active electrophilic metabolites. The latter interacts with nucleophilic DNA groups, causing malignancy[4] of cells [25-26].

It is especially important to note that the main way to activate the carcinogenic activity of a number of substances is enzymatic oxidation. For example, chloroethylene oxide proved to be a carcinogenic metabolite of vinyl chloride. In this case, for each carcinogen, there may be, apparently, not one, but several ways of metabolic activation [27].

Thus, if as a result of any (especially oxidative) effect on the pitch, analytical studies show a decrease in the content of specific PAH recognized as indicators of carcinogenic activity, this does not mean a reduction in the oncological danger of the pitch. As an illustration of this, Table 4 shows the data on the content of BAP and Aiboll index obtained for electrode pitches subjected to various special processing techniques [3, 7, 22]. Among the agents of such processing in the literature very exotic ones, for example, γ-irradiation can come across.

Table 4. The study results of carcinogenic activity of modified pitches

Pitch Name	Softening point accordint to K&S, %	Mass fraction of BaP, %	Aiboll index
Industrial, initial	69,4	1,1	44,2
Industrial, electrode, grade B	86,0	2,1	39,5
No. 1, subjected to γ-irradiation	71,0	0,7	33,1
No. 2, thermoaired with ozone	73,0	1,2	39,3
No. 2, reated with gaseous chlorine	84,3	0,8	9,5

As can be seen from the data presented, even a significant decrease in BaP content is accompanied only by a slight improvement in the biological index of Aibolla. With the thermal aeration of the pitch (i.e., when it is oxidized by ozone), the biological index does not change at all, although the mass fraction of BaP decreases by almost half.

The only exception is the chlorinated pitch. However, both the technology of processing coal tar pitch with gaseous chlorine and the use of a chlorinated binder in the electrode production, do not appear to be technological.

[4] Malignization (from Latin malignus) - the acquisition by cells of normal or pathologically altered tissue of the body (including benign tumors) of the properties of a malignant tumor.

The same can be said about a decrease in the carcinogenicity of the pitch by its sulfonation. According to the data of the work [13], such a pitch contains no BaP and has Aiboll index equal to zero. At the same time, according to the data of the work [7], sulfonation gives the coal pitch very uncharacteristic properties for it, for example, water solubility.

4. Conclusion

Thus, from the above mentioned, we can draw the following conclusions:

1. The technological value of the coal tar electrode pitch is largely determined by the high content of condensed polyaromatic compounds in its composition.
2. An attempt to change the chemical composition of the coal tar electrode pitch in order to reduce the content of carcinogenic PAH will bring it closer to oil binders that are significantly inferior in their technological properties, or inform them of the new properties that are not desirable from the consumer's point of view.
3. Involving carcinogenic PAH in the process of chemical transformations, whose products are not determined by analytical methods as indicators of cancer risk, will not necessarily lead to a decrease in the carcinogenic risk of coal tar pitch as a physicochemical system.
4. Efforts to reduce the carcinogenic hazards of coal tar pitches should be focused on improving the production technology and application of these materials in order to minimize their contacts on personnel.

References

[1] Pityulin IN. Scientific and technological foundations of production of coal tar carbon-containing materials for large electrodes; Monograph; Contrast: Kharkov, 2004; p. 480.
[2] Privalov VE, Stepanenko MA. Coal tar pitch: production, processing, application; Metallurgy: Moscow, 1981; p. 208.
[3] Kleshnya GG, Cheshko FF, Pityulin IN. Problems of modern domestic production of electrode coal tar pitch. J. Coal Chem. 2006; 5-6: 63-67.
[4] Zuss R, Kintsel V, Skribner D. Cancer: experiments and hypotheses; Mir: Moscow, 1977; p. 360.
[5] Yanyisheva NYa, Kireeva IS. Protection of the environment from carcinogens at ferrous metallurgy enterprises; Znanie: Kiev, 1988, p. 16.
[6] Yanyisheva NYa, Chernichenko IA, Balenko NB. On methodological issues of rationing the chemical carcinogenic substances in the environment. Hygiene and sanitation. 2003; 1: 54-57.
[7] Mochalov VV. Theoretical foundations and technology of production of new carbon-containing materials on the basis of coal tar pitches and high-boiling fractions of coal tar: a thesis for the degree of Doctor in technical science, UKHIN: Kharkov, 1984; p. 435.
[8] Toxicological Profile for Polycyclic Aromatic Hydrocarbons / U.S. Department of Health and Human Services, August 1995; Electronic resource: https://www.atsdr.cdc.gov/toxprofiles/tp69.pdf.
[9] The Carcinogenic Effects of Polycyclic Aromatic Hydrocarbons; Under the editorship of Andreas Luch; Imperial College Press: London, 2005; p. 489.
[10] Kanilo PM, Solovey VV, Kostenko KV. Problems of atmospheric pollution of cities with carcinogenic-mutagenic super toxicants. Bulletin of the Kharkov Automobile Road University. 2011; 52: 47-53.
[11] Gogoleva TYa, Shustikov VI. Chemistry and technology of coal tar processing; Metallurgy: Moscow, 1992; p. 256.
[12] Andreykov EI, Amosova IS, Pervova MG. Determining the content of polycyclic aromatic hydrocarbons in industrial samples of coal tar and pitch. Coke Chem. 2008; 8(51): 321-325.
[13] Sidorov OF, Seleznev AN. Prospects of production and improvement of consumer properties of coal tar electrode pithes. Russian Chemical Journal. 2006; 1(50): 16-24.
[14] Vershinina EP, Gildebrandt EM, Selina EA. Trends in the development of binder production for anodes of aluminum electrolyzers. Journal of Siberian Federal University: Engineering & Technologies. 2012; 5: 752-759.
[15] Ugapev AA, Kim IV, Doshlov IO, Lubinskiy MI, Sinshinov PA. Research, development of technology and production of a new composite binder - petroleum pitch HDPE. Polzunovsky almanac. 2010; 2: 314-316.

[16] Perez M, Granda M, Menendez R. Preparation of binder pitches by blending coal-tar and petroleum pitches. Light Metals. 2001; 573-579.
[17] Perez M, Granda M, Garcia R et al. Petroleum derivatives as an alternative to binder coal-tar pitches. Light Metals. 2000; 531-536.
[18] Lazarev VD, Mahalova NP, Tarasevich NI et al. Rus. Patent 2116383 RU, 1998.
[19] Hayrutdinov IR, Ahmetov MM, Telyashev EG. State and prospects of development of coke and pitch production from petroleum raw materials. Russian Chemical Journal. 2006; 1(50): 25-28.
[20] Cheshko FF, Shustikov VI. Catalytic effect on the group and chemical composition of coal tar pitch. Problems of catalysis in coal chemistry (Collection of scientific works); Naukova dumka: Kiev, 1992; p. 289.
[21] Sidorov OF. Carcinogenic activity of pithes depending on the technology of their production. Coke&Chemistry. 2006; 6: 36-40.
[22] Lebedev VA, Branin OB, Dyukanov AG. Reducing the content of benzpyrene in a coal tar binder. Coke&Chemistry. 1988; 8: 36-37.
[23] Anshits AG, Kurteeva LI, Dyukanov AG. Comparative assessment of the emission of carcinogenic substances using medium- and high-temperature pitches. Chemistry for sustainable development. 2001; 9: 345-352.
[24] Rubchevskii VN, Chernyshov YuA, Volokh VM, Kovalev ET, Pityulin IN. Exclusion of oxygen in electrode-pitch production. Coke Chem. 2009; 4(52): 161-167.
[25] Seyts IF, Knyazev PG. Molecular oncology; Medicine: Leningrad, 1986; p. 352.
[26] Belitskiy GA. Chemical carcinogenesis. Problems of Clinical Medicine. 2006; 1(5): 10-15.
[27] Napalkov NP. General Oncology; Medicine: Leningrad, 1989; p. 646.

To whom correspondence should be addressed. Dr. Fedor Cheshko, Ukrainian State Coal-Chemistry Institute (UKHIN), 61023, 7 Vesnina str., Kharkov, Ukraine, chishkof@ukr.net

Petroleum and Coal

Article **Open Access**

Experimental Study and Pore-Scale Numerical Modeling of Permeability Impairment Resulting From Asphaltene Precipitation in Porous Medium

Abbas Khaksar Manshad[1,5], Rouhollah Fatehi[2], Amir H. Mohammadi[3*], Jagar A. Ali[5], Siavash Ashoori[4], Rasoul Hassanalizadeh[3]*

[1] *Department of Petroleum Engineering, Abadan Faculty of Petroleum Engineering, Petroleum University of Technology (PUT), Abadan, Iran*
[2] *Department of Mechanical Engineering, School of Engineering, Persian Gulf University, Bushehr, Iran*
[3] *Discipline of Chemical Engineering, School of Engineering, University of KwaZulu-Natal, Howard College Campus, Durban 4041, South Africa*
[4] *Department of Petroleum Engineering, Ahwaz Faculty of Petroleum Engineering, Petroleum University of Technology (PUT), Ahwaz, Iran*
[5] *Department of Petroleum Engineering, Faculty of Engineering, Soran University, Kurdistan Region- Iraq*

Received February 7, 2018; Accepted April 23, 2018

Abstract

Asphaltene precipitation affects the formation by reducing the porosity and permeability. In this study the permeability reduction asphaltene precipitation in granular porous media has been modeled using pore-scale simulation. In this way, the pore-scale geometry of a granular porous medium is used, and governing equations are solved numerically by an improved version of weakly compressible Smoothed Particle Hydrodynamics (SPH). Based on the results of the pore-scale simulation, a model is proposed for the permeability change of a single cell (grain) in the porous media. In this model, there are two parameters; final to initial permeability and characteristics time of precipitation that are evaluated through pore-scale simulation. Then, the proposed model is averaged through an up-scaling process to lead to a macro-scale relation which independently of the changes in the porosity predicts the time evolution of the permeability reduction. Experimental procedure has been conducted in a synthetic porous medium made of the slim tube, which was filled with glassy beds. Different flood tests were carried out at different temperatures and injection rates to test the volume ratio of oil to solvent. A predictive model has been developed to assess the permeability reduction via asphaltene precipitation. The main assumption for the model is based on the theory of deep bed filtration and the relationship between damaged and initial permeability, which is a function of the porosity change with asphaltene deposition. The developed model simulates the permeability reduction in flooding tests using computer code. The model provides good fit from the experimental data, which is an indication of the reliability of the developed model.

Keywords: *Permeability Impairment; Asphaltene Precipitation; Porous Media; Smoothed particle Hydrodynamics; Model.*

1. Introduction

Asphaltene is a mixture of a set of hydrocarbon(s) that can precipitate at different reservoir conditions. After starting the precipitation, the fine particles aggregate. The mentioned process is reversible which allows the collected particles to dissociate and make the initial fine particles. Rock surface is capable of adsorbing and trapping the aggregates on their pores, which depends on the size of the porous media (plugging). Due to high local velocity known as shear, it can be returned into the oil phase. Effective mobility of hydrocarbon can be reduced with asphaltene by:

a) Reducing the permeability of the rock by blocking the pore throats,
b) Changing the formation wettability started with adsorption to rock surface, which diminishes the permeability and increases the oil saturation as it cannot be reduced again.
c) Forming an ionized solution (colloidal) in the oil phase, which increases the viscosity of the reservoir fluid.

Asphaltene precipitation reduces the porosity. Correlating the porosity reduction to the rock permeability declination can be considered using power law relationship. The power low relationship gives the ratio of the permeability K to the initial permeability K_{init} at time t, e.g., in the way used by Civan [1].

When asphaltene forms without water and under saturated oil, the permeability declination is the main mechanism of damage. The radius of damage depends on the draw down, and it occurs deep in the reservoir. There are plenty of developed models for the precipitation of the asphaltene in core tests. Civan [2-3] categorized flow channels of porous media into the groups of plugging and non-plugging trajectories. For the modelling, pore throat plugging of surface adsorption and dragging the precipitates are considered.

Ali and Islam [4] assumed the suspension of asphaltene in crude oil, which is ready to precipitate. Further factors of the model include entrainment of the deposits and surface adsorption. Wang *et.al.* [5-6] used ideal solution theory to simulate deposition process. Two factors to model the asphaltene deposition are plugging of the surface adsorption and entrainment.

In this study, a numerical model has been developed to predict a reduction of permeability due to asphaltene precipitation. To this end, pore scale geometry of a granular porous medium is used, and governing equations are solved numerically, which is Smoothed Particle Hydrodynamics (SPH). This method is not applying the Lagrangian mesh, which makes it a popular method of computational fluid dynamics (CFD) modelling approaches. It is easy to implement and flexible while handling large displacements and interfaces of complex fluids. Lucy [7] and Gingold and Monaghan [8] initially developed the SPH method in the same time for simulating astrophysical problems which was extended to many fields of fluid flows and solid mechanics [9].

In this work, an improved version of weakly compressible SPH was used as suggested in recent work of Fatehi and Manzari [10]. This improvement includes more consistent scheme for discretization of second derivatives in conjunction with a numerical filter for reduction of non-physical oscillations and a new method for implementation of wall boundary condition. Another novelty of this work is that in contrast with the common models in the literature the model proposed to predict the time evolution of the permeability inclination is independent of the changes in the porosity.

In the following, first, the phenomenon is studied in pore-scale. The computational domain governing equations and the numerical method are described, and the obtained results are presented. In the next section, based on the results of pore-scale simulation a model is proposed for the permeability change of a single cell (grain) in the porous media. Then, the proposed model is averaged through an up-scaling process to lead to a relation for the permeability reduction due to asphaltene precipitation in a slim tube.

2. Experiments of the slim tube

2.1. Material and equipment

Table 1 shows properties of the target crude oil which were taken from an oil field in the Southern part of Iran. It is heavy oil (relatively) which has a gravity index equal to 20° API with asphaltene content of 11 weight percent. The sample (crude oil) was kept at specific laboratory conditions (almost three months) to eliminate the volatile components and reach to a fixe composition for the equilibrium condition. In association with oil production, further, than oil, there are possible contaminations such as sand and clay. Hence, Whattman paper filter (number 42) was applied to eliminate the mentioned impurities. In our gravimetric experimental method, n-heptane was taken as the precipitant to measure the quantity of the deposited asphaltene.

Several experiments were conducted on the porous medium (the synthetic medium) at high temperature and pressure (reservoir condition) to study the asphaltene deposition phenomenon. Figure 1 shows the experimental apparatus. It consists of a slim tube submerged in an oil bath, vacuum and liquid pumps, a transparent capillary tube connected to a heating jacket, which helps to monitor the fluid flow, a pressure regulator for resulting oil, a container to collect the final oil, and connected pressure gauges.

Table 1. Composition and characteristics of the crude oil [13-15, 17]

Component	Mole %	Property	Value
H_2S	0.192	Reservoir Oil MW (g/gmol)	156.67
Nitrogen	0	Test temperature (F)	225
CO_2	2.204	MW C_{7+} (g/gmol)	316.49
Methane	26.945	SG C_{7+}	0.9272
Ethane	8.008	Density of reservoir fluid @ Pb (g/cc)	0.7646
Propane	6.426	Bubble point pressure (psia)	1890
i-Butane	1.134	Asphaltene content in stock tank oil, wt%	11
n-Butane	3.682		
i-Pentane	1.742		
n-Pentane	2.233		
Hexanes	4.202		
Heptanes+	43.212		

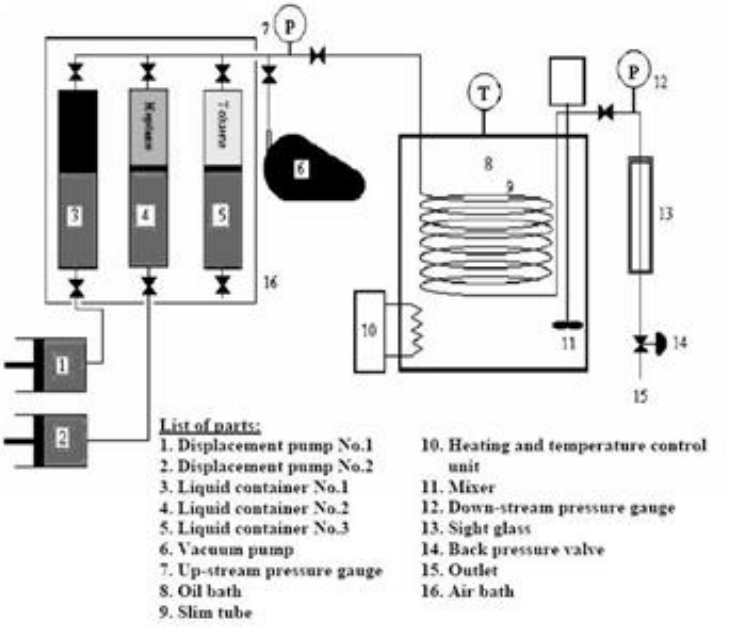

Figure 1. A schematic diagram of the experimental setup [14-16]

A Ruska tube was used to measure the quantity of the lost permeability resulting from asphaltene deposition in the porous medium. The tube is made of stainless steel tube coil with outside diameter and inside diameter of 7.9 and 6.2 mm, respectively with the length of 18.3 m. The tube is coiled (up to 20 cm of diameter). Small round glass beds of 150-170 micrometre are used to pack the slim column.

The porosity of the porous medium is almost 27 % with an approximate absolute permeability of 4.93×10^{-12} m^2 (5 Darcies). The total approximate volume of the available voids is 150 cm^3.

The isothermal oil bath can be heated up to 175°C using a heat insulated tank which is controlled thermostatically with an approximate volume of 60 liters. The circulating mixer and heating element are mounted by a duct which leads to the full circulation of the fluid inside the bath. It is equipped with a temperature controller with 1°C resolution. The tube is placed

vertically, and the inlet valve and outlet valve are located on top side of the temperature bath. To distribute the temperature evenly, the tube is submerged fully into the bath. The transparent high pressure tube is located at the end of the slim tube (downstream). The passing fluid can be either one phase or two-phase slug flow.

Two pressure gauges are connected to the tube with the aim to monitor the pressure of the upstream and downstream which is controlled using a backpressure regulator connected to the downstream side after flushing the resulting oil to the atmospheric condition.

There are two cylinder-pistons of 500 m^3 volume inside the pump with a variable flow rate of 1 to 1999 cm^3/hr. The accuracy of the pump is 0.0025 cm^3 using a calibrated ruler which can work up to 70 MPa and controlled by computer and manual as well.

2.2. Experimental technique

The two categories of the experimental technique are as follows:

2.2.1. Initial activities

The initial activities include:

a. To wash the slim Rusk tube
b. To dry the tube
c. To evacuate the tube
d. To fill the vessel of fluid transfer
e. To measure the pore volume
f. To study the system in terms of flow behavior
g. To measure the permeability
h. To calculate the porosity of packed bed using the equation of Carman-Kozeny.

2.2.2. Flooding experiments

The effect of injection rate, temperature, and solvent to oil ratio on permeability declination (resulted from asphaltene deposition) were studied by conduction several flooding experiments and considering the factor of time. The calculated Reynolds number for injection rate was less than unity, which leads to Darcy's low as a method to obtain the permeability.

Initial activities were conducted to find the operational condition of the flooding tests on the porous medium. The flood test procedure is as follows:

1. The filtered crude oil is filled to one of the vessels of fluid transfer and n-heptane to the other one.
2. The fluid transfer vessels are connected with a line to each other from top valves of the vessels using a T-junction between them.
3. Each vessels bottom is connected to a pump which is set to the flow rate that is desired and evacuated to eliminate the possible impurities such as air.
4. The porous medium is then connected to the T-injection outlet of the evacuated vessel.
5. Fluids are injected to mix the n-heptane with crude oil. The pump is activated at the same time that the porous medium's inlet valve is opened with recording the initial time.
6. Internal pressure to the porous medium is monitored and recorded every 2 minutes. The mixture of the n-heptane and crude oil passes through the porous medium. After filling the medium with the volume of one pore (150 cm^3) of the mixture, the entrance pressure starts to increase. The exit valve is opened to produce the mixture consequently. The inlet pressure drops and in a short time reaches a steady state condition. Increasing the pressure is the reason that shows asphaltene precipitates. After observing the product at the outlet valve, it is necessary to take a sample after every 10 minutes. Continues sampling process stops after injection of at least 4 times of pore volume to the tube. The highest allowed pressure to ovoid safety problems is 28 MPa.
7. The obtained samples are used to obtain the deposited asphaltene, which leaves the tube and remains in the taken samples.

Either the porous medium permeability versus time or injected fluid pore volume can be calculated using Darcy's law as well as the obtained data from the step 6. This experiment can show the effect of different factors on severity of the damage due to permeability reduction. Measured data at the 7th step shows the concentration of the deposited asphaltene with varying time. Table 2 reports the conditions for these experiments.

3. Pore-Scale simulation

To predict the behavior of the porous media in asphaltene precipitation process a pore scale model of a two-dimensional granular porous medium (as shown in Figure 2) is considered. It is constructed from similar circular cylinders all of diameter D which are infinitely placed in a regular inline arrangement. Here, the spacing in both transversal and longitudinal directions is equal S.

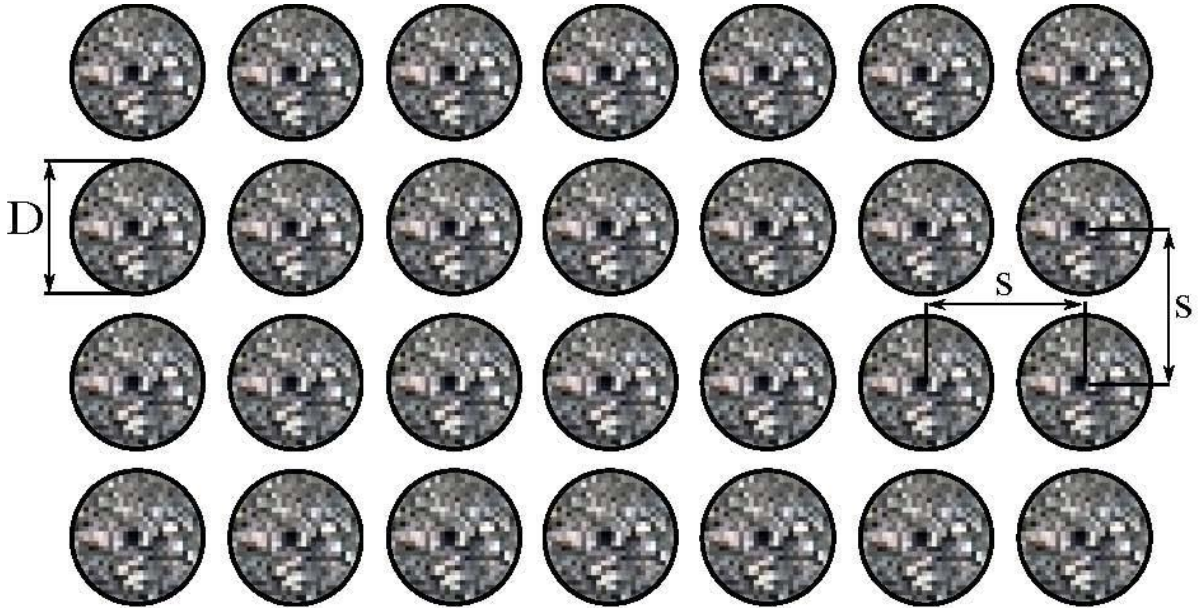

Figure 2. Schematic of the regular granular medium used here for pore-scale simulations

Initially, the medium is filled with an oil free from asphaltene particles at the time t=0 another heavy oil with precipitated asphaltene flocs of concentration C_i is injected from the right hand boundary. This causes the whole fluid in the medium to flow from right to left. As the asphaltene flocs approach to the low speed regions near the grains they merge and form deposits attached to the solid walls. This leads to two consequences; first, the cross section area of the fluid flow is reduced which means a reduction in porosity and permeability of the medium. The other consequent of asphaltene precipitation is that the fluid flows in the remaining area more rapidly providing the flow rate be constant. This increase in velocity prevents more asphaltene particles from settling. Precipitation of particles first occurs at the first grain, and then it promotes in the way of the flow to the next grains.

3.1. Governing equations

Here, mass and momentum conservations are applied. Since the numerical method (SPH) uses the Lagrangian approach, the conservation equations are written in the Lagrangian form. For the solution, mass conservation is

$$\frac{d\rho}{dt} = -\rho \nabla y \qquad (1)$$

In addition, momentum conservation assuming Newtonian fluid and incompressible flow leads to

$$\rho \frac{dv}{dt} = -\frac{1}{\rho}\nabla P + \mu\nabla^2 v + \rho g \quad (2)$$

Here, μ and ρ denote viscosity and density of the solution, respectively.

In addition, V and P are velocity vector and pressure, respectively. For the concentration of asphaltene flocs, one can write a transport equation like

$$\frac{dC}{dt} = D\nabla^2 C \quad (3)$$

where, C is a concentration of precipitated asphaltene flocs in mole/m^3 and D is diffusion coefficient.

Since asphaltene precipitates and forms into flocs; this diffusion cannot be Fickian or molecular diffusion. However, in practice, there is always diffusion effect due to the Brownian motion of particles and other possible effects.

3.2. Numerical method

To solve the governing equations based on numerical methods, as mentioned earlier, a Lagrangian method known as SPH is used. In this section, general discretization plans for the first spatial derivatives and second spatial derivatives of field values and boundary conditions adopted for this problem are introduced. More details of discretization and solution algorithm for a discrete form of governing equations (1) to (3) can be found in reference [10].

3.2.1. SPH formulation

The SPH method is based on the interpolation concept. For a random function of the field such as u, the value, which is interpolated (u) for the neighboring particles values uj, can be calculated using the following equation:

$$\left(u(r)\right) = \sum_j \omega_j u_j W(r - r_j, h) \quad (4)$$

where, ω_j denotes the volume or weight of particle j, r denotes the position vector, W denotes the kernel or smoothing function and h denotes the circular compact support radius.

Here, the quantic Wend land function [11] is used. For obtaining the first derivative's numerical approximation $(u)_i$ the following equation can be used [12]:

$$(\nabla u)_i = \sum_j \omega_j B_i . \nabla W_{ij}(u_j - u_i) \quad (5)$$

where, $W_{ij} = W(r_i - r_{j,h})$ is the value of smoothing or kernel function of particle i at the position of particle j. Also,

$$B_i = -\left[\omega_j r_{ij} \nabla W_{ij}\right]^{-1} \quad (6)$$

is a renormalization tensor in which $r_{ij} = r_i - r_j$ shows the distance of i and j particles. For the second derivative, a consistent scheme is used,

$$(\Delta . \nabla u)_i = \hat{B}_i : \sum_j 2\omega_j e_{ij} \nabla W_{ij} \left(\frac{u_i - u_j}{r_{ij}} - e_{ij} . \sum_j \omega_j (u_i - u_j) B_i \nabla W_{ij}\right) \quad (7)$$

where $r_{ij} = |r_{ij}|$ and $e_{ij} = \dot{r}_{ij}/r_{ij}$ is a unit vector in the direction of inter-particle.

It is noticeable that (u) is calculated as in Eq. (5) and B is a new renormalisation tensor for the second derivative calculated by

$$\hat{B}_i : \left[\sum_j \omega_j r_{ij} e_{ij} e_{ij} \nabla W_{ij} + \left(\sum_j \omega_j e_{ij} e_{ij} \nabla W_{ij}\right) . B_i \left(\sum_j \omega_j r_{ij} r_{ij} \nabla W_{ij}\right)\right] = -1 \quad (8)$$

3.2.2. Boundary conditions

Since the domain is geometrically periodic and the Reynolds' number of the flow is very small, the modified pressure and velocity $\tilde{P} = P + \rho g x$ of the domain can be treated using some finite number of solid grains with periodic boundary conditions on all outer boundaries. Figure 3 shows a sample of the computational domain. In this figure, also the initial arrangement of SPH particles can be seen. Here, dark dots are fluid particles and lights are solid particles, which represent the wall boundaries of grains.

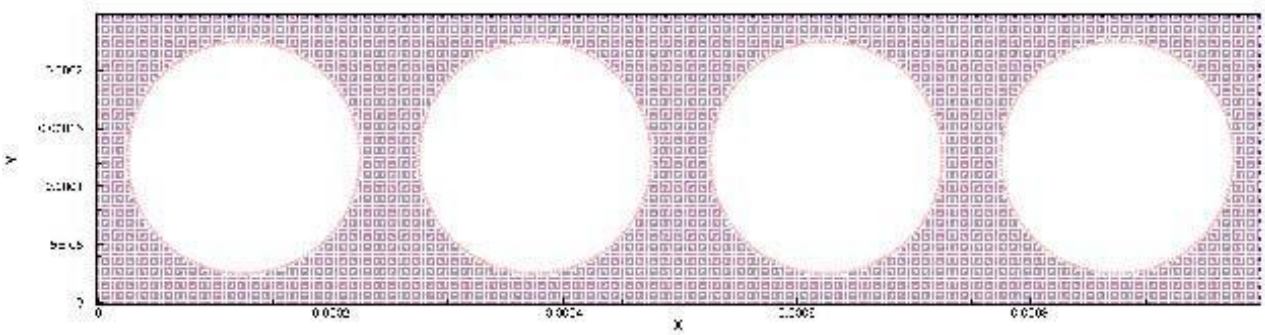

Figure 3. A Sample of computational domain with initial arrangement of SPH particles. All outer boundaries (solid lines) are treated as periodic boundary conditions in mass and momentum equations

Each SPH particle exiting the right-hand boundary enters at the corresponding point from the left boundary with the same properties including velocity and modified pressure. However, this condition cannot be applied for the concentration of asphaltene flocs C. The entering SPH particles from the left boundary necessarily bring the particular amount of asphaltene flocs C_{in} that is defined using the thermodynamic properties of the injected heavy oil.

3.2.3. Wall boundaries and precipitation

In the momentum equation (2), the surfaces of grains are treated as a no-slip condition. Since the velocity of the fluid particles is similar to the wall, consequently their acceleration is equal to zero. Then we have:

$$\frac{\nabla P}{\rho}.n = g.n \qquad (9)$$

where *n* denotes the unit vector.

The unit vector is normal to the wall, which is obtained by summing the kernel gradients. It can be shown as follow:

$$n_i = \frac{\sum_j \omega_j \nabla W_{ij}}{|\sum_j \omega_j \nabla W_{ij}|} \qquad (10)$$

Hence, assuming the location of particle *i* on the wall, one can conclude that its velocity is apparent (that would be zero for the fixed wall) and the pressure for the next step (P_i^{n+1}) can be found from,

$$P_i^{n+1} = \frac{\left(\sum_j \omega_j \frac{P_i^{n+1}}{\overline{\rho_{ij}}} B.\nabla W_{ij}\right).n_i - g.n_i}{\left(\sum_j \omega_j \frac{1}{\overline{\rho_{ij}}} B.\nabla W_{ij}\right).n_i} \qquad (11)$$

here *j* denotes all particles in the neighboring of particle *i*, which includes the particles on the wall.

Thus, calculation of the new time-step pressure P^{n+1} needs a limited number of iteration (i.e., 3 iterations) with wall particles [10]. When an asphaltene floc approaches the walls of the grains, it may settle down depending on its velocity and concentration of asphaltene near the wall. Here, precipitation of asphaltene floc in the porous medium is simulated using some rules. An SPH particle deposes on the wall provided that:

- Its asphaltene concentration C is higher than a critical value C_{cr};
- The distance to the nearest particle on a wall or a deposed SPH particle is less than h;
- Its velocity magnitude V is less than a critical value V_{cr}.

After a particle was deposited, its velocity is set to zero, and the viscosity is enlarged by ten times to better simulate the properties of the deposits.

4. Numerical results

The aforementioned problem was solved numerically using the SPH method described in the previous section. Physical properties and numerical parameters of the problem are summarized in table 3 where Courant number is defined as $C_r = c\Delta x/\Delta t$ in which Δx and Δt are

initial spacing between SPH particles and time-step size, respectively. In this case, using $\Delta x = 4.17 \times 10^{-6}$ m leads to approximately 7700 SPH particles. The initial arrangement of particles is illustrated in Figure 3. The kernel function for smoothing radius (h) is selected as 2.5 Δx in this simulation, which for each particle; it is equivalent to approximately 20 neighbors.

Table 3. Physical properties and numerical parameters of the simulated problem

Parameter	Symbol	Value	Unit
Diameter of grains	D	$2.0*10^{-4}$	m
Grains spacing	S	$2.5*10^{-4}$	m
Fluid's density	ρ	10^{-3}	kg/m^3
Fluid's viscosity	μ	10^{-3}	Pa.s
Diffusion coefficient	Đ	10^{-7}	mm^2/s
Body force acceleration	G	10^{-2}	m/s^2
Critical velocity	V_σ	$2.0*10^{-4}$	m/s
Artificial speed of sound	C	0.2	m/s
Courant number	Cr	0.3	-

The obtained results of asphaltene flocs concentration are shown in Figure 4. In this figure, the contour plot of the fraction of asphaltene flocs concentration C to the inlet value C_{in} is illustrated for six different times after injection. In early times, two channels are formed up and down the grain, and the fluid preferred to flow thorough these channels. Thus, the domain can be divided into high-speed regions, i.e., these channels and low-speed regions which include the spaces between the grains in the middle of the domain horizontally. In high-speed regions, the dominant effect is advection while in the latter diffusion effect is more significant.

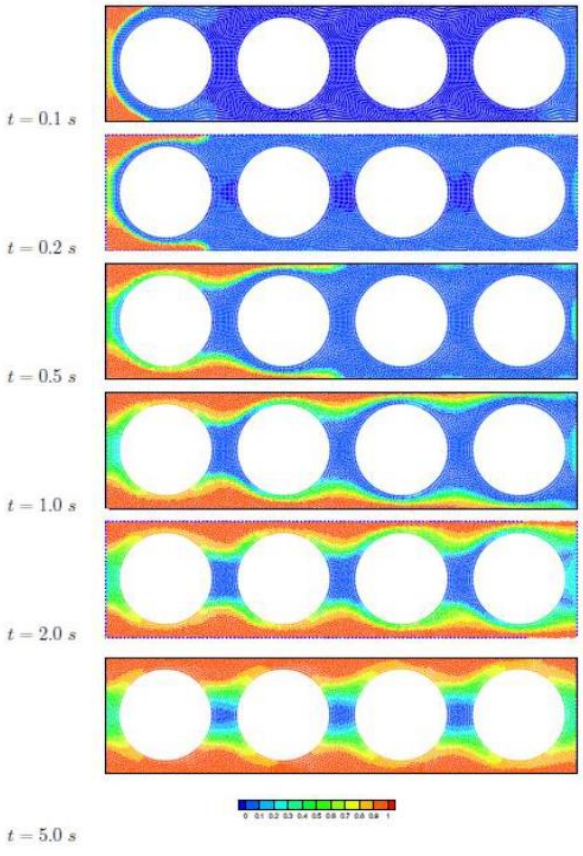

Figure 4. The results of normalized concentration of asphaltene for different times

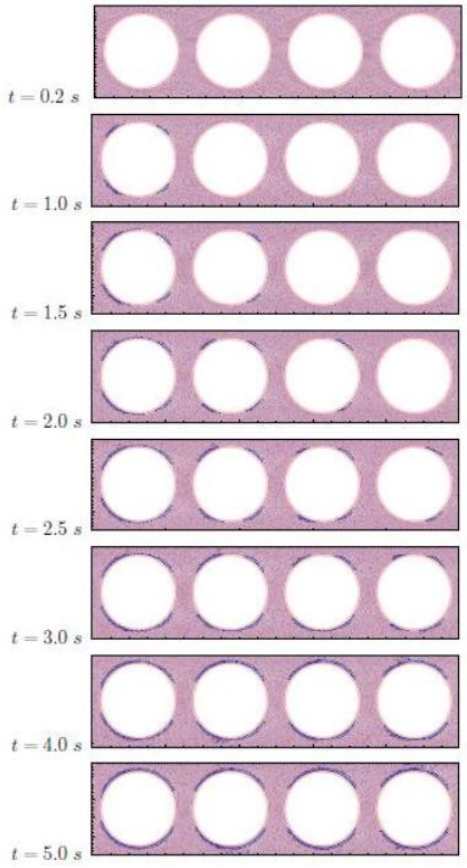

Figure 5. The results of asphaltene flocs precipitation during time. (Dark particles represent asphaltene deposits.)

In early times, two channels are formed up and down the grain, and the fluid preferred to flow thorough these channels. Thus, the domain can be divided into high-speed regions, i.e., these channels and low-speed regions which include the spaces between the grains in the middle of the domain horizontally. In high-speed regions, the dominant effect is advection while in the latter diffusion effect is more significant.

At t =1.0 s the front of injected fluid reaches the outlet boundary, and after that, the diffusion effect extends the influenced region to the whole domain slowly.

The particles near the walls have a chance to be deposited because of their low velocity if their concentration were higher than the critical value C_{cr}. In this simulation, C_{cr} was selected as 0.5 C_{in}. Figure 5 indicates the amount of deposited SPH particles in the numerical results by dark dots. In this figure, it can be seen that after a certain time asphaltene flocs concentration of the particles near the wall of the first grain reaches the critical value C_{cr} and they settle down. For more clarity, the above results are also shown in Figure 6 for the first grain (periodic cell). In this figure, in addition, velocity vectors of the SPH particles are illustrated. It can be seen that in the earlier time (t ≤ 2) asphaltene flocs gradually settle on the surface of the grain. Then, it develops a stable layer. After this time, any floc added to the deposited layer is removed by the shear stress of the flowing fluid. The same phenomenon occurs for the other gains with a certain delay, which can be recognized in Figure 5.

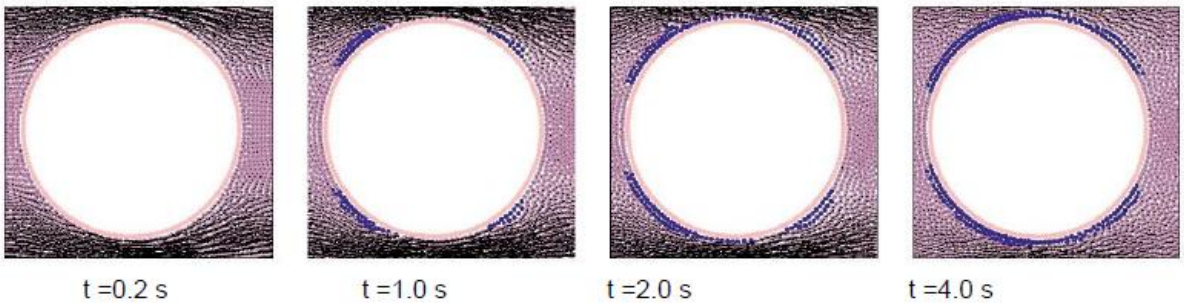

Figure 6. Particles distributions and velocity vectors for four different times around the first grain. (Dark particles represent asphaltene deposits.)

5. Modeling and discussion

To determine the permeability change using the results of numerical simulations one should average the velocity field V over the spatial domain to obtain Darcy's velocity u which in the discrete form is,

$$u = \Phi \frac{\sum_i^N V_i \omega_i}{\sum_i^N \omega_i} \qquad (12)$$

where φ is the porosity of medium, which in this case is equal $1 - \pi D^2/4s^2 = 0.50$. Then Darcy's law for the averaged volume reads

$$K = \frac{u_x \mu}{\rho g} \qquad (13)$$

where u_x is the x_i component of Darcy's velocity, and K is the (absolute) permeability.

5.1. Permeability change for a single cell

The above procedure was done for the obtained numerical results of the previous section for every time-step, and the resulted permeability is plotted versus time in Figure 7. To better show the evolution of the permeability, in this figure, it is normalized by using the initial value of the permeability of the medium K_{init}.

In Figure 7, three regions can be recognized. The schematic diagram of these regions (based on Figure 7) is shown in Figure 8 for an arbitrary periodic cell in the medium. In the first region (I), no precipitation has been formed. In this region, the local permeability of the intended cell is constant, and it is equal to the initial permeability of the medium K_{init} in single-

phase flow of oil. At a certain time t_i , the precipitation of asphaltene is begun. Here, it is denoted as the onset of permeability changes.

The local permeability in the region (II) is strictly descending. The rate of this process decreases as the time passes. The reason is the increase in velocity caused by decreasing the cross-section of flow. It also causes some deposited flocs to be removed from the surface of the grains. Therefore, after a certain time (τ) the asphaltene precipitation process will be stable.

Consequently, the net rate of precipitation will be zero. In this state, the flow in the considered cell becomes steady. Then, the region (III) is begun. In this region, the local permeability is constant and equal to K_{fin}.

It must be mentioned that the above behavior occurs under conditions when the flow rate is kept constant. Otherwise, the third region is not formed. Meanwhile, it is likely that the porous media become blocked completely. In addition, in the constant flow rate conditions it is concluded that for one alternative media the parameters in Figure 8. τ, K_{init} and K_{fin} are almost the same for all cells. Their difference is only the time of beginning the second region t_i. Let consider the normalized permeability for the cell i be $K_i/K_{init} = f_i(t)$. Then

$$\frac{K_i}{K_{init}} = f_{i-1}(t-\Delta t) = f_0(t-i\Delta t) \qquad (14)$$

where $f_0(t)$ is the permeability change function for the first grain (cell). It is supposed that $t_0 = 0$. In addition, Δt is the time between the onsets of permeability change for two adjacent cells, i.e., $\Delta t = t_i - t_{i-1}$. Note, the difference between τ and Δt. The value of Δt may be assumed to be equal to the time it takes for the flow to pass through a cell. That is $\Delta t = s/u_x$. A suitable relation, which fits well with the aforementioned model, is

$$\frac{K_i}{K_{init}} = \left(1 + \frac{\frac{K_i}{K_{init}}-1}{2}\left(1 + tanh\left(\alpha\left(2\frac{t-t_i}{\tau}-1\right)\right)\right)\right)^{-1} \qquad (15)$$

where α is a tuning parameter which is set here to 3. For the numerical results in Figure 7 and the other parameters are $K_{fin}/K_{init} = 0.17$ and $\tau = 5$ s.

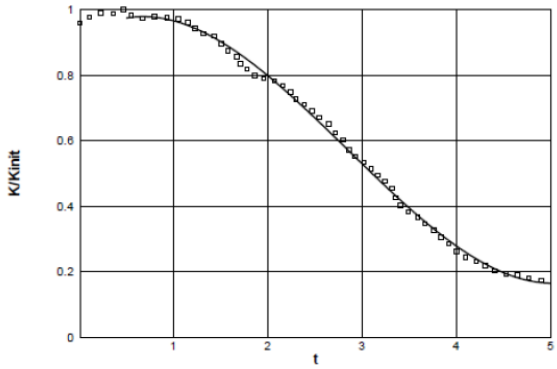

Figure 7. Fraction of absolute permeability to the initial permeability versus time

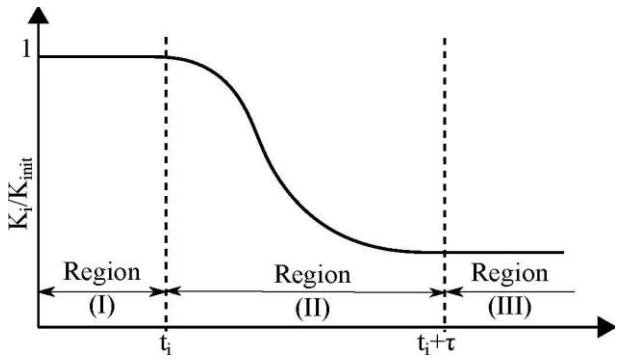

Figure 8. Schematic diagram for normalized permeability changes in time for a periodic cell *i*

5.2. Permeability change for a slim tube

The above model is appropriate for only one cell in the medium. For a slim tube with numerous grain arranged in series, the permeability of each cell at a certain time should be averaged. In the following, an averaging process is presented to obtain a model for the permeability change for a slim tube based on the numerical results and modeling of the previous sections.

If $K_n(t)$ is the average permeability of a porous medium including n periodic cells and since the cells are series it follows:

$$\frac{1}{\bar{K}_n(t)} = \frac{1}{nK_{init}} \sum_{i=0}^{n-1} \frac{1}{K_i(t)} = \frac{1}{nK_{int}} \sum_{i=0}^{n-1} \frac{1}{f_i(t)} \quad (16)$$

Regarding the periodic property of f(t) in Eq. (14) the sum in Eq. (16) can be rewritten as one integral approximation as

$$\frac{K_{init}}{K_n(t)} = \frac{1}{n\Delta t} \int_0^{n\Delta t} \frac{dt'}{f_0(t-t')} \quad (17)$$

where K_{init} is also the initial permeability of the slim tube. Then by replacing the value of $\Delta t = s/u_x$ and changing the variable one has

$$\frac{K_n(t)}{K_{init}} \cong \frac{L}{u_x \int_{t-L/ux}^{t} \frac{d\eta}{f_0(\eta)}} \quad (18)$$

in which $L = n_s$ is the length of the tube. By defining

$$(t) = \int_0^t \frac{d\eta}{f_0(\eta)} \quad (19)$$

Eq. (18) can be simplified as,

$$\frac{K_n(t)}{K_{init}} \cong \frac{T}{F(t)-F(t-T)} \quad (20)$$

where $T = L/u_x$ is the time needed for the flow to pass through the slim tube. Now by substituting the new model presented in Eq. (15) for a cell in Eq. (20) one can conclude that

$$\frac{K_n(t)}{K_{init}} \cong \frac{1}{1+\beta+\frac{\beta\tau}{2\alpha T} l.n\left(\frac{\cosh\left(\alpha\left(2\frac{t}{r}-1\right)\right)}{\cosh\left(\alpha\left(2\frac{t-T}{r}-1\right)\right)}\right)} \quad \text{where } \beta = \frac{K_{int}}{K_{fin}} - 1/2 \quad (21)$$

This equation simply relates the macro-scale average permeability of a slim tube to the pore-scale parameters K_{fin}/K_{init} and τ.

Using this up-scaling process the macro-scale permeability reduction of a porous medium can be predicted using pore-scale data. For example, using the previous data of Figure 7 the permeability reduction plots of two "short" and "long" slim tubes with T = 100s and T = 500s are shown in Figure 9. In this figure, it is observable that for the "short" slim tube (T = 100s) the permeability decreases during the time until the front of the injected asphaltene reaches the end of the tube (t = T). After that, the whole tube is at a stable condition with deposited asphaltene, so the permeability reaches its final value K_{fin}.

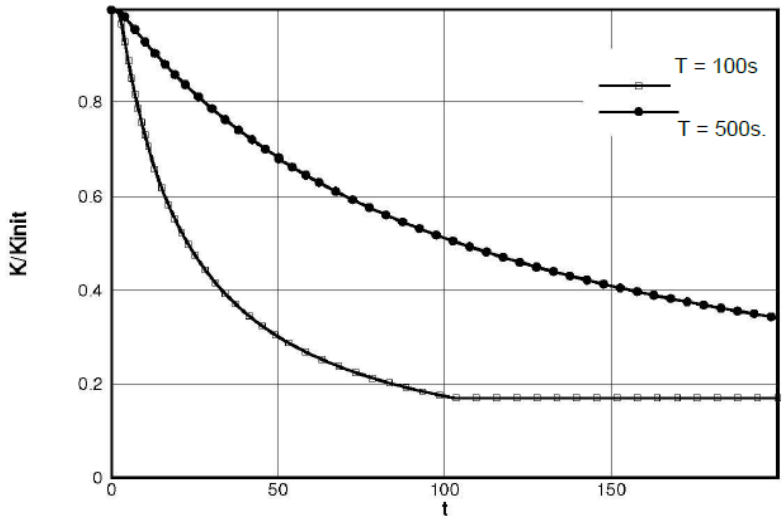

Figure 9. The results of permeability reduction of versus time based on the pore-scale simulation results for two slim tubes with T = 100s and T = 500s

For the "long" slim tube (T = 500s) (is shown in Figure 9), the time of the supposed experiment in Figure is not enough to reach the final stable condition. Thus, the permeability is strictly reducing during the experiment. This is more common in the real experiments. The same trend can be seen for instance in the works by Ashoori *et al.* [13] and Alizadeh *et.al.* [14].

For such conditions in which $\tau \ll t \ll T$ the Eq. (21) can be simplified more as

$$\frac{K_n(t)}{K_{init}} \cong \frac{1}{1+\beta\frac{t}{T}} \qquad \beta = \frac{K_{int}}{K_{fin}} - 1/2 \qquad (22)$$

This relation has only two parameters β and L and the first parameter belongs to the pore-scale phenomena while the latter is just a property of the flow in the slim tube.

6. Conclusion

In the current work, asphaltene precipitation in the granular porous medium was simulated in pore scale using an improved version of the Lagrangian particle-based method SPH. Using the numerical results of pore-scale simulation a model for the permeability reduction versus time (Eq. (15)) was developed for a single grain (periodic cell). Based on this model and using an up-scaling process another relation (Eq. (21)) was presented which describes the evolution of the permeability of a slim tube during precipitation of asphaltene. The main outcomes of this study can be expressed as below.

The results of the SPH method in the pore-scale simulation properly show the physical behavior of the flow including asphaltene flocs concentration velocity and pressure fields. In a constant flow rate, a repeated phenomenon for each grain can be recognized in which a deposited layer is gradually developed and reaches the steady state.

- ✓ A hyperbolic function model (Eq. (15)) can describe the evolution of the permeability of a single grain (periodic cell) during precipitation of asphaltene. In this function, there are two parameters; final to initial permeability K_{fin}/K_{init} and characteristic time of precipitation τ that should be evaluated through pore-scale simulation.
- ✓ By up scaling the model of a single grain the time evolution of the permeability of a slim tube or similar porous media is obtained. Here the suggested model (Eq. (21)) just needs the length of the tube and Darcy's velocity in addition to the aforementioned Pore-scale parameters.
- ✓ For enough long slim tubes, the model can be simplified to the form, which fits well with the laboratory experiments. The proposed models describe the permeability change with no need to know the changes of porosity.
- ✓ The developed model simulates the permeability reduction in flooding tests using computer code. The model provides good fit from the experimental data, which is an indication of the reliability of the developed model.

References

[1] Civan F. Scale effect on porosity and permeability: Kinetics, model, and correlation. AIChE journal, 2001; 47(2): 271-287.

[2] Civan F. Modeling and simulation of formation damage by organic deposition, in: First international symposium in colloid chemistry in oil production: Asphaltenes and wax deposition. JSCOP, 1995: 26-29.

[3] Civan F. Formation damage mechanisms and their phenomenological modeling-an overview. in: European Formation Damage Conference, Society of Petroleum Engineers, 2007.

[4] Ali M, Islam M. The effect of asphaltene precipitation on carbonate-rock permeability: an experimental and numerical approach. SPE production & facilities, 1998; 13(3): 178-183.

[5] Wang S, Civan F. Productivity decline of vertical and horizontal wells by asphaltene deposition in petroleum reservoirs, in: SPE international symposium on oilfield chemistry, Society of Petroleum Engineers, 2001.

[6] Wang S, Civan F, Strycker, AR. Simulation of paraffin and asphaltene deposition in porous media, in: SPE international symposium on oilfield chemistry, 1999: 449-458.

[7] Lucy LB. A numerical approach to the testing of the fission hypothesis. The astronomical journal, 1977; 82: 1013-1024.

[8] Gingold RA, Monaghan JJ. Smoothed particle hydrodynamics: theory and application to non-spherical stars, Monthly notices of the royal astronomical society. 1977; 181(3): 375-389.
[9] Monaghan JJ. Smoothed particle hydrodynamics. Reports on progress in physics, 2005; 68(8): 1703.
[10] Fatehi R, Manzari M. A consistent and fast weakly compressible smoothed particle hydrodynamics with a new wall boundary condition. International Journal for Numerical Methods in Fluids, 2012; 68(7): 905-921.
[11] Wendland H. Piecewise polynomial, positive definite and compactly supported radial functions of minimal degree. Advances in computational Mathematics, 1995; 4(1): 389-396.
[12] Randles P, Libersky L. Smoothed particle hydrodynamics: some recent improvements and applications. Computer methods in applied mechanics and engineering, 1996; 139(1-4): 375-408.
[13] Ashoori S, Manshad AK, Alizadeh N, Masoomi M, Tabatabaei S. Simulation and Experimental Investigation of the Permeability Reduction due to Asphaltene Deposition in Porous Media. Iranian Journal of Chemical Engineering, 2010: 3-16.
[14] Alizadeh N, Khaksar Manshad A, Fadili A, Leung E, Ashoori S. Simulating the permeability reduction due to asphaltene deposition in porous media. in: International Petroleum Technology Conference, International Petroleum Technology Conference, 2009.
[15] Manshad AK, Manshad MK, Ashoori S. The application of an artificial neural network (ANN) and a genetic programming neural network (GPNN) for the modeling of experimental data of slim tube permeability reduction by asphaltene precipitation in Iranian crude oil reservoirs. Petroleum Science and Technology, 2012; 30(23): 2450-2459.
[16] Menshad AK, Mofidi AM, Shariatpanahi F, Edalat M. Developing of scaling equation with function of pressure to determine onset of asphaltene precipitation. Journal of the Japan Petroleum Institute, 2018; 51(2): 102-106.

To whom correspondence should be addressed: Dr. Amir H Mohammadi, Discipline of Chemical Engineering, School of Engineering, University of KwaZulu-Natal, Howard College Campus, Durban 4041, South Africa, E-mail: amir_h_mohammadi@yahoo.com and Dr. Abbas Khaksar Manshad, Department of Petroleum Engineering, Abadan Faculty of Petroleum Engineering, Petroleum University of Technology (PUT), Abadan, Iran, Email: khaksar@put.ac.ir

Petroleum and Coal

Article **Open Access**

THE USING OF COAL BLENDS WITH AN INCREASED CONTENT OF COALS OF THE MIDDLE STAGE OF METAMORPHISM FOR THE PRODUCTION OF THE BLAST-FURNACE COKE. MESSAGE 1. PREPARATION OF COAL BLENDS

E. O. Shmeltser[1], V. P. Lyalyuk[1], V. P. Sokolova[1], D.V. Miroshnichenko[2]*

[1] Kryvyi Rig Metallurgical Institute, Ukraine National Metallurgical Academy, 50006, Kryvyi Rig, Ukraine
[2] National Technical University "Kharkov Polytechnic Institute", 61002, Kharkiv, Ukraine

Received March 13, 2018; Accepted May 31, 2018

Abstract

Laboratory and industrial research confirm that decrease in the coking properties of bituminous coal with a high level of fluidity (HFC) when it is present to excess in the coking blend improves the strength of blast-furnace coke. If coal blend containing >70% HFC is crushed until its content of the ≤ 3 mm class is 90%, the crushability M_{25} may be increased by 1.8%, with a decrease in the abrasion strength M_{10} by 0.8%. This behavior may be explained in that increase in the specific surface of the coal particles reduces the fluidity of the plastic mass and hence increases its viscosity. Consequently, the residence time of the gaseous products in the plastic zone increases. That results in the formation of a large quantity high-molecular gas, creating higher expansion pressure. The overall outcome is greater utilization of the destruction products as plasticizers; the formation of an additional liquid from the gaseous products within the grains; and improvement in the contact conditions.

Keywords: *coal blend; coal with a high level of fluidity grindability; coking properties; coke strength.*

1. Introduction

In previous work, we analyzed the reasons for the decline in quality of the coke produced at ArcelorMittal Kryvyi Rig [1–5]. They include the purchase of coal concentrates from a multitude of suppliers; the instability of the coke supplies for coking (sometimes as many as 60–80 changes in blend composition within a month); incorrect selection of the optimal degree of blend crushing (that is, the content of the ≤3 mm class), so that the packing density of the blend and the content of the poorly coking 0–0.5 mm class in the blend are not optimal with varying rank composition of the blend; elevated moisture and ash content of the blend sent for coking; and very variable coal and blend quality.

Attempts to improve blend preparation with the coal supplies currently available in Ukraine entail selection of the optimal degree of crushing of coal blend with a very high content of HFC [6]. Since the content of the ≤3 mm class varied from 76 to 89% in coke production at ArcelorMittal Kryvyi Rig, while the content of HFC (bituminous coal) varied from 56 to 89%, it is of interest to analyze the influence of these two factors on coke quality. If the content of HFC in the blend is 70–89%, the strength of the coke increases with increase in the degree of crushing. If the content of the ≤3 mm class in the blend is increased from 76 to 89%, with a corresponding increase in the <0.5 mm class from 37 to 47%, M_{25} increases from 85.6 to 87.3%, on average.

Obviously, if the content of HFC in the blend is too high to permit the production of coke with satisfactory strength, we must reduce the coking properties of the blend by further crushing. Note that the crushing of valuable HFC to reduce its coking properties should be regarded as a last resort to improve the coke quality when the content of the HFC in the blend is excessive. In other circumstances, it cannot be recommended for use in the preparation of coking blend.

It is expedient to investigate why the strength of the blast-furnace coke produced from a blend with >70% HFC improves if the content of the ≤3 mm class in the blend is increased from ~80 to ~90%. We will also study the change in the strength of the coke produced from a blend with <70% HFC.

2. Experimental

In the experiments, we use concentrates obtained from coal of different ranks available in Ukraine: Taltek (Russia); Kievskaya (Ukraine); Cherkasov Kamen' (Russia); and Kalinovskaya Vostochnaya (Ukraine).

Tables 1–3 present the technological properties, petrographic characteristics, and granulometric composition of the coal concentrates. Note that, since the experiment is conducted in two stages, we use two samples of Kievskaya concentrate and two samples of Kalinovskaya Vostochnaya coal. We know that oxidation of the coal samples has a considerable influence on their properties [7–9]. Therefore, we use only unoxidized coal (Δt < 6ºC).

Table 1. Technological properties of coal concentrate

Component; country	Proximate analysis, %			Thickness of plastometric lager, mm	Hardgrove grindability, un.	Oxidation index, °C
	A^d	S^d_t	V^{daf}	x	HGI	Δt
Taltek' coal; Russia	8,7	0,51	36,5	10	53	3
Kievskaya coal; Ukraine, sample 1	8,8	1,56	31,2	22	76	2
Kievskaya coal; Ukraine, sample 2	8,7	1,57	30,9	22	78	1
Kalinovskaya Vostochnaya coal; Ukraine, sample 1	8,2	1,41	21,6	16	98	3
Kalinovskaya Vostochnaya coal; Ukraine, sample 2	7,7	1,64	21,5	16	91	2
Cherkasov Kamen' coal; Russia	9,6	0,53	27,9	14	67	1

Table 2. Petrographic characteristics of coal concentrate

Component; country	Petrographic composition (without mineral impurities), %					Mean vitrinite reflection coefficient, %	Distribution of vitrinite reflection coefficient, %					
	V_t	S_v	I	L	ΣFC	R_0	0.50–0.64	0.65–0.89	0.90–1.19	1.20–1.39	1.40–1.69	1.70–2.59
Taltek' coal; Russia	71	0	27	2	27	0,63	63	37	0	0	0	0
Kievskaya coal; Ukraine, sample 1	90	0	8	2	8	1,04	0	7	79	14	0	0
Kievskaya coal; Ukraine, sample2	91	0	8	1	8	1,04	0	3	95	2	0	0
Kalinovskaya Vostochnaya coal; Ukraine, sample 1	92	0	8	0	8	1,33	0	0	6	72	22	0
Kalinovskaya Vostochnaya coal; Ukraine, sample 2	90	0	10	0	10	1,40	0	0	3	49	48	0
Cherkasov Kamen' coal; Russia	57	0	43	0	43	0,99	0	15	85	0	0	0

Table 3. Granulometric composition of coal concentrates

Component; country	Granulometric composition (%) by class (mm)								Mean particle diameter, mm
	>25	13–25	6–13	3–6	1–3	0.5–1.0	<0.5	≤3	d_{me}
Taltek' coal; Russia	19.1	16.7	16.4	16.6	14.1	6.0	11.1	31.2	13.00
Kievskaya coal; Ukraine, sample 1	–	0.8	2.5	7.0	29.7	24.8	35.2	89.7	1.57
Kievskaya coal; Ukraine, sample 2	–	–	5.0	9.2	21.7	23.4	40.7	85.8	1.60
Kalinovskaya Vostochnaya coal; Ukraine, sample 1	–	1.3	3.9	11.1	22.7	14.9	46.1	83.7	1.80
Kalinovskaya Vostochnaya coal; Ukraine, sample 2	–	1.9	5.1	14.3	19.5	19.1	40.1	78.7	2.10
Cherkasov Kamen' coal; Russia	9.1	14.2	9.7	13.8	19.9	9.1	24.2	53.2	8.18

Analysis of Tables 1–3 indicates that the coal samples may be divided into two groups.

1. Taltek and Cherkasov Kamen', characterized by an elevated content of fusinized components (27–43%), poor coking properties (y =10–14 mm), and low Hargrove grindability (53–67 units). Coal in this group contains 33.0–52.2% of the >6 mm class and no more than 31.2–53.2% of the <3 mm class.

2. Kievskay and Kalinovskaya Vostochnaya, which are petrographically uniform ($\sum FC < 25\%$), with good coking properties (y = 16–22 mm) and Hardgrove grindability of 76–98. 2 units. Coal in this group contains 3.3–7.0% of the >6 mm class and 78.7–89.7% of the <3 mm class.

Table 4 presents the composition of the experimental blends. Blends 1–3 correspond to the actual blend composition used in coking at a Ukrainian plant, with 42% Kievskaya coal. In other words, the content of HFC is significant but less than 70%. In blends 4 and 5, the content of Kievskaya coal exceeds 70%; in fact, it is 80%. That may be due to temporary disruption of normal coal supplies to the plant.

Table 4 Composition of coal blends

Batch component; country	Blend, %	
	1–3	4, 5
Taltek' coal; Russia	35	15
Kievskaya coal; Ukraine, sample 1	42	0
Kievskaya coal; Ukraine, sample 2	0	80
Kalinovskaya Vostochnaya coal; Ukraine, sample 1	10	0
Kalinovskaya Vostochnaya coal; Ukraine, sample 2	0	5
Cherkasov Kamen' coal; Russia	13	0
Total	100	100

The whole blend is crushed at once. The content of the ≤3 mm class is 82.7–90.3% in blends 1–3 and 81.0–90.0% in blends 4 and 5. Increasing the degree of crushing decreases the mean diameter of the coal particles: from 1.68 to 1.45 in the first series (Table 4, blends

1–3); and from 2.39 to 1.56 mm in the second series (blends 4 and 5). Table 5 presents the granulometric composition of the experimental blends. Table 6 presents their technological properties, while Table 7 summarizes their petrographic characteristics.

Table 5. Granulometric composition of coal blends

Blend	Granulometric composition (%) by class (mm)					Mean particle diameter, mm
	>3	1–3	0.5–1.0	<0.5	≤3	d_{me}
1	17.3	34.5	17.3	30.9	82.7	1.68
2	13.5	38.1	17.1	31.3	86.5	1.58
3	9.7	39.9	18.8	31.6	90.3	1.45
4	19.0	49.0	14.0	18.0	81.0	2.39
5	10.0	49.0	16.0	25.0	90.0	1.56

Table 6. Technological properties of coking batches

Blend	Proximate analysis, %			Thickness of plastometric lager, mm	Expansion pressure, kPa	Gieseler plastic properties				
	A^d	S^d_t	V^{daf}	y	P^n_{max}	t_1, °C	t_{max}, °C	t_{so}, °C	Δt, °C	F_{max}, ddpm
1	8.7	1.07	31.7	16	3.4	421	451	480	59	100
2	8.8	1.06	31.6	15	3.5	421	457	481	60	119
3	8.8	1.06	31.5	15	3.7	425	456	484	59	125
4	8.4	1.41	31.3	20	4.2	408	447	480	72	335
5	8.4	1.41	31.3	20	7.4	414	447	480	66	135

Table 7. Petrographic characteristics of coal blends

Blend	Petrographic composition (without mineral impurities), %					Mean vitrinite reflection coefficient, %	Distribution of vitrinite reflection coefficient, %					
	V_t	S_v	I	L	ΣFC	R_0	0.50–0.64	0.65–0.89	0.90–1.19	1.20–1.39	1.40–1.69	1.70–2.59
1	78	0	21	1	21	0.94	19	22	48	7	4	0
2	81	0	18	1	18	0.95	23	25	38	12	2	0
3	80	0	19	1	19	0.95	25	18	43	10	4	0
4	88	0	11	1	11	1.00	9	8	77	4	2	0
5	88	0	11	1	11	1.00	9	8	77	4	2	0

For better assessment of how the degree of crushing affects the strength of blast furnace coke, we determine the expansion pressure and the Gieseler plasticity of the coal blends. The expansion pressure is the pressure applied by the coal mass in a plastic state when the free expansion is impossible [10].

In the tests, we record the following temperatures (ºC): the onset of softening t_1; maximum fluidity t_{max}; solidification t_{so}; and the plastic range $\Delta t = t_1 - t_{so}$. The most important of the measured characteristics is the maximum fluidity F_{max}, ddpm (dial divisions per minute), which characterizes the viscosity of the plastic mass.

3. Results and discussion

Analysis indicates that the results of the proximate and plastometric analysis are practically the same for the two series of blends. This indicates agreement of the actual and specified compositions.

If the content of the ≤3 mm class is increased from to 90.3% in the first series (Table 5, blends 1–3), the fluidity of the plastic mass increases somewhat (from 100 to 125 ddpm). That may be due to the more uniform distribution of petrographically distinct Taltek and Cherkasov Kamen' coal particles within the blend. With the increase in the degree of crushing in the second series (batches 4 and 5), the fluidity of the plastic mass declines considerably (from 335 to 135 ddpm), and its viscosity increases accordingly.

In that case, we may observe the effect noted in [11-12]: if coal blend with a high content of HFC is more finely crushed, the infusible grains are better dispersed in the surrounding plastic mass, with consequent increase in the concentration of the disperse phase and the viscosity of the dispersion medium. In those circumstances, the expansion pressure tends to increase (from 4.2 to 7.4 kPa). That may be explained by an increase in the proportion of vapor gas phase and hence in its pressure on the plastic layer. For example, a decrease in particle size is accompanied by an increase in the total surface of the disperse phase and decrease in the quantity of free dispersion medium, which results in increased viscosity of the plastic mass and improved coke quality.

If we regard blends 4 and 5 as practically the same, we may agree with the conclusion in [13]: "for all coal ranks, a more fluid plastic mass is formed with greater crushing." The increase in fluidity of the plastic mass in HFC is due to the greater delay in the formation of liquid products within the large grains, their tendency to plasticize the remainder of the grain, and its more complete transition to the plastic state, according to [13]. The crushing of the coal increases the specific surface of the particles, accelerates the evacuation of gases, and slows reduction processes, according to [14]. The overall result increases in the viscosity of coal in the plastic state.

Since the expansion pressure reflects the gas pressure developed within a volume surrounded by a plastic layer, we may expect that this pressure will increase with an increase in viscosity of the plastic layer, other conditions being equal [15].

By increasing pressure within the plastic zone and the contact between the particles, the increase in viscosity of the plastic mass hinders gas liberation. That extends the period during which the destruction products are plastic. In view of the foregoing, the increase in expansion pressure from 4.2 to 7.4 kPa when blend with a high content of HFC is more finely ground is entirely predictable.

The next step is box coking of the coal blends. The blends are placed in 200 × 200 × 300 mm iron boxes; three boxes are used for each coking blend. The packing density is 800 kg/m^3 in all cases; the coking time is 22 h; the actual temperature in the heating channels is 1167ºC on the machine side and 1174ºC on the coke side.

After coking, the boxes are cooled in water and opened. The coke is placed on trays and dried in a chamber to constant mass. Table 8 presents the characteristics of the coke produced.

The results indicate that the coke produced in each series is characterized by similar yield, ash content, and total sulfur content. The volatile matter is low (0.1–0.3%). That indirectly indicates that the coking process is over and the coke has been fully cooked.

It follows from Table 8 that, if blends containing <70% of HFC (blends 1–3) are more intensively crushed, the resultant increase in strength of the coke is slight. That is consistent, in particular, with the slight increase in expansion pressure (from 3.4 to 3.7 kPa). The crushability M_{25} increases by 0.4–0.6%, with a decrease in the abrasion strength M_{10} by 0.1–0.2%.

Table 8. Characteristics of the coke produced

Blend	Coke yield B_{co}, %	Proximate analysis, %			Mechanical strength, %	
		A^d	S^d_t	V^{daf}	M_{25}	M_{10}
1	74.5	11.7	0.90	0.1	90.9	7.7
2	74.6	11.8	0.89	0.2	91.3	7.6
3	74.5	11.7	0.87	0.1	91.5	7.5
4	74.8	11.2	1.19	0.3	89.3	8.4
5	74.9	11.3	1.21	0.2	91.1	7.6

In the present case, the increase in coke strength may be attributed to decrease in the local stress due to the coking of coal particles with different petrographic composition and hence volatile matter, thermal stability, and the physical properties [14].

If blends containing >70% of HFC (blends 4 and 5) are more intensively crushed, we note a considerable increase in the strength of blast furnace coke: the crushability M_{25} is increased by 1.8%, with a decrease in the abrasion strength M_{10} by 0.8%.That is due to the considerable increase in expansion pressure (from 4.2 to 7.4 kPa). On account of the increase in viscosity of the plastic mass, the residence time of the gaseous products in the plastic zone increases. That is associated with the formation of a larger quantity of high molecular gases, which create higher expansion pressure.

Therefore, in this case, the improvement in coke strength is predominantly due to increases in the expansion pressure of the coal blend, which results not only in the greater use of the liquid destruction products as plasticizers but also in the formation of an additional liquid from the gaseous products within the grains. That is associated with better softening of the coal grains and more complete contact between the grains (in some cases, their coalescence) [16].

Thus, we have studied how greater crushing of coal blend with a high content of HFC affects the properties of the plastic mass and the mechanical strength of the coke formed. Our research illuminates the factors responsible for the increase in the coke strength and confirms that, as previously determined by analysis, a decrease in the coking properties of HFC when it is present in the blend in excessive quantities improves the strength of blast-furnace coke.

Symbols

A^d	*ash content of coal in the dry state, %;*
S^d_t	*sulphur of coal in the dry state, %;*
V^{daf}	*volatile matter in the dry ash-free state, %;*
y	*thickness of the plastic layer, mm;*
HGI	*hardgrove grindability index, units;*
Δt	*oxidation index, °C;*
Vt	*vitrinite, %;*
Sv	*semivitrinite, %;*
I	*inetinit, %;*
L	*liptinite, %;*
$\sum FC$	*sum of fusinized components, %;*
R_0	*mean vitrinite reflection coefficient, %;*
d_{me}	*mean diameter of coals particles, mm;*
P^h_{max}	*expansion pressure of coal (blend), kPa;*
t_1	*temperature of the onset of softening, °C;*
t_{max}	*temperature of maximum fluidity, °C;*
t_{so}	*temperature of soliditication, °C;*
F_{max}	*maximum fluidity, ddpm;*
M_{10}, M_{25}	*indices of resistance of coke abrasion and crushability, respectively, %.*

References

[1] Lyalyuk VP, Uchitel' AD, Lyakhova IA, Kassim DA, and Zaitsev GL. Preparation of coking batch. Coke and Chemmistry, 2011; 54(8): 271–286.

[2] Lyalyuk VP, Sokolova VP, Lyakhova IA, and Kassim DA. Ensuring stable quality of blast-furnace coke. Coke and Chemistry, 2012; 55(8): 304–308.

[3] Shmeltser EO, Lyalyuk VP, and Sokolova VP. The effect of preparation of coal charges on the quality of metallurgical coke. Vestn. Priazovsk. Gos. Tekh. Univ., 2015; 30: 27–36.

[4] Lyalyuk VP, Shmeltser EO, Lyakhova IA, and Kassim DA. Changes in the petrographic composition of coal batch on crushing. Coke and Chemistry, 2017; 60(2): 55–58.

[5] Romanyuk IV, Sikan II, Mukina NV. et al. Prospective development of the coal resource base of the Arcelor Mittal Krivoy Rog coke chemical production. Uglekhim. Zh., 2016; 3–4: 12–18.

[6] Lyalyuk VP, Sokolova VP, Lyakhova IA, and Kassim DA. Quality fluctuations of coking coal. Coke and Chemistry, 2013; 56(1): 1–6.

[7] Miroshnichenko DV. Influence of oxidation on the packing density of coal. Coke and Chemistry, 2014; 57(5): 183–191.

[8] Miroshnichenko DV. Crushing properties of coal. Coke and Chemistry, 2013; 56(12): 449–455.

[9] Desna NA, and Miroshnichenko DV. Oxidized coal in coking: a review. Coke and Chemistry, 2011; 54(5): 139–146.

[10] ISO 10329:2009: Coal-Determination of Plastic Properties Constant-Torque Gieseler Plastometer Method, Geneva: Int. Org. Standard., 2009.

[11] Taits EM, Enik GI, and Rizaev VV. The degree of crushing of high-sintering coal and coke strength. Koks Khim., 1987; 11: 37–39.

[12] Gofman MV. Prikladnaya khimiya tverdogo topliva (Applied Solid Fuel Chemistry), Moscow: Metallurgizdat, 1963.

[13] Sklyar MG. Fiziko-khimicheskie osnovy spekaniya uglei (Physical and Chemical Basis of Coal Sintering), Moscow: Metallurgiya, 1984.

[14] Gryaznov NS. Osnovy teorii koksovaniya (Fundamental Theory of Coking), Moscow: Metallurgiya, 1976.

[15] Miroshnichenko DV, Kaftan YS, Desna NA, and Sytnik AV. Oxidation of bituminous coal. 1. Expansion pressure. Coke and Chemistry, 2015; 58(10): 376–381.

[16] Miroshnichenko A.. Sostavlenie ugol'nykh shikht dlya koksovaniya (Composition of Coal Charge for Coking), Kiev: Tekhnika, 1965.

To whom correspondence should be addressed Dr. E. O. Shmeltser, Kryvyi Rig Metallurgical Institute, Ukraine National Metallurgical Academy, 50006, Kryvyi Rig, Ukraine, E-mail: shmelka0402@gmail.com

Petroleum and Coal

Article **Open Access**

IDENTIFICATION OF CARBON NANOSTRUCTURES IN COALS AND CARBONIZATION PRODUCTS

Vladimir M. Shmalko[1], Oleg I. Zelenskii[1], Elena Yu. Spirina[1], Alexey V. Sytnik[1], Andrey B. Grigorov[2]

[1] *Ukrainian State Coal-Chemistry Institute, 61023, Kharkov, 7 Vesnina Str., Ukraine*
[2] *National Technical University «Kharkov Polytechnic Institute», 61002, 2 Kirpichova str., Kharkov, Ukraine*

Received March 13, 2018; Accepted May 31, 2018

Abstract

The article contains experiments on the extraction of carbon nanostructures from coal and coal carbonization products, namely, coke, pith coke, coal tar pitch, coke dust and carbon deposits from coke and coke-pitch chambers were carried out. With the help of transmission electron microscopy method extracted carbon nanostructures were investigated. The rationale of the derived nano-structures technologic origin is given in this paper. It was found that the average nanoparticle size in the suspension is 40 nm. It is shown that in coke and carbonizations products nanoparticles including nanotubes have been revealed. Nanotubes in coke and other coking products are supposedly formed in coking chamber in the course of carbonizing coals. In the coals studied spherical and elongated carbon nanostructures (supposedly two-phase) were found. Their composition and origin are not yet clear. During storage of nanoparticles suspension from coal and carbonization products, the processes of self-organization of carbon nanostructures are processing to form fractal structures.

Keywords: *carbon nanostructures; coal; coke products; suspensions; electron microscope.*

1. Introduction

At present, the main ways to produce carbon nanostructures (CNS) are arc methods, laser ablation and chemical vapor deposition (CVD). The range of materials used as precursors is widening by years. However, the use of coal as a precursor material to produce CNS is of special interest. Due to its characteristic features and structure as well as vast resources coal is very promising as a raw material source to obtain CNS.

CNS is produced from coal since 1991 [1], and considerable success has recently been made in the production of one-wall, two-wall and multiwall nanotubes [2-11]. The main method of CNS synthesis from coals lies in using coal to produce electrodes substituting for graphite in the arc synthesis. Coal electrodes are made by carbonizing coal mixed with a binder and a catalyst at temperatures of 900 - 1200°C.

At the same time, we believe it reasonable to consider coal carbonization products (coke and other products) as a source to obtain CNS. If one compares the main features of CVD reactors and those of coke ovens a conclusion can be made that in a coking chamber especially in its upper part (referred to as oven headspace or gas collecting space) the operating conditions similar to CVD reactors are actually existing. Fig. 1 shows a schematic diagram of a CVD reactor and the headspace of a coking chamber. It is evident that a temperature range in the oven headspace falls within that used in CVD reactors. Hydrocarbon raw materials decompose on a catalyst to form CNS on its surface and in the whole space of the reactor. In a coke oven, there are hydrocarbons releasing from the coal charge during coking. Mineral components of a coke can serve as a catalyst and silica of refractories may be a catalyst 0n the surface of brickwork. Supposedly, it is CNS deposited on the surface of coke oven walls that initiate carbon deposition in coke ovens.

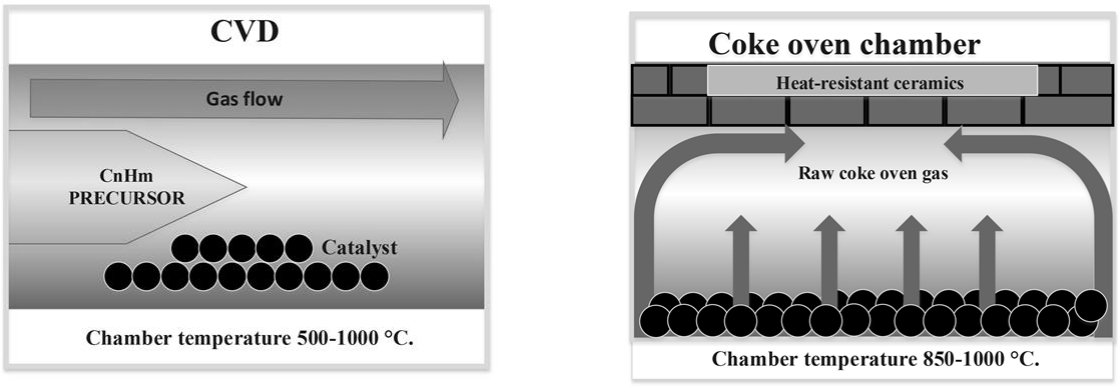

Fig.1 CVD reactor and coking chamber

2. Experimental

In order to check the supposition that CNS can be formed in a coking chamber like in a CVD reactor we have investigate carbon-containing materials of various kinds, namely coke from coal, carbon deposits in coking chambers, coal tar, medium temperature pitch, pith coke, deposits in pitch coke ovens, as well as dust from dust free pushing (DFP) units and dry coke quenching (DCQ) units. In addition, samples of coking and fat coals (key components of the coal blend for production of coke) were examined in order to check whether CNS could be introduced into the coking chamber together with the coal charge.

The characteristics of the samples used are presented in Tab. 1-3.

Table 1. The characteristics of the coals

Coal used	A^d, %	S^d_t, %	V^{daf}, %
Bituminous coal	2.9	1.04	34.4
Coke-grade coal	2.8	0.64	28.9

Table 2. The characteristics of the coal carbonization products

Samples	A^d, %	S^d_t, %	V^{daf}, %
Coke from coal	12.1	0.95	1.7
Carbon deposits from coking chamber	3.1	1.46	0.9
Pitch coke	0.6	0.54	0.6
Carbon deposits from pitch coke chamber	0.3	0.62	0.4
Dust from DCQ unit	14.3	0.82	1.1
Dust from DFP unit	11.0	0.99	3.4

Table 3. The characteristics of the coal tar and the coal tar pitch

Samples	W, %	A, %	S, %	V, %	D, kg/m^3	α, %	α_1, %
Coal tar	1.3	0.14	0.45	-	1177	6.7	1.9
Coal tar pitch	-	0.27	0.56	56.2	1281	20.4	5.6

The samples crushed to ≤ 0.2 mm were dispersed in distilled water by ultrasonic and separated in a centrifuge. Coal tar samples were heated to turn them into a flowing state.

After centrifugation, the solid precipitate was removed, and the centrifugate was studied. Light dispersion in a beam of red laser with a wavelength of 405 nm (Tyndall effect) was used as a test for the presence of nanoparticles.

The concentration of nanoparticles in their suspensions was measured by weight after evaporation of water. CNS were identified by transmission electron microscope (TEM).

3. Result and discussion

The centrifugate of all samples studied exhibited the Tindal effect. This means that all water suspensions of the tested samples contained particles the size of 40 nm and higher (0.1 of the wavelength of light). Nanoparticles in water suspensions are not stable, and during storage, they aggregated to give filaments, whiskers and the like visible by the naked eye. The content of particles in suspensions is presented in Tab. 4.

Table 4. The content of nanostructures in suspensions

Samples	Content of CNS, % of sample weight
Coke from coal	0.1
Carbon deposits from coking chamber	1.8
Coal tar	1.4
Coal tar pitch	1.0
Pitch coke	1.3
Carbon deposits from pitch coke chamber	1.9
Dust from DCQ unit	1.2
Dust from DFP unit	0.4

The amounts of CNS presented in Table 4 were obtained by a single treatment of the samples by ultrasound.

The lowest quantity of CNS was found in coke and coke dust after dry quenching. Possibly, CNS concentrate on the surface of coke lumps, and due to abrasion, they come to dust in DCQ unit where their amount is four times higher.

A considerable amount of CNS in the dust from DFP units is explained by the fact that this dust by its structure is nearer to pyrocarbon than to coke and possibly the bulk of this dust is a product of carbon clusters condensation which forms CNS. Condensation of carbon clusters from the gaseous phase is occurring also on oven walls, and at our suggestion, this is one of the main causes of carbon deposition in a coking chamber.

Probably, part of clusters is carried over by coke oven gas. When gas has cooled the clusters associated and come to coal tar. It is in this way that one can explain the occurrence of CNS in coal tar. Some quantity of CNS comes from coal tar to the tar distillation products, but the major part probable remained in pitch.

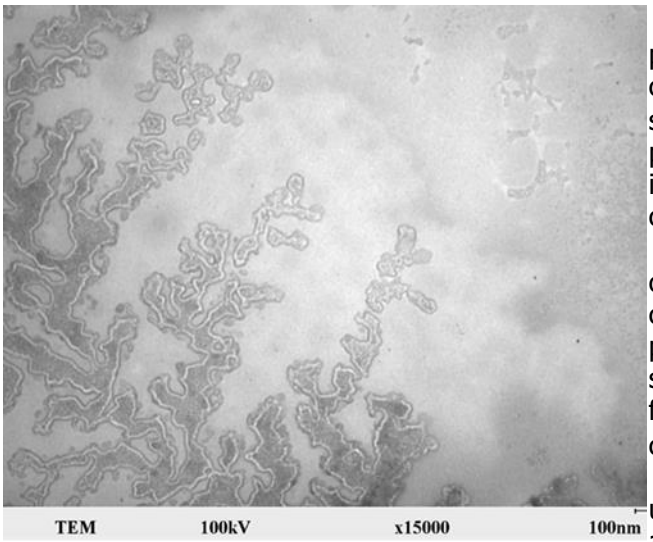

Fig. 2 CNS fractal structure from coke

A little amount of CNS is determined in pitch coke and carbon deposits in a pitch coke oven. This can be explained by the secondary formation of CNS when coking pitch. In other words, CNS is formed both in coke oven chambers and in pitch coke chambers.

Figures 2-7 show photographs of CNS obtained from water suspensions of various carbonization products. Practi-cally in all suspensions, there are nano-particles of the shoot. This can be explained by unsatisfactory separation of solid particles in the centrifugal field of the centrifuge used.

As shown in Fig. 2-7, CNS in the coals under study as well as in coking products are rather different and can be distinguished by their shape, struc-ture, and size.

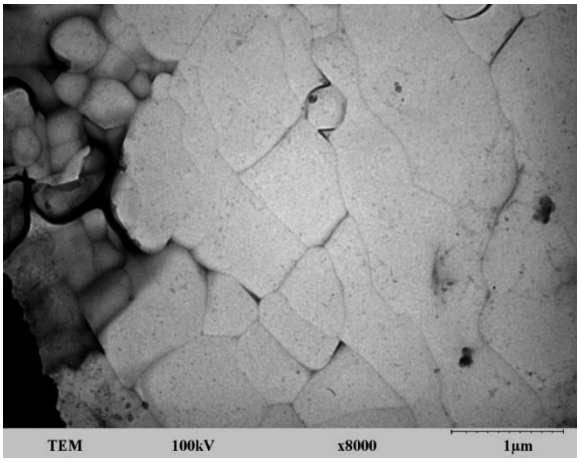

a.

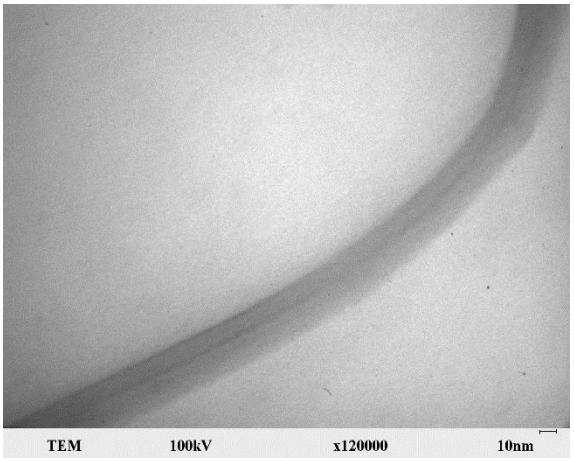

b.

Fig. 3. CNS from carbon deposits in coking chamber: (a) foam-shape particles; (b) and (c) carbon nanotubes

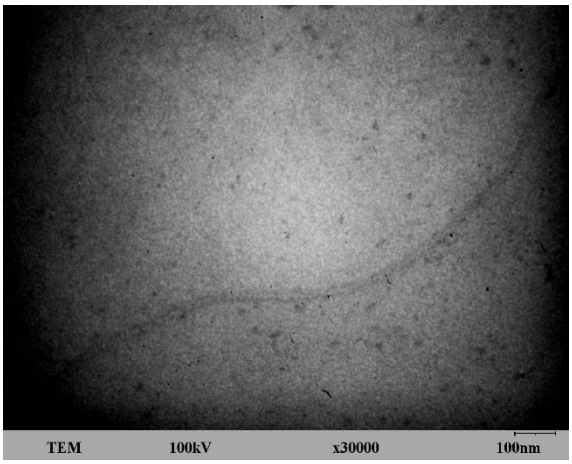

c.

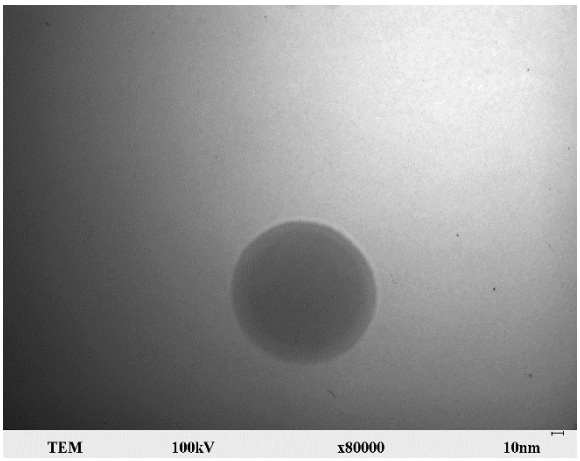

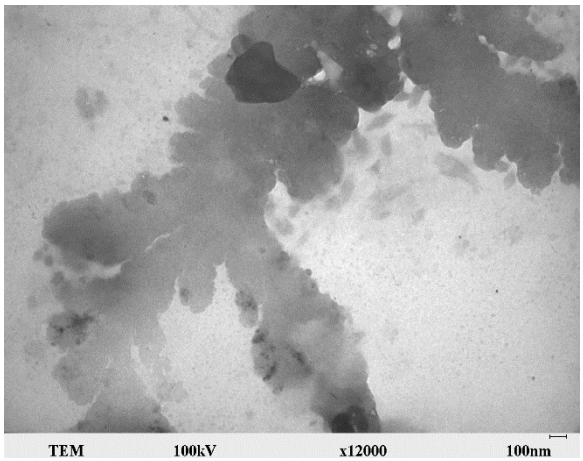

Fig.4. CNS from pitch: (a) spherical two-phase nanoparticle, (b) fractal "assemlage"

CNS in the form of nanotubes have been found in coke (Fig. 2), in dust from DCQ units, in carbon deposits in coke ovens (Fig.3, b-c) and pitch coke ovens, in dust from DFP units (Fig. 5) and in pitch coke (Fig. 6). In pitch coke, there were found helical CNS of about 360 nm in diameter which may be the products of self-organization of carbon nanotubes during storage of suspensions.

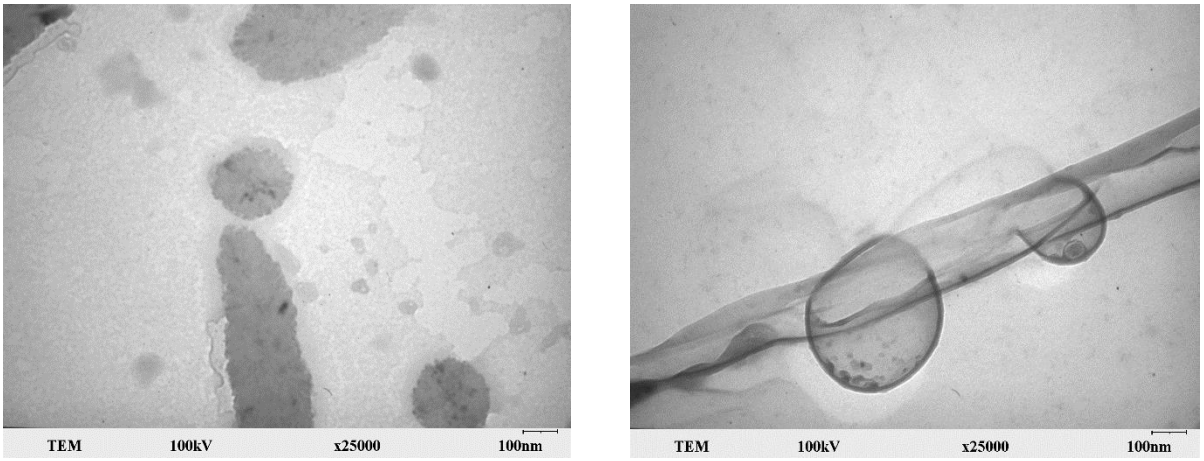

Fig.5. CNS from dust in DFP units: (a) fractal structure; (b) nanotubes

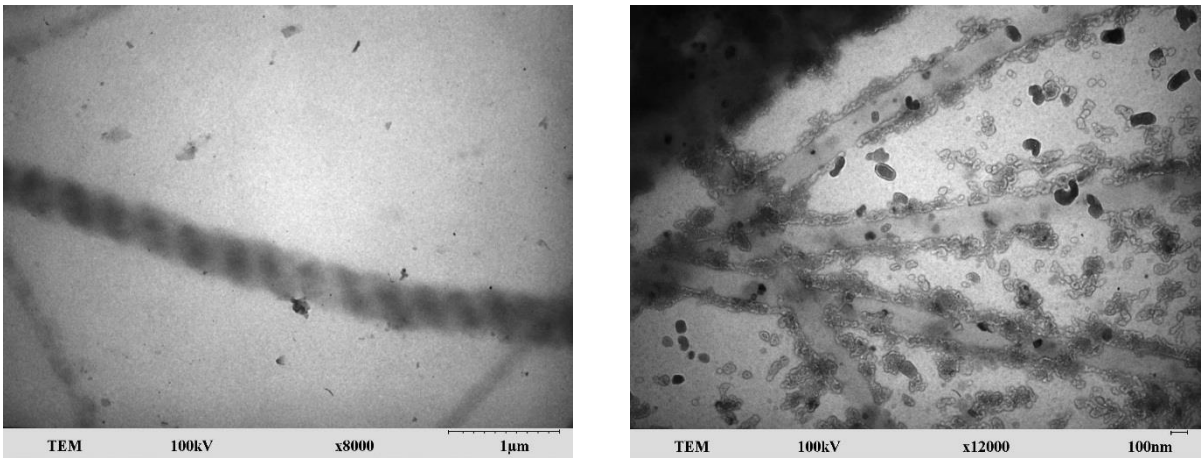

Fig. 6. CNS in pitch coke: (a) helical nanotubes, (b) nanotubes with adsorbed spherical two-phase particles

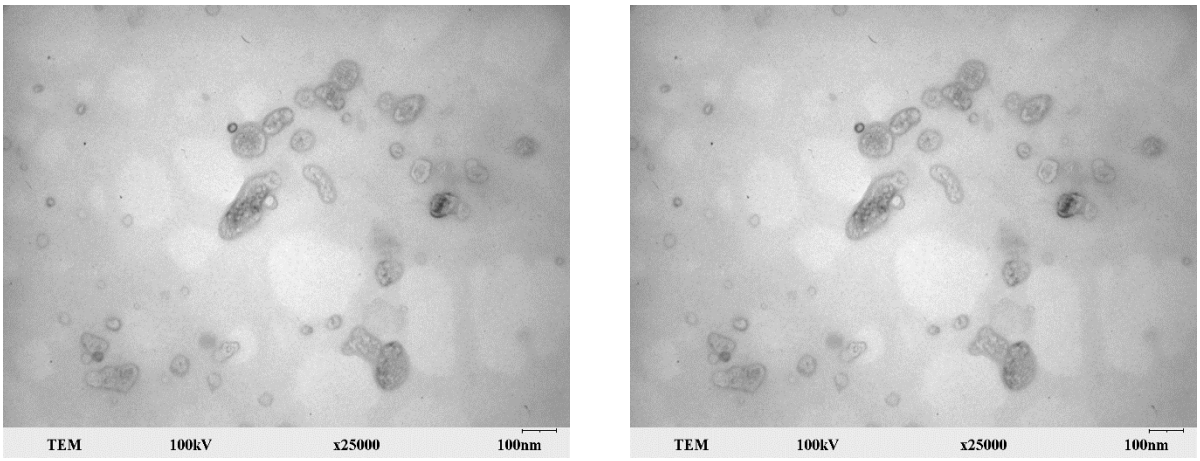

Fig.7. CNS in coals: (a) in bituminous coal; (b) in coke-grade coal

In the coal, samples studied nanotubes have not been found that gives good grounds to believe that nanotubes in coke and carbonization products are forming in coking chamber in the course of carbonization.

Nevertheless, in coals, CNS has been also revealed. These are two-phase nanoparticles with the core and shell which aggregate in the process of self-organization during storage of suspensions to form longer nanoparticles. All the particles in coals are of crystalline nature that is shown on diffraction patterns.

4. Conclusion

Examination of the results obtained during the determination of CNS in coke and other carbonization products permits the following basic conclusion:
1. In coke and carbonizations products nanoparticles including nanotubes have been revealed. Nanotubes in coke and other coking products are supposedly formed in coking chamber in the course of carbonizing coals.
2. In the coals studied spherical and elongated CNS (supposedly two-phase) were found. Their composition and origin are not yet clear.
3. During storage of nanoparticles suspension from coal and carbonization products, the processes of self-organization of CNS are processing to form fractal structures.

Symbols

W	*moisture in the analysis sample, %;*
A	*ash content, %;*
Ad	*ash content in the dry state, %;*
V	*volatile matter, %;*
Vdaf	*volatile matter in the dry ash-free state, %;*
S	*sulphur content, %;*
Sdt	*sulphur in the dry state, %;*
D	*density, kg/m3;*
α	*mass fraction of substances insoluble in toluene, %;*
$\alpha 1$	*mass fraction of substances insoluble in quinoline, %.*

References

[1] Pang LSK, Vassallo AM, Wilson MA. Fullerenes from coal. Nature. 1991; 352: 480.
[2] Qiu JS, Zhou Y, Wang LN, Tsang SC. Formation of carbon nanotubes and encapsulated nanoparticles from coals with moderate ash content. Carbon. 1998; 36(4): 465-467.
[3] Qiu JS, Zhou Y, Yang ZG, Wang DK, Guo SC, Tsang SC, Harris PJF. Preparation of fullerenes using carbon rods manufactured from Chinese hard coals. Fuel. 2000; 79(11): 1303-1308.
[4] Qiu JS, Zhang F, Han HM, Zhou Y, Hu DS, Tsang SC, Harris PJF. Carbon nanomaterials from eleven caking coals. Fuel. 2002; 81(11-12): 1509-1514.
[5] Qiu JS, Li YF, Wang YP, Wang TH, Zhao ZB, Zhou Y, Li F, Cheng HM. High-purity single-walled carbon nanotubes synthesized from coal by arc discharge. Carbon. 2003; 41(11): 2170-2173.
[6] Yu J, Lucas J, Strezov V, Wall T. Coal and carbon nanotube production. Fuel. 2003; 82(15-17): 2025-2032.
[7] Doherty SP, Buchholz DB, Chang RPH. Semi-continuous production of multiwalled carbon nanotubes using magnetic field assisted arc furnace. Carbon. 2006; 44(8): 1511–1517.
[8] Arora N, Sharma NN. Arc discharge synthesis of carbon nanotubes: Comprehensive review. Diamond and related materials. 2014; 50: 135-150.
[9] Qiu J, Chena G, Li Z, Zhao Z. Preparation of double-walled carbon nanotubes from fullerene waste soot by arc-discharge. Carbon. 2010; 48(4): 1312–1315.
[10] Berkmans J, Jagannatham M, Reddy R, Haridoss P. Synthesis of thin bundled single walled carbon nanotubes and nanohorn hybrids by arc discharge technique in open air atmosphere. Diamond and Related Materials. 2015; 55: 12–15.
[11] Nan Y, Li B, Shen S, Song X. Positive pressure assisted-arc discharge synthesis of single-walled carbon nanohorns. Materials Letters. 2016; 180: 313-316.

To whom correspondence should be addressed Dr. Vladimir Shmalko, Ukrainian State Coal-Chemistry Institute, 61023, 7 Vesnina str., Kharkov, Ukraine; tel.: +3-8050-684-27-01; e-mail: v.shmalko@gmail.com

Petroleum and Coal

Article **Open Access**

SYNTHESIS, CHARACTERIZATION AND THERMAL PROPERTIES OF GREEN ABC MIKTOARM STAR TERPOLYMERS

Rabab M. Nasser, Nehal S. Ahmed, Amal M. Nassar

Egyptian Petroleum Research Institute, Department of Petroleum Applications, Nasr city, Cairo, Egypt

Received March 12, 2018; Accepted April 27, 2018

Abstract

Six (Jojoba-Divinyl Benzene–Alkylacrylate) and five (jojoba–divinyl benzene–α-olefins) ABC miktoarm star terpolymers were prepared by free radical polymerization using (1: 0.2: 1.8) molar ratios. The prepared terpolymers were characterized using FT-IR and ^{1}H-NMR analysis. The weight average molecular weight Mw, the number average molecular weight Mn and the poly-dispersity index PDI were determined from GPC (gel permeation chromatography). Thermal properties (DSC and TGA analysis) of the prepared terpolymers were determined. The morphology of the prepared star polymers were done using SEM (Scanning Electron Microscopy).

Keywords: *Miktoarm Star polymers; jojoba; divinyl benzene; alkylacrylate; thermal analysis; SEM.*

1. Introduction

The preparation of polymers with well-defined forms of branching has posed a challenge to polymer chemists for many years. Star-branched polymers consisting of several linear chains linked together at one end of each chain constitute the simplest form of branching. Perhaps the earliest attempt to synthesize such molecules was that of Shaefgren and Flory [1]; who polymerized e-caprolactam in the presence of either a tetra-functional or an octa-functional carboxylic acid to produce polymers of the type $(R\text{-}CO(NH(CH_2)_5\,CO)n\text{-}OH)_x$ where x = 4 or 8. Another technique has been used which involves divinylbenzene as coupling agent [2-4]. Star-shaped polymers are characterized as structures in which all the chains of a molecule are linked together to a small-molar-mass core. The interest in star polymers arises not only from the fact that they are models for branched polymers but also from their enhanced segment densities [5].

Miktoarm star polymers, in general, are defined as star polymers with at least three arms of molecular weight, chemical or topological asymmetry (Scheme 1) [6]. Various review articles dealing with the synthesis of miktoarm star polymer systems were published during the last two decades, highlighting the interest in such complex materials and their high potential [6-11]. However, in the following, the main focus will be set on ABC miktoarm star terpolymers, which display the corresponding branched analogues of the intensively studied linear ABC triblock terpolymers [12-18].

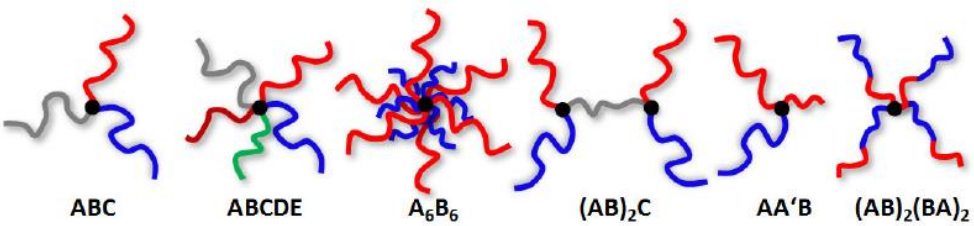

Scheme 1. Examples of miktoarm star polymers with chemical (ABC, ABCDE, A_6B_6, $(AB)_2C$)), molecular weight (AA`B) or topological asymmetry ($(AB)_2(BA)_2$).

In the present work, eleven miktoarm stars branched terpolymers were prepared by free radical polymerization and elucidated using FT-IR, ^{1}H-NMR, and the average molecular weight was determined using GPC. Thermal analysis (DSC and TGA) were determined; while morphologies of polymers surface were determined using SEM.

2. Experimental

2.1. Materials

Divinylbenzene (DVB), 79%, acrylaic acid 97%, octyl alcohol 98.0%, decyl alcohol 99.0%, dodecylaclcohol 98.0%, tetradecyl alcohol 97.0%, hexadecyl alcohol 98.0%, octadecyl alcohol 97%, 1-octene 98%, 1-dodecene 99%, 1-tetradecene, 97 %, 1-hexadecene 99 %, benzoyl peroxide 98%, *p*- toluene sulphonic acid hydrated 97%, *p*- hydroquinone 99% were from Sigma-Aldrich Chemical Company; while jojoba oil was obtained from the Egyptian Company of Natural Oils, Egypt.

2.2. Instrumentation

The molecular weight of the prepared terpolymers was determined by using Agilent GPC/SEC, Germany Poly Strogel, particle size 100, 104, 105A°, using tetra-hydro-furan "THF" as a solvent. Differential scanning calorimetric thermos-grams were recorded using Simultaneous Q-600 DSC/TGA (USA). Calculations were made based on the corrected sample weight. Fourier Transform Infrared (FTIR) spectra were determined using FTIR- spectrometer, Model Type Mattson Infinity series Bench Top 961. ^{1}H-NMR Spectrometer Type (300MHz Spectrophotometer- W-P-300, Bruker), using tetra-methyl silane "TMS" as internal standard and dimethyl sulphoxide "DMSO-D_6" as a solvent. The microscopic characterization of polymers was carried out using scanning electron microscope (JEOL JSM-5410, Japan). The energy of the acceleration beam employed was 30 KV. All micrographs were taken at a magnification power (X 500).

2.3. Methods and procedures

2.3.1. Synthesis of alkylacrylate

Octylacrylate, decylacrylate, dodecylacrylate, tetradecylacrylate, hexadecylacrylate, and octadecylacrylate were prepared as mentioned at literature [19-24].

2.3.2. Synthesis of (Jojoba- DVB- alkylacrylate) miktoarm star terpolymers

In 250mL three necked bottomed flask provided with a magnetic stirrer and N_2 inlet, 1mole of jojoba was added to 0.2mole of DVB and 1.8mole of alkylacrylate; the alkylacrylate used were (octylacrylate, decylacrylate, dodecylacrylate, tetradecylacrylate, hexadecylacrylate and octadecylacrylate) separately, the desired amount of benzoyl peroxide was used at 80±10°C. After the completion of the reaction, the product was poured drop by drop in cooled methanol, filtered off and dry, Scheme 2.

2.3.3. Synthesis of (Jojoba- DVB- α olefins) miktoarm star terpolymers

In 250mL three necked bottomed flask provided with a magnetic stirrer and N_2 inlet, 1mole of jojoba was added to 0.2mole of DVB and 1.8mole of α-olefins; the α-olefins used were (octene, dodecene, tetradecene, hexadecane, and octadecene) separately, the desired amount of benzoyl peroxide was used at 80±10°C. After the completion of the reaction, the product was poured drop by drop in cooled methanol, filtered off and dry, Scheme 3.

3. Results and discussion

Eleven miktoarm terpolymers were prepared by free radical polymerization using jojoba, alkylacrylate, α-olefins and technical grade divinylbenzene DVB, and benzoyl peroxid (BPO) as initiator at 80±10°C. The terpolymers symbol, designation, feed ratio (%), and the actual composition (%) of the prepared terpolymers are given at Table 1.

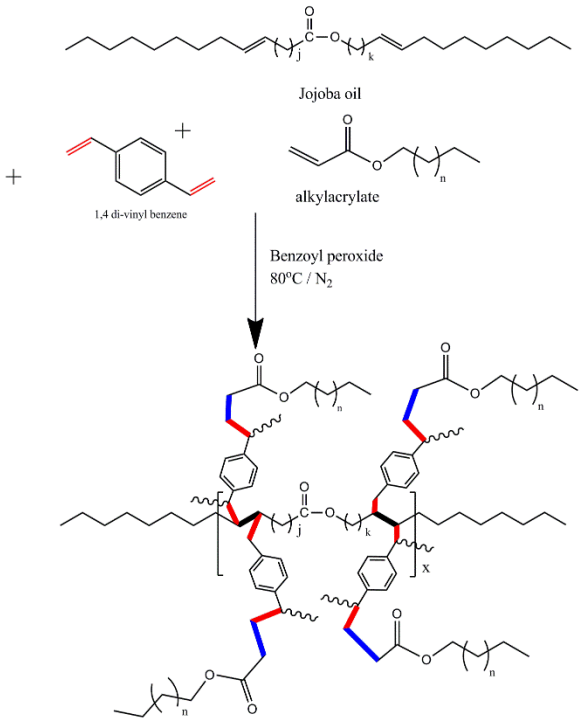

Scheme 2. (Jojoba- DVB- alkylacrylate) miktoarm star terpolymers

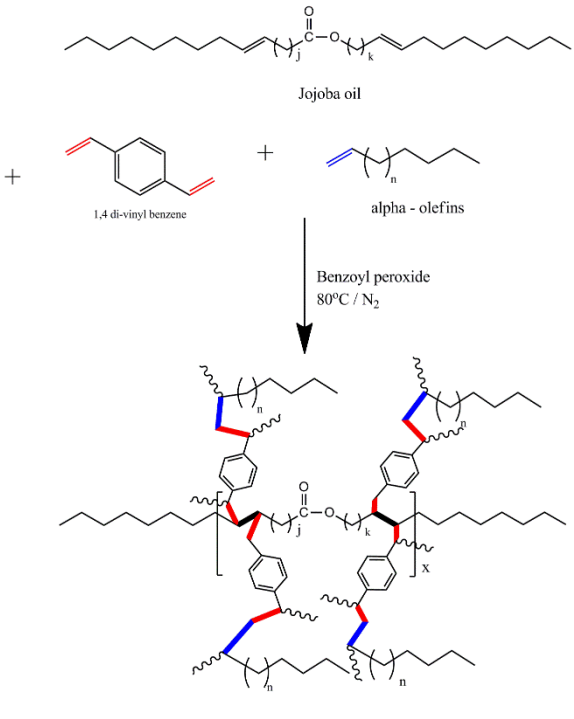

Scheme 3. (Jojoba- DVB- olefins) miktoarm star terpolymers

Table 1. Miktoarm terpolymers symbol, designation, feed ratio (%), and the actual composition (%) of the prepared terpolymers

Symbol	Terpolymer designation	Feed ratio (%)	Terpolymers composition (%)	Symbol	Terpolymer designation	Feed ratio (mole)	Terpolymers composition (%)
A_1	Jojoba: DVB: octylacrylate	33.53: 6.67: 60.00	30: 6.20: 63.80	B_1	Jojoba: DVB: Octene	33.53: 6.67: 60.00	32.12: 6.60: 61.28
A_2	Jojoba: DVB: decylacrylate		27.90: 6.30: 65.90	B_2	Jojoba: DVB: dodecene		30.32: 6.54: 63.14
A_3	Jojoba: DVB: dodecylacrylate		26.12: 6.46: 67.42	B_3	Jojoba: DVB: tetradecene		28.16: 6.42: 65.42
A_4	Jojoba: DVB: tetradecylacrylate		24.68: 6.64: 68.68	B_4	Jojoba: DVB: hexadecane		25.46: 6.20: 68.34
A_5	Jojoba: DVB: hexadecylacrylate		21.86: 6.86: 71.28	B_5	Jojoba: DVB: Octadecene		24.60: 6.12: 69.28
A_6	Jojoba: DVB: octadecylacrylate		20.66: 6.98: 72.36				

3.1. Characterization of the prepared ABC Miktoarm star polymers

The prepared Miktoarm star terpolymers were characterized using GPC (SEC), thermal analysis (DSC and TGA), microscopic characterization (SEM), structural characterization using (^{1}H-NMR and FTIR).

3.1.1. Chromatographic characterization of the prepared terpolymers

The prepared terpolymers were characterized using GPC/SEC chromatography, Table 2. It was found that the molecular weight increase with increasing the chain length of both alkylacrylate and α-olefin used.

Table 2. Mean molecular weight (Mn), average molecular weight (Mw) and poly dispersity index (PDI) of the prepared Miktoarm terpolymers

Terpolymer designation	Mn	Mw	PI	Terpolymer designation	Mn	Mw	PDI
A_1	16660	26656	1.60	B_1	1363	1664	1.22
A_2	18984	31893	1.68	B_2	1412	1765	1.25
A_3	20778	38231	1.84	B_3	1496	1900	1.27
A_4	24556	52059	2.12	B_4	1541	2034	1.32
A_5	27641	67306	2.435	B_5	1583	2216	1.40
A_6	32534	81335	2.5				

3.1.2. Thermal analysis

Thermal analysis refers to a variety of techniques in which a property of a sample is continuously measured as the sample is programmed through a predetermined temperature profile. Among the most common techniques are thermal gravimetric analysis (TGA) and differential scanning calorimetry (DSC) [25].

3.1.2.1. TGA analysis

Jojoba: DVB: alkylacrylate and Jojoba: DVB: α-olefin (33.33: 6.67: 60) miktoarm terpolymers were subjected to thermal degradation in air at heating rate 10°C/min., from room temperature to 700°C and results have been summarized in Tables 3 and 4. Initial degradation temperature (IDT), the temperature at 30%, 50%, 70% decomposition of (A_1-A_6) and (B_1-B_5), and integral procedural decomposition temperature (IPDT, a relative measure of thermal stability) were determined. As noticed from Tables (3, 4), star polymers based on alkylacrylate are more stable than that prepared from α- olefins, and as the chain length increases the thermal stability decrease. It can be explained that as the length of alkyl chain increases in the backbone of C–C bond, the bond dissociation energy of the chain decreases and flexibility of the chain increases thus making the polymeric chain more susceptible towards thermal degradation.

Table 3. Thermal properties of Jojoba: DVB: alkylacrylate terpolymers.

Jojoba %	DVB %	Alkylacrylate %	IDT (°C)	Temperature (°C) at weight loss			IPDT (°C)
				T_{30}	T_{50}	T_{70}	
33.33	6.67	Octylacrylate (60)	310	339	373	397	420
33.33	6.67	Decylacrylate (60)	307	364	387	401	410
33.33	6.67	Dodecylacrylate (60)	306	344	371	388	408
33.33	6.67	Tetradecylacrylate (60)	303	353	379	398	407
33.33	6.67	Hexadecylacrylate (60)	296	371	390	405	406
33.33	6.67	Octadecylacrylate (60)	290	336	366	386	396

Table 4. Thermal properties of Jojoba: DVB: α-olefin terpolymers.

Jojoba %	DVB %	α-olefin %	IDT (°C)	Temperature (°C) at weight loss			IPDT (°C)
				T_{30}	T_{50}	T_{70}	
33.33	6.67	Octene (60)	307	375	392	407	406
33.33	6.67	Dodecene (60)	288	327	370	388	404
33.33	6.67	Tetradecene (60)	141	185	353	388	402
33.33	6.67	Hexadecene (60)	109	195	323	380	400
33.33	6.67	Octadecene (60)	95	262	364	391	388

3.1.2.2. DSC

By studying Figures (1 and 2) there were small endothermic peaks around 370°C-380°C, this is the temperatures which were required to break the polymer backbone, and these prove the stability of the prepared polymers toward thermal degradation.

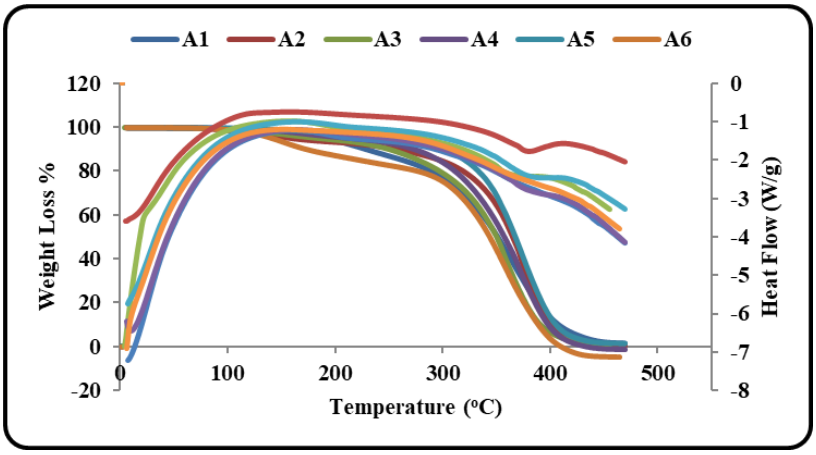

Figure 1. TGA and DSC analysis of (A_1-A_6) star polymers

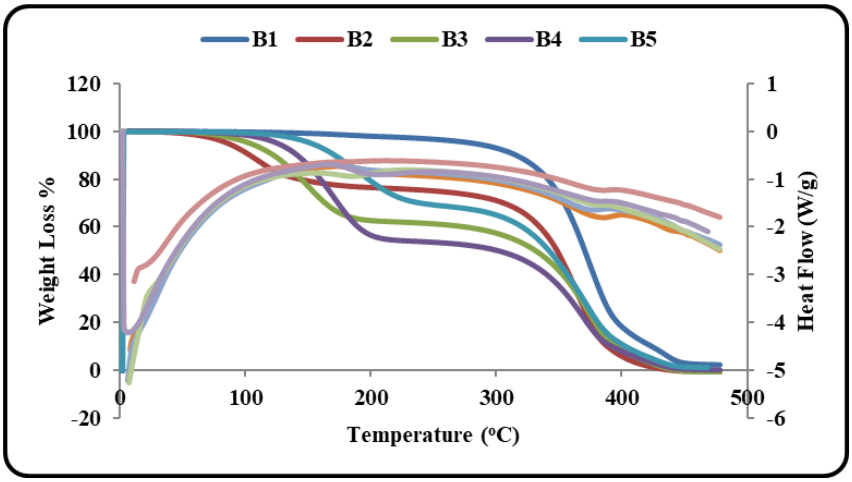

Figure 2. TGA and DSC analysis of (B_1-B_5) star polymers

3.1.3. Surface morphology (SEM)

The prepared star polymers were subjected to surface morphology study by scanning electron microscopy. Terpolymers prepared in the presence of alkylacrylate and α-olefins were cut by a sharp blade at liquid nitrogen temperature, Figure 3.

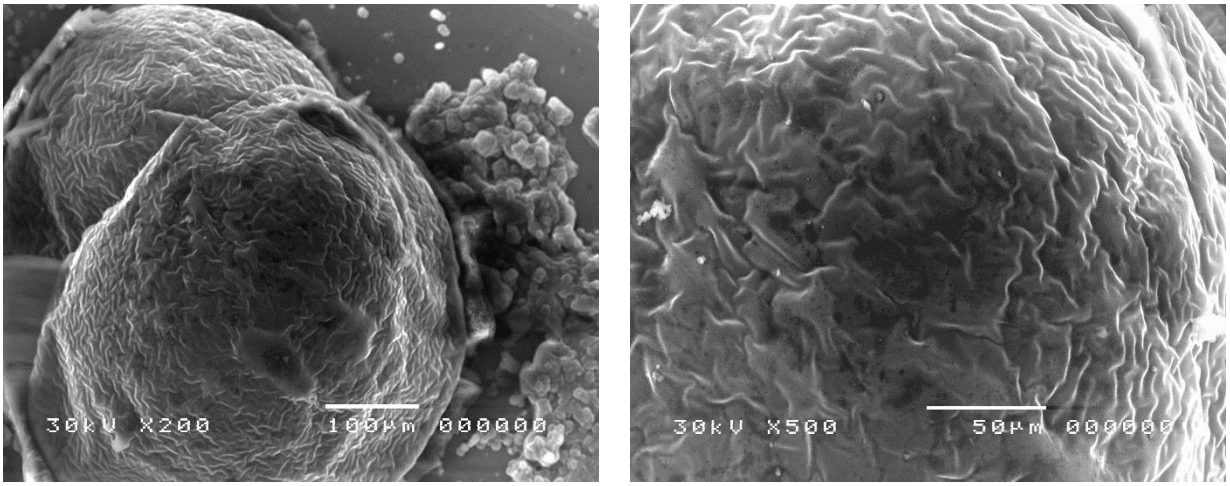

Figure 3. Surface morphology of A_6 miktoarm terpolymer

3.1.4. Structural characterization

3.1.4.1. FT-IR

Characteristic absorption bands of jojoba-DVB-alkylacrylate terpolymers were observed in the FTIR spectra. IR spectra show absorption due to phenyl ring of DVB (aromatic C–H stretching) and aliphatic C–H stretching, characteristics IR peaks of C=O (carbonyl) and C–O–C (esters) confirming the incorporation of alkylacrylates in jojoba chains Sharp peaks of aromatic ring chain vibration, C–O vibration and disubstituted aromatic ring C–H bending vibration was also observed in FTIR spectra of terpolymers Table 5.

Table 5. IR data of the prepared (A_1-A_6) and (B_1-B_5) miktoarm terpolymers

Symbol	Aliphatic (CH –stretching cm^{-1})	Carbonyl stretching cm^{-1})	C-O-C stretching cm^{-1})	Aromatic (C – C stretching cm^{-1})	Ring C-H bending cm^{-1}
A_1	2930	1736	1174	1460	720
A_2	2925	1735	1178	1459	720
A_3	2929	1736	1171	1460	720
A_4	2938	1736	1172	1460	720
A_5	2929	1736	1172	1460	720
A_6	2930	1735	1170	1462	721
B_1	2925	1738	1174	1459	719
B_2	2940	1736	1175	1459	721
B_3	2924	1738	1174	1459	719
B_4	2945	1739	1174	1643, 1460	720
B_5	2925	1739	1174	1640, 1459	721

3.1.5. ^{1}H-NMR

The structure of the prepared miktoarm terpolymers was confirmed by using ^{1}H-NMR, as in Figure 4, ^{1}H-NMR spectrum of (A_1), it was found characteristics peak signals corresponding to (δ-0.90 for ($-CH_3$), δ-4.13 for ($-O-CH_2$), δ-2.53 for – ($CO - CH_2$)) of alkyl acrylate, (δ-2.27 for – ($COO - CH_2$), δ-1.29 for – $(CH_2)_{j \text{ and } k}$ -, δ-0.88 for)of jojoba oil, and peak signals around δ- 7.02-7.25 corresponding to phenyl group of DVB. Figure 5; illustrates the spectrum of B_1 as an example of the olefins star polymers. It was found a characteristic peak signals at δ-0.88 for $-CH_3$, δ-CH_2 – CH_3, δ-1.25 – $(CH_2)_n$-, δ-2.55 –CH-Ph., δ-1.54 – (CH_2- CH- Ph.) (δ-2.27 for – ($COO - CH_2$), δ-1.29 for – $(CH_2)_{j \text{ and } k}$ -, δ-0.88 for)of jojoba oil, and peak signals around δ- 7.02-7.25 corresponding to phenyl group of DVB.

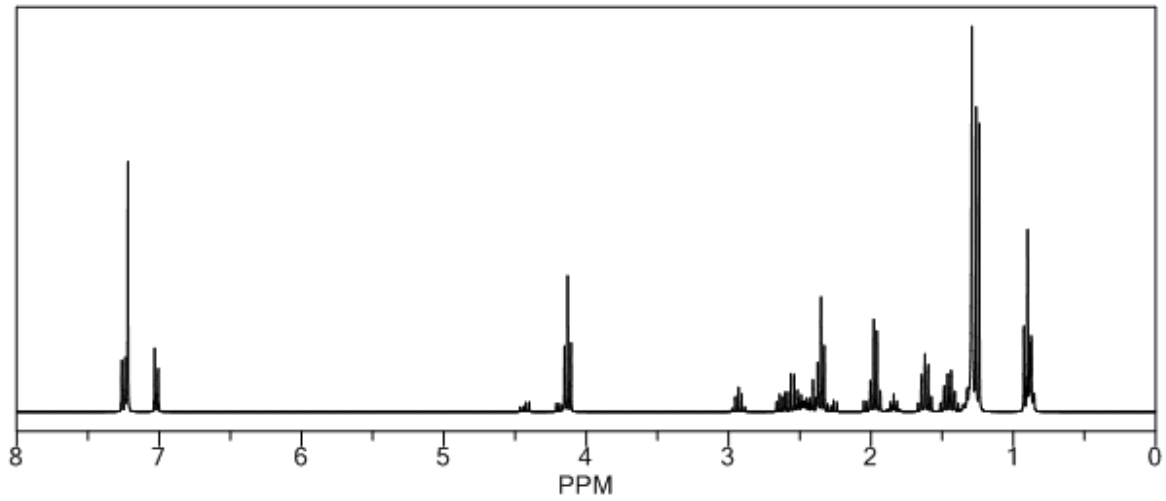

Figure 4. ^{1}H-NMR spectrum of the A_1 terpolymer.

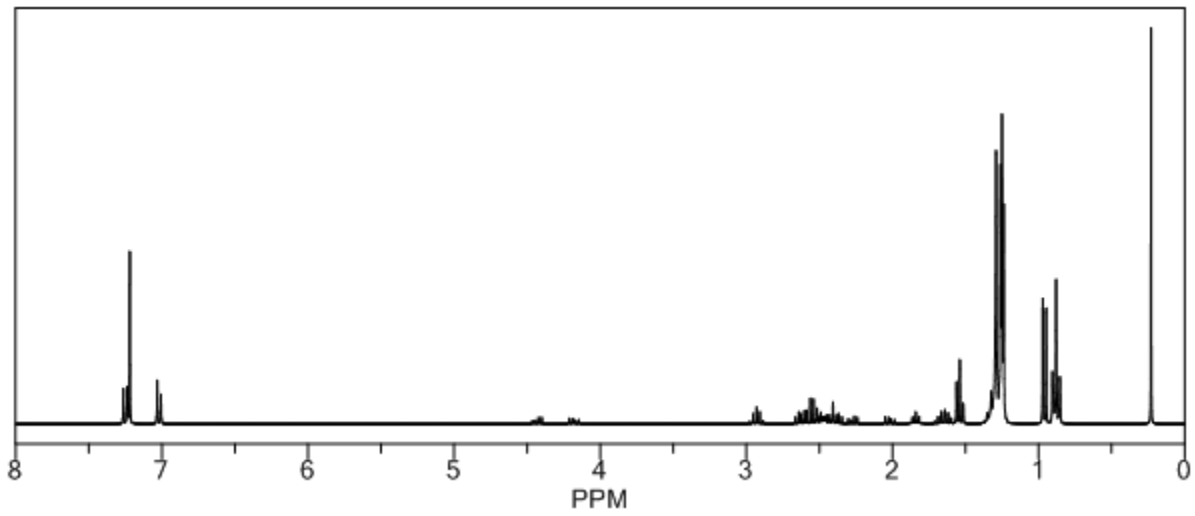

Figure 5. ^{1}H-NMR spectrum of the B_1 terpolymer

4. Conclusion

A green approach for synthesizing eleven miktoarm star terpolymers based on (Jojoba: DVB: alkylacrylate) and (jojoba: DVB: α-olefin) was performed easily (one step reaction), via free radical polymerization using benzoyl peroxide as an initiator, and DVB as tetra-functional cross-linker. The prepared star terpolymers were characterized using GPC/SEC for determination of Mn, Mw, and PDI. The morphological structure was characterized using SEM. Thermal analysis for the prepared star polymers were done, and it was found that they exhibit good thermal stability properties. Star polymers structural characterization was performed by FT-IR and ^{1}H-NMR.

Acknowledgment

We would like to acknowledge Egyptian Petroleum Research Institute, for providing us with chemical and analysis.

References

[1] Schaefgren JR, Flory PJ. J. Am. Chem. Soc.,1948; 70: 2709.
[2] Decker D, Rempp P. C. R. Acad. Sci.,1965; 261: 1977.
[3] Zilliox J-G, Decker D, Rempp P. C. R. Acad. Sci., 1966; 262: 726.
[4] Zilliox J-G, Rempp P, Parrod J. J. Polym. Sci. (Part C), 1968; 22: 145.
[5] Ishizu K, Kitano H, Ono T, Uchida S. Polymer, 1999; 40: 3229–3232.
[6] Hadjichristidis N. J. Polym. Sci., Part A: Polym. Chem., 1999; 37: 857-871.
[7] Hadjichristidis, N, Iatrou H, Pitsikalis M, Mays J. Prog. Polym. Sci., 2006; 31: 1068-1132.
[8] Khanna K, Varshney S, Kakkar A. Polym. Chem., 2010; 1: 1171-1185.
[9] Higashihara T, Hayashi M, Hirao A. Prog. Polym. Sci., 2011; 36: 323-375.
[10] Altintas O, Vogt AP, Barner-Kowollik C, Tunca U. Polymer Chemistry, 2011; 3: 34-45.
[11] Iatridi Z, Tsitsilianis C. Polymers, 2011; 3: 1911-1933.
[12] Breiner U, Krappe U, Stadler R. Macromol. Rapid Commun., 1996; 17: 567-575.
[13] Suzuki J, Furuya M, Iinuma M, Takano A, Matsushita Y. J. Polymer Sci., Part B: Polym. Phys., 2002; 40: 1135-1141.
[14] Erhardt R, Zhang M, Böker A, Zettl H, Abetz C, Frederik P, Krausch G, Abetz V, Müller AHE. J. Am. Chem. Soc., 2003; 125: 3260-3267.
[15] Fukushima S, Miyata K, Nishiyama N, Kanayama N, Yamasaki Y, Kataoka K. J. Am. Chem. Soc., 2005; 127: 2810-2811.
[16] Sperschneider A, Schacher F, Gawenda M, Tsarkova L, Müller AHE, Ulbricht M, Krausch G, Köhler J. Small, 2007; 3: 1056-1063.
[17] Docampo P, Stefik M, Guldin S, Gunning R, Yufa NA, Cai N, Wang P, Steiner U, Wiesner U, Snaith HJ. Adv. Energy Mater., 2012; 2: 676-682.

[18] Hanisch A. Synthesis and self-assembly of novel ABC miktoarm star terpolymers, Ph.D. Dissertation, Bayreuth university, 2013.
[19] Nassar AM, Nasser RM, Khattab AF, and Abdel Azim AAA. Synthesis and evaluation of some polymeric compounds as pour point depressants and viscosity index improvers for lube oil. Petroleum Science and Technology, 2008; 26: 1390-1402.
[20] Ahmed NS, Nassar AM, Nasser RM, Khattab AF, and Abdel- Azim AA. Synthesis and Evaluation of Some Polymers as Lubricating Oil Additives. Journal of Dispersion Science and Technology, 2012; 33: 668-675.
[21] Ahmed NS, Nassar AM, Nasser RM, Raouf MEA, and El-Kafrawy AF. Novel Terpolymers as pour point depressants and viscosity modifiers for lube oil. Journal of Petroleum Science and Technology, 2014; 32: 680-687.
[22] Ahmed NS, Nassar AM, Nasser RM, Raouf MEA and El-Kafrawy AF. The rheological properties of lube oil with terpolymeric additives. Journal of Petroleum Science and Technology, 2014; 32(17): 2115 – 2122.
[23] Nasser RM. The Behavior of Some Acrylate Copolymers As Lubricating Oil Additives. OmniScriptum GmbH &Co.KG, Germany, ISBN:978-3-659-31639-5, (2015).
[24] Nasser RM. Synthesis and Evaluation of Some Lubricating Oil Viscosity Index Improvers and Pour Point Depressants. OmniScriptum GmbH &Co.KG, Germany, ISBN:978-3-330-33270-6, (2017).
[25] Cheremisinoff NP. Polymer Characterization Laboratory Techniques and Analysis; Chapter 2, Noyes Publications, USA, 1996.

To whom correspondence should be addressed Dr. Rabab M. Nasser, Egyptian Petroleum Research Institute, Department of Petroleum Applications, Nasr city, Cairo, Egypt, rabab_nasser@yahoo.com

Petroleum and Coal

Article **Open Access**

PAINT MATERIALS BASED ON PETROLEUM RESINS

Vladimir G. Bondaletov, Lyudmila I. Bondaletova, Nguyen Van Thanh*

School of Earth Sciences & Engineering, Tomsk Polytechnic University, Russia

Received March 22, 2018; Accepted May 31, 2018

Abstract

Petroleum resins synthesized by ionic polymerization (catalyst – $TiCl_4$-$Al(C_2H_5)_2Cl$) of different fractions of liquid pyrolysis products have been modified using peracetic acid prepared as a product of *in situ* reaction between hydrogen peroxide and acetic acid in the presence of sulfuric acid.

This modification leads to the introduction of the following polar groups into the resin: carboxyl (acid number 3.7-16.8 mg/g) and epoxy (epoxy number 2.9-8.9 %) groups. It has been shown that initial and modified petroleum resins are suitable for the formation of paint and varnish coatings. Modified resin coatings have improved elasticity and increased adhesion to metal surfaces and can be used as a part of bitumen-resin compositions.

Keywords: *fraction of liquid pyrolysis products; petroleum resin; modification, bitumen, bitumen-resin composition.*

1. Introduction

A promising direction of utilization of petrochemical industry waste or by-products is their use in the synthesis of new organic compounds. By-products of pyrolysis plants with ethylene and propylene as their target products contain 30-50 % of unsaturated compounds, so their prospective processing is polymerization with the formation of petroleum polymer resins (PR). A distinctive feature of the petroleum resin production is that the industry's by-products (feedstock for polymerization) have a complex composition. The feedstock contains a significant amount of differently structured monomers that have different reactivity in a mixture with unpolymerizable hydrocarbons. Thus, the synthesis of PR represents the copolymerization process of monomers in solution [1].

The by-products of pyrolysis plants, the so-called liquid pyrolysis products, are divided into narrow fractions of saturated, unsaturated and aromatic hydrocarbons. The composition of different fractions varies considerably depending on the pyrolysis conditions and the type of raw material used in the pyrolysis process. The hydrocarbon fraction C_5 (initial and final boiling point of 25-35°C and 70-75°C respectively) contains a considerable amount of diene monomers (isoprene, cyclopentadiene, pentadienes, etc.). Their content varies within a fairly wide range, which is explained by different conditions of sampling and storage of fractions. In the higher-boiling fraction C_9 (initial and final boiling point of 120-125°C and 200-205°C respectively) reactive arylalkenes and dicyclopentadiene are present. In accordance with the classification of PR, aliphatic resins are obtained in the polymerization of unsaturated hydrocarbons of the C_5 fraction, aromatic resins – of the C_9 fraction, copolymer resins –of the C_5 and C_9 fractions. Copolymer resins can also be obtained by polymerization of unsaturated hydrocarbons of wide C_{5-9} fraction (initial and final boiling point of 25-35°C and 200-205°C respectively). The properties of resins produced from different fractions vary significantly. Aromatic resins in comparison with aliphatic resins have a higher density, softening point, heat resistance and lower bromine number, which determines the unsaturated nature of the resins. Copolymer resins obtained by copolymerization of aliphatic and alkenyl aromatic monomers contained in C_5 and C_9 fractions respectively occupy an intermediate position according to their properties [2].

One of the drawbacks that limit the use of PR in the composition of polymer materials is their poor compatibility with many, usually polar, substances. This property is explained by the absence of functional groups in the resin structure. Therefore, the development and implementation of new types of resins and, above all, modified ones is an urgent task at present.

Modified petroleum resins are obtained by copolymerization [3-4] of liquid pyrolysis product fractions and polar monomers (vinylacetate, maleic anhydride, acrylic, methacrylic and other α, β-unsaturated acids, methyl methacrylate, butyl methacrylate, acrylonitrile) or by treatment [5] of the petroleum resins with chemical agents (oxygen, ozone, hydrogen peroxide, α, β-unsaturated dicarboxylic acids and anhydrides). The most common method of the PR functionalization is oxidation. The presence of unsaturated bonds in the PR composition makes it possible to use them in the process of oxidation by hydrogen peroxide according to the Prilezhaev's reaction [6]. Thus, the modification of aliphatic and aromatic resins with hydrogen peroxide by the Prilezhaev's reaction leads to the introduction of carboxyl and epoxy groups into their composition and to the decrease in the overall unsaturation of the resins, which entails a change in the properties of paint coatings based on them.

Petroleum resins as film-forming agents hold a special place among synthetic vegetable oil substitutes in the paint and varnish industry and are widely used in the development of oil-resin or bitumen-resin compositions. The developed polymerization methods and the different compositions of the initial fractions of liquid pyrolysis products determine the variety of chemical structures and properties of the resins. Therefore, different types of PR have different properties as film-forming substances.

Consequently, the purpose of this paper is to study the technical characteristics of paint coatings based on the initial and modified resins obtained by polymerization of the C_5, C_9, C_{5-9} fractions and the dicyclopentadiene fraction, and to study the possibility of using these resins as part of bitumen-resin compositions.

2. Experimental

2.1. Objects of research

The object of the study is petroleum resin obtained by polymerization of unsaturated compounds of various hydrocarbon fractions: C_5 fraction (boiling point of 30-70°C), C_9 fraction (boiling point of 110-190°C), C_{5-9} wide fraction of hydrocarbons (boiling point of 30-190°C) and enriched with dicyclopentadiene fraction (DF, boiling point of 110-190°C). The polymerization of unsaturated compounds of the fractions was carried out in a solution of saturated hydrocarbon under the action of the $TiCl_4$-$Al(C_2H_5)_2Cl$ catalyst system. $TiCl_4$ concentration was 2 %, the component ratio of the catalytic system was 1: 1. The process temperature was maintained at 80°C, and the process duration was 2 hours. Polymerization of high-boiling fractions (C_9, DF) was carried out at atmospheric pressure, polymerization of fractions C_{5-9} and C_{5-9} – at a pressure of 0.13 MPa. The catalytic system was deactivated with propylene oxide at the end of the process; the reaction product was kept in the composition of the obtained resins.

The modification of petroleum resins (PR_{C5}, PR_{C5-9}, PR_{C9}, PR_{DF}) synthesized on the basis of different fractions (C_5, C_{5-9}, C_9, DF) was carried out with peracetic acid obtained *in situ* at an equimolar ratio of hydrogen peroxide and acetic acid in the 30 % toluene solution of the resin. The process duration was 3 hours; the process temperature was 70-75 °C. The weight ratio of resin to the oxidative system was 1 to 0.25. At the end of the process, the reaction mass was washed from acid impurities, and the resin was isolated by removal of the solvent [7].

BN 90/10 bitumen was used (GOST 6617-76 "Petroleum construction bitumens. Technical specifications"). The bitumen-resin composition was prepared by mixing 40 % bitumen solutions and 40 % resin solutions (solvent – xylene).

2.2. Methods of research

The functional numbers of the modified resins (MPR_{C5}, MPR_{C5-9}, MPR_{C9}, MPR_{DF}) were determined by standard methods [8].

The paint coatings were obtained on metal plates (plate size – 9 x 16 x 0.1 cm), using a core applicator for liquid paint materials. The metal plates had been cleaned and degreased by gasoline and acetone beforehand.

The thickness of the liquid paint material was monitored with the "Measuring comb" instrument, the thickness of the dry paint material (the paint coating) with the "Thickness gauge-pencil Constant M1" instrument. The coating was dried in air, and then the strength characteristics were determined. The thickness of the bituminous or bituminous coatings was 100-140 μm, the resin coating thickness – 20-25 μm.

The adhesion strength of the coating was measured by the detachment method with the "Adhesimeter OR" device (GOST 32299-2013 (ISO 4624: 2002) "Paint materials. Pull-off test for adhesion") or by the method of lattice incisions (GOST 15140-78 "Paintwork materials. Methods for determination of adhesion").

The bending strength of coatings was determined in accordance with GOST R 52740-2007 (ISO 1519-2002) "Paints materials. Method for determination of film strength while bending around cylindrical mandrel". This property characterizes the elasticity of coatings.

The impact strength of coatings was measured in accordance with GOST R 53007-2008 "Paint materials. Rapid deformation (impact resistance) test method".

The hardness test was performed according to ISO 6441-2 : 1999 "Paints and varnishes. Determination of micro-indentation hardness. Part 2: Knoop hardness by measurement of indentation depth under load".

The water absorption measurement of the coating was carried out according to GOST 21513-76 "Paint materials. Methods for determination of paint film. Water- and moisture absorptivity".

The wetting angle was determined on a Drop Shape Analyzer DSA 25-Kruss by the drop method at 25°C. The bitumen, resins or their bitumen compositions were dissolved in toluene at a material: solvent ratio of 1: 1.5.

3. Results and discussion

The analysis of scientific and patent literature on the PR application in the paint and varnish industry shows that there is high demand for them due to the availability of raw materials (petrochemical industries by-products containing unsaturated hydrocarbons) and their low cost. The application of PR in paint and varnish materials allow to effectively save the deficient monomers or the vegetable oils used to produce film-forming.

The advantages of using PR as paint materials include water resistance, acid-, salt- and alkali-inertness, high binding and adhesive capacity, good solubility in many solvents, high drying speed and coating hardness. The disadvantages are low light and weather resistance, brittleness, insufficient strength and adhesion characteristics, poor compatibility with drying or semi-drying oils and other polar substances. These disadvantages are eliminated by means of the introduction of polar groups or during the preparation of composite materials using low molecular weight, oligomeric and polymeric plasticizers: for example, phthalic and phosphoric acid esters, paraffin, waxes, transformer oils [9], low molecular weight or oxidized rubbers [10].

In the present work, petroleum polymer resins (PR_{C5}, PR_{C5-9}, PR_{C9}, PR_{DF}) obtained by polymerization of unsaturated compounds of various hydrocarbon fractions and modified resins (MPR_{C5}, MPR_{C5-9}, MPR_{C9}, MPR_{DF}) obtained by oxidation with peracetic acid obtained *in situ* by the Prilezhaev's reaction were used. Characteristics (functional numbers) of the initial and modified petroleum resins – bromine number (BN, g/100 g), acid number (AN, mg/g), epoxy number (EN, %)) are given in Tab. 1.

The modification leads to a decrease in the unsaturated nature of the resins and the introduction of polar (carboxyl and epoxy) groups in the polymer chain. The multicomponent composition of the initial fractions and different reactivity of the monomers in the polymerization process do not allow a strict correlation between the structure of PR_{C5}, PR_{C5-9}, PR_{C9}, PR_{DF}, MPR_{C5}, MPR_{C5-9}, MPR_{C9}, MPR_{DF} and functional numbers of the initial and modified petroleum resins.

Table 1. Functional numbers of initial and modified petroleum resins

Characteristics	Functional numbers of initial and modified petroleum resins			
	PR_{C5}	PR_{C5-9}	PR_{C9}	PR_{DF}
Bromine number, g/100 g	27.2	19.0	33.2	32.3
Acid number, mg/g	0.7	0.6	0	0
Epoxy number, %	0	0	0	0
	MPR_{C5}	MPR_{C5-9}	MPR_{C9}	MPR_{DF}
Bromine number, g/100 g	14.8	2.6	14.2	13.6
Acid number, mg/g	3.7	14.6	10.1	16.8
Epoxy number, %	5.0	2.9	8.2	8.9

Properties of coatings derived from 40 % solutions of initial and modified resins in toluene are given in Tab. 2.

Table 2. Properties of coatings based on initial and modified resins

Characteristics	Properties of coatings based on initial and modified resins			
	PR_{C5}	PR_{C5-9}	PR_{C9}	PR_{DF}
Adhesion, points	2	2	3	3
Adhesion, MPa	1.0	1.2	0.8	0.9
Impact strength, cm	5	5	2	5
Bending strength, mm	3	1	3	3
Hardness, kg	0.2	0.2	0.7	0.2
Water absorption, %	0.5	0.3	0.6	0.5
	MPR_{C5}	MPR_{C5-9}	MPR_{C9}	MPR_{DF}
Adhesion, points	1	1	2	1
Adhesion, MPa	1.4	1.5	1.0	1.5
Impact strength, cm	10	10	4	10
Bending strength, mm	1	1	1	1
Hardness, kg	0.2	0.4	0.8	0.2
Water absorption, %	0.5	0.1	0.6	0.5

The test results showed that the type of resin affects the coating properties, but this effect is insignificant. For example, aromatic resins (PR_{C9}, MPR_{C9}) are more brittle and have lower adhesion values, but they are harder. In general, the results (Table 2) indicate an improvement of adhesion and strength properties (impact and bending strength) of coatings based on modified resins (MPR_{C5}, MPR_{C5-9}, MPR_{C9}, MPR_{DF}).

The improvement of adhesion properties is directly related to the change in the wetting angle (Tab. 3, Figure 1). Adhesion characterizes the interfacial interaction, as a result of the desire of the system to reduce surface energy. A quantitative measure of the interfacial interaction of a material with a metal surface is adhesion work, determined by the Dupre-Young equation [11]:

$$Wa = \sigma \cdot (1 + \cos\theta),$$

where: *Wa* – the adhesion work, mN/m^2; σ – the surface tension of the material at the boundary with air, mN/m^2; θ –the wetting angle.

According to the above equation, the adhesion work increases with a decrease in the wetting angle, hence, the adhesion of the material to the metal surface increases.

Thus, a decrease in the wetting angle with the use of modified resins naturally leads to an increase in adhesion (Table 2, 3).

Table 3. Wetting angle values

Wetting angle values, degree			
PR_{C5}	PR_{C5-9}	PR_{C9}	PR_{DF}
8.6	9.2	11.1	8.5
MPR_{C5}	MPR_{C5-9}	MPR_{C9}	MPR_{DF}
7.4	8.3	9.9	8.2

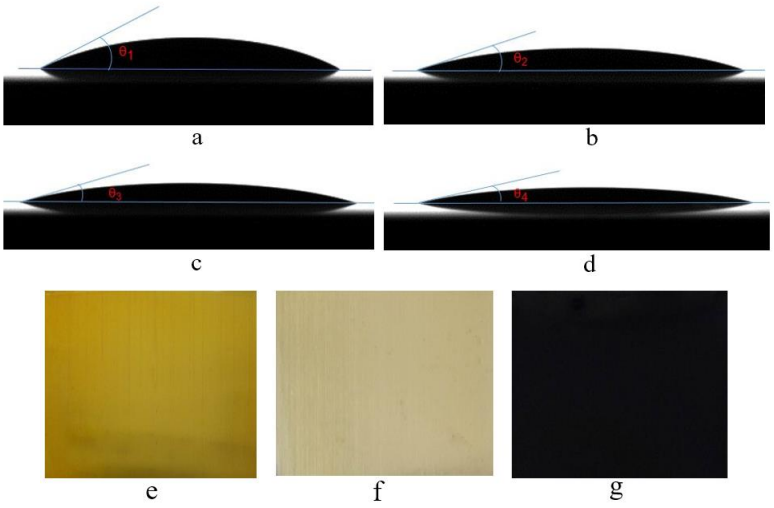

Fig. 1. Wetting angle by solutions of bitumen (a), bitumen-MPR$_{C9}$ resin composites (b), initial PR$_{C9}$ resin (c), modified MPR$_{C9}$ resin (d) and surface view of initial PR$_{C9}$ resin (e), modified MPR$_{C9}$ resin (f), bitumen-MPR$_{C9}$ resin composite (g)

As an independent film-forming compound or in combination with vegetable oils, natural resins or synthetic film-forming agents, bitumen is used in paintwork materials [12]. Previously rosin and products of its processing (natural resins) in combination with bitumen were mainly used, but at present, such materials are practically not applicable in industry. Natural materials (rosin, vegetable oils, etc.) in the bituminous composites are replaced with synthetic polymers without deterioration of the composite properties. The oil-free bituminous varnishes are divided into bitumen composite, which consists of bitumen and solvent, and bitumen-resin composite, which is a mixture of the bitumen and resin solution. The bituminous varnish is the basis for the production of the paint coating, which is reliable anticorrosive protection for metal surfaces and has good conservation properties at a reasonably low cost.

Initial and modified resins can also be used to prepare bitumen-resin composites. Examples of main properties of bituminous paint coatings, which contain 90% bitumen and 10% resin, are given in Tab. 4.

Table 4. Bitumen-resin coating properties

Characteristics	Properties of bitumen-resin coatings based on initial or modified petroleum resins				
	Bitumen – PR	Bitumen – PR$_{C5}$	Bitumen – PR$_{C5-9}$	Bitumen – PR$_{C9}$	Bitumen – PR$_{DF}$
Composition, %	100 – 0	90 – 10	90 – 10	90 – 10	90 – 10
Adhesion, points	1	1	1	1	1
Adhesion, MPa	2.4	2.7	2.7	2.1	2.8
Impact strength, cm	35	40	42	50	35
Bending strength, mm	1	1	1	1	1
Hardness, kg	0.2	0.4	0.4	0.4	0.3
Water absorption, %	0.8	0.1	0.1	0.1	0.1
	Bitumen – MPR	Bitumen – MPR$_{C5}$	Bitumen – MPR$_{C5-9}$	Bitumen – MPR$_{C9}$	Bitumen – MPR$_{DF}$
Composition, %	100 – 0	90 – 10	90 – 10	90 – 10	90 – 10
Adhesion, points	1	1	1	1	1
Adhesion, MPa	2.3	2.8	2.9	2.1	2.8
Impact strength, cm	35	45	47	50	45
Bending strength, mm	1	1	1	1	1
Hardness, kg	0.2	0.3	0.4	0.5	0.4
Water absorption, %	0.8	0.1	0.1	0.1	0.1

Higher adhesion values of coatings containing modified resins in comparison with coatings based on initial resins are well correlated with the wetting angle values of the metal surface with bitumen-resin composite solutions (Tab. 5, Fig. 1).

Table 5. Wetting angle values with bitumen-resin solutions (90 % bitumen, 10 % resin)

Wetting angle values, degree				
Bitumen	Bitumen – PR_{C5}	Bitumen – PR_{C5-9}	Bitumen – PR_{C9}	Bitumen – PR_{DF}
19.9	14.1	14.4	17.3	14.3
Bitumen	Bitumen – MPR_{C5}	Bitumen – MPR_{C5-9}	Bitumen – MPR_{C9}	Bitumen – MPR_{DF}
19.9	12.1	12.7	14.9	13.1

4. Conclusions

1. Initial petroleum resins were synthesized by ionic polymerization of unsaturated compounds of various liquid pyrolysis product fractions with $TiCl_4$-$Al(C_2H_5)_2Cl$ catalyst system. These resins were then further modified.
2. Resin modification with peracetic acid obtained *in situ* results in the introduction into the resin of polar groups: carboxyl (acid number 3.7-16.8 mg/g) and epoxy (epoxy number 2.9-8.9 %).
3. Initial and modified resins are suitable for obtaining paint and varnish coatings. It has been shown that coatings based on modified resins have increased adhesion to metal surfaces (1.0-1.5 MPa) and improved elasticity (bending strength – 1 mm) as compared to coatings based on initial resins (adhesion – 0.8-1.2 MPa, bending strength – 3 mm)

Obtained resins can be used in the bitumen-resin compositions to improve the protective coatings properties

References

[1] Zohuriaan-Mehr MJ, Omidian H. J. Macromol. Sci. Rev. Macromol. Chem. Phys., 2000, C 40 (1): 23.
[2] Dumskii YuV, No BI, Butov GM: Khimiya i Technologiya Neftepolimernikh Smol; Khimiya: Moskva, 1999.
[3] Shikhalizade PD, Aliev SM, Metkhiev SI, Muradova MO. Azerbaijan Chemical Journal 1977; 3: 58.
[4] Sutyagin VM, Bondaletov OV, Fiterer EP, Bondaletov VG, Bondaletova LI, Grigoreva ON: Izvestiya Vysshikh Uchebnykh Zavedeniy. Seriya "Khimiya I Khimicheskaya Tekhnologiya" 2009; 52(5): 98.
[5] Sukhov VD, Krasnobaeva VS, Demina EN, Ermilova TA, et a.: Lakokrasochnie materialy I ikh primenenie. (Russian Coatings Journal), 1989; 2: 45.
[6] Prilezhaeva YeI: Reaktsiya Prilezhaeva. Elektrofilnoye okisleniye; Nauka: Moskva, 1974.
[7] Bondaletov V, Bondaletova L, Nguyen Van Thanh, Prokopyeva T. Pet Coal, 2016; 58(5): 578.
[8] Odabashyan GV: Laboratornyj praktikum po himii i tekhnologii osnovnogo organicheskogo i neftekhimicheskogo sinteza; Khimia: Moskva, 1978.
[9] Ignatyuk VP, Lapina VA, Poddubnii AK: Lakokrasochnie materialy I ikh primenenie (Russian Coatings Journal) 1989, 1, 7.
[10] Ryazanova TA, Selivanova MP, Mogilevich MM, et al. Lakokrasochnie materialy I ikh primenenie (Russian Coatings Journal) 1985; 1: 6.
[11] Frolov YuG: Kurs kolloidnoj himii. Poverhnostnye yavleniya i dispersnye sistemy; Khimiya: Moskva, 1988.
[12] Gun, R.B.: Petroleum bitumens; Khimiya: Moskva, 1973.

To whom correspondence should be addressed: prof. Dr. Lyudmila I. Bondaletova, School of Earth Sciences & Engineering, Tomsk Polytechnic University, 30, Lenin Avenue, Tomsk, 634050, Russia; tel.: (+7-3822) 606-121; fax: (+7-3822) 564-320; e-mail: bondli@tpu.ru

Petroleum and Coal

Article **Open Access**

SIMULATION STUDIES ON NATURAL GAS SWEETENING USING PIPERAZINE AMINE

Nagamalleswara Rao K[1], Babu Ponnusami A[2]*

[1] *Centre for Disaster Mitigation and Management, VIT University, Vellore, Tamilnadu, India*
[2] *Department of Chemical Engineering, School of Civil and Chemical Engineering, VIT University, Vellore, Tamilnadu, India*

Received March 24, 2018; Accepted May 31, 2018

Abstract
This work aims at studying acid gas removal from natural gas with piperazine (PZ) amine by using Aspen HYSYS V9.0. Design of acid gas removal process is explained using sensitivity analysis. Plant capacity enhancement studies are performed by considering the crucial parameters like sour gas feed rate, amine recirculation rate and regenerator reboiler duty etc. The optimum feed temperature is identified as 31^0C. Optimum concentration and flow rate of amine is 30 wt% and 350 m^3/hr respectively. Rigorous hydraulic studies are performed for absorber to know the operational issues like flooding and weeping in the column. Arranging the packing in the absorber solved the operational issues and improved the CO_2 and H_2S removal efficiencies by 58% and 20% respectively. By arranging packing revenue losses are minimized by 2.1%. The techno-economic analysis results of this study are useful for process engineers working in gas plants to take reasonable decisions in operating the gas plant.

Keywords: *Acid gas; Gas plant; Hydraulic studies; Natural gas; Sensitivity analysis; Process Simulation; Gas Sweetening.*

1. Introduction

The worldwide market for liquefied petroleum gas (LPG) and natural gas liquids (NGL) is continuously increasing [1]. Presence of H_2S, CO_2, mercaptans, CS, elemental sulfur and contaminated water decreases the quality of sales gas and their presence is not acceptable, since they corrodes the equipment, pipelines and release in to atmosphere leads to acid rains [2]. Chemical solvents, physical solvents, adsorption processes, hybrid solvents and physical separations especially membranes are the available acid gas removal techniques [3]. According to the environmental regulations the acceptable limits for H_2S and CO_2 are 4 ppm and 2 mole % respectively.

Aspen HYSYS V9.0 acid gas removal model supports various amines in its data base [4]. Continuous investigations are going on to invent the new efficient amines and their blends for efficient removal of CO_2 from gas mixtures. Piperazine is one of the amine [5]. Bishnoi *et al.* [6] conducted modelling experiments and revealed that the carbon dioxide removal rate is more for PZ amine compared to the other amines like MDEA, MEA, DEA and their blends. Kinetic studies by [7], VLE studies by [8], absorption studies by [9-11], high pressure absorption studies by [12] concluded that piperazine in alone and in combination with methyldiethanolamine has reported improved absorption rates of CO_2 from aqueous solutions. Aqueous solutions containing piperazine is used as washing agent for removing H_2S, CO_2 and COS present in natural gas, coke-oven gases, and synthesis gases [13]. Configurations and methods of acid gas removal to meet the pipe line requirements are explained by [14]. A process for removal of H_2S and CO_2 from an acid gas stream is explained by [15-16] using various amines.

Silhavy *et al.* [17] provided simulation based operational data base for acid gas removal plant. The author [18-20] conducted numerical simulation and optimization studies using process simulators like Aspen HYSYS. In their studies they used diethanol amine for acid gas removal. Similarly, the autors [21-22] used MEA. Pellegrini *et al.* [23] used diethanolamine (DEA)

and methyldiethanolamine (MDEA), Kazemi *et al.* [24] used mixed amines and checked the feasibility of the process by improving the acid gas removal efficiency. The authors [25-26] tested impact of operating conditions like absorption temperature, pressure, number of absorber trays and solvent recirculation rate on acid gas removal are tested to identify the optimum conditions. The authors [27-28] identified optimum conditions from the steady state and dynamic studies and these observations are useful for safety and economy of the processes. Øi *et al.* [29] tested alternative flow sheet arrangements in improving the acid gas removal rates. Zare Aliabad *et al.* [30] used MDEA and DEA amines in combined form and studied the effect of major operating parameters like operating pressure of the absorber column, temperature of the amine, sour gas feed rate and morpheme efficiency, on the rate of absorption and on energy point of view [31]. Optimization studies are conducted by [32] for optimum absorber working pressure to get 99% purity of the methane.

The above studies motivated the present research to do acid gas removal using piperazine (PZ) amine from natural gas. Objective of this work is to analyse the effect of process parameters like amine temperature, feed gas flow rate on acid gas removal and to check the role of column hydraulic studies in improving the acid gas removal efficiency and feasibility. This work is useful for process engineers to optimize their gas processing units and to take decisions on retrofit studies.

2. Process description

Equipment involved in the Aspen HYSYS V 9.0 acid gas cleaning simulation model are: extractor, absorber, separator, rich amine heater, regenerator, lean amine cooler, booster pump and makeup operation. Process flow sheet is shown in figure 1. In the extractor contaminants are removed by passing the acid gas through the amine solution. In the absorber sour gas is passed through the bottom and the lean amine enters from the top of the absorber as a result of absorption, sweet gas comes out from the top of the absorption column and the rich amine comes out from the bottom part of the absorber. Rich amine obtained from the absorber column bottom, is send to the separator. In the separator low hydrocarbons are removed and the remaining rich amine is send to the regenerator. In the regenerator, sufficient heat is provided by the reboiler for the separation of impurities present in the amine solution. Separated hydrogen sulfide (H_2S) and carbon dioxide (CO_2) are sent for processing. Losses in amine quantities are makeup using the make-up block.

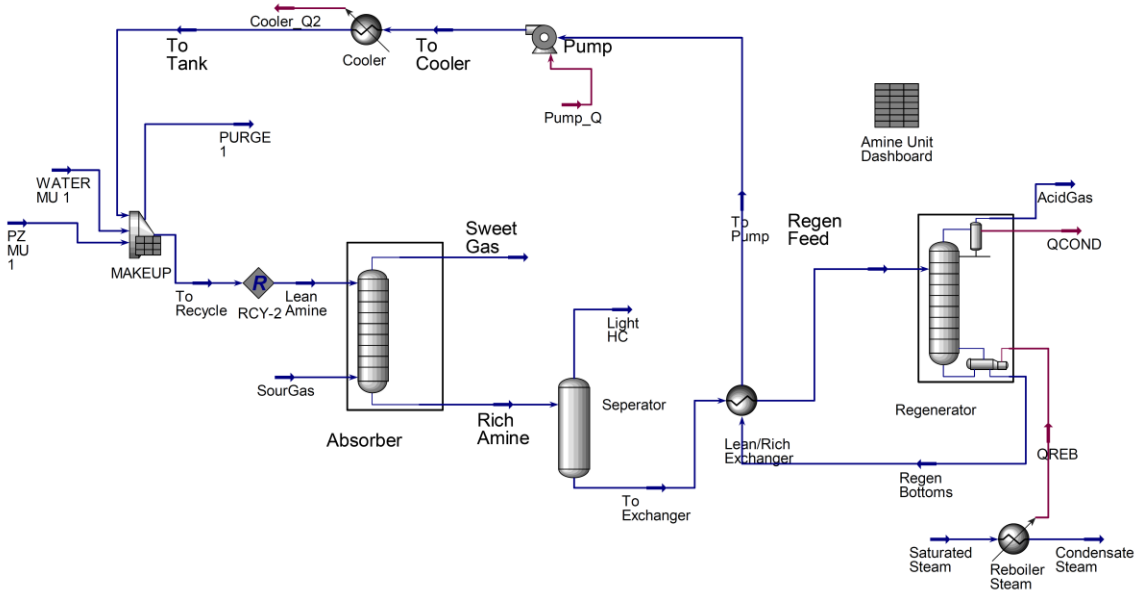

Figure 1. Aspen HYSYS acid gas cleaning flow sheet

3. Process simulation

The flow sheet for natural gas sweetening using PZ was developed in Aspen HSYS V9.0. The fluid package used in this study is acid gas cleaning package. The composition of the sour gas is given in table 1. The design capacity of this process plant is 1128 m^3/hr or 1.703×10^5 barrel/day. Sour gas feed enters at 40^0C and 20 bar pressure is feed to the bottom of the absorber.

Absorber contains 20 number of stages. Lean amine is entering the top of the absorber and its concentration is 30 wt% and temperature 42^0C. Lean amine temperature is higher than the sour gas temperature. When the sweetening process is completed and the regenerated piperazine (PZ) is recycled back to the absorber, Aspen HYSYS recalculates the actual operating composition. In makeup block aspen HYSYS, ADJUST operation is the inbuilt operation and it adjusts the circulation rate of lean amine.

Table 1. Feed gas composition of sour gas

Component	Mole fraction	Component	Mole fraction
CO_2	0.0202	Ethane	0.0707
H_2S	0.0202	Nitrogen	0.0303
Methane	0.8656		

Sensitivity analysis studies are conducted using various process parameters like feed gas flow rate, feed gas temperature, amine recirculation rate to calculate the composition of the acid gases in sweet gas. Desirable concentrations of CO_2 and H_2S in sweet gas will be maintained by optimizing the reboiler duty and the recirculation rate of the amine in the surge tank. Hydraulic studies for the absorber are conducted to improve the performance of absorber. Packing material is used as a substitute for trays to avoid the hydraulic problems in the column. Acid gas removal and the economic study values of the both tray column and packed column are compared.

4. Results and discussion

4.1. Effect of PZ amine concentration

Increasing concentrations of PZ amine in lean amine stream positively affected the acid gas removal. Figure 1 illustrates the effect of varying concentrations of PZ on extraction of CO_2 and H_2S. From 10 to 30 wt% of PZ amine concentration, acid gas removal is good. It indicates the desired concentration of PZ is 30 wt%. At 30 wt% of PZ concentration, acid gas concentration in sweet gas is 1.51×10^{-4} mole% for CO_2 and 0.0198 ppm for H_2S.

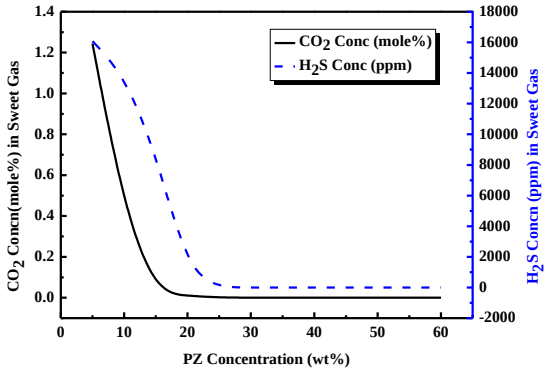

Figure 1. Effect of PZ concentration on acid gas concentration in sweet gas

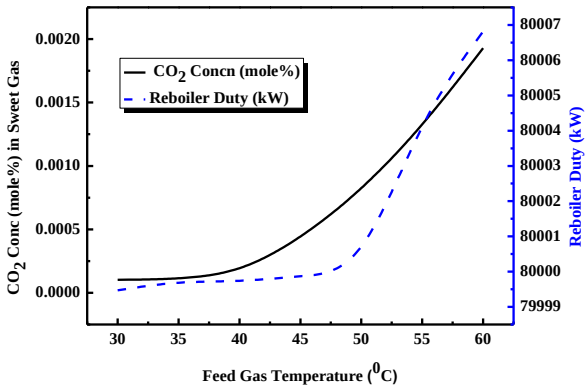

Figure 2. Effect of feed gas temperature on CO_2 concentration in sweet gas

4.2. Effect of feed gas temperature

Plant behaviour is predicted for various temperatures of the feed gas. Temperature is varied from 30^{0}C to 60^{0}C. Observed parameters are CO_2 and H_2S concentrations in sweet gas. As the feed gas temperature is increased from 30^{0}C to 60^{0}C, CO_2 and H_2S concentrations are increased in sweet gas and the reboiler duty also increased.

Reboiler duty remains constant between 35^{0}C to 40^{0}C. Beyond 40^{0}C reboiler duty increased to higher values, it shows that acid gas cleaning demands more reboiler duties. From figure 2 and from figure 3 the optimum temperature range for acid gas cleaning is in between 35^{0}C to 40^{0}C.

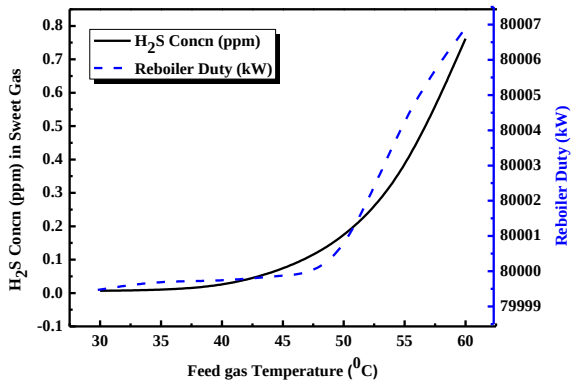

Figure 3. Effect of feed gas temperature on H_2S concentration in sweet gas

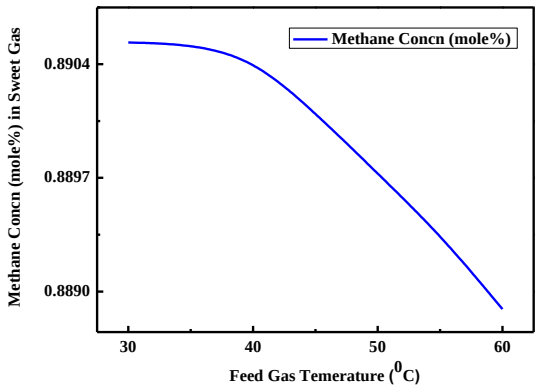

Figure 4. Effect of feed Gas temperature on methane concentration in sweet gas

Increasing temperatures decreased the concentrations of methane in sweet gas. Figure 4 illustrates that methane concentration is constant with temperature of the feed gas in between 30^{0}C and 35^{0}C. Maximum concentration of methane i.e 89 mole% is observed at 30^{0}C.

4.3. Effect of feed gas flow rate

Effect of feed gas rate on acid gas concentration in sweet gas is illustrated in figure 5. CO_2 concentration in sweet gas increased 3.8×10^{-6} mole % to 6.87 $\times10^{-5}$ mole %. It is evident that CO_2 concentration is increased nearly ten times. At the same time H_2S concentration decreesed from 0.93 ppm to 0.41 ppm. For feed gas flow rate of 35000 kg/hr, H_2S and CO_2 concentrations are optimum and their values are: CO_2 concentration is 4.32×10^{-5} mole% and the H_2S concentration is 1 ppm.

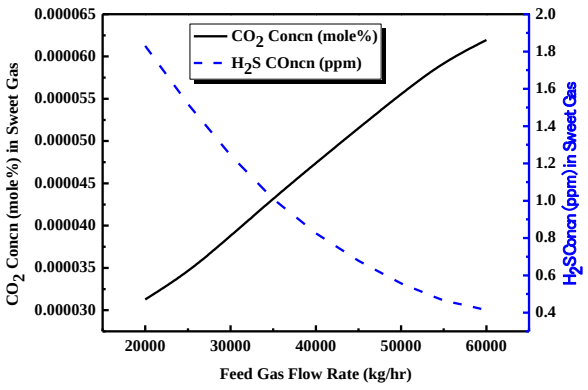

Figure 5. Effect of feed gas flow rate on acid gas concentration in sweet gas

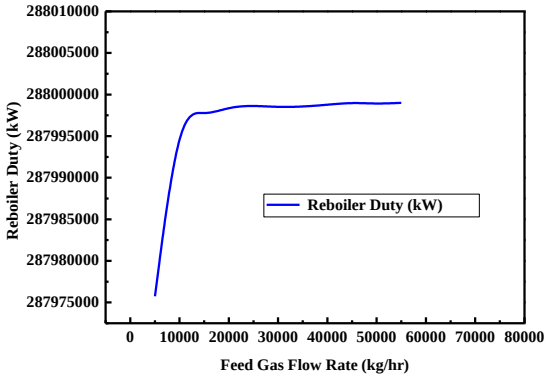

Figure 6. Effect of feed gas flow rate on reboiler duty (kW)

Effect of feed gas rate on reboiler duty is given in figure 6. For feed gas flow rate of 5000 kg/hr reboiler duty is 2.879×10^{8} kW and it is the minimum reboiler duty recorded. Reboiler duty is constant from the 20000 kg/hr to 55000 kg/hr. In this region CO_2 concentration is from 3.13×10^{-5} mole% to 5.94×10^{-5} mole% and the H_2S concentration is from 1.83 ppm to 0.46 ppm.

4.4. Effect of lean amine recirculation rate

Lean amine recirculation rate is changed from 284.65 m^3/hr to 641.18 m^3/hr and it is shown in figure 7. Increased amine recirculation rates decreased the concentration of H_2S in sweet gas. Increased amine recirculation rates increased the reboiler duties. Minimum reboiler duty observed is 2.878×10^{8} kW.

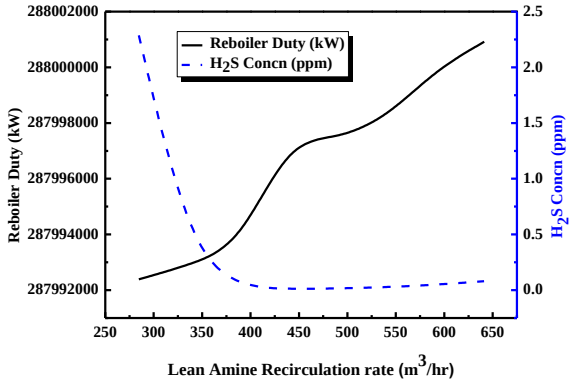

Figure 7. Effect of amine recirculation rate on reboiler duty

4.5 Absorber hydraulic studies

Hydraulic studies of absorber are performed for two cases. First case is absorber fitted with trays and the second case is absorber fitted with packing material. Absorber fitted with trays is considered as the base case. Base case hydraulic plots are illustrated in figure 9.

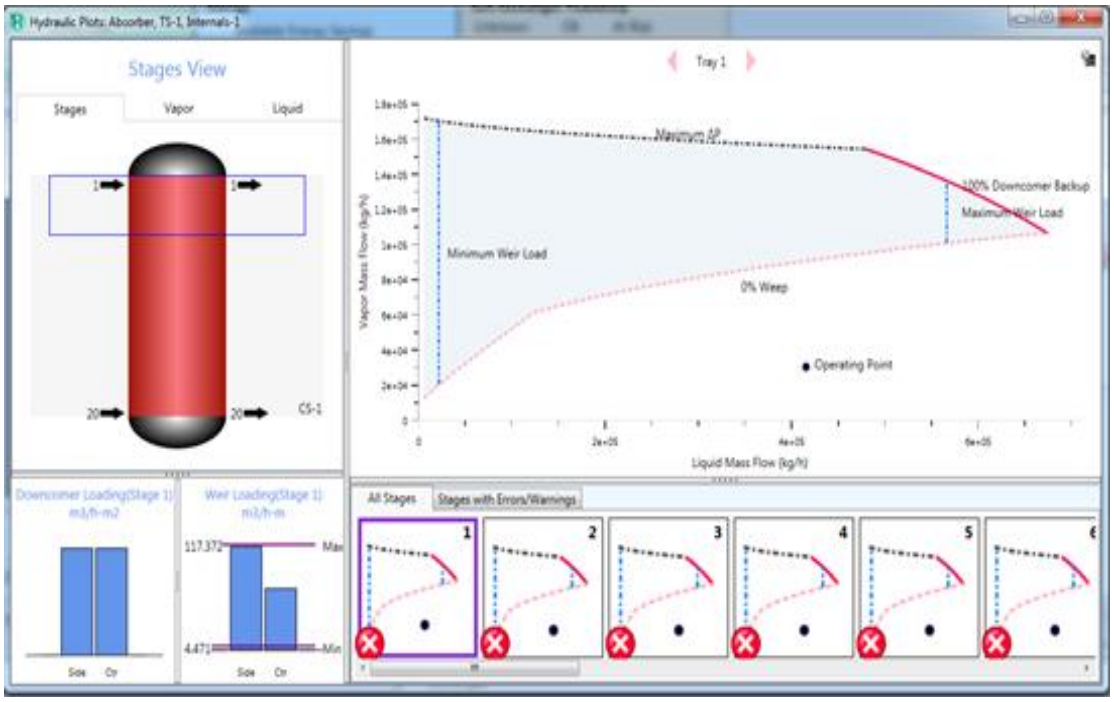

Figure 9. Hydraulic profile of absorber fitted with trays

Area under the plot gives the operating area of the tray column and it shows operating issues existing in the column. General operating issues are flooding and weeping. For stage 1 of the absorber hydraulic plot is shown in figure 10. The upper limit curve indicates the maximum pressure drop allowable in the column. The minimum limit curve indicates the minimum pressure drop allowable in the column. Area between the upper limit curve and the lower limit curves gives the absorber operation area.

Operation conditions reaching the upper point indicates the increased pressure drop in the column, it shows flooding in the column. Operation conditions reaching the minimum point in the plot indicates the weeping in the column.

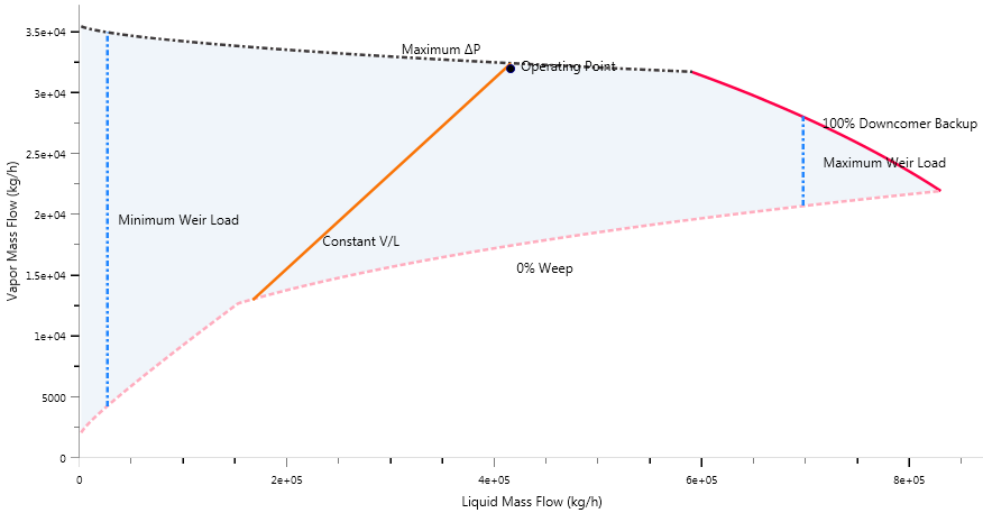

Figure 10. Hydraulic plot for stage 1 of the absorber fitted with trays

In figure 10, operating point reached the upper curve. It indicates flooding is present in the column and it reduces the efficiency of the column. Flooding should be avoided and this operating issue is solved by arranging packing material in the absorber. Trays are replaced with packing material of type raching ring made up of ceramic material. Size of the raching ring is 1 inch. Hydraulics of absorber filled with packing material is shown in figure 11.

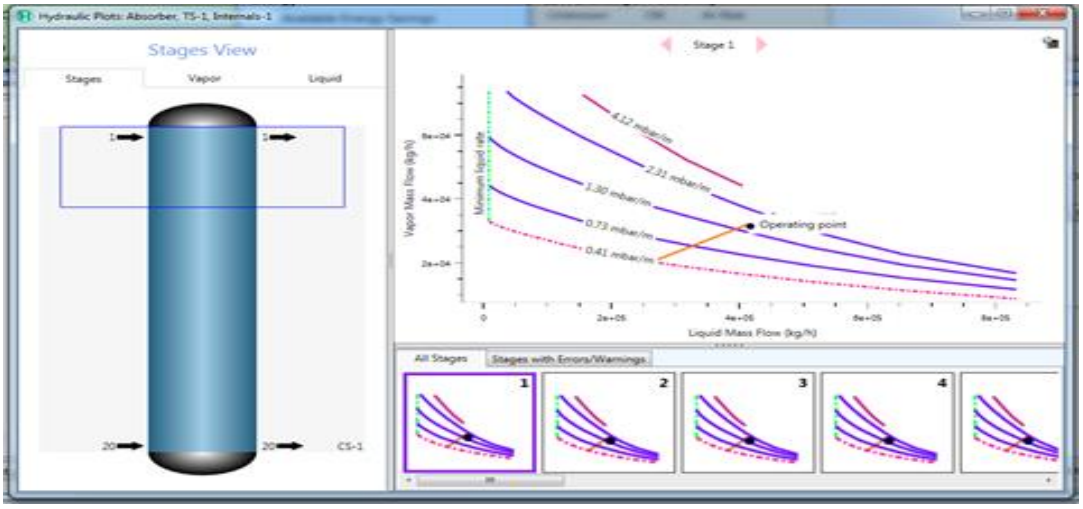

Figure 11. Hydraulics of packed column

It is observed that there are no operational issues for absorber filled with packing material. Absorber filled with packing material eliminated the operation issues of all stages in the column. Figure 12 shows the hydraulic plot of first stage of the absorber with packing material.

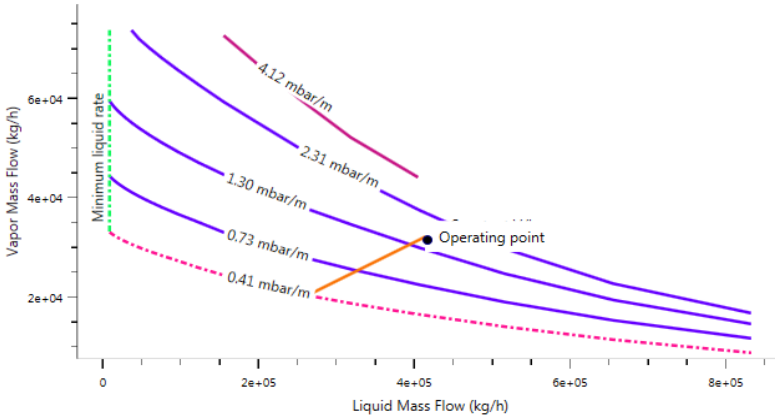

Figure 12. Hydraulic plot for packing column

Operating point is present in between the maximum pressure drop of 4.12 mbar/m and lower operating pressure of 0.41 mbar/m for the first stage of the column. Similarly the same pattern is observed for the remaining stages. The reason for improved operation is packing material provided more contact area for Vapour-Liquid contacting simultaneously it decreased the re-boiler duty demands. Results of the absorber column without operating issues are used for design calculations of the absorber. Absorber design data for rigorous rating calculations is given in Table 2.

Table 2. Absorber design data for rating calculations

Parameter	Values
Section Starting Stage	1
Section Ending Stage	20
Column diameter [m]	2.496
Packed Height Per Stage [m]	0.5
Section Height [m]	10.0
Maximum % Capacity (Constant L/V) [%]	80
Maximum Capacity Factor [m/s]	0.01645
Section Pressure Drop [mbar]	84.2
Average Pressure Drop / Height [mbar/m]	8.4
Average Pressure Drop / Height (Frictional) [mbar/m]	7
Maximum Stage Liquid Holdup [m^3]	0.49
Maximum Liquid Superficial Velocity [m^3/h-m^2]	84.37
Surface area [m^2/m^3]	190
Void Fraction	0.74
1st Stichlmair Constant	2.24
2nd Stichlmair Constant	3.24
3rd Stichlmair Constant	2.728

In table 3, acid gas removal and economics results of both base cases i.e tray column and packed column are given. CO_2 concentration is reduced from 1.56×10^{-4} mole% to 6.192×10^{-5} mole%, which shows 58% improvement in CO_2 recovery. H_2S concentration is reduced from 0.3868ppm to 0.3094 ppm indicates 20% improvement in H_2S removal from the natural gas. Arranging packing in the column reduced the total cost by 2.1%.

Table 3. Absorber comparison table

	Tray column	Packed column
Capital cost (USD)	98 323 200	96 183 500
Operating Cost(USD)	28 368 600	27 772 859
CO_2 (mole%)	1.56×10^{-4}	6.192×10^{-5}
H_2S (ppm)	0.3868	0.3094

5. Conclusions

Acid gas removal of natural gas using piperazine (PZ) amine is studied. Effect of feed gas flow rate, temperature, amine concentration and effect of amine recirculation rate on acid gas removal are studied. Effect of amine recirculation rate on reboiler duty is observed. Rigorous hydraulic studies are performed and the packed column design data is tabulated. Absorber operational efficiency is improved by improving the acid gas removal rates. CO_2 removal enhanced by 58% and the H_2S removal enhanced by 20%. Economic performance improved by 2.1%. The methodology and the results of this study are useful for process engineers those who are using piperazine (PZ) amine or other amines for the acid gas removal in their acid gas cleaning plants.

Acknowledgement

The authors are grateful to VIT University, Vellore, Tamilandu, India for providing the necessary facilities for the successful completion of this research work.

References

[1] Kumar S, Kwon H. T, Choi K. H, Cho J. H, Lim W, Moon I. Current status and future projections of LNG demand and supplies: A global prospective, Energy Policy, 2011; 39(7): 4097-4104.

[2] Moore CW, Zielinska B, Petron G, Jackson R. B. Air impacts of increased natural gas acquisition, processing, and use: a critical review, Environmental science & technology, 2014; 48(15): 8349-8359.

[3] Ebenezer SA, Gudmunsson JS. Removal of carbon dioxide from natural gas for LNG production, Semester project work, 2005.

[4] AspenTech Knowledge base

[5] Munoz DM, Portugal AF, Lozano AE, José G, de Abajo J. New liquid absorbents for the removal of CO_2 from gas mixtures, Energy & Environmental Science, 2009; 2(8): 883-891.

[6] Bishnoi S, Rochelle GT. Absorption of carbon dioxide in aqueous piperazine/methyldiethanolamine, AIChE Journal, 2002; 48(12): 2788-2799.

[7] Zhang X, Zhang CF, Qin SJ, Zheng ZS. A kinetics study on the absorption of carbon dioxide into a mixed aqueous solution of methyldiethanolamine and piperazine, Industrial & engineering chemistry research, 2001; 40(17): 3785-3791.

[8] Xu G. W, Zhang CF, Qin SJ, Gao WH, Liu HB. Gas– Liquid Equilibrium in a CO_2 - MDEA-H_2O System and the Effect of Piperazine on it, Industrial & engineering Chemistry research, 1998; 37(4): 1473-1477.

[9] Samanta A, Bandyopadhyay SS. Absorption of carbon dioxide into piperazine activated aqueous N-methyldiethanolamine. Chemical engineering journal, 2011; 171(3), 734-741.

[10] Samanta A, Bandyopadhyay SS. Kinetics and modeling of carbon dioxide absorption into aqueous solutions of piperazine. Chemical Engineering Science, 2007; 62(24), 7312-7319.

[11] Bishnoi S, Rochelle GT. Absorption of carbon dioxide into aqueous piperazine: reaction kinetics, mass transfer and solubility, Chemical Engineering Science, 2000; 55(22): 5531-5543.

[12] Kadiwala S, Rayer AV, Henni A. High pressure solubility of carbon dioxide (CO_2) in aqueous piperazine solutions, Fluid Phase Equilibria, 2010;292(1): 20-28.

[13] Appl M, Wagner U, Henrici HJ, Kuessner K, Volkamer K, Fuerst E. Method for neutralizing a stream of fluid, and washing liquid for use in one such method, U.S. Patent No. 4,336,233, 1982.

[14] Mak J. Configurations and methods of acid gas removal, U.S. Patent No. 7,637,987, 2009.

[15] Brok TJ, van der Zwet GP. Process for removal of hydrogen sulphide and carbon dioxide from an acid gas stream, U.S. Patent No. 8,765,086, 2014.

[16] Schubert CN, Frank TC. Regeneration of acid gas-containing treatment fluids, U.S. Patent No. 8,303,685, 2012.

[17] Silhavy B, Erdos L, Mizsey P, Koczka K, Szanyi A, Mika L, Benko T. Generation of Simulation Based Operational Database for an Acid Gas Removal Plant with Automatic Calculations, Periodica Polytechnica. Chemical Engineering, 2016; 60(1):24-28.

[18] Gutierrez JP, Benitez LA, Ruiz ELA, Erdmann EA. sensitivity analysis and a comparison of two simulators performance for the process of natural gas sweetening, Journal of Natural Gas Science and Engineering, 2016; 31: 800-807.

[19] Abdulrahman R, Sebastine IM. Natural gas sweetening process simulation and optimization: a case study of the Khurmala field in Iraqi Kurdistan, WIT Transactions on Engineering Sciences, 2012; 81: 37-46.
[20] Elfattah STA, Eldrainy YA, Attia A. Numerical Simulation to Optimize Di-Ethanol-Amine (DEA) Strength for Achieving the Highest Methane Purity from Biogas, Int. J. Adv. Sci. Tech. Res, 2015; 4(5):742-751.
[21] Sanggie FW. Process Modeling And Comparison Study Of Acid Gas Removal Unit by Using Different Aqueous Amines, Doctoral dissertation, UMP, 2011.
[22] Qiu, K, Shang JF, Ozturk M, Li TF, Chen SK, Zhang LY, Gu XH. Studies of methyldiethanol-amine process simulation and parameters optimization for high-sulfur gas sweetening, Journal of Natural Gas Science and Engineering, 2014; 21: 379-385.
[23] Pellegrini LA, Moioli S, Picutti B, Vergani P, Gamba S. Design of an acidic natural gas purification plant by means of a process simulator, Chemical Engineering Transactions, 2011; 24: 271-276.
[24] Kazemi A, Malayeri M, Shariati A. Feasibility study, simulation and economical evaluation of natural gas sweetening processes–Part 1: A case study on a low capacity plant in Iran, Journal of Natural Gas Science and Engineering, 2014;20:16-22.
[25] Qiu K, Zhu L, Bagajewicz M, Kim SY, Ozturk M. A simulation study on the impact of operating conditions on desulphurisation selectivity in high-sulphur gassweetening, International Journal of Oil, Gas and Coal Technology, 2013; 6(3): 348- 366.
[26] Abdulrahman R, Sebastine I. Effect of lean amine temperature on amine gas sweetening: case study and simulation, Chemistry and Technology of Fuels and oils, 2013; 49(4): 293-297.
[27] Pouladi B, Hassankiadeh MN, Behroozshad F. Dynamic simulation and optimization of an industrial-scale absorption tower for CO_2 capturing from ethanegas, Energy Reports, 2016; 2:54-61.
[28] Al-Lagtah NM, Al-Habsi S, Onaizi SA. Optimization and performance improvement of Lekhwair natural gas sweetening plant using AspenHYSYS, Journal of Natural Gas Science and Engineering, 2015; 26: 367-381.
[29] Øi L. E, Brathen T, Berg C, Brekne S. K, Flatin M, Johnsen R, Thomassen E. Optimization of configurations for amine based CO_2 absorption using Aspen HYSYS, Energy Procedia, 2014; 51: 224-233.
[30] Zare Aliabad H, Mirzaei S. Removal of CO_2 and H_2S using aqueous alkanolamine solutions, World Academy of Science, Engineering and Technology, 2009; 49(1):194-203.
[31] Angaji MT, Ghanbarabadi H, Khodabandehlo H. Study and examining the processing parameters on function of MDEA and DEA solvents for measuring removal units of CO_2 and H_2S, European Journal of Experimental Biology,2013; 3(3):609-616.
[32] Elfattah STA, Eldrainy YA, Attia A. Utilization of Aspen HYSYS simulation to determine the optimum absorber working pressure needed to achieve more than 0.99 methane purity from Egyptian biogas, International Journal of Information Research and Review, 2016; 3:1739-1744.

To whom correspondence should be addressed: prof. Dr. Nagamalleswara Rao K., Centre for Disaster Mitigation and Management, VIT University, Vellore, Tamilnadu, India,

Petroleum and Coal

Article **Open Access**

PHYSICOCHEMICAL, MINERALOGICAL, AND THERMOGRAVIMETRIC PROPERTIES OF NEWLY DISCOVERED NIGERIAN COALS

Bemgba B. Nyakuma[1], Aliyu Jauro[2], Olagoke Oladokun[1], Aliyu A. Bello[1], Habib Alkali[1], Mohammed A. Modibo[3], Mustapha Abba[4]*

[1] *Department of Chemical Engineering, Universiti Teknologi Malaysia, 81310 Skudai, Johor Bahru, Malaysia*
[2] *National Centre for Petroleum Research & Development (NCPRD), Abubakar Tafawa Balewa University, P.M.B 0248, Bauchi State, Nigeria*
[3] *Department of Surveying & Geoinformatics, Abubakar Tafawa Balewa University, P.M.B 0248, Bauchi State, Nigeria*
[4] *Department of Microbiology, Bauchi State University, P.M.B 65, Gadau, Bauchi State, Nigeria*

Received March 27, 2018; Accepted May 31, 2018

Abstract

Coal is an abundant and accessible energy source despite growing environmental concerns about its use. It is a critical driver of socio-economic growth and development particularly in nations with vast proven reserves. The discovery of new coal deposits in Nigeria has renewed interest in its utilisation. However, the scarcity of data has limited the energy utilization. Therefore, this study examines and reports data for the physicochemical, mineralogical, and morphological fuel properties of coals from Obomkpa (BMK), Ihioma (IHM) and Ogboligbo (OGB). The results revealed BMK contains the highest C and H, but OGB has the highest N, S, and O content. Morphology revealed coarse-grained coal particles with distinct lustre comprised of C, O, Si, Al, S, Fe, Ti, K, and Ca. Thermal analysis revealed IHM is the most reactive coal, whereas OGB is the least reactive. The DTG revealed two endothermic peaks for drying (30 – 200°C) and devolatilization (200°C to 600°C). The highest mass loss was observed in IHM, which confirmed its higher reactivity compared to BMK and OGB. The heating values were: 15.55 MJ/kg, 19.40 MJ/kg, and 19.66 MJ/kg for OGB, IHM, and BMK, respectively. Based on the findings, the coals are classified as lignite with potential for thermal energy recovery.

Keywords: *Fuel Characterization; Flash Pyrolysis; Lignite; Coal; Nigeria.*

1. Introduction

Despite global concerns about greenhouse gas emissions, coal remains the dominant fuel for electric power generation [1]. Currently, coal accounts for 40% of global power generation or about 64% of economically recoverable resources [2]. It provides an economical, reliable, and efficient source of energy for various industries around the globe [3]. Furthermore, the global importance of coal is augmented by its widespread accessibility and abundance [4]. As a result, coal plays a critical role in the socio-economic growth and sustainable development in emerging nations such as China, India and South Africa [5]. Therefore, the discovery of large coal deposits in Nigeria – Africa's largest economy and the most populous nation has renewed interest in the coal sector. However, coal does not currently contribute to the electric power production despite the nation's large coal deposits currently estimated at 2.8 billion tonnes [3].

Over the years, successive governments have made initiatives to revive the nation's moribund coal sector through policies reforms and strategic investments aimed at generating 30% of the nation's electricity from coal [6-7]. According to experts, coal utilisation for electric power generation is hampered by numerous socio-economic, environmental, and technological challenges [8-10]. The most notable technological challenges include lack of comprehensive data on

coal such as its elemental, mineralogical and calorific properties [11-12]. The outlined coal properties are critical to the design, optimisation and scale-up of efficient conversion processes [13]. Furthermore, the assessment of coal properties is an important step in defining its rank, energy application, or potential emissions [14-16]. Such information is a crucial dynamic in debates on the future coal and its applications particularly in the age of global warming and climate change.

With this in focus, several studies have examined the fuel properties of various Nigerian coals. The study by Ryemshak and Jauro [17] examined the proximate, rheological properties and potential applications of selected coals from Garin Maiganga, Shankodi-Jangwa and Tai environs in Nigeria. Chukwu, Folayan [3] examined the fuel characteristics of selected Nigerian coals for power generation. The study examined the ultimate-proximate, calorific, petrograp-hic and thermal properties of Odagbo, Owukpa, Amansiodo, Ezimo, Inyi, Odagbo, and Owukpa coals from Nigeria. Similarly, Sonibare, Ehinola [18], examined the thermal and kinetic proper-ties of Agbogugu, Enugu, Chikila and Lamja coals under oxidative and non-oxidative thermosgravimetry. Other studies have also examined the mineralogical, morphological and microstructural properties of Nigerian coals in the literature [19-21]. However, there is an absence of comprehensive data on the fuel properties of many newly discovered Nigerian coals in the literature. These include the recent discoveries of coal deposits in Obomkpa, Ihioma, and Ogboligbo in Delta, Imo and Kogi States, respectively, in Nigeria. The new deposits are strategically located in three out of the six geopolitical zones in the country. This revelation presents significant prospects for electric power generation required for socio-economic growth and development in the country.

To the best of the authors' knowledge, there is limited knowledge on the fuel properties of the Obomkpa (BMK), Ihioma (IHM) and Ogboligbo (OGB) coals. Therefore, this study will examine the physicochemical, mineralogical, and thermogravimetric characteristics of the newly discovered coals.

2. Experimental

The three (3) coal samples; Obomkpa (BMK), Ihioma (IHM) and Ogboligbo (OGB) were acquired from the National Metallurgical Research and Development Centre (NMRDC) Jos in Plateau State Nigeria. The coal samples were originally sourced from the following coal fields: Obomkpa (BMK) in Aniocha-North Local Government Area of Delta State; Ihioma (IHM) in Orlu Local Government Area of Imo State; and Ogboligbo (OGB) in Igalamela-Odolu Local Government Area of Kogi State. The coal samples were crushed and pulverised in a dry miller and then sieved through the 250 μm analytic test sieve based on the procedure described in a previous study [22].

The pulverised coal samples were subjected to the physicochemical analyses; ultimate, proximate, and bomb calorimetry to determine the elemental composition, fuel properties and higher heating values. The ultimate analysis was done using the vario MICRO Cube™ Elemental Analyzer (Germany) based on ASTM D5291-16. The proximate analysis was performed through thermogravimetric analysis (TGA) according to the procedure described in the literature [23-24]. Lastly, the higher heating value (MJ/kg) was determined by bomb calorimetry using the IKA C2000 (USA) combustion calorimeter based on ASTM standard D2015. Each test was performed in duplicate to ensure the accuracy and reliability of the measurements.

The mineralogical, morphological and microstructural characterisation of the coal samples were done by Scanning Electron Microscopy/Electron Dispersive X-ray (SEM/EDX) analysis. The tests were performed on the JEOL-JSM IT 300 LV (Germany) Scanning Electron Microscope (SEM) equipped with an Energy Dispersive X-Ray (EDX) detector. For each test, microscopic amounts of the samples were sprinkled on the SEM/EDX carbon stubs. Next, the samples were sputter coated with platinum using the Quorum Q150R S Sputter coater for 10 minutes before SEM/EDX analysis. The analysis was performed at 20 kV and 5 mm working distance to obtain micrographs at magnifications of ×1000. The AZTEC EDX software from Oxford Instruments, UK was used to analyse the captured SEM images. The elemental composition of the samples was quantified in wt. % based on a charge balance and the EDX peaks acquired.

The thermal degradation characteristics of the coals were examined through non-isothermal thermogravimetric analysis (TGA) under flash heating conditions. The rapid heating (flash) test conditions were selected to simulate the conditions for pulverised coke production. For the TGA runs, about 15 mg of each coal sample was placed in an alumina crucible and heated at 50°C/min from 30°C to 900°C. The TG runs were performed on the Shimadzu TG-50 analyser. The TGA was continuously purged with ultra-pure nitrogen gas (99.99%, Air Liquide, Malaysia) at a flow rate of 20 mL/min during the experiments. On completion, the TGA was cooled to RT, and the data files were retrieved and processed on the Shimadzu TA-60WS Workstation.

Based on the recovered TA ASCII data, the mass loss (TG), and derivative degradation (DTG) curves were plotted against temperature to determine the thermogravimetric characteristics and temperature profiles (TPC) of each coal. The TPCs deduced included; ignition (T_{on}), midpoint (T_{mid}), and maximum decomposition (T_{max}), and burnout (T_{off}) temperatures along with the mass loss rate (MLR, %/min) and residual mass (R_M, %). The T_{on} is the temperature at which the sample begins to decompose after drying is completed during TGA. The midpoint temperature or T_{mid} is the half-way point on the TG plot. However, the T_{max} is the temperature at which maximum decomposition or mass loss rate (M_{LR}, %/min) of the sample occurs, as denoted by a large peak (DTG) during TGA. The burnout temperature (T_{off}) is the temperature at which thermal degradation or devolatilization of the sample is completed. Lastly, the residual mass (R_M, %) is the final mass of the sample at the final TGA temperature. It is a measure of the coke or ash yield of thermally decomposing materials.

3. Results and discussion

3.1. Physicochemical analysis

The physicochemical fuel properties; ultimate (elemental), proximate and calorific values of Obomkpa (BMK), Ihioma (IHM) and Ogboligbo (OGB) coals are presented in Table 1 in as received (*a.r*) basis.

Table 1. Physicochemical properties of BMK, IHM, and OGB

Analyses	Element	Symbol	BMK	IHM	OGB
Ultimate	Carbon	C (wt. %)	50.38	46.80	37.48
	Hydrogen	H (wt. %)	5.62	5.39	3.51
	Nitrogen	N (wt. %)	0.59	0.64	0.80
	Sulphur	S (wt. %)	0.96	1.52	2.33
	Oxygen	O (wt. %)	42.45	45.64	55.88
Proximate	Moisture	M (wt. %)	3.63	4.75	3.12
	Volatiles	VM (wt. %)	58.05	69.52	51.43
	Ash	A (wt. %)	11.73	2.43	1.03
	Fixed Carbon	FC (wt. %)	26.61	23.30	44.41
	Fuel Ratio	F_R	0.46	0.34	0.86
	Mineral Matter	M_m	13.20	3.46	2.39
Heating Value	Higher Heating Value	HHV (MJ/kg)	19.66	19.40	15.55
	Lower Heating Value	LHV (MJ/kg)	18.64	18.41	14.75

The ultimate analysis indicates the coal samples contain high proportions of the combustible elements C, H, O along with the pollutant precursor elements N and S. BMK coal sample has the highest C and H content along with the lowest N, S, and O content (Table 1). Conversely, OGB contains the highest N, S, and O, indicating its potential for generating significant amounts of NOx, SOx and other greenhouse gases (GHG). The OGB coal also exhibited the lowest C and H content which accounts for its poor heating values ranging from 14.75 to 15.55 MJ/kg compared to IHM (18.41 to 19.40 MJ/kg) and BMK (18.64 to 19.66 MJ/kg).

The proximate analysis of the coal samples revealed high VM and FC along with low moisture and ash contents. IHM coal contains the highest M, and VM whereas BMK and OGB contain the highest Ash and FC, respectively (Table 1). Conversely, the lowest M, VM and Ash were observed in OGB, whereas IHM contains the lowest FC. Based on the findings, the high M and VM properties of IHM indicate that it may be suitable as a feedstock for coal gasification into syngas or flue gases for energy production. Conversely, the low M, VM, A and high FC indicate that OGB is best suited for pyrolysis or coke production.

The fuel ratio (F_R) is a ratio of the fixed carbon to the volatile matter [2]. At high F_R, coal combustion will result in high residues of unburnt coal and ultimately poor boiler efficiency [25]. Therefore, F_R is a good measure of the reactivity or the combustibility of coals. The F_R for the coals are: 0.46 (BMK), 0.34 (IHM) and 0.86 (OGB) (Table 1). This indicates that the conversion of OGB coal will result in high deposits (ash or coke), compared to IHM and BMK. Hence, the most reactive coal is IHM, followed by BMK whereas OGB is the least reactive coal. Lastly, the physicochemical properties and calorific values of the coals, indicate that all the coal samples (BMK, IHM and OGB) are lignite (brown) low-rank coals (LRC) with potentials for power generation and cement manufacture.

3.2. SEM/EDX Analysis

The SEM/EDX micrographs for BMK, IHM and OGB are presented in Figures 1-3 (a). The EDX plots showing the mineralogical composition of the coals are presented in Figures 1-3(b) and Table 2.

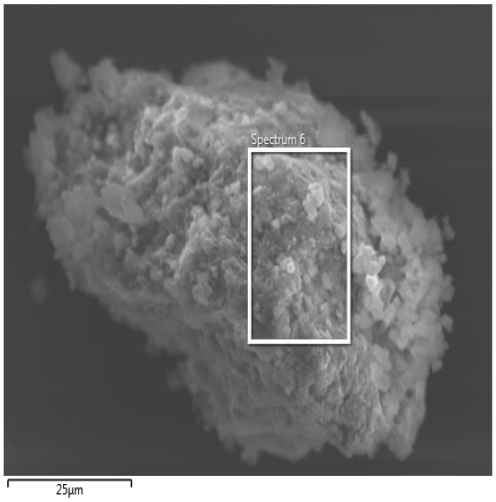

Figure 1(a). BMK Coal

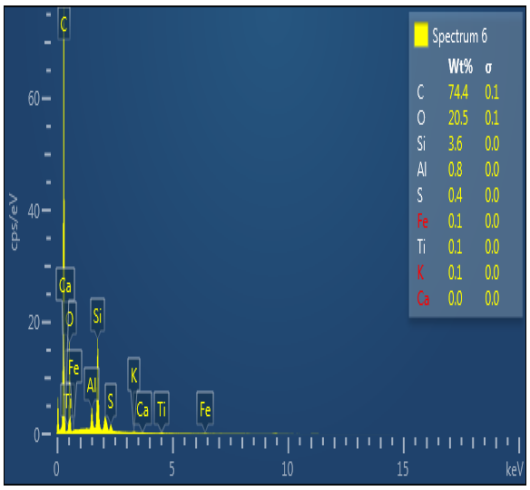

Figure 1(b). BMK Coal

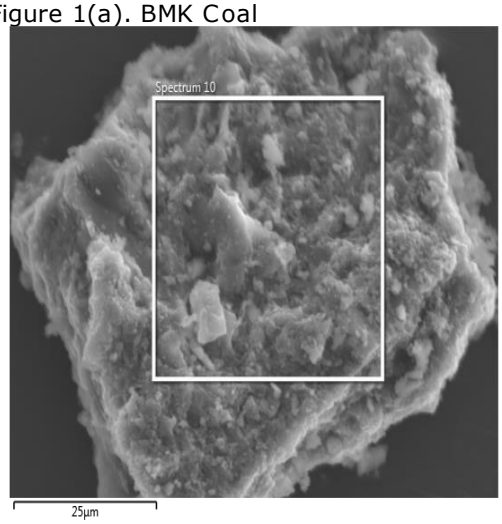

Figure 2(a). IHM Coal

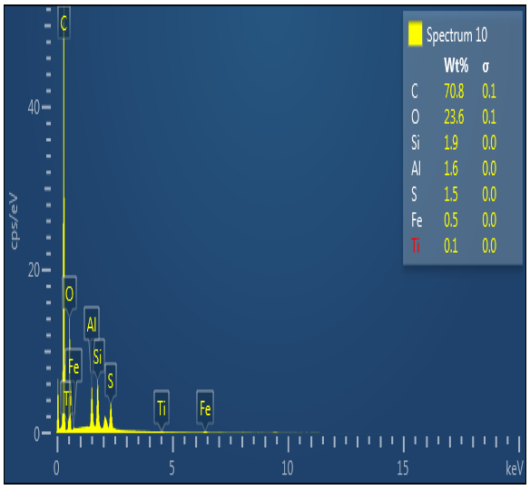

Figure 2(b). IHM Coal

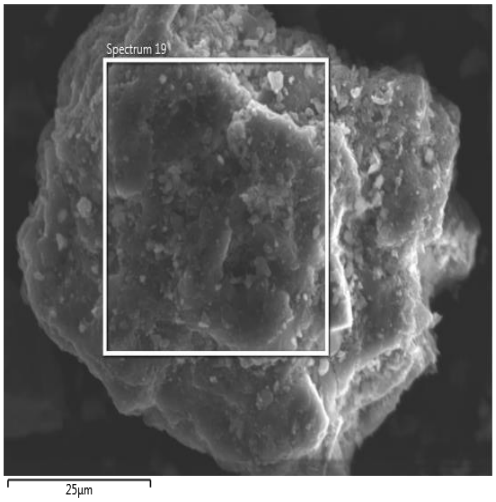

Figure 3(a) OGB Coal

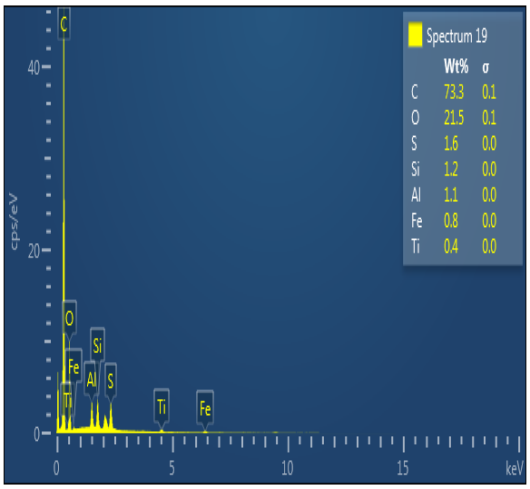

Figure 3(b). OGB Coal

The EDX plots revealed that the coals comprise of C, O, Si, Al, S, Fe, Ti, K, and Ca, although K and Ca were not detected (ND) in the IHM and OGB samples. However, for all samples, the highest elements observed were C, O, Si, and Al whereas the lowest were Ca, K, Ti, and K (Figures 1-3(b) and Table 2.

Table 2. EDX Elemental composition of BMK, IHM and OGB coals

Elements	Symbol	BMK (wt. %)	IHM (wt. %)	OGB (wt. %)
Carbon	C	74.38	70.85	73.34
Oxygen	O	20.46	23.62	21.54
Silicon	Si	3.59	1.91	1.23
Aluminum	Al	0.85	1.61	1.11
Sulfur	S	0.37	1.49	1.63
Iron	Fe	0.14	0.45	0.75
Titanium	Ti	0.12	0.08	0.41
Potassium	K	0.05	ND	ND
Calcium	Ca	0.04	ND	ND

In comparison, BMK exhibited the highest composition of C and S but the lowest O content. This may somewhat be responsible for its porosity and grindability along with its high heating value (Table 1). However, the lowest C composition and highest O content were observed in the IHM coal sample. It is widely reported that the high O content in carbonaceous fuels can result in over oxidation during thermal conversion resulting in high NO_x, SO_x and other greenhouse gases (GHG). Hence, the IHM has the potential to be highly reactive during thermoschemical conversion. Furthermore, the high concentration of metallic elements such as Al and Fe in IHM can potentially catalyse thermal conversion processes for energy recovery.

3.3. Thermogravimetric analysis

The TG-DTG plots for the flash pyrolysis and thermal degradation of the BMK, IHM and OGB coals are presented in Figures 4 and 5, respectively.

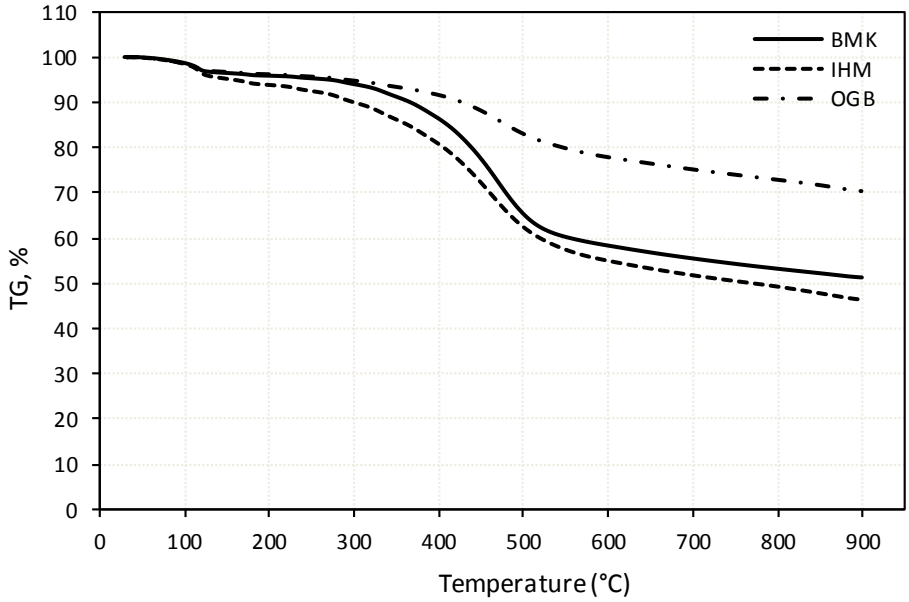

Figure 4. TG Plots for Flash Pyrolysis of Nigerian Lignite Coals

As observed in Figure 4, the TG curves exhibited downward sloping trends from left to the right of the plot. The trends indicate an increase in temperature from 30 to 900°C resulted in a progressive loss of mass during thermal degradation of the samples. However, the thermal degradation and mass loss observed in BMK and IHM were more significant compared to OGB coal. This could be ascribed to the higher contents of C, H, VM and HHV in BMK and IHM compared with OGB (Table 1). The findings indicate that BMK and IHM are more reactive than OGB coal. To confirm this, the reactivity of the coals was further examined by its characteristic temperature profiles (TPC) from the TG plots, as presented in Table 3.

Table 3. TPCs for Flash TG-Pyrolysis of BMK, IHM, and OGB

Characteristic Profiles	Symbol	BMK (°C)	IHM (°C)	OGB (°C)
Onset Temperature	T_{on}	364.94	319.36	340.69
Midpoint Temperature	T_{mid}	453.34	437.41	465.66
Burnout Temperature	T_{off}	543.36	556.86	592.62
Residual Mass (%)	R_M	51.27	46.43	70.35

As observed in Table 3, the ignition temperatures (T_{on}) for the coal samples ranged from 319.36 °C to 364.94°C or an average of 341.66°C. The lowest and highest values of T_{on} were observed for IHM and BMK coals, respectively. The midpoint (T_{mid}) temperatures ranged from 437.41°C to 465.66°C or an average of 452.14°C. The lowest and highest values of T_{mid} were observed for IHM and OGB, respectively. However, the burnout (T_{off}) temperatures ranged from 543.36°C to 592.62°C or an average of 564.28°C. The lowest and highest values of T_{off} was observed for BMK and OGB, respectively. Lastly, the residual mass (R_M, %) for the coals ranged from 46.43% to 70.35%. The lowest and highest values of R_M was observed for IHM and OGB, respectively. Based on the TPC values derived from the TG plots, IHM is the most reactive of the coals whereas OGB is the least reactive.

The reactivity of the coal samples was examined from the DTG plots presented in Figure 5. As observed, the thermal decomposition of the samples resulted in two sets of endothermic peaks. The first peak was observed from RT to 200°C, whereas the second larger peak was from 200°C to 600°C. The mass loss in the temperature range of the first peak was 4.11% for BMK, 6.09% for IHM and 3.82% for OGB. The values are marginally higher than the moisture

content of BMK (3.63%), IHM (4.75%) and OGB (3.12%) reported in Table 1. This indicates the mass loss in this range can be ascribed not only to drying but also the loss of low molecular weight compounds during thermal decomposition of the coals.

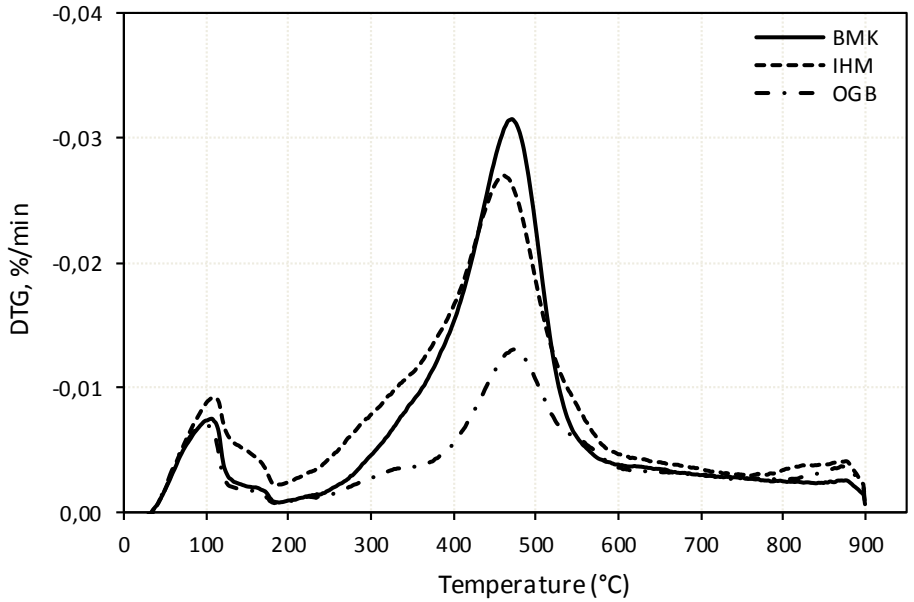

Figure 5. DTG Plots for Flash Pyrolysis of Nigerian Lignite Coals

The second peaks observed from 200°C to 600°C resulted in mass losses of 37.59% for BMK; 38.90% for IHM; and 18.35% for OGB coals. The highest mass loss and thermal decomposition was observed for IHM, followed closely by BMK and finally OGB coal. This confirms that IHM is the most reactive whereas OGB is the least reactive of the coals examined. Furthermore, the mass loss observed is much lower than volatile matter content for BMK (58.05%); IHM (69.52%); and OGB (51.43%). Therefore, the complete or higher decomposition of the coals may require higher temperatures and slower heating rates in future energy conversion systems. These conditions will potentially improve the TPCs and energy recovery potential of the coals. The TPCs deduced from the DTG plots for flash pyrolysis of the coals are presented in Table 4.

Table 4. DTG TPCs for flash pyrolysis of BMK, IHM, and OGB

Characteristic Profiles	Symbol /Unit	BMK (°C)	IHM (°C)	OGB (°C)
Drying peak	T_{dry}	166.90	32.20	98.32
Decomposition peak	T_{max}	470.59	460.98	473.07
Mass Loss	M_L, %	48.73	53.58	29.65

As observed, the results show that IHM exhibited the lowest value of drying peak temperature whereas the BMK had the highest at 166.90°C. This indicates that the process of drying BMK requires more energy input and reaction time compared to OGB and IHM. In contrast, the highest maximum peak decomposition temperature (T_{max}) was observed for OGB, followed by BMK and IHM which has the lowest. These results indicate that based on T_{max}, the IHM coal is the most reactive as its maximum decomposition occurs at 460.98°C which is lower than BMK (470.59 °C) and OGB (473.07°C).

Lastly, the mass loss (M_L, %) of the coals was examined to highlight the potential solid product formed from the decomposition process. As observed in Table 4, the highest M_L (%) was observed for the IHM coal sample whereas the lowest was observed for OGB. Since the product of coal pyrolysis is typically coke, the results demonstrate that OGB has highest coke

forming potential (based on the residual mass R_M values in Table 3), followed by BMK and lastly IHM. However, further tests are required to verify this inference.

4. Conclusions

The coal samples from Obomkpa (BMK), Ihioma (IHM) and Ogboligbo (OGB) contain high proportions of C, H, O along with N and S elements. The BMK coal sample has the highest C and H content along with the lowest N, S, and O. However, OGB contained the highest N, S, and O indicating a high potential for NOx, SOx and other GHG emissions. OGB has the lowest C and H content and the corresponding least HHV (15.55 MJ/kg) compared to IHM (19.40 MJ/kg) and BMK (19.66 MJ/kg). Hence, the coals BMK, IHM and OGB coals are classified as lignite (brown) or low-rank coals (LRC) with potential for thermal energy recovery. The morphological analysis revealed that BMK, IHM and OGB coals are comprised of particles of various shapes and sizes. The mineralogical analyses revealed the coal composition consists of C, O, Si, Al, S, Fe, Ti, although K and Ca were not detected in IHM and OGB.

The thermal degradation behaviour and TPCs were also examined. The findings show that IHM and BMK are more reactive than OGB coal. Based on the TGA derived TPCs, IHM is the most reactive coal whereas OGB is the least reactive under the conditions examined in this study. The DTG revealed two endothermic peaks for drying (RT – 200°C) and devolatilization (200°C to 600°C). The highest mass loss and thermal decomposition were observed in IHM, followed by BMK and finally OGB coal. This confirms that IHM is the most reactive whereas OGB is the least reactive of the coals examined. In conclusion, the Obomkpa (BMK), Ihioma (IHM) and Ogboligbo (OGB) coal samples possess the requisite physicochemical, mineralogical, morphological fuel properties for future energy conversion and recovery systems in Nigeria.

Acknowledgement

The authors wish to acknowledge the National Metallurgical Research and Development Centre (NMRDC, Jos) Plateau State Nigeria for providing the coal samples. The technical assistance of Dr T.A.T Abdullah of the Hydrogen Fuel Cell Laboratory (Universiti Teknologi Malaysia, UTM Malaysia) along with Nurleyana Binti Salleh and Ahmad Safuan Bin Borhan of UiRL UTM Skudai is gratefully acknowledged.

References

[1] IEA. Market Series Report: IEA Coal 2017 in Analysis and Forecasts to 2022. 2017; International Energy Agency: Paris, France. p. 1-8.
[2] Speight JG. The Chemistry and Technology of Petroleum. 3 ed. Chemical Industries. 2014; Boca Ranton FL, USA: CRC Press (Taylor & Francis Group). 845.
[3] Chukwu M, Folayan C, Pam G, and Obada D. Characterization of some Nigerian coals for power generation. Journal of Combustion, 2016; 1(1): 1-12.
[4] Nyakuma, BB and A Jauro. Physicochemical Characterization and Thermal Decomposition of Garin Maiganga Coal. GeoScience Engineering, 2016; 62(3): 6-11.
[5] Shaw TM, Cooper AF, and Antkiewicz A. Global and/or regional development at the start of the 21st century? China, India and (South) Africa. Third World Quarterly, 2007; 28(7): 1255-1270.
[6] Ohimain EI. Can Nigeria generate 30% of her electricity from coal. International Journal of Energy and Power Engineering, 2014; 3(1): 28-37.
[7] Okoro O and Chikuni E. Power sector reforms in Nigeria: opportunities and challenges. Journal of Energy in Southern Africa, 2017; 18(3): 52-57.
[8] Ajao K, Ajimotokan H, Popoola O, and Akande H. Electric energy supply in Nigeria, decentralized energy approach. Cogeneration and Distributed Generation Journal, 2009; 24(4): 34-50.
[9] Oyedepo SO. On energy for sustainable development in Nigeria. Renewable and sustainable energy reviews, 2012; 16(5): 2583-2598.
[10] Aliyu AS, Ramli AT, and Saleh MA. Nigeria electricity crisis: Power generation capacity expansion and environmental ramifications. Energy, 2013; 61(1): 354-367.
[11] Olajir, A, Ameen A, Abdul-Hammed M, and Adekola F. Occurrence and distribution of metals and porphyrins in Nigerian coal minerals. Journal of Fuel Chemistry and Technology, 2007; 35(6): 641-647.

[12] Nyakuma B. Physicochemical Characterization and Thermal Analysis of newly discovered Nigerian coals. Bulgarian Chemical Communications, 2016; 48(1): 4.
[13] Antoniou N and Zabaniotou A. Re-designing a viable ELTs depolymerization in circular economy: Pyrolysis prototype demonstration at TRL 7, with energy optimization and carbonaceous materials production. Journal of Cleaner Production, 2018; 174(1): 74-86.
[14] Nyakuma BB and Jauro A. Chemical and Pyrolytic Thermogravimetric Characterization of Nigerian Bituminous Coals. GeoScience Engineering, 2016; 62(3): 1-5.
[15] Oboirien B, North B, Obayopo S, Odusote J, and Sadiku E. Analysis of clean coal technology in Nigeria for energy generation. Energy Strategy Reviews, 2018; 20(1): 64-70.
[16] Nyakuma B, Jauro A, Oladokun O, Uthman H, and Abdullah T. Combustion Kinetics of Shankodi-Jangwa Coal. Journal of Physical Science, 2016; 27(3): 1-12.
[17] Ryemshak SA and Jauro A. Proximate analysis, rheological properties and technological applications of some Nigerian coals. International Journal of Industrial Chemistry, 2013; 4(1): 7.
[18] Sonibare O, Ehinola O, Egashira R, and KeanGiap L. An investigation into the thermal decomposition of Nigerian Coal. Journal of Applied Sciences, 2005; 5(1): 104-107.
[19] Sonibare OO, Jacob DE, Ward CR, and Foley SF. Mineral and trace element composition of the Lokpanta oil shales in the Lower Benue Trough, Nigeria. Fuel, 2011; 90(9): 2843-2849.
[20] Sonibare OO, Haeger T, and Foley SF. Structural characterization of Nigerian coals by X-ray diffraction, Raman and FTIR spectroscopy. Energy, 2010; 35(12): 5347-5353.
[21] Akinyemi S, Gitari W, Akinlua A, and Petrik L. Mineralogy and geochemistry of sub-bituminous coal and its combustion products from Mpumalanga Province, South Africa. in Analytical Chemistry. 2012, InTech.
[22] Nyakuma BB, Oladokun O, Jauro A, and Nyakuma DD. Evaluating the Energy Recovery Potential of Nigerian Coals under Non-Isothermal Thermogravimetry. IOP Conference Series: Materials Science and Engineering, 2017; 217(1): 012013.
[23] Karatepe N and Küçükbayrak S. Proximate analysis of some Turkish lignites by thermogravimetry. Thermochimica Acta, 1993; 213(1): 147-150.
[24] Donahue CJ and Rais EA. Proximate Analysis of Coal. Journal of Chemical Education, 2009; 86(2): 222.
[25] Asthana A. Coal Blending and its effects on Boiler Performance. 2015; Available from: http://bit.ly/2FcMhQI.

To whom correspondence should be addressed: Bemgba B. Nyakuma, Department of Chemical Engineering, Universiti Teknologi Malaysia, 81310 Skudai, Johor Bahru, Malaysia, bbnyax1@gmail.com, bnbevan2@live.utm.my

Petroleum and Coal

Article **Open Access**

WATER STABILIZATION IN CLOSED CIRCUITS BY PHOSPHATE COMPOUNDS

Laleh Shirazi[1]*

[1] *Gas Division, Research Institute of Petroleum Industry (RIPI), Tehran, Iran*

Received March 25, 2018; Accepted May 31, 2018

Abstract

The stabilization of circulating water is meant to optimize water conditions to prevent the formation of deposits or corrosion. Calcium carbonate precipitation in pipes water decreases water carrying capacity and increase cost of transportation. Water should be stabilized to prevent these problems. Water stabilization is the adjustment of the pH, Ca^{+2}, and alkalinity to its $CaCO_3$ saturation equilibrium. Accordingly, stabilized water neither dissolves nor precipitates $CaCO_3$. In this study suitable chemicals for decreasing hardness, alkalinity and suspended solid from water are selected. Also the effects of some parameters such as pH, alkalinity, hardness, temperature, phosphate dosage and additive starch are studied on water stabilization.

Keywords: *water stabilization; phosphate; starch; sediment.*

1. Introduction

Suran was the first to use phosphates to remove calcium and magnesium salts from water [1]. Hall was first used sodium triphosphate to prevent the formation of calcium carbonate precipitation and control it in boiler water. He noted that sodium triphosphate is dissolved in water and reacts with calcium and magnesium salts, and converts to calcium phosphate and magnesium, which are in the form of sludge. He also suggested that use of triphosphate calcium, which has a low solubility and a stable solubility, is positive. He examined the problem by mathematical method and assumed that the phosphate would displace the remaining hardness, preventing corrosion, and displacing precipitated deposits which were previously formed [1-2].

Hall explained the mechanism of sediment formation in the walls of steam boilers. Sticky and hard sediments formed due to the direct crystallization of low soluble solids on heated walls that have reached saturation. These sediments can also contain water suspended matter. If the solubility of the soluble in solution is shown as S and the temperature as T, at $dS/dT<0$, the formation of the precipitate is certain and the resulting sediments are highly adhesive and very hard. At $dS/dT>0$, the formed sediments have little adhesion and are formed in cool parts and often remain suspended in sediment. Hall, used Graham salt $(NaPO_3)_6$ which is now called sodium hexametaphosphate, for the first time for boiler water treatment [1].

W.F. Langelier was related calcium carbonate solubility to several effective variables in dissolution. By defining the parameter of the saturation index, a tendency to precipitation or corrosion of water is obtained qualitatively. But this method is useful for water with low amount of soluble solids with pH=6.5-9.5. Langelier with the naming of pH water, which has neither a tendency to corrosion nor to precipitate to saturation pH (pH_s) and to compare it with real pH of water, could have gotten an idea of water instability [1]. This index is defined as $LSI=pH-pH_s$. pHs can be determine by analyzing water and by using the following formula:

$$pHs=11.017+0.197\log(TDS)-0.995\log(Ca)_t-1.041\log(Alk.)_t-0.016\log(Mg)_t+0.021\log(SO4)_t$$

whwre TDS is total dissolved solids that equal to total water soluble solids (total concentration of all the ions in the water).

If pH_s=pH then LSI=0, so, the solution is saturate and water does not have tendency to precipitate or corrosion. The positive LSI, shows pH>pH_s, under these conditions (temperature, alkalinity and soluble solids), the water is supersaturated from calcium carbonate and tends to precipitate. The negative LSI indicates that chemical equilibrium is not yet established, and if there is a precipitate in the system, it will dissolve in water and water may also attack to metal and cause corrosion.

This index is corrected for the water with high levels of soluble as follow:

LSI = pH-PCa-PAlk.-K PCa = -log[Ca] Palk. = -log[Alk.]

where K is a constant which relates to temperature and ion concentration of water.

Ryznar due to the work carried out by Langelier, presented a new method for the tendency of water sedimentation. He believed that the Langelier saturation index was qualitative and his suggested index represents a quantitative amount to determine the content of calcium carbonate that can precipitate up to 200°C. By Ryznar index can specified corrosive and sediment water [2]. Ryznar stability index = 2pH_s-pH.

If the stability index is equal to 6 or less, the sedimentation property of the water will be high, and if this index is greater than 7, the precipitate will not be formed, and if this index is more than 7.5 or 8, the risk of corrosion will increase.

Feither investigateed the constraints of Langelier and Ryznar saturation indexes and stability of them. He introduced a new concept called critical pH, which was about 1.7 to 2 unit higher than the predicted value of the Langelier index [3].

Puckorius and Brooke were studied the formation of calcium carbonate precipitation in cooling water systems. According to their idea, the existing indexes for the formation of calcium carbonate deposition at pH above 7.5 in a cooling water tower are not accurate [4]. The percentage of water stabilization is calculated by using the following formula [4]:

$$Stabilization = \frac{(LSI)_{initial} - (LSI)_{final}}{(LSI)_{initial}} * 100$$

2. Water stabilization

The goal of water stabilization is provide adequate water for drinking, for boilers and coolants. Also in the industry, the aim is create a thin layer of protective calcium carbonate on the inner wall of the water distribution system. Due to the issues facing most industries today, water stabilization is one of the most important issues [5]. For this purpose, different materials such as chromate, silicate, sodium carbonate and phosphates can be used [6].

Phosphates are one of the most commonly used substances for stabilizing circulating water, which are used in a better and more effective manner than any other material mentioned above and there are different combinations in the market. Increasing their value depends on several factors such as sedimentation potential, reaction time, amount of phosphate added, pH and temperature [7].

The effect of the above parameters on the proper selection of suitable phosphate compounds, which will increase the efficiency and increase the time of unit operation, has always been a topic of interest in the industry [8].

The purpose of this paper is to investigate the effect of phosphate compounds on water stabilization in closed circuits. To achieve this goal, obtain of the best material for reducing hardness, suspended particles and alkalinity and determining the effective physical factors on increasing stabilization efficiency such as temperature, pH and reaction time are the objectives of the study. In this research, only water stabilization has been studied to optimize water conditions to prevent sediment formation, and the corrosion problem has not been discussed [9].

2.1. The effect of phosphates on hardness and water stabilization

Phosphates are one of the most common and effective materials for stabilizing circulating waters. Phosphates form complexes with dissolved calcium ions in the environment and reduces the equilibrium concentration of calcium ion prevent deposition of calcium carbonate in

the water pipes, boilers and coolants. In this way reduces water hardness and causes water stabilization [10].

2.2. Types of phosphates in stabilization of water

The major phosphates used in water stabilization are polyphosphates, glassy phosphates & metaphosphates. Also, the special phosphates are used in water stabilization, which are produced by heating of various types of orthophosphate salts which called dehydrated phosphates such as $Na_4P_2O_7$, $NaPO_3$, $Na_2H_2P_2O_7$, $(NaPO_3)_3$ & $(NaPO_3)_6$.

Effectively, the low amount of phosphate compounds prevents sedimentation. Excessive use of phosphates may result in the deposition of calcium phosphates or iron phosphates which is harmful [10]. Also, long contact time for some phosphates is harmful due to reversible reactions. To control sediment with phosphates, factors such as maximum temperature in the system, time dependence and precipitation potential are important [11].

2.3. Effect of different doses of phosphate on water stabilization at different times

According to the Figure 1, it can be seen that higher doses of phosphate increase the stabilization efficiency, the cause can be explained by the greater complexity factor (phosphates) and the greater involvement with hardness and calcium and magnesium ions in the environment.

According to the Figure 2, we find that over two hours, the efficiency goes up by about 30% while at 30 min, efficiency is 25%. This shows that over time, more complexes are formed.

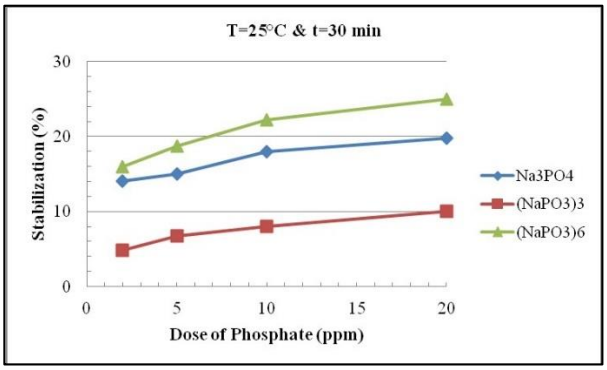

Figure 1. Effect of different doses of phosphate on water stabilization percent at t= 30 min

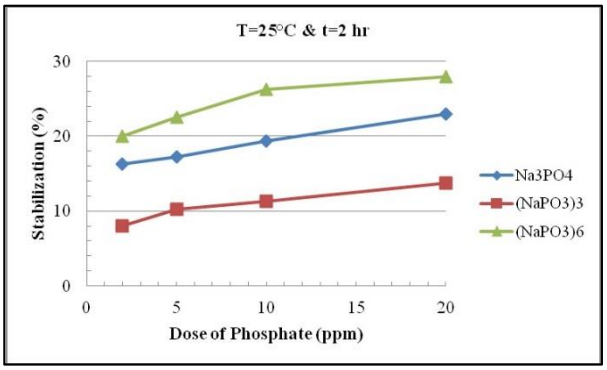

Figure 2. Effect of different doses of phosphate on water stabilization percent at t= 2 hr

Also, according to the Figure 1 & 2, hexa methaphosphate is better than two other phosphates. Because polyphosphates have better efficiency than orthophosphates (Na_3PO_4). Unlike orthophosphates, which are deposited in calcium and magnesium phosphate, polyphosphates do not precipitate and keep calcium and magnesium ions in solution.

2.4. Effect of pH on the function of phosphates

According to the Figure 3, 4 & 5, we find that sodium hexametaphosphate has the best performance at pH=8. Sodium metaphosphate is an acidic phosphate that is better in alkaline medium. But it decomposes to orthophosphate at pH above 8 and decreases the efficiency. So, the efficiency at pH = 9 is lower than at pH=8. In pH= 6 because the environment is acidic, acidic sodium hexametaphosphate does not have good performance.

Figure 4 & 5, show the effect of the reaction time on the stabilization percentage at pH= 6 and 9, respectively. Due to its high alkalinity properties, this phosphate acts better at pH=6 and also has a better efficiency at 2 hours.

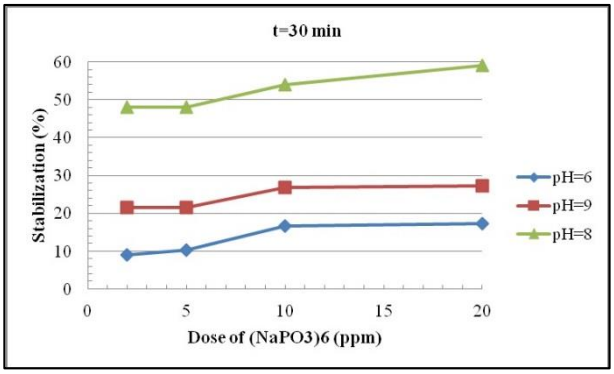

Figure 3. Effect of pH on water stabilization with $(NaPO_3)_6$ at t= 30 min

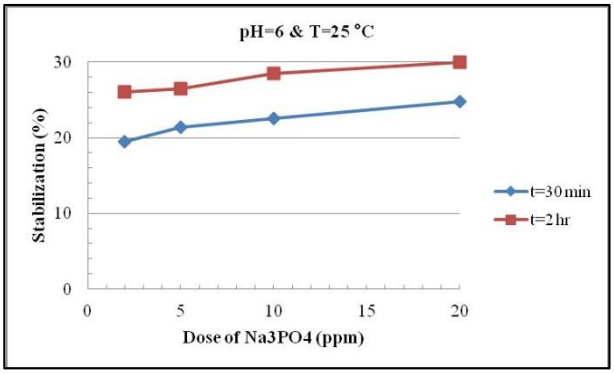

Figure 4. Effect of reaction time on water stabilization with Na_3PO_4 at pH=6 & T= 25°C

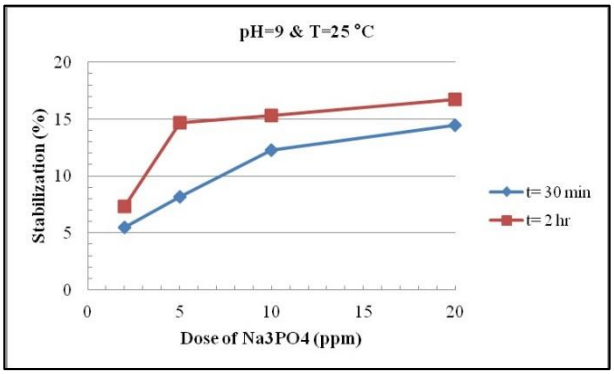

Figure 5. Effect of reaction time on water stabilization with Na_3PO_4 at pH=9 & T= 25°C

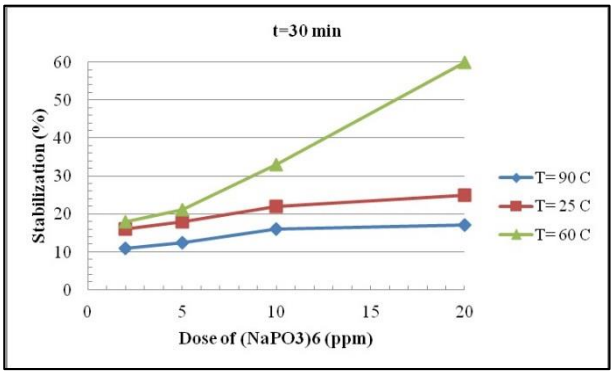

Figure 6. Effect of reaction temperature on water stabilization with $(NaPO_3)_6$ at t= 30 min

The results for $(NaPO_3)_3$ is same as $(NaPO_3)_6$, but the efficiency is slightly lower, because it is a weaker polyphosphate than $(NaPO_3)_6$. In terms of economic, it is better that use of $(NaPO_3)_6$ in alkaline environments and Na_3PO_4 in acidic environments.

2.5. Effect of temperature on stabilization efficiency

According to the Figure 6 & 7, we find that an increase in the temperature up to 60°C, raises the efficiency, which may be due to carbonate decomposition into bicarbonate and CO_2 and increase alkalinity of environment, which results in better efficiency of the acidic $(NaPO_3)_6$.

But at 90°C, the polyphosphate is severely decomposed and converted to orthophosphate, the efficiency goes down even lower than 25°C.

According to Figure 7, by increasing the time reduces the stabilization efficiency, which can be explained by the decomposition of the polyphosphate and its conversion to orthophosphate. The result for $(NaPO_3)_3$ is as same as $(NaPO_3)_6$, only it has less efficiency.

The results for Na_3PO_4 indicate that the efficiency at T=90°C does not decrease too low (compared with $(NaPO_3)_6$), and the reason is that Na_3PO_4 is an orthophosphate, and the orthophosphate remains as the temperature rises. Only by increasing the temperature, carbonate decomposes and becomes bicarbonate and CO_2 which enters the environment and increases alkalinity, the efficiency decreases. Because Na_3PO_4 in a medium with high alkalinity, has less efficiency

2.6. Effect of starch with phosphate on stabilization efficiency

According to Figure 8, it is clear that add starch improves the stabilization efficiency and this due to the starch colloidal property which by creating a covering around sediments prevents them from sticking. This effect sees better at lower times and higher doses of starch.

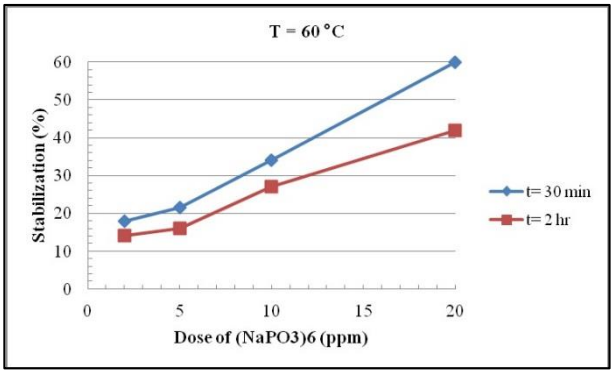

Figure 7. Effect of reaction time on water stabilization with $(NaPO_3)_6$ at T= 60°C

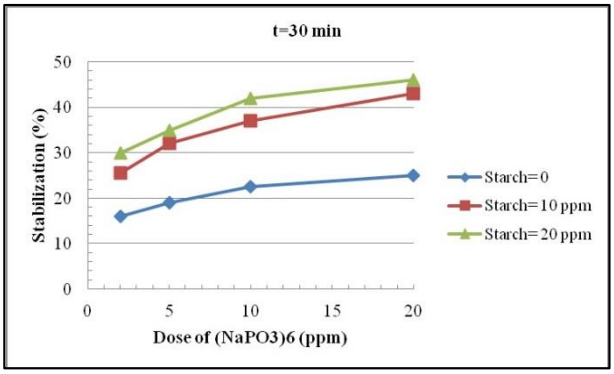

Figure 8. Effect of starch on water stabilization with $(NaPO_3)_6$ at t= 30 min

2.7. Hardness effect on the stabilization percentage

According to the Figure 9, the lower hardness has better stabilization efficiency. Because when the hardness is low, the phosphate can be more complex with them, but when calcium ions increase, phosphate can be less involved with them and can complex. As time passes, the efficiency becomes better because the phosphate has more time to form the complex

2.8. Alkalinity effect on the stabilization percentage

According to the Figure 10, we find that at the higher alkalinity, sodium hexameta-phosphate, has higher efficiency, which is due to its acidity. The result for two hours, shows that the efficiency is higher than 30 min, due to the surrounded more calcium ions.

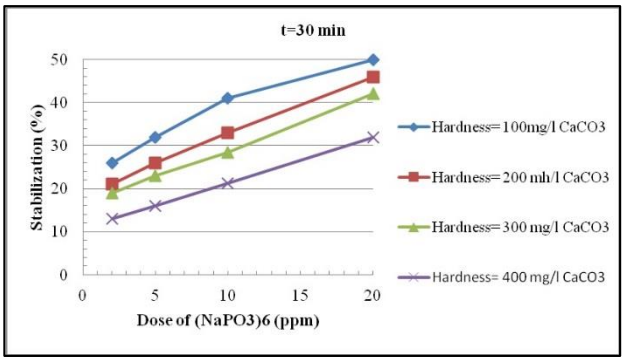

Figure 9. Effect of hardness on water stabilization with $(NaPO_3)_6$ at t= 30 min

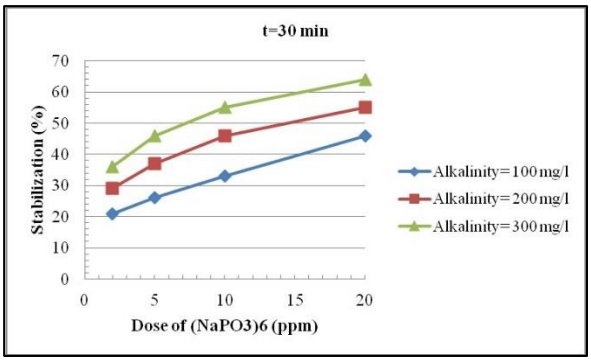

Figure 10. Effect of alkalinity on water stabilization with $(NaPO_3)_6$ at t= 30 min

3. Conclusion

Generally, the use of low phosphate dose (lower than 20 ppm), effectively prevents the formation of calcium carbonate precipitation. Also, for economic saving can be used less amount phosphate (10 ppm). Phosphates have different performance at different operating conditions, and the percentage of water stabilization at the same temperature and amount of phosphate, does not follow a given order for a different contact time. The stabilization efficiency with phosphate at different temperatures and times is between 20% and 80%.

The use of polyphosphates has better results than orthophosphates (about 3 times). At higher temperatures, the use of polyphosphates is not very suitable because it decomposes and converts to orthophosphate, and at higher temperatures it is better to use Glassy type polyphosphate.

In high alkaline environments, the use of sodium hexametaphosphate as an acidic property has better results in stabilizing efficiency, whiles the results in low alkalinity with Na_3PO_4 with

high alkaline properties, and is better. Usually, the time of 2 hours has the better stabilization efficiency

The use of useful additives such as starch increases the efficiency, and it is better to use lower doses (10-25 ppm) to make economically saving. In the environment with low hardness, the stabilization efficiency is improved, which is due to the effective function of phosphates in the formation of a complex with calcium ions

To prevent water corrosion, it is necessary to have a saturation index greater than zero to ensure that not only does corrosion not occur, but also a thin layer of sediment will be created. Depending on whether chemical inhibitors are used or not, LSI is chosen about 0.6-1. Today, in units where the water temperature is not high, they use the Langelier Saturation Index to control water quality, which is known as water stabilization.

It is emphasized that the Langelier Saturation Index or sediment index is merely a qualitative indication of the tendency to precipitate or corrosion, and does not determine the amount of sediment content is created or the amount of corrosion.

For example, water with high hardness and positive saturation index leads to a large amount of sediment, while the water with low hardness and the same amount of saturation index, may not produce considerable sedimentation.

References

[1] Langelier WF. Chemical Equilibria in Water Treatment. American Water Works Association, 1946; 38(2): 169-178, 1946.

[2] Ahmadun FR, Pendashteh A. Process for treating wastewater. US patent 9145316B2, 2008.

[3] Schock M R. Temperature and Ionic Strength Corrections to the Langelier Index Revisited. Journal of American Water Works Association, 1984; 76(8): 72-76.

[4] Langelier WF, Caldwell DH, Lawrence WB, and Spaulding CH. Scale Control in Sea Water Distillation Equipment - Contact Stabilization. Ind. Eng. Chem., 1950; 42(1): 126–130.

[5] Aiman EAl-R, Ehab MAl-Sh. Assessment of tap water resources quality and its potential of scale formation and corrosivity in Tafila Province, South Jordan. Desalination, 2007; 206(1–3): 322-332.

[6] Loewenthal RE, Morrison I, Wentzel MC. Control of corrosion and aggression in drinking water systems, Water Science & Technology, 2004; 49(2): 9-18.

[7] Igunnu ET, Chen GZ. Produced water treatment technologies, International Journal of Low-Carbon Techno-logies, 2014; 9(3): 157–177.

[8] Kababya S, Gal A, Kahil K, Weiner S, Addadi L, Schmidt A. Phosphate-water interplay tunes amorphous calcium carbonate metastability: spontaneous phase separation and crystallization vs stabilization viewed by solid state NMR. J. Am. Chem. Soc., 2015; 137(2): 990-8.

[9] Nguyen BT, Nicolai T, and Benyahia L. Stabilization of Water-in-Water Emulsions by Addition of Protein Particles. Langmuir, 2013; 29(34): 10658–10664.

[10] Feodorov V. Modern Technologies of Treatment and Stabilization for Sewage Sludge from Water Treatment Plant. Agriculture and Agricultural Science Procedia, 2016; 10: 417-430.

[11] Dickhout JM, Moreno J, Biesheuvel PM, Boels L, Lammertink RGH, de Vos WM. Produced water treatment by membranes: A review from a colloidal perspective. Journal of Colloid and Interface Science, 2017; 487: 523-534.

To whom correspondence should be addressed: Laleh Shirazi, Gas Division, Research Institute of Petroleum Industry (RIPI), Tehran, Iran, shirazil@ripi.ir

Petroleum and Coal

Article **Open Access**

QUANTITATIVE PETROPHYSICAL EVALUATION AND RESERVOIR CHARACTERIZATION OF WELL LOGS FROM "DATOM" OIL FIELD, NIGER DELTA

*Lawson-Jack Osaki[1], and Alexander Ifeanyichukwu Opara[2]**

[1] Rivers State University of Science and Technology, Nkporo, Rivers State, Nigeria
[2] Department of Geology, Federal University of Technology, Owerri, Nigeria

Received March 31, 2018; Accepted June 20, 2018

Abstract

This paper presents a detailed reservoir characterization of three wells in "Datom" Oil Field, Niger Delta using well logs data. The distributions and thicknesses of sand bodies were determined within each of the wells in the field using interactive petrophysical (IP) software. The quantitative and qualitative analysis were done for the three exploration wells with the depth ranges of 8700-9200ft for Datom North well , 8900-9400ft for Datom West well, and 9000-9500ft for Datom East well. Two distinctive porous sand bodies were identified across the field (A and B), Datom North has it reservoirs as 1A (8815-8903ft) and 1B (9100-9157ft), Datom West has its reservoir as 2A (8996-9095ft) and 2B (9263-9321ft) and Datom East as 3A (9101-9219ft) and 3B (9357-9418ft). Petrophysical evaluation was made from a suite of wire-line logs comprising of gamma ray, resistivity, neutron and density logs of the wells. The average porosity values obtained are in the range of 0.18-0.22 with average net pay permeability values ranging from 322.70mD to 733.20mD. The water saturation obtained for each reservoir unit in combination with the resistivity index was used to prove the presence of hydrocarbon in the sand units. The hydrocarbon saturation of the reservoirs are in the range of 0.6-0.7 across the prospect zones with gas effect of the combination logs of neutron and density indicating the hydrocarbon accumulation is predominantly gas. The average net to gross ratio across the reservoirs (0.7-0.9) is defined using an average porosity ($\emptyset$) and volume of clay (V_{clay}) cut offs values of ≥ 0.1 and ≤ 0.5 respectively. With a moveable hydrocarbon index (MHI=S_W/S_{XO}) less than 0.7 across the sand units, it shows favorable hydrocarbon moveability in the reservoirs. The results clearly revealed that the gas bearing sand units have good reservoir potentials favorable for hydrocarbon production.

Keywords: *Petrophysics; Net-to-Gross; Niger delta; well logs; Porosity; Water and Hydrocarbon Saturation.*

1. Introduction

The search for hydrocarbons starts with a regional knowledge of the prevailing geology in a geologic basin, where the geologist is in charge of the sedimentary sand deposition. After the geophysicist conducts seismic surveys and data processing, risky wildcat exploration wells may be drilled to test the best geological and seismic structural model. If a hydrocarbon discovery is made, data must be collected to evaluate the scale, quality, and quantity of the discovery. The resolution of moving an exploration well to completion is depended on its economic valiabity. To establish this viability a qualitative and quantitative analysis of all available well data is paramount. This analysis carried out at about the midpoint of a critical financial investment in the field development study will eventually determine whether to proceed with well completion and incur the relative cost or otherwise. Unarguably petrophysics plays a sensitive role in the evaluation of well and field potential.

Petrophysics actually converts resistivity, gamma ray and porosity tool measurements into reservoir properties, resistivity and porosity are the single most important measurements made by convectional logging tools and form the foundation on which the entire industry is built. Petrophysics evaluation combines well log, core, mud log, and other disparate data

sources for the purpose of analyzing, predicting, and establishing formation lithology and porosity, hydrocarbon saturation, permeability, producibility, and estimating the economic viability of a well. According to Asquith and Krygowski [1], well logs are used to correlate zones suitable for hydrocarbon accumulation, identify productive zones, determine depth and thickness of zones, distinguish between gas, oil and water in a reservoir and to estimate hydrocarbon reserves.

Qualitatively the petrophysical evaluation is centered on translating geophysical responses to geological parameters, for instance, what natural radioactivity means as regard shale content; how sonic velocity can be interpreted as regard shale compaction; what bulk density means in terms of mineral composition etc. The ambit of this independent study is limited to the use of geophysical well log data to achieve not only the lithology and fluid type of the prospect zones but also the average water saturation and the productive capabilities will be predicted. However, as relevant as log parameters are, they should not be applied without the consultation of other necessary data like drill stem test, mud log evaluation, sample shows, nearby production etc, before taking a decision to drill.

In this study therefore, we carried out petrophysical evaluation and volumetric estimation of the "Datom" Field from a suite of wire-line logs comprising of gamma ray, resistivity, neutron and density logs of the wells. The analyses carried out involved the delineation of lithologies, identification of reservoirs and fluid types, wells correlation and determination of petrophysical parameters (porosity, hydrocarbon saturation, volume of shale, formation resistivity, net to gross ratio, water saturation, permeability etc) of the identified reservoirs. The objective of this study therefore was to carry out a detailed hydrocarbon reservoir characterization of the "Datom" Field using well log data.

1.1. Location and geology of the study area

The 'Datom' Oil Field is located within the central swamp depobelt of Niger delta basin, Nigeria (Figure 1). Several earlier scholars have presented detailed information on the regional geology, stratigraphy and structure of the Niger delta basin in several key publications [2-10]. Niger Delta according to Klett *et al.* [11] is situated within the Gulf of Guinea with extension throughout the Niger Delta Province. It is located in the southern part of Nigeria between the longitude 4^0 –9^0 E and latitude 4^0-6^0 N. It is situated on the West African continental margin at the apex of the Gulf of Guinea, which formed the site of a triple junction during continental break-up in the Cretaceous [12].

From the Eocene to the present, the Niger delta has prograded south-westward, forming depobelts that represent the most active portion of the delta at each stage of its development [12]. These depobelts form one of the largest regressive deltas in the world with an area of some 300, 000km^2 , a sediment volume of 500,000 km^3 and a sediment thickness of over 10 km in the basin depocenter [13]. Niger Delta Province contains only one identified petroleum system referred to as the Tertiary Niger Delta (Akata –Agbada) Petroleum System [13-14]. Extended research by Tuttle *et al.* [15] confirmed this one petroleum system with the delta, which was formed at the triple junction related to the opening of the southern Atlantic beginning in the late Jurassic and continuing into the Cretaceous. The delta began its development in the Eocene with the accumulation of sediments that are now about 10 kilometers thick [12-14]. The area is geologically a sedimentary basin, and consists of three basic Formations: Akata, Agbada and the Benin Formations. The Akata is made up of thick shale sequences and it serves as the potential source rock. It is assumed to have been formed as a result of the transportation of terrestrial organic matter and clays to deep waters at the beginning of Paleocene [12]. According to Doust and Omatsola. [12] the thickness of this formation is estimated to about 7,000 meters thick, and it lies under the entire delta with high overpressure. Agbada Formation is the major oil and gas reservoir of the delta, It is the transition zone and consist of intercalation of sand and shale (paralic siliciclastics) with over 3700 meter thick and represent the deltaic portion of the Niger Delta sequence [13,16]. Agbada Formation is overlain by the top Formation, which is Benin. Benin Formation is made of sands of about 2000m thick [2].

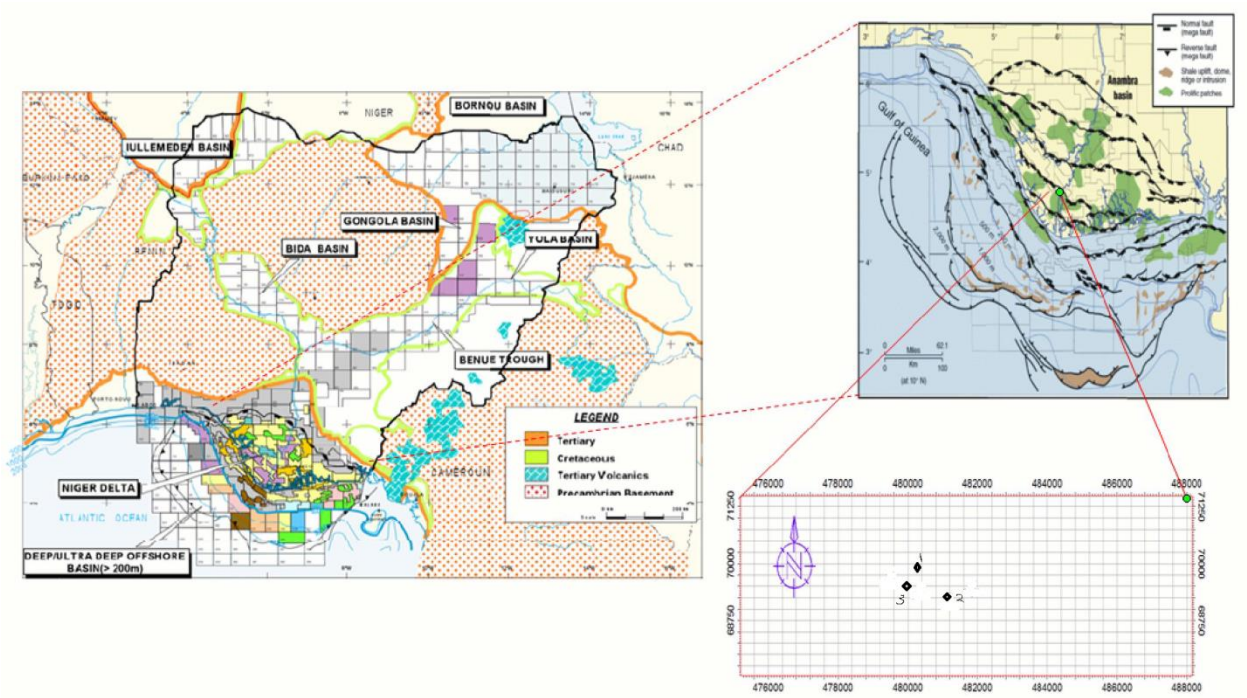

Fig 1. Map of Nigeria Showing the Location of the Niger Delta and the Base map of Datom oil field with well locations (well 1,2,3) representing Datom North, Datom East and Datom West respectively *(Modified from Whiteman [16])*

2. Methodology

Log analysis, or formation evaluation was done with Interactive petrophysics (IP) software. The evaluation requires the synthesis of logging tool response physics, geological knowledge, and auxiliary measurements or information to extract the maximum petrophysical information concerning the subsurface formations. The qualitative and quantitative analyses were carried out on the available petrophysical logs (GR,Resistivity, neutron and Density logs) of the Datom oil field. While qualitative analysis involves the assessment of reservoir properties, fluid type from log pattern, quantitative analysis deals with the numerical estimation of reservoir properties viz; % of gas, oil and water. Empirical formulae were used to estimate the petrophysical properties of the mapped reservoir units delineated on the well logs.

The first task is to identify the zones with a low-volume fraction of shale since such zones (clean zones) are more likely to produce accumulated hydrocarbons. This task has traditionally been accomplished through two measurements: the gamma ray and combine effect of the neutron and density log, In the reservoir units, gamma ray (GR) log which measures natural radioactivity in formations reflects the shale contents while the compensated neutron/density log was use to validate the porosity and the lithology both logs were used for the identification of sand / shale lithology in the Datom field. The resistivity log in combination with the GR logs were used to differentiate between hydrocarbon and non-hydrocarbon bearing zones since hydrocarbon is a nonconductor. The combination of the neutron and density log further validates the sand-shale zones and detection of gas bearing zones. The reservoir units were further characterized quantitatively to arrive at petrophysical parameters, which includes: volume of shale, formation factor, porosity, water saturation, permeability and so on. Some of these parameters are discussed.

Gamma Ray Index

The gamma ray log is generally used to determine the gamma ray index using the formula according to Asquith and Gibson [17] as given in equation 1:

$$I_{GR} = (GR_{LOG} - GR_{MIN})/(GR_{MAX} - GR_{MIN}) . \quad (1)$$

where: I_{GR} =gamma ray index; GR_{LOG}=gamma ray reading of formation from log ; GR_{MIN}=minimum gamma ray (clean sand); GR_{MAX}= maximum gamma ray (shale).

Volume of shale

The volume of shale was calculated by applying the gamma ray index in the appropriate volume of shale equation according to Larionov [18] for tertiary rocks as given in equation 2:

$V_{sh} = 0.083[2^{(3.7 \times IGR)} - 1.0]$... (2)

where: V_{sh}=volume of shale ,I_{GR}= gamma ray index.

Porosity

The computation of porosity was done in stages, the first involved the use of the Wyllie equation to estimate the density derived porosity (ϕ_D), and then the neutron-density porosity (ϕ_{N-D}), was estimated using the neutron (ϕ_N) porosity coupled with the density derived porosity. The Wyllie equation for density derived porosity is given as shown in equation 3 [19]:

$\phi_D = (\ell_{max} - \ell_b)/(\ell_{max} - \ell_{fluid})$ (3)

where:ℓ_{max} =density of rock matrix = 2.65 g/cc; ℓ_b = bulk density from log; ℓ_{fluid} = density of fluid occupying pore spaces (0.74g/cc for gas, 0.9g/cc for oil and 1.1 g/cc for water).

The Neutron – Density porosity could be calculated according to The Neutron-Density porosity could be calculated using the equation of Hussien *et al*. [20] as:

$\phi_{N-D} = (\phi_N + \phi_D)/2$ *for oil and water column* (4)

$\phi_{N-D} = (2\,\phi_D + \phi_N)/3$ *for gas bearing zones*... (5)

Formation factor

The estimation of the Formation Factor was achieved using the popular Humble Equation [39]:

$F = a/\emptyset^m$ (6)

where, F = formation factor; a = tortuosity factor = 0.62 ; Ø = porosity; m=cementation factor = 2.15

Formation water resistivity (Ωm)

Using the Archie's equation that related the formation factor (F) to the resistivity of a formation at 100% water saturation (R_o) and the resistivity of formation water (R_w), the resistivity of the formation water was estimated as:

$R_w = R_o/F$ ... (7)

Water saturation

Determination of the water saturation for the uninvaded zone was achieved using the Archie [21] equation given.

$S_w^2 = (F \times R_w)/R_T$ (8)

But, $F = R_o/R_w$ (9)

Thus, $S_w^2 = R_o/R_T$ (10)

where: S_w = water saturation of the uninvaded zone; R_o= resistivity of formation at 100% water saturation; R_T= true formation resistivity.

Hydrocarbon saturation

This was obtained directly by subtracting the percentage of water saturation from 100.

Thus $S_{hy} = 1 - S_w$ r S_{hy} %= 100 - S_w% (11)

where: S_{hy} is the hydrocarbon saturation (expressed as a fraction or as percentage).

Resistivity Index

This was estimated using the ratio of formation true resistivity (R_t) to resistivity of formation at 100% saturation (Ro) as given in equation 12:

$I = R_t/R_o$ ... (12)

where: I is the resistivity index. When I is equal to unity, it implies that the reservoir is at one hundred percent (100%) water saturation, The higher the value of I, the greater the percentage of hydrocarbon saturation.

Bulk volume water

Bulk volume of water (BVW) was estimated as the product of water saturation (S_w) of the uninvaded zone and porosity ($Ø_{N-D}$). Thus, the bulk volume of water is shown in equation 13:

$BVW = S_w \times Ø_{N-D}$ ... (13)

where: $Ø_{N-D}$ = neutron-density porosity.

Hydrocarbon pore volume

The hydrocarbon pore volume (HCPV) is the fraction of the reservoir volume occupied by hydrocarbon. This was calculated as the product of neutron-density porosity and hydrocarbon saturation as shown in equation 14:

$HCPV = Ø_{N-D} \times (1 - S_w)$ (14a)

$HCPV = Ø_{N-D} \times (S_h)$ (14b)

Irreducible water saturation

The irreducible water saturation was calculated using the following relationship in equation 15. However, this theoretical estimate of irreducible water is majorly useful in the estimation of relative permeability.

$S_{wirr} = (F/2000)^{1/2}$ ... (15)

where: S_{wirr} = irreducible water saturation; F =formation factor.

Permeability

This was based on the relationship between permeability, porosity, and irreducible water saturation according to Wyllie and Rose [19]. The relationship is expressed in equation 16 as:

$K = [(250 \times (Ø_{N-D})^3)/S_{wi}]^2$ ... (16)

Shaliness (V_{sh} Total)

This is the total volume of shale represented as a depth factor within a well. It is calculated by using equation 17:

Average V_{sh} x Gross thickness ... (17)

Net thickness

This is the column of the reservoir that is occupied by reservoir formation (e.g. sand) only and exclusive of non-reservoir formations (e.g. shale). It is calculated by using equation 18:

Gross Thickness – V_{sh} Total ... (18)

Net to Gross ratio (NTG)

This is the ratio between the net reservoir thickness and the gross reservoir thickness. However in terms of hydrocarbon pay, it could be calculated as the ratio between the net pay thickness and the gross pay thickness. The four main steps in the application of a net-pay cut off to a particular reservoir interval are to establish a standard, calibrate one or more logs to the chosen standard, confirm that the calibration step produces results consistent with the standard, and apply the calibrated model to all wells [22-23]. The primary geological considerations in determining pay and non pay in the reservoir interval are depositional environment and hydrocarbon and structural history. The "net-to-gross ratio" or "net/gross" (N/G) is the total amount of pay footage divided by the total thickness of the reservoir interval (for simplicity, the well is assumed here to be vertical). The depositional environment provides a picture of whether the overall reservoir interval is sand rich (high N/G) or shale rich (low N/G) and the nature of the interbedding of high-quality rock with poor-quality rock. If the reservoir interval is quite interbedded with high-quality rock intimately layered with poor-quality rock

on the scale of a few inches to a few feet, the poor-quality rock intervals, if they contain hydrocarbons, will likely contribute to production [24-26]. However, if the layering is on a much larger scale with thick high-quality rock intervals separated from thick low-quality rock intervals, then the poor-quality rock intervals are much less likely to contribute significantly to production [22-26]. The NTG is generally estimated using equation 19:

NTG = Net thickness ÷ Gross Thickness (19)

Effective Porosity

This is the porosity of the interconnected pore spaces. It assumes the absence of shale from the reservoir. It can be calculated using the following relationship as shown in equation 20:

$\Phi_{effective} = (1 - V_{SHALE}) * \phi_{N-D}$ (20)

Storage Volume

This is the capacity to store hydrocarbon in the reservoir. The storage volume is always higher than the hydrocarbon pore volume within a well because the net pay zone is inclusive of the grain matrix whereas the grain matrix is absent in the hydrocarbon pore volume computation as only the hydrocarbon in the pore spaces is calculated for. The storage volume is generally estimated using the formula given in equation 21.

Storage Volume = ϕ_{N-D} * Net Pay Thickness … (21)

3. Result interpretation

In this study based on the analysis, two hydrocarbon bearing zones (Reser A and B) were identified for further interpretation.The sand units (Reser A and B) were delineated as hydrocarbon bearing sands within the Agbada formation of the field as shown from the correlation of three wells using well logs (Figure 2). The sands were identified to be highly prolific in hydrocarbon yield and were completely analyzed to estimate their petrophysical parameters. Increasing trend of the thickness of the shale units with depth indicate that the sequence is approaching the Akata Formation. The parameters deduced from the analysis include gamma ray index, porosity, net to gross, volume of shale, formation factor, irreducible water saturation, hydrocarbon saturation, water saturation and hydrocarbon pore volume etc. These parameters help to effectively quantify the reservoirs.

Datom North

The reservoirs (1A and 1B) of the Datom North well have its top and base at a depth interval of 8815.50ft - 8903.50ft and 9100ft - 9157.50ft respectively with a gross thickness of 88ft and 57.50ft, net pay interval of 79.25 and 38ft, N/G are 0.9 and 0.6 .The average neutron-density derived porosity for the reservoirs are 20% and 18%, Average water saturations are 0.32 and 0.33 respectively. The net pay permeability of reservoir 1A and 1B is fair to good,733mD and 598mD,average water of the flushed zone (S_{XO}) is 0.82 and 0.79 respectively (table 1.).

Table 1. Summary of the calculated averages of Petrophysical parameters of Datom North

Zone Name	Top reserv.MD (ft)	Base reserv.MD (ft)	Gross interval (ft)	Net pay interval MD (ft)	N/G ratio	Av.Phie (%)	Av Sw (%)	Swirr (%)	Av Vcl (%)
RESER 1A	8815.50	8903.50	88.00	79.25	0.90	20	32	31	22
RESER 1B	9100.00	9157.50	57.50	38.00	0.66	18	34	32	36

Zone Name	Net pay permeability (md)	S_{xo}	BVW	MHI	HCPV	S_h
RESER 1A	733.20	0.82	0.06	0.39	13.56	0.68
RESER 1B	598.60	0.79	0.06	0.43	11.90	0.66

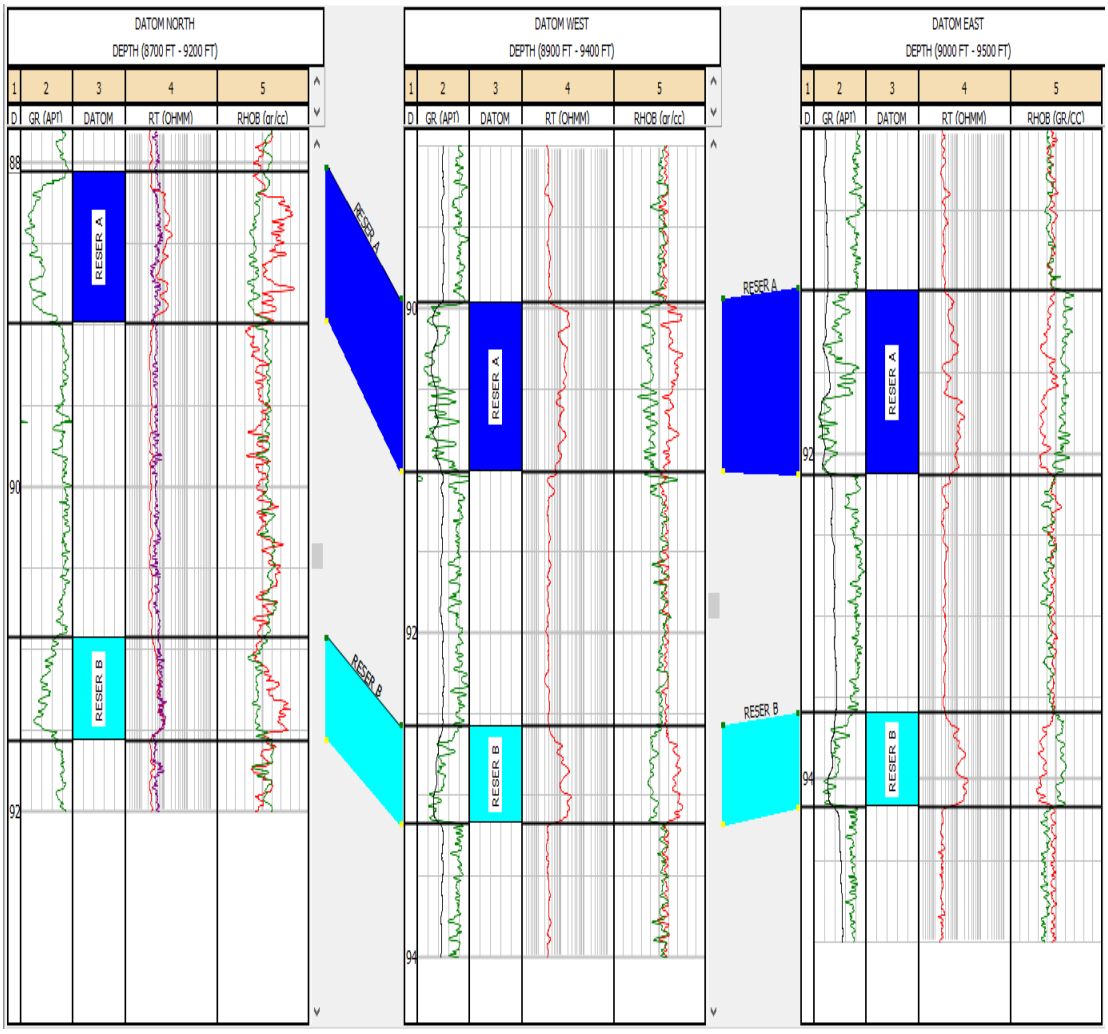

Fig 2. Well-to-well correlation panel of the study area showing hydrocarbon bearing sand units

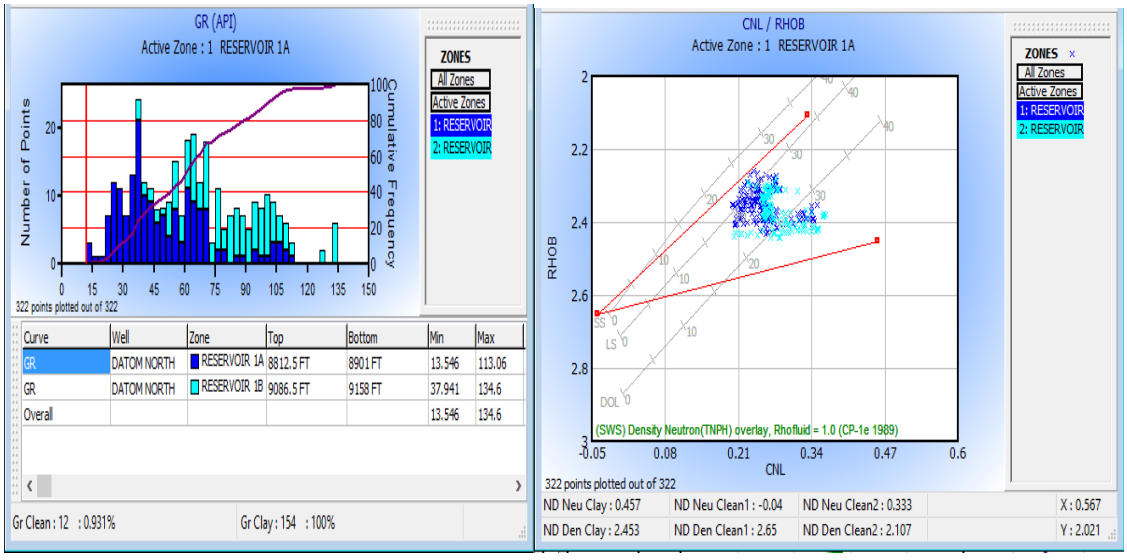

Fig 3. showing GR log histogram and cross plot of neutron-density log of reservoir 1A and 1B of the Datom north well for shale volume estimation

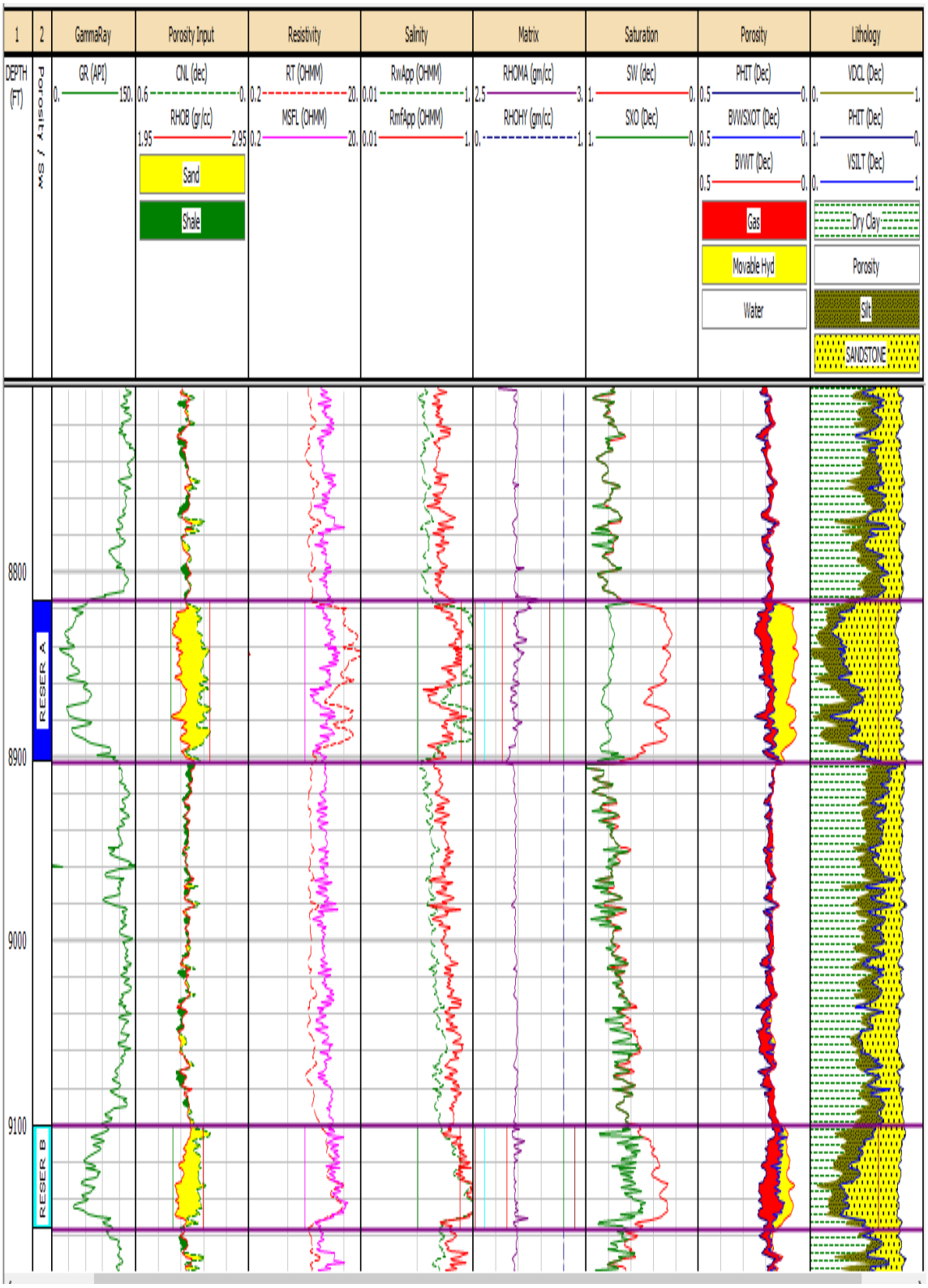

Fig 4. Comparison of petrophysical parameter logs of Datom north to validate lithology, fluid type, hydrocarbon producibilty

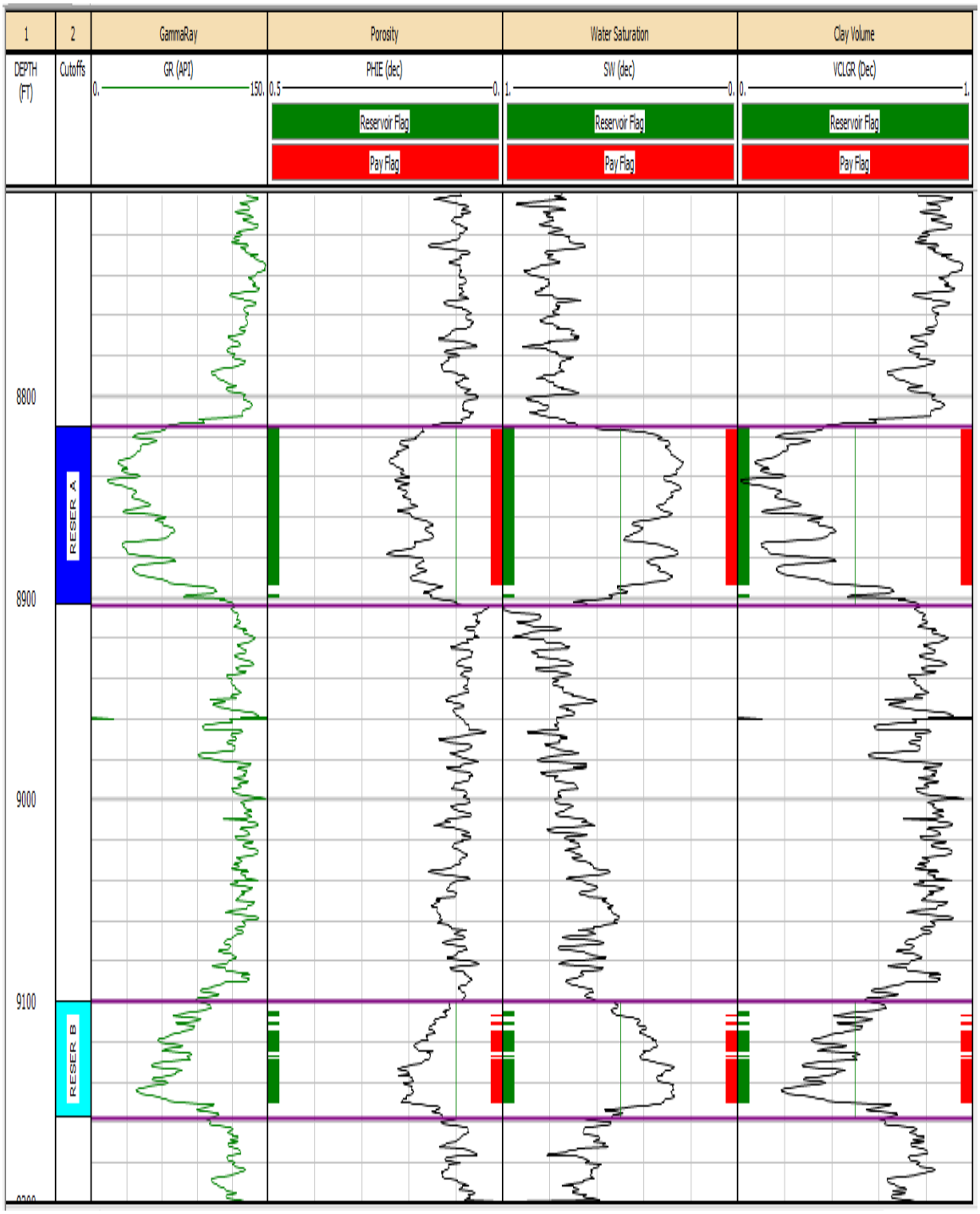

Fig 5. Showing summary of cut off from average porosity, volume of clay, water saturation to estimate net pay zones of Datom north well

Datom West

The average porosity of the reservoirs (2A and 2B) of the Datom West well is approximately 18%, with well top and base at 8996.50ft-9095ft and 9263ft-9321ft respectively. It has a gross thickness of 98ft and 58ft, Net pay thickness of 86.50ft and 48ft with a N/G ratio of 0.878 and 0.828. The water saturation is relatively good at 0.38 and 0.32. The permeability

of the net pay zone and the water saturation of the flushed zone for reservoir 2A and 2B are 640mD and 471mD (permeability) and approximately 0.9 for (S_{XO}) (table 2).

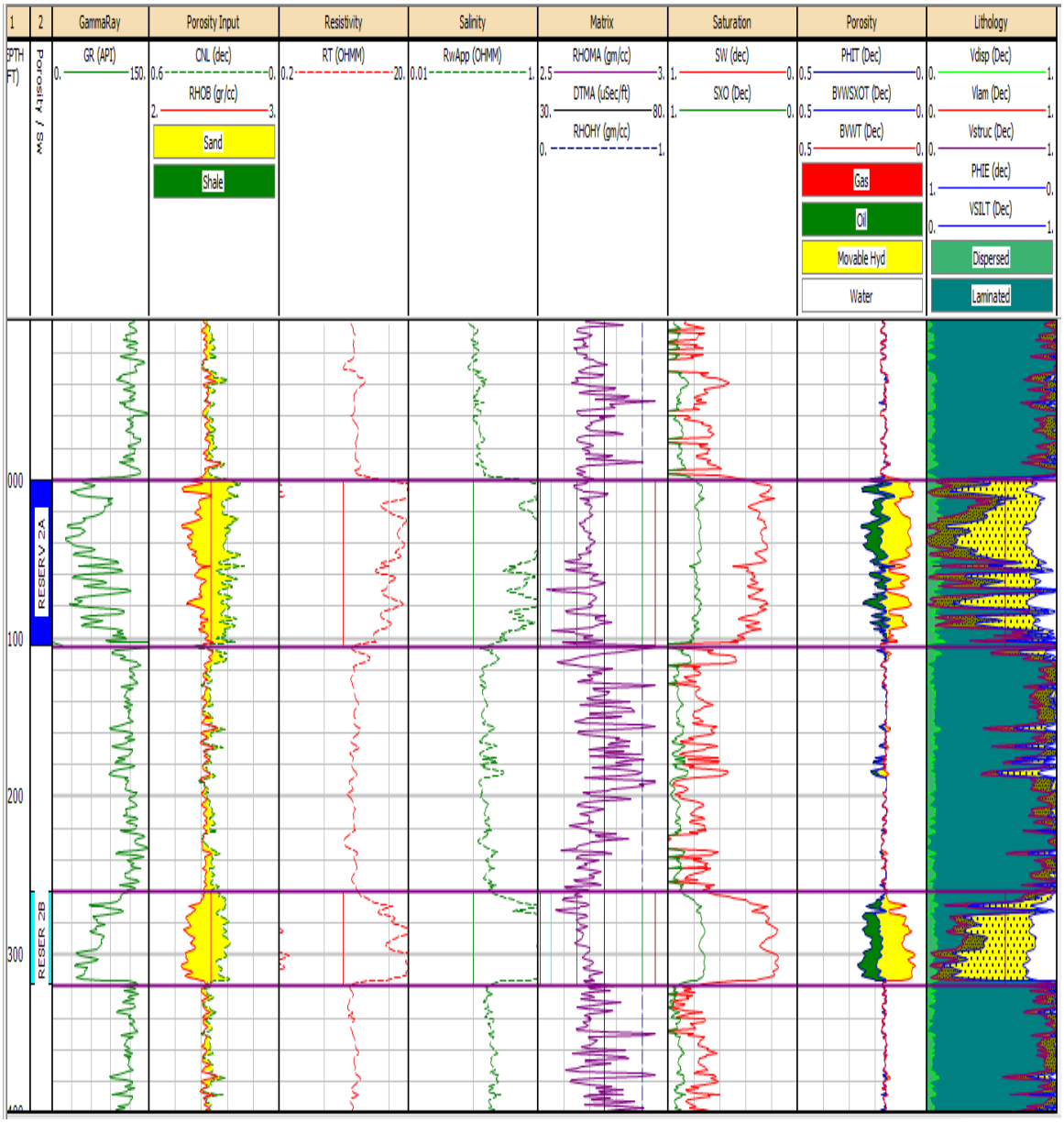

Fig 6. Comparison of petrophysical parameter logs of Datom west to validate lithology, fluid type, hydrocarbon producibilty

Table 2. Summary of the calculated averages of Petrophysical parameters of Datom west

Zone Name	Top reserv.MD (ft)	Base reserv. MD(ft)	Gross interval. MD, (ft)	Net pay interval MD(ft)	N/G ratio	Av.Phie (%)	Av Sw (%)	Sw irr (%)	Av Vcl
RESER 2A	8996.50	9095.00	98.50	86.50	0.88	19	37	35	0.14
RESER 2B	9263.00	9321.00	58.00	48.00	0.83	18	32	31	0.13

Zone Name	Net pay permeability, (md)	S_{xo}	BVW	MHI	HCPV	S_h
RESER 2A	640.5	0.88	0.07	0.26	11.84	0.62
RESER 2B	471.9	0.84	0.06	0.38	12.22	0.68

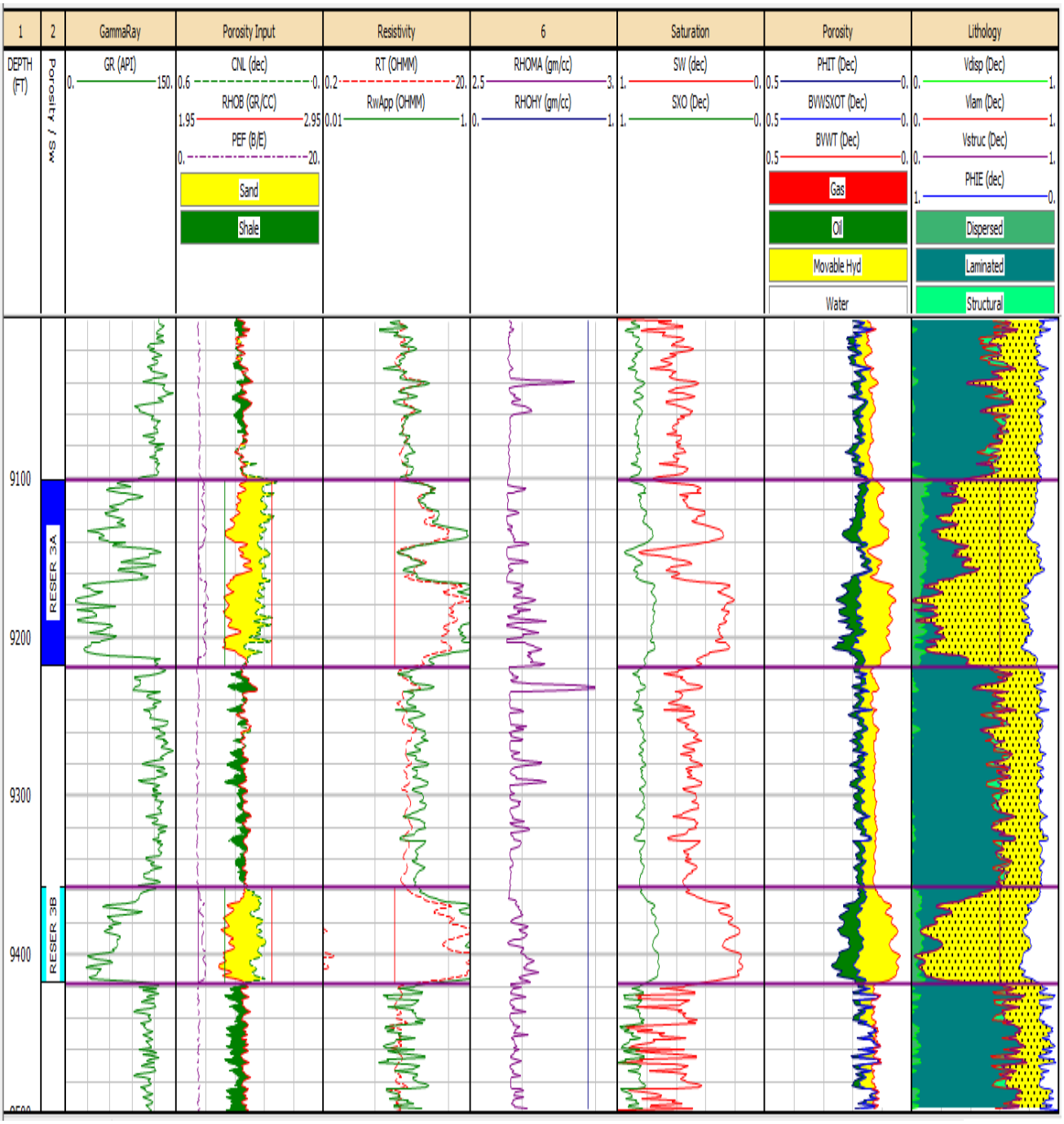

Fig 7. Comparison of petrophysical parameter logs of Datom east to validate lithology, fluid type, hydro - carbon producibilty

Datom East

The reservoirs in this well have average thicknesses from 9101ft -9219ft in reservoir 3A and 9357.50ft-9418ft in reservoir 3B. The average neutron-density derived porosity for the reservoirs are between 19% and 22%, which indicates good average porosity. The water saturation of the reservoirs is 0.34 and 0.22 with a gross interval of 118ft and 61ft respectively. The net pay thickness is 88.50ft and 48ft,N/G ratio of approximately 0.8, Average net pay permeability

is 587mD and 322mD with water saturation of flushed zone to be 0.81 and 0.79 respectively (table 3).

Table 3. Summary of the calculated averages of Petrophysical parameters of Datom East

Zone Name	Top reserv.MD (ft)	Base reserv. MD(ft)	Gross interval. MD, (ft)	Net pay interval MD(ft)	N/G ratio	Av.Phie (%)	Av Sw (%)	Sw irr (%)	Av Vcl
RESER 2A	9101.00	9219.00	118.00	88.50	0.75	19	34	34	36
RESER 2B	9357.50	9418.50	61.00	48.00	0.79	22	21	20	35

Zone Name	Net pay permeability, (md)	S_{xo}	BVW	MHI	HCPV	S_h
RESER 2A	587.30	0.81	0.07	0.42	12.50	0.66
RESER 2B	322.70	0.79	0.05	0.27	17.25	0.78

4. Discussion

A careful examination of the logs recorded through the three wells Datom (North, West and East) oil field shows two distinctive porous and permeable sand bodies (fig 3),where the shallow reservoir is indicated as Reservoirs (1A,2A,3A)and reservoirs (1B,2B and 3B) as the deeper reservoir of the three wells. The average porosity and net pay permeability are hydrocarbon production friendly and also the consistent decrease of these lithological properties with depth is perhaps due to compaction resulting from the weight of the overburden. While the resistivity logs were used to detect the presence of hydrocarbon in the reservoirs, the combination response (gas effect) of the neutron-density log through the sand units (clastic reservoirs) indicates that the hydrocarbons will dominantly be gas inferred from Figures 4, 6 and 7 [26-27].

The bulk water volume (BVW) of the reservoirs was calculated at several depths and are almost constant (0.06-0.07), this indicates homogeneity of the reservoirs and is validated by the close values of the water saturation (S_W) and irreducible water saturation (S_{wirr})as shown in tables 1,2&3.The implication is that hydrocarbon production from the zones at irreducible water saturation should be water free [28].With a moveable hydrocarbon index (MHI=S_W/S_{XO}) less than 0.7 across the sand units shows favorable hydrocarbon moveability in the reservoirs [29], this is in agreement with the increase in average water saturation (S_{XO}) of the flushed zones relative to water saturation (S_W) across the entire reservoir (table 1,2,3). The average net to gross ratio across the reservoirs (0.7-0.9) is defined using an average porosity ($\emptyset$) and volume of clay (V_{clay}) cut offs values of $\geq 0.1\ and\ \leq 0.5$ respectively (fig 5), validates the high level of clean sand in the reservoirs, such sand bodies confirm that the permeability and porosity are prospective [30-32]. An average hydrocarbon saturation (1-S_W) ranging from 0.6-0.7 (table 1,2,3) indicates that hydrocarbon is relatively higher than water in the reservoir, it is important to note that water saturation does not represent the ratio to hydrocarbon that will be produced from the reservoir but a reflection of relative proportion of the fluids contained in the reservoir.

Petrophysical analysis of the study area revealed average porosity values of 18-22% while the permeability values ranged from 322.70 – 733.20 md across the reservoirs. Hydrocarbon saturation and reservoir thickness across the reservoirs ranges from 66 - 78% and 48-98.50 ft respectively. The escalator regression sedimentation model of the Niger Delta makes it clear that younger sediments are found in the distal part of the basin with pronounced thickness greater than that on the proximal part [33]. Compaction was initiated early in the older rocks of proximal facies of the Depobelts of the Niger Delta and graded down basin ward. Similarly, the net-to- gross across the study area varies from 0.60- 0.9. Since it is well known that the lower the volume of shale the higher the N/G and the better the reservoir quality, therefore the higher N/G values across the study area is indicative of very good hydrocarbon reservoirs. Since it is generally believed by some authors that the sealing capacity of faults in a reservoir is a function of the shale percentage / shale content or the shale-sand ratio in a reservoir, it therefore means that the faults of the reservoir with more shale content may be more sealing

than the faults of the reservoir with lower shale content [12,34]. There also seem to be a gradual decrease in sand percentage moving away from the structure building bounding faults towards the distal flanks [35]. The stacked thicknesses of the reservoirs ranging between 18.20-33.86m and 31.48-77.47m for reservoirs Sand_A and Sand_B are relatively high.

5. Summary, Conclusion and Recommendation

Gamma ray, neutron, density, resistivity/conductivity logs were employed in the evaluation and examination of three wells, Datom (North, West and East). Two gas rich bearing sand units were delineated across the formation, with porosity ranging from 0.18 to 0.22 indicating a suitable reservoir quality, Favorable net pay permeability values from 322.70mD to 733.20mD derived from logs and hydrocarbon saturation range of 0.62 to 0.78 implied high hydrocarbon production. These results in addition with the hydrocarbon movability index (MHI) values suggest high hydrocarbon potential and a reservoir system whose performance is considered satisfactory for hydrocarbon production.

However, as relevant as log parameters are, they should not be applied without the consultation of other necessary data like drill stem test, mud log evaluation, sample shows, nearby production etc before taking a decision to drill. Secondly, the hydrocarbon reserve was not estimated due to unavailability of the area extent of the reservoir therefore I recommend that 3-D seismic data should be incorporated to allow for detailed and complimentary study of "Datom" Oilfield, which includes necessary parameters to enable an accurate static and dynamic model of the reservoir to be constructed. This will enhance the geometry of the geologic features, reveal the area extent of prospect zones and reduce inherent uncertainty.

References

[1] Asquith G and Krygowski D. Relationships of Well Log Interpretation in Basic Well Log Analysis Method in Exploration Series. American Association of Petroleum Geologists; 2004; 16: 140.

[2] Avbovbo. Tertiary lithostratigraphy of Niger Delta. American Association of Petroleum Geologists Bulletin, 1978; 62: 295-300.

[3] Short KC, and Stäuble AJ. Outline of geology of Niger Delta. Ame. Assoc. of Petrol. Geol. Bull., 1965; 51:761-779.

[4] Hospers J. 1965. Gravity field and structure of the Niger Delta, Nigeria. West Africa. Geol. Soc. of Ame. Bull., 1965; 76: 407-422.

[5] Hospers J. The geology of the Niger delta area. In: F.M. Delany (Editor), Continental Margin, Geol. E. Atlantique, SCOR Conference, Cambridge 1970. HMSQ: 123-142.

[6] Evamy BD, Haremboure J., Kamerling P, Knaap WA, Molloy FA, and Rowlands PH. Hydrocarbon habitat of Tertiary Niger Delta. Ame. Assoc. of Petrol. Geol. Bull., 1978; 62:277-298.

[7] Nton ME. and Adesina AD. Aspects of structures and depositional environment of sand bodies within Tomboy Field, Offshore Western Niger Delta, Nigeria. Mater. & Geo-environ., 2009; 56(3): 284–303.

[8] Ejeh OI. Sedimentary Fill Modelling Relationships to Sequence Stratigraphy and its implications for Hydrocarbon Exploration in the Niger Delta. Nig. Pacif. Jour. of Scie. & Tech., 2010; 11 (1): 502 – 509.

[9] Olowokere MT and Abe SJ. Structure and Facies Development Resulting from Neogene Gravity Tectonics and Depositional Processes: Application to Afo Field Niger Delta, Nigeria. Jour. of Emer. Trends in Engi. & Appl. Scie., 2013; 4(3):5-41.

[10] Edigbue PI, ,Komolafe AA, Adesida AA, and Itamuko OJ. Hydrocarbon reservoir characterization of "Keke" field, Niger Delta using 3D seismic and petrophysical data. Amer. Jour. of Sci. & Industr. Resear., 2014; 5(2): 73-80; DOI:10.5251/ajsir.2014.5.2.73.80.

[11] Klett TR, Ahlbrandt TS, Schmoker JW, and Dolton JL. Ranking of the world's oil and gas provinces by known petroleum volumes. U.S. Geological Survey Open-file Report-97-463, 1997.

[12] Doust H, and Omatsola E. Niger Delta, in, Edwards, J. D., and Santogrossi, P.A., eds., Divergent/passive Margin Basins, AAPG Memoir 48, 1990, Tulsa, American Association of Petroleum Geologists;p 239-248.

[13] Kulke H. Nigeria, in, Kulke, H., ed., Regional Petroleum Geology of the World. Part II: Africa, America, Australia and Antarctica. Berlin 1995, Gebrüder Borntraeger, p. 143-172

[14] Ekweozor CM, and Daukoru EM. 1994. Northern delta depobelt portion of the Akata-Agbada Petroleum System, Niger Delta, Nigeria, in The Petroleum system—from source to trap: AAPG Memoir, 1994; 60: 599-613.
[15] Tuttle MLW, Charpentier RR, and Brownfield ME.The Niger Delta Basin Petroleum System: Niger Delta Province, Nigeria, Cameroon, and Equatorial Guinea, Africa. Open- File Report 99-50-H, United States Geological Survey, World Energy Report:44, 1999.
[16] Whiteman A. Nigeria: its petroleum geology, resources and potential: Graham & Trotman, London 1982. 1: 390-394.
[17] Asquith GB, and Gibson CR. 1982. Basic Well Log Analysis for Geologists Methods in Exploration Series),The American Association of Petroleum Geologists(AAPG) ; 1982: 216pp
[18] Larionov VV. Radiometry of boreholes (in Russian), NEDRA 1969, Moscow.
[19] Wyllie MRJ, and Rose WD. 1950. Some Theoretical Considerations Related to the Quantitative Evaluation of the Physical Characteristics of Reservoir Rock from Electric Log Data," Trans., AIME, 1950; 189: 105.
[20] Hussein S, Hassan S, Klimentos T, Boyd A and Zeid A. Using NMR and Electrical Logs for Enhanced Evaluation of Producibility and Hydrocarbon Reserves in Gas Reservoirs with High Irreducible Water Saturation; 40th SPWA Logging Symposium, 30 May-3 June.,1999, Oslo, Norway;Paper HH.
[21] Archie GE. 1941. The electrical resistivity log as an aid in determining some reservoir characteristics. Transactions of AIME, 1941; 146: 54–62.
[22] Cobb WM, and Marek FJ. Net Pay Determination for Primary and Water flood Depletion Mechanisms. Presented at the Socie. Petrol. Engin. (SPE) Annual Technical Conference and Exhibition 1998, New Orleans, Louisianna, USA, 27–30 September. 1998; SPE-48952-MS. http://dx.doi.org/10.2118/48952-MS.
[23] Egbele E, Ezuka I and Onyekonwu R. Net-To-Gross Ratios: Implications in Integrated Reservoir Management Studies. Nigeria Annual International Conference and Exhibition of the Socie. of Petrol. Engi (SPE), 1-3 August,2005, Abuja, Nigeria. SPE-98808-MS; https://Doi.org/10.2118/98808-MS
[24] Inichinbia S, Sule PO, Hamza H, and Ahmed AL. 2014. Estimation of net-to-gross of among hydrocarbon field using well log and 3D seismic data. IOSR Jour. of Appl. Geol. and Geophys., 2014; 2(2): 18-26.
[25] Maharaja A. Global net-to-gross uncertainty Assessment at reservoir appraisal stage. Doctor of Philosophy Thesis, Department of Energy Resources Engineering 2007, Stanford University, USA: 144.
[26] Doust H. The Niger Delta hydrocarbon potential, a major Tertiary NigerProvince. Proceedings of KNGMG Symposium 1989, Coastal Lowstands, Geology andGeotechnology, The Hague, Kluiver Acad. Publ., Dordrecht.p22-25.
[26] Zee Ma Y, Moore W, Kaufman P, Luneau B and Gomez E. Identifying Hydrocarbon Zones in Unconventional Formations by Discerning Simpson's Paradox. Soc. of Petrol. Engi.(SPE) Western North American and Rocky Mountain Joint Regional Meeting, Denver, Colorado, USA, 16–18 April 2014; SPE 169495-MS:11.
[27] La Vigne J, Herron M, and Hertzog R. Density-Neutron Interpretation in Shaly Sands. In Trans., Society of Petrophysicists and Well Log Analysts: 35th Annual Logging Symposium. Paper EEE.
[28] Morris RL and Biggs WP. Using log-derived values of water saturation and porosity. Soc. Professional Well Log Analysts, 8th Ann Logging Symp 1967, p. 13.
[29] Schlumberger Educational Services, Log Interpretation Principles/ Applications. 1989.
[30] Osaki LJ. 3D Seismic Attributes Analysis And Reserve Estimation Of ''Guramala Field'', Coastal Swamp Depobelt, Niger Delta. (Unpublished M.Sc Dissertation) Federal University Of Technology 2015, Owerri;142p.
[31] Osaki LJ, Opara AI, Adiela UP, Njoku IO, Emberga TT,and Eluwa N. 3D Seismic Interpretation and Volumetric Estimation of "Osaja Field" Niger Delta, Nigeria. Int. Lett. Nat. Sci., 2016; 59: 14-28.
[32] Opara AI. 2010. Prospectivity Evaluation of "Usso" Field, Onshore Niger Delta Basin, Using 3-D Seismic and Well Log Data. 2010; Pet Coal 52(4): 307-315.
[33] Knox GJ, and Omatsola EM. Development of the Cenozoic Niger Delta in Terms of the "Escalator Regression" Model and Impact on Hydrocarbon Distribution. In: van der Linden, W.J.M., et al., eds., Proceedings of KNGMG Symposium on Coastal Lowlands 1989, Geology, Geotechnology, Kluwer Academic Publishers, Dordrecht: 181-202.

[34] Weber KJ, and Daukoru EM. Petroleum geology of the Niger Delta. Proceedings of the Ninth World Petroleum Congress, Volume 2, Geology: London, Applied Science Publishers 1975, Ltd: 210-221.
[35] Stacher P. Present understanding of the Niger Delta hydrocarbon habitat. in, Oti, M.N., and Postma, G., eds., Geology of Deltas: Rotterdam 1995, A.A. Balkema: 257-267.
[36] Dresser. Log interpretation charts, Houston Dresser Industries 1979, Inc. pp. 107.
[37] Bhuyan K, and Passey QR. Clay Estimation from GR and Neutron-Density Porosity Logs. PWLA 35th Annual Logging Symposium, 19-22 June, Tulsa, Paper D.
[38] Nwajide CS. 2013.Geology of Nigeria's Sedimentary Basins. CSS Bookshops Limited, Lagos, Nigeria 2013:120; ISBN: 978-978-8401-67-4.
[39] Winsauer WO, Shearin HM, Masson PH, and Williams M. 1952. Resistivity of brine Saturated Sands in Relation to pore Geometry. AAPG Bulletin, 1952; 36: 253-277.

To whom correspondence should be addressed: Alexander Ifeanyichukwu Opara, Department of Geology, Federal University of Technology, Owerri, Nigeria, oparazanda2001@yahoo.com

Petroleum and Coal

Article **Open Access**

ENHANCING THE PHYSICO-MECHANICAL/RHEOLOGICAL PROPERTIES OF ASPHALT 60/70 IN DIFFERENT MEDIA VIA MA-PP COMPATIBILIZED POLYPROPYLENE/ACRYLONITRILE BUTADIENE RUBBER BLENDS (PP/NBR)

M. M. Badr[1], M. El-Shafie[2], A. A. Ragab[2]

[1] *Petrochemical Department, Egyptian Petroleum Research Institute (EPRI), Nasr City, Cairo, Egypt*
[2] *Petroleum Applications Department, Egyptian Petroleum Research Institute, Nasr City, Cairo, Egypt*

Received April 2, 2018; Accepted June 25, 2018

Abstract

Elastic reverse deformation and enhance the mechanical / rheological properties at low temperatures are desired in asphalt modification. So, thermoplastic elastic blends 3, 5, 7and 10% PP/NBR with and without using PP-MA were used. PMAs were evaluated using Penetration Index (PI), temperature susceptibility, shear stress / shear rate, dynamic viscosity and mechanical properties in different media air and water, tensile shear strength and elongation. The results showed that the addition of polymers to asphalt reduces its thermal susceptibility at different temperatures since the asphalt become more elastic, PMAs have thixotropic property, high yield stress, good gunnability and lack of flow on vertical surfaces. It is found also, the tensile shear strength for the obtained blends increases with polymer content with using PP70/MA more than PP70. In both water and air PP70 & PP70/MA enhancing the mechanical properties of asphalt but in air is the best, while the suitable ratio is 7 & 5% according to workability. Finally, PMAs have a higher tensile strength means asphalt can tolerate higher strains before failing (i.e. cracking). Additionally, the moisture susceptibility of the asphalt mixture can be evaluated by comparing the tensile strength of asphalt mixtures exposed to wet and dry conditions.

Keywords: *Asphalt; thermoplastic elastic; polypropylene, enhancing; susceptibility; rheological.*

1. Introduction

The history of polymer blends is quite long and strictly correlated with that of polymers themselves [1]. Along with over increasing growth in the application of engineering polymers such as polymer blends [2] composites [3-5] and nanocomposites [6], understanding of their mechanical behavior under long-term loading conditions becomes more significant and challenging.

Indeed, blending two or more polymers may give rise to new polymeric systems with new, interesting properties, different from those of the two components, thus eliminating the long and expensive route of synthesizing new polymers [7-10]. Nevertheless, an important shortcoming in blending different polymers is that the polymers often form immiscible and incompatible blends, displaying a coarse morphology with particles of dispersed phase badly adherent to the matrix and badly distributed. Consequently, a compatibilization process is necessary in order to modify the interfacial properties in the immiscible polymer blend, thus leading to a reduction of the interfacial tension coefficient and the formation and stabilization of the desired morphology. Several compounds have been used as compatibilizers including, more recently, nanoparticles that can modify the final morphology of the polymer blend [1]. A recent outstanding book [11] outlines the behavior of many polymer blends used in several applications or just investigated.

The simple blending of crystalline thermoplastic and elastomeric polymer results in a new class of material termed a thermoplastic olefin (TPO). The properties of the resultant TPO will be derived from the properties of each of the two polymers and dependent on the composition

and the interaction between their phases [12–15]. An approach to further improve the performance of TPO is to develop dynamically vulcanized TPO [16]. During dynamic vulcanization, the rubber is vulcanized in the presence of the molten thermoplastic under shear forces. Since crosslinked rubber is unable to coalesce, rubber particles are dispersed in the thermoplastic matrix even at high rubber content [16]. The effect of the dynamic vulcanization on morphology and mechanical properties has been extensively studied, and some important reviews are available in the scientific literature. Acrylonitrile butadiene rubber (NBR) is a commonly used oil-resistant rubber. Polypropylene (PP)/NBR-based TPO combines the oil resistance of NBR as well as excellent chemical and moisture resistance, good ductility and stiffness, low density, and easy processing characteristics of PP [17]. The large difference in the solubility parameter between the polar NBR and the non-polar PP leads to poor compatibility of blends. As a result, PP and NBR are highly incompatible and usually exhibit phase-separated morphology because of poor physical, mechanical and chemical interactions across the phase boundaries [18]. The interfacial adhesion and mechanical properties of PP/NBR blends can be improved by the addition of compatibilizers or interfacial agents. Phenolic-modified PP and maleic anhydride-modified PP are two main types of a compatibilizer for PP/NBR blends. George *et al.* [19] have reported several works about the effect of phenolic-modified PP and maleic-modified PP as compatibilizers on the properties of PP/NBR blends.

Thermoplastic elastomers (TPEs) are a class of copolymers or a physical mixture of polymers (usually a plastic and a rubber) which consist of materials with both thermoplastic and elastomeric properties. TPEs have attracts more attentions in the industry since they combine the properties of vulcanized rubber with the ease of processing of thermoplastics [20–25]. Styrene–butadiene–styrene copolymer (SBS) is a typically synthesized copolymer and the largest TPE being used as asphalt modifier because of its good compatibility with asphalt, workability and high performance.

However, the poor oxidation resistance caused by the presence of double bonds in the backbone of SBS and high cost are the main challenges before selecting it as asphalt modifier [26–30]. Therefore, more competitive TPEs are deserved to develop for asphalt modification.

Maleic anhydride and irradiation approach are also used to improve compatibility [31]. Magioli [20] has reported using dynamic vulcanization technology to enhance the properties of TPE.

In modification of a paving asphalt, it is desirable to increase its softening point, make penetration less temperature-dependent, make asphalt less susceptible to elastic reverse deformation, increase the ductility (especially at low temperatures), enhance the adhesion of the asphalt to mineral fillers of asphalt concrete, and extend the range of working temperatures [32]. To this end, it is first necessary to ensure good compatibility of rubbers with asphalts. However, elastoplastics are not all compatible with asphalts. Their compatibility depends on the chemical composition of both asphalts and elastoplastics.

It is known that high-molecular-weight rubbers to be compounded with asphalt require, for swelling and subsequent dissolution, a larger amount of oils than that contained in paving asphalts. Furthermore, these rubbers (elastoplastics) can induce coagulation of asphaltenes, which are the major structuring components of asphalts; this is inadmissible in the production of high-performance paving asphalts [33-34].

In this paper, thermoplastic elastic blends (PP/NBR in percentages 3, 5, 7 and 10 wt/wt%) use to achieve desired properties in the presence of maleic anhydride (10 wt/wt%) as a compatibilizer for good compatibility blends. PMAs were evaluated via Physical characterization (PI, temperature susceptibility, and routine tests), rheological (shear stress/ shear rate, dynamic viscosity) and mechanical properties in different media (air and water) (Tensile shear strength and elongation). The results showed that as expected the addition of polymers to asphalt reduces its thermal susceptibility at temperatures and guarantees a greater constancy of its properties since the asphalt become more elastic. Increasing the ratio of polymer added found to improve the physical and rheological properties, rheological data PMAs indicates that the PMAs have thixotropic property and high yield stress, good gunnability and lack of flow on vertical surfaces. It is found. Also, the tensile shear strength (N/cm^3) for the obtained blends

increase with polymer % content and for that forming with using PP70/MA more than that with using PP70 so, addition of TEPs (PP70& PP70/MA) enhancing the mechanical properties of virgin asphalt 60/70 in both water and air but in air is the best. Finally, polymer modified asphalt samples have a higher tensile strength means asphalt can tolerate higher strains before failing (i.e., cracking). Additionally, the moisture susceptibility of the asphalt mixture can be evaluated by comparing the tensile strength of asphalt mixtures exposed to wet and dry conditions.

2. Experimental

2.1. Materials

Local virgin asphalt cement of penetration grade (AC 60/70) produced by El-Nasr Petroleum Company in Suez, Egypt. PP70/ NBR30, PP70/NBR30/10% MA which prepared according to Motawie *et al.* [35].

2.2. Experimental procedure

The testing program included the following steps.

2.2.1. Characterization of virgin asphalt 60/70

The virgin asphalt sample was tested as illustrated in Table 1 for penetration (ASTM D5), softening point (ASTM D36), specific gravity (ASTM D70), Brookfield viscosity (ASTM D4402) and n-heptane insoluble (ASTM D3297). The results are illustrated in Table 1.

Table 1. Physical and chemical properties of asphalt samples AC 60/70 used for modification

Physical properties of asphalt samples AC 60/70					
Penetration 0.01mm 25°C	Ductility, cm	Kinematic viscosity 135°C, C.st	Absolute viscosity 60°C	Softening point, °C	Specific gravity, g/cm^3
62	150	259	1088	50.6	1.1763
API	Penetration temperature susceptibility	Penetration index	Specific heat Btu pound per °F	Thermal conductivity	
-11.20	0.0273	-0.51	0.391	0.6330	
Chemical properties of asphalt samples AC 60/70					
Wax %		Oil %	Resin %	Asphaltene content %	
6.88		28.90	55.10	16.41	

2.2.2. Preparation and evaluation of PP/NBR blends

PP/NPR blends of various weight compositions with and without compatibilizers were prepared with a Brabender plasticorder (PL 2100, 350S). At the start, PP was introduced into the Brabender plasticorder preheated to 180°C for 2 min, the tested compatibilizer was incorporated, and NBR was added thereafter. The mixer was operated at 180°C; the rotor speed is maintained at 60 rpm for 6 min. Upon using MAH, benzoquinone (0.75 parts) and dicumyl peroxide (3 parts) were added in a Brabender plasticorder at 180°C with the above mentioned technique 5,16 giving maleic acid-modified PP (MA-PP) as a compatibilizer.

Property evaluation

The tensile strength (rR), elongation at break (eR), and young's modulus (E) were determined with a universal tension testing machine (type M-10 Hunge Ta Instruments). The compressed sheets were cut into dumbbell-shaped specimens with appropriate punching dies with a width of 4 mm (DIN 53504). The specimens, with a width of 4 mm, a neck length of 50 mm, a thickness of 1–1.5 mm, were tested at a crosshead speed of 50 mm/min.17 The hardness of test specimens at least 6-mm thick was measured with a shore A durometer (PTC instrument of Model 306L18). Mass swell percentages of the test pieces were carried out in the

benzene/acetone solvent mixture. About 0.1–0.2 g of each specimen (square test pieces with 5-mm dimensions and 1-mm thick) was weighed in a weighing bottle, which was covered with benzene/acetone solvent mixture 50/50 for 24 h. The swollen samples were weighed and then dried in an oven to a constant weight. The last weight was taken as the correct weight of the sample free from dissolved matter. The mass swell percentages Q of the samples were calculated as follows:

$Q = [(m-m_o)/m_o] \times 100$ (1)

where m and m_o represent the weights of the samples after swelling and original one, respectively.

All these tests were performed at room temperature (25°C ± 1°C), and the reported results were averaged from a minimum of five specimens.

2.2.3. Evaluation of polymer blends carried out according to the following subsections

2.2.3.1. Mechanical measurements for polymer blends with and without MA as a compatibilizer

Tensile strength (T_s) MPa, elongation at break (E_b) %, absorbed energy Kgf.mm, Young's modulus MPa, and hardness, were measured for the all prepared samples.

Table 2. Mechanical Properties of PP/NBR and PP70/10 MA Binary Blend Samples with Different Ratios of Blending

Sample	Ratio PP : NBR		Tensile Strength (MPa)	Elongation at Break (%)	Absorbed Energy (Kgf.mm)	Young's Modulus (MPa)	Hardness Shore A
	PP	NBR					
PP_{100}(Pure PP)	100	0	33.2	15.2	206.6	518.6	96
PP_{90}	90	10	25.0	66.6	182.6	437.5	96
PP_{80}	80	20	21.3	80.1	164.9	366.3	96
PP_{70}	70	30	17.2	96.3	137.7	278.5	96
PP_{60}	60	40	13.7	69.8	75.5	219.6	95
PP_{50}	50	50	8.7	45.7	47.9	161.3	94
PP_{40}	40	60	7.1	41.9	25.6	91.7	90
PP_{30}	30	70	3.6	38.6	11.1	52.7	83
PP_{20}	20	80	2.7	244.9	5.3	28.1	75
PP_{10}	10	90	1.6	663.8	1.8	5.2	64
PP_0(Pure NBR)	0	100	0.8	1250.0	0.2	1.6	31
PP70/ 10% MA	70	30	20.3	75.0	217.6	576.0	99

Stress-strain measurements

Five individual dumbbells shaped specimens for the tensile test were cut using a steel die of standard width 4 mm and length of 50 mm by Punch Press model 1701 Germany. The stress strain behavior of the test specimens prepared from vulcanized rubbers film samples with a thickness approximately 1 mm. Thickness measured by Digital thickness gauge, a gauge graduated to one hundred of mm.

Tensile strength (T_s), elongation at break (E_b), absorbed energy, and Young's modulus was determined directly according to ASTM D638-98, at room temperature using (Tension Machine Type M-10 HUNG-TA, connected with data analysis, at cross-head speed 100 mm/min.

a. Tensile strength

It is defined as the force per unit area of the original cross sectional area which is applied at the time of rupture of a specimen and is expressed in MPa [36-37]. The tensile strength of the specimen at break can be calculated as follows:

Tensile Strength (T_S) = (L/T.W) x 10 MPa (2)

where: L is load in kgf, which necessary to cause a break; W is width of the specimen in mm;

T is thickness of the sample in mm.

b. Elongation at Break

Elongation at break is an indication of material elasticity, and expressed as the percent elongation of the original distance between benches marks attained at the moment of rupture and is calculated according to:

E_b (%) = $(L - L_o)/L_o$ x 100 (3)

where: L is length of the specimen at the moment of rupture; L_o is length between bench marks.

c. Absorbed energy

The absorbed energy is an indication of the material toughness, which is the amount of energy that material must absorb before breaking. Absorbed energy value determined by experiment according to ASTM D182 and D2289, toughness can be calculated as the area under stress strain curve.

d. Young's Modulus

Young's modulus of a specimen is a physical constant of the material, gives an indication of material stiffness, and determined by experiment in the same units of stress, i.e., MPa, and can be calculated from values of stress and strain of the initial straight part of the curve, by using the following equation:

Young's modulus = Stress / Strain = MPa (4)

2. Hardness measurement

Hardness determined for all prepared samples which must have a flat surface, at room temperature. The measurement was applied according to, (ASTM-D 2240), using Durometer of Model 306 L Type A. The unit of hardness is expressed in (Shore A).

2.2.4. Modification of asphalt using prepared polymers (PP70 and PP70/MA)

In this step; asphalt was modified via using four percent of PP70 and PP70 + 10% MA (3, 5, 7 and 10 percent by weight of asphalt). The samples were prepared in suitable cans using a high shear mixer rotating at 3000 rpm. The polymer was added gradually at a rate of 5 g/min. The temperature was kept within 180 ± 1°C during the polymer addition and subsequent mixing. Then, stirring was performed for 2 hours after complete addition of polymer [38-39].

2.2.3. Characterization of polymer modified asphalt samples (PMAs)

2.2.3.1. Physical properties

Penetration Index (PI) and temperature susceptibility

The penetration index represents a quantitative measure of the response of bitumen to variation in temperature. Knowing the penetration index of particular bitumen, it is possible to predict its behavior in an application. Therefore, asphalt binders with high penetration numbers (called "soft") are used for cold climates while asphalt binders with low penetration numbers (called "hard") are used for warm climates. All bitumen display thermoplastic properties, i.e. they become softer when heated and harden when cooled. Several equations exist that define the way that the viscosity (or consistency) changes with temperature. One of the best known is that developed by Pfeiffer and Van Doormaal which states that: If the logarithm of penetration, P, is plotted against temperature, T, a straight line is obtained such that [40]:

log P = AT + K (5)

where: A is the temperature susceptibility; P is penetration at temperature T; K is constant.

The value of A varies from 0.0015 to 0.06 showing that there may be a considerable difference in temperature response. Pfeiffer and Van Doormaal developed an equation for the temperature response that assumes a value of about zero for road bitumen. For this reason, they defined the penetration index (PI) as:

$$\frac{20-PI}{10-PI} = 50A \quad (6)$$

or explicitly,

$$PI = \frac{20\ (1-25A)}{1+50A} \quad (7)$$

The value of PI ranges from around -3 for high temperature susceptible bitumens to around +7 for highly blown low temperature susceptible (high PI) bitumen. The PI is an unequivocal function of A, and hence it may be used for the same purpose. The values of A and PI can be derived from penetration measurements at two temperatures,T1 and T2 using the equation:

$$A = \frac{\log pen\ at\ T1 - \log pen\ at\ T2)}{T1-T2} \quad (8)$$

Pfeiffer and Van Doormaal (year) found that most bitumens had a penetration of about 800 dmm (deci-millimetre) at the ASTM softening point temperature. Replacing T2 in the above equation by the ASTM softening point temperature and the penetration at T2 by 800 they obtained equation (9):

$$A = \frac{\log pen\ T1 - \log 800)}{T1 - ASTM\ softining\ point} \quad (9)$$

Substituting equation (9) in equation (7) and assuming a penetration test temperature of 25 °C gives:

$$PI = \frac{1952 - 500 \log pen\ T1 - 20 softining\ point}{50 \log pen - softining\ point - 120} \quad (10)$$

Equations (7) and (9) were applied in this study to calculate first for A (temperature susceptibility of bitumen) and PI (penetration index). These were calculated from the measured softening point temperatures and penetrations.

2.2.3.2. Rheology of asphalt using Brookfield viscometer (ASTM D4287, 1994)

The Brookfield DV-III Ultra Programmable Rheometer measures fluid parameters of shear stress and viscosity at given Shear Rates. Viscosity is a measure of a fluid's resistance to flow. The principle of operation of the DV-III Ultra is to drive a spindle (which is immersed in the test fluid) through a calibrated spring. The viscous drag of the fluid against the spindle is measured by the spring deflection. Spring deflection is measured with a rotary transducer. The viscosity measurement range of the DV-III Ultra (in centipoise or cP) is determined by the rotational speed of the spindle.

2.2.3.3. Mechanical characteristic; tensile shear strength and elongation measurements for modified asphalt samples using PP70 and PP70/MA

To examine adhesion properties of asphalt and asphalt- polymer blends, shear strength was measured for standard 10 cm length and 2 cm width plain steel plates (bonded area 2.5 cm) solvent degreased after 14 days curing. The tensile shear strength was carried out by Instron testing machine (model 1026) at 23±2°C with cross head speed 100 mm/min, chart speed 200 mm/min and load cell range 0 - 500 Newton according to ASTM D638-77a. Measurements were carried out for samples after being suspended in Air and immersed in water for 24 hrs, at room temperature.

Test procedure [41]:

1. Cut or injection molds your material into one of the five "dumbbell" shapes. The exact shape you use is dependent upon your material's rigidity and thickness.
2. Load the specimen into tensile grips.
3. Attach the extensometer to the sample
4. Begin the test by separating the tensile grips at a constant rate of speed. Speed depends on specimen shape and can range from 0.05 - 20 inches per minute. The target time from start of the test to break should be from 30 seconds to 5 minutes.
5. End the test after sample break (rupture)

Analysis obtained: tensile strength, elongation at yield, elongation at break, nominal strain at break (grip separation), modulus of elasticity, secant modulus, Poisson's ratio (requires transverse extensometer).

3. Results and discussion

3.1. Evaluation of blending ratios of PP/ NBR for choosing optimum ratio

3.1.1. Optimization of blending ratios of PP/NBR

Different mixing ratios of PP and NBR are required to study the characterization of PP/NBR blends. Prepared blends of PP/NBR, respectively take these ratios, [(pure PP = PP_{100} = 100/0), (PP_{90} = 90/10), (PP_{80} = 80/20), (PP_{70} = 70/30), (PP_{60} = 60/40), (PP_{50} = 50/50), (PP_{40} = 40/60), (PP_{30} = 30/70), (PP_{20} = 20/80), (PP_{10} = 10/90), and (pure NBR = PP_0 = 0/100)], formulations are presented in Table 2.

Mechanical properties measurements were used to evaluate the prepared blend samples. Results of tensile strength, elongation at break, absorbed energy, young's modulus and hardness are presented in Table 2. Mechanical properties measurements were used to evaluate the prepared blend samples. Results of tensile strength, elongation at break, absorbed energy, young's modulus and hardness are presented in Table 2.

From the data obtained it is clear to see that PP has the highest values of tensile strength, absorbed energy, and young's modulus combined with the lowest value of elongation at break, while NBR gives lowest values of tensile strength, absorbed energy, young's modulus, and hardness combined with highest value of elongation at break. These behaviors may be due to the high crystalline content of PP and very low content of crystalline content in NBR, which is an amorphous polymer [42]. observed that the crystallinity of the PP/NBR blend was decreased by the incorporation of NBR, from 55.3 for pure isotactic PP to 33.9 and 13.7 for both incorporation 30 and 70 wt/wt% NBR, respectively.

The strength of PP/NBR blends depends on the strength of the PP phase, which in turn depends on the extent of crystallinity of the blend, was decreased by the incorporation of NBR. It is also observed that increasing NBR content in PP/NBR blend decreases absorbed energy and Young's modulus, which may be due to the presence of the soft rubber phase and fall in crystallinity of the PP phase. Hence, decreasing the crystalline content of the blend occurred [43]. have shown that the spherules growth of PP in blends with rubber is hindered by the presence of the rubber phase. It can also be deduced that the tensile strength, absorbed energy and young's modulus values for blends will show a negative deviation, i.e., blend properties lie below the additive line. The negative deviation is due to poor interfacial adhesion between the non-polar PP and polar NBR phases, which causes poor stress transfer between matrix and the dispersed phase. A clear change in the slope of this tensile composition curve is seen between the composition ranges 50/50 to 30/70 PP/NBR. The observed change in mechanical properties composition curves have been reported by [44] for the PP/EPDM system.

In immiscible blends, the elasticity usually depends on the particle size of the dispersed phase. Data indicate that elongation at break slightly increases with the addition of NBR with ratios 10, 20 and 30% in the region of PP_{90}, PP_{80} and PP_{70} blends. It can be considered that NBR with ratio ≤ 30% act as a plasticizer to PP, that is where particles of NBR in this ratio of blending formed small spheres, which dispersed in the continuous phase of PP. Increasing ratio of NBR from 30 to 40, 50, 60 and 70 increase growth of the particle size of the NBR dispersed phase, which hinders blend to give elasticity, this is clearly described by the continues reduction in values of elongation at break from PP_{70} to PP_{30}. This decrease in elongation at break at higher rubber content is due to the bigger particle size of the dispersed NBR phase and poor interfacial adhesion between the polymers have shown that elongation at break decreases with increase in particle size of the dispersed rubber phase of PP/EPDM blend. The poor interfacial adhesion causes premature failure as a result of the usual crack-opening mechanism. Smaller and uniformly distributed particles are more effective at initiating crazes and terminating them before they develop into catastrophic sizes. Increasing rubber content

over 70% companied with sharply increase in elongation at break continuously with the further addition of NBR. This sharp increase in elongation at break may be due to the continuous nature of NBR phase, which forms a co-continuous structure with the plastic phase; similar results were reported in the case of the PP/EVA system [45]. NBR give the highest value of elongation at break. The elongation at break also shows negative deviation from the additive line.

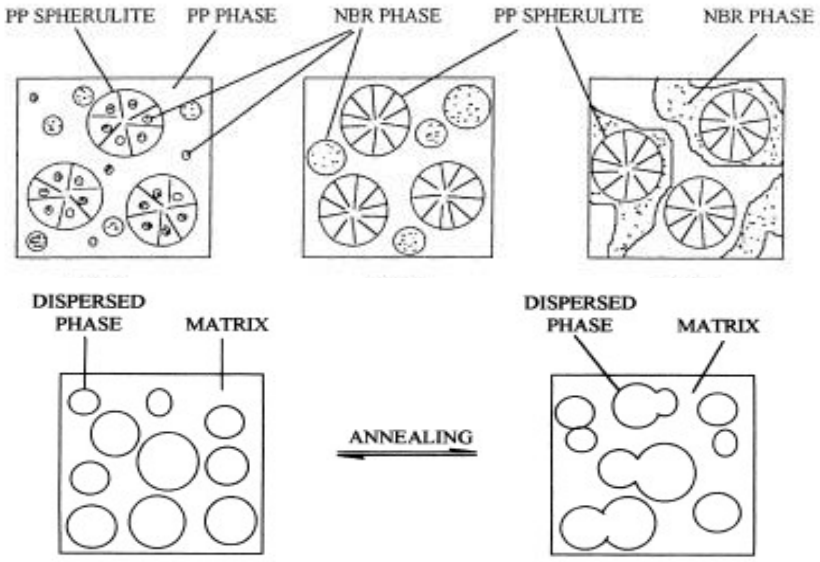

Fig 1. Representation of dispersed phase (NBR) in the matrix of the continuous phase (PP), *(George et al. [42])*.

It is also observed that hardness values do not give any change with a low ratio of NBR addition (from 10 to 30%), which may be due to high crystallinity of PP not affected with the small particle of NBR formed in the PP matrix as shown in Fig 1. Low rate decrease in values of hardness was observed with increasing NBR concentration from 30 to 70%. Here the particle size of NBR dispersed in the matrix of PP increased, but PP stilled the continuous phase and formed the matrix. More rate of reduction in hardness values and the slope change in the curve at higher proportions of NBR (≥ 70%) can be explained by the phase inversion of NBR from dispersed to the continuous phase to form co-continuous phase of both PP and NBR on passing from the 50/50 PP/NBR to the 30/70 PP/NBR blend. It is interesting to see that the hardness values show a positive deviation.

It is can be deduced clearly from all the above mentioned data of mechanical properties for all ratio of PP/NBR blends that; the sample of PP70 with blending ratio PP/NBR (70/30) has the most reasonable required collection of mechanical properties that is in means of high values of tensile strength, absorbed energy, young's modulus, and hardness combined with high value of elasticity. It is noteworthy that any another sample will have deficient in one or more value of mechanical properties than PP70.

3.1.2. Determination of suitable type and ratio of C compatibilizers, for PP/NBR (70/30) Blends [35]

The mechanical properties of immiscible polymer blends are affected by the addition of compatibilizers. Data obtained in Table 2 show the variation of tensile strength, elongation at break, absorbed energy, young's modulus, and hardness of 70/30 PP/NBR blend and copolymers with the presence of compatibilizer,

In the case of MA-PP compatibilized copolymers, the increase in tensile strength may be due to the increased dipolar interaction between the MA-PP and NBR phase, which causes an increase in interfacial adhesion between PP and NBR phases, although there is no reduction in particle size with the increase in MA-PP concentration beyond 1%.

The tensile strength of the blends could be predicted by Coran's equation where the MA-PP and Ph-PP are found to act as compatibilizers in PP/NBR system. With the increase in the concentration of compatibilizer, the domain size of the dispersed NBR phase decreases, followed by a leveling off at higher concentrations, which is an indication of interfacial saturation. The theories of Noolandi and Hong predict a linear decrease of interfacial tension with compatibilizer volume fraction for concentrations less than the CMC. Considering the fact that the interfacial tension is directly proportional to the domain size, it is demonstrated that the experimental data are in agreement with these theories.
It is also seen that the **absorbed energy, young's modulus, and hardness** of the blend is found to increase significantly with the addition of compatibilizer. The rate of increasing in these parameters found to increase with a number of H_2O_2 moles added per each mole of oil in an epoxidation process. MA-PP used as compatibilizer gives the highest values of absorbed energy, young's modulus, and hardness
Values of **elongation at break** give noticeable decrease with the addition of MA as a compatibilizer. Further decreases of elongation at break are obtained as a result of the further addition of MA.

3.1.3. The mechanism of compatibilization

The mechanism of compatibilization process using PP-MA as a compatibilizer for PP/NBR (70/30) blend, maleic anhydride is the leading monomeric candidate for reactive compatibilization. Particularly in the production of the graft copolymer (PP-MA) that is the effective compatibilizer, this graft copolymer acts as an emulsifier at the interface and thus reduces interfacial tension. The maleic anhydride (MA) groups are grafted onto the PP chain backbone to form maleic anhydride grafted polypropylene MA-PP as shown in Scheme (1) [35].

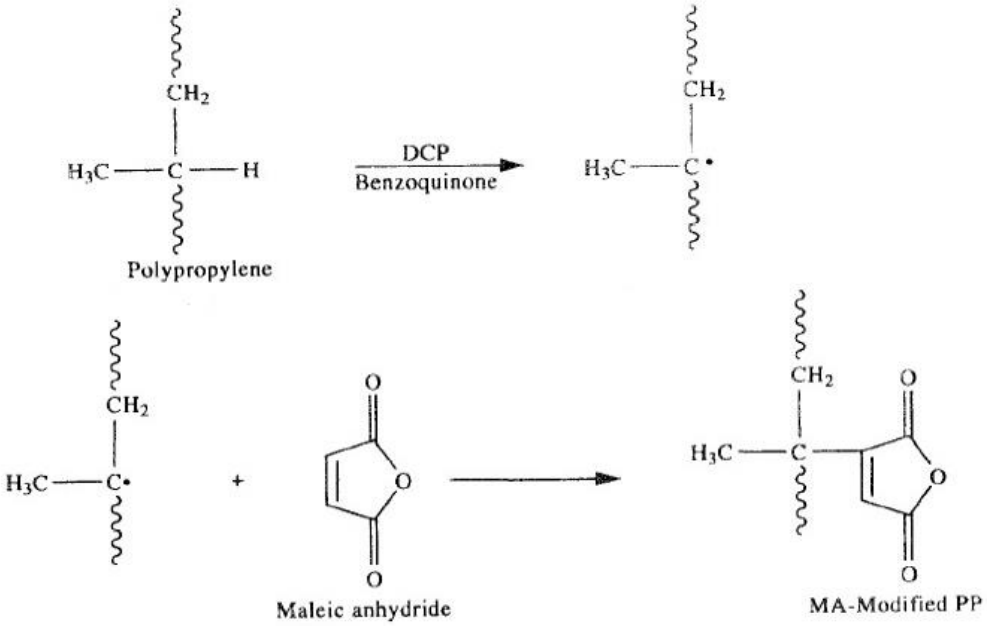

Scheme 1. The Rreaction of maleic anhydride (MA) with polypropylene (PP) to produce maleic anhydride modified polypropylene (MA-PP)

3.2. Characterization of polymer modified asphalt samples (PMAs)

PMA samples were prepared as previously mentioned using 3, 5, 7 and 10% PP70 and PP70/MA. The characteristics of all samples will be detected as follows:-

In Table 1 the properties and performance of asphalt 60/70 dramatically change with the polymer modification.

3.2.1. Physical characteristics modified samples

Generally, data in Table 3 and Figure 2 indicated that the modified samples are more hardening than the virgin one as there was an increase in softening point, specific gravity, and dynamic viscosities and decrease in penetration value. These results are attributed to the effect of addition both of PP70 and PP70/MA which blended with asphalt. Also, it is noticed from Tables 4 and 5) that, hardness in case of using PP70/MA is more than that recorded in case of using PP70.

With the increase of PP70 levels as 3,5,7 & 10 wt/wt% noticed that comparing to virgin AC properties the penetration value of PMAs decreased in percentages of 32.26, 54.8, 62.9 and 72.6%, while softening point increased in percentages of 10.67, 26.48, 34.4 and 44.27% respectively. Also, the dynamic viscosity at 60°C increased in percentages of 338.5, 393.0, 456.4 & 892 and at 130°C increased in values of 6.7, 73.24 & 258.53 respectively. While the penetration indexes increased from -0.51 to -0.21, 0.38, 0.65 & 0.85 respectively, as well as the specific gravity, increased in the same manner.

While, increasing the PP70/MA content from 3 to 10 wt/wt% penetration of PMAs decreased in percentages of 32.3, 56.45, 72.6 and 88.7%, while softening point increased in percentages of 10.87, 42.29, 58.1 and 73.9% respectively with the addition of RRNP as 3, 5, 7 and 10%. Also, the dynamic viscosity at 60 °C increased in percentages of 473.0, 546.4, 678.5 & 1036.5 and at 130 °C increased in percentages of 8.6, 68.24, 196.53 & 221.64 respectively. While the penetration indexes increased from -0.51 to -0.21, 2.83, 3.18 & 4.3 respectively, as well as the specific gravity, increased in the same manner.

This is attributed to nature and accordingly the chemical molecular composition of the PP70/MA which react with asphaltene in the matrix.

3.2.2. Temperature susceptibility of all asphalt samples

The temperature susceptibility of the modified samples was investigated by calculating PI values. From Table 3 and Figure 3 with comparing to virgin AC the PI values also, increased from -0.51 for virgin AC to -0.21 & 0.38 & 0.64 & 0.85 for 3, 5, 7 and 10% of PP70 content respectively and -0.21& 2.83& 3.12& 4.3 for 3, 5, 7 and 10% of PP70/MA content respectively. Also, in case of using rubber materials the increase in P.I will increase the resistance of asphalt samples to cracking at low temperature.

The penetration index of all modified asphalt samples from Table 3 the PI proved a rather powerful indicator for classifying asphalt rheological behavior, and it was observed that blown asphalt had typically PI < 1 when straight-run asphalt had −1 > PI > +1. Only very susceptible materials such as coal tar gave PI > −1. Therefore, PI was thought to be a good indicator of asphalt type, with PI < 2 being indicative of a gel asphalt whereas PI > 0 is typical of a sol. In general, PI varies between −2.6 and 8 when including all types of asphalt (including blown ones) but typically lies between −2 and +2 for paving grades asphalt. Solvent deasphalted asphalt could give PI values between −2 and +2, based on the exact process used (especially type of solvent and yield. Still, negative values were more frequent, and deasphalted asphalt is generally considered more susceptible than straight run ones. Van der Poel showed that asphalt with the same PI had similar rheological master curves. Since a mathematical model turned out to be quite difficult to propose, Van der Poel developed a nomograph from which the complex (or creep) modulus at whatever temperature and frequency (or time) can be predicted for given asphalt, knowing only its PI and Ring and ball softening temperature. This device still gives acceptable values.

Hardness and stability of modified samples are obviously noticed for PP70/MA addition rather than in case of using PP70.

Table 3. Physical properties of PMAs using PP70 and PP70/MA

Asphalt sample	Penetration 0.01 mm 25 °C	Ductility cm	Kinematic viscosity 135 °C, C.st	Absolute viscosity 60 °C	Softening point °C	Specific gravity gm/cm^3	(1) API	2* PTS	3* PI	*4 C, Btu pound per °F	*5 thermal conductivity	Dynamic viscosity mpa.s, 60 °C 1198.08 S^{-1}
3	44	129	375	1645	56	1.023	-8.563	0.0361	-0.21	0.385	0.6530	1176.54
5	28	120	435	1732	64	1.0910	-7.713	0.0281	0.38	0.377	0.667	1560.69
7	23	80	450	1820	68	1.1431	-3.008	0.0247	0.64	0.2320	0.834	2201.12
10	17	50	495	1921	73	1.1510	-1.254	0.0201	0.85	0.2291	1.021	3301.56
With MA												
3	42	125	450	1720	56	1.024	-6.415	0.0344	-0.21	0.360	0.748	1350.23
5	27	115	503	1850	72	1.028	-2.568	0.0305	2.38	0.342	0.862	1820.36
7	17	75	560	1930	80	1.030	-0.652	0.0250	3.12	0.202	1.025	2830.56
10	7	30	630	2140	88	1.032	1.542	0.0184	4.3	0.160	1.458	4238.14

**2 - penetration temperature susceptibility; *3 - penetration index; *4 - Specific heat; *5 - Thermal conductivity*

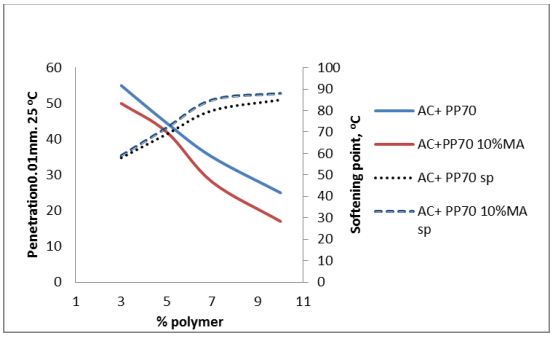

Fig. 2. Penetration and softening point of PMAs with percentages of blends addition

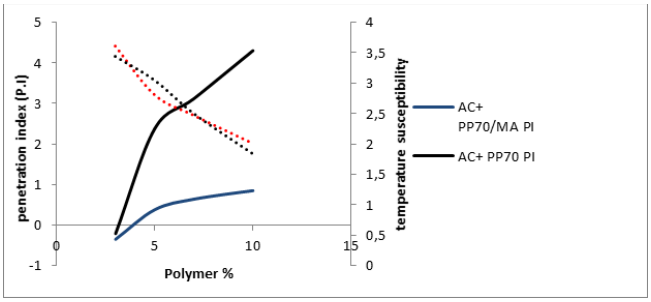

Fig. 3. Penetration index and temperature susceptibility of PMAs with percentages of blends addition

3.2.3. Rheological properties

3.2.3.1. Viscosity and temperature

In this test, the effect of temperature variation as sever conditions for which the coating may be exposure on the viscosity for all samples is detected. The test is also used to develop temperature–viscosity charts. As shown in Figures 4,5 it can be observed that the viscosity values reduce as the test temperature increases regardless of the polymer type and content. The blend viscosity increased with the increase in polymer content at the chosen temperatures from 60 to 150°C, and this increase was observed in both the viscous and elastic moduli. As shown in Figures 4,5 the viscosity of PMAs samples are highly remarkable decrease as compared to the unmodified sample. This is due to the presence of PP/ NBR particle which causes improvement in rheological properties of virgin asphalt. dynamic viscosity decreases in case of using PP70/MA & PP70 at temperature 60 °C in percentages of 3, 5, 7 and 10% wt/wt in percentages of 100, 200, 225, 250% & 300, 350, 360 and 600% respectively while at 130°C dynamic viscosity decreases in percentages 47, 50, 52 & 53 and 20, 30, 43 & 45 respectively. As expected, there is an increase in the asphalt viscosity with the polymer addition, and it is important to stress that samples with compatibilizer agents, which have a plasticizer effect, showed higher viscosities than the pure asphalt [46].

The high differences between the two modifiers is due to presence of MA-PP as a compatibilizer in PP70/MA which interact with asphalt to form very strong network causes the asphalt to become highly viscous.

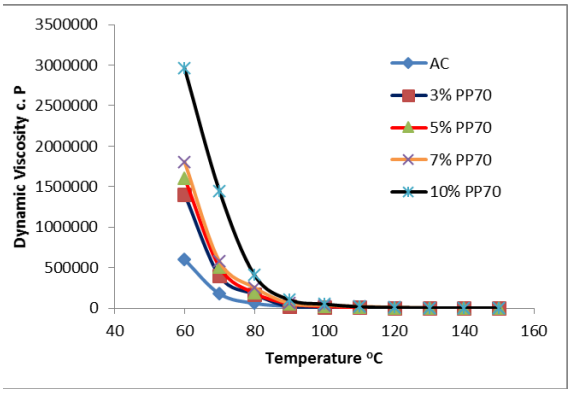

Fig. 4. Dynamic viscosity with temperature of PMA using PP70

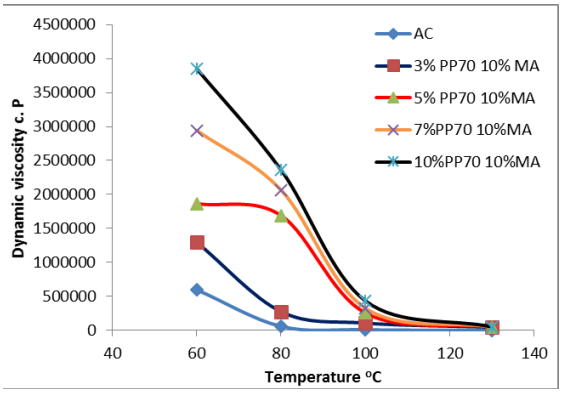

Fig. 5. Dynamic viscosity with temperature of PMA using PP70/MA

*3.2.3.*2. Shear rate and shear stress

Figures 6-9 show that the virgin asphalt and PMAs samples do not undergo stress rates proportional to the applied shear stress that's means that all samples are undergo non- Newtonian matters.

The viscosity of such fluids will therefore change as the shear rate is varied. Thus, the experimental parameters of Viscometer model, spindle and speed all have an effect on the measured viscosity of the non-Newtonian fluid. Non-Newtonian flow can be envisioned by thinking of any fluid as a mixture of molecules with different shapes and sizes. As they pass by each other, as happens during flow, their size, shape, and cohesiveness will determine how much force is required to move them. At each specific rate of shear, the alignment may be different and more or less force may be required to maintain motion. There are several types of non-Newtonian flow behavior, characterized by the way a fluid's viscosity changes in response to variations in shear rate. As shown in Figures 6-9 it is noticed that the elasticity modulus of PMAs increase with increasing the polymer addition level in the order of 3, 5, 7 and 10% wt/wt for both modifiers namely PP70 & PP70/MA but in case of using PP70/MA, the elasticity modulus is remarkable highly increased. This attributed to that the increased dipolar interaction between the MA-PP and NBR phase, which causes an increase in interfacial adhesion between PP and NBR phases. This bond should prevent phase separation and improve storage stability [38].

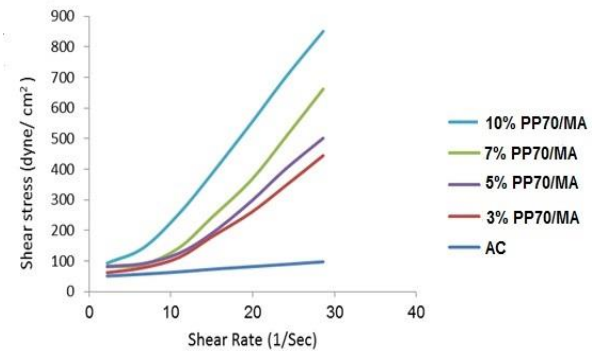

Fig.6. Shear stress shear rate curves of PMA using PP70/MA at 130°C

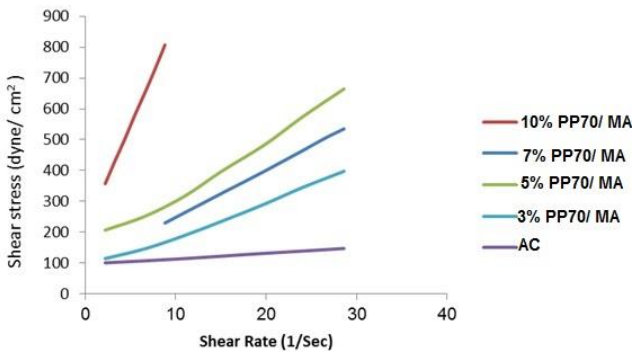

Fig. 7. Shear stress shear rate curves of PMA using PP70/MA at 80°C

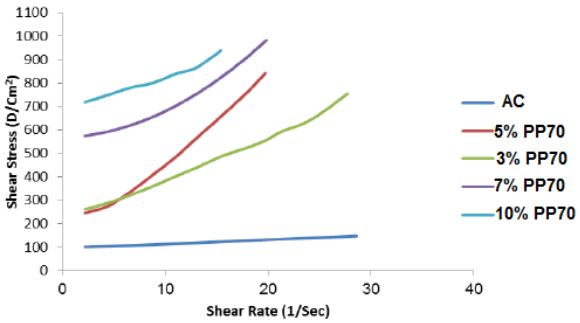

Fig. 8. Shear stress shear rate curves of PMA using PP70 at 60°C

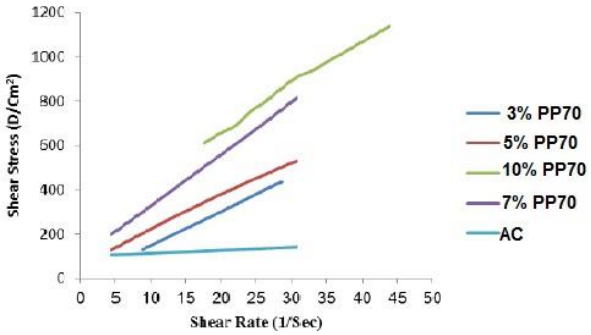

Fig. 9. Shear stress shear rate curves of PMA using PP70 at 130°C

3.2.4. Tensile shear strength and elongation measurements for modified asphalt samples using PP70 and PP70/MA

The purpose of tensile strength testing is to evaluate asphalt mixtures fatigue potential and moisture susceptibility. Chapuis *et al.* [47] has indicated the tensile strength of hot-mix asphalt is related to fatigue cracking.

A higher tensile strength means asphalt can tolerate higher strains before failing (i.e., cracking). Additionally, the moisture susceptibility of the asphalt mixture can be evaluated by comparing the tensile strength of asphalt mixtures exposed to wet and dry conditions.

From Figs 10-13 and Table 4, the data revealed that the tensile shear strength values measured for different samples in air and water give interesting behavior. The tensile shear strength for all samples is slowly increasing with increasing the percentages of polymer added. It is noticed from the results that the PMAs with using PP70/MA acquire better tensile strength as compared with those based on PP70 without MA. Comparison of PMAs using PP70/MA in the air and in water shows that the order of increase in tensile shear strength follows the sequence 10% polymer > 7% > 5% > 3%. The tensile strength ratio (TSR) [48] for samples conditioned with water is shown in Figures 10-13 and Table 4. The value of TSR is calculated as:

Tensile strength ratio = Tensile strength of conditioned sample/Tensile strength of the dry sample.

In Figures 10-13 and Table 4 TSR testing would have a value of less than 1.00 in case of blended PP/NBR with and without MA because it is expected that the conditioned samples would suffer moisture damage and exhibit lower tensile strength with comparing to PMAs; this phenomenon was observed in the control sample. However, it was found that all polymer modified asphalt samples exhibited TSR values greater than 1.00 [49]. This indicated that the sample after conditioning has higher tensile strength. Overall, it was concluded that the addition of TEPs (PP70& PP70/MA) would reduce a mixture's moisture susceptibility in most cases.

The different ratios added from PP70 & PP70/MA were found to have the potential to improve material strength and fatigue characteristics while enhancing ductility and other durability properties of engineering materials in different media.

Table 4. Tensile shear strength, (N/cm^3) and elongation (El., %) for PMAs with PP70 & PP70/10% MA after 24 hrs immersion in different media, at room temperature

Sample	In air		In H_2O	
	N/cm^3	El, %	N/cm^3	El, %
PP70	825	40.4	800	80
PP70 /MA	1370	41.7	1165	100
3% PP70	420	60	523	140
5% PP70	523	80	623	120
7% PP70	795	100	795	100
10% PP70	823	120	1180	80
3% PP70/MA	623	80	573	160
5% PP70/MA	707	100	1180	140
7% PP70/MA	975	120	1225	120
10% PP70/MA	1115	140	1295	100

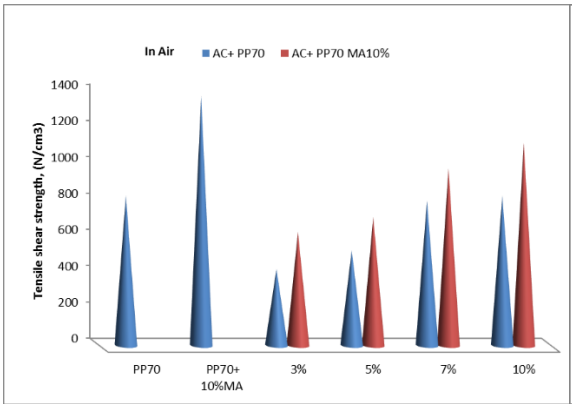

Fig. 10. Tensile shear strength of PMAs with % blends added in air

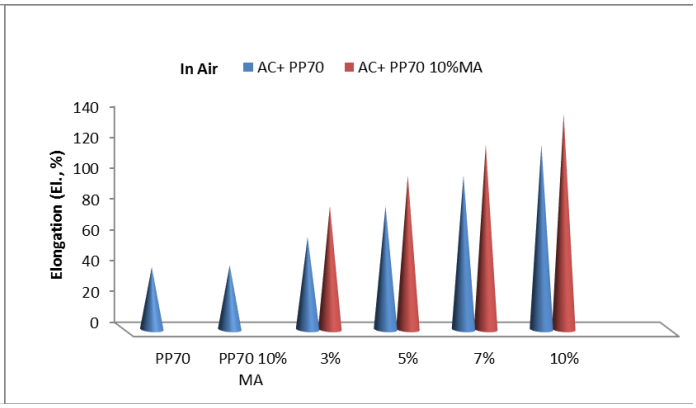

Fig. 11. Elongation of PMAs with % blends added in air

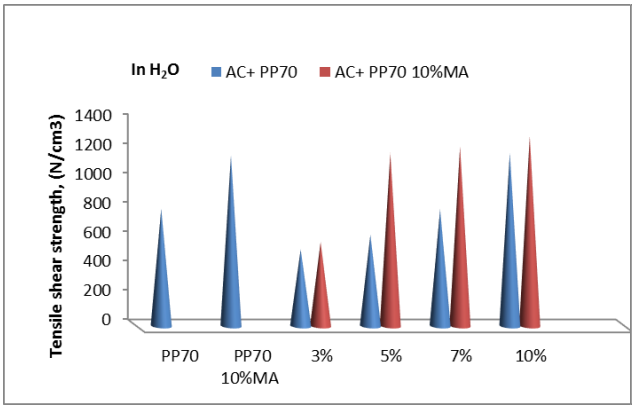

Fig. 12. Tensile shear strength of PMAs with % blends added in water

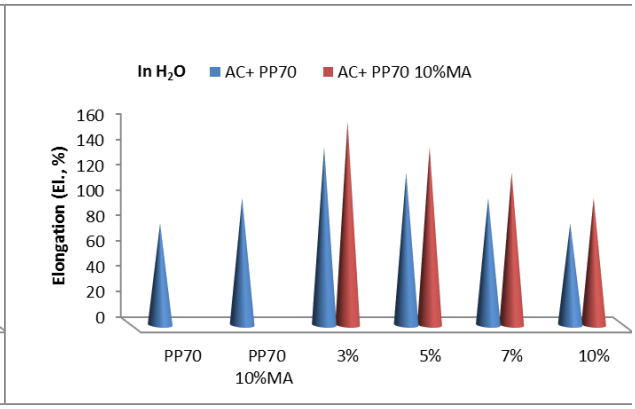

Fig. 13. Elongation of PMAs with % blends added in water

4. Conclusion

This research aims to use Thermoplastic elastomers (TPEs) which are a class of copolymers or a physical mixture of polymers (usually a plastic and a rubber) which consist of materials with both thermoplastic and elastomeric properties in the modification of asphalt 60/70 to produce very specific asphaltic material for use in infrastructure applications in different media. TPEs have attracts more attentions in the industry since they combine the properties of vulcanized rubber with the ease of processing of thermoplastics. The new asphaltic material is low cost and has a high quality performance at low temperature. To achieve the aim of the study, blend PP/ NBR with and without compatibilizers (MA) were used as additives to modify asphalt 60/70 in percentages of 3, 5, 7 & 10 wt/wt% The results of the study concluded that;

- The compatibility of PP and NBR is poor and can be enhanced by the addition of compatibilizers.
- In this study, PP/NBR (70/30 wt/wt%) blends were modified by the addition of compatibilizers, that is, MAH. Ternary blends with compatibilizers (10 wt/wt%) showed an improvement in mechanical and rheological properties compared with uncompatibilized ones
- As expected the addition of polymers to asphalt reduces its thermal susceptibility at temperatures and guarantees a greater constancy of its properties since the asphalt becomes more elastic.
- Increasing the ratio of polymer added found to improve the physical and rheological properties, and the suitable ratio is 7% according to workability
- Rheological data PMAs indicates that the PMAs have thixotropic property and high yield stress

- The phenomenon of low viscosity at a high shear rate, and lack of flow at low shear rate which is gained by prepared blends is very important from the practical point of view since the application requirements for sealants necessitate both good gunnability and lack of flow on vertical surfaces.
- The tensile shear strength (N/cm^3) for the obtained blends is found to increase with polymer % content and for that forming with using PP70/MA more than that with using PP70.
- Addition of TEPs (PP70 & PP70/MA) enhancing the mechanical properties of virgin asphalt 60/70 in both water and air but in the air is the best.
- Polymer modified asphalt samples have a higher tensile strength means asphalt can tolerate higher strains before failing (i.e., cracking). Additionally, the moisture susceptibility of the asphalt mixture can be evaluated by comparing the tensile strength of asphalt mixtures exposed to wet and dry conditions.

References

[1] La Mantia FP, Morreale M, Botta L, Mistretta MC, Ceraulo M, Scaffaro R. Degradation of polymer blends: A brief review.Polymer Degradation and Stability, 2017; 145: 79- 92.

[2] Paran SMR, Abdorahimi M, Shekarabi A, Khonakdar HA, Jafari SH, Saeb MR. Modeling and analysis of the nonlinear elastoplastic behavior of compatibilized polyolefin/polyester/clay nanocomposites with emphasis on interfacial interaction exploration. Composites Science and Technology, 2018; 154: 92-103.

[3] Jouyandeh M, Moini Jazani O, Navarchian AH, Saeb MR. High-performance epoxy-based adhesives reinforced with alumina and silica for carbon fiber composite/steel bonded joints, J. Reinf. Plast. Compos., 2016; 35(23): 1685-1695.

[4] Truong LT, Larsen ÅG, Roots J. Morphology, crystalline features, and tensile properties of syndiotactic polypropylene blends. J. Appl. Polym. Sci., 2017 134: 44611.

[5] Ebrahimi Jahromi HR, Bakhshandeh GR, Ebrahimi Jahromi A, Saeb MR, Ahmadi Z, Pakdel AS.A comparative study to assess structure-properties relationships in (acrylonitrile butadiene rubber)-based composites: recycled microfillers versus nanofillers. J. Vinyl Addit. Technol., 2017; 23(1): 13-20.

[6] Jahromi AE, Jahromi HRE, Hemmati F, Saeb MR, Goodarzi V, Formela K. Morphology and mechanical properties of polyamide/clay nanocomposites toughened with NBR/NBR-g-GMA: a comparative study Compos. Part B Eng., 2016; 90: 478-484.

[7] Sionkowska A. Current research on the blends of natural and synthetic polymers as new biomaterials: Review, Prog. Polym. Sci., 2011; 36: 1254-1276.

[8] Shokoohi S., Arefazar A. A review on ternary immiscible polymer blends: morphology and effective parameters, Polym. Adv. Technol., 209; 20: 433- 447.

[9] Okada O., Keskkula H., Paul DR. Mechanical properties of blends of maleated ethylene propylene rubber and nylon 6, Polym. Guildf., 2001; 42: 8715- 8725.

[10] Yu L, Dean K, Li L. Polymer blends and composites from renewable resources, Prog. Polym. Sci., 2006; 31: 576- 602.

[11] Utracki LA, Mukhopadhyay P, Gupta RK.Polymer blends: introduction, in: L.A. Utracki, C.A. Wilkie (Eds.), Polym. Blends Handb, Springer, Netherlands, Dordrecht 2014, p. 3e170.

[12] Chakraborty P, Ganguly A, S Mitra, Bhowmick AK. Influence of phase modifiers on morphology and properties of thermoplastic elastomers prepared from ethylene propylene diene rubber and isotactic polypropylene. Polym. Eng. Sci., 2008; 48: 477– 489.

[13] Chen YZ, Li HL. Phase morphology evolution and compatibility improvement of PP/EPDM by ultrasound irradiation. Polymer, 2005; 46: 7707–7714.

[14] Kim DH, Fasulo PD, Rodgers WR, Paul DR. Effect of the ratio of maleated polypropylene to organoclay on the structure and properties of TPO-based nanocomposites. Part I: Morphology and mechanical properties. Polymer, 2007; 48: 5960 –5978.

[15] Yang H, Zhang Q, Guo M, Wang C, Du RN, Fu Q. Study on the phase structures and toughening mechanism in PP/EPDM/SiO2 ternary composites. Polymer, 47: 2106–2115.

[16] Martin G, Barres C, Sonntag P, Garois N, Cassagnau P. Morphology development in thermoplastic vulcanizates (TPV): Dispersion mechanisms of a pre-crosslinked EPDM phase. Eur. Polym. J., 2009; 45: 3255–3266.

[17] Soares BG, Almeida MSM, Deep Urs MV, Kumaraswamy GN, Ranganathaiah C, Mauler SR. Influence of curing agent and compatibilizer on the physicomechanical properties of polypropylene/nitrile butadiene rubber blends investigated by positron annihilation lifetime technique. J. Appl. Polym. Sci., 2006; 102: 4672–4681.
[18] George S, Neelakantan NR, Varughese KT, Sabu T. Dynamic mechanical properties of isotactic polypropylene/nitrile rubber blends: Effects of blend ratio, reactive compatibilization, and dynamic vulcanization. J. Polym. Sci. B Polym. Phys., 1997; 35: 2309- 2327.
[19] Xu Ch, Cao X, Jiang X, Zeng X, Chen Y. Preparation, structure and properties of dynamically vulcanized polypropylene/acrylonitrile butadiene rubber/zinc dimethacrylate ternary blend composites containing maleic anhydride grafted polypropylene. Polymer Testing, 2013; 32: 507–515.
[20] Magioli M, Sirqueiraand AS, Soares BG. The effect of dynamic vulcanization on the mechanical, dynamic mechanical and fatigue properties of TPE based on polypropylene and ground tire rubber, Polym. Testing, 2010; 29(7): 840–848.
[21] Zhang ZX, Zhang SL, Lee SH, Kang DJ, Bang D, Kim JK. Microcellular foams of thermoplastic vulcanizates (TPEs) based on waste ground rubber tire powder, Mater. Lett., 2008; 62(28): 4396–4399.
[22] Sridhar V, Xiu ZZ, Xu D, Lee SH, Kim JK, Kang DJ., Bang D-S. Fly ash reinforced thermoplastic vulcanizates obtained from waste tire powder, Waste Management,2009; 29(3): 1058–1066.
[23] Lee SH, Shanmugharaj AM, Sridhar V, Zhang ZX, Kim JK. Preparation and characterization of polypropylene and waste tire powder modified by allylamine blends. Polym. Adv. Technol., 2009;20(7): 620–625.
[24] Satapathy S, Nag A, Nando GB. Thermoplastic elastomers from waste polyethylene and reclaim rubber blends and their composites with fly ash, Process Saf. Environ. Prot., 2010; 88(2): 131–141.
[25] Zhang SL, Xin ZX, Zhang ZX, Kim JK. Characterization of the properties of thermoplastic elastomers containing waste rubber tire powder, Waste Management, 2009;29(5): 1480–1485.
[26] Mouilet V, Lamontagne J, Durrieu F, Planche JP, Lapalu L. Infrared microscopy investigation of oxidation and phase evolution in bitumen modified with polymers. Fuel, 2008;87(7): 1270–1280.
[27] Arega AZ, Bhasin A, De TK. Influence of extended aging on the properties of asphalt composites produced using hot and warm mix methods. Constr. Build. Mater, 2013;44: 168–174.
[28] Lu XH, Isacsson U. Effect of ageing on bitumen chemistry and rheology. Constr. Build. Mater, 2002; 77(9/10): 15–22.
[29] Cerni G, Cardone F, Colagrande S. Low–temperature tensile behavior of asphalt binders: application of loading time–temperature conditioning time superposition principle, Constr. Build. Mater., 2011; 25(4): 2133–2145.
[30] Lins VFC, Araújo MFAS, Yoshida MI, Ferraz VP, Andrada DM, Lameiras FS. Photo degradation of hot–mix asphalt", Fuel; 87;15–16 (2008) 3254–3261.
[31] Karger-Kocsis J, Meszaros L, Barany T. Ground tyre rubber (GTR) in thermoplastics, thermosets, and rubbers. J. Mater. Sci., 2013; 48: 1–38.
[32] Essawy AI, Saleh AMM, Zaky MT, Farag RK, Ragab AA. Environmentally friendly road construction. Egyptian Journal of Petroleum, 2013; 22(1): 189-198
[33] Syroezhko AM, Begak OYu, Fedorov VV, Proskuryakov VA, and Semenova EB. Modification of Paving Asphalts with an Elastoplastic. Russian Journal of Applied Chemistry, 2002; 75(9): 1525-1528. Translated from Zhurnal Prikladnoi Khimii, 2002; 75(9): 1559-1562.
[34] Padhan RK, Gupta AA. Preparation and evaluation of waste PET derived polyurethane polymer modified bitumen through in situ polymerization reaction. Construction and Building Materials, 2018; 158(15): 337-345.
[35] Motawie AM, Abdel-Aziz MM, Rabia AM, Mazrous AM, Badr MM, Sadek EM. Compatibility Study of Polypropylene and Acrylonitrile Butadiene Rubber Blends. Journal of Applied Polymer Science, 2010; 118: 2056–2061.
[36] Walker BM. Handbook of Thermoplastic Elastomers"; New York, NY: Van Nonstrand Reinhold; 1979.
[37] Abd El Rahman AMM, El-Shafie M, El Kholy SA. Modification of local asphalt with epoxy resin to be used in pavement. Egyptian Journal of Petroleum, 2012; 21: 139- 147

[38] Ragab AA, Farag RK, Kandil U, El-Shafie M, Saleh AMM and El-Kafrawy AF. Thermo-mechanical properties improvement of asphalt binder by using methylmethacrylate/ethylene glycol dimethacrylate". Egyptian Journal of Petroleum; 25 (2016) p. 397–407.
[39] Saroufim E, Celauro C, Mistretta MCh. A simple interpretation of the effect of the polymer type on the properties of PMBs for road paving applications. Construction and Building Materials, 2018; 158: 114–123.
[40] Ehinola OA, Falode OA and Jonathan G. Softening point and Penetration Index of bitumen from parts of Southwestern Nigeria. NAFTA, 2012; 63(9-10): 319-323.
[41] ADMET Home 2015 www.admet.com.
[42] George J, Reethamme J, Sabu T, Varughese KT. High density polyethylene/acrylonitrile butadiene rubber blends: Morphology, mechanical properties, and compatibilization. J Appl Polym Sci, 1995; 57(4): 449-465.
[43] Martuscelli E, Silvestre C, and Abate G. Morphology, crystallization and melting behavior of films of isotactic polypropylene blended with ethylene-propylene copolymers and polyisobutylene, Polymer, 1982; 23(2): 229-237 .
[44] Danesi S, and Porter RS. Blends of isotactic polypropylene and ethylene-propylene rubbers: rheology, morphology and mechanics. Polymer, 1978; 19(4): 448-457 .
[45] Thomas S. Tensile impact strength of blends of polypropylene and ethylene-vinyl acetate copolymer. Materials Letters, 1987; 5(9): 360-364 .
[46] Fernandes MRS, Forte MMC, Leite LFM. Rheological evaluation of polymer-modified asphalt binders, Mat. Res., 2008; 11(3): 381-386.
[47] Goh SW, Akin M, You Zh, Shi X. Effect of deicing solutions on the tensile strength of micro- or nano-modified asphalt mixture. Construction and Building Materials, 2011; 25: 195–200.
[48] Zh You, Mills-Beale J, Foley JM, Samit R, Odegard GM, Dai Q, Goh SW. Nanoclay-modified asphalt materials: Preparation and characterization. Construction and Building Materials, 2011; 25: 1072–1078.
[49] Liu D-L, Yao H-B, Bao S-Y. Performance of nano-calcium carbonate and SBS compound modified asphalt. Zhongnan Daxue Xuebao (Ziran Kexue Ban)/J Cent South Univ (Sci Technol), 2007; 38(3): 579–82.

To whom correspondence should be addressed: Dr. A. A. Ragab, Petroleum Applications Department, Egyptian Petroleum Research Institute, Nasr City, Cairo, Egypt, chemragab83@yahoo.com

Petroleum and Coal

Article **Open Access**

Data Modeling and Analysis of a Reflux Splitter Column (RSC) Using Artificial Neural Network Methodology (ANN) Implemented in R

Sepehr Sadighi[1*], *Davood Faraji*[2]

[1] *Research Institute of Petroleum Industry (RIPI), Catalysis Technologies Development Division, P.O. Box 14665137, Tehran, Iran*
[2] *Hydrocracking Unit (HCU) of Imam Khomeini Shazand Refinery, Arak, Iran*

Received May 8, 2018; Accepted June 25, 2018

Abstract

This paper deals with developing an artificial neural network (ANN) model for the reflux splitter column (RSC) of a commercial vacuum gas oil hydrocracking unit. RSC separates light product, light naphtha, heavy naphtha, kerosene and diesel from the feed, and the residue is pumped back to the feed line of the hydrocracking reactors. The input-output data required for training and testing ANN is obtained from an Iranian refinery. The ANN model is implemented in R program which is an open source program and has access to certain system functions. The input layer of ANN model developed for RSC includes volume flow rate and temperature of rich oil, pressure of overhead, volume flow rate and temperature of super heat steam, flow rate and temperature of the reflux, flow rates of diesel, kerosene and heavy naphtha splitter vapors, temperature of fifth tray of RSC, and the value of pressure between trays 5 and 6. The networks are arranged to predict flow rates of LPG, light naphtha, heavy naphtha, kerosene, and diesel products. They are trained and cross validated based on 153 data points gathered from the target RSC unit by applying 'neuralnet' package obtained from the CRAN repository. The networks compared against the testing data, and it is shown that AADs% of unseen data for the heavy naphtha, kerosene, and diesel are 5.86%, 3.42% and 3.95%, respectively.

Keywords: *Artificial Neural Network; Reflux Stripping Column; Distillation, R software.*

1. Introduction

Mathematical modeling is well appreciated in the field of chemical engineering for the sake of designing, operating, controlling and optimizing the process plant. For any target process, a model should be developed to predict product yields and qualities versus variables such as pressure, flow rate and temperature [1]. Process models are computer-based programs that commonly comprise a system of interconnected elements which should be solved synchronously for disclosing the nature of the system.

Distillation is one of the most imperative process equipment in petroleum refining, and it is indispensable to be controlled close to the optimum operating conditions. The task of a distillation tower is to separate a feed consisting different compounds into two or more other streams, based on the difference in the volatility of those components. To develop a reliable, rigorous model for a distillation column working in a crude oil refinery, the complexity of the feed mixture makes it highly difficult to describe its components at a molecular level. For this reason, in refinery applications, any oil stream is typically characterized based on a distillation assay [2]. Existing commercial simulators like Aspen plus or Hysys from Aspen Technology and PetroSim from KBC do not have such limitations for the number of species, and it is possible to use a unique set of pseudo components for petroleum assay streams; but, this method increases the calculation time, and following reports become unnecessarily sophisticated.

Recently, soft computing methods mainly artificial neural networks (ANN) and fuzzy logic were widely applied for modeling, controlling and optimizing many chemical engineering processes [3-19]. ANN is an information processing paradigm that is inspired by the way of the biological nervous, and it is in an excursion to simulate the human brain for emulating human action, i.e., to function intelligently [20]. This modeling strategy has the following benefits: 1. it is highly nonlinear; thus, its architecture can be more rigorous and more representative than most other fundamental models; 2. its topology does not have to be pre-specified; therefore, they are completely resilient models [21].

However, studies focus on applying ANN for modeling a multi-cut distillation column in a crude oil refinery are scarce [22-24]. In order to discus on the idea of this research, using data points obtained from an industrial scale reflux splitter column (RSC) located in a VGO hydrocracking plant, a feed-forward ANN is developed in R program to predict the side products of the target distillation tower. These products are light petroleum gas (LPG), light naphtha (LN), heavy naphtha (HN), kerosene (Ker) and diesel (Dis). After training the ANN model by available tools in R program (i.e., nueralnet), the capability of developed networks to simulate the flow rate of RSC are validated against the unseen data.

2. Process description

In the Isomax process studied in this research, VGO hydrocracking is carried out at elevated temperature and pressure in a hydrogen atmosphere. The pressure at reactor inlet is about 180 barg, and the temperature at the inlet is started from 370°C to about 410°C at the end of the run (EOR) [25]. This single stage VGO hydrocracking process executes both hydrocracking and hydrotreating in a single catalytic reactor with three parallel trains. After the hydrocracking reactors, and high and low pressure separators, the feed to the fractionation section still have everything from hydrogen and hydrogen sulfide to the heaviest fractions, and it is essential to divide this stream into the favorite products such as liquefied petroleum gas (LPG), gasoline, kerosene, and diesel which are accepted by the market. The fractionation unit includes the following sections:

1. Sponge absorber tower
2. Recycle splitter column (RSC) with side cut strippers (Figure 1)
3. Diesel and kerosene strippers
4. Naphtha stripper
5. Gasoline stabilizer

The sponge absorber is designed to separate LPG fraction from the vapor of the splitter feed flash drum. In the RSC which is the target of this study, the light product and light naphtha are seized overhead, and the other fractions, i.e. heavy naphtha, kerosene, and diesel are taken as side cuts. The recycle splitter overhead then routed to the stabilizer column to recover light naphtha, LPG, and light gases.

The feed of the recycle splitter enters the lower portion of the column and is warmed up to the required flash zone temperature. This distillation column is a steam stripped column with several side cut draw offs. The overhead from the column is condensed and routed to the reflux accumulator. Heavy naphtha and kerosene as the recycle splitter side cut products are conducted to the corresponding strippers, and they are bared with vapor. The lowest side cut product is a diesel with a TBP range of about 260°C-360°C. This commodity is regularly a high quality, low pour point stream. Due to control its pour point, the end point of that must be adjusted meticulously to pass the required specifications. Finally, down the 370°C, it is removed from the bottom of the distillation tower and returned as the recycle feed to the reactor.

3. Developing the ANN for the RSC

R is a language and environment for statistical computing and graphics developed at Bell Laboratories (formerly AT&T, now Lucent Technologies) by John Chambers and colleagues. R provides a wide variety of statistical (linear and nonlinear modeling, classical statistical tests, time-series analysis, classification, and clustering) and graphical techniques, and is highly

extensible. The advantage of using this software is its availability as free software under the terms of the Free Software Foundation's GNU General Public Licensein source code form. The ability and accuracy of R for modeling chemical engineering processes using its ANN package has been validated and reported in the previous work [26].

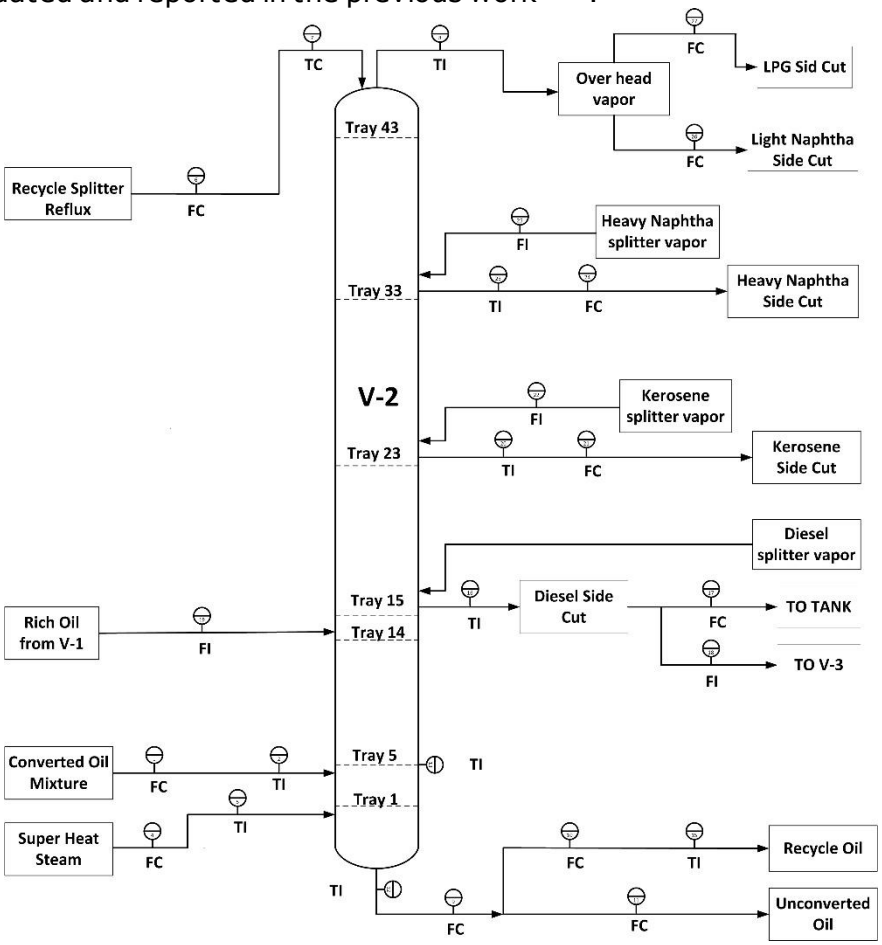

Figure 1. Block flow diagram (BFD) of the main fractionation tower of Isomax unit FC: flow controller; TI: temperature indicator

In this study, neural networks are developed in R software (Version 3.4.1, Copyright 2017) for predicting flow rates of output streams (i.e., LPG, LN, HN, Ker, and Dis) coming from an RSC hydrocracking plant. The package 'neuralnet' (Version 1.33) obtained from the CRAN repository is applied to develop and construct the corresponding ANN models. This package permits resilient settings through custom-choice of error and activation function, and also the calculation of generalized weights [27] is implemented. The globally convergent algorithm of 'neuralnet' is based on the resilient back-propagation without weight back-tracking and additionally modifies one learning rate, either the learning rate associated with the smallest absolute gradient [28].

The most widely employed networks have one hidden layer only. Each node within a given layer is connected to all of the nodes of the previous layer. The node sums up the weighted inputs and bias, and it passes the result through a linear function as follows [29]:

$$a_j = \sum_{i=0}^{m} w_{ji} y_i + b_j \quad (1)$$

where w_{ji} is the weight that goes from the input (i) to the hidden neuron (j); b is the bias to the node, and $x_i$is the input unit of the neuron. By utilizing an activation function (f), the output of the neuron can be written as follows:

$$Z_j = f(a_j) \quad (2)$$

By using 'neuralnet' package, a feed-forward ANN with one hidden layer is developed to simulate the target RSC plant. The input layer of the ANN model consists volume flow rate and temperature of rich oil (Fin and Tin), pressure of overhead (PT), volume flow rate and temperature of super heat steam (Fsin and TS1), flow rate of reflux (FR1), temperature of the reflux (TR1), flow rates of diesel, kerosene and heavy naphtha splitter vapors (R14, FRK24 and FRHN34, respectively), temperature of fifth tray (T5), and the value of pressure between trays 5 and 6 (P56). It should be mentioned that to prevent memorizing instead of learning, only 3 neurons are selected for the hidden layer such that the number of coefficients is less than the number of actual data.

4. Results and discussions

During the period of data collection (about 300 days), 153 valid points are obtained which is randomly divided into two categories including training and testing datasets by using the 'sample' command of the R software. These groups consist 91 and 62 data points (60% and 40% of total data), respectively. All data points are scaled based on the maximum and minimum values of the actual data. In the next step, up to reaching the minimum relative mean squared error (RMSE), networks are trained by using 'neuralnet' package installed in the R environment. The number of iterations, AAD% of training and testing datasets for the flow rates of output streams from the RSC, i.e. LPG, LN, HN, Ker and Dis are presented in Table 1, respectively. From this table, it can be concluded that R can learn the pattern of distillation products. The total CPU time for training each network is less than 3 sec which can be an advantage for developing ANNs using R software. However, this table shows that the iteration is stopped for LPG and LN in less than 100 steps, and training is terminated. Moreover, it results that the AAD% of training for LPG and LN are higher than 5%, in consequence with raising the AAD% of prediction for unseen data (testing). It is supposed that due to the high volatility and vapor pressure of these streams, measuring their flow rate has the abnormal gross error. Moreover, our observations confirm that setting the flowrates of these streams by adjusting the manipulated variables of the RSC is tremendously difficult, and any nuance changes create an enormous deviation in the set point volume flow rates of LPG and LN. Therefore, the collected data for these outputs are not certain which are clearly justified by results of developed ANNs. Additionally, the feasibility of some faults such as signal transmission, calibration, and power fluctuation should not be neglected. Thus, the ANN model cannot test and train flow rates of LPG and LN based on the adjusted variables obtained from the target RSC.

Table 1. Number of iterations and AAD% of training and testing data for VGO hydrocracking neural networks

Product	AAD%_train	Steps	AAD%_test
LPG	7.07	92	17.4
LN	25.66	46	56.28
HN	2.56	798	5.86
Ker	1.55	1874	3.42
Dis	2.1	3009	3.95

The topology of ANNs which are constructed by R for flow rates of LPG, LN, HN, Ker, and Dis are illustrated in Figures 2 to 6, respectively. As seen, each network consist of 42 weights and 4 biases, totally 46 coefficients. As mentioned before, for training a network, there are 91 data points for the yield of each hydrocracking product. Hence, the degree of freedom (DOF) for each ANN is equal to 45. This positive DOF slightly prevents memorizing (over learning) instead of training. It is obvious that increasing the number of data points prevents the over learning, and enhances the resiliency of the ANN model.

After training ANNs, the unforeseen (predicting) data set are injected into the model, and the corresponding flow rate for each distillation stream is estimated and de-scaled using the 'compute' command in the R. As seen from Table 2, the AADs% of predicting data for all products are higher than the AADs% of testing data points, and except to those of LPG and

LN, they are near to the AAD% of trained data. In order to further investigation the reliability of the model, actual yields of LPG, LN, HN, Ker, and Dis are sketched versus the predicted values as parity plots in Figures 7 to 11, respectively. All these figures are achieved by graphical tools provided in the R software. As seen, ANNs for predicting HN, Ker, and diesel flow rates have high certainty; thus, they can be utilized for the purpose of planning, sensitivity analysis and optimizing the target RSC plant.

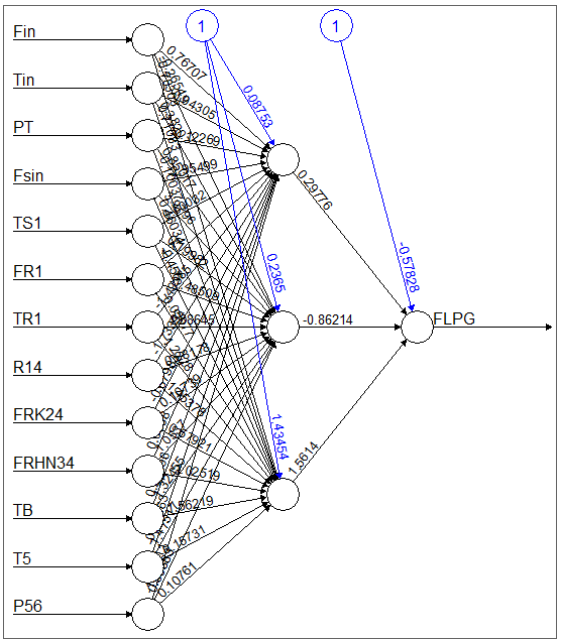

Figure 2. Structure of ANN constructed by R for predicting the yield of LPG

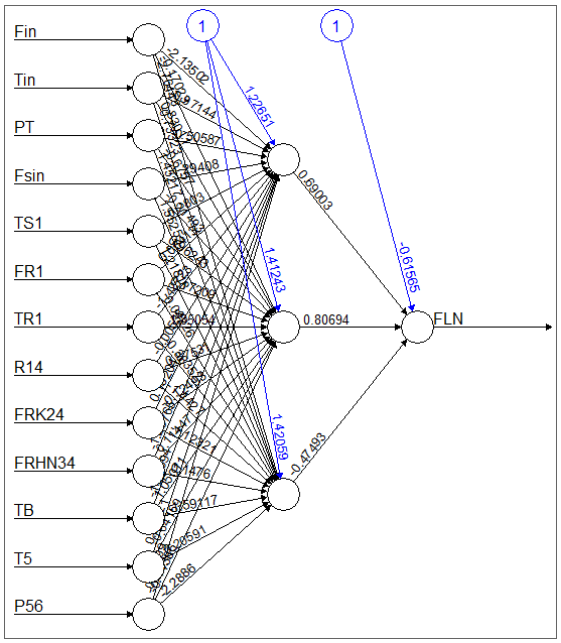

Figure 3. Structure of ANN constructed by R for predicting the yield of LN

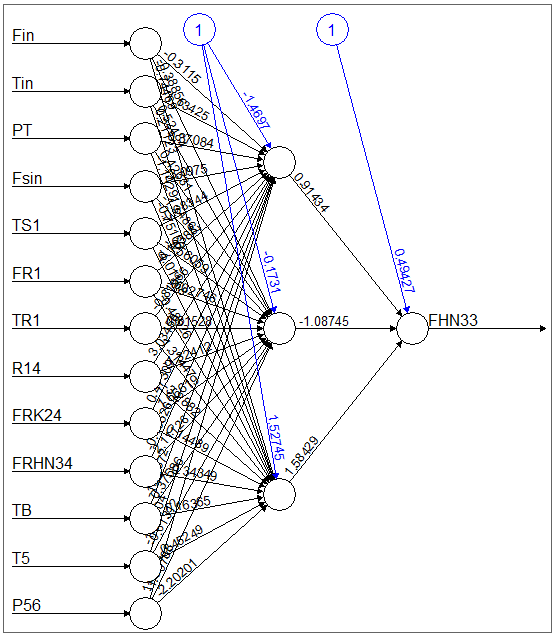

Figure 4. Structure of ANN constructed by R for predicting the yield of HN

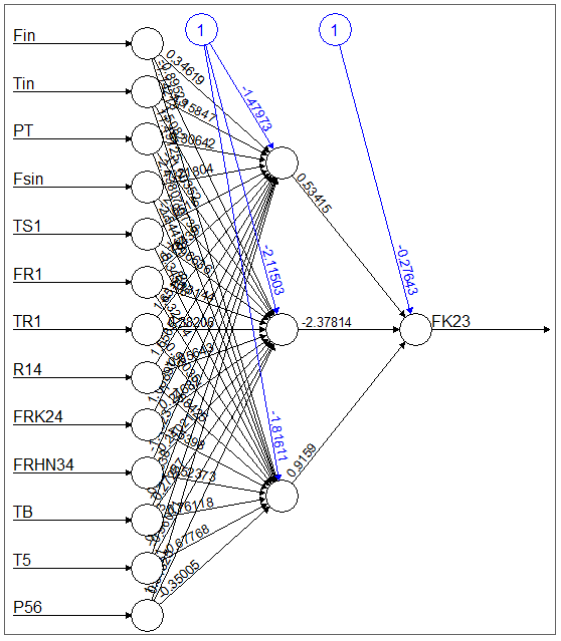

Figure 5. structure of ANN constructed by R for predicting the yield of kerosene

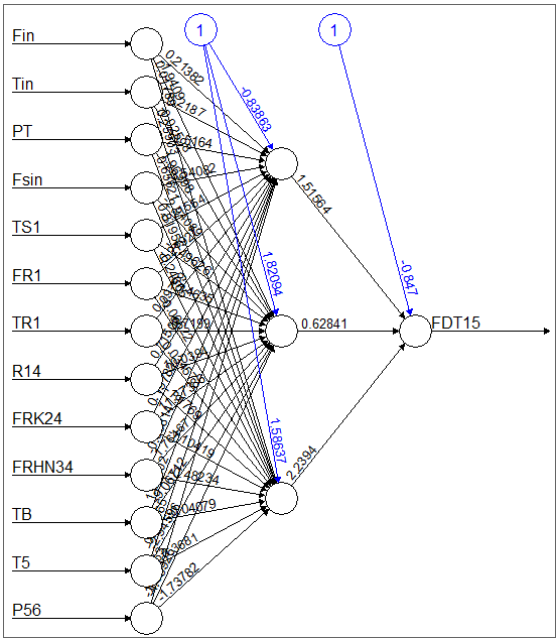

Figure 6. Structure of ANN constructed by R for predicting flow rate of diesel

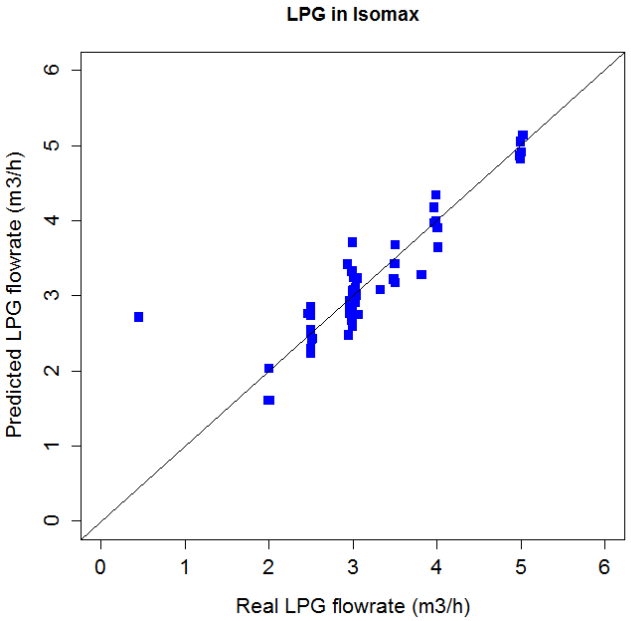

Figure 7. Comparison between actual and predicted values of LPG flow rate predicted by R

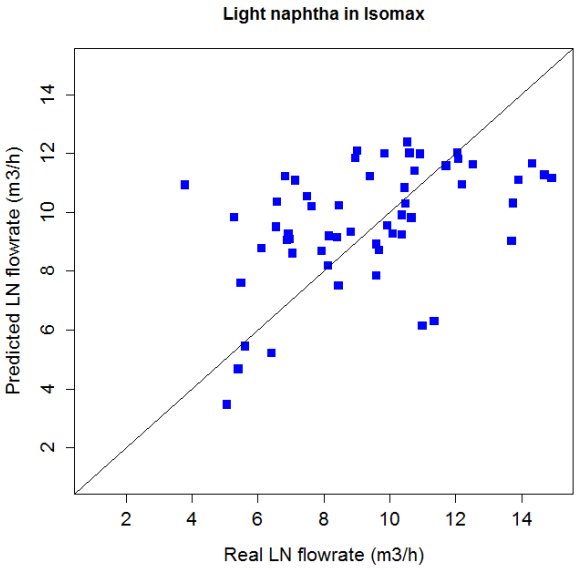

Figure 8. Comparison between actual and predicted values of LN flow rate predicted by R

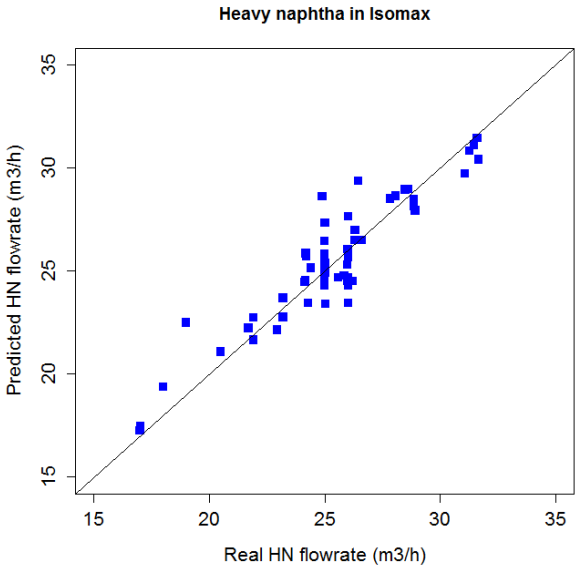

Figure 9. Comparison between actual and predicted values of HN flow rate predicted by R

5. Conclusions

This research demonstrated that the reflux splitter column (RSC) of a commercial scale VGO hydrocracking plant could be molded by using a feed forward artificial neural network. This model was implemented in R software by using 'neuralnet' package. Neural networks could learn about the connection among manipulating variables of the distillation column and flow rates of LPG, light naphtha, heavy naphtha, kerosene and diesel cuts.

To develop the ANN model, 153 actual data points gathered from the target RSC unit. The architecture of ANN models was designed based on a feed-forward neural network with 13 neurons in the input layer and 3 neurons in the hidden layer. For training step, 91 of data points were randomly chosen, and it was performed by using the back-propagation method. Other unseen data points (i.e., 62 data points) were utilized to investigate predicting ability of ANN models constructed in R environment. Results showed that these models could predict flow rates of heavy naphtha, kerosene, and diesel with appreciable accuracy; however, for that of light naphtha and LPG, the predictions were not reliable. This methodology did not need the huge amount of efforts and time such as the mechanistic approaches. Therefore, it can be applied for optimizing and planning the performance of the target RSC unit.

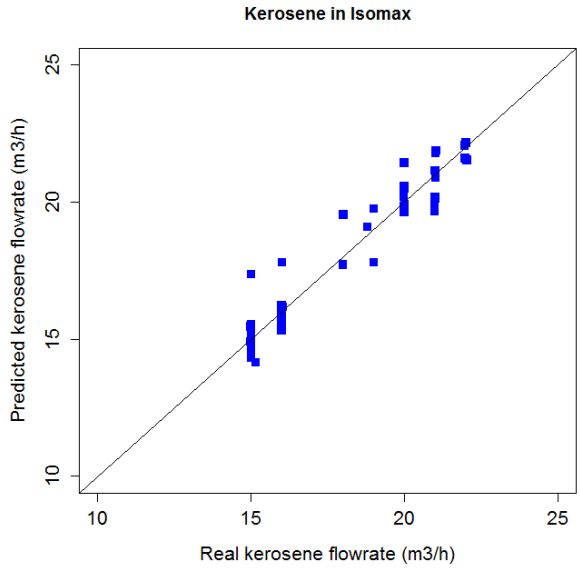

Figure 10. Comparison between actual and predicted values of kerosene flow rate predicted by R

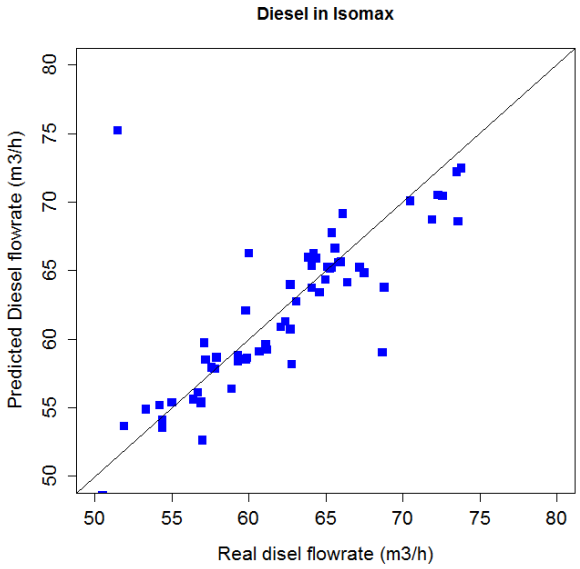

Figure 11. Comparison between actual and predicted values of diesel flow rate predicted by R

Acknowledgements

The authors would like to thank Mr. Mohammad Nabi Golkar Araghi (Engineering supervisor of Isomax Plant) for his helpful advice, and Mr. Yousef Ghaderi (Senior engineer of hydrogen plant) for his efforts during data gathering.

References

[1] Sadighi S. J. Chem. Eng. Jap., 2016; 49(12), 979.
[2] Nikolaychuk E, Stratiev D, Velkov I, Veli A, Sotirov S, Mitkova M, Pet. Coal, 2015; 57(3): 266-279.
[3] Sadighi S, Zahedi S, Hayat, R, Bayat M. Ener. Technol., 2013; 1: 743.
[4] Sadighi S, Mohaddecy R, Norouzian A. Bull. Chem. React. Eng. Catal., 2015; 10: 210.
[5] Sadighi S, Mohaddecy R, Pet. Coal, 2017; 59(2): 195-201.
[6] Taskin H, Kubat C, Uygun O, Arslankaya S. Comput. Chem. Eng., 2006; 30: 850.
[7] Bas D, Dudak FC, Boyaci IH. J. Food Eng., 2007; 79: 622.
[8] Riverol C, Pilipovik MV. Chem. Eng. J., 2007; 133: 133.
[9] Bhutani, N.: Rangaiah, G.P.: Ray, A.K., Ind. Eng. Chem. Res., 2006; 45: 7807.
[10] Niae A, Towfighi J, Khataee AR. Rostamizadeh K. Petrol. Sci. Technol, 2007; 25: 967.
[11] Istadi I, Amin NAS. Ind. Eng. Chem. Res. Catal., 2006; 45: 6655.
[12] Istadi I, Amin NAS, Bull. Chem. React. Eng. Catal., 2007; 2: 37.
[13] Zahedi G, Mohammadzadeh S, Moradi M. Energy& Fuels, 2008; 22: 2671.
[14] Alhajree I, Zahedi, GR, Manan ZA, Mohammad Zadeh S. J. Pet. Sci. Eng., 2011; 78: 627.
[15] Vasseghian Y, Ahmadi M. J. Chem. Pet. Eng., 2014; 48(2): 125.
[16] Sadighi S, Mohaddecy RS. Int. J. Technol., 2013; 2. 102-111.

[17] Sadighi S, Mohaddecy R, Norouzian A. Bull. Chem. React. Eng. Catal., 2015; 10: 210.
[18] Sadighi S, Ghorbani Y, Pet Coal, 2017; 59(6): 777.
[19] Sadighi S, Mohaddecy SR, Abbasi A. Int. J. Technol., 2018; 9(1): 99.
[20] Kusumoputro B, Sutarya D, Faqih A. Int. J. Technol., 2016; 4: 709.
[21] Himmelblau DM. Korean J. Chem. Eng., 2000; 17(4): 373.
[22] Biyanto R Widjiantoro BL, Jabal AA, Budiati T. Int. J. Eng. Sci. Technol., 2010; 2(6): 177-188
[23] Ahmed DF, Khalaf AH. Journal of Chem. Eng. Process Technol., 2016; 7: 272.
[24] Pipoola LT, Babagana G, Susu AA. Int. J. Recent Res. Appl. Studies, 2013; 15(3): 337.
[25] Sadighi S, Ahmad A. Can. J. Chem. Eng., 2013; 91: 1077.
[26] Sadighi S, Mohaddecy SR. Pet. Coal, 2018; 60(3): 358.
[27] Intrator O, Intrator N. Using Neural Nets for Interpretation of Nonlinear Models. Proceedings of the Statistical Computing Section, 1993, 244-249, San Francisco: American Statistical Society.
[28] Fritsch S, Guenther F, Suling M, Mueller SM. Package 'neuralnet': Training of Neural Networks, 2016, https://cran.r-project.org/web/packages/neuralnet/neuralnet.pdf.
[29] Haykin S, Hamilton O. Neural Networks. 2nd ed., Prentice Hall International, Upper Saddle River, NJ, 1998.

To whom correspondence should be addressed: Dr. Sepehr Sadighi, Research Institute of Petroleum Industry (RIPI), Catalysis Technologies Development Division, P.O. Box 14665137, Tehran, Iran, sadighi_sepehr@yahoo.com

Petroleum and Coal

Article **Open Access**

Reservoir Characterization of the "Bawi Field", Greater Ughelli Depobelt, Niger Delta, Nigeria using 3-D Attributes Assisted Seismic Interpretation

A. I. Opara[1], S. A. Chukwu[1], S.O.Onyekuru, A. C. Ekwe[2], C. N. Okereke[1], U. O. Anyiam[1], I. O. Njoku[1], H. N. Echetama[1]*

[1] *Department of Geosciences, Federal University of Technology, PMB 1526, Owerri, Imo State, Nigeria*
[2] *Department of Geology/ Geophysics, Federal University Ndufu-Alike Ikwo, Abakaliki Nigeria*
[3] *Department of Geology, Oklahoma State University, United States of America*

Received April 1, 2018; Accepted June 20, 2018

Abstract

Seismic interpretation of the "Bawi Field", Greater Ughelli Depobelt Niger Delta Nigeria was carried out with the objective of characterizating the reservoirs of the study area using 3-D seismic attributes. Hydrocarbon exploration of complex subsurface configuration as found in the study area requires an enhanced seismic interpretation approach. Several extracted seismic attributes which include variance, acoustic impedance, average energy, spectral decomposition, etc were used to enhance the interpretation of subtle hydrocarbon traps. Suites of signatures from wire-line logs and seismic volume were utilized to gain insight into the hydrocarbon saturated areas and the possible hosting (trapping) units outside the vicinity of well control. Well-to-seismic tie revealed that reservoir tops are tied to direct hydrocarbon indicators (Bright spots) on the vertical seismic section. Seismic variance attribute greatly enhanced geologic discontinuities and aided fault interpretation across the study area while spectral decomposition technique helped to delineate channel geometry and to appropriately select the best band for channel in-fill identification. Two major growth faults (F1 and F2, trending northwest to southeast respectively) were mapped at the central part of the field were revealed to have demarcated the field into three major blocks. Fault 1 (F1) has a southerly dip, while Fault 2 (F2) has a northerly dip. Six faults designated F1, F2, F4, F5, F6& F8 and four seismic horizons of interest were identified and mapped. Structural maps generated from the study revealed that the main hydrocarbon trapping mechanism in the field are fault closures. The trapping elements that can be distinguished include anticlinal dip closures, up thrown fault closures, and down thrown fault closures. Prospective hydrocarbon accumulation spots identified in the study area occur in the downthrown side of F1 and F2 and within the enclosed channel-fill sands in the "Bawi" Field. Four hydrocarbon bearing reservoirs (R1, R2, R3, and R4) were delineated.The reservoirs have an average porosity range of 19% to 38%; water saturation range of 28% to 44%, and net to gross range of 60% to 88%. Estimation of hydrocarbon volume in place revealed that R1 has less than a million cubic feet aof gas while R2 contains 795 million barrels of oil. Reservoirs R3 and R4 have estimated volume reserves of 177 and 227million barrels of oil respectively.

Keywords: *Seismic attribute; spectral decomposition; reservoir characterization; petrophysics; reservoir; Niger delta.*

1. Introduction

Innovative seismic attributes have the potential for revealing subtle geologic features from conventional seismic amplitude data. Chopra and Marfurt [1] defined seismic attribute as any measure of seismic data that helps the seismic interpreter to visually enhance or quantify features of interpretation interest. A seismic attribute is therefore any property of seismic data that helps us better visualize or quantify features of interpretation interest. Seismic attributes have proliferated in the last three decades at a rapid rate and have helped in making accurate predictions in hydrocarbon exploration and development [2]. They are most often widely used for lithological and petrophysical prediction of reservoir properties. Attributes are related to

the fundamental information in seismic data which include time, amplitude, frequency, and attenuation. Generally, time-derived attributes help to discern structural details while amplitude/frequency derived attributes are better suited for addressing problems of stratigraphy and reservoir characterization [44-45]. Amplitude attributes are the most robust and are most often used while frequency attributes may help to resolve problems associated with subtle stratigraphic traps and may reveal additional geologic layering [3]. One of the frequency attributes that has gained popularity and wide application in the hydrocarbon industry over the past few decades is spectral decomposition [46-47]. Spectral decomposition is an innovative seismic attribute used for reservoir imaging and interpretation technology [4]. The technology utilizes a sequence of seismic frequency slices through an area of interest to create a suite of frequency maps which can be selectively combined to yield much higher resolution images of reservoir boundaries, lithologic heterogeneities and interval thicknesses than traditional broad-band seismic displays [5]. Castagna *et al.* [6] mentioned four effects or ways in which spectral decomposition can help in the direct detection of hydrocarbons, which include: 1) abnormally high attenuation, 2) low-frequency shadows, 3) tuning frequency anomalies (also called differential reservoir reflectivity or preferential reservoir illumination), and 4) frequency-dependent Amplitude Variation with Offset (AVO).

Seismic attributes have evolved over the past three decades and have been invaluable in making far better accurate predictions and characterization of reservoir properties [7-11]. They are specifically applied in hydrocarbon exploration and development and are widely used for lithological and petrophysical prediction of reservoir properties [11]. Common seismic attributes such as complex trace [12], coherence [13], curvature [14], and spectral decomposition attributes [4] use mathematical formulations to capture the geometry or other physical properties of the subsurface and can be used to clarify subtle geologic features of interest [48-49]. A methodology has now been proposed and described for 3-D structural characterization based on the combination of specific attributes of interest and other visualization techniques [1,50-52]. The correct combination and sequence of these attributes can enhance the final goal of identifying features that were not visible before.

Radical development of new technology has led to the discovery of new attributes like texture attributes [15]. Sangree and Widmier's [15] pioneered this discovery which suggested that zones of common seismic signal character are related to the geologic environment in which their constituent sediments were deposited. This concept have been used by Love and Simaan [16] to attempt the extraction of patterns using texture analysis. Texture is defined by the spatial configuration of rock units and is more diagnostic of and relevant to deformational fabrics, depositional facies, and reservoir properties than an averaged acoustic property [17]. The methodology follows the way a seismic interpreter analyzes seismic amplitudes and waveforms. In the past decade, the idea of studying seismic 'textures' has been revived. While the term was earlier applied to seismic sections to pick out zones of common signal character [18], several studies have been carried out which use statistical methods to classify and clarify textural signatures using gray-level co-occurrence matrices [9-10,19-22]. Some of the statistical measures used are energy (denoting textural homogeneity), entropy (measuring predictability from one texel or voxel to another), contrast (emphasizing the difference in amplitude of neighboring voxels) and homogeneity (highlighting the overall smoothness of the amplitude). Homogeneity, contrast and entropy have been found to be the most effective in characterizing seismic data. Texture attributes are promising and can aid the geophysicist for making more accurate interpretations.

The evaluation of the intrinsic properties of a reservoir like thickness, net-to-gross ratio, pore fluid, porosity, permeability, water saturation and volumetric reserve is what is most often regarded as reservoir characterization [53-55]. Most of these reservoir properties were previously estimated using information from borehole logs. However, in the past few years, most of these properties have been mapped with the help of seismic attributes especially when calibrated with available well data within the study area [55-57]. This methodology has certain inherent advantages which includes the high spatial coverage as well as the fact that the

seismic data can be used for interpolating and extrapolating within and beyond the locations of the few available well data [23]. Seismic attributes are characteristics of a seismic data and often represented by analytical maps that aids the interpreter in better interpretation and visualization of geological features of interest [44,51,54]. This work would therefore focus among other things on showing how derived seismic attributes can be used to enhance seismic interpretation and reduce risks in prospect prediction. The ability of the seismic data to image the sub-surface and assess interpreted structures and their closures for potential reservoirs for hydrocarbon entrapment and accumulation will also investigated.

2. Regional geology of the study area

The study area is located within the Greater Ughelli Depobelt of the Niger Delta basin, southern Nigeria as shown in Fig.1. The geology, stratigraphy, petroleum and structural geology of the Niger delta basin have been extensively discussed in several key publications [24-33]. The Niger Delta basin is a world class petroleum province which lies approximately within longitudes 4°E and 8°E and latitudes 4°N and 6°N [59-59]. Its areal extent is about 75,000km^2 with a clastic fill of about 12,000m [34].It ranks amongst the world's most prolific petroleum producing tertiary deltas that together account for about 5% of the world's oil and gas reserves [60-61]. The onshore portion of the Niger Delta includes the geologic extent of the Tertiary Niger Delta (Akata-Agbada) Petroleum System and is delineated by the geology of southern Nigeria [35]. The northern boundary is the Benin flank - an east-northeast trending hinge line south of the West Africa basement massif [58-59]. The northeastern boundary is defined by outcrops of the Cretaceous on the Abakiliki High and further east (south-east) by the Calabar flank-a hinge line bordering the adjacent Precambrian rocks (Fig.2).

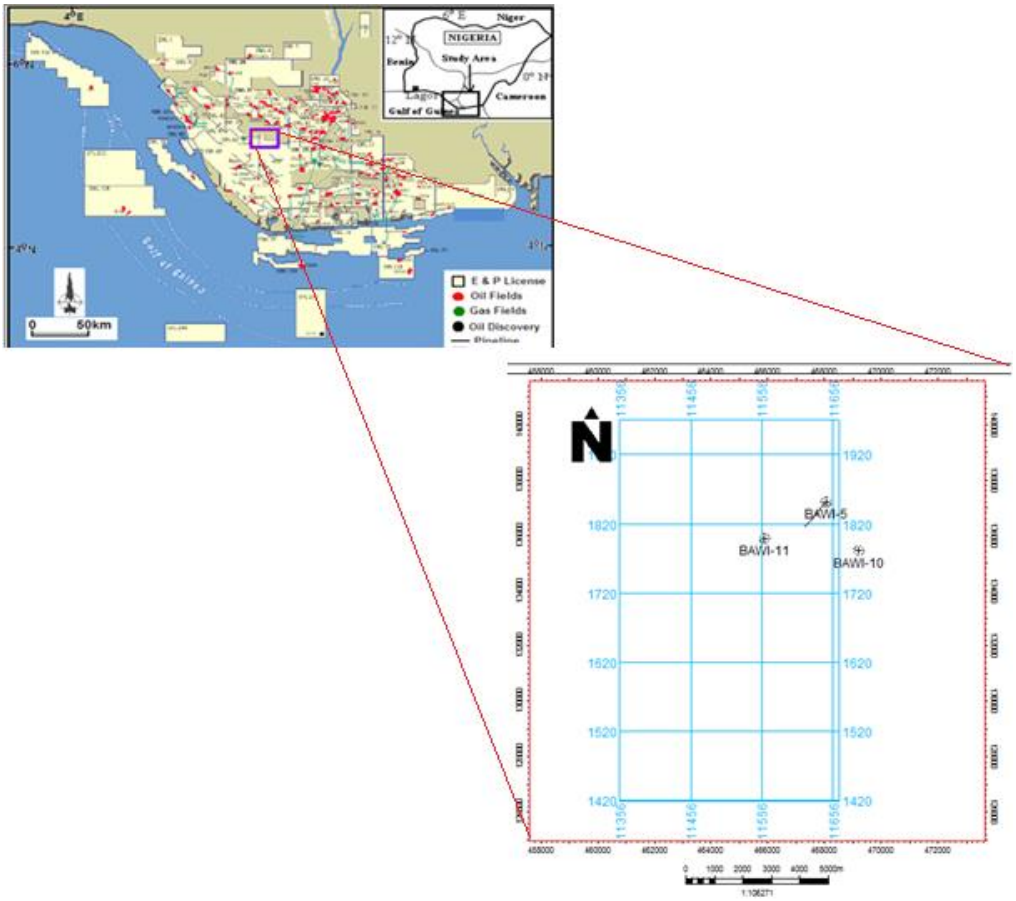

Fig.1a Base map and location of the study area showing the seismic lines and wells drilled

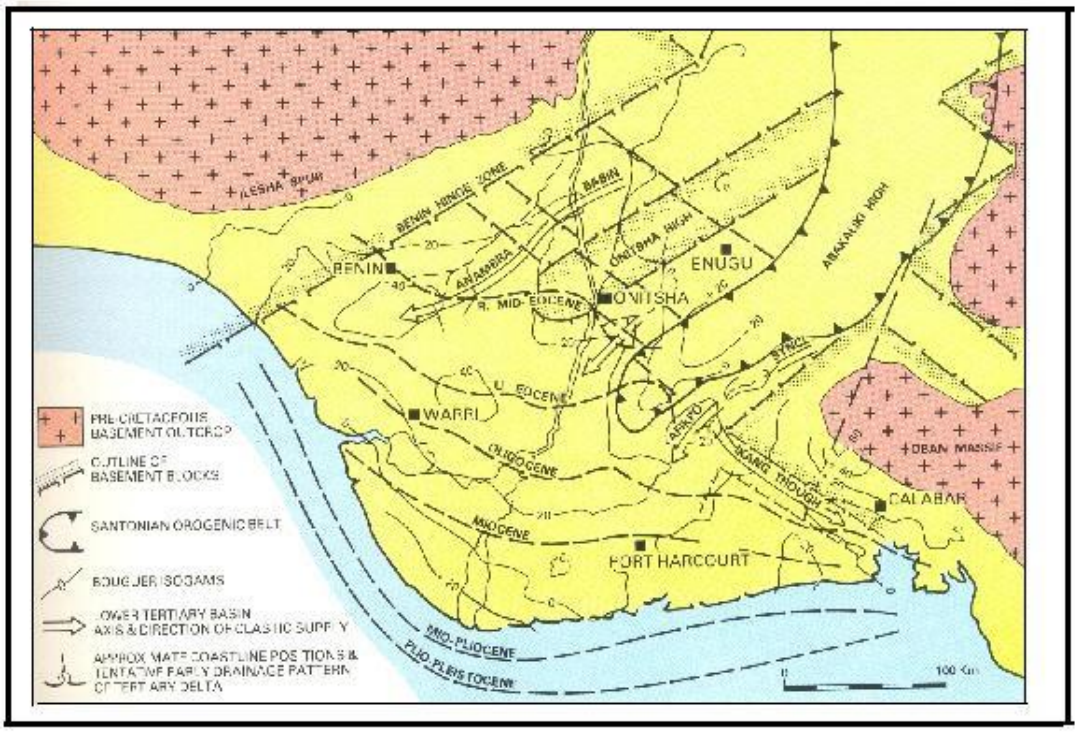

Fig. 1b.Geological map of the Niger Delta (modified after Whiteman [30]

The composite Tertiary sequence of the Niger Delta consists, in ascending order the Akata, Agbada and Benin Formation. The Akata Formation which is at the base of the delta is predominantly undercompacted, overpressured sequence of thick marine shales, clays and siltstones (potential source rock) with turbidite sandstones (potential reservoirs in deep water). It is estimated that the formation is up to 7,000 meters thick [28,36]. The Agbada Formation which is the major petroleum-bearing unit is about 3700m thick and is made up of an alternating sequence of paralic sandstones, clays and siltstone [24,35,37]. The upper Benin Formation overlying the Agbada Formation consists of massive, unconsolidated continental sandstones. These three major lithostratigraphic units decrease in age basin ward, reflecting the overall regression of depositional environments within the Niger Delta clastic wedge. The deposition of the three formations and the progradation of the Niger Delta has been dependent on the interaction between rates of subsidence and sediment supply, and modified by faulting. Several growth-fault bounded sedimentary units (depobelts) are therefore present. These depobelts succeeded one another as the delta prograded through time under the influence of off lapping siliciclastic sedimentation cycles [35,38]. Sedimentation in the depobelts is a function of sediment supply and of accommodation space created by basement subsidence and growth faulting. Growth faults, triggered by a pene-contemporaneous deformation of deltaic sediments are the dominant structural features in the Niger delta [60-61]. For any given depobelt, gravity tectonics were completed before deposition of the Benin Formation and are expressed in complex structures, including shale diapirs, rollover anticlines, collapsed growth fault crests, back-to-back features, and steeply dipping, closely spaced flank faults [24,39]. These faults mostly offset different parts of the Agbada Formation and flatten into detachment planes.

Petroleum in the Niger Delta is produced from sandstone and unconsolidated sands predominantly reservoir rocks of Eocene to Pliocene in age and are often stacked, ranging in thickness from less than 15 meters to about 45 meters [24]. Based on reservoir geometry and quality, the lateral variation in reservoir thickness is strongly controlled by growth faults, with the reservoir thickening towards the faults of the downthrown block [39].

3. Methodology

This research attempts to identify and characterize prospects in the "Bawi" field, Niger Delta through an integrated seismic attribute assisted interpretation of the study area. The well data used include well header, check shots, well deviation and well log data. Biostratigraphic information was only available for one well. Interpretative geophysical softwares utilized include Petrel 2013 and OpendTect 4.2.0. A quick look interpretation was carried out using gamma ray and resistivity logs for lithofacies and hydrocarbon pay zone (reservoir) determination of three wells (Bawi-11, Bawi-5& Bawi-10). Gamma ray log was used to delineate lithology (sand and shale bodies). Sand bodies were identified by deflection to the left due to the low concentration of radioactive minerals in sand while deflection to the right signifies shale which is as a result of high concentration of radioactive minerals. Reservoirs were identified by using the log signatures of both gamma and deep resistivity logs. Intervals that have high resistivity are considered to be hydrocarbons while low resistivity zones are thought to be water bearing.

Well correlation was carried out to determine the continuity and equivalence of lithologic units for the reservoir sands and marker sealing shales of the wells in the study area (Figs.2&3). Regional markers from biostratigraphic information obtained for well 3(Bawi-10), were matched on the Niger Delta chronostratigraphic chart for maximum flooding surfaces determination and correlated across the field using the gamma ray log motifs. The gamma ray log motif was used for an initial lithologic interpretation to identify the major sandstone and shale units, and then further combined with the deep resistivity logs for detailed correlation work with emphasis on the shale sections. Four reservoirs of interest R1, R2, R3&R4 were identified and correlated in the Oil field. Reservoir tops sand 001, sand 002, sand 003 and sand 004 were correlated to depths of 2886 m, 3527m, 3856m and 4024m in Bawi-11 and 3160m, 3850m, 4000m and 4177m in Bawi-5. Well section analysis revealed that each of the sand units were revealed to extend through the field and vary from 70 to 77m in R1, 63 to 73m in R2, 45 to 64m in R3 and 35 to 50m in R4. Some sand units occur at greater depth than their adjacent units (possibly an evidence of faulting). The shale layers were observed to increase with depth along with a corresponding decrease in sand layers.

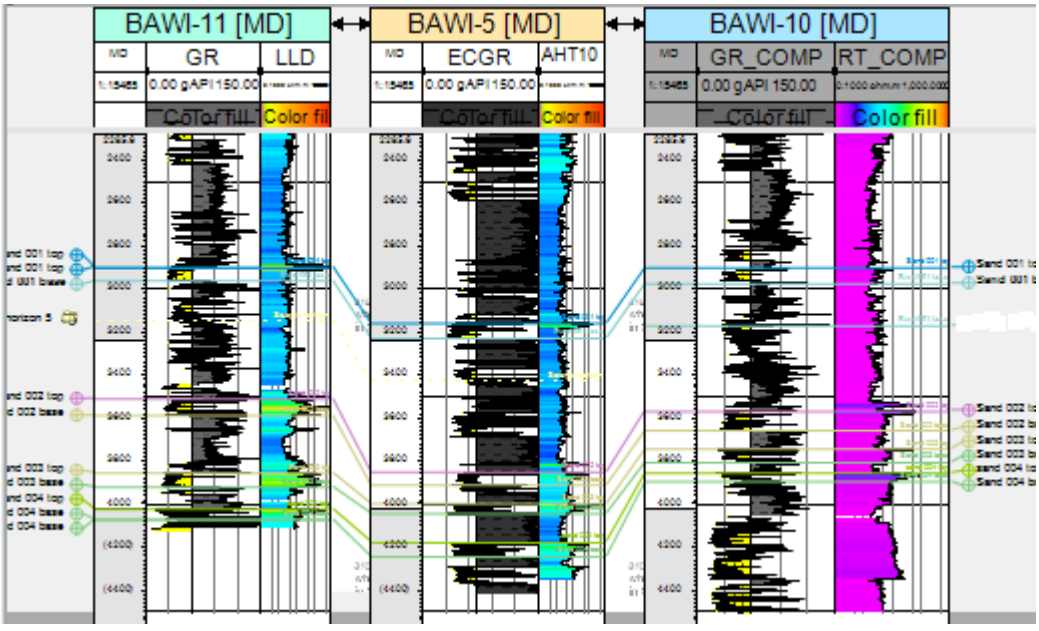

Figure 2. Display of Well log correlation across the Oil field

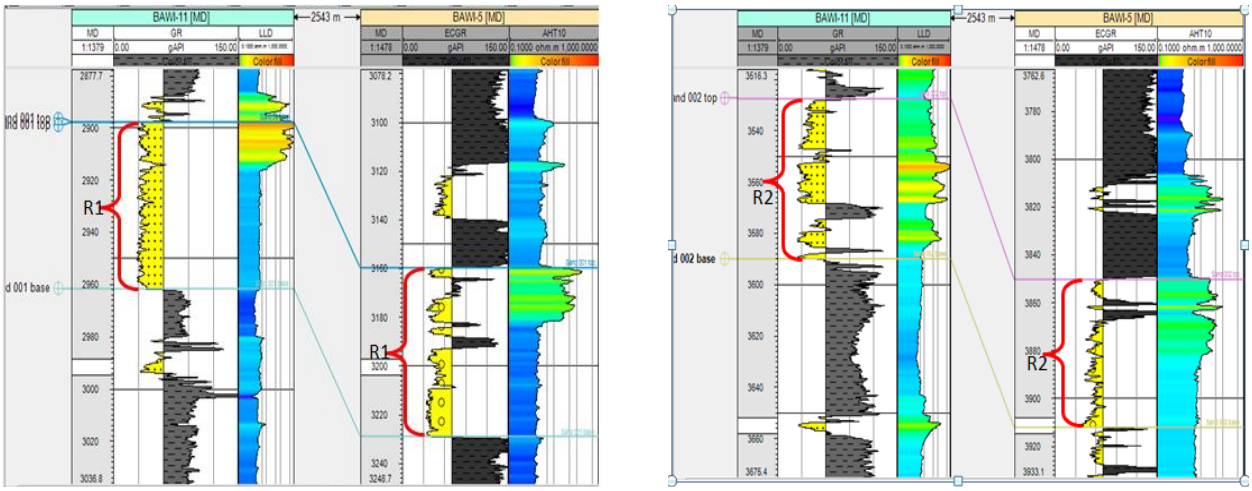

Figure 3a. Reservoir delineation from well logs (a) Reservoir R1 (b) Reservoir R2

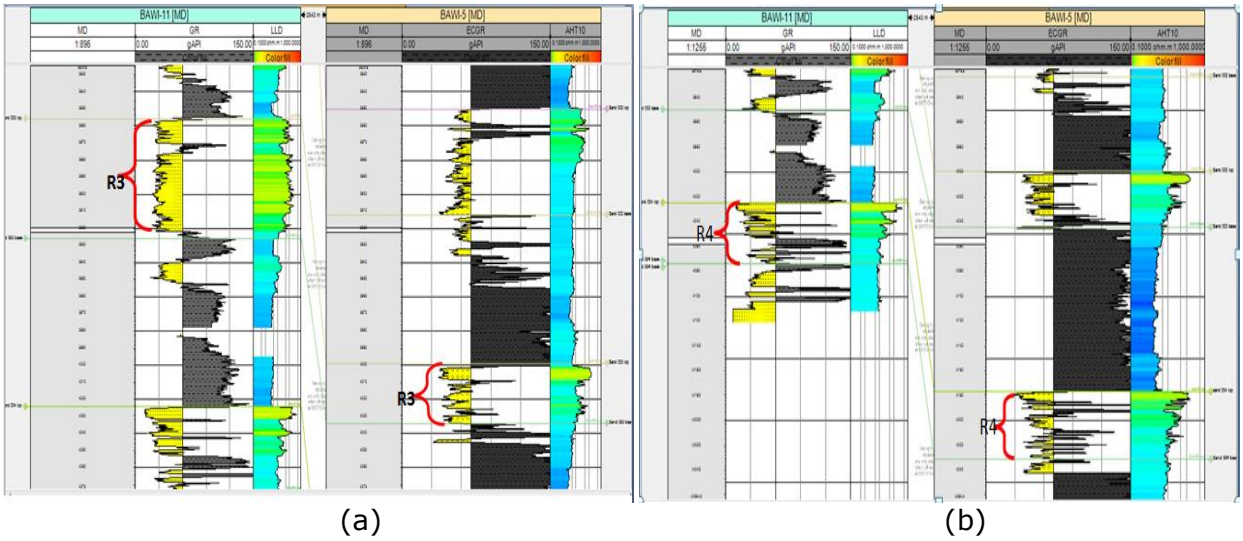

Figure 3b. Reservoir delineation from well logs (a) Reservoir R3 (b) Reservoir R4

Similarly, well to seismic tie was carried out with information extracted from Bawi-11 well, in order to calibrate the seismic data and also identify its polarity (Fig.4). A synthetic seismogram was generated for this purpose, using sonic and density logs. First, corrected sonic and density logs was used to generate the Acoustic impedance and a reflection coefficient was computed. The generated reflection coefficient was convolved with extracted wavelet from the seismic (zero phase wavelet) to generate the synthetic seismogram. Well to seismic correlation revealed that reservoir tops tied to bright reflections on seismic sections. High amplitudes were interpreted as peaks, while low amplitudes represent troughs.

4. Result interpretation and discussion

4.1. Horizon picking, fault Mapping and map generation

The seismic reflection data quality was low in certain places and therefore fault trends were not readily apparent on seismic sections due to poor resolution. Seismic variance attribute was employed to reveal subtle details in the seismic data and to guide fault mapping. Major and minor faults were mapped based on linear features observed in the seismic data. Key reflections corresponding to well tops on seismic sections were identified and mapped across

the seismic volume. Four horizons were picked in both in lines and cross lines. Interpretations were first made in the volume near the wells that were tied, and then extended outwards from the well. Seismic attribute (Relative acoustic impedance) showed great promise for determining reflector continuity. Time maps were generated from the picked horizons, and fault polygons developed. Furthermore, a velocity function generated from the T-Z data was used to convert the time maps to depth maps.

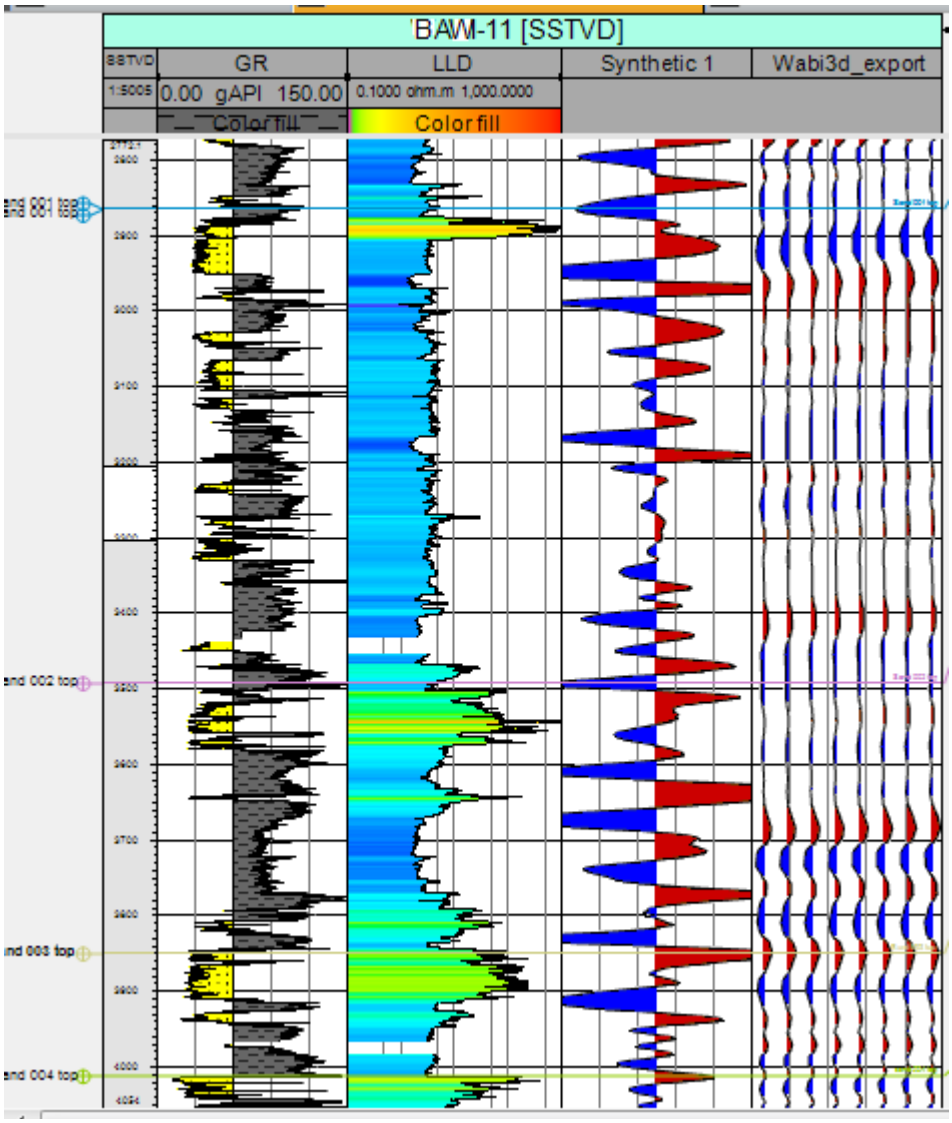

Figure 4.Well to Seismic tie section (Bawi-11). High amplitude events correspond to peaks

Seismic variance attribute revealed discontinuities on seismic sections and aided fault interpretation. Structural interpretation of the study area revealed a preponderance of northwest to southeast (NW-SE) trending faults in the field(Fig.5). Two major growth faults (F1 and F2) were mapped at the central part of the field thereby dividing the field into three major blocks. These faults are the major structure building faults. These two faults extend throughout the field as seen on the interpreted seismic sections. Fault (F1) is dipping to the south while fault (F2) is dipping to the north. Other faults mapped include a synthetic fault (F5), and minor faults (F4, F6 and F8). Displacement of seismic facies across the faults generally increased with depth. This could be attributed to sediment deposition on the downthrown part of the fault.

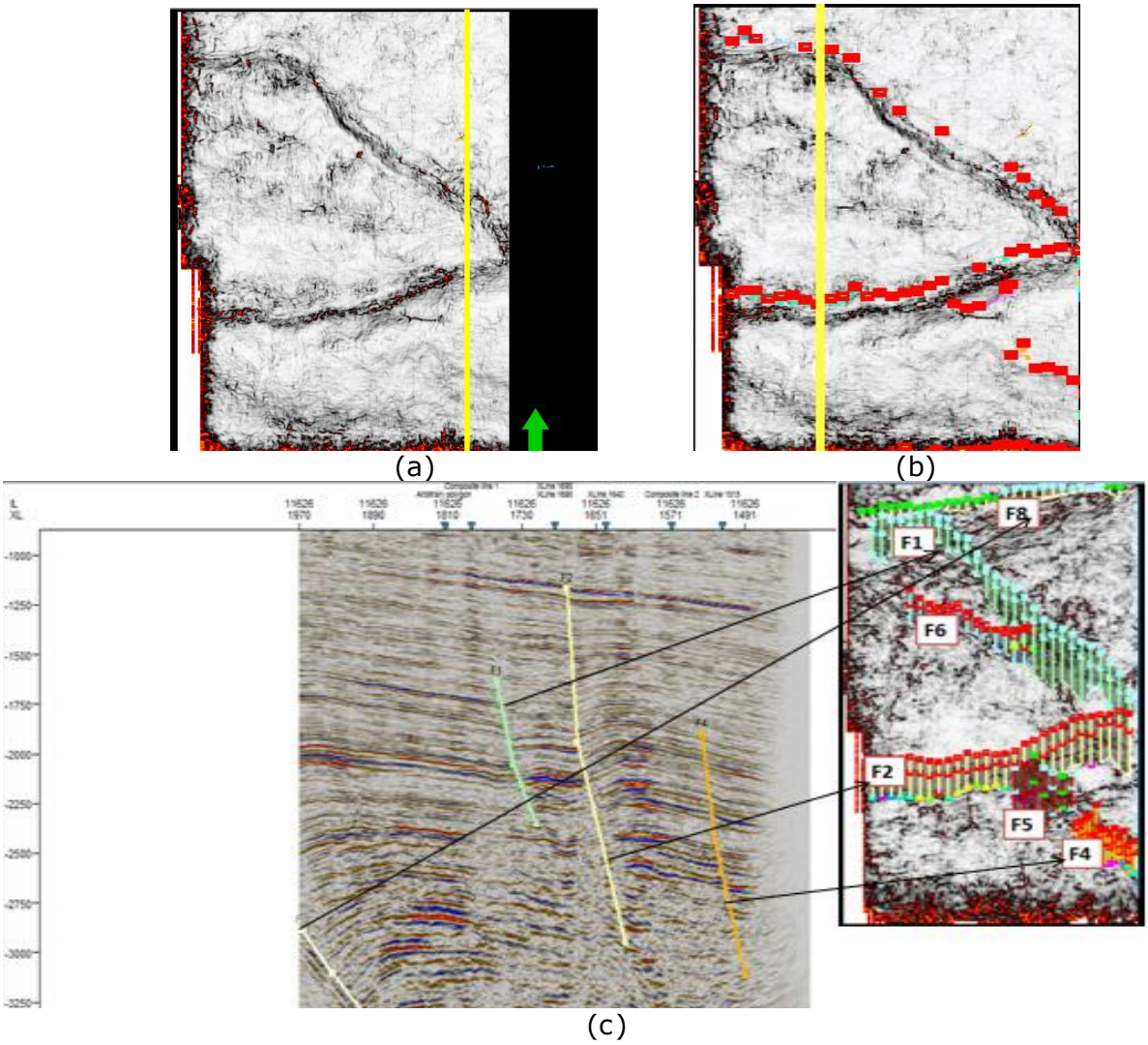

Figure 5. (a) Variance slice at 2000ms (b) Variance slice at 2000ms with fault sticks of picked faults (c) Faults picked on seismic section (inline 11626) and corresponding fault sticks on variance slice (2900ms)

Key seismic reflections identified were moderately continuous and truncated in places by faults. Altogether, four horizons were picked on both in lines and cross lines across the field (fig. 6). Time structure maps were generated from the picked horizons with depth structure maps depth converted from the time maps using a velocity model (Figs.7-10). The depth converted map of the horizons reflected the structure of the subsurface. Large faulted anticline take up most of the study area. The anticline trends NE- SW and is asymmetrical in shape. The complexity of the anticline increases from the top (horizon 1) to the bottom (horizon 4). This field is characteristically associated with fault closures and roll-over anticlines, which are considered to be the main hydrocarbon trapping mechanisms.

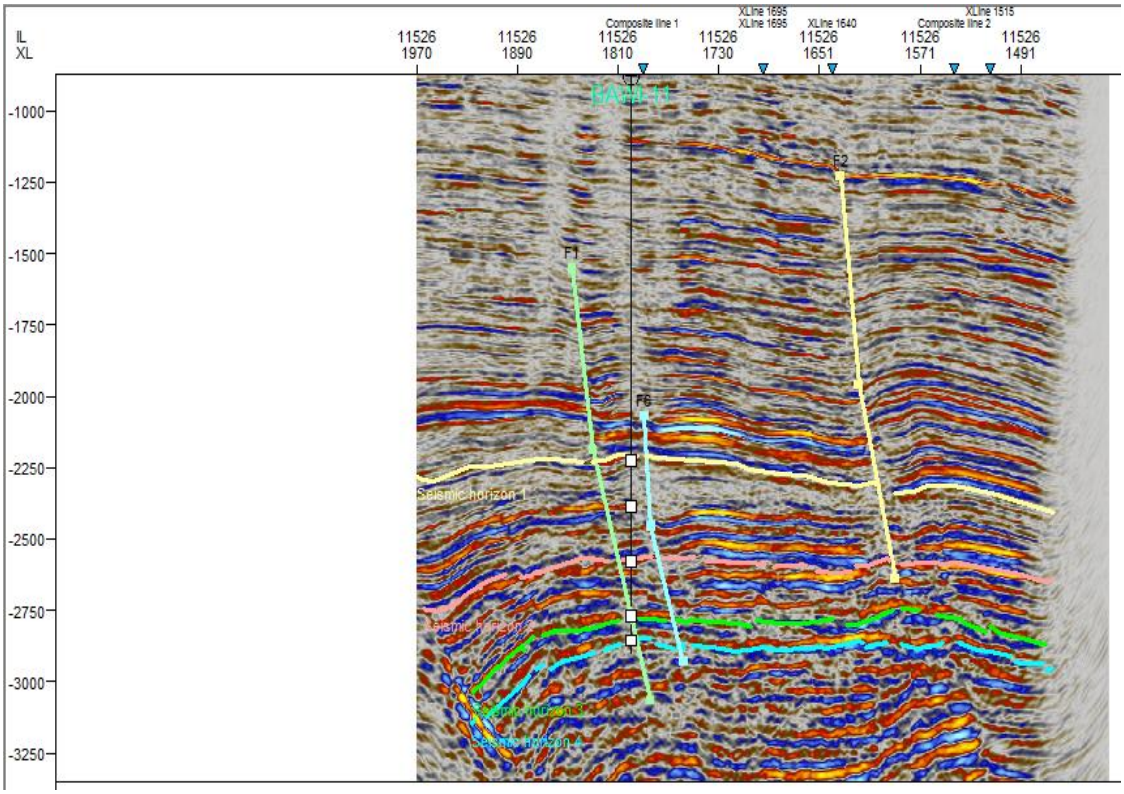

Figure 6. Showing Acoustic impedance attribute enhanced reflections and picked horizons (inline 11526)

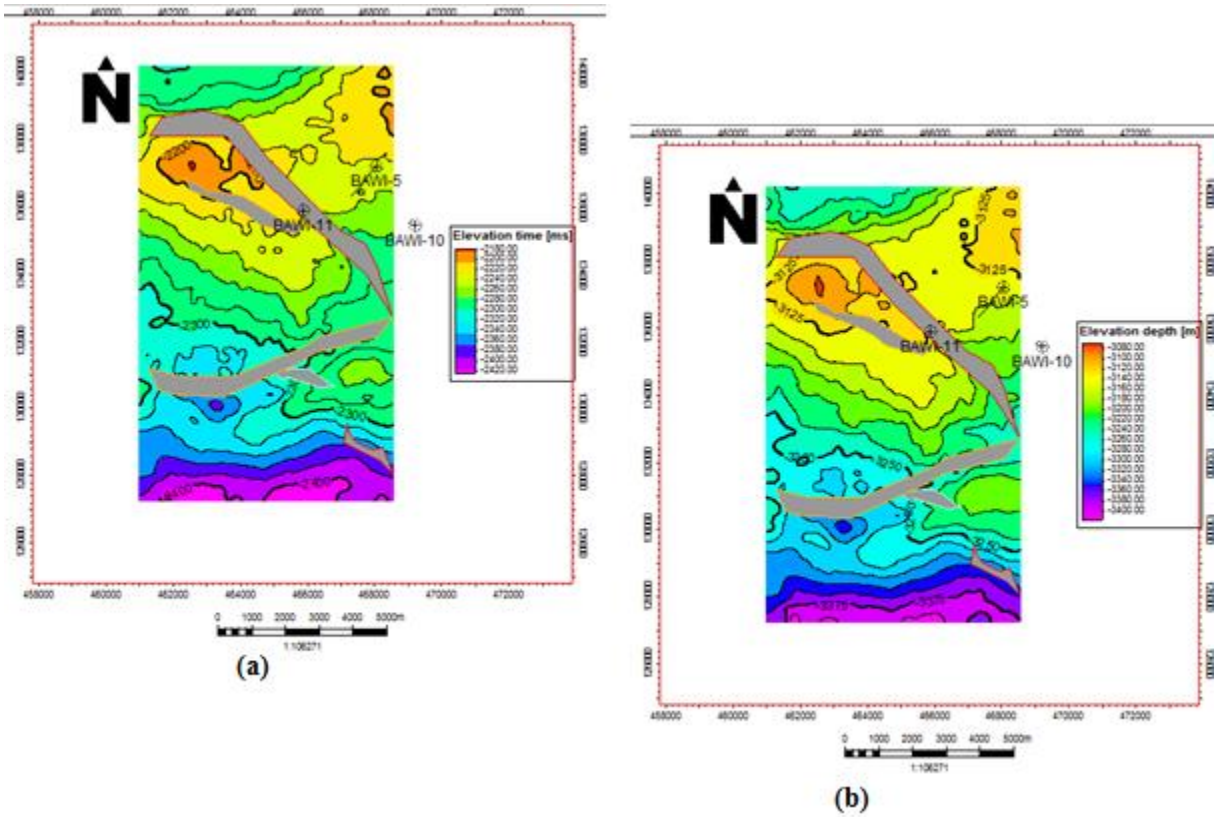

Figure 7. Structural maps from horizon 1 (a) Time map (b) Depth map

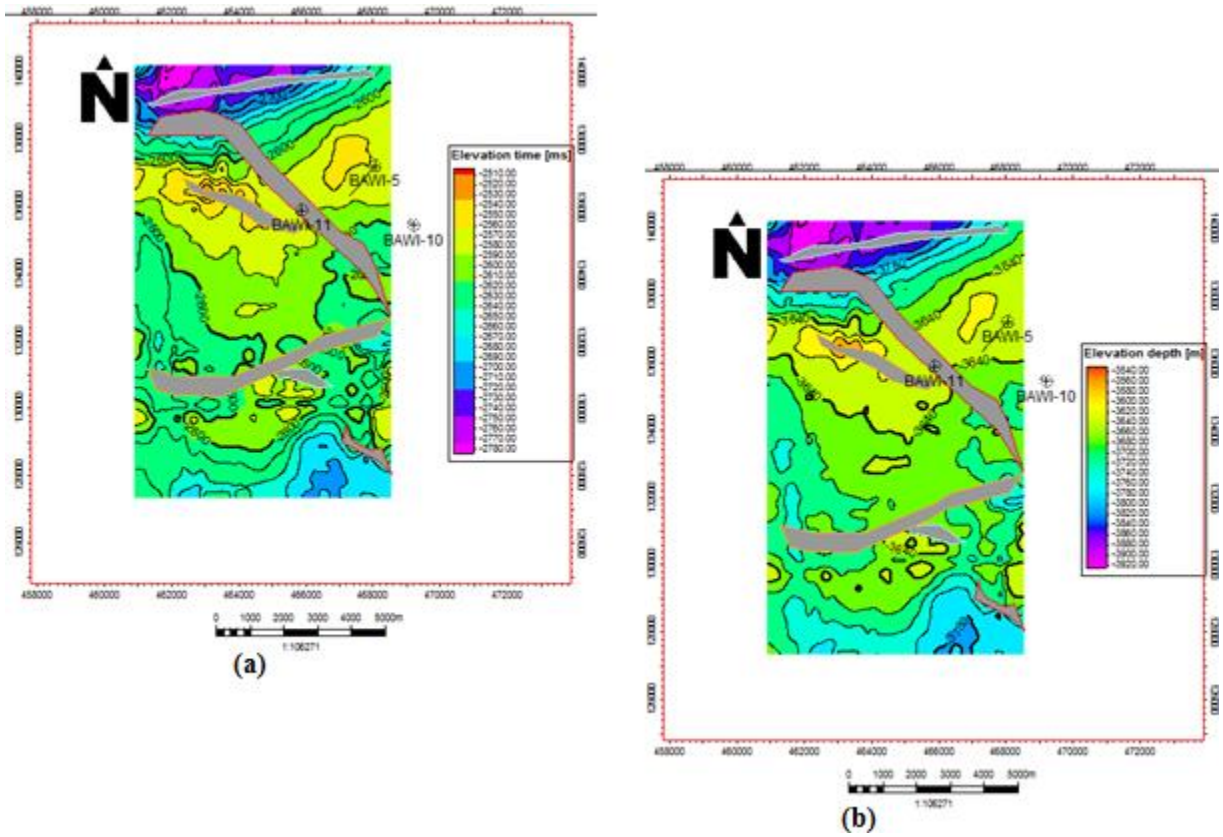

Figure 8. Structural maps from horizon 2: (a) Time map (b) Depth map

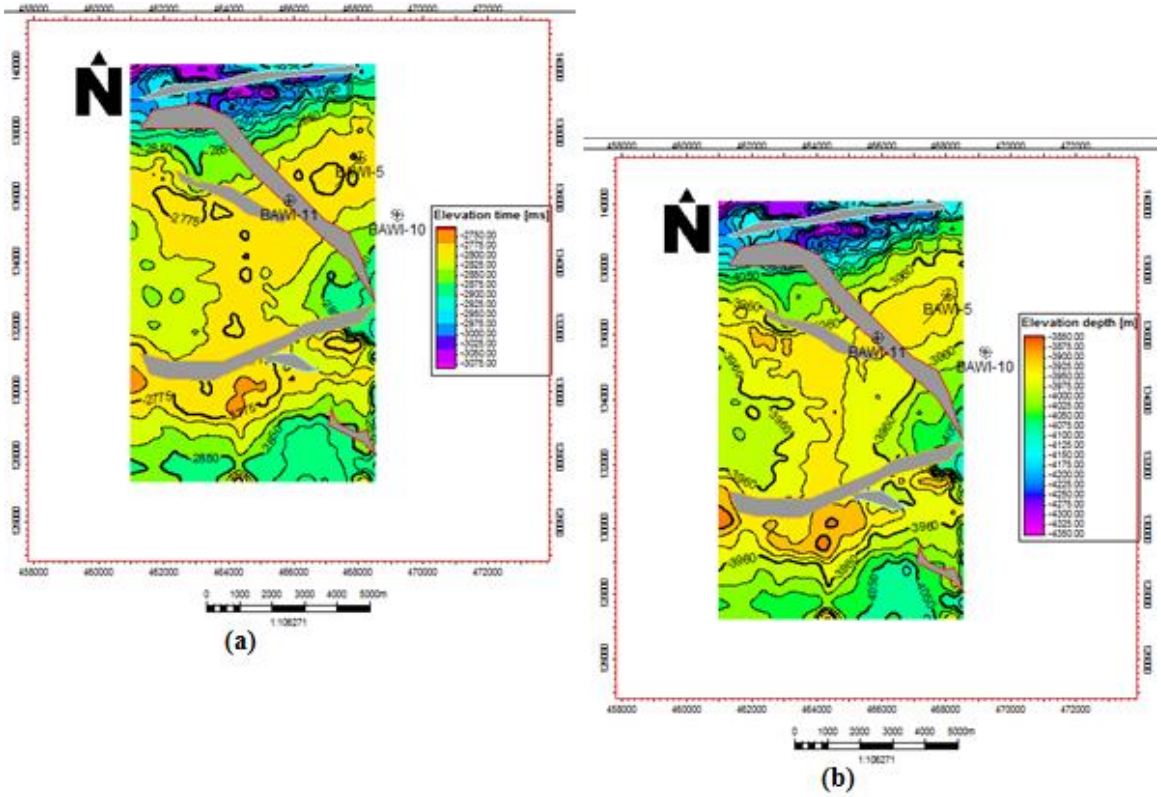

Figure 9. Structural maps from horizon 3: (a) Time map (b) Depth map

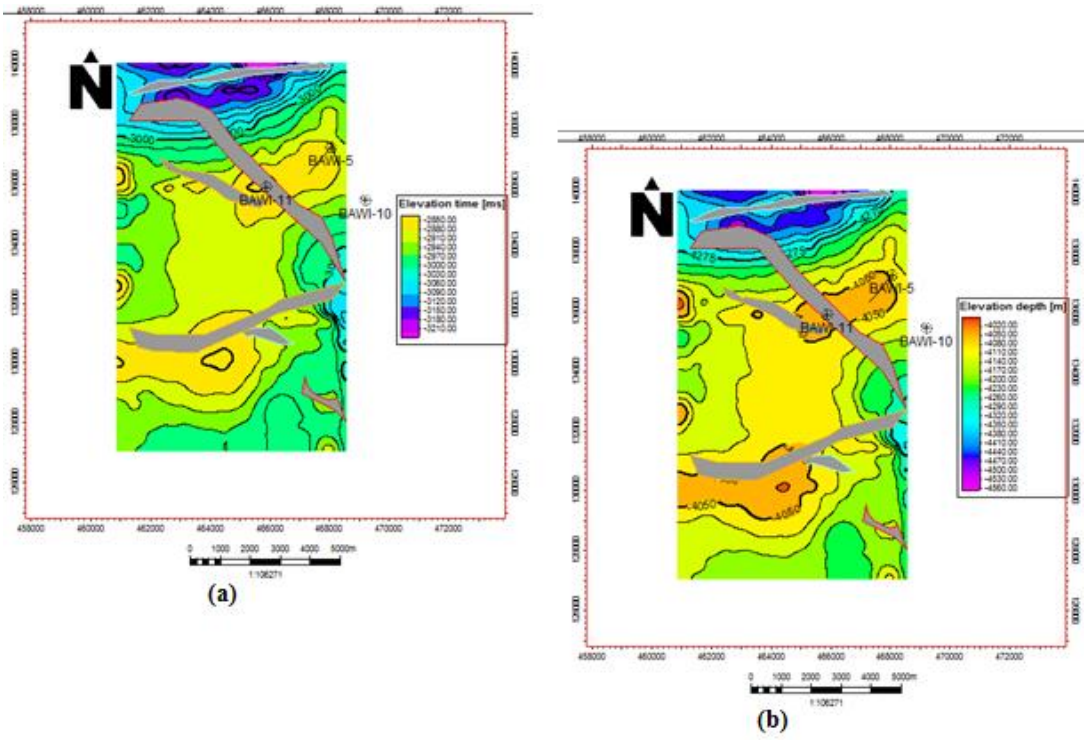

Figure10. Structural maps from horizon 4: (a) Time map (b) Depth map

4.2. Seismic attribute analysis

The acronym DHI refers to Direct Hydrocarbon Indicators. DHI attributes are attributes that when observed in a seismic horizon, they indicate directly the presence of hydrocarbon to a very high degree. The primary DHI attribute used for this work was the average energy, which predicts areas of high amplitudes. The average energy was complemented by other seismic attributes which include instantaneous bandwidth attribute (to detect relative uniformity or otherwise of predicted lithology), and relative acoustic impedance attribute (a porosity indicator).Similarly, stratigraphic channel investigation was carried out in the study area using a combination of envelope, iso-frequency, and spectral decomposition. Spectral decomposition helped to generate series of maps in order to observe the response of reservoir characteristics to different frequency bands. These were integrated to determine the part of the channel with thickest reservoir continuity.

From the average energy map, higher energy spots are believed to be indicative of hydrocarbon (Fig.11a). Variation in the Instantaneous bandwidth suggests sharper amplitude changes related to changes in lithology, while zero instantaneous bandwidth represents uniform lithology (Figs.11b&11c). Although the exact lithology type may not be predictable, it gives an idea about where the lithofacies are uniform in the reservoir. The Relative Acoustic Impedance (RAI) is a porosity indicator. There is a high negative correlation between porosity and acoustic impedance. Bouvier *et al.* [36] reported that acoustic impedance contrast is negative for hard shale to soft sandstone and that in Nigeria, sandstones have comparatively lower acoustic impedance than shales; hydrocarbon bearing sandstones having even lower acoustic impedance than water-bearing sandstones with increased positive amplitude. By comparing with generated Relative Acoustic Impedance map, the lithology types associated with areas with uniform lithology (zero bandwidth) are assumed to be sands (because of associated high porosity). This is confirmed by good match between gamma ray and instantaneous bandwidth at well locations. This guided our prospect prediction. Identified prospects are labeled P1, P2 and P3 (Figs.11-13).

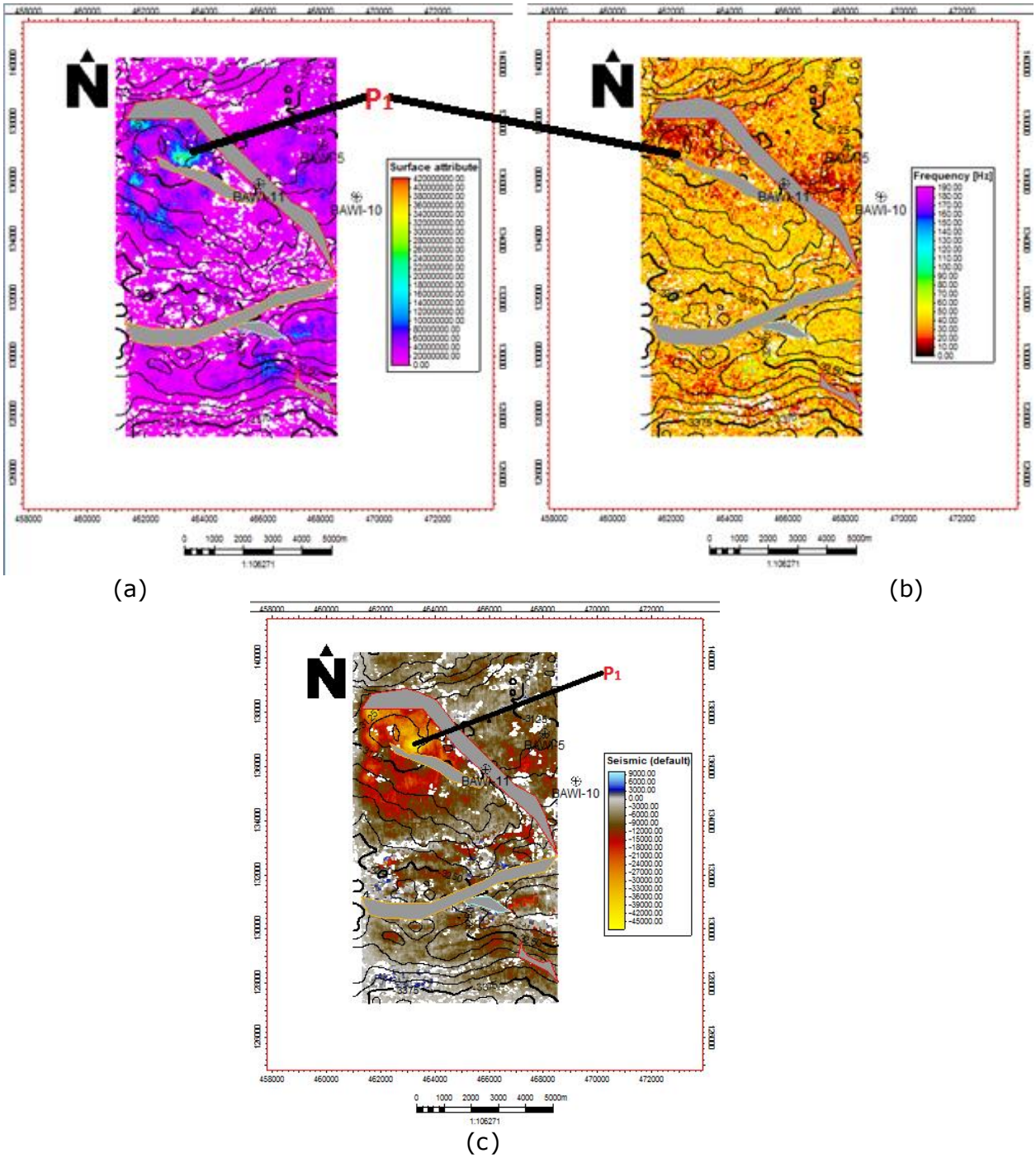

Figure 11. Seismic attribute analysis for horizon 1. Prospective area P1was identified (a) Average energy (b) Instantaneous bandwidth (c) Relative acoustic impedance

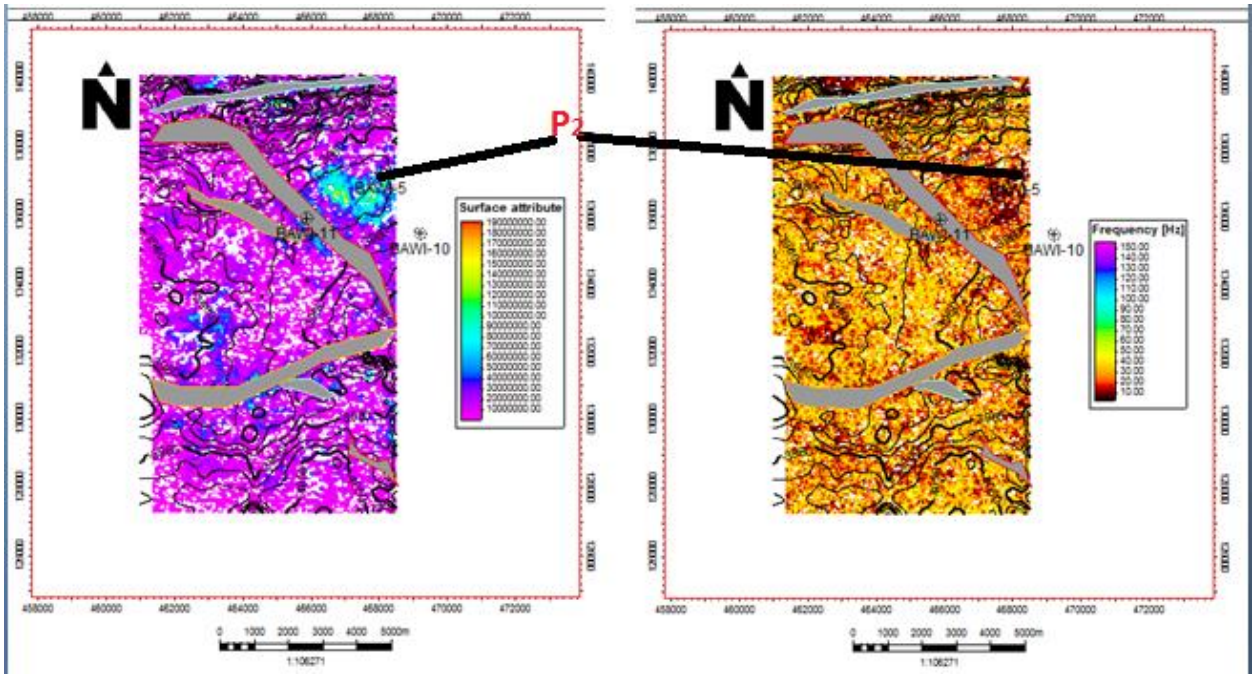

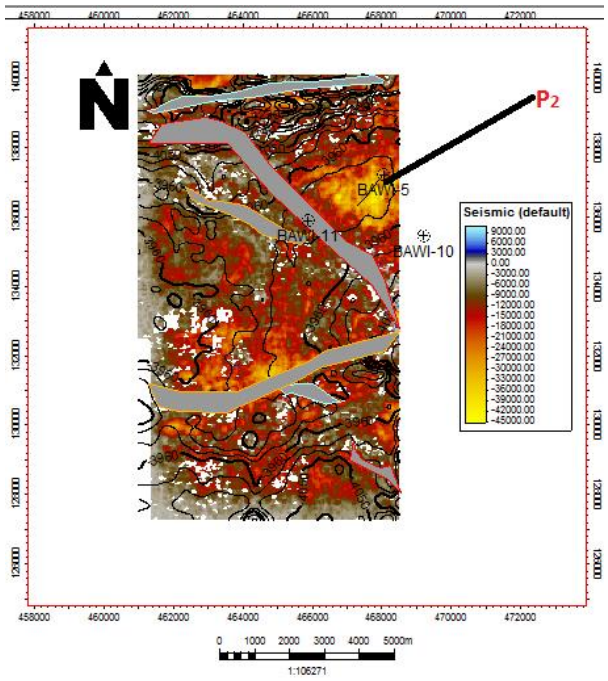

Figure 12. Seismic attribute analysis for horizon 3. Prospective area P2 was identified (a) Average energy (b) Instantaneous bandwidth (c) Relative acoustic impedance

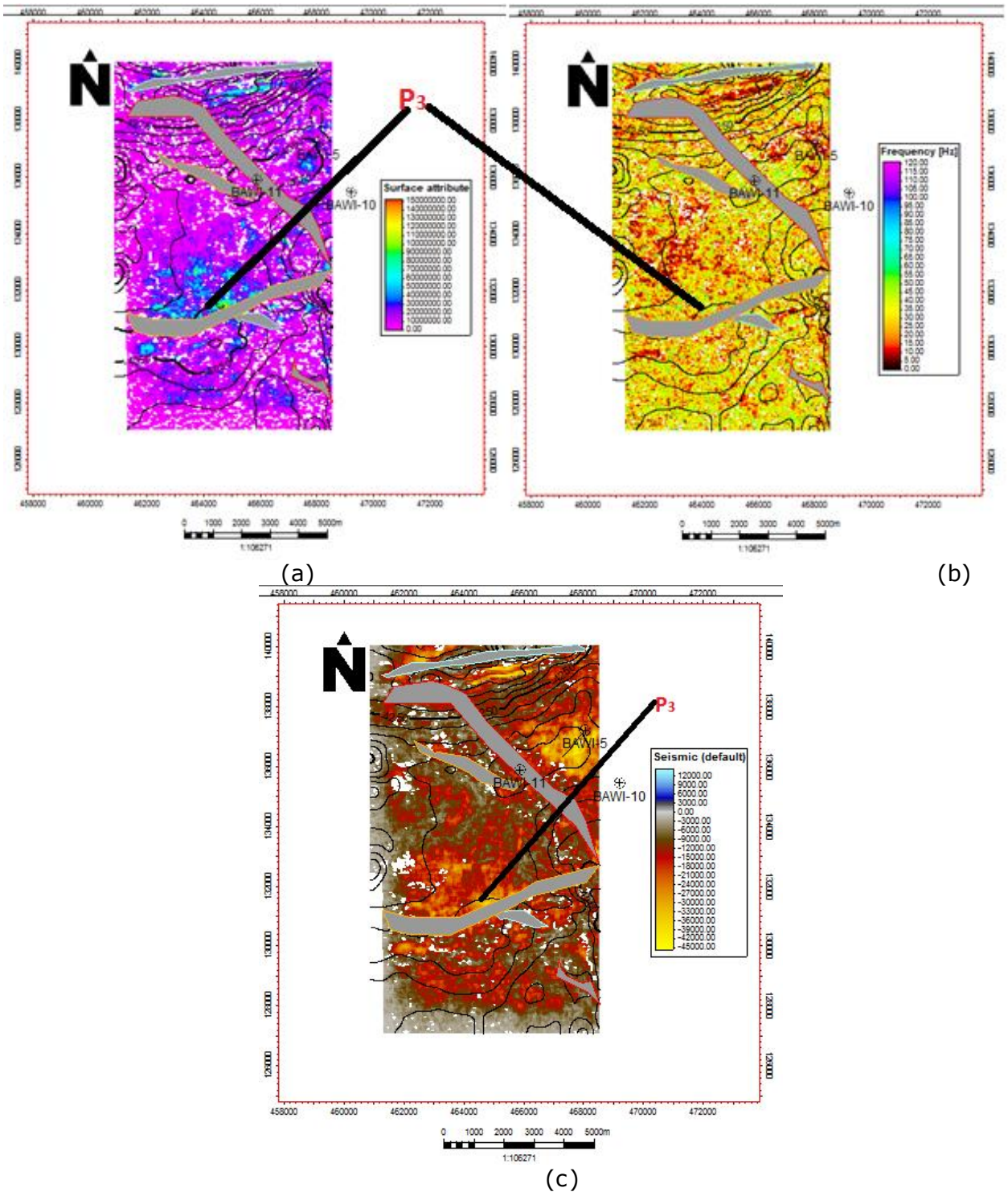

Figure 13. Seismic attribute analysis for horizon 1. Prospective area P3 was identified (a) Average energy (b) Instantaneous bandwidth (c) Relative acoustic impedance

4.3. Stratigraphic channel investigation

Sinuous features were conspicuous at time slice 2600ms in the default seismic section. The observed features were further analyzed using seismic attributes. The time-slice (default seismic) and derived seismic attribute slices (Iso-frequency component and Envelop) are as shown in figure 14 below.

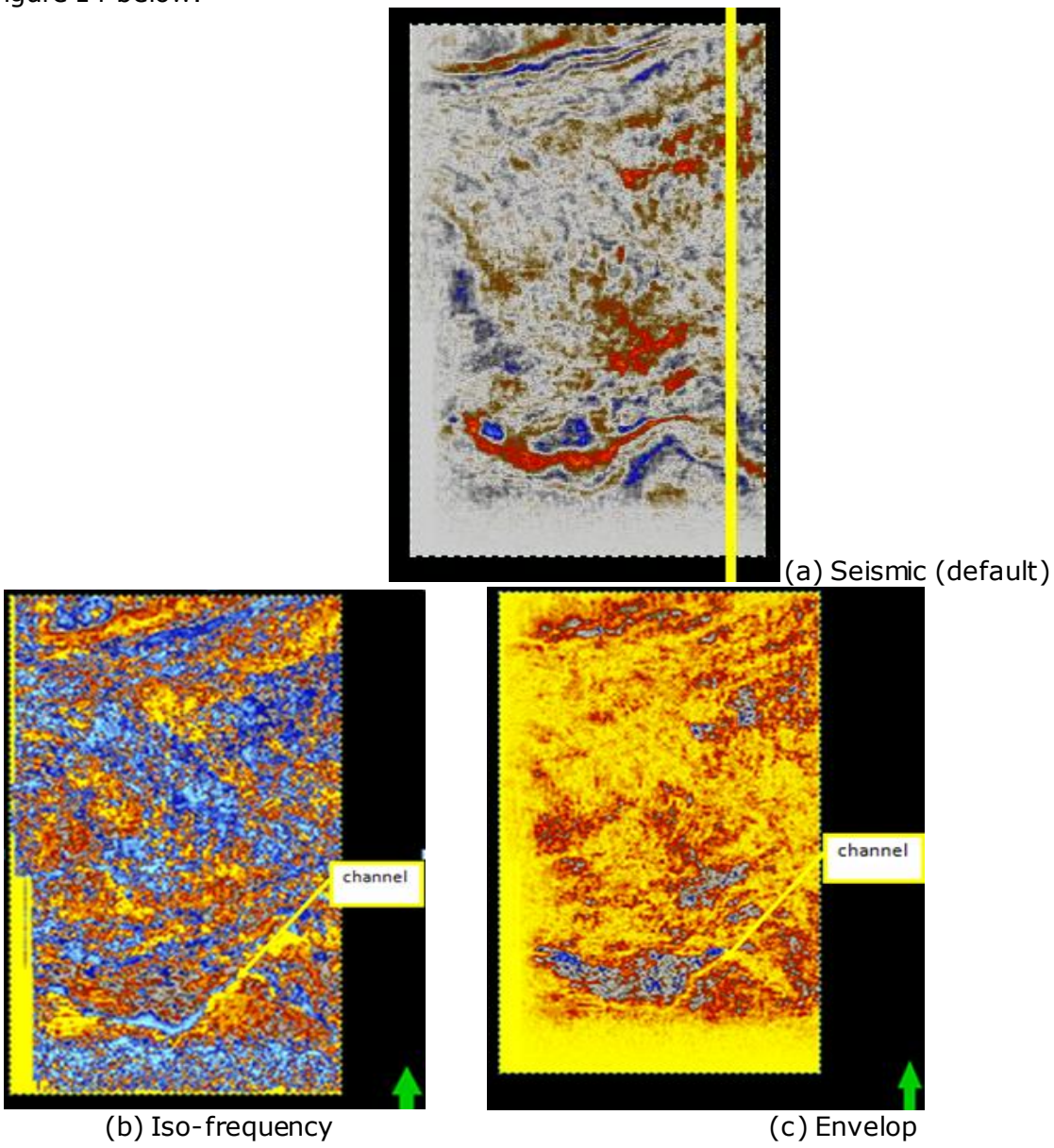

(a) Seismic (default)

(b) Iso-frequency

(c) Envelop

Figure 14. Time slice and derived seismic attribute slices at 2600ms (a) Seismic (default) (b) Iso-frequency (c) Envelop

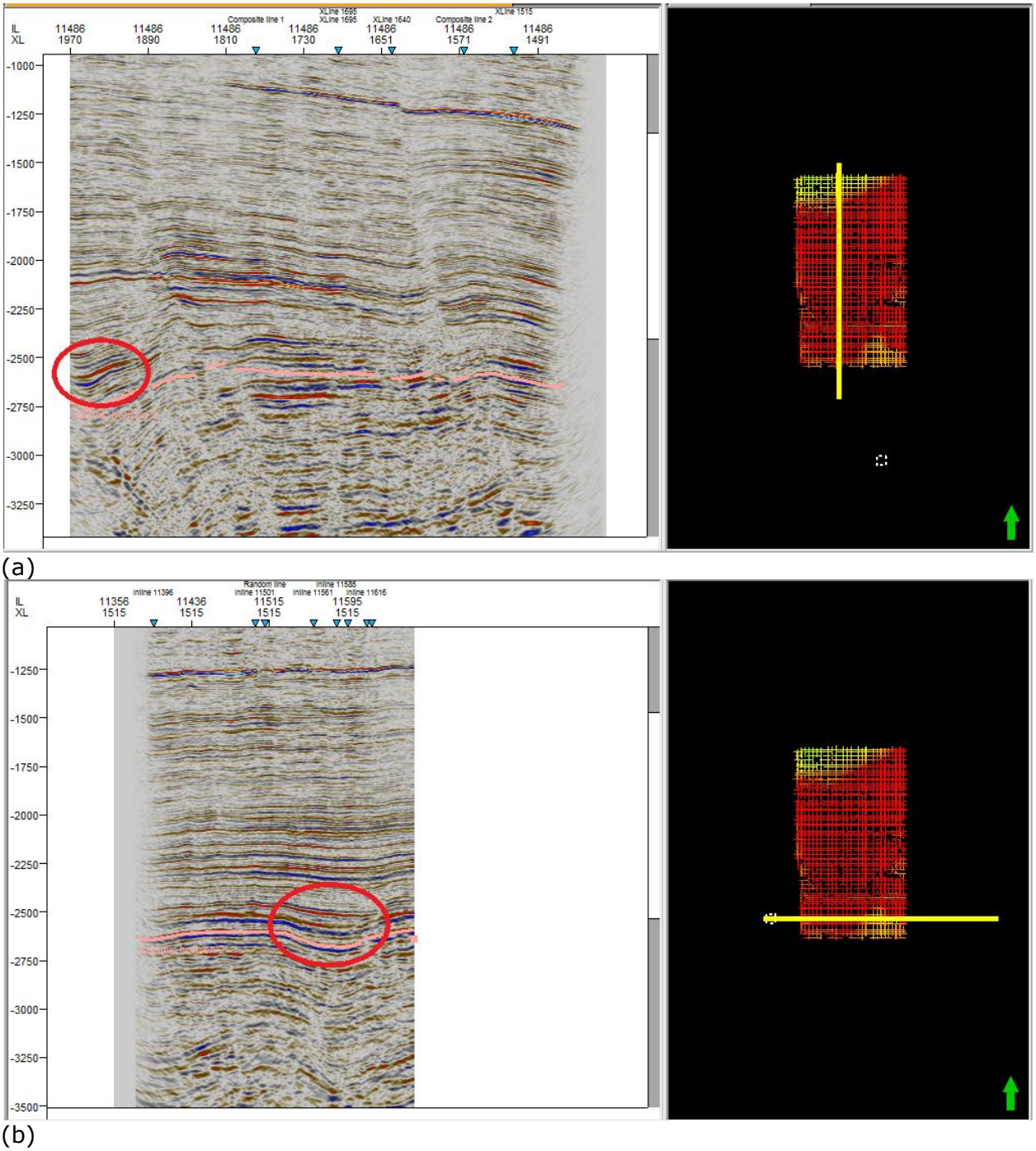

Figure 15. (a) Channel observed around 2600ms on seismic section (Inline 11486) (b) Channel observed around 2600ms on seismic section (Inline 1515). For both the inline and crossline - horizon picked (horizon 2) passed through channel region.

The sinuous features seen were confirmed to be channels from the seismic sections of inline 11486 and cross line 11436 are shown in figure 15 above. However, it was observed that the channel geometry shown by Iso-frequency attribute as seen on generated attribute map differs substantially from that on the generated envelop attribute map (Fig.14). This observation suggests that we could be dealing with stacked and amalgamated channels. To resolve some of the subtle characteristics of the channel, spectral decomposition was employed which better

improved channel imaging and thickness delineation. The concept behind spectral decomposition is that, a reflection from a thin bed has characteristic expression in the frequency domain that is indicative of temporal bed thickness. In other words, higher frequencies image thinner beds better, and lower frequencies image thicker beds. The spectral decomposition workflow focused on processing Discrete Fourier Transform (DFT) at time slice 2600ms, transforming the amplitude/phase data into the frequency domain. Prior to running the spectral decomposition, 3-D seismic data was loaded on the OpenD Tect software and the dominant frequency of the seismic data determined (approximately 35Hz) as shown in figure 16 below.

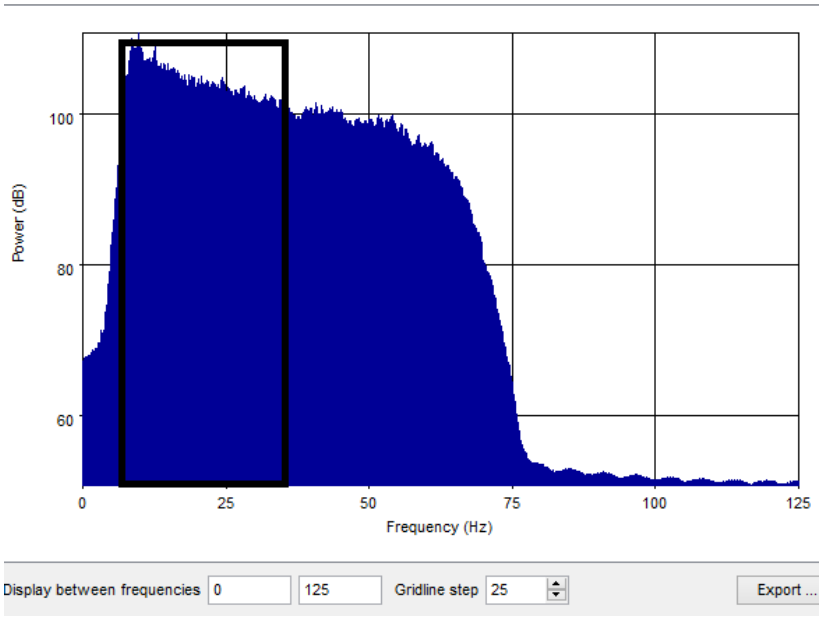

Figure 16. Amplitude spectrum for the Bawi Field. The dominant frequency band is highlighted.

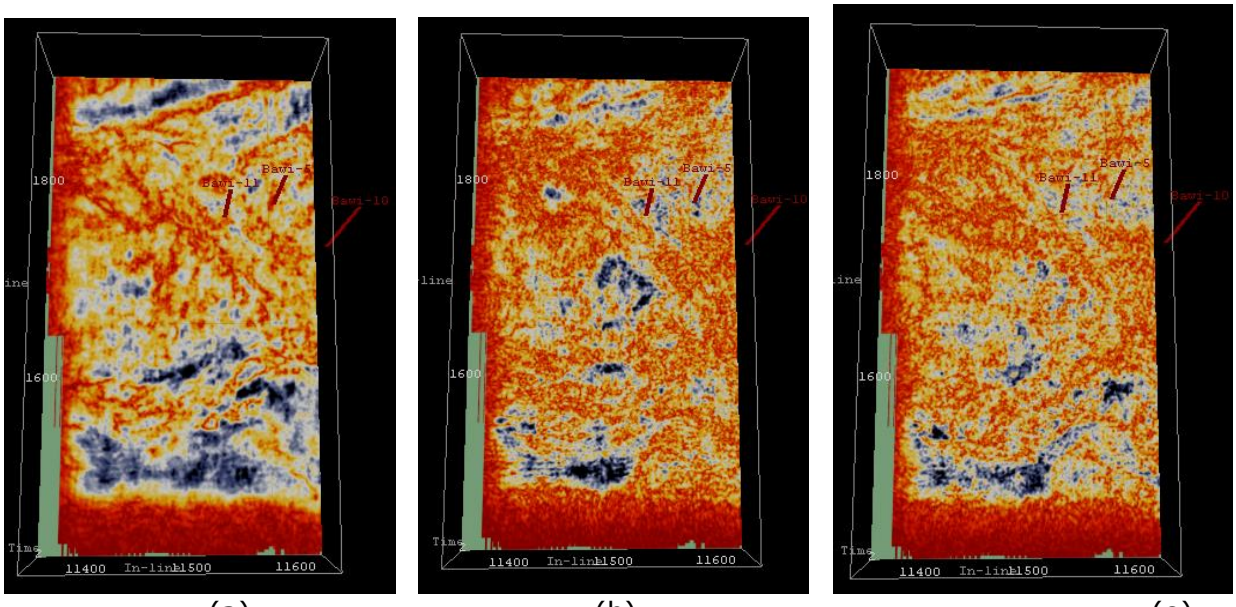

(a) (b) (c)

Figure 17. Spectral decomposition of seismic data at time slice 2600ms showing channel-fill sand (a) 5Hz (the lowest frequency band) (b) 35Hz (the dominant frequency band) (c) 70Hz (the highest frequency band).

Where we have a stratigraphic feature that varies in thickness, if the frequency content is high, thinner stratigraphic features will be "tuned in" and highlighted by higher amplitude. But, if the frequency content is lower, thicker stratigraphic features will stand out [41]. Typically, amplitude maps are dominated by the frequency content of seismic data and will best image stratigraphy with thickness related to the dominant frequency. The channel fill tuning frequency therefore may be either greater or less than the overall seismic dominant frequency (approximately 35Hz).

Based on the above theory, we incorporated the highest frequency band and lowest frequency band in our analysis as shown in figure 17. When we observed the response of the reservoir to different frequencies, it was discovered that 5Hz best imaged the channel feature in the lowest frequency band while 70Hz best imaged the channel in the highest frequency band. We used the Red-Green-Blue (RGB) colour blended map to integrate maps derived from our analysis. Each colour correspond to a specified frequency band i.e. 5Hz (lowest frequency band in Red colour), 35Hz (dominant frequency band in Green colour), and 70Hz (highest frequency band in Blue colour); see fig.17. The colors when additively combined produced the full-spectrum image shown in fig.17. White hue shows that the red (5Hz), green (35Hz) and blue (70Hz) have coincident high amplitude responses in that area (Fig.18). This is the part of the channel with the thickest reservoir.

Comparing the results of the spectral decomposition with the average energy attribute map of horizon 2, the thickest part of the channel can be seen to match a strong amplitude anomaly (Fig.19). Following the correlation observed on relative acoustic impedance attribute map, the lithology was interpreted as high porosity sand (Fig.19). This makes this part of the channel a good drilling location for hydrocarbon.

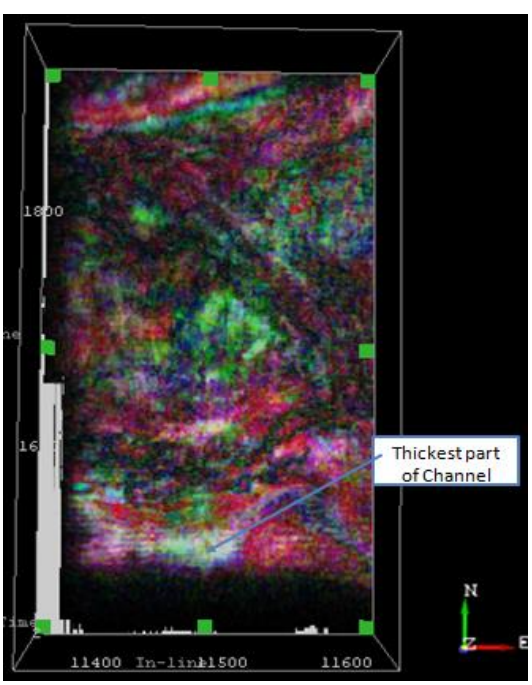

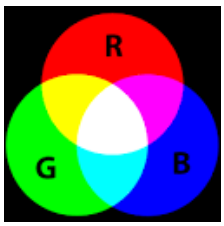

Figure 18. Colour blended frequency map showing the thickest part of the channel-fill sand. Note that the thickest part of the channel appear in white colour (all frequency ranges are present). The three colors used are shown in the color code.

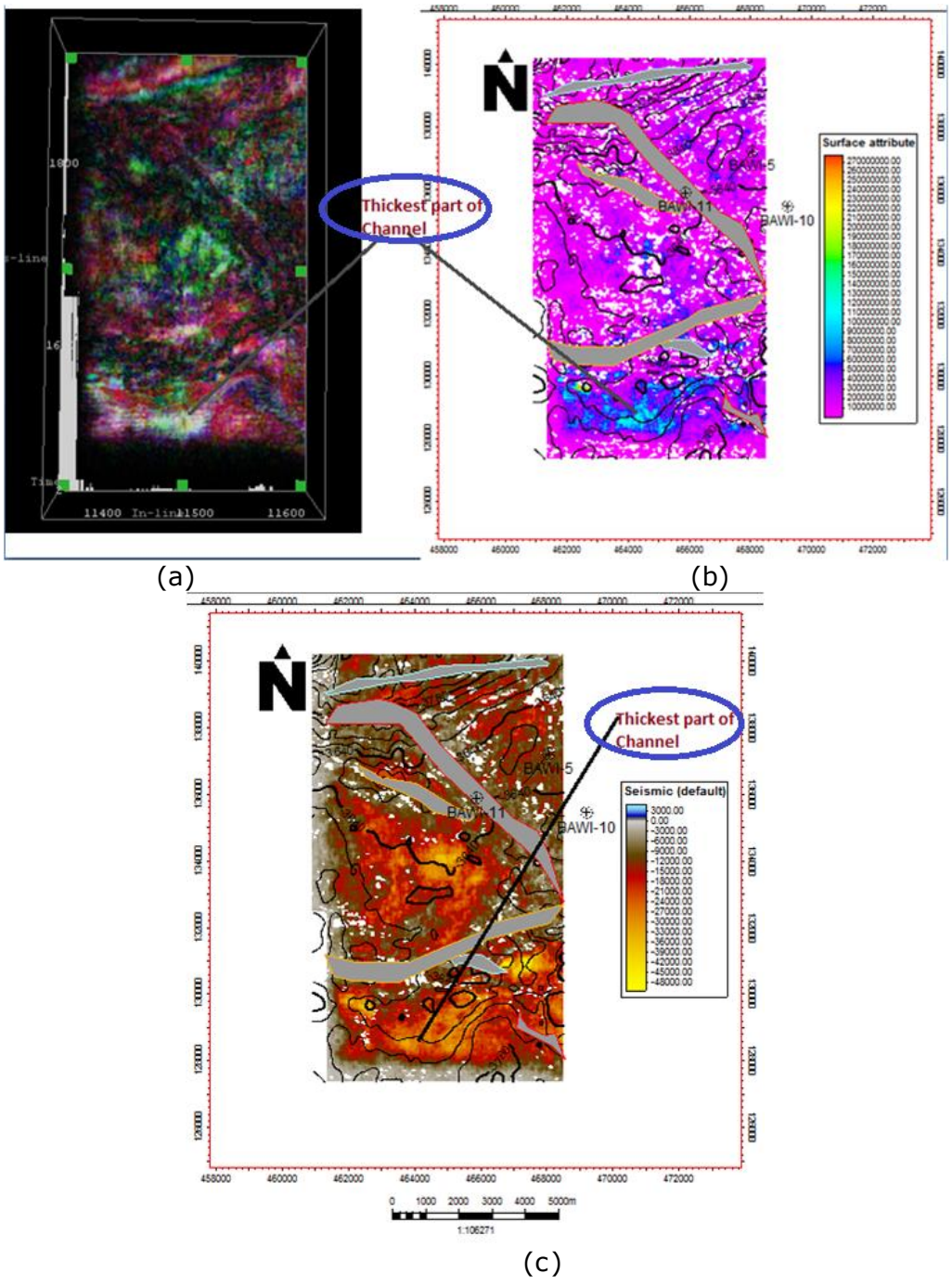

Figure 19. Seismic attribute analysis of channel-fill sand (a) Colour blended frequency map (b) Average energy attribute map of horizon 2 (c) Relative Acoustic Impedance map of horizon 2

4.4. 3-D Model generation of the study

Several models were then generated for the interpreted horizons to gain more information of interpretation interest. Models generated include 3-D structural models of the field, structural model based on seismic observation, and a general fault model of the field. The generated subsurface fault model of the study area is shown in fig.20. Fault models help to better appreciate fault relationships and assist in reservoir studies (Fig.20).The generated fault model revealed cross-fault juxtaposition around the central part of the study area. Cross-fault

juxtaposition is the most important fault seal process [40], as examples of capillary sealing by faulted rocks are fewer and more difficult to predict.

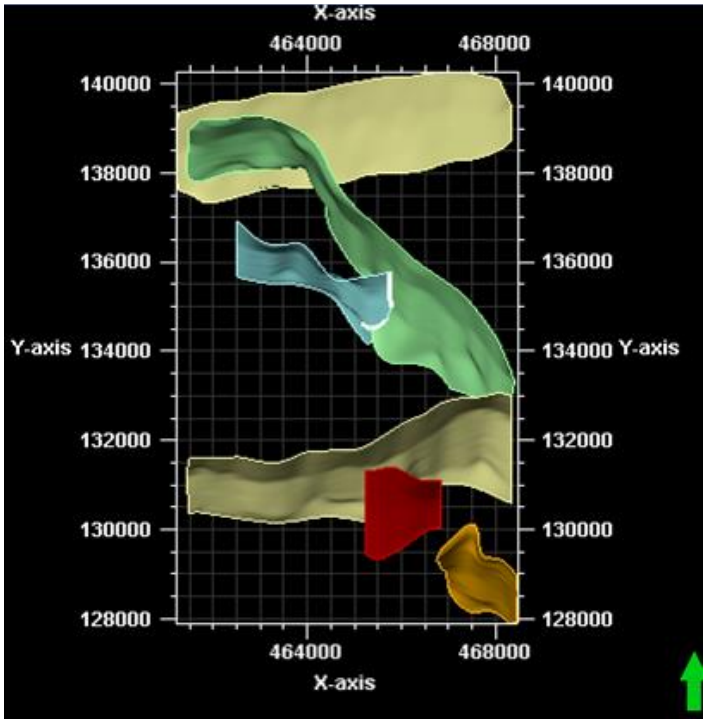

Figure 20. Showing a fault model of the field. Observe that one fault (F6) is cross-juxtaposed against another fault (F1) at the central part of the field. This has implications for the sealing capacity of the faults

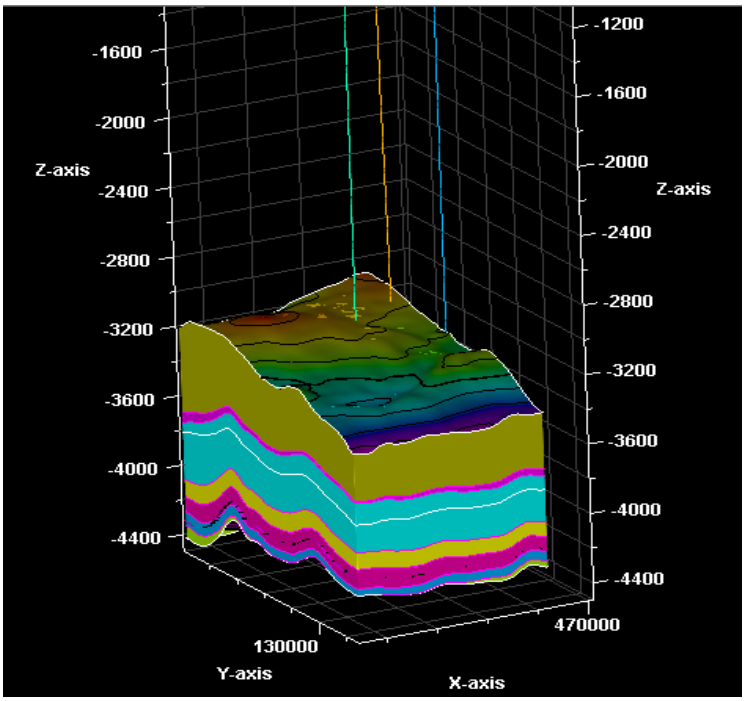

Figure 21. Showing 3D structural model of the Agbada sands (Bawi field). Compressional style deformation is observed. Displacements (upthrow/downthrow) caused by two major structure building faults in the field are better understood.

3-D structural models generated from the study area also revealed an anticline trending towards the southwestern part of the oil field. A smaller anticline trends to the southeastern part of the field. Structural highs are observed to be followed by a compression axis, and then structural lows. This could be a regressive trend towards the south of the Oil field. The models show clear evidence of compression style deformation (Fig. 21). Displacements (up throw/ down throw) caused by the two major structure building faults in the field are therefore better understood from this model.

An amplitude supported structural model generated shows maximum amplitude attribute extracted along the surface of Sand 001 top superimposed to show a better view of the high amplitude feature of the identified prospect P1 Fig.22). High amplitudes were also observed within the vicinity of drilled wells in the area.

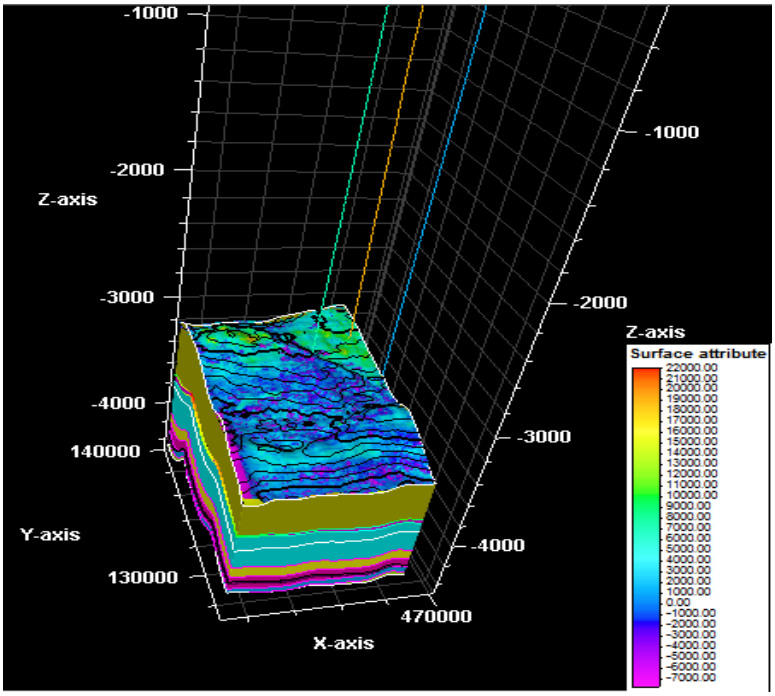

Figure 22. Structural model based on seismic observation in the Bawi field. Maximum amplitude attribute extracted along the surface of Sand 001 top superimposed to show a better view of the amplitude feature of the identified prospect P1. High amplitudes are also observed within the vicinity of drilled wells.

4.5. Petrophysical analysis and volumetric determination

Gross reservoir thickness interval is the interval covering shale and sand within a reservoir. Net thickness of sand is the interval covering only sand within a reservoir. It is called net productive sand. The gross reservoir thickness is determined by knowing interval covering both sand and shale within the reservoir studied using gamma ray log.Net sand thickness is determined by subtracting the interval covering the shale from gross reservoir thickness. Well log data were used in this analysis to generate rock properties using the following formulae: The net-to-gross ratio (NTG) is mathematically expressed as:

$$NTG = (NST/GST) \ldots\ldots\ldots\ldots\ldots\ldots\ldots\ldots\ldots\ldots\ldots\ldots\ldots\ldots\ldots\ldots\ldots\ldots\ldots\ldots\ldots\ldots\ldots\ldots\ldots\ldots\ldots\ldots\ldots\ldots\ldots\ldots\ldots.(2)$$

where NST is the net sand thickness (if shale is present in the formation) while GST is gross sand thickness.

Similarly, the gamma ray log was used to calculate the volume of shale in a porous reservoir. The first step used to determine the volume of shale from a gamma ray log was the calculation of the gamma ray index using the equation:

$$I_{GR} = \frac{GR_{log} - GR_{min}}{GR_{max} - GR_{min}} \ldots\ldots\ldots\ldots\ldots\ldots\ldots\ldots\ldots\ldots\ldots\ldots\ldots\ldots\ldots\ldots\ldots\ldots\ldots\ldots\ldots\ldots\ldots\ldots\ldots..\ldots\ldots\ldots(3)$$

where I_{GR} = gamma ray index, GR_{log} = gamma ray reading of the formation, GR_{min} = minimum gamma ray (clean sand) while GR_{max} = maximum gamma ray (shale). All these values were read off within a particular reservoir. Having obtained the gamma ray index from equation 2 above, volume of shale was then calculated using the Dresser Atlas [42] formula for tertiary consolidated sand given as:

$$V_{sh} = 0.083(2^{3.7xI_{GR}} - 1) \quad \ldots\ldots (4)$$

Another very important rock property is porosity which is defined as the percentage of voids to the total volume of rock. The Formation density log was used to determine formation porosity. The porosity was determined by substituting the bulk density readings obtained from the density log within each reservoir into the equation 4 [42,52].

$$\emptyset_{den} = \frac{\rho_{ma} - \rho_b}{\rho_b - \rho_f} \quad \ldots\ldots (5)$$

where, $\emptyset_{den}$ is the density derived porosity, ρ_{ma} is the matrix density and is given as 2.65 gm/cm^3(for sand/ sandstone), ρ_f is the fluid density which has a value of 1.1gm/cm^3 (fluid density) and ρ_b is the formation bulk density.

Determination of the water saturation for the uninvaded zone was achieved using the Archie's (1942) equation:

$$S_w^2 = \frac{F \times Rw}{Rt} \quad \ldots\ldots (6)$$

$$F = \frac{Ro}{Rw}, \quad S_w^2 = \frac{Ro}{Rt}$$

$$S_w = \sqrt{\frac{Ro}{Rt}} \quad \ldots\ldots (7)$$

where, S_w = water saturation of the uninvaded zone, Ro = resistivity of formation at 100%water saturation, Rt = true formation resistivity, F = formation factor and Rw = formation water resistivity

4.6. Volumetrics (Reserve estimation) of the "Bawi" Field

Integrating the petrophysical parameters calculated, oil/water contacts determined, and value of recovery factor known, volume of hydrocarbon in place was then computed. The petrophysical parameters deduced from well logs are water saturation (Sw), porosity (φ), Net to Gross (NTG) and Volume of Shale (Vsh). The tables below summarizes the average results of these important petrophysical parameters utilized as variables for reserve estimation. The volumetric analysis was limited to Hydrocarbon Pore Volume (HCPV) estimation due to non-availability of value for Formation Volume Factor (FVF). Using a recovery factor of 20%, reserve estimate calculated for reservoir R2 gave 795 million barrels; reservoir R4 has a total of 227 million barrels and reservoir R3 has a total of 177 million barrels. Reservoir R1, which is thought to be predominantly gas because of its very high resistivity, contains very little quantity of hydrocarbon (less than a million cubic feet). The total HCPV estimate is about 1.2 billion barrels.

Table 1. Petrophysical evaluation results of the "Bawi" Field

Reservoir sand	Porosity φ	Net to gross	V shale	Sw	Sh
Sand 001	0.380	0.878	0.168	0.443	0.557
Sand 002	0.220	0.862	0.097	0.283	0.717
Sand 003	0.205	0.603	0.040	0.315	0.685
Sand 004	0.190	0.665	0.187	0.333	0.667

Table 2. Volumetric estimation results of the Bawi Field

Horizon	Contact	HC Area [*10^6 m^3]	Bulk Volume [*10^6 m^3]	Net Volume [*10^6 m^3]	Pore Volume [*10^6 m^3]	HCPV[*10^6 m^3]
1	2915.00	0.00	0	0	0	0
2	3737.21	77.86	5843	5037	1108	795
3	3975.67	52.24	2086	1258	258	177
4	4129.98	51.86	2696	1793	341	227

4.7. Integrated prospect ranking and risk analysis

In the identified prospects, fault closures form the main hydrocarbon trapping mechanism. In terms of trap integrity, trapped hydrocarbon may be compromised if the faults are non-sealing. The risk is lower where cross-fault juxtaposition is established. Similarly, faults that display growth are commonly sealing, but those without growth may also seal if there is sufficient clay smear, or if reservoir sands are juxtaposed against shales [28]. Prospects of the same closure type but with higher attribute anomaly are ranked higher provided there is no significant difference in estimated volume whereas prospects associated with low volumes are considered to have high risk. A Channel is given a high rank, as channel sands form good stratigraphic traps for hydrocarbon entrapment [43]. Table 3 below is an integrated ranking and risk analysis of identified prospects in "Bawi field".

Table 3. Integrated prospect ranking and risk analyses of Bawi Field

Prospect	Horizon	Attribute Anomaly	Associated volume	Closure Type	Risk	Rank	Remarks
P1	1	Evident	Low	Upthrown/ Footwall Fault closure	High	4	
P3	4	Evident	High	Downthrown/ Hanging Wall Fault closure	Low	3	Fault shows considerable growth
P2	3	Evident	High	Downthrown/ Hanging Wall Fault closure	Low	2	Cross fault juxtaposition observed
Stratigraphic Channel Prospect	2	Evident	High		Low	1	Thickest part of channel targeted

5. Conclusion and recommendation

5.1. Conclusion

This study has demonstrated how a methodology that integrates seismic attributes in seismic interpretation technique can help overcome pitfalls in interpretation and make for a more precise prospect identification and prediction. The trapping elements that were distinguished in the study area include anticlinal dip closures, up thrown fault closures and down thrown fault closures. Growth structures (faults) characterize the structural style in the Oil field. Their complexity increases generally towards the lower section of the delta region. Mapped fault trends were observed to be in the NW-SE direction. The environment of deposition based on wire line logs can be described as a fluvial and "fluvio-deltaic" system. Fining and coarsening upward facie successions were clearly defined. The fluvial system deposited the topmost sand body which is the thickest. The main heterogeneities identified correspond to increasing shaliness in the reservoir due to the environment of deposition. It was deduced that reservoir R2 is the most oil prolific while R1 is the least within the study interval. The total hydrocarbon pore volume (HCPV) in the Oil field is 1.2 billion barrels.

5.2. Recommendation

It is recommended that detailed analysis involving sequence stratigraphy and seismic stratigraphy be incorporated into field studies for better understanding of the stratigraphic plays in the area. Sequence stratigraphic analysis would better define the environment of deposition of the stratigraphic successions, while seismic stratigraphy will better reveal stratigraphic traps in the Oil field. From previous studies, overpressure zones are likely where channels exist in an Oil province like the Niger Delta. Predrill pore-pressure prediction should be carried out to support drilling plan for the stratigraphic channel prospect identified in the Oil field.

Acknowledgement

The authors are sincerely grateful to the management of Total E & P Nigeria Limited and the Department of Petroleum Resources (DPR), Nigeria for their various roles in provision of research data and materials for this work.

References

[1] Chopra S, and Marfurt KJ. Seismic attributes for prospect identification and reservoir characterization. Society of Exploration Geophysicists geophysical development series 2007, no. 11.
[2] Chopra S, Pruden D and Alexeev V., 2004. Multi-attribute seismic analysis – tackling non-linearity. First Break, 2004; 22(12): 43-47.
[3] Brown AR Understanding seismic attributes. Geophysics, 2001; 66:47– 48.
[4] Partyka G, Gridley J, and Lopez J. Interpretational applications of spectral decomposition in reservoir characterization; The Leading Edge, 1999; 18:353–360, doi:10.1190/1.1438295.
[5] Burns S, and Street K. Spectral decomposition highlights faults. Hart"s E&P, March 2005, http://www.epmag.com/archives/digitalOilField/2135.htm.
[6] Castagna JP, Sun S, and Siegfried RW. Instantaneous spectral analysis: detection of low-frequency shadows associated with hydrocarbons. The Leading Edge, 2003; 22: 120-127.
[7] Dorn GA. Modern 3-D seismic interpretation. The Leading Edge, 1998; 17(9): 1262–1272
[8] Jones TA and Helwick SJ. Methods of generating 3-D Geologic models incorporating geologic and geophysical constraints, United States Patent, USOO5838634A., Nov, 1998.
[9] Gao D. Volume texture extraction for 3-D seismic visualization and interpretation. Geophysics, 203; 68: 1294-1302.
[10] Gao D. Texture model regression for effective feature discrimination: Application to seismic facies visualization and interpretation. Geophysics, 2004; 69: 958- 967.
[11] Chopra S and Marfurt K. Seismic Attributes – a promising aid for geologic prediction. CSEG RECORDER, Special Edition, 2006: 111-121.
[12] Taner MT, Koehler F, and Sheriff RE. Complex seismic trace analysis. Geophysics, 1979; 44: 1041–1063.
[13] Bahorich M and Farmer S. 3-D seismic discontinuity for faults and stratigraphic features: The coherence cube. The Leading Edge,1995; 14: 1053–1058.
[14] Marfurt KJ and Kirlin RL. 3-D broad band estimates of reflector dip and amplitude. Geophysics, 2000; 65:.304–320.
[15] Sangree JB, and Widmier JM. Interpretation of depositional facies from seismic data: Geophysics, 1979; 44:, 131-160,165–184.
[16] Love PL, and Simaan M. Segmentation of stacked seismic data by the classification of image texture: 54th Annual International Meeting 1984, SEG, session S7.3.
[17] Gao D. Latest developments in seismic texture analysis for subsurface structure, facies, and reservoir characterization: A review. Geophysics, 2011; 76(2): W1–W13.
[18] Love PL. and Simaan M. Segmentation of stacked seismic data by the classification of image texture: 54th Annual International Meeting 1984, Society of Exploration Geophysicists, Session:S7.3.
[19] Vinther R, Mosegaard K, Kierkegaard K, Abatzis I, Andersen C, and If F. Seismic texture classification: A computer-aided approach to stratigraphic analysis. 65th Annual International Meeting 1995, Society of Exploration Geophysicists Expanded Abstracts, 153-155.
[20] Vinther R. Seismic texture classification applied to processed 2-D and 3-D seismic data. 67th Annual International Meeting 1997, Society of Exploration Geophysicists Expanded Abstracts, 721- 724.
[21] Whitehead P, Fairborn J, and Wentland R. Identifying stratigraphic units by seismic patterns, 69th Annual International Meeting 1999, Society of Exploration Geophysicists Expanded Abstracts, 942-945.
[22] West B, May S, Eastwood JE, and Rossen C. Interactive seismic facies classification using textural and neural networks. The Leading Edge, 2002; 21:1042-1049.
[23] Cooke DA and Muryanto T. Reservoir Quantification of B Field, Java Sea via Statistical and Theoretical Methods. Submitted for presentation at the SEG International Exposition and Meeting 1999, Houston, TX USA.
[24] Evamy DDJ, Haremboure P, Kamerling WA, Knaap F, Molloy A, Rowlands MH. Hydrocarbon habitat of the Tertiary Niger Delta. American Association of Petroleum Geologists Bulletin, 1978; 62: 1–39.

[25] Avbovbo AA.1978. Tertiary lithostratigraphy of Niger Delta. American Association of Petroleum Geologists Bulletin, 1978; 62: 295-300.
[26] Merki PI. Structural Geology of Cenozoic Niger Delta. First African Regional Geological Conference Proceedings Ibadan University Press 1971, Ibadan, Nigeria;p.251 –266.
[27] Ejedawe JE. Patterns of incidence of oil reserves in Niger Delta Basin: American Association of Petroleum Geologists, 1981; 65: 1574-1585.
[28] Doust H and Omatsola E.1990. Niger Delta, in, Edwards JD, and Santogrossi PA, eds., Divergent/passive Margin Basins, AAPG Memoir 48: Tulsa, American Association of Petroleum Geologists, 1990; 239-248.
[29] Ekweozor CM, Okogun JI, Ekong DEU and Maxwell JR. Preliminary organic geochemical studies of samples from the Niger Delta, Nigeria: Part 1, Analysis of crude oils for triterpanes: Chemical Geology, 1979; 27: 11-28.
[30] Whiteman AJ. Nigeria: Its Petroleum Geology: Resources and Potential. 1&2. Graham and Trottan: London 1982, UK;p.394.
[31] Beka FT and Ot, MN. The distal Offshore Niger Delta: frontier prospects of a mature petroleum province, in, Oti, M.N., and Postma, G., eds., Geology of Deltas: Rotterdam 1995, A.A. Balkema; p. 237- 241.
[32] Bilotti F and Shaw JH, 2005.Deepwater Niger Delta Fold and Thrust Belt modeled as a Critical – Taper Wedge: The Influence of Elevated Basal Fluid Pressure on Structural Styles. AAPG Bulletin, 2005; 89(11): 1475-1491.
[33] Owoyemi AO and Willis BJ. Depositional Patterns Across Syndepositional Normal Faults, Niger Delta, Nigeria; Journal of Sedimentary Research, 2006; 76: 346-363.
[34] Weber KJ. 1987.Hydrocarbon distribution patterns in Nigerian growth fault structures controlled by structural style and stratigraphy; Journal of Petroleum Science and Engineering., 1987; 1: 91-104.
[35] Tuttle MLW, Charpentier RR and Brownfield ME. The Niger Delta Basin Petroleum System: Niger Delta Province, Nigeria, Cameroon, and Equatorial Guinea, Africa; Open- File Report 99-50-H, United States Geological Survey World Energy Report 1999, 44pp.
[36] Bouvier JD, Kaars-Sijpesteijn CH, Kluesner DF and Onyejekwe CC. 1989. Three- Dimensional Seismic Interpretation and Fault Sealing Investigations". Nun River Field, Nigeria. AAPG Bulletin., 1989; 73(11): 1397 – 1414.
[37] Etu-Efeotor JO. Fundamentals of Petroleum Geology. Africana-Fep Publishers, Onitsha 1997, Nigeria, pp: 111-123.
[38] Stacher P. Present understanding of the Niger Delta hydrocarbon habitat. [In:] M.N. Oti & G. Postma (Eds): Geology of Deltas. Balkema, Rotterdam 1995, 257–268.
[39] Xiao H and Suppe J.1992. Origin of Rollover. American Association of Petroleum Geologists Bulletin, 1992; 76: 509-229.
[40] Jolley SJ, Fisher QJ, and Ainsworth RB. 2010. Reservoir compartmentalization: an introduction. Geological Society, London, Special Publications 2010; 347: 1- 8.
[41] Laughlin K, Garossino P, and Partyka G. Spectral Decomposition for Seismic Stratigraphic Patterns. Online Journal for E&P Geoscientists, 2003.
[42] Dresser Atlas.,1979. Log interpretation chartsDresser Industries Inc, Houston, Texas, p.107.
[43] Caldwell J, Chowdhurry A, van Bemmel, Engelmark F, Sonneland L and Neidell NS. Exploring for stratigraphic traps. Schlumberger Oilfield Review 1997; pp.49-61.
[44] Eichkitz CG, Schreilechner MG, and Groot PD, and Amtmann J. 2014.Mapping directional variations in seismic character using gray-level co-occurrence matrix-based attributes. Interpretation, 2014; 3(1): T13–T23.
[45] Xia S, Li Q, Wang X, Sun C, Wang Y, Hu A, Li X and Zheng Q.,2010. Application of 3-D fine seismic interpretation technique in Dawangzhuang Area, Bohai Bay Basin, Northeast China. Arabian Journal of Geosciences, 2010; 1-11, DOI 10.1007/s12517-013-1225-6.
[46] Abdul Kalid NZ, Hamzah U, and Samsudin AR. Seismic Attributes And Their Application In Faults Interpretation of Kupe Field, Taranaki Basin, New Zealand. EDJE, 2016; 21(6): 2169-2184.
[47] Kluesner JW and Brothers DS., 2016. Seismic attribute detection of faults and fluid pathways within an active strike-slip shear zone: New insights from high-resolution 3D P-Cable™ seismic data along the Hosgri Fault, offshore California. Interpretation,2016; 4(1): SB131-SB148.
[48] Castanie L, Bosquet F and Levy B. Advances in seismic interpretation using new volume visualization techniques. First Break, 2005; 23: 69-72.

[49] Sullivan MD, Jensen GN, Goulding FJ, Jennette DC, and Stern D. 2000.Architectural analysis of deep- water outcrops: Implications for exploration and production of the Diana sub-basin, Western Gulf of Mexico. In: P. Weimer et al.(eds) Deep-Water Reservoirs of the World. GSC-SEPM Foundation 20th Annual Bob F. Perkins Research Conference, pp. 1010-1031.
[50] Malleswar MR and Marfurt KJ. Seismic texture analysis for reservoir prediction and characterization. The Leading Edge, 2010; Special Edition; p.1116-1121.
[51] Pereira LA. Seismic attributes in hydrocarbon reservoirs characterization. Universidade de Aveiro 2009, p. 1- 183.
[52] Kendall CG. Template for "conceptual models" used to interpret depositional systems USC Sequence Stratigraphy. http://strata.geol.sc.edu/index.html, University of South Carolina.
[53] Hamed EM and Kurt JM. Structural interpretation of the Middle Frio Formation using 3-D seismic and well logs: An example from the Texas Gulf Coast of the United States. The Leading Edge, 2008; 27 (7):840-854.
[54] Khan HM, Woobaidullah ASM and Quamruzzaman C. 2013. Seismic Interpretation of 2-D Data over Kailashtila Gas Field, NE Bangladesh. International Journal of Emerging Technology and Advanced Engineering, 2013; 3(11): 23-34.
[55] Wiener RW, Helwig JA, and Rongpei J. Seismic Interpretation and Structural Analysis of the Rifted Thrust Belt, Jianghan Basin, China. The Leading Edge, 1997; 60(8): 1177 – 1183.
[56] Opara AI. Prospectivity Evaluation of "Usso" Field, Onshore Niger Delta Basin, Using 3-D Seismic and Well Log Data. Pet Coal, 2010; 52 (4).307-315.
[57] Mejias M. A Geological Interpretation of 3-D Seismic Data of a Salt Structure and Subsalt Horizons in the Mississippi Canyon, Subdivision of the Gulf of Mexico; University of New Orleans Theses and Dissertations 2006, 438p.
[58] Reyment RA. Aspects of the geology of Nigeria, university of Ibadan press 1965, Nigeria; 145p.
[59] Short KC and Stäuble AJ. Outline of geology of Niger Delta: American Association of Petroleum Geologists Bulletin., 1965; 51: 761-779.
[60] Doust H. The Niger Delta hydrocarbon potential, a major Tertiary Niger Province; Proceedings of KNGMG Symposium, Coastal Lowstands, Geology and Geotechnology, The Hague, Kluiver Acad. Publ. 1989, Dordrecht., p.22-25.
[61] Weber KJ and Daukoru EM. Petroleum geology of the Niger Delta: Proceedings of the Ninth World Petroleum Congress 1975, volume 2, Geology: London, Applied Science Publishers, Ltd;p.210-221.
[62] Castillo F. Seismic Attributes for 3-D Fracture Interpretation; Geo-Canada 2010 – Working with the Earth 2010, pp.1-4.
[63] Posamentier HW, and Allen GP. Siliciclastic sequence stratigraphy - concepts and applications: SEPM Concepts in Sedimentology and Paleontology, 2000; 7: 210.
[64 Serra, O. Sedimentary environments from wireline logs: Houston, Schlumberger 1985, 211 p.
[65] van Rensbergen P, and Morley CK. 3-D Seismic study of a shale expulsion syncline at the base of the Champion delta, offshore Brunei and its implications for the early structural evolution of large delta systems. Journal of Marine and Petroleum Geology, 2000; 17: 861–872.

To whom correspondence should be addressed: Dr. A. I. Opara, Department of Geosciences, Federal University of Technology, PMB 1526, Owerri, Imo State, Nigeria, oparazanda2001@yahoo.com

Petroleum and Coal

Article **Open Access**

Effect of Composite Membrane for Desulfurization Diesel in Pervaporation Process: Fabrication of Polydimethylsiloxane and Using Tetra-Ethyl-Ortho-Silicate as Cross-Linking Agent

Mohsen Farsi[1], Bizhan Honarvar[2], Amir Heydarinasab[1], Mehdi Arjmand[1]

[1] *Department of Chemical Engineering, Science and Research Branch, Islamic Azad University, Tehran, Iran*
[2] *Department of Chemical Engineering, Marvdasht Branch, Islamic Azad University, Marvdasht ,Iran*

Received April 4, 2018; Accepted June 25, 2018

Abstract

The multi composite membranes were fabricated through a blend of polydimethylsiloxane (PDMS), polyethyleneglycol (PEG), polyethersulfonic (PES) and cross-linked polyacrylnitrile (PAN) with tetra-ethyl-ortho-silicate (TEOS) to decrease the sulfur content in diesel fuel. The structural morphology of the composite membranes was characterized by scanning electron microscope (SEM). Experimental results indicated that 20% of the crosslinking agent amount was more preferable. The composite membranes were employed in pervaporation separation of thiophene mixtures in diesel. The pervaporation performances of the membranes under various crosslinking agent amounts, feed sulfur content, feed temperature, permeate pressure and feed flow rate on the separation efficiency and total flux was investigated experimentally. The increase of sulfur content in feed resulted in a higher total flux but a lower sulfur enrichment factor. By increasing the feed temperature, the total flux increased while sulfur enrichment factor decreased. Low permeate pressure and high feed flow rate were beneficial to improve total flux and sulfur enrichment factor. The prepared membrane displayed an optimum desulfurization performance with permeation flux of 9.98 kg/(m^2h) and the selectivity of 2.56 towards thiophene in model diesel.

Keywords: *Composite Membrane; Sulfur Content Removal; Cross-linking Agent; PDMS; Pervaporation.*

1. Introduction

The presence of sulfur compounds in liquid hydrocarbons and its products creates various problems such as corrosion, poisoning factories catalyst receiving gas and liquid products, environmental problems, reduced heat value and reduced the price. Environmental concerns about fuel quality are one of the most important topics in oil refineries. Reducing sulfur below the 30 ppm for diesel and gasoline in many developed countries is according to the Environmental Protection Agency (EPA) rules that have been adopted in 2006 [1]. However, new methods for removing sulfur deeper may be necessary for the near future (sulfur content less than 10 ppm) [1-2]. (Common sulfur compounds can be founded in diesel and gasoline fuels contain mercaptans (RSH), sulfides (R2S), disulfides (RSSR), thiophene and its derivatives [1,3]). Thiophene compounds attributed itself more than 80% of sulfur impurities among other compounds of sulfur in gasoline and diesel [4].

The used membrane materials for removing sulfur are mostly including hydrophobic membranes such as polyurethane, polyurea/polyurethane, polyamide, natural rubber, polystyrene-butadiene and Polydimethylsiloxane. Hydrophilic properties of the membranes clearly increase the selectivity to the sulfur compounds which usually are more polar than hydrocarbons. The most common methods for making membranes with high selectivity and flux include cross-linking, blending, filling and copolymerization. Lin et al. studied the solubility of gasoline blending in polyethylene glycol [5]. They concluded that sulfur recovery rate by increasing the

amount of cross-linking agent and the cross-linking time increases. Lin *et al.* [6] used polyethylene glycol and polyurethane polymers for fluidized bed catalytic cracking unit gasoline desulfurization. Wu *et al.* [7] improved the stability of the interface between the active layer of Polydimethylsiloxane and base layer of polyethersulfone by the aminosilane and amino propyl trimethoxysilane. Their results showed that with an increase of cross-linking agent penetration flux is uniformly reduced. The effect of tetraethyl ortho silicate on the increasing selectivity in the Polydimethylsiloxane membrane has been studied by Xu *et al.* [8]. In another study, manufacturing of *Polydimethylsiloxane* and polyamide composite membrane in separation heptane from thiophene was studied [9]. Rajesha et al. [10] synthesized oxide-zeolite composite membranes for benzophenone-3 removal from water. They concluded that membrane performances were significantly improved after the addition of ZnO-zeolite in the cellulose acetate solution. Ghasemian *et al.* [11] used polyvinylidene fluoride (PVDF) and nano-porous silica particle. Their results show that PVDF/SiO_2 nano-composite membranes exhibited enhanced antifouling property compared to neat PVDF membrane [11]. Xu *et al.* [12] manufactured a gradient cost-efficient composite membrane. They concluded that when the additive amount of OMWCNTs was 1wt%, the composite membranes presented an excellent flux.

Esfahan oil refining company operates in Iran. The company offers liquefied petroleum gas, solvents, unleaded gasoline, kerosene, gasoil, light and heavy fuel oil, light and heavy lubecut, and sulfur. In this study, the total sulfur in diesel product of Esfahan oil refinery was reduced from 6380 ppm to 1700 ppm by using composite membranes of PDMS, PDMS + PEG, PDMS + PES and PDMS + PAN, as well as the cross-linking technique by TEOS in a module of flat sheet membranes.

2. Materials and Methods

2.1. Materials

In order to manufacture the composite membranes, the following laboratory material was used: Tetraethyl ortho-silicate (TEOS) with an average molecular weight of approximately 208 g/mol (Merck, Germany); oligomers *of* polydimethylsiloxane (PDMS) with an average molecular weight of approximately 40000 g / mol and viscosity 5000 MPa.sec (Aldrich, USA); polyethylene glycol (PEG) with an average molecular weight of approximately 4000 g / mol (BASF, Germany); polyethersulfone (PES) with an average molecular weight of about 58000 g / mol (flakes, BASF, Germany); polyacrylonitrile (PAN) with an average molecular weight of about 45000 g / mol (Merck, Germany); polyvinylpyrrolidone (PVP) k90 as a filler with an average molecular weight of approximately 360000 g/mol (Merck, Germany); dimethyl acetamide (DMac) as a solvent (Merck, Germany); dibutyltindilaurate (Fluka, Switzerland); ammonia (Merck, Germany); the asymmetric nano filter based membrane of polyester (PlasmachemGmbH, Germany); n-heptane (Romil, UK); SPAN 80 (Merck , Germany); distilled water.

2.2. Composite membrane preparation

A certain amount of Span 80 as a surfactant, silicone propulsion (tetraethyl-ortho-silicate) with various weight percentages with oligomers of polydimethylsiloxane and polyethylene glycol in n-heptane (solvent) at room temperature for making homogeneously solution mixed together. Ammonia in water (anti-solvent) with half the molar concentration of the solution is solved to build a solution with pH = 9. However, a certain amount of this solution is added into a homogeneous solution under difficult conditions of stirring. The mass ratio between solvent to polymer is about 3.5, and the mass ratio between the polymers used in this study is equal. The use of ammonia as catalyst cause agglomerate silica has been done at the interface of water/homogeneous solution. After mixing for thirty minutes, a small amount of dibutyltindilaurate*as* bubble removing is added to this mixture. After removing bubbles in homogeneous solution, the solution is laying the base layer, and the film device is used. The solution to building a base film by deposition technique made by immersion; so, a 15% the mass of solution polyethersulfone and 3% the mass of the Polyvinylpyrrolidoneas filler in the dimethylacetamide solvent is made. This solution is built on the base of nano-filter asymmetric

polyester, and after using the film immersed quickly in distilled water to remove residual dimethylacetamide. For other types of base layer, a 15% solution of polyethersulfone, 10% polyethylene glycol and 3% Polyvinylpyrrolidonein dimethylacetamide are used. Membranes initially are placed in the open air for 24 hours and then to complete the cross-linking process and evaporate the remaining solvent at the time of cross-linking (0.5-2.5 h) determined and at the time of cross-linking time (65-85℃) placed inside an electric furnace. Finally, the membranes are washed with distilled water and placed between sheets of filter paper and dried. All of the membranes before used in the membrane module and the membrane performance be measured should be placed in a free of dust and dry environment.

The other homogeneous solutions parallel with the above active membrane (PDMS + PEG) can be made only with this difference that the polyethylene glycol in the production of the homogeneous solution is removed from the environment and replaced with polyethersulfone and polyacrylicnitrile in each stage. In the entire process of construction of active membrane (derived from homogeneous solution), construction of basement membrane is the same way.

3. Membrane characterization

3.1. Scanning electronic microscopy spectroscopy

In order to investigate the membrane structure, SEM characterization of the prepared membraneshas been carried out. For this purpose, the membrane samples were fractured in liquid nitrogenand then coated with Au–Pd under vacuum conditions. The cross section and surface membranemorphology was taken by SEM (JSM-6301F scanning electron microscope). Membrane Characterization. In this study, a device with a model of VEGA3SBH\\TESCAN is used for the morphology of the cross-sectional structure of composite membranes. First, membrane samples are be broken in liquid nitrogen and then coated with a thin layer of gold in a vacuum.

3.2. Fourier Transform Infrared Spectra (FTIR-ATR)

Information about the presence of specific functional groups of the prepared membrane surfaceswas obtained by a Nicolet IR 560 spectrometer with horizontal attenuated total reflectance(ATR) accessory equipped with a ZnSe crystal. For evaluation, a total of 32 scans were performed at a resolution of 4 cm-1 at a temperature of 25±1°C. Meanwhile, Fouriertransform infrared (FTIR) spectra were recorded within the range of 4,000–400 cm^{-1}.

4. Pervaporation experiments

The schematic pervaporation apparatus is shown in Fig. 1. The feed solution was continuously circulated from a feed tank through the tube side of the membrane module using a variable speed feed pump. Vacuum on the permeate side was monitored by a digital vacuum gauge. The permeated vapor was collected by turns in liquid nitrogen traps. About 2 h after starting the PV process, a mass transfer equilibrium was established, and PV performance reached stable. At steady state, the weight of permeate collected in the cold trap was measured to obtain the total flux, J:

The total flux can be obtained from the following equation [13]:

$$J = \frac{m}{A \times t};\left[g.m^{-2}.h^{-1}\right] \quad (1)$$

and partial flux, J_i:

$$J_i = w_i^p J \quad (2)$$

where M is the total mass permeated; A the effective membrane area; t the experiment time interval, and w_i^p the weight fraction of component i in the permeate samples.

The total sulfur contents of the feed and permeated samples were analyzed by gas chromatography (GC-2014, SHIMADZU, Japan, equipped with FID). The sulfur enrichment factor, E, is defined as

$E=w^p/w^f$ (3)

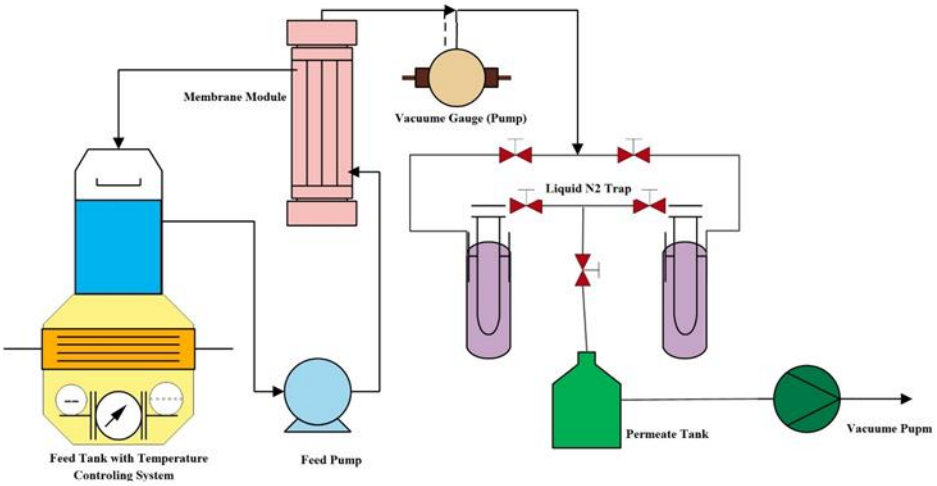

Fig. 1. Schematic diagram of experimental apparatus.

Feed is containing about three liters of diesel with the total sulfur content of 6380 ppm. After using any appropriate membrane, the remaining diesel is poured inside the feed tank and to experiment with new membrane will be replaced with a new diesel. The pump has been used that leads diesel with different flow rates and pressures set (5-9 times) into the membrane module. Membrane modules are manufactured from stainless steel and membranes used with an active area of 2100 cm. Membranes used to achieve steady state to be kept wet approximately one hour before the start of each test in the input feed to the modulus. For each test, approximately three hours were taken, and operating temperature range is between 30-50°C.

5. Results and discussion

5.1. SEM Photographs of PDMS–TEOS composite membrane

As demonstrated in the SEM photographs, there is a clear boundary between the top layer and the support layer. Meanwhile, the cross-sectional structure of the composite membrane consisted of an ultrathin skin layer and a porous finger-like structure. The surface morphology of the composite membrane was shown in Fig. 3 and Fig. 4.

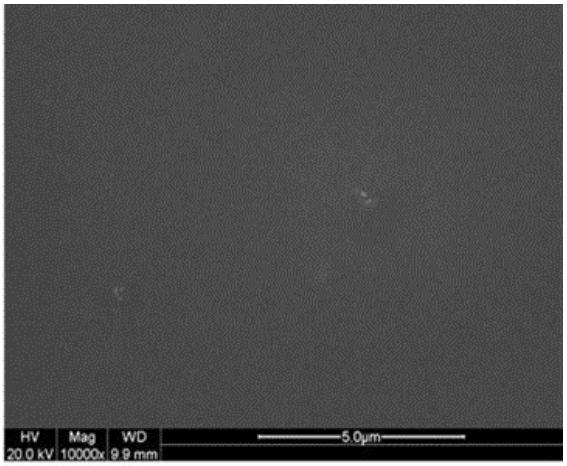

Fig. 2. The surface morphology of the PDMS composite membrane

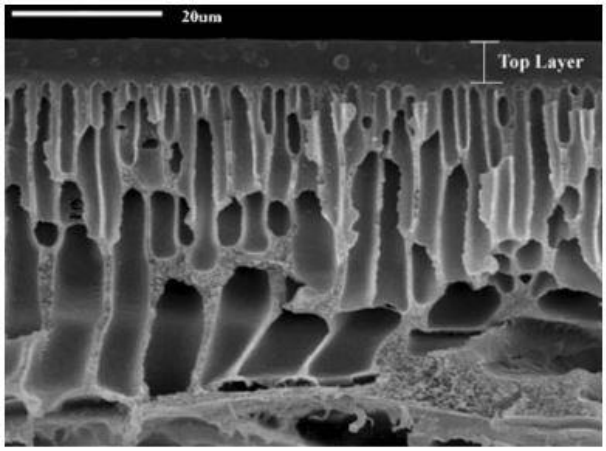

Fig. 3. The cross section morphology of the PDMS composite membrane

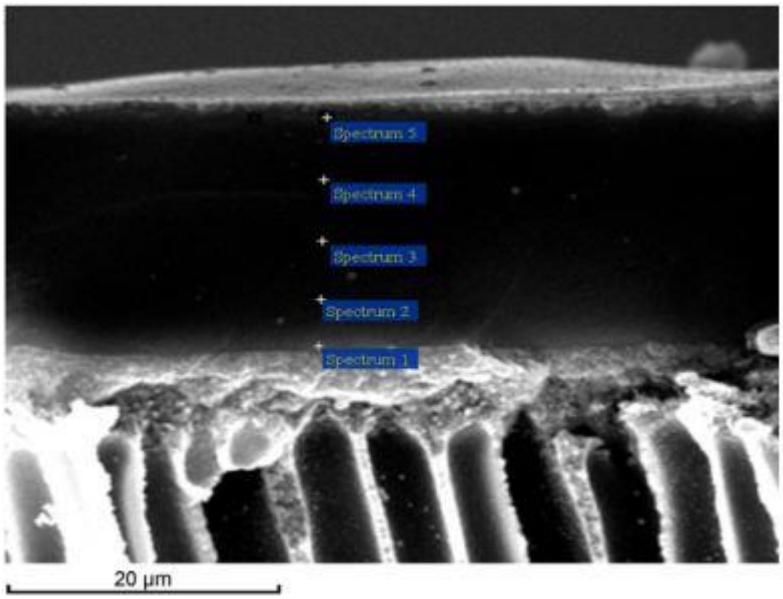

Fig. 4. SEM images of the cross-section of composite PDMS membrane

From these figures, the originally porous surface of the main substrate was covered by a flat, featureless layer, and the top PDMS layer, functioning as the basis of selectivity, had a nonporous and tight structure. The surface of the composite is dense, and there is no pinhole or crack, which is important for the practical application.

5.2. FTIR Spectra of PDMS composite membrane

The attenuated total reflection Fourier transform infrared spectroscopy is a commonly used method to characterize the chemical structure of the surface. The ATR technique enables the identification of specific molecules and groups located within 100 nm from the surface layer. In order to obtain accurate information about the structural changes of PDMS composite membranes resulting from cross-linking modification, FTIR spectra of the surface of PDMS composite membranes were recorded in Fig. 5 using the ATR technique.

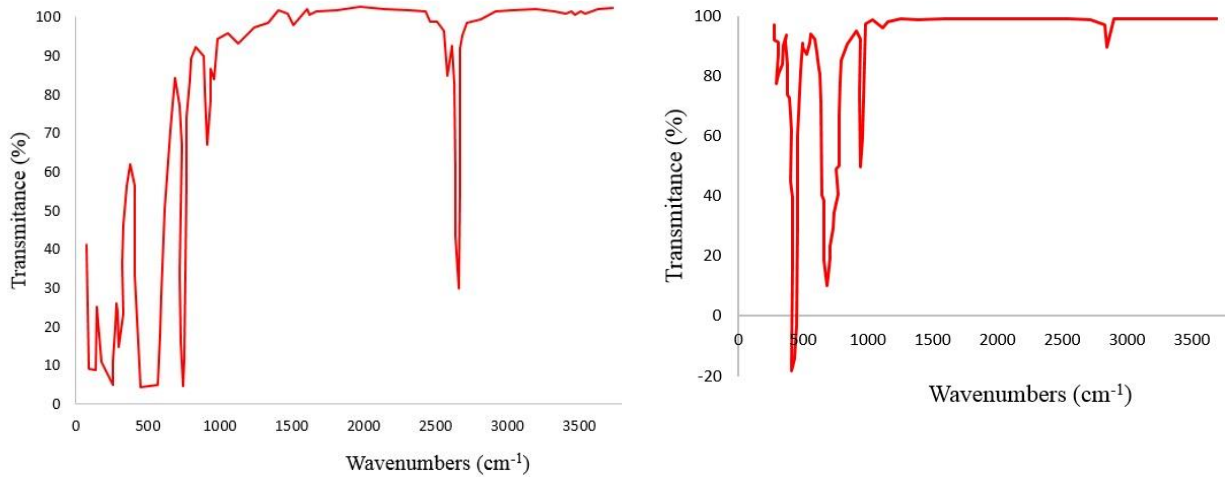

(a) (b)

Fig. 5. FTIR spectra of PDMS composite membrane. (a) Before cross-linking modification, (b) after crosslinking modification

5.3. The effect of cross-linking agent amount on membrane performance

In order to improve the selectivity and limiting the swelling behavior of the active PDMS layer, the effect of crosslinking agent amount on membrane performance was investigated. From Fig. 6, the sulfur enrichment factor increased by increasing the amount of crosslinking agent as envisage, while the total flux decreased. When the crosslinking agent was added to the PDMS solution, the chemical connection occurred between macromolecules and reticular spatial structure formed, which was desirable for swelling resistance of membranes in diesel. And then the mobility of macromolecules and chain segments weakened with the inter chain free volume reduced, which estimated for the decline of permeation flux. However, because of thiophene species having a stronger affiliation to the membrane, the permeation flux of the thiophene species decreased more slowly than that of hydrocarbon species. Therefore, the sulfur enrichment factor increased with the addition of the crosslinking agent.

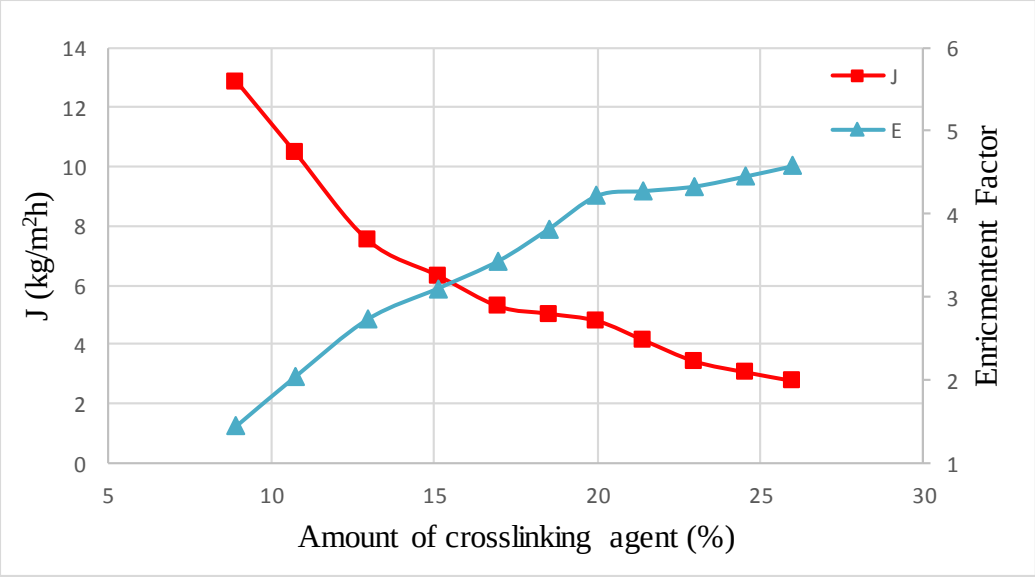

Fig. 6. Effect of crosslinking agent amount on the pervaporation performance of PDMS composite membrane

Meanwhile, excessive addition of crosslinking agent solution brought a higher viscosity solution, which was hard to be coated on the support layer uniformly. So the amount of crosslinking agent at 20% should be more practical due to the trade-off between permeation flux and sulfur enrichment factor.

5.4. Feed temperature

Feed temperature is an important factor in membrane separation performance for desulfurization. As shown in Fig. 7, when the temperature increased, the total flux increased, whereas the sulfur enrichment factor decreased. The increase of the feed temperature cause speed up the mobility of the polymer chains and prepared larger available free volume within the membrane for diffusion. In addition, higher temperature resulted in higher vapor pressure difference which would enhance the transport driving force.

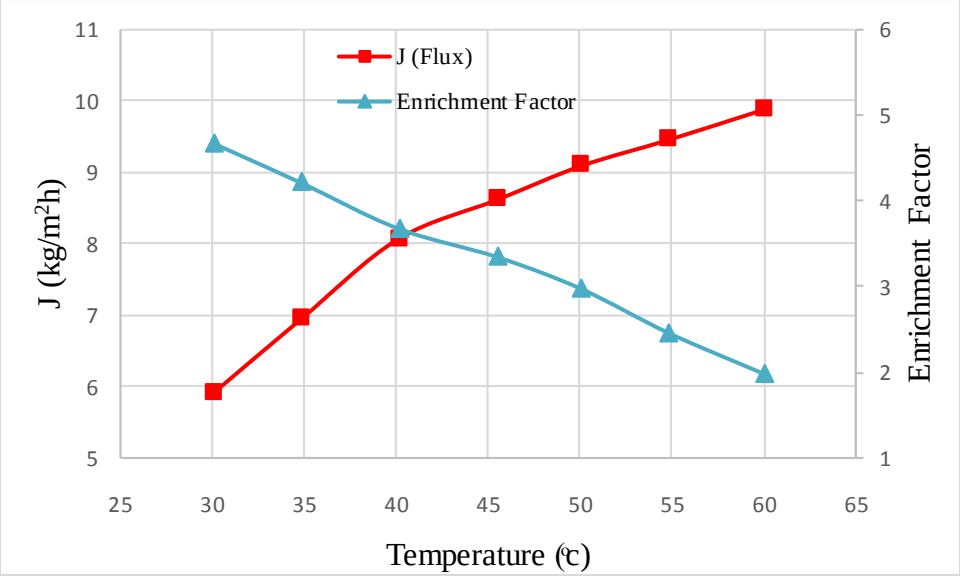

Fig. 7. Effect of operating temperature on the pervaporation performance of PDMS composite membrane

5.5. Permeate pressure

A vapor pressure difference through the membrane is the crucial driving force for pervaporation process. Fig. 8 shows the effect of permeate pressure on the membrane performance for desulfurization. As the permeate pressure increased, the total flux decreased significantly because there was a reduction of driving force for transport of components. In contrast, the sulfur enrichment factor decreased gently. The above results showed that relatively high vacuum (low permeate pressure) was useful to improve both total flux and sulfur enrichment factor.

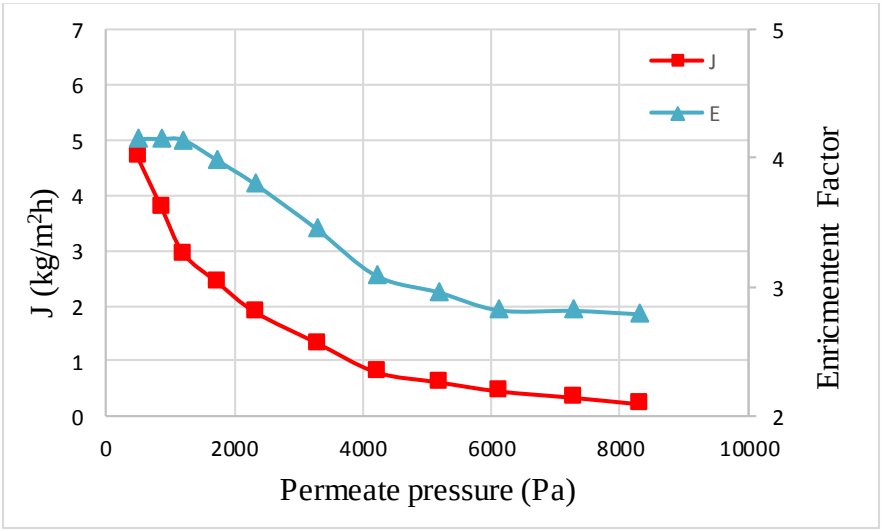

Fig. 8. Effect of operating pressure on the pervaporation performance of PDMS composite membrane

5.6. Feed flow rate

The effect of feed flow rate on pervaporation performance for desulfurization is representd in Fig. 9. Total flux and sulfur enrichment factor both increased with increasing the feed flow rate. The increase of feed flow rate was favorable to the reduction of concentration polarization

and thickness of liquid boundary layer. Meanwhile, a reduction of concentration polarization meant that thiophene concentration near the membrane surface was close to that in bulk, which could enhance sorption and swelling of thiophene in the membrane. Consequently, both total flux and sulfur enrichment factor increases.

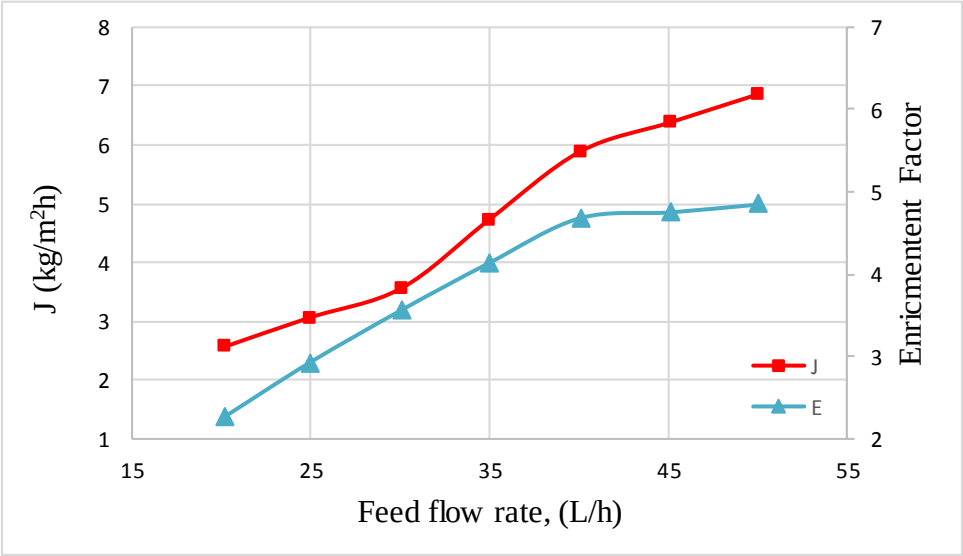

Fig. 9. Effect of feed flow rate on the pervaporation performance of PDMS composite membrane

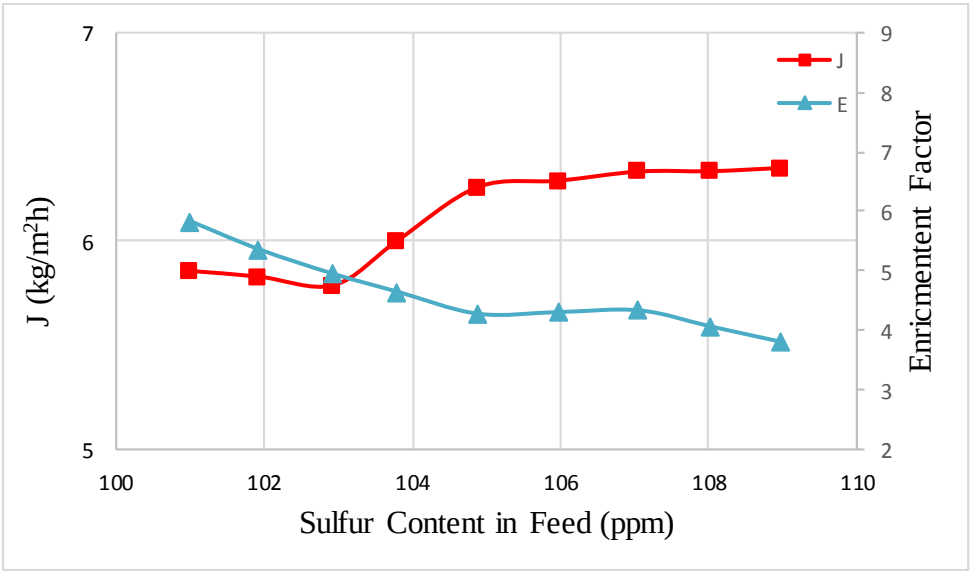

Fig. 10. Effect of sulfur content in feed flow on the pervaporation performance of PDMS composite membrane

5.7. Sulfur content in feed

Fig. 10 illustrates the effect of sulfur content on pervaporation performance for desulfurization. A higher feed sulfur content resulted in a higher total flux but a lower sulfur enrichment factor. while sulfur content increases, the thiophene molecules dissolve more and more in the polymer chains of the membrane, leading to the extensive swelling of the membrane. Consequently, the thiophene components permeated through the membrane easily, and total flux increases. The increasing swelling of the membrane would weaken difference of sorption and diffusion characteristics of the individual component. Therefore, the sulfur enrichment factor decreases.

6. Conclusions

Cross-linked PDMS composite membranes were utilized for removal of sulfur impurities from diesel by pervaporation process. Experimental results showed that the total flux increases with the increase of feed temperature and sulfur content, while in this situation the sulfur enrichment factor decreases. A relatively low permeate pressure was desirable for an optimal total flux and sulfur enrichment factor. On the other hand, both the total flux and sulfur enrichment factor increase s little with increasing the feed flow rate. Our study indicated that the cross-linked PDMS composite membranes had a good sulfur removal efficiency and were potential candidates to be used for practical and industrial desulfurization.

7. Acknowledgement

The authors gratefully acknowledge the scientific institutes and companies that they sincerely helped to this research. Among them can be mentioned the following: Esfahan Oil Refining Company, Iran Polymer and Petrochemical Institute (IPPI), Chemistry & Chemical Engineering Research Center of Iran (CCERCI), and Razi University.

References

[1] Song Ch, Ma X. New design approaches to ultra-clean diesel fuels by deep desulfurization and deep dearomatization. Appl Cat B. Env., 2003; 41(1): 207-238.

[2] Kaufmann TG, Kaldor A, Stuntz GF, Kerby MC, Ansell LL. Catalysis science and technology for cleaner transportation fuels. Catal Today, 2000; 62(1): 77-90.

[3] R Qi, Ch Zhao, Li J, Wang Y, Zhu S. Removal of thiophenes from n-octane/thiophene mixtures by pervaporation. J Membr Sci., 2005; 269(1): 94-100.

[4] Lin L, Wang G, Qu H, Yang J, Wang Y, Shi D, Kong Y. Pervaporation performance of cross-linked polyethylene glycol membranes for deep desulfurization of FCC gasoline. J Membr Sci, 2006; 280(1): 651-658.

[5] Lin L, Kong Y, Zhang Y. Sorption and transport behavior of gasoline components in polyethylene glycol membranes. J Membr Sci, 325(1): 438-445.

[6] Lin L, Kong Y, Xie K, Lu F, Liu R, Guo L, Shao Sh, Yanga J, Shi D, Zhang Y. Polyethylene glycol/polyurethane blend membranes for gasoline desulphurization by pervaporation technique. Sep Purif Technol, 2007; 61(3): 293-300.

[7] Wu H, Zhang X, Xu D, Li B, Jiang Zh. Enhancing the interfacial stability and solvent-resistant property of PDMS/PES composite membrane by introducing a bifunctional aminosilane. J. Membr. Sci, 2009; 337(1): 61-69.

[8] Xu R, Liu G, Dong X, Jin W. Pervaporation separation of n-octane/thiophene mixtures using polydimethylsiloxane/ceramic composite membranes. Desalination, 2010; 258(1): 106-111.

[9] Lin L, Zhang Y, Li H. Pervaporation and sorption behavior of zeolite-filled polyethylene glycol hybrid membranes for the removal of thiophene species. J Colloid Interface Sci., 2010; 350(1): 355-360.

[10] Rajesha BJ, Vishaka VH, Balakrishna GR, Padaki M, Nazri NAM. Effective composite membranes of cellulose acetate for removal of benzophenone-3. J Water Proc Eng. 2017 in press; doi:10.1016/j.jwpe.2017.06.003.

[11] Ghasemian S, Sahari MA, Barzegar M, Gavlighi HA. Omega-3 PUFA concentration by a novel PVDF nano-composite membrane filled with nano-porous silica particles. Food Chemistry, 2017; 230: 454-462.

[12] Xu Z, Li X, Teng K, Zhou B, Ma M, Shan M, Jiao K, Qian X, Fan J. High flux and rejection of hierarchical composite membranes based on carbon nanotube network and ultrathin electrospun nanofibrous layer for dye removal. J. Membr. Sci., 2017; 535: 94-102. d

[13] Zellers ET. Three-dimensional solubility parameters and chemical protective clothing permeation. I. Modeling the solubility of organic solvents in Viton® gloves. J Appl Polym. Sci., 1993; 50(3): 513-530.

To whom correspondence should be addressed: Dr. Amir Heydarinasab, Department of chemical engineering, Science and Research Branch, Islamic Azad University, Tehran, Iran, amir.heydarinasab@hotmail.com

Petroleum and Coal

Article **Open Access**

EVALUATION OF THE LEVEL OF BIODEGRADATION OF BONNY LIGHT, UGHELLI BLEND AND OKORDIA-IKARAMA CRUDE OILS FROM NIGER DELTA NIGERIA

M. C. Onojake, and S. O. Adesi*

Petroleum Chemistry Research Group, Department of Pure and Industrial Chemistry, University of Port Harcourt, P.M.B 5323, Choba, Port Harcourt, Nigeria

Received April 23, 2018; Accepted June 27, 2018

Abstract

Representative samples of Bonny light, Ughelli Blend and Okordia-Ikarama Crude oils collected from some oil fields in the Niger Delta were quantitatively analysed using oil Gas chromatography flame ionization detector to determine the extent at which biodegradation has impacted on the crude oil quality. The chromatograms of crude oil samples show loss of lower hydrocarbon range from nC_1 to nC_9 either due to evaporative loss during fractionation or biodegradation. The paraffinicity and aromaticity of the crude oil sample were determined using various ratios. The percentage loss of the paraffin showed Bonny light 75.40%, Ughelli Blend 78.36%, and Okordia-Ikarama 46.24%; while the percentage loss of aromatics showed Bonny light 66.02%, Ughelli Blend 78.62%, and Okordia-Ikarama 55.38%. Pristane/nC17 and Phytane/nC18 ratios were used to complement the results of the percentage loss of paraffinic and aromatic content. The results showed that Ughelli Blend crude oil was heavily biodegraded with extensive loss of the parrafins and the aromatics. While the Bonny light and Okordia-Ikarama crude oils were slightly biodegraded. Biodegradation of hydrocarbons is undesirable because it can lead to lowering of the API gravity, impact crude oil quality and consequently affect the commercial value.

Keywords: *Biodegradation; crude oils; Gas chromatography; Paraffinicity; aromaticity.*

1. Introduction

The general growth in the world's population and industrialization has constantly made the demand for energy on the increase worldwide. These have led to increasing oil exploration activities to obtain crude oil, which is the principal source of energy, to meet societal energy demand. Crude oil is an intricate combination of thousands of C_1 to C_{60+} aliphatic, alicyclic and aromatic hydrocarbons. One of the problems facing the hydrocarbon production is biodegradation. Biodegradation of crude oil and the subsequent deterioration in the value of crude oil is mostly encountered in reservoirs cooler than nearly 80°C [1-2]. When crude degrade progressively in the reservoir saturated hydrocarbons are removed first, making the substantial polar and asphaltene fractions to be concentrated in the remaining oil. This tends to reduce the commercial value of the crude oil by lowering the value of API gravity and increasing viscosity, sulphur, and metals content. The commercial significance of the crude oil largely decreases with biodegradation due to a reduction in the volume of the refinery distillates and an unprecedented rise in vacuum residue yields. Additionally, biodegradation increases the amount of naphthenic acid formed, leading to an upsurge of the acidity of the crude oil, which is customarily computed as Total Acid Number (TAN). TAN can cause a reduction in the value of the crude oil and perhaps add to production and handling problems encountered in the downstream sector, which includes emulsion formation and corrosion [3]. Other compounds present in crude oils are the asphaltic (nitrogen, sulphur, and oxygen compounds), some organometallic compounds of sulphur and vanadium, and dissolved gases, such as hydrogen sulphide [4].

Hydrocarbons from the productive basin in the Niger Delta occurs at different prospects are from separate depth [5]. Whole oil gas chromatography permit for the appraisal of an array of hydrocarbons in crude oil or source rock extract which enables a geochemist to infer the level of biodegradation, thermal maturity by applying some peak ratios to establish the extent of thermal cracking for oil generation, and source characteristics such as a marine, lacustrine, fluvial, or terrestrial depositional environment. Furthermore, comparing peaks and some peak ratios from the chromatograms obtained from the whole gas chromatographic analysis, reservoir continuity can be ascertained.

The aim of this research is to establish the level of biodegradation of crude oils from some fields in the Niger Delta and ascertain its influence on crude oil quality and the commercial value.

2. Materials and methods

2.1. Regional geology of study area

The province geology is that of the Niger Delta Basin where crude oil samples were collected. It is located in the Gulf of Guinea and lengthens through the Niger Delta Region [6]. The geologic formations in the area are The Benin Agbada and Akata Formations [7]. The region ranks one of the largest hydrocarbon provinces in the world with approximately 34.5 billion barrels of recoverable oil and 93.8 trillion cubic feet of recoverable gas. The depobelts of the area is one of the principal regressive deltas in the world with an expanse of 300,000 km^2, a sediment capacity of 500,000 km^3 and a sediment thickness of more than 10 km in the basin depocenter [8]. The petroleum system of the study area is known as the Tertiary Niger Delta or Akata –Agbada Petroleum System (Figure 1).

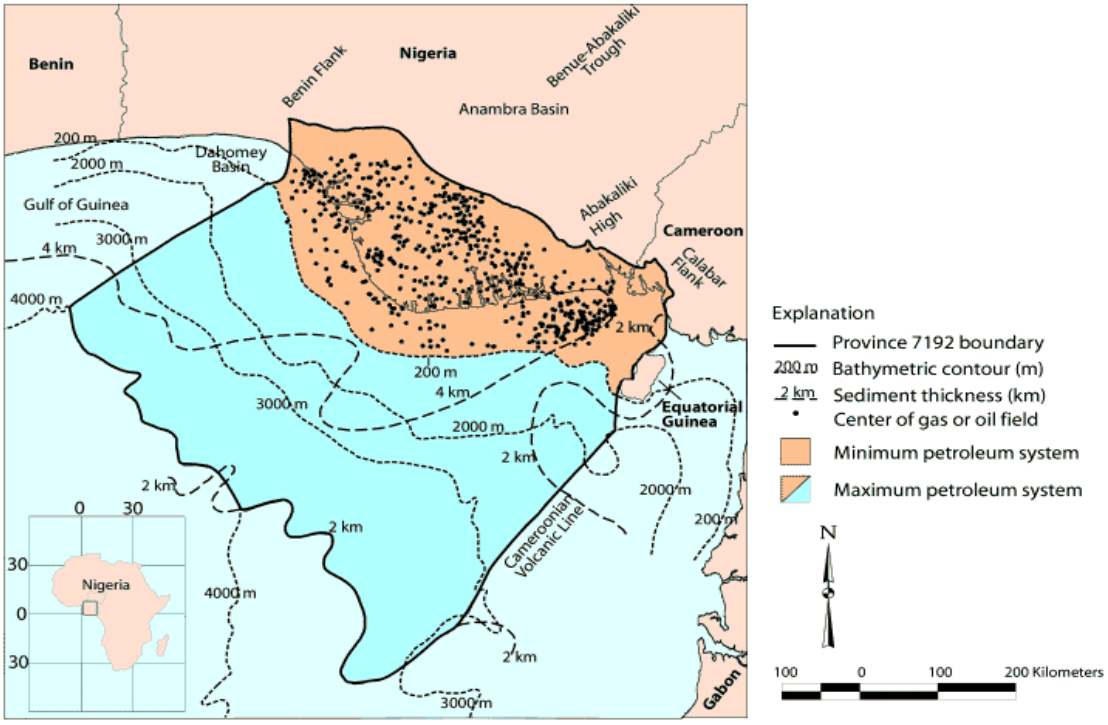

Figure 1. Map of the Niger Delta showing Province outline. *(Source: U. S. Geological Survey Open File Report)*

The onshore part of the study area (Niger Delta Region) is synonymous with the geology of southern Nigeria and south-western Cameroon (Figure 1). The northern margin is the Benin border, an east-northeast trending hinge line south of the West Africa basement massif. The north-eastern margin is demarcated by outcrops of the Cretaceous on the Abakaliki high and

further east-south-east by the Calabar margin; a hinge line is bordering the adjacent Precambrian. The offshore margin of the region is demarcated by the Cameroon volcanic line to the east, the eastern border of the Dahomey basin to the west, and the two kilometer sediment thickness contour or the 4000-meter bathymetric contour in zones where sediment depth is more than two kilometres to the south [9-10].

2.2. Sample collection

Representative samples of crude oils were obtained from producing fields in the Niger Delta region. Glass vials used for sampling were rinsed with trioxonitrate (v) acid, distilled water and properly dried. The crude oil samples were then placed in a cooler containing ice block at a temperature of about 4°C preceding laboratory analyses.

2.3. Whole - Oil Gas chromatographic analysis

The Gas chromatographic analysis of crude oil samples was done using Gas Chromatograph, fitted with Flame Ionization Detector model Shimadzu 14B series with a film thickness of 30m × 0.25 mm and 0.25 µm fused silica capillary columns, coated with methyl silicone. One micro litre (1 µL) of crude oil sample was introduced in splitless mode with a syringe through a rubber septum into the column. The flame ionization detector (FID) and injector temperatures were kept at 250 and 280°C, respectively. The oven temperature was automated from 60 to 280°C at 4°C /min with an original hold time of 1 min and final hold time of 15 mins. The carrier gas used was Helium at a linear velocity of 2 mL/min. The data were collected from retention time: 0-71 minutes [11].

3. Results and discussion

Representatives crude oil samples of Bonny light (BL), Ughelli blend (UB) and Okordia Ikarama (OI) crude oils were analysed using Gas Chromatographic Flame ionization detection (GC-FID) to ascertain the different degrees of degradation.

Detailed examination of the chromatograms of the samples shows a complete depletion of the n-alkanes from C_1 to C_9 (Figure 2) which are an indication of severe degradation of the samples. The n-alkanes, cycloalkanes, 2-methylhexanes through 1, 1- dimethylcyclopentanes are somewhat reduced as shown in Table 1. The ratio of parafinicity for all crude oils was also calculated as shown in Table 2. The ratio of n- Heptane/(Cyclohexane + Mcyclohexanes ranges from 0.0004, 0.0092 and 0.729 for BL, UB, and IO crude samples, n-heptane/Mcyclohexane ranges from 0.0008, 0.0664 and 1.2011, (n-hexane+n-heptane)/(cyclohexane+Mcyclohexane) are also low for all crude oil samples (Table 2) is an indication that the amount of paraffin in the crude oil samples has been significantly affected.

Bonny light (BL)

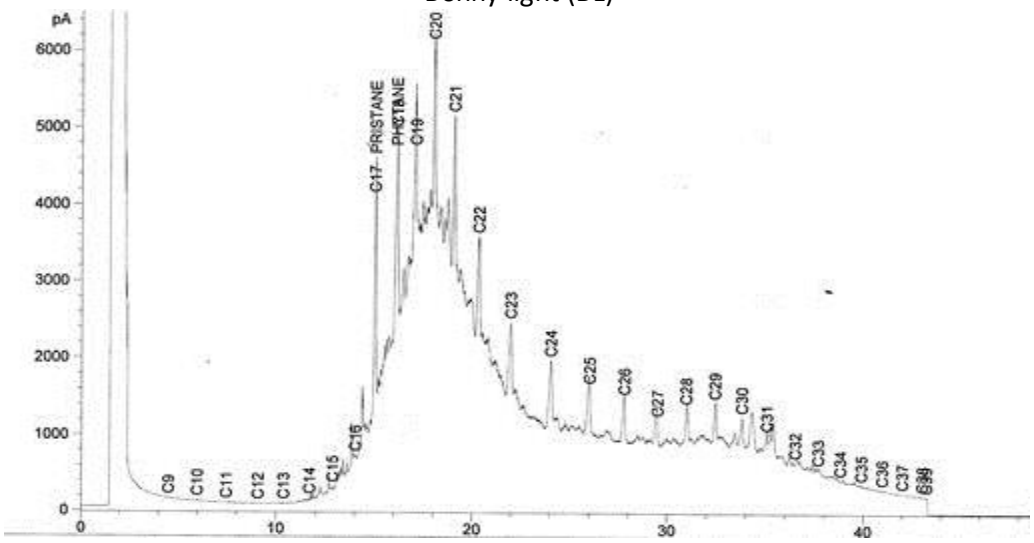

Ughelli Blend (UB)

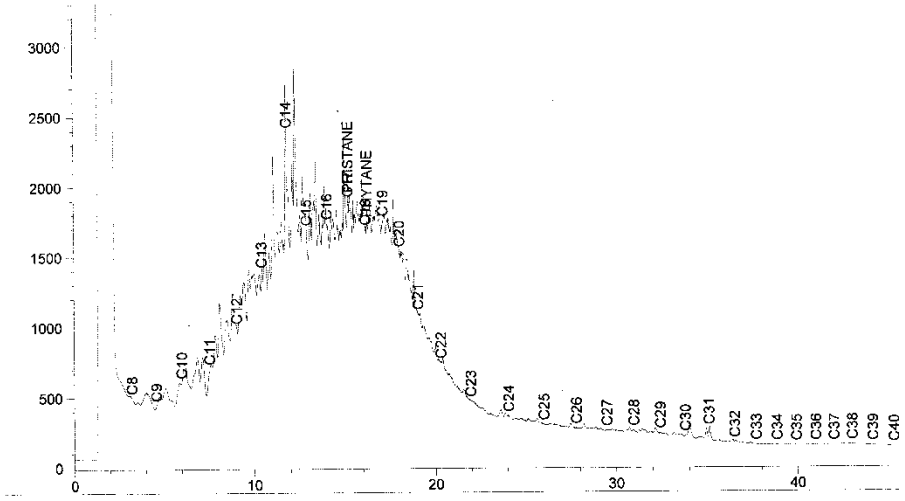

Ikordia Ikarama (OI)

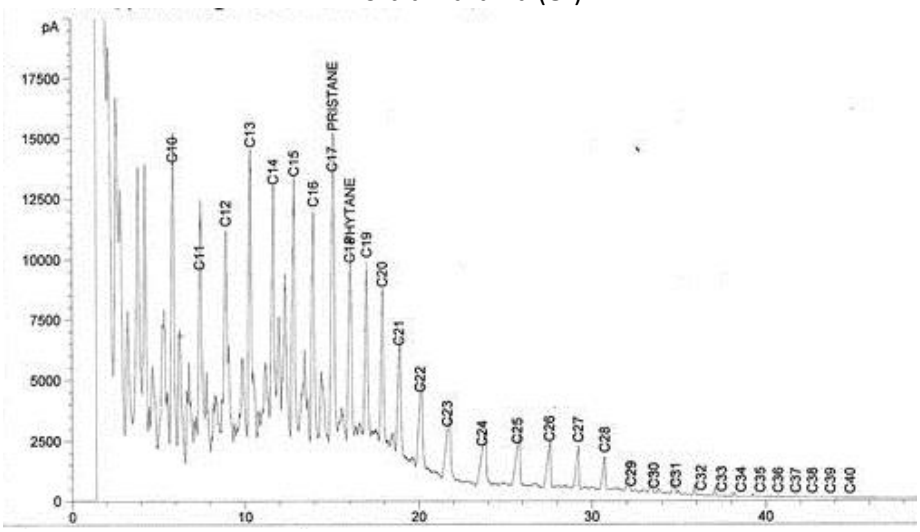

Figure 2. Gas chromatogram of crude samples

Table 1. Results of the percentage area (PA) of crude oil samples

Name	Hydrocarbon	Oil sample	Bonny light	
		BL	**UB**	**OI**
n- Hexane	nC_{10}	19809.80	84.57	52420.20
2,4-DMP	nC_{11}	158.55	49877.90	349.98
Benzene	nC_{12}	76.42	41.04	16.41
Cyclohexane	nC_{13}	4671.68	964.64	3991.76
2-Mhexane	nC_{14}	99.83	650.64	178.77
2,3-DMP	nC_{15}	208.33	114.08	2990.48
1,1-Dimethycyclopentane	nC_{16}	2606.10	172.46	20861.70
Pristane	Pr	48.96	42.89	39.70
3-Mhexane	nC_{17}	20.32	136.62	15.60
1-c-3-DMCP	nC_{18}	37.24	138.81	19.85
Phytane	Ph	989.73	33.03	780.05
1-t-2-DMCP	nC_{19}	37.62	101.76	254.71
2,2,4-TMP	nC_{20}	31.80	31.62	37.44
n- Heptane	nC_{21}	3.31	10.33	7407.11

Name	Hydrocarbon	Oil sample	Bonny light	
		BL	**UB**	**OI**
McycloHexane	nC22	3960.24	155.66	6166.73
2,5-DMhexane	nC23	5.39	11.36	7.03
2,3,4-TMP	nC24	4.55	20.64	7.34
Toluene	nC25	11.78	7.64	5.27
3-Mheptane	nC26	6.74	56.27	1177.06
2,2,5-TMP	nC27	16.25	83.84	3.68
Cycloheptane	nC28	2.50	20.76	2.77
n-Octane	nC29	1.87	7.82	9.30
Ethylbenzene	nC30	1.89	58.91	93.21
m-Xylene/p-Xylene	nC31	1.58	12.11	53.77
o-Xylene	nC32	5.92	26.08	36.43
n-Nonane	nC33	1.14	2.19	29.32
Cyclooctane	nC34	8.85	1.38	16.06
	nC35	12.95	1.70	9.07
	nC36	2.41	1.27	0.00
	nC37	3.40	6.05	5.89

BL= Bonny light, UB = Ughelli Blend, IO = Okordia-Ikarama

Table 2. The calculated paraffinicity of crude oil samples

Parameters	Crude oil samples		
	BL	UB	IO
n- Heptane/(Cyclohexane + Mcyclohexanes)	0.0004	0.0092	0.7292
n- Heptane/ McycloHexane	0.0008	0.0664	1.2011
(n-hexane+n-heptane)/(cyclohexane+Mcyclohexane)	2.2953	0.0847	5.8894
2, & 3 Mcylohexanes/DMcyclopentanes)	1.6049	3.2724	0.7079
Total	3.9015	3.4327	8.5276
%Remained	24.59666	21.64111	53.76223
%lost	**75.40334**	**78.35889**	**46.23777**

Table 3. The calculated aromacity of crude oil samples

Parameters	crude oil samples		
	BL	UB	IO
Benzene/nhexane (C_{12}/C_{10})	0.0039	0.4853	0.0003
Toulene/n heptane (C_{25}/C_{21})	3.5540	0.7394	0.0007
Xylene/nOctane (C_{31}/C_{29})	0.8471	1.5483	5.7827
Total	4.4049	2.7729	5.7837
%Remained	33.9843	21.39354	44.62216
%lost	**66.0157**	**78.60646**	**55.37784**

Table 4. The calculated ratios used in crude oil biodegradation studies

Ratios	Crude oil samples		
	BL	UB	IO
Pr/Ph	0.05	0.03	0.05
Pr/nC_{17}	2.41	0.31	2.54
Ph/nC_{18}	26.57	0.24	39.30

The percentage of the paraffin lost were also calculated, and this indicates the BL 75.40%, UB 78.36% and is 46.24% for the IO crude oils (Table 3, Fig. 3). The low values of the paraffinicty of the oils show the light-end of the hydrocarbons have been severely depleted, and the paraffinic content of the crude samples have been greatly reduced. Some researchers have shown that those anaerobic sulphate-reducing bacteria are in charge of the slight biodegradation [12]. More also the light ends ranging from (C_1 – C_9) fraction have been totally removed from the gas chromatograms of the crude oil samples (Fig.2). This may be due to anaerobic bacteria attack deep in the reservoir or loss of the volatile light ends through evaporative fractionation or phase separation [13]. The aromatic content of oil crude oils samples under study are shown in Table 3. The ratios Benzene/nhexane (C_{12}/C_{10}), Toulene/n heptane (C_{25}/C_{21}) and Xylene/nOctane (C_{31}/C_{29}) is low for the crude oil samples. The aromatics have

shown to be more resistant to biodegradation, but the low values indicate that they have remained seriously degraded, therefore may be under sulphate reducing conditions [14].

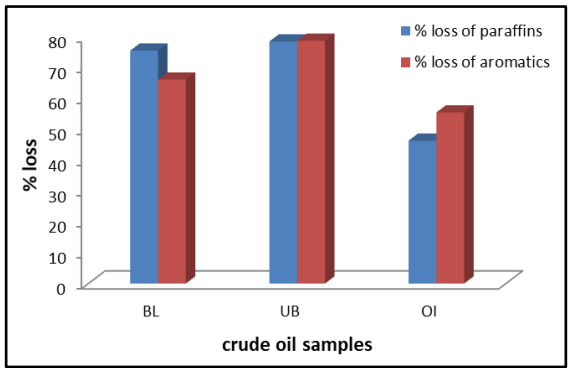

Figure 3. Comparison of the % loss of the paraffins and aromatics in crude oil samples

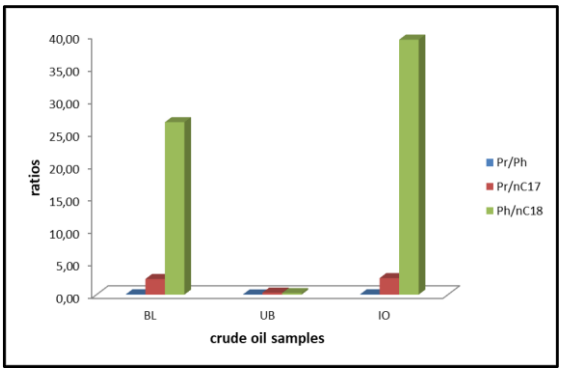

Figure 4. Plot of biodegradation ratios for crude oil samples

These low ratios show that the aromatics have been degraded. The percentage of aromatics lost to biodegradation are 66.02% for BL, 78.60 for UB and 55.38% for IO oil showing that the UB is more affected by the degradation followed by the BL oils (Table 3). The UB crude oils are obtained from the onshore fields in the coastal swamp depobelt of the Niger Delta. The superficial onshore reservoirs may have an influx of meteoric water which is originator high degree of biodegradation [15]. Most researchers have shown that fresh, oxygenated waters which usually come in contact with crude oil in reservoirs can cause extensive aerobic biodegradation. Also, it is acknowledged that fermenting and anaerobic sulphate reducing bacteria can also degrade petroleum [15].

The level of biodegradation in the crude oil samples from the calculated percentages can be ranked (BL>UB>IO), these will affect the fluid properties and hence the value and producibility of the oil accumulations in the basin [16]. The calculated Pr/Ph ratios for the BL are 0.05, UB is 0.03 and OI are 0.05 (Table 4). The ratios are low for the all crude oil samples which is a strong indication of degradation of the oils and a reducing source of organic matter [17].

The near loss to low ratios of Pr/Ph, Pr/nC_{17}, and Ph/nC_{18} (Table 4) portray heavy biodegradation for UB crude oil samples and slight biodegradation for BL and OI crude oil [15]. The Ph/nC_{18} ratio is 26.57 for BL, and 39.30 for IO crude oil samples (Table 4, Figure 4). These values are high for the two crude oil samples which show that the oil samples are moderately biodegraded [12]. All components of petroleum such as the gases, alkanes (paraffins), cycloalkanes (naphthenes) and aromatics are vulnerable to microbial degradation. The preferential attack of low molecular weight hydrocarbon components increases the high density (low API 23 gravity) of the unconsumed hydrocarbons. Meteoric water penetrates into a basin and alters any petroleum accumulation in that basin. Water moving past an oil field preferentially dissolves the most soluble hydrocarbons such as methane, ethane, benzene, and toluene. Microbes in the water can also consume the small hydrocarbon molecules producing heavy oils with low API gravity. Meteoric waters have been shown to be responsible for degraded hydrocarbons especially in the Niger Delta [18].

4. Conclusion

The whole oil gas chromatographic analyses of the three crude oil samples under investigation elucidate a progression of biodegradation. This was confirmed by the high percentage loss of the paraffinic and aromatic content of the crude oil samples. The ratios of Pr/Ph, Pr/nC_{17}, and Ph/nC_{18} were used to complement the results of the percentage loss of paraffinic and aromatic content. The results revealed that crude oils were biodegraded with extensive loss of the parrafins and the aromatics. The intensities of biodegradation could be caused by fresh, oxygenated waters which usually come in contact with crude oil in reservoirs. Also, it is

acknowledged that fermenting and anaerobic sulphate reducing bacteria can also degrade petroleum hydrocarbons which can lead to lowering of the API gravity, impact crude oil quality and consequently affect the commercial value. In addition to low-quality crude produced as a result of biodegradation, completely new compounds such as naphthenic acids can be formed during biodegradation which could be also undesirable for crude oil quality.

Acknowledgements

The Department of Petroleum Recourses of Nigeria is acknowledged for the permission and approval to access crude oil samples used for this research. The authors wish to also thank Jawura Environmental Laboratories for the use of their laboratories during the analyses of the crude oil samples.

References

[1] Connan J, Biodegradation of crude oils in reservoirs. In:Brooks J, Welte DH (eds) Advances in petroleum geochemistry, vol 1. Academic Press, London1984, pp 299 –335.
[2] Barnard PC and Bastow MA. Hydrocarbon generation, migration, alteration, entrapment and mixing in the Central and Northern North Sea. In: England WA, Fleet AJ (eds) Petroleum migration, geological society. Special Publication, London, 1991 pp 167–190
[3] Laredo GC, Lopez CR, Alvarez RE., Cano JL. Naphthenic acid, total acid number and sulphur content profile characterization in Isthmus and Maya crude oils. Fuel, 2004; 83: 1689 - 1695.
[4] Onojake MC, Abrakasa S, and Osuji LC. Chemometric representation of molecular marker data of some Niger Delta crude oils. Egyptian J. Petrol., 2015; 24(2): 139-143.
[5] Sonibare O, Alimi H, Jarvie D and Ehinola OA. Origin and occurrence of crude oil in the Niger Delta, Nigeria. J. Petrol Sci. Eng., 2008; 61: 97–107.
[6] Klett TR, Ahlbrandt TS, Schmoker JW and Dolton JL. Ranking of the world's oil and gas provinces by known petroleum volumes. U.S. Geol. Surv. Open-File Report 97- 463.
[7] Sundararaman C, Nicholas J and Diedjomahor JO. Niger Delta Petroleum System: Reg. Geol., org. facies and Thermal Maturity. AAPG annual meeting March 10-13, 2002, Houston Texas.
[8] Kaplan A, Lusser CU and Norton IO. Tectonic map of the world, panel 10. American Assoc. of Petrol. Geolo. 1994, Tulsa.
[9] Kulke H. Nigeria. In: Kulke H (ed) Regional Petroleum Geology of the World. Part II: Africa, America, Australia and Antarctica. Gebru¨der Borntraeger, Berlin 1995, pp 143–172.
[10] Michele LWT, Ronald RC, and Michael EB. The Niger Delta Petroleum System: Niger Delta Province, Nigeria, Cameroon, and Equatorial Guinea, Africa. U. S. Department of the Interior U.S. Geol. Surv. Open-File Report 99-50-H.
[11] Peters KE, and Moldowan JN. The Biomarker Guide: Interpreting Molecular fossils in Petroleum and Ancient sediments prentice Hall. Englewood Cliffs 1993, New Jersey
[12] Mode AW, Anyiam OA, Amobi JO and Nweke SU. Gas chromatographic analysis of whole oil samples: implications for biodegradation in the Niger Delta J. Petrol. Explor. Prod Technol., 2017; 7: 389–398.
[13] Oforka NC, Osuji LC, and Onojake MC. Petroleum hydrocarbon fingerprinting of crude oils from umutu/bomu oil fields in Niger Delta, Nigeria. Arch. Appl. Sci. Res, 2012; 4(1), 246-253.
[14] Margesin R and Schinner F. 2001. Biodegradation and bioremediation of hydrocarbons in extreme environments. J Appl Micro Biotechnol., 2001; 56: 650–663.
[15] Wenger LM., Davis CL and Isaksen GH. 2002. Multiple controls on petroleum biodegradation and impact on oil quality. SPE Reserv Evaluat & Engr, 2002; 5(05): 375-383.
[16] Miiller DE, Holba AG and Huges WB. Effects of biodegradation on crude oils. In: Meyer RF (ed) Exploration for heavy crude oil and natural bitumen. AAPG studies in geology. AAPG 1987, Tulsa, pp 233–241.
[17] Hunt JM. Petroleum geochemistry and geology, 2nd ed. WH Freeman and Co. 1995, USA, p 743.
[18] Ahsan A, Karlsen DA and Patience RL. 1997. Petroleum biodegradation in the Tertiary reservoirs of the North Sea. Mar and Petrol Geol, 1997; 14(1): 55-64.

To whom correspondence should be addressed: Dr. M. C. Onojake, Petroleum Chemistry Research Group, Department of Pure and Industrial Chemistry, University of Port Harcourt, P.M.B 5323, Choba, Port Harcourt, Nigeria, mudiaga.onojake@uniport.edu.ng

Petroleum and Coal

Article **Open Access**

Application of Transgressive-Regressive Technique in Sequence Stratigraphic Analysis and Its Implication for In-fill Well Locations: A Case Study from "Imaemi" Field, Offshore Niger Delta

D. E. N. Ubulom[1], J. I. Nwachukwu[2], and U. K. Benjamin[2]*

[1] *Zircon Geo Pet Limited, Lagos, Nigeria*
[2] *Department of Geology, Obafemi Awolowo University, Ile-Ife. Nigeria*

Received April 11, 2018; Accepted June 27, 2018

Abstract

The transgressive-regressive technique was used to delineate sequence boundaries identified on well logs from 25 wells in "Imaemi Field", offshore Niger Delta. The study was aimed at enhancing current understanding of the importance of reservoir basinal sequences in exploration. Eleven sequence boundaries; Sequence Boundary-1 through to Sequence Boundary-11 (SB-1 to SB-11) were identified and delineated in the field. Reservoir architectural analysis yielded twenty four vertically stacked, youngest to oldest reservoir bodies (A-Sand through Q-Sand) within channel-fill, abandonment phase, delta plain and prodelta depositional settings. The transgressive-regressive technique presents a simple scientific approach to anatomize the Niger Delta stratigraphic sequences. This approach significantly fast-tracked the pace of characterizing reservoirs in the studied field, fosters prediction of sand body geometry and continuity within a depositional architecture and can enhance selection of new in-fill wells locations in a field. For example, the geologic continuity of the H-Sand reservoir, including its hydrocarbon spatial distribution in the field is predictable. The H-Sand, I-Sand and N-Sand can be selected as in-fill wells objectives at some locations between well Imaemi-01 and well Imaemi-19. H-Sand, I-Sand and J-Sand are suitable objectives between Imaemi-27 and Imaemi-02, while H-Sand, M-Sand and N-Sand can be targeted between Imaemi-33 and Imaemi-31 wells in the field.

Keywords: *Sequence stratigraphy; Transgressive-Regressive; In-fill Well Location; Stratigraphic Architecture; Offshore Niger Delta.*

1. Introduction

The stratigraphic architecture of a basin often reflects the complexity of interplay among sedimentation, eustatic sea-level changes, tectonism and paleotopography. Sequel to the emergence of modern sequence stratigraphic analysis, many workers had adopted several techniques to evaluate the sedimentary fill and architecture of basins. For example, Type 1 and Type 2 depositional sequences [1] and Genetic stratigraphic sequence type which used maximum flooding surfaces as sequence boundaries [2]. A later sequence stratigraphic methodology utilized the transgressive-regressive sequence boundaries, based on changes from prograding to retrograding parasequence set stacking pattern [3].

Sediment supply, accommodation space and relative sea level fluctuations in the Niger Delta created repetitive vertical stacking of marine interbedded silts, sands and clays followed by shore-face sand, then coastal plain deposits; each stack being an autocyclic fourth-order sequence [4-5]. It has been recognized that stratigraphic architecture is signified by the degree of third–order cycles or sequences, which are fundamental units of regional subsurface stratigraphic subdivision and correlation [5]. Mazzullo [6], for instance, attributed the stratigraphic and depositional architecture of Chase Group in Mid–Continent USA, to interplay among paleobathymetry, glacio–eustasy and periodic syndepositional tectonism. Using wireline logs from

"Imaemi" field, offshore Niger Delta, this study employed the transgressive-regressive technique to delineate sequence stratigraphic boundaries. The study also highlights the importance of the technique as an invaluable tool for reservoir characterization and well planning.

2. Study area and the geologic setting of the Niger Delta

"Imaemi" Field is located 8.00 km offshore, western part of the Niger Delta at water depth of approximately 9 m (29.5 ft). The field is situated in the palaeogeographic zone referred to as the Upper Miocene/Pliocene and Pliocene/Pleistocene of the delta formation cycle [7]. In the Niger Delta, there are the Northern depobelt, Greater Ughelli, Central Swamp, Coastal Swamp and Offshore depobelts. These depobelts occur in onshore, continental shelf and deep offshore environments, determined by regional faults [5]. They defined the structural styles and zones in the Niger Delta. These are known as the extensional, transitional and compressional zones, characterized by three categories of structural styles; growth faults, diapirs and toe-thrust structures respectively. Imaemi Field is in the continental shelf, shallow offshore depobelt (Fig. 1) distinguished by growth faults. The study area is within the extensional province of the shelf.

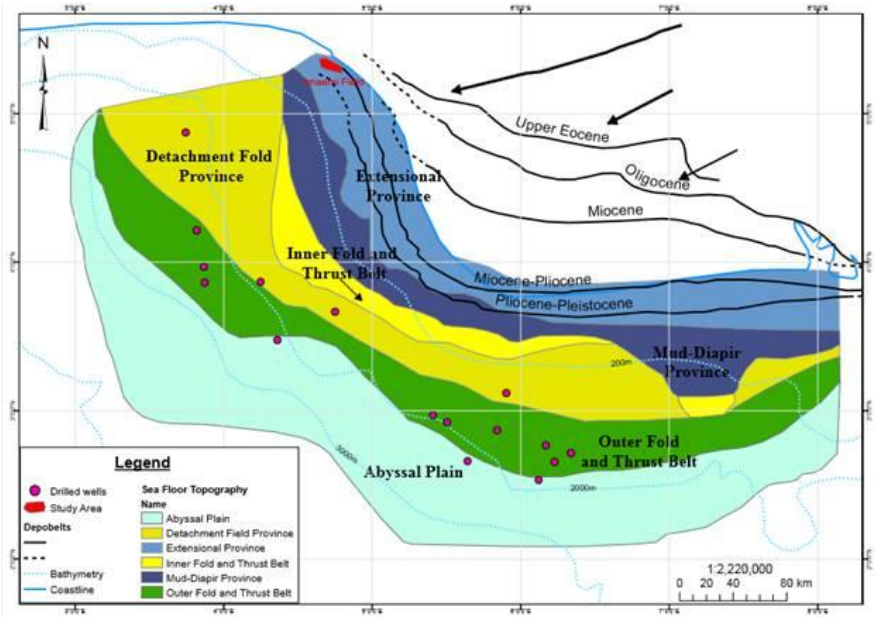

Figure 1. A structural map of the Niger Delta region, showing the study area *(Modified from Tuttle et al. [47]; Corredor et al.[44]; Kostenko et al. [46])*.

The tectonic framework of the Niger Delta may be understood within the context of the African continental margin. A host of rift systems had developed, associated with pre-Cretaceous lineaments in the lithosphere, which were zones of pre-existing weakness [8]. These resulted in the parting of the Atlantic Ocean in the Cretaceous. The Tertiary Niger Delta covers an area of approximately 75,000 km^2 (28, 957 sq. miles) In the east, the delta is bounded by a line of volcanic rocks comprising the Cameroon volcanic zone and Guinea ridge [7], with structures like the Calabar flank, a jigsaw of NW–SE trending Ikang Trough (Fig. 2), Itu High and the Calabar Hinge Line [5], and the Abakaliki Trough [9-10]. Westward, the delta complex fuses across the Benin hinge line and Okitipupa high into the Dahomey basin. The Chain and Charcot oceanic transform faults helped the Benue Trough growth, while transform fault propagation controlled Niger Delta subsidence [5]. The Niger Delta generally fits the overlying, earlier transform basin systems of the Atlantic-type passive margin basin classification [11]. Three major sedimentary cycles occurred in the Niger Delta since Early Cretaceous [12]. The Late Maestrichtian–Paleocene transgression terminated the second cycle and marked the beginning of the third depositional cycle. The Tertiary Niger Delta is a sedimentary deposit formed as a complex regressive offlap sequence of clastic sediments ranging in thickness from

9000 – 12000 m (29528 – 39370 ft). Short and Stauble [9] first named the three subsurface stratigraphic units as Akata, Agbada and Benin Formations from bottom to the top, in the order of decreasing age in the modern or Cenozoic Niger Delta.

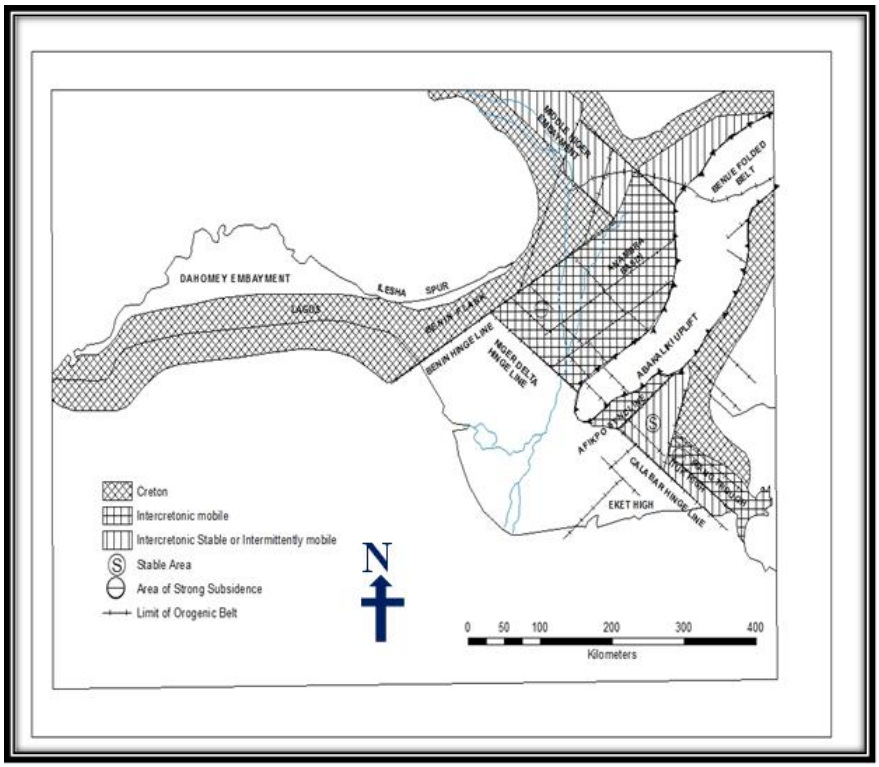

Figure 2. Megatectonic Frame: Campanian to Eocene, Showing Prominent Bounding Structures of the Niger Delta *(After Murat [12])*

2.1. Akata Formation

The Akata Formation is a massive marine shale or clay, often overpressured and 0 - 6000 m (0 – 19685 ft) thick. Its deposition began during the Palaeocene transgression and it extends over the entire Niger Delta basin, outcropping along its edges. It is a prodelta marine megafacies, comprising of gray shale, occasional sandstone and siltstone, with plant remains at the top [5,7,13]. Its sandstone units occur as thin lenses close to the contact of the overlying Agbada Formation.

2.2. Agbada Formation

The Agbada Formation contains the main hydrocarbon reservoirs in the Niger Delta [14-16]. The formation is a paralic sequence, characterized by alternation of sandstones and shales, diagnostic of environments distinguished by differential subsidence, variation in sediment supply and shift in the depositional axis [7,9,13,17] The alternation of fine and coarse clastics provides multiple reservoir stratigraphic seal couplets, while structural traps are related to rollovers and growth faults [17]. It is a delta front lithofacies, made of several offlap rhythms [7], unconsolidated to fairly consolidated point bars, distributary channels and coastal barriers. The prevalence of growth faults coupled with facies changes led to structural and stratigraphic traps acting together in many of the reservoirs and influence depth to sand bodies.

2.3. Benin Formation

The Benin Formation is the topmost formation in the Niger Delta, extending from the west across the whole delta area and southward beyond the present coastline. This Formation has been variously reported in the literature [5,7,9,13,18]. It has been described to consist of massive

continental sands and gravels (over 90%), partly unconsolidated, coarse-grained, gravelly to locally fine-grained sand stone. Asseez [13] identified point bars, channel fills, natural levees, backswamp deposits and oxbow fills, within this formation, which are indicative of the variability of the shallow water depositional medium. Dearth of fauna contents constitutes dating difficulty [7], although an age range of Oligocene to Recent is often accepted. The formation has five clay members in the eastern Niger Delta and Opuama in the west [5,18]. Only traces of hydrocarbon shows have been known in it and these are mainly towards its base [7].

3. Historical development of the concept of sequence stratigraphy

Stratigraphy describes the vertical and lateral relationships of rocks. Embry [19] gave a working definition of the subject. He noted that sequence stratigraphy consists of the recognition and correlation of changes in depositional trends in the rock record. These changes generated by the interplay of sedimentation and shifting base level, are recognized by sedimentological criteria and geometrical relationships. One of the earliest known proponents of this concept was Nicholaus Steno, who identified that strata are formed as heavy particles settle out of a fluid. Steno's enduring stratigraphic principles are: that younger layers lie on top of older layers; layers are initially horizontal, and continue until they run into a barrier [20]. A notable addition to stratigraphy was from Gressly, especially in the areas of facies concept and applications, stratigraphic correlation and palaeogeographic reconstruction [21]

Modern stratigraphy began in the late 18th century, and was driven by two contrasting research models or cognitive styles; inductive and the deductive models [22-27]. The inductive stratigraphy led to the creation of a data base of stratigraphic units, and constitutes the basis of modern chronostratigraphic time scale [27]. The deductive models began with Hutton's uniformitarianism, and employed underlying geologic controls to explain Earth processes. Deductive school of thought sought evidence of regularity or cyclicity in the Earth processes or "the pulse of the earth", which includes the modern global-eustasy model [27].

A distinguished German philosopher, Heidegger [26] explained geological practices in a process termed the hermeneutic circle. This involves a sequence of induction and deduction. The iterative processes incorporate observation, generalization and theorizing or induction, then construction of hypotheses and seeking of new observation to test and abandon or refine the theory or deduction. Fairbridge [29] summarized the main mechanisms of sea level changes. He stated that tectonic hypothesis is localized to a region, while eustatic or sea level changes are widespread and apply worldwide. Fairbridge [29] therefore, proposed integration of multidisciplinary theory for solution to stratigraphic concepts.

Earlier stratigraphic hypotheses were harmonized and its modern state enunciated [1,30-35]. Sloss [30] for instance, grouped layers of rocks into unconformity-bounded sequences based on lithology. In 1977 Vail, a student of Sloss introduced seismic stratigraphy, by interpreting unconformities based on tying together global sea-level change, local relative sea-level change and seismic reflection patterns. The end result of Vail's work was the production of global charts for the distribution of major unconformities derived from seismic [36]. This new application of stratigraphy fosters linkage of seismic, log, fossil and outcrop data at local, regional and global scale.

Modern work on the chronostratigraphic time scale is based on empirical principles, culminating in the definition of global section and boundary stratotypes for the major chronostratigraphic units [37]. Presently, sequence stratigraphic concepts as recognized by scientists are based on the assumption that sea level changes are the predominant control on stratigraphic architecture, geometries and facies, while they admit that tectonics, subsidence, isostasy and compaction contribute to creation of space for sediment accommodation. As noted above, sequence stratigraphy depends on the intricate subdivision of the Earth's sedimentary deposits into layers or sequences. These sequences vary in types; hence, the succeeding section focuses on sequence types.

4. Stratigraphic sequence types

There are four stratigraphic sequence types, each with a different set of bounding surfaces. Vail *et al.* [1] defined Types 1 and 2 depositional sequences. Galloway [2] suggested genetic stratigraphic sequence type, while Embry and Johannessen [3] proposed the Transgressive-Regressive Sequence. The Type 1 sequence uses subaerial unconformity as the unconformable portion of the boundary. Its timeline matches the start of base level fall for correlative conformity. It is difficult to apply this sequence type due to difficulty of objectively identifying a timeline that coincides with the start of base level fall [19]. The Type 2 sequence similarly used subaerial unconformity as the unconformable portion of the boundary, but utilizes a timeline equivalent to the end of base level fall for the correlative conformity. Embry [19] observes difficulty to identify time line equivalent to end of base level fall or start of base level rise. Galloway [2] proposed the application of ma-ximum flooding surfaces (MFS) as sequence boundaries and termed the unit a Genetic Stratigraphic Sequence. The advantage of this method [19] includes alleviation of subjectivity in boundary recognition, inherent in Type 1 and Type 2 sequence types, since maximum flooding sequence is determined by objective scientific means. The limitation of the genetic sequence is lack of coherency in basin margins, because subaerial unconformity can occur within the sequence. Embry and Johannessen [3] initiated the transgressive-regressive sequence. It uses the subaerial unconformity as the conformable portion of the sequence boundary and the maximum regressive surface as the correlative conformity [19]. The emphasis here is on the use of changes in depositional trends as boundaries to define the transgressive-regressive sequence type (Table 1). In this ca-se, transgressive system tract may be below and a regressive systems tract above.

Table 1. A Comparison of System Tract Schemes for a Type 1 Depositional Sequence, a Type 2,Depositional Sequence and a Transgressive-Regressive Sequence

Event	Type 1	Type 2	T-R
Start Transgression			SB
Start B.L. Rise	LST late / early	LST / SB / FRST (FSST)	RST
Start B.L. Fall	SB		
Start Regression	HST	HST	
	TST	TST	TST
Start Transgression			SB
Start B.L. Rise	LST late / early	LST / SB	RST

LST: Lowstand System Tract; TST: Transgressive Systems Tract; HST: Highstand Systems; Tract; FRST: Forced Regressive Systems Tract; FSST: Falling Sea Level Systems Tract; RST:Regressive Systems Tract; SB: Sequence Boundary; (T-R): Transgressive-Regressive Sequence (Modified from [3,19]

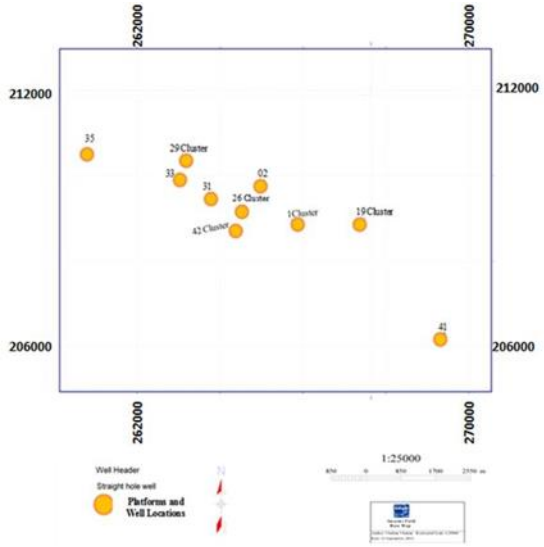

Figure 3. Base map of Imaemi Field showing the location of 10 Platforms from which 25 wells used in this study were drilled and the surface positions of the wells

5. Methodology

The Gamma Ray, Resistivity, and Neutron-Density logs were combined to pick and correlate stratigraphic surfaces and sequence boundaries. At intervals where only Gamma Ray log curve exists, it was used to define changes from prograding parasequence set to retrograding parasequence set stacking pattern [3,19,38]. Changes in depositional trends were used as boundaries [38]. For instance, change from sedimentation to subaerial erosion or change from transgressive or deepening of the environment to a regressive or shallowing upward trend. Thus, subaerial unconformity was seen as change from sedimentation to subaerial erosion [38]. Maximum flooding surfaces were defined by change from transgression to regression. The four log curves were used thus;

1) Flooding surfaces (FS), were picked based on Neutron-Density separations and Resistivity readings. The interval with highest Neutron-Density values and related lowest Resistivity reading close to other flooding surfaces was picked as the Maximum Flooding Surface (MFS).

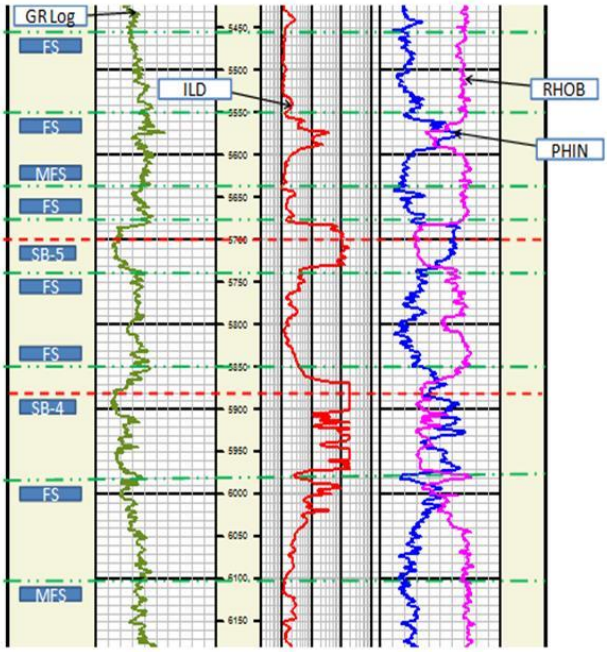

Figure 4. Part of Imaemi-01 Well Log Showing Positions of Flooding Surfaces (FS),Maximum Flooding Surfaces (MFS) and Sequence Boundaries (SB) Delineated and PickedUsing the Transgressive-Regressive Method. Note: ILD = Deep Induction Log; GR =Gamma Ray; RHOB = Bulk Density; PHIN = Neutron Porosity Log; Depth values on the Log are given in feet.

2) Trends of upward-increasing FS Resistivity and upward-decreasing FS Neutron-Density correspond to forward stepping or progradation of delta cycles. Conversely, trends of decreasing FS Resistivity and increasing FS Neutron-Density correspond to a back-stepping or retrogradation of the delta. The two patterns are separated by a sequence boundary (SB), a surface that reflects time of maximum basinward shift of the shoreline position within the cycle. Stacking patterns were used to link, FS, MFS and SB. This approach was used to delineate sequences in the field (Fig. 4), as presented in the succeeding section. The base of Benin Formation, that is, the top of the underlying Agbada Formation was first defined and used as a datum prior to picking of tops and bases of reservoirs. The datum was identified in each well by marked drop in typically high Resistivity reading of the fresh to brackish water of the Benin Formation with concomitant change in Gamma Ray log from dominantly low reading sandy sections to high Gamma Ray value and low Resistivity shale break. The shale break or layer is directly succeeded by transitional paralic Agbada sequences.

6. Sequence Stratigraphy of Imaemi Field

6.1. Sequence Boundary 1

Sequence 1 is the lowest sequence boundary picked in this work and is correlated field-wide along northwest-southeast portion or in the coastline direction (Fig. 5). The sequence boundary was picked within N-Sand. It is well preserved to the southeast and gradually eroded to the northwest part of the field. Sequence Boundary 1 separates a lower prograding parasequence stack from an aggrading upper transgressive parasequence. Below the sequence

boundary are lobes of upward coarsening channel sands, bifurcated by shale lenses. The sequence boundary depicts the time of the lowest sea mark from the land or position of maximum sea retreat.

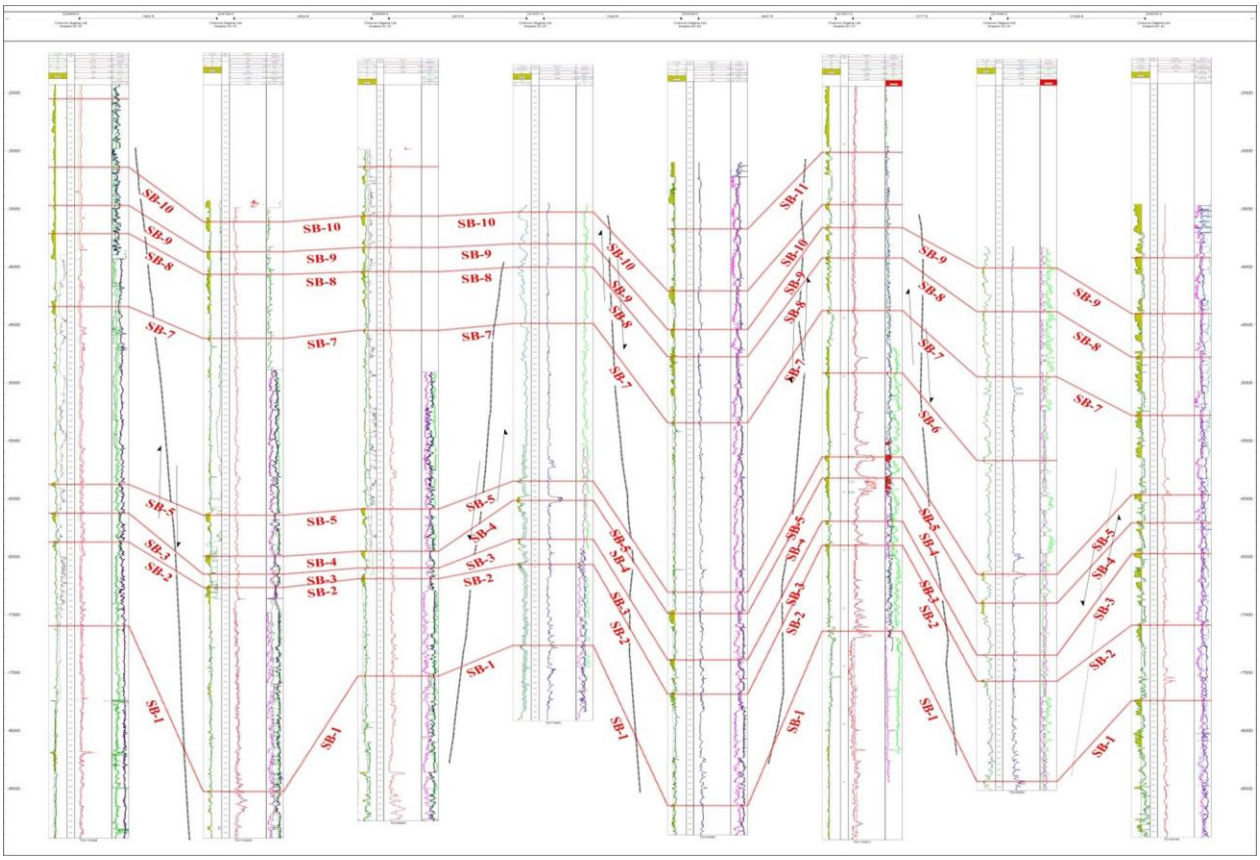

Figure 5. The Sequence Stratigraphy of Imaemi Field Showing 11 Sequence Boundaries, SB-1 to SB-11 Picked on Well Logs

6.2. Sequence Boundary 2

Sequence Boundary 2 starts with an erosional base and comprises an aggradational stacking pattern parasequence. It formed over a long time with relatively stable eustatic changes, reflected as minor regressions and transgressions which resulted in agradded beds of fine sand, silty sand, shaly sand, silt and shale. Within this sequence occurs deep marine facies transiting to marine shoreface facies, with M2-Sand, M1-Sand, M-Sand and the L-Sand as the main reservoirs. Its top represents a progradational stacking pattern as the shoreline regressed, resulting in sand deposition that was abruptly terminated by marine transgression, giving L-Sand sharp contact with overlying marine shale bed (Figs. 6 and 7), in the strike and dip sections of Imaemi Field.

6.3. Sequence Boundary 3

This sequence began with subaerial erosional truncation and or channel incision, with basinward shift in environments. The sea level dropped, with flooding surfaces picked in Imaemi-43 at 2359.15 and 2330.50 m (7740.00 and 7646.00 ft) MD, while maximum flooding surfaces, MFS were picked at 2356.10 and 2322.27 m (7730.00 and 7619.00 ft) MD. The sequence boundary, SB 3 at 2282.95 m (7490.00 ft) MD, depicts maximum seaward shift of the shoreline. The main reservoir is the K-Sand, a channel fill with gradational shale to silty sand base to sand rich top. The sequence is preserved in the SE to the NW. It pinches to thin lenticular shaly bed by erosion at Imaemi-31 and 33 wells.

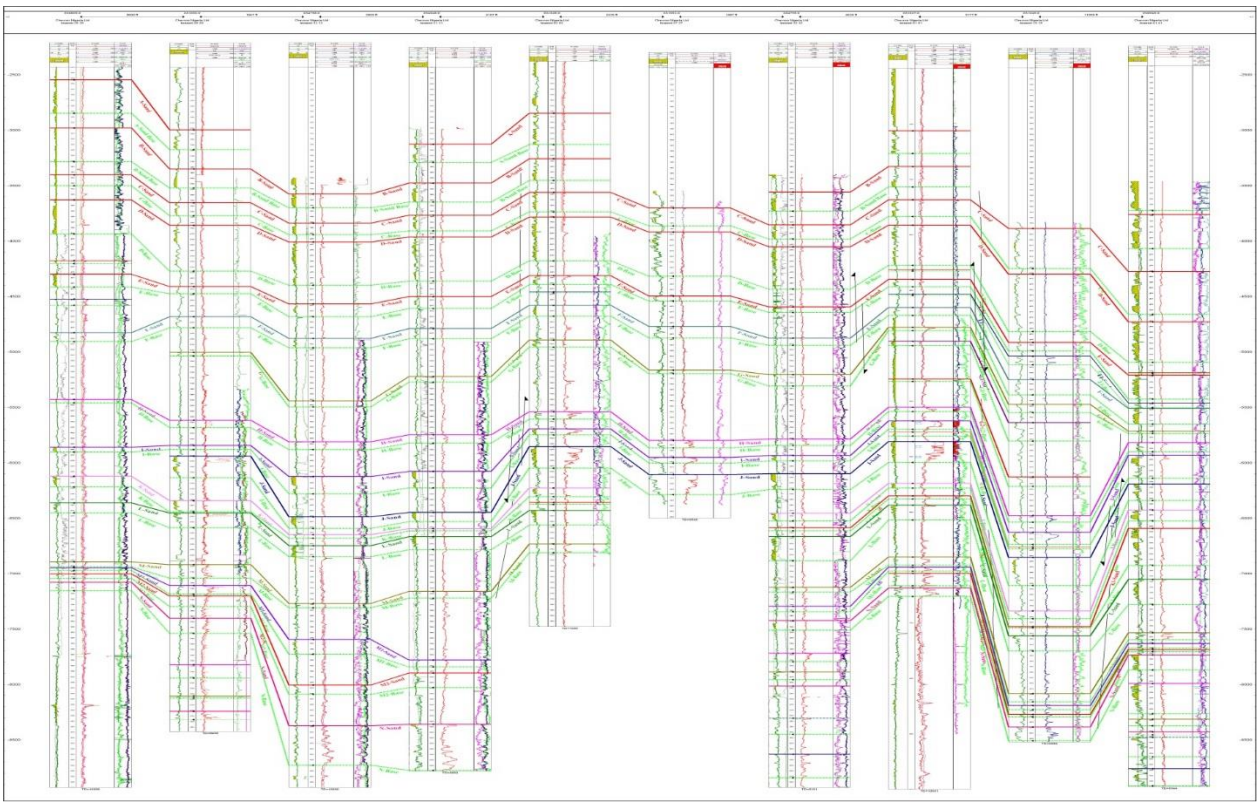

Figure 6. Stratigraphic Cross Section Along Strike, NW–SE Direction in Imaemi Field, Showing the Architectural Stacking Pattern of the Reservoirs, Tops and Bottoms of the Reservoirs and Non-Reservoir Units

6.4. Sequence Boundary 4

Transgression prompted erosion of the top layer of K-Sand reservoir, prior to deposition of shale as energy waned. Flooding surfaces, FS were observed at 1903.17 m (6244.00 ft) MD, 1898.90 m (6230.00 ft) MD, 1892.20 m (6208.01 ft) MD, 1875.74 m (6154.00 ft) MD, and 1860.19 m (6103.00 ft) MD in Imaemi-01. The MFS was also observed at 1886.71 m (6190.00 ft) MD in Imaemi-01, followed by gradual eustatic sea level lowering, which concomitantly increased depositional energy and shallowing of the water column, while shale beds at the base steadily improved in sand content. There were short-lived switches of transgressions. Thus, the sand-rich top became bifurcated by thin lenticular shale beds. The reservoir interval here is the J-Sand.

6.5. Sequence Boundary 5

Sequence Boundary 5 lies unconformably over Sequence Boundary 4 and has the I-Sand reservoir, with erosional base. It represents another cycle of transgression. In Imaemi-33 the sequence is 106.68 m (350.00 ft) thick. The basal part of the sequence consists of homogenous marine shale to sandy shale. The upper part is a progradational deposit, made of lobes of coarsening upward sand.

6.6. Sequence Boundary 6

This sequence depicts aggradational deposits. It has varied thicknesses due to erosion and palaeogeomorphic setting. It is 221.28 m (725.98 ft) thick in In Imaemi-01 and 299.31 m (981.99 ft) thick in Imaemi-19. Sequence Boundary 6 lies unconformably on I-Sand reservoir, a relatively clean coarsening upward sand and incorporates the H-Sand, G2-Sand and G1-Sand. The H-Sand is very diagnostic, while G2-Sand and G1-Sand are thin lenticular beds,

confined to few wells toward the southeast and pinched out to the north, northwest segment of the field.

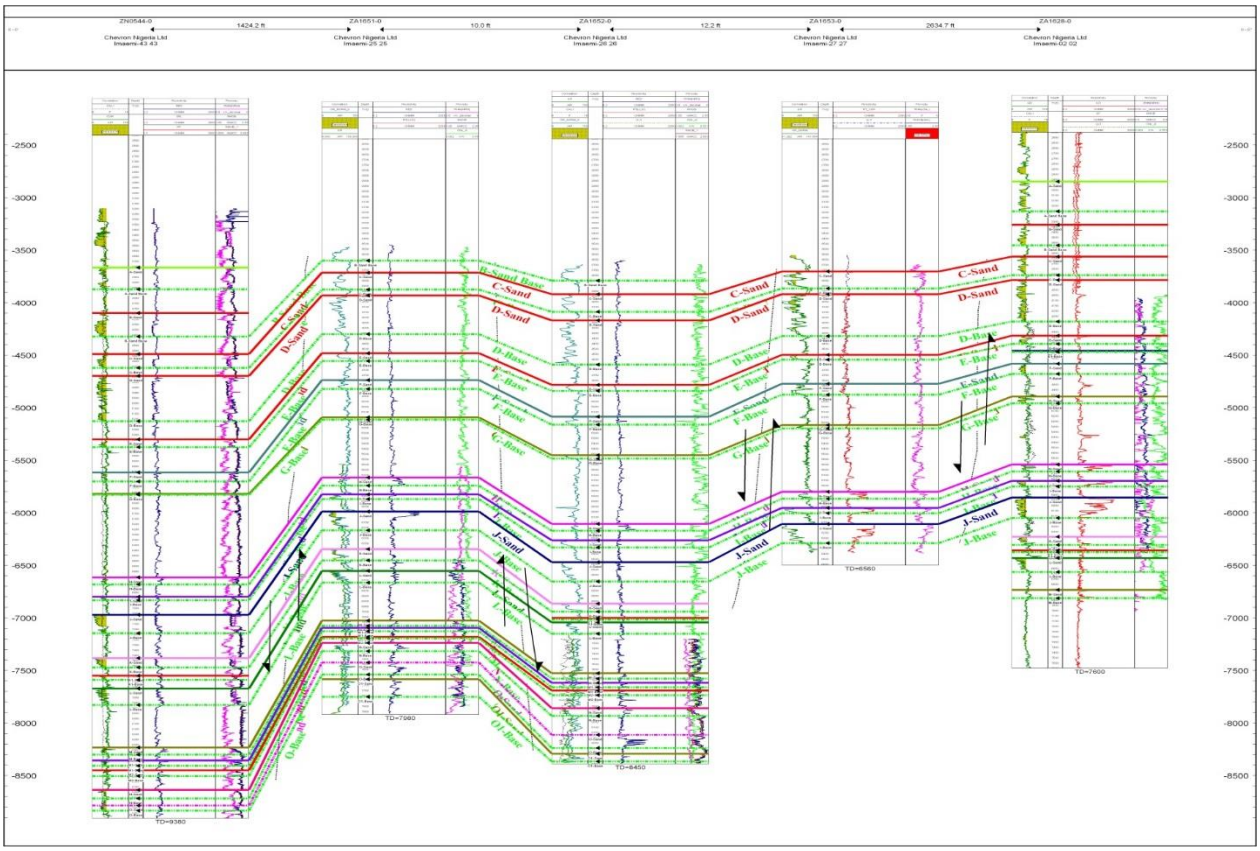

Figure 7. Imaemi Field NNE-SSW Dip Cross Section, Showing the Field Architectural Stacking Pattern, Tops and Bottoms of the Reservoir and Non-Reservoir Units

6.7. Sequence Boundary 7

Sequence Boundary 7 started with transgression and led to the deposition of shale above G1-Sand, a fining upward sand body. The G-Sand, F-Sand, E1-Sand and E-Sand are the main reservoirs in this sequence. The G-Sand coarsens upward and pinched out to the northwest in Imaemi-35, while the F-Sand consists of lobes of coarsening upward fine to silty sand bodies bifurcated by thin lenticular shale beds. The E1-Sand is limited in extent and present in Imaemi-01, 19, and 41 wells. It has two hydrocarbon bearing lobes in Imaemi-19 well. The E-Sand is the uppermost reservoir in this sequence and is extensive. In Imaemi-01 it splits into three coarsening upward sand lobes.

6.8. Sequence Boundary 8

A shale layer representing transgressive system tract marks its base. The sequence has D1 and D-Sand reservoirs. The D1-Sand is sheet-like and limited in extent. The D-Sand consists of six to nine sand lobes aggraded on one another, separated by thin shale lenses, which wedged out in places to result in amalgamated, relatively homogenous thick sand bodies. Each of the sand lobes is coarsening upward in trend. The top of Sequence Boundary 8, picked at the cleanest sand of the lowstand deposit, represents the farthest shoreline shift before another transgression.

6.9. Sequence Boundary 9

This sequence began with the deposition of relatively low resistivity, largely homogenous transgressive marine shale bed of varied thickness, indicative of stable and wide spread event, which accounts for its field-wide correlation. It attained an average thickness of 23.77 m (77.99 ft) within the northwest portion, 20.19 m (66.24 ft) in the southeast and an overall average of 21.95 m (72.01 ft) thick along strike direction in the field. The C-Sand facies in the sequence consists of two main coarsening upward, smooth or slightly serrated lobes, separated by thin shale bed and sharp to cylindrical upper boundaries, as seen in Imaemi-41 and Imaemi-01 wells respectively (Fig. 5).

6.10. Sequence Boundary 10

This sequence unconformably overlies Sequence Boundary 9, with largely homogenous basal shale facies, having 43.99 m (144.32 ft) average thickness from 6 wells (Imaemi-33, 31, 25, 43, 01 and 41), taken in the NW-SE direction. Continued shallowing of the water column due to progradation of the deltaic clastic deposits resulted in high energy and progressive increase in sand content to funnel shape log motif of B-Sand. The sand is bifurcated into upper and lower compartments.

6.11. Sequence Boundary 11

Sequence Boundary 11 is identified in this work to mark the top of the paralic sequence, on which lies the base of a shale bed that separated Agbada Formation from the continental Benin Formation. This sequence is correlated field-wide based on well logs. It consists of the A-Sand as the main reservoir body, homogeneous shale bed underneath this sand and the silty to shaly sand uppermost part of B-Sand. The primary sand, that is, A-Sand within this sequence is serrated into three coarsening upward lobes, each with abrupt top and gradational base.

7. Discussion

The thicknesses of the Benin Formation and Agbada Formations intersected by wells used in this study ranged from 799.00 to 1193 m (2621.39 to 3914.04 ft) for the Benin Formation and up to 1524 m (5000.00 ft) for the Agbada Formation.

The sequence stratigraphic, Transgressive-Regressive technique resulted in the recognition and delineation of Sequence Boundaries (SB1 to SB11), each of approximately 2 to 4 million years cycles. The stratigraphic panel diagram of the field was constructed from H-Sand to N-Sand, incorporating the reservoir and non-reservoir facies with the intercalating shale beds (Fig. 6.2). Correlations of reservoirs and non-reservoir lithofacies in stratigraphic positions within the delineated Sequence Boundaries aided determination of sand geometry, reservoirs heterogeneity; which are factors of scale and complexity [39-40]. Understanding the Sequence Boundaries, their relative positions are vital to reservoirs distribution predictability. The reservoirs are seen to be laterally continuous and bifurcated by variably thick shale intercalations. The laterally continuous nature of the reservoir sands and intercalated shale beds suggest repeated Transgressive-Regressive cycles. Shale breaks with reasonable continuity are known to have a negative influence on hydrocarbon recovery [41-42]. Conversely, the presence of shale lenses tends to limit the danger of early gas or water break called conning.

Infill wells placement may be effectively planned if reservoir distribution knowledge is integrated with spatial spread of fluid contacts in a field. Thus, infill wells can be planned between Platform-19 and Platform-41 wells to the southeast, and Imaemi-35 and Imaemi-29 wells to the northwest.

7.1. Implicatin for hydrocarbon exploration

Further exploration for petroleum resources or search for appraisal or infill well locations, especially in an existing field requires diligent use of available data set. As shown in this study, the Transgressive-Regressive method eases the identification and delineation of sequences

around Imaemi Field. Once sequence boundaries are established, reservoir distribution within the sequences in terms of sand bodies' continuity, shaliness and pinch-out directions become predictable. The geologic continuity of the H-Sand reservoir, for instance, coupled with its hydrocarbon spatial distribution in the field is predictable. The H-Sand occurs between SB-5 and SB-6 (Figs. 5, 6 and 7). The reservoir is observed to thicken toward the Southeastern part of the field, while it pinches out to the Northwest (Fig. 6). Similarly, it was noted that the shale content of H-Sand increases from the Southeast to the Northwest. In-fill well locations, where H-Sand reservoir could be targeted were identified as between Imaemi-33 and Imaemi-31, Imaemi-31 and Imaemmi-02, Imaemi-02 and Imaemi-27, Imaemi-27 and Imaemi-32, Imaemi-32 and Imaemi-01 (Figs. 3and 6). It is also possible to predict and target multiple reservoirs for appraisal and in-fill wells drilling through this technique. The H-Sand, I-Sand and N-Sand can be selected as objectives at a location between Imaemi-01 and Imaemi-19, while H-Sand, I-Sand and J-Sand are suitable objectives between Imaemi-27 and Imaemi-02. Moreover, in-fill wells drilling locations can be selected to target H-Sand, M-Sand and N-Sand between Imaemi-33 and Imaemi-31 wells in the field.

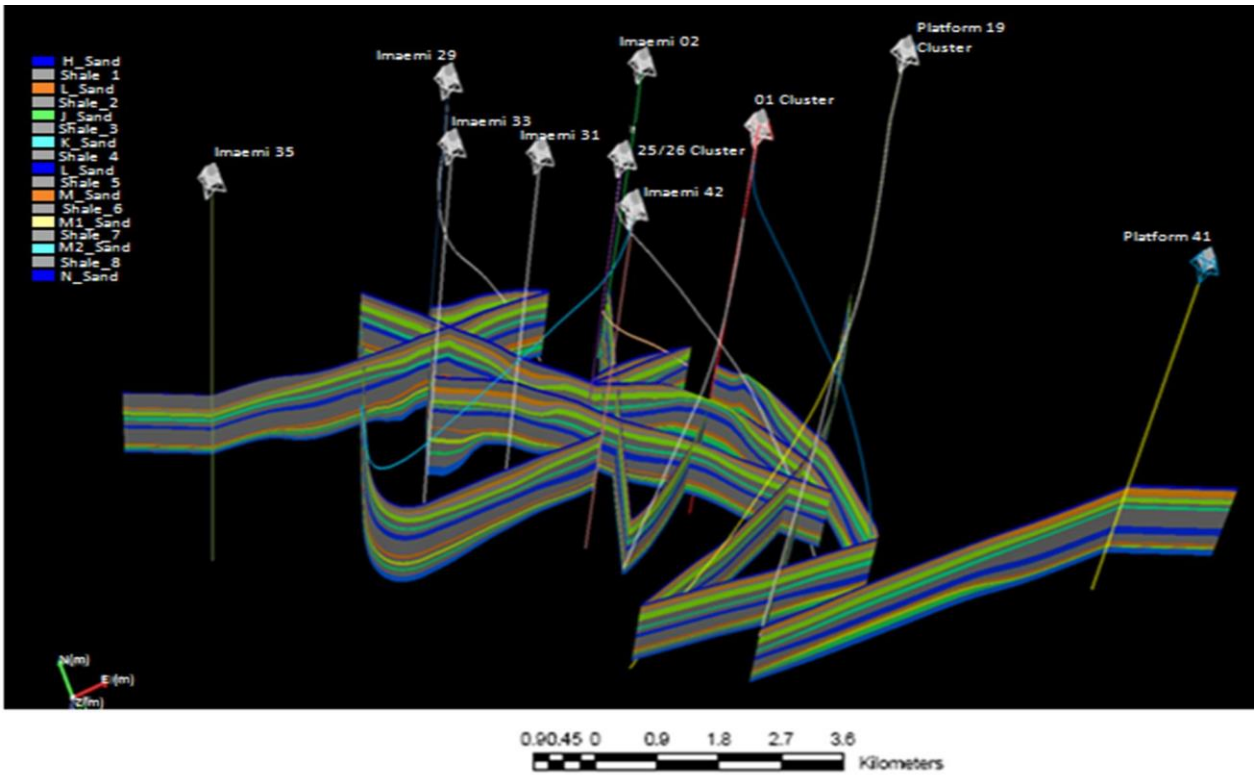

Figure 8. Stratigraphic Panel Diagram of Imaemi Field Showing Reservoirs Architecture from H-Sand to N-Sand, Viewing from the Southern Direction

8. Conclusion

It can be concluded that the application of the transgressive-regressive sequence stratigraphic technique in the study has led to the delineation of 11 Sequence Boundaries (SB-1 through to SB-11) which were correlated across the field, based on changes from prograding parasequence set to retrograding parasequence set stacking patterns. The reservoir architectural analysis yielded 24 vertically stacked, different reservoir bodies, informally named A-Sand through to Q-Sand, starting from the shallowest to the deepest. This approach eased reservoir location, correlation and characterization.

It is also possible to predict and target multiple reservoirs for appraisal and in-fill wells drilling through this approach. The geologic continuity of the H-Sand reservoir, including its hydrocarbon spatial distribution in the field, for instance, is predictable (Fig. 8). The H-Sand,

I-Sand and N-Sand can be selected as in-fill wells objectives at locations between Imaemi-01 and Imaemi-19. The H-Sand, I-Sand and J-Sand are suitable objectives between Imaemi-27 and Imaemi-02, while H-Sand, M-Sand and N-Sand can be targeted between Imaemi-33 and Imaemi-31 wells in the field. Such development drilling could increase ultimate recovery from the field in case of future declining productivity.

Acknowledgement

The authors are grateful to Chevron Nigeria Limited for providing the data used for this work and to the Department of Petroleum Resources, Lagos for facilitating release of the data. We are also grateful to numerous authors whose publications were consulted in course of this work.

References

[1] Vail PR, Mitchum Jr. RM, Todd RG, Widmier JM, Thompson III S, Sangree JB, Bud JN, and Hatleid WG. (1977): Seismic stratigraphy and global changes of sea level. AAPG Memoir, 1977; 26: 49-214.

[2] Galloway WE. Genetic stratigraphic sequences in basin analysis 1: architecture and genesis of flooding surface bounded depositional units: AAPG Bull., 1989; 73: 125 – 142.

[3] Embry AF, and Johannessen EP. T-R sequence stratigraphy, facies analysis and reservoir distribution in the uppermost Triassic-Lower Jurassic succession, western Sverdrup Basin, Arctic Canada. In: Vorren, T. O., Bergsager, E., Dahl-Stamnes, O. A., Holter, E., Johansen, B., Lie, E., Lund, T. B., (Eds.), Arctic Geology and Petroleum Potential, vol. 2 (Special Publication). Norwegian Petroleum Society 1992 (NPF), p. 121-146.

[4] Evamy ED, Haremboure J, Kamerling P, Knaap WA, Molloy FA, and Rowlands PH. (1978): Hydrocarbon habitat of Tertiary Niger Delta. AAPG Bull., 1978; 62: 1 – 39.

[5] Reijers TJA. Selected Chapters On Geology, Sedimentary Geology and Stratigraphy in Nigeria. Shell Petroleum Development Company 1996: 103 - 117.

[6] Mazzullo SJ. (1998): Stratigraphic Architecture of Lower Permian, Cyclic Carbonate Reservoirs (Chase Group) in the Mid-Continent USA, Based on Outcrop Studies. AAPG Bull., 1998; 82(3): 464 – 483.

[7] Etu-Efeotor JO. Fundamentals of Petroleum Geology. Paragraphics, Port Harcourt 1997, p. 146.

[8] Neumann ER and Ramberg IB. Paleorifts – Concluding Remarks. In I. B. Ramberg and E. R. Neumann (eds.). Tectonics and Geophysics of Continental Rifts 1976, p. 409 – 424.

[9] Short KD, and Stauble AJ. Outline of the geology of the Niger Delta. AAPG Bull., 1967; 51: 761.

[10] Merki P. Structural geology of the Cenozoic Niger Delta. (ed. T. F. J. Dessauvagie & A. J. Whiteman), African Geology, Ibadan Univ. Press 1972, 635-646.

[11] Bally AW, and Snelson S. (1980): Realms of subsidence. In: Miall, A. D., (ed.), Facies and principles of world petroleum occurrence. Canadian Society of Petroleum Geologists, Memoir 1980; 6:1003.

[12] Murat RC. Stratigraphy and palaeogeography of the Cretaceous and Lower Tertiary in Southern Nigeria. In: Dessauvagie, T. F. J. and Whiteman, A. J. (Eds.): African Geology, Ibadan Univ. Press 1972, p 251 – 265.

[13] Asseez LO. Review of the stratigraphy, sedimentation and structure of the Niger Delta. In: Geology of Nigeria, (edited by Kogbe C. A.), Elizabethan Publication Company 1976, Nigeria, p. 259 – 272.

[14] Kulke H. Nigeria, in, Kulke, H., ed., Regional Petroleum Geology of the World. Part II:Africa, America, Australia and Antarctica: Berlin, Gebrüder Borntræger 1995, p. 143-172.

[15] Hooper RJ, Fitzsimmons RJ, Grant N, and Vendeville BC. (2002): The role of deformation in controlling depositional patterns in the south-central Niger Delta, West Africa. Journal of Structural Geology, 2002; 24: 847-859.

[16] Anyiam AO, Mode AW, and Ekwe AC. (2010): Formation evaluation of an Onshore appraisal well 'KG-5', "green field", Niger Delta Nigeria. Am. J. Sci. Ind. Res., 2010; 1(2): 262-270.

[17] Reijers TJA, Petters SW, and Nwajide CS. The Niger Delta Basin, in Selley, R. C., ed., African Basins – Sedimentary Basin of the World 3: Amsterdam, Elsevier Science 1997, p. 151-169.

[18] Petters SW. An ancient submarine canyon in the Oligocene-Miocene of the Western Níger Delta. Sedimentology, 1984; 31: 805 – 810.

[19] Embry AF. Transgressive-regressive (T-R) sequence stratigraphy. In: Armentrout, J.M., and Rosen, N. C., Eds., Sequence Stratigraphic Models for Exploration and Production: Evolving Methodology, Emerging Models and Application Histories. 22nd Annual Gulf Coast Section SEPM Foundation, Bob F. Perkins Research Conference 2002: Houston, Gulf Coast Section, SEPM, p. 151-172.
[20] Neal J, Risch D, and Vail P. (1993): Sequence stratigraphy – A global theory for local success. Oilfield Review, 1993; 5(1): 51 – 62.
[21] Cross TA, and Homewood PW. (1997): Amanz Gressly's role in founding modern Stratigraphy. Geological Society of America Bulletin, 1997; 109: 1617–1630.
[22] Johnson D. (1933): Role of analysis in scientific investigation. Geological Society of America Bulletin, 1933; 44: 461 – 493.
[23] Beaumont C. (1981): Foreland basins. Geophysical Journal of the Royal Astronomical Society, 1981; 65: 291 – 329.
[24] Rudwick MJS. Cognitive styles in geology. In: M. Douglas, Ed., Essays in the sociology of perception. London 1982: Routledge and Kean Paul, p. 219 – 241.
[25] Hallam A. Great geological controversies, second edition. Oxford University Press, 244 pp.
[26] Frodeman R. Geological reasoning: geology as an interpretive and historical science.Geological Society of America Bulletin, 1995; 107: 960 – 968.
[27] Miall AD, and Mail CE. (2001): Sequence stratigraphy as a scientific enterprise: the evolution and persistence of conflicting paradigms. Earth-Science Reviews, 2001; 54: 321-348.
[28] Miall AD. Empiricism model building in stratigraphy: The historical roots of present-day practices. Stratigraphy,1961; 1(1): 3 – 25.
[29] Fairbridge RW. Eustatic changes in sea level. In: Ahrens L. H., Press F., Rankama K, and Runcom S. K. (Eds): Physics and Chemistry of the Earth, vol. 4. London 1961, England: Pergamon Press Ltd, p. 99 – 185.
[30] Sloss LL. (1963): Sequences in cratonic interior of North America. Geol. Soc. Am. Bull., 1963; 74: 93 – 114.
[31] Mitchum RM, Jr, Vail PR, and Thompson III S. Seismic stratigraphy and global changes of sea level, part 2: the depositional sequence as a basic unit for stratigraphic analysis. In Payton, C. E., (ed.), Seismic stratigraphy-application to hydrocarbon exploration: Tulsa, Ok, AAPG Memoir,1977; 26: 516.
[32] Posamentier HW, Jervey MT, and Vail PR Eustatic controls on clastic deposition. Conceptual framework. In: Wilgus, C. K., Hastings, B. S., Kendall, C. G. St. C., Posamentier, H. W., Ross, C. A., and Van Wagoner, J. C., (Eds.), Sea Level Changes-An Integrated Approach, 1988; 42: 110-124,SEPM Special Publication.
[33] Posamentier HW, and Allen GP. (1999): Siliciclastic sequence stratigraphy: concepts and applications. SEPM Concepts in Sedimentology and Palaeontology, 1999; 7: 210.
[34] van Wagoner JC, Mitchum RM, Campion KM, and Rahmanian VD. Siliciclastic sequence stratigraphy in well logs, cores and outcrops. AAPG Methods in Exploration 1990 series 7, 55p.
[35] Catuneanu O. (2002): Sequence stratigraphy of clastic systems: concepts, merits, and pitfalls. Journal of African Earth Sciences, vol. 35, p. 1-43.
[36] Haq BU, Hardenbo J, and Vail PR. (1987): Chronology of fluctuating sea levels since the Triassic. Science, 1987; 235: 1156-1166.
[37] Miall AD Principles of Sedimentary Basin Analysis. Springer-Verlag, New York 1990, 2nd Ed., 668 pp.
[38] Rider MH. (2002): The Geological Interpretation of Well Logs: Whittles Publishing, 2nd Edition, p. 251-266.
[39] Yeats RS, and Beall JM. Stratigraphic controls of oil fields in the Los Angeles basin: a guide to migration history. In: K. T. Biddle, ed., Active margin basins: AAPG Memoir, 1991; 52: 221 – 237.
[40] Yerkes RF, McCulloh TH, Schoelhamer JE, and Vedder JG. Geology of the Los Angeles basin, California–an introduction: U.S. Geological Survey Professional Paper. 1995:420–A, p. A1–A57.
[41] Zeito GA. Interbedding of shale break and reservoir heterogeneities. Journ. Pet. Tech. (October 1965), p. 1223 – 1228.
[42] Weber KJ. Influence of common sedimentary structures on fluid flow in reservoir models. Journ. Pet. Tech. 1982; 34(): 665 – 672.
[43] Allen TO. Production Operations: Well Completion, Workover and Simulation, OGCI, Tulsa, 1982; 1: 10 – 27.

[44] Corredor F, Shaw JH, and Bilotti F. Structural styles in the deep-water fold and thrust belts of the Niger Delta: AAPG Bull., 2005; 8: 753 – 780.
[45] Galloway WE. Depositional architecture of Cenozoic Gulf coastal plain fluvial systems: In: Recent and Ancient None-marine Depositional Environment: Models for Exploration (eds.) Frank G. Ethridge and Romoe M. Flores: Society of Economic Palaeontologists and Mineralogists. Special Publication, 1981; 31: 127–155.
[46] Kostenko OV, Naruk SJ, Hack W, Poupon M, Meyer H, Glukstad M, Anowai C, and Mordi M. Structural evaluation of column-height controls toe-thrust discovery, deep-water Niger Delta. AAPG Bull., 2008; 92: 1615 – 1638.
[47] Tuttle MlW, Brownfield ME, and Charpenter RR. Tertiary Niger Delta (Akata-Agbada) Petroleum System (No. 701901), Niger Delta Province, Nigeria, Cameroon, and Equatorial Guinea, Africa. In Tuttle, M. L. W., Charpenter, R. R. and Brownfield, M. E., Eds.: The Niger Delta Petroleum System: Niger Delta Province, Nigeria, Cameroon, and Equatorial Guinea, Africa. 1999, Open-File Report 99-50-H.

To whom correspondence should be addressed: Dr. D. E. N. Ubulom, Zircon Geo Pet Limited, Lagos, Nigeria, Daniel Ubulom <info@zircongeopet.com>

Petroleum and Coal

Article **Open Access**

INTEGRATION OF 3D SEISMIC AND WELL LOG DATA FOR THE EXPLORATION OF KINI FIELD, OFFSHORE NIGER DELTA

Adesoji O. Akanji[1], Oluseun A. Sanuade[2], SanLinn I. Kaka[2], Isaac D. Balogun[3]

[1] *A-S Lionbridge Resources, Lagos, 23401, Nigeria.*
[2] *Geosciences Department, College of Petroleum Engineering & Geosciences, King Fahd University of Petroleum & Minerals, Dhahran, 31261, Saudi Arabia*
[3] *Stratahills Technologies, Lagos, 23401, Nigeria*

Received April 7, 2018; Accepted June 27, 2018

Abstract

Initial interpretation of the available data in Kini-field offshore Niger Delta suggests huge uncertainty in the hydrocarbon volume. Thus, additional exploration procedure is required to minimize economic risk before progressing to the next stage of the field development. An independent interpretation of the 3D seismic data and well logs of the Kini-1 well was carried out to highlight the sources of the key uncertainties in the geology and make a necessary recommendation on additional data acquisition to minimize the uncertainties. Four oil-bearing grains of sand (A, B, C and D reservoirs) were identified for petrophysical evaluation. These sands have a good gross thickness ranging from 21 to 33 m and average net-to-gross (NTG) of 0.62. Porosity varies between 0.22 and 0.30 indicating good reservoir quality having hydrocarbon saturation (S_h) between 69 to 76 %. Kini-1 well did not encounter hydrocarbon water contact thereby creating uncertainty in the fluid contact, hydrocarbon column and in a way the extent of the hydrocarbon fluid in the reservoir. This study also revealed that the seismic data did not completely capture the overall extent of the reservoir structures as indicated in the top structure maps of the four reservoirs and thus could not properly describe the trapping system of the NW-SE striking anticline as well as the area extent of the hydrocarbon bearing zone because the northern arm of the structure was not captured by seismic. Few east-west striking synthetics (F1, F2, F3, F6, F7) and antithetic (F4, F5, and F8) faults identified in the southern part of the field did not appear to control the fluid entrapment in these reservoirs. Only low case gross rock volume (GRV) and hydrocarbon reserve (of 663 MMbl) were calculated using oil-down-to (ODT) of Kini -1 well because of the highlighted huge structural uncertainties do not permit base and high case estimates. Consequently, it was recommended that the result should not be used to make an economic decision unless until more data are available to minimize the risks. To minimize the highlighted uncertainties, additional 3D seismic data covering an area extent of about 1430000 square meters was proposed at the northern and eastern parts of the field. This is expected to fully capture the reservoir structure and help estimate the GRV more accurately. Two wells (Kini-2 and Kini-3) were strategically positioned to target the fluid contact, examine lateral variation in the petrophysical properties and ultimately yield a more reliable hydrocarbon volume estimates.

Keywords: *Exploration; reservoir structure; stratigraphic trap; uncertainty; petrophysical property.*

1. Introduction

Kini field is located at a water depth of about 1000 m at offshore Niger Delta (Fig. 1). The field was discovered by Kini-1 well which encountered stacked reservoir set with notable thickness. After discovery, additional exploration is required to ascertain the petroleum potential of the field as well as to meet the future production forecast of the field. Hence, the knowledge of exploration potentials is vital for the Kini field. Regional studies carried out in the offshore area indicated structural complexity which poses serious challenges to Geoscientists as a number of exploration wells that drilled at other fields did not yield meaningful results [1-5]. Thus, to

minimize such economic risk in Kini field and ultimately firm up the technical confidence of the subsurface geology, more exploration data are needed.

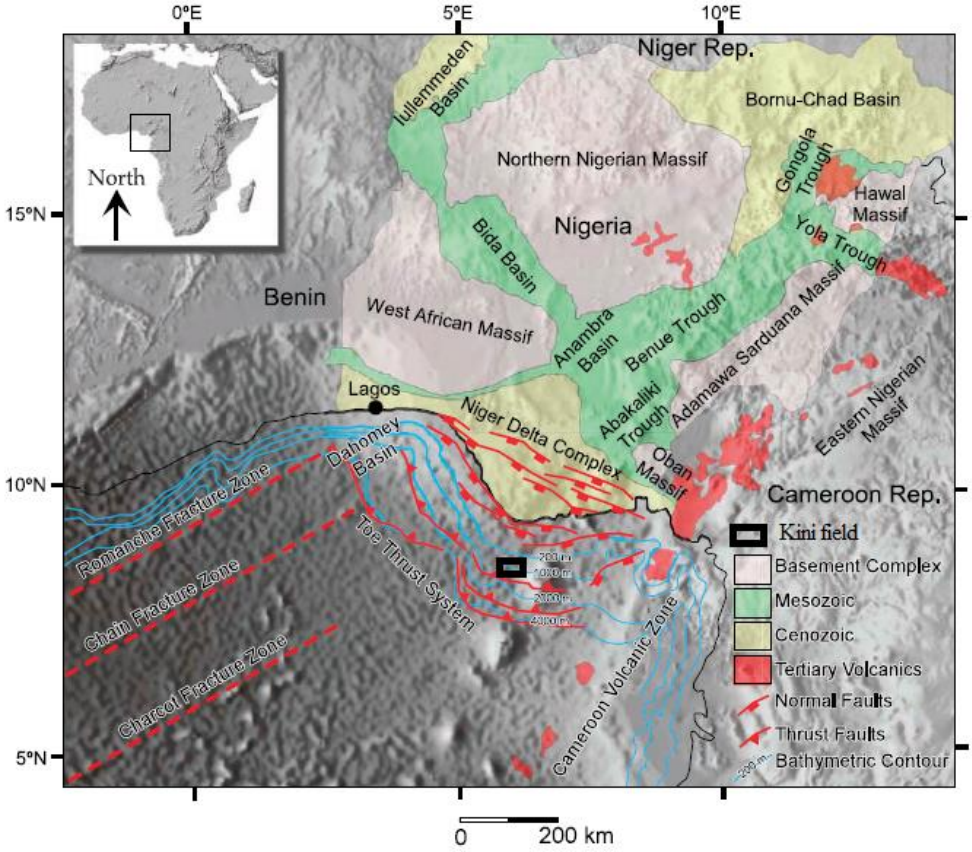

Fig. 1. Location Map of Kini Field Offshore Niger Delta, Nigeria *(Modified from Corredor et. al. [15])*

Previous studies have shown that integration of 3D seismic data and well log data could serve as a useful tool to understand the structural frame work and to estimate reserves [6-8]. Therefore, this study was undertaken to present the initial interpretation of the available information about the subsurface geology with the objectives of proffering recommendation procedure for data acquisition and to highlight the sources of the key uncertainties to minimize the uncertainties in the field.

The proposed acquisition is expected to capture the whole extent of the reservoir structure, and its interpretation should provide a more reliable hydrocarbon potential of the field thereby minimizing economic risk while progressing to the next stage of the field development.

2. Geological framework

The Niger Delta basin was formed during the breakup that occurred between the plates of South America and that of Africa at the failed arm of a triple junction. The basin is made up of three main Formations: Akata, Agbada, and Benin (Fig. 2). The oldest (Akata) formation is about 6000 m thick and mainly composed of marine shale that is believed to have changed the form of the clastic wedge of the Niger Delta Basin [9]. Streaks of sand found in the formation are believed to be of turbidity origin flow. The effect of over-pressure, ductility, and depth of this marine shale in the Akata formation led to the formation of syndepositional normal faults formed during progradation of the delta. The overlying formation is a paralic sequence of fluvial-deltaic sand and marine shale of about 4,000 m thick notably Agbada formation. It is Eocene to Pleistocene in age [9]. The youngest Formation is the Benin Formation which composed of non-marine sands believed to be of upper coastal plain or alluvial origin [9]. The Benin Formation is Oligocene to Recent in age [10].

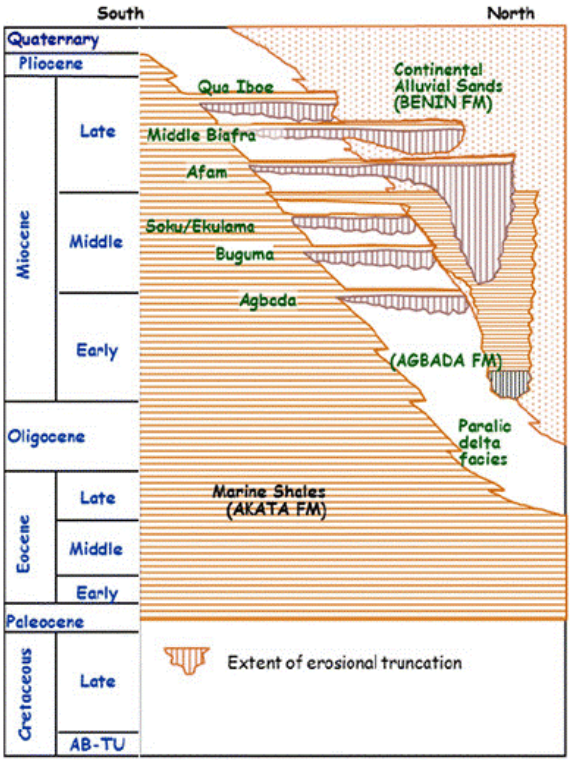

Fig. 2. Regional stratigraphy of the Niger Delta *(modified after Corredor et al.* [15]*)*

Akata Formation is the main source rock while Agbada Formation is the main reservoir rock in the Niger Delta basin. The interbedded shale in the Agbada Formation serves as the primary seal rocks [9,11-13].

The Niger Delta is known to have accumulations of a lot of giant oil and gas and many unexplored opportunities that are being trapped in many structural styles ranging through the continental shelf to the continental slope within the Nigerian Offshore depobelt. The gas-to-oil ratio is believed to increase towards the south within the depobelts in the Niger delta basin. This is as a result of the complex hydrocarbon distributions in the Niger Delta [9].

3. Datasets and methodology

Available 3D seismic data and Kini-1 well log suite data were processed and interpreted using *Petrel* software to describe the structure and the intrinsic properties of the hydrocarbon bearing sands (reservoirs). These were used to evaluate the petrophysical parameters and Gross Rock Volume (GRV) of the reservoirs**.** Structural features were identified and mapped on the seismic section and the reflection events (horizons) that correspond to hydrocarbon bearing sands were mapped after well to seismic tie. Time structure maps of these horizons were then generated and then converted to depth maps which were used to calculate the GRV and the hydrocarbon volume. Petrophysical parameters (such as porosity, the volume of shale (V_{shale}), net-to-gross (NTG), net sand, water saturation and hydrocarbon saturation) of the selected reservoirs were calculated at Kini-1 well location using necessary log suites and equations.

4. Results and discussion

Four oil-bearing reservoirs (A, B, C, and D) with significant gross sand thickness were identified considered for this evaluation (Figure 3). Observable Gross sand thickness of these reservoirs ranges from 21 to 33 m with an average net to gross of 0.62 (Table 1). Porosity generally reduces with depth ranging between 0.22 and 0.30 indicating that the reservoirs are generally of good sand quality with hydrocarbon saturation (S_h) between 69 to 76 %. Kini-1

well did not encounter Oil Water Contact (OWC) in any of these reservoirs thus creating uncertainty in fluid contact.

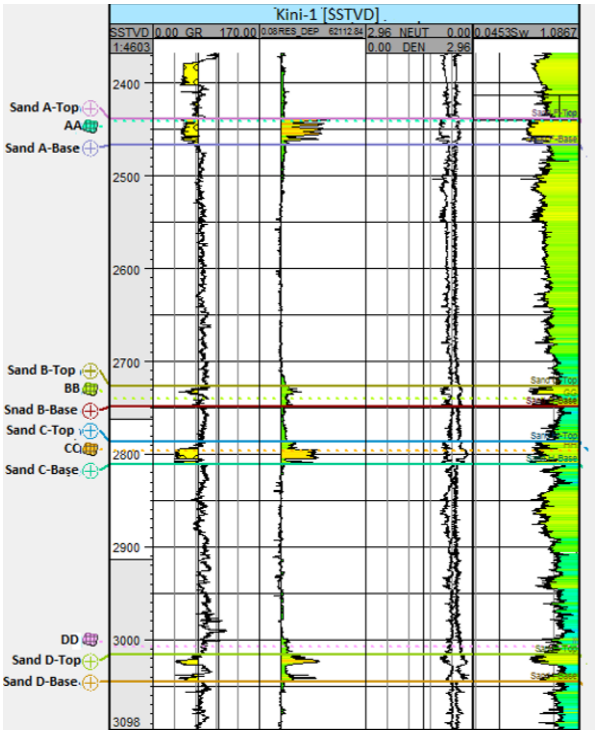

Fig. 3. Log signature of reservoirs A, B, C and D in Kini-1 well

Table 1. Summary of petrophysical properties of the selected reservoirs at Kini-1 well location

Well	Reservoir	Top (m) tvdss	Base (m) tvdss	Gross (m)	Net (m)	NTG	Av. ϕ	Sw	Oil Down To (m) tvdss
Kini-1	A	2433.71	2466.88	33.17	24.17	0.73	0.30	0.24	2462.01
Kini-1	B	2727.18	2748.55	21.37	12.37	0.58	0.25	0.31	2748.55
Kini-1	C	2785.21	2809.03	23.82	14.82	0.62	0.25	0.30	2809.03
Kini-1	D	3016.67	3045.18	28.51	15.51	0.54	0.22	0.30	3045.18

Notable structures identified are growth faults and channels. Synthetic faults (F1, F2, F3, F6, F7) generally strike east-west (E-W) and dip to south while the antithetic ones (F4, F5, and F8) are north dipping following the regional structural framework of offshore fields in Niger Delta province [3,14-15], Fig. 4).

Top structure maps (Figure 5a-d) of the selected reservoir shows that the seismic data did not capture the overall extent of the reservoir structures, and thus one could not properly describe the trapping mechanism and the area extent of the hydrocarbon bearing zone as the northern arm of the structure which could likely give a clue to the trapping system was not covered by the available seismic data. However, the structure appears to be a NW-SE striking anticline penetrated at the crest by Kini-1 well. This suggests either a three-way, a four-way dip closure or a combination trap. Since no fluid contact was established only low case GRV and hydrocarbon reserve were calculated using ODT of Kini -1 well. The huge uncertainty in the area extent of the hydrocarbon bearing interval and the contact do not permit the definition of base and high case hydrocarbon volumes as indicated in Figure 6.

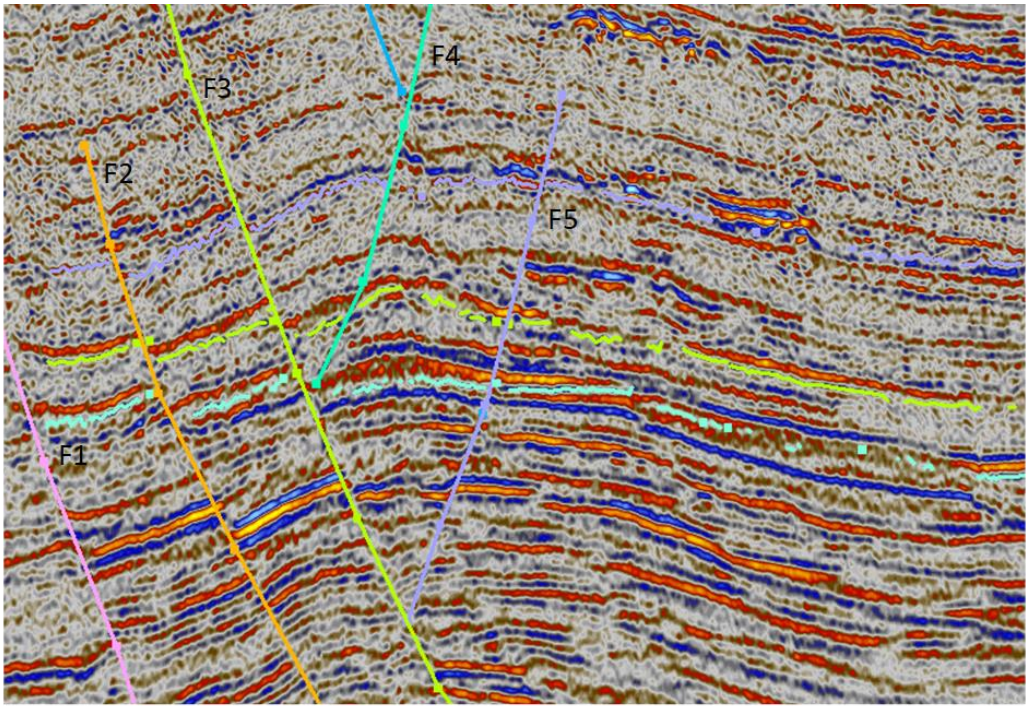

Fig. 4. Synthetic and Antithetic Faults identified in Kini field

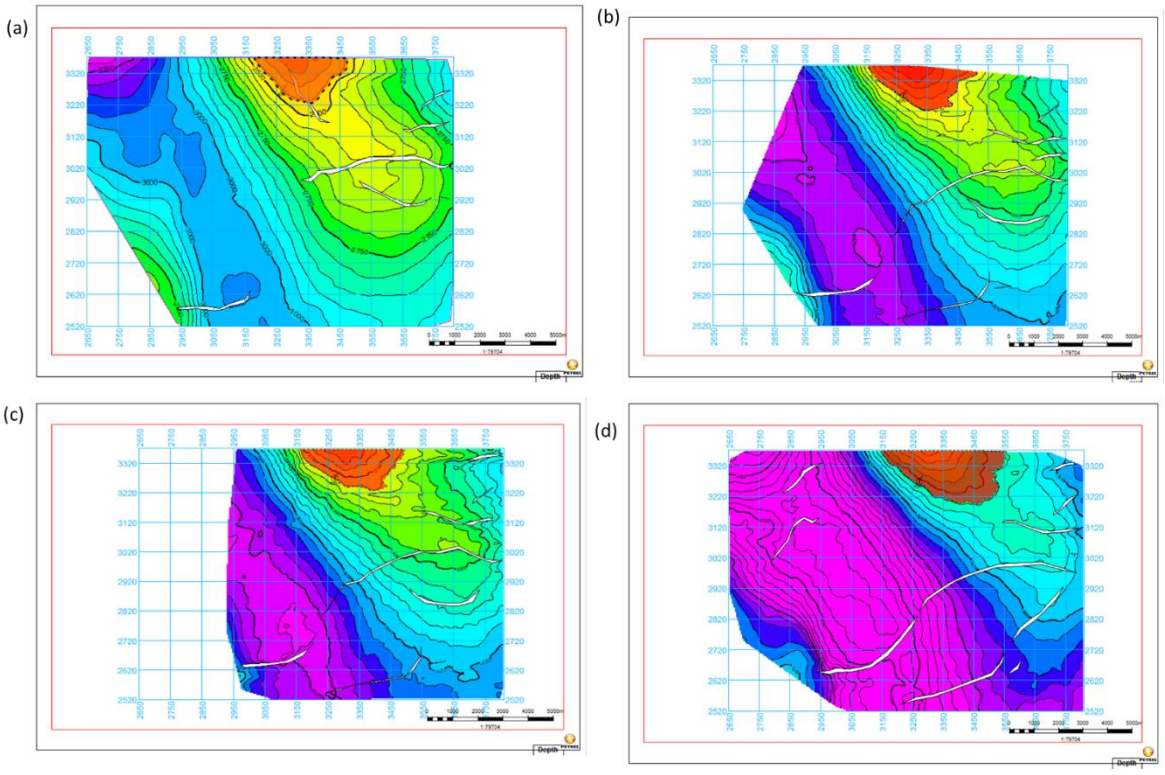

Fig. 5. (a) Top structure map of reservoir sand A showing ODT (brown) of Kini-1 well (b) Top structure map of reservoir sand B showing ODT (brown) of Kini-1 well (c) Top structure map of reservoir sand C showing ODT (brown) of Kini-1 well (d) Top structure map of Reservoir D showing ODT (brown) of Kini-1 well

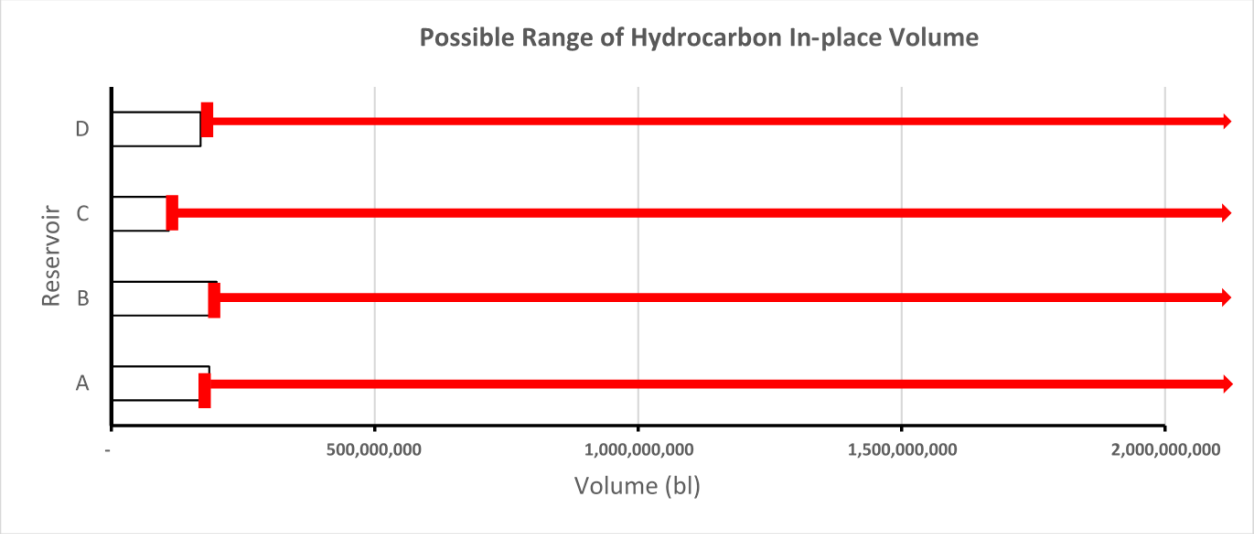

Fig. 6. Possible range of hydrocarbon volumes in reservoirs A, B, C & D

GRV and hydrocarbon-in-place volumes were estimated using only the area filled with a hydrocarbon in the seismic data and the ODT in Kini-well 1. It should be noted that this could underestimate the low case volume provided in Table 2. All the reservoirs have STOIIP of 663 MMbl (Table 2).

Table 2. Hydrocarbon volume in-place (low case)

Reservoirs	STOIIP (bl)	Reservoirs	STOIIP (bl)
A	185,825,708	C	108,832,435
B	199,645,173	D	169,363,684

Figure 6 shows a pictorial representation of the estimated hydrocarbon volume. However, the left bar indicates the lowest possible volume which is subject to uncertainty in the area extent of the hydrocarbon in the reservoir and fluid contact. However, this low case could be greatly underestimated as the cumulative effect of the major parameters of uncertainty. Thus, this result should not be used to make an economic decision. The red arrows indicate that the upper limit could not be defined as a result of insufficient data (especially in the seismic coverage).

4.1. Further exploration proposal

As a result of huge subsurface uncertainties in Kini field, this study highlighted key subsurface uncertainties in order of importance and then recommended exploration procedures as seen in Table 3.

Table 3. Key Subsurface uncertainties and the recommended data acquisition

Key subsurface uncertainty	Volume parameter	Recommendation
Geometry and size of Reservoir Tank	GRV	Seismic Data Acquisition
Fluid contact	GRV	Drilling well
Reservoir structure	GRV	Seismic Data Acquisition
Uncertainty in reservoir properties	Petrophysics	Drilling Well
Compartmentalization of the reservoirs	GRV	Drilling Well
Aquifer Activity	Petrophysics	Production test
Fault sealing	GRV	Drilling Well

As shown in Table 3, the major source of uncertainty in the area extent of the reservoir filled with hydrocarbon bearing, fluid contact, reservoir structure, compartmentalization and fault sealing. These create huge uncertainty in GRV. Other sources of uncertainty include reservoir properties and aquifer activity.

However, much effort should be focused on minimizing structural uncertainty as described below.

4.2. Seismic data acquisition

Due to uncertainty associated with the subsurface structure, additional 3D Seismic data covering a total area of about 1430000 square meters is proposed to be acquired at the northern and eastern segment of the field (Figure 7). This will help capture the reservoir structure, estimate the area extent of the hydrocarbon bearing zone and ultimately inprove confidence level in GRV estimates and hydrocarbon reserves.

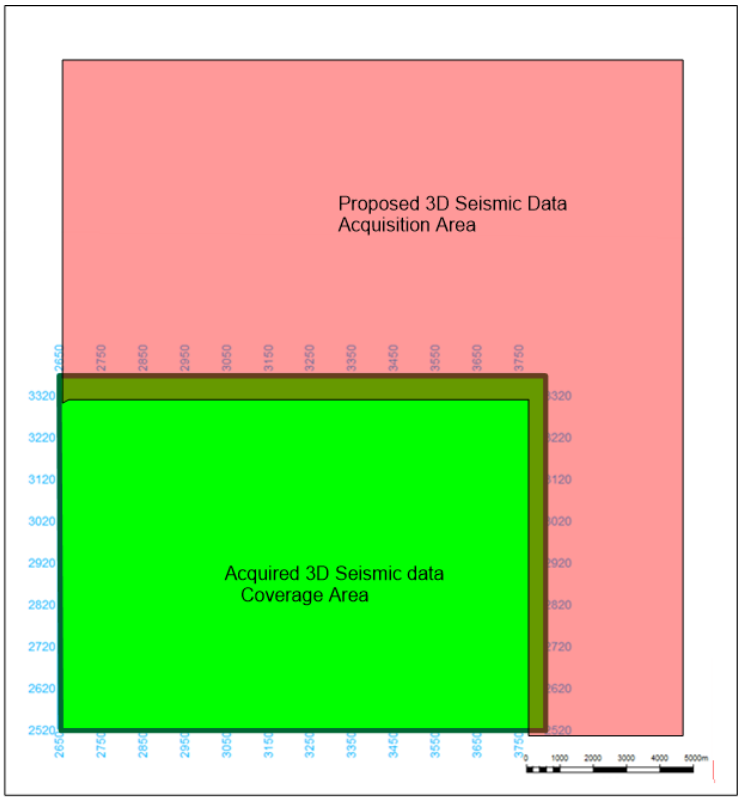

Fig. 7. Proposed 3D seismic data acquisition

4.3. Well drilling

Two appraisal wells (Kini-2 and Kini-3) are proposed down dip of Kini-1 after acquiring additional 3D seismic data and field re-evaluation to target fluid contacts in selected reservoirs, determine petrophysical properties and further explore deeper prospects (Figure 8). Kini-2 should be drilled first and the result obtained will determine whether to proceed with drilling Kini-3. However, the locations of the wells might change after interpreting the proposed seismic study.

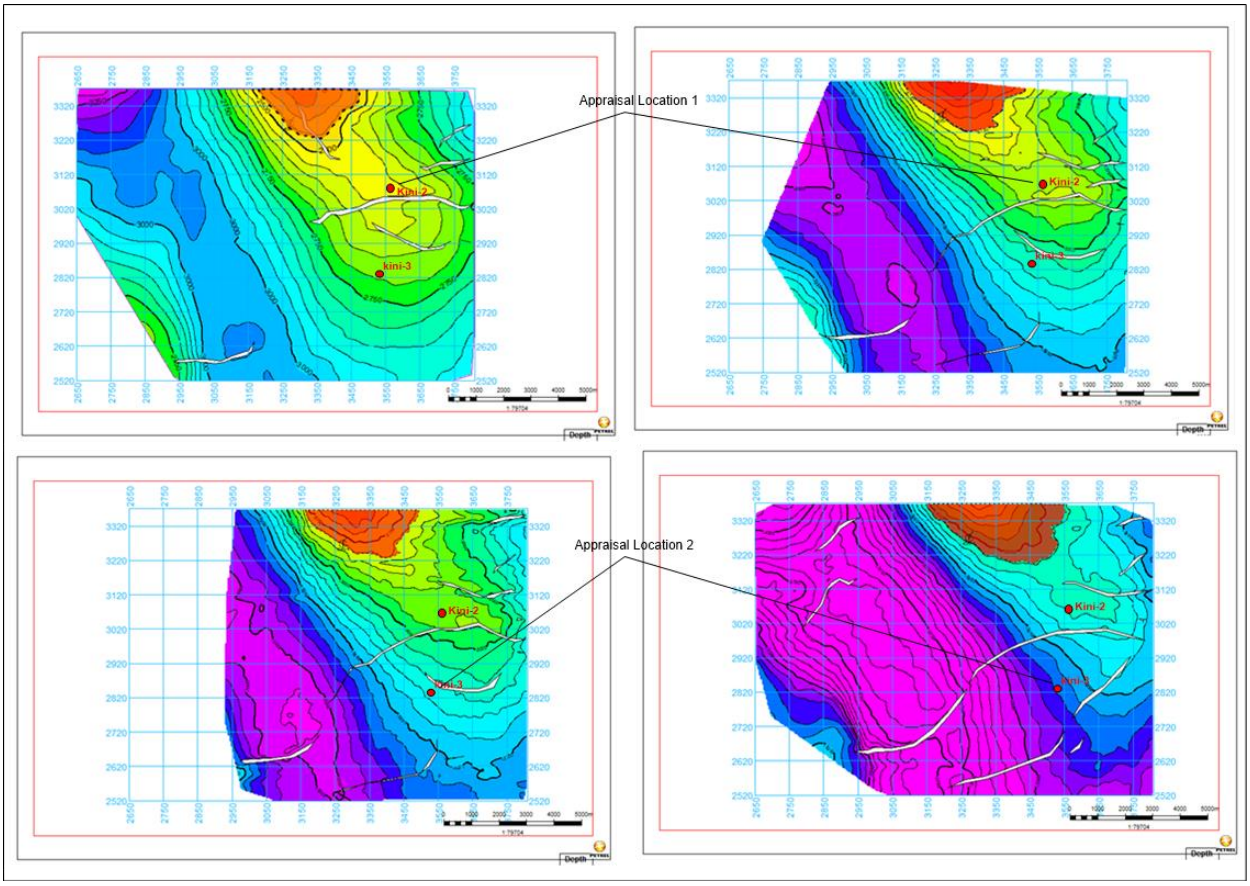

Fig. 8. Location of the proposed wells (Kini-2 and Kini-3 wells)

The exploration/appraisal program will help to estimate a more reliable range of in-place hydrocarbon volume by addressing the major subsurface uncertainty in Kini field which includes reservoir structure and trapping mechanism, area extent of the reservoir, fluid contacts, reservoir petrophysical properties, and compartmentalization. This procedure will impact decisions related to field development and translate into risk reduction, confidence building or higher profitability for the project.

5. Conclusions

This study was carried out using 3D seismic and well log data from one well to describe the subsurface features of the field and recommend on additional data to be acquired to reduce the major uncertainty highlighted in the present study. Four oil-bearing reservoirs (A, B, C, and D) were identified and evaluated for petrophysical characteristics. Kini-1 well encountered hydrocarbon in the selected reservoirs at oil-down-to (ODT) condition creating uncertainty in the fluid contact. Gross sand thickness ranges from 21 to 33 m with average NTG of 0.62. Porosity varies between 0.22 and 0.30 indicating that the reservoirs are of good quality with hydrocarbon saturation (S_h) between 69 to 76 %. The area of the zone covered by hydrocarbon was estimated using the top depth structure maps and was used to estimate low case GRV and hydrocarbon volume in-place. The present interpretation shows that synthetic faults in the field are E-W striking and south dipping while the antithetic faults are north dipping. The top structure maps of the selected reservoir show that the seismic data did not completely capture the overall extent of the reservoir structures and thus one could not properly describe the trapping mechanism and the area extent of the hydrocarbon bearing zone as the northern arm of the structure was not covered. However, the structure appears to be an NW-SE striking anticline penetrated at the crest by Kini-1 well. This suggests either a three-way, a four-way

dip closure or a combination trap and that there is no evidence that these faults controlled the fluid distribution. Since no fluid contact was established only low case GRV and hydrocarbon reserve was calculated using ODT of Kini -1 well and area restricted to available seismic. The huge uncertainty in the area extent of the hydrocarbon bearing interval and the fluid contact does not permit the definition of base and high case hydrocarbon volumes. Low case hydrocarbon cumulative minimum (low case) stock tank original oil-in-place (STOIIP) of the four reservoirs amount to 663 MMbl. These uncertainties are related to reservoir structure, area extent of the hydrocarbon bearing zone, fluid contact, compartmentalization and fault seal which created huge uncertainties in the GRV. To minimize the highlighted uncertainties, additional 3D seismic data covering an area extent of about 1430000 square meters was proposed to be acquired at the northern and eastern parts of the field. This is expected to result in structural uncertainty and help to more accurately estimate the GRV. Two appraisal wells (Kini-1 and Kini-2) were strategically positioned to target the fluid contact and also examine lateral variation in the petrophysical properties. This procedure will impact decisions related to field development and translate into risk reduction, confidence building or higher profitability in the field.

Acknowledgements

The authors thank College of Petroleum Engineering and Geosciences, King Fahd University of Petroleum & Minerals Saudi Arabia for the provision of valuable software.

References

[1] Adeoti L, Onyekachi N, Olatinsu O, Fatoba J, Bello M. Static reservoir modeling using well log and 3-D seismic data in a KN field, offshore Niger Delta, Nigeria. International Journal of Geosciences, 2014; 5:93–106.

[2] Amigun JO, Bakare NO. Reservoir evaluation of 'Danna' field Niger Delta using petrophysical analysis and 3D seismic interpretation. Pet Coal,20; 13 55:119–127.

[3] Sanuade OA, Akanji AO, Oladunjoye MA, Olaojo AA, Fatoba JO. (2017a) Hydrocarbon reservoir characterization of "AY" field, deep-water Niger Delta using 3D seismic and well logs. Arabian Journal of Geosciences, 2017; https://doi.org/10:151 DOI 10.1007/s12517-017-2941-0.

[4] Sanuade OA, Akanji AO, Olaojo AA, Oyeyemi KD (2017b) Seismic interpretation and petrophysical evaluation of SH field, Niger Delta. Journal of Petroleum Exploration and Production Technology,2017; https://doi.org/10.1007/s13202-017-0363-x.

[5] Shepherd M The reservoir framework. In: Shepherd M (ed) Oil field production geology. American Association of Petroleum Geologists Memoir,2009; 91: 81–92.

[6] Ihianle OE, Alile OM, Azi SO, Airen JO, Osuoji OU. Three dimensional seismic/well logs and structural interpretation over 'X-Y' field in the Niger Delta area of Nigeria. Science and Technology, 2013; 3:47–54.

[7] Oyedele K, Ogagarue D, Mohammed D. Integration of 3D seismic and well log data in the optimal reservoir characterization of "Emi" field, off shore Niger delta oil province, Nigeria. American Journal of Scientific and Industrial Research, 2013; 4: 11–21.

[8] Onayemi J, Oladele S. Analysis of facies and depositional systems of "Ray" field, onshore Niger Delta basin, Nigeria. 2014 edition of the Society of Exploration Geophysicists Technical Program (Expanded Abstract), Denver, Oct. 26-31 2014, p. 2724-2728.

[9] Doust H, Omatsola M. (1990) Petroleum geology of the Niger delta. In: Brooks, J. (ed.), Clastic Petroleum Provinces, Vol. 50: Geological Society of London 1990, Special Publications 50:365–365.

[10] Short K, Stauble A. Outline of geology of Niger delta. American Association of Petroleum Geologists Bulletin, 1967; 51, 761–779.

[11] Bustin R. Sedimentology and characteristics of dispersed organic matter in tertiary Niger delta: origin of source rocks in a deltaic environment. American Association of Petroleum Geologists Bulletin,1988; 72:277–298.

[12] Ekweozor CM, Okoye NV. Petroleum source-bed evaluation of Tertiary Niger Delta. American Association of Petroleum Geologists Bulletin,1980; 64:1251–1259.

[13] Evamy B, Haremboure J, Kamerling P, Knaap W, Molloy F, Rowlands P. Hydrocarbon habitat of tertiary Niger delta. American Association of Petroleum Geologists Bulletin,1978; 62:1–39.

[14] Adelu AO, Sanuade OA, Oboh EG, Offeh EO, Adewale T, Mumuni OS, Oladapo IM, Omolaiye, EG. Hydrocarbon field evaluation: case study of 'Tadelu' field shallow offshore Western Niger Delta, Nigeria. Arabian Journal of Geosciences, 2016; 9:116.
[15] Corredor F, Shaw JH, Bilotti F. Structural styles in the deep-water fold and thrust belts of the Niger Delta. American Association of Petroleum Geologists Bulletin,2005; 89:753–780.
[16] Stacher P. Present understanding of the Niger delta hydrocarbon habitat: Geology of Deltas. AA Balkema, Rotterdam 1995, 267 p.
[17] Tuttle ML. Charpentier RR, Brownfield ME. The Niger delta petroleum system: Niger delta province, Nigeria, Cameroon, and Equatorial Guinea, Africa. Open-file report 99-50-H, U.S. Geological Survey, Reston 1999, 65 p.
[18] Whiteman A. Nigerian petroleum geology, resources and potential. Graham and Trotman 1982, 166 p.

To whom correspondence should be addressed: Oluseun A. Sanuade, Geosciences Department, College of Petroleum Engineering & Geosciences, King Fahd University of Petroleum & Minerals, Dhahran, Saudi Arabia, sheunsky@gmail.com; oluseun.sanuade@kfupm.edu.sa

Petroleum and Coal

Article **Open Access**

EVALUATION OF HYDROCARBON CONTAMINATION OF SELECTED WATERS OF UGWUEME AND LOKPANTA IN ENUGU NIGERIA AND ITS SPREAD MECHANISM

*Chinenye F. Onyeabor[1], Kovo G. Akpomie[2]**

[1] *Department of Geology and Minning, Enugu State University of Science and Technology, Enugu, Nigeria*
[2] *Department of Pure and Industrial Chemistry, University of Nigeria, Nsukka, Nigeria*

Received March 23, 2018; Accepted May 31, 2018

Abstract

This evaluation was aimed at the determination of organic contaminants in water bodies in Ugwueme and Lokpanta in Enugu, Nigeria. The analytical study involved the sampling of water bodies both from both locations in order to conduct a comparative and qualitative study of the organic pollutants of the area..The points of sampling include; Oguta river, Lokpanta, Ugwueme spring, Seepage point at Ugwueme, Ugwueme stream and Obilagu river. The obtained result showed in mg/L; phenol (137.93 to 168.58), COD (4.07 to 9.95), BOD (11.89 to 23.99), synthetic detergent (59.6 to 74), grease (0.02 to 0.08%), pH (6.4 to 6.8), Cl (7.81 to 8.56), Br (0.19 to 0.2), asphalthene (133.2 to 178.4), ethylene (125.8 to 180.3), benzene (15.15 to 36.34), tetramethylene (77.3 to 159.1) and naphthene (10.7 to 17.2). The spread flow varied with respect to distance and altitude from the oil seep. The result revealed that the oil seep migration does not flow only at the seen point but gradually soaks into the Owelli from other parts of the contact. The close range of the organic parameter investigation confirms that the seep affects the entire mapped area, thus affecting the waters in the study area adversely showing polluted water.

Keywords: *Ugwueme-Lokpanta; organic contaminant; spread mechanism; oil seep.*

1. Introduction

It is a known fact that without water, the biosphere cannot be sustained; water is life. The water accessible to humans is basically surface and ground water. The surface waters are usually contaminated due to exposure to agents of contamination and possibly pollution. In south eastern Nigeria, there are available water bodies utilized by the local populace, such as Ugwueme and Lokpanta waters. The acessessment of the pollution level of such water is therefore necessary since its been utilized by the people. Ozoko and Onyeabor [1] in their work, considered the inorganic elements of Ugwueme surface and groundwater systems and confirmed them safe and potable. Although they recommended that the organic content ought to be checked in subsequent studies. However, research on the organic content of these water bodies is yet to be established. Ugwueme is a notable town in eastern Nigeria which experiences oil seep draining into the neighborhood streams. This was first observed by Reyment [2], in his work, he described the entire area (including Lokpanta and Ngusu and their environs) as oil soaked/oil bearing sandstone. The seep is observed at the base of Owelli Sandstone [1-2]. Ekweozor and Unomah [3] described the area as oil shale deposit of Eze-Aku Shale; having the oil soaked Owelli Sandstone overlying uncomfortably on the shales of the Eze-Aku. The total organic carbon (TOC) of the oil-soaked formation ranges from 0.07 to 1.13wt% with kerogen type 111, thus generating more gas compared to oil within optimal thermal maturity [4]. The thickness of the oil band increases from Ugwueme to Lokpanta in a S.E. direction via the exposed scarp at Ugwueme and core drilling at Lokpanta [2]. This is a low threshold for exploitation, but a high pollution threshold when exposed to the drainage of

the area. This drainage is absorbed by the soil, hence affecting both the soil and the vegetation. Okeke and Enoh [4] in their work observed the decrease in vegetation cover of Ugwueme over the years (1996 to 2016) due to hydrocarbon seepage effect on the vegetation. The Lokpanta oil shales were also enriched in some potentially hazardous trace elements; V, Cr and Ni, which according to Sonibare *et al.* [5] are not the same with what is obtainable in oil shale from other parts of the world. The study was therefore aimed at investigating the hydrocarbon content of Ugwueme and Lokpanta water bodies and their spread mechanisms to provide information on the organic contaminant levels of such useful waters.

2. The study area

2.1. Location and study extent

The study area lies within latitude $5^{0}57^{1}$N to $6^{0}02^{1}$ and longitude $7^{0}25^{1}$E to $7^{1}30^{1}$E covering an area extent of about 85.25km on a scale map of 1:25,000 (Fig 1). The study area includes Ugwueme town, Lokpanta, and fringes of Lekwesi. Lokpanta and Lekwesi are situated towards the valley of the escarpment while Ugwueme is situated on the escarpment.

The area is accessible via the Enugu–Port-Harcourt express road, Enugu, Nigeria. Ugwueme is about 2km east of the Enugu-Port-Harcourt express road, making a haphazard link to Ugwueme-Amuda-Mbala road through the Y junction along the express road. The Lokpanta and Lekwesi axis could be rightly accessed via Awgu-Orji river road which passed through Mgbidi town. It has an estimated population of about 15,000 people [6] and found at the hill /top of the Awgu escarpment, about 7.5km south of Awgu market in Awgu town which host the local government headquarters of the area. Ugwueme town is strategically located on top of the Awgu cuesta and is underlain by iron stone beds with other sedimentary facies.

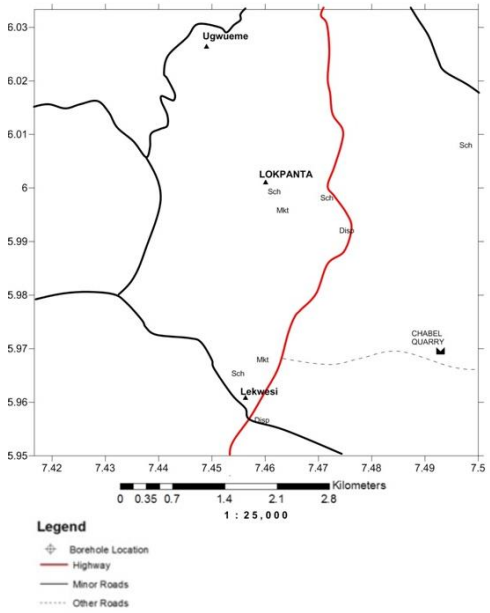

Fig.1. Accessibility map of Ugwueme-Lokpanta, Southeastern Nigeria

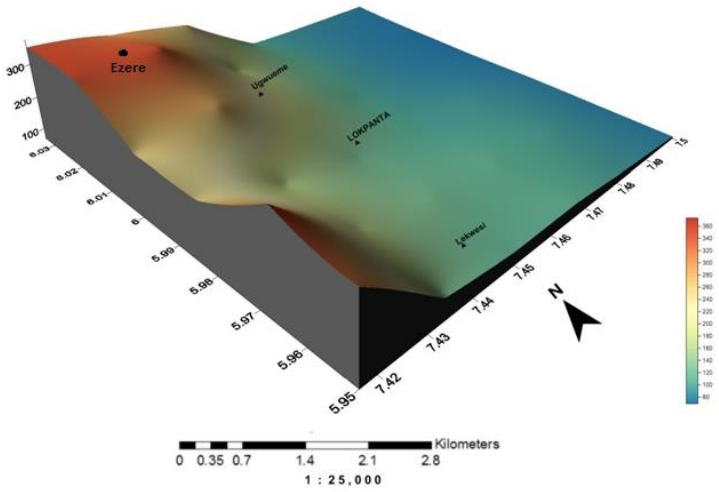

Fig. 2. Elevation map of Ugwueme-Lokpanta, Southeastern Nigeria

2.2. Physiography, climate, and vegetation

The study area has steep highlands at the escarpment area which includes Ezere, Nkwe, Mbala and Ugwueme towns of the study and also low lying plains. The low lying plains are basically found within the Lokpanta and Lekwesi axis of the map (Fig.2). The area is dominantly characterized by high, rugged and undulating topography which are in place due to the area's geomorphology and the tectonic folding and faulting of the Santonian age. The peak height is at Achara (350m, $N6^{0}0^{1}53^{11,}$ and $E7^{0}23^{1}49^{11}$) while the lowest is located around

Lekwesi (93m, N5^{0}58^{1}34.6^{11,} and E7^{0}28^{1}10.4^{11}). The major climatic conditions are the wet season (April to September) and the dry season (November to March). The average mean annual rainfall data in the area (2009 – 2015) ranges from 1750 to 2000mm [7]. The dry season which is characterized by little or no rainfall, high sunshine, and dryness is associated to the North-easterly trade wind of the Sahara. The study area is enveloped by the woodland and tall grasses of the Guinea Savanna [7]. Plants show luxuriant growth at the base of the valleys and spurs, and progressively become sparse at the escarpment. The luxuriant growth is dominated by grasses and few trees. Over the years, the vegetation in the area has supported the cultivation of crops such as cassava, vegetables, cashew and root tubers. The area is drained by several streams such as Obae, Iyiohimiri, Ngene Uhie, Ogwunnu, Ndumoku, Aguta-Lokpanta and Echie streams in a dendritic pattern, which took its source from the top of the escarpment (Fig.1). They all drain into the surface water flow of the NE-SW trending water shed created by the Awgu-Lokpanta escarpment hence, flowing westward into Igwu River, Abia state and eastward into the Ivo River in Ebonyi state.

2.3. The geology

The geology of Ugwueme and its environs is elucidated in the geologic map (Fig 2). Ugwueme is underlain by several lithological facies and four formations. These facies are; the dark gray shale, coarse grained sandstone, medium grained sandstone, heterolith sediments and white cross bedded sandstone while the formations are Awgu Shale, Owelli Sandstone, Mamu Formation and Ajalli Formation. Dark gray carbonaceous fissile shale with inclusions of sandstone and limestone cobbles are obvious along the stream sections, southeastern part of the map (Lokpanta-lekewsi). The shales are fissile, bluish grey, pyritic, calcareous, micaceous and occasionally gypsiferous [2]. The coarse grained sandstone is poorly sorted angular to sub-angular in shape with the incidence of quartz pebbles which are positively skewed. It appears dark coloured in some places. This lithologic unit is obvious around the border lines (elevations) between Ugwueme and Lokpanta maintaining a peak value (height of 300m). Ripple marks, orphiomorpha burrows and pelecipod inoceramus impressions are found within this facie [2]. This coarse grained sandstone is extended to Awgu town. There is the presence of oolitic iron stone capping the Owelli Sandstone. The medium grained sandstone is poorly sorted while the heterolith facies are assemblages of siltstone, clay, shale, mud, and ironstone. The friable unit is poorly sorted and angular to sub-angular in shape.

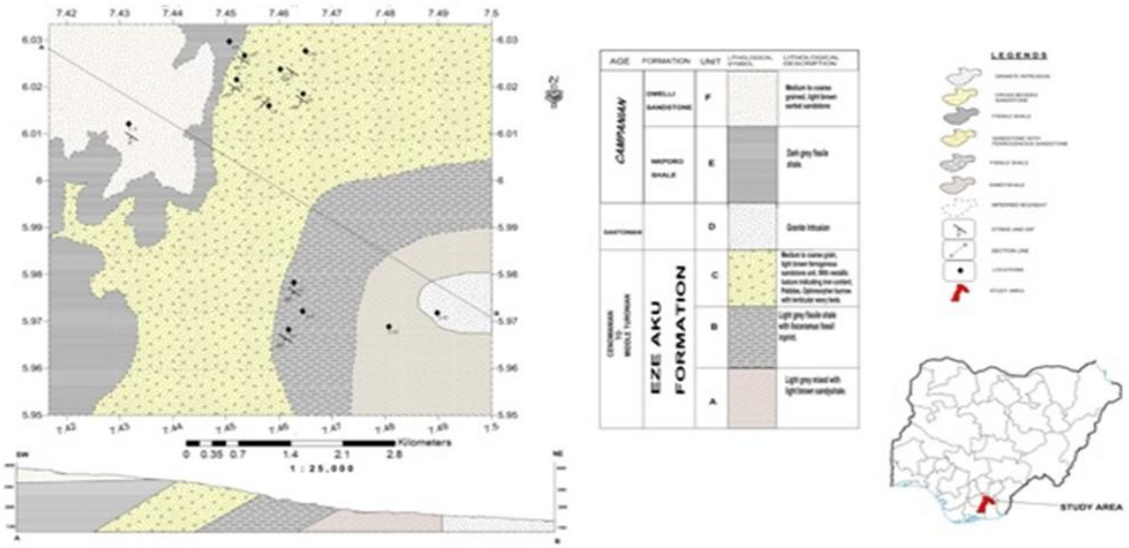

Fig.3. Geologic map of Ugwueme-Lokpanta, Southeastern Nigeria

At some points ($N6^{0}0^{1}28^{11}$ and $E7^{0}26^{1}53^{11}$), the coarse sandstone reveals resemblance of dark coloration which is attributed to oil stain. This was supported [2], according to the report, at a distance of 6km south of Awgu, oil seepage issues at the base of Owelli Sandstone was described at that point as coarse grey, the basal bed which rests uncomformably on the folded shales. This is located at the escarpment, between the Awgu Shale and Owelli Sandstone just before Lokpanta town. The oil seepage at Ugwueme is geo-referenced Lat.$06^{0}01^{1}47.5^{11}$N and Long. $07^{0}27^{1}18.7^{11}$E. The regional trend is NE-SW trend with an average dip of 8^{0} and a synclinal fold around Lokpanta. The heterogeneous facies are obvious at the Mmamo stream section. The afore mentioned facies are correlatable to the Awgu shale, Npkoro shale/Owelli sandstone, Mamu formation and Ajali formation (Fig.3) [2,8]. The study area is dissected by an NE-SW trending watershed of the Awgu-Lokpanta escarpment. This is drained by Obae, Ngene-Uhie, Ogwunnu, Oyiohimiri, Oguta, Obilagu and Echie streams which took its source from the sandstone unit at the scarp face of the escarpment and washes into the Ivo river in Ebonyi state. The Mmamo and Ngene meander through spurs and valleys into Awgu river in Mbala Isuochi Abia state.

3. Materials and methods

A desk study of the area was conducted, followed by field work and laboratory analysis of water samples for the organic pollutant. The field work involved the delineation of lithological facies and identification of the streams in order to checkmate the time/distance organic contamination of the water bodies consumed by the Locals.

Five water samples (including the water body directly receiving the seepage, (Fig.4.) were obtained with respect to topography, infiltration, recharge and discharge points. Organic parameters such as Biochemical Oxygen Demand (BOD), Chemical Oxygen Demand (COD), asphaltthene, ethylene, benzene, tetramethylene, naphthene and organic halogens were analyzed. Nitrogen quantification was done using Micro-Kedjehl method [9]. The pH was measured with Hanna 98127. The BOD was obtained via the difference between the initial oxygen in the sample and final oxygen after 5 days of incubation at 27^{0}C. Gravimetric method [10] using n-hexane was used to measure the grease content while the synthetic detergent was obtained using methylene method, using alkyl benzene sulphonate and methylene blue in a soluble chloroform complex to determine the colour for spectrophotometric reading at a wavelength of 560nm. The Chemical Oxygen Demand (COD) was determined via incubation of K-dichromate for 6 hrs before measuring the absorbance in a standard curve at an absorbance of 520nm. All the other parameters (asphalthene, ethylene, benzene, organic halogens and tetramethylene) were prepared with the standard reagents for each, before reading the measurement in a UV-spectrophotometer (model 752p Techmel & Techmel USA) at variously recommended wavelength [11] except for chlorine which was determined using the titrimetric method with silver nitrate.

Fig.4. Oil seepage at Ugwueme

4. Results and discussion

The results obtained from the physicochemical analysis are tabulated in Table 1. The results in mg/L showed phenol ranging from 137.93 to 149.43, COD.; 4.07 to 9.95, BOD; 11.89 to 23.99, synthetic detergent; 59.6 to 74, % grease; 0.02 to 0.08, organic halogens: Cl; 7.81 to 8.56 and Br; 0.19 to 0.2, asphalthene; 143.2 to 212.5, ethylene; 125.8 to 180.3, benzene; 15.15 to 36.34, tetramethylene; 77.3 to 159.1 and naphthene; 10.7 to 15.6. The peak values reside within the seepage point and the stream it flows into except for synthetic detergent, pH, ethylene and tetramethylene an indication that the seepage occurs beyond the observed point at Ugwueme (Lat.$06^{0}01^{1}47.5^{11}$N and Long. $07^{0}27^{1}18.7^{11}$E). The Biochemical Oxygen Demand (BOD) and COD are very useful parameters in accessing the quality of water bodies. Both parameters are known to affect directly the amount of dissolved oxygen (DO) available in the water. The greater the BOD and COD the more rapidly oxygen is used up in the water, and this implies corresponding decrease in the DO value and the less oxygen available to aquatic life. The BOD values were higher than the WHO recommended limit 15mg/L except that obtained for the stream along hydrocarbon contaminated seepage point. This could have an adverse effect on aquatic lives. However, the COD values were all within the WHO recommended a range of 40 mg/L [12].

Table 1. Physicochemical analysis of the water bodies

Parameters	ROGT	UGS	HCSP	SAHCSP	ROBL
pH	6.8	6.6	6.4	6.5	6.7
Phenol	149.4	141.5	168.6	137.9	148.7
COD	4.07	5.41	9.95	6.68	4.21
BOD	23.8	20.0	21.0	11.9	23.9
Grease	0.04	0.02	0.02	0.08	0.04
Organic-Cl	8.41	8.17	7.81	8.56	8.32
Organic-Br	0.2	0.2	0.19	0.2	0.2
Ethylene	180.3	125.8	145.8	146.2	164.5
Benzene	22.7	33.3	15.15	36.63	20.4
Tetramethylene	159.1	77.3	145.6	157.6	82.4
Naphthene	15.8	14.95	10.7	17.2	15.2
Asphalthene	151.1	165.1	212.5	178.4	143.2

**ROGT=River Oguta, UGS=Ugwueme spring, HCSP=Hydrocarbon seepage point, SAHCSP= stream along hydrocarbon contaminated seepage point, ROBL= River Obilagu, All parameters are in Mg/L except pH and grease (%).*

The variation maps (Fig. 5 and 6) showed the peak points, and the spread pattern as across a given spread as mixing and dilution occur along the drainage system. A synthetic detergent which serves as a natural cleanser has a better residence in the moving waters (the rivers) hence providing a soapy cleanser function therein. The grease value is relatively low, and the pH values are close to 7.0. The required oxygen of BOD and COD are beyond the detection limits; peaks at the seepage point for COD and at River Obilagu for the BOD. The corrosive, poisonous compound (C_6H_5OH) which is usually present in tars of coal and wood exceeded the permissible limits. Fig. 5 shows an enclosure at the seepage point indicating high phenol content at the point of seepage and its progressive dilution in different water bodies. The organic halogens are closely ranged, with the point of seepage in both bromine and chloride having the lowest values (Fig. 5). Ethylene has its peak at River Oguta with an elevation of 103m and lowest at Ugwueme spring (elevation: 203m). This is an indication that the oil seep predominates the contact between the Owelli Sandstone and Agwu Shale and Owelli Sandstone and Eze-Aku Shale where it uncomformably overlies the Eze-Aku. Benzene, an aromatic hydrocarbon is found beyond the detection limits in all the samples and having its peak in the stream. The tetramethylene and naphthalene are organic compounds with simple polycyclic aromatic hydrocarbons. They are toxic to animals via putative toxicity [13].

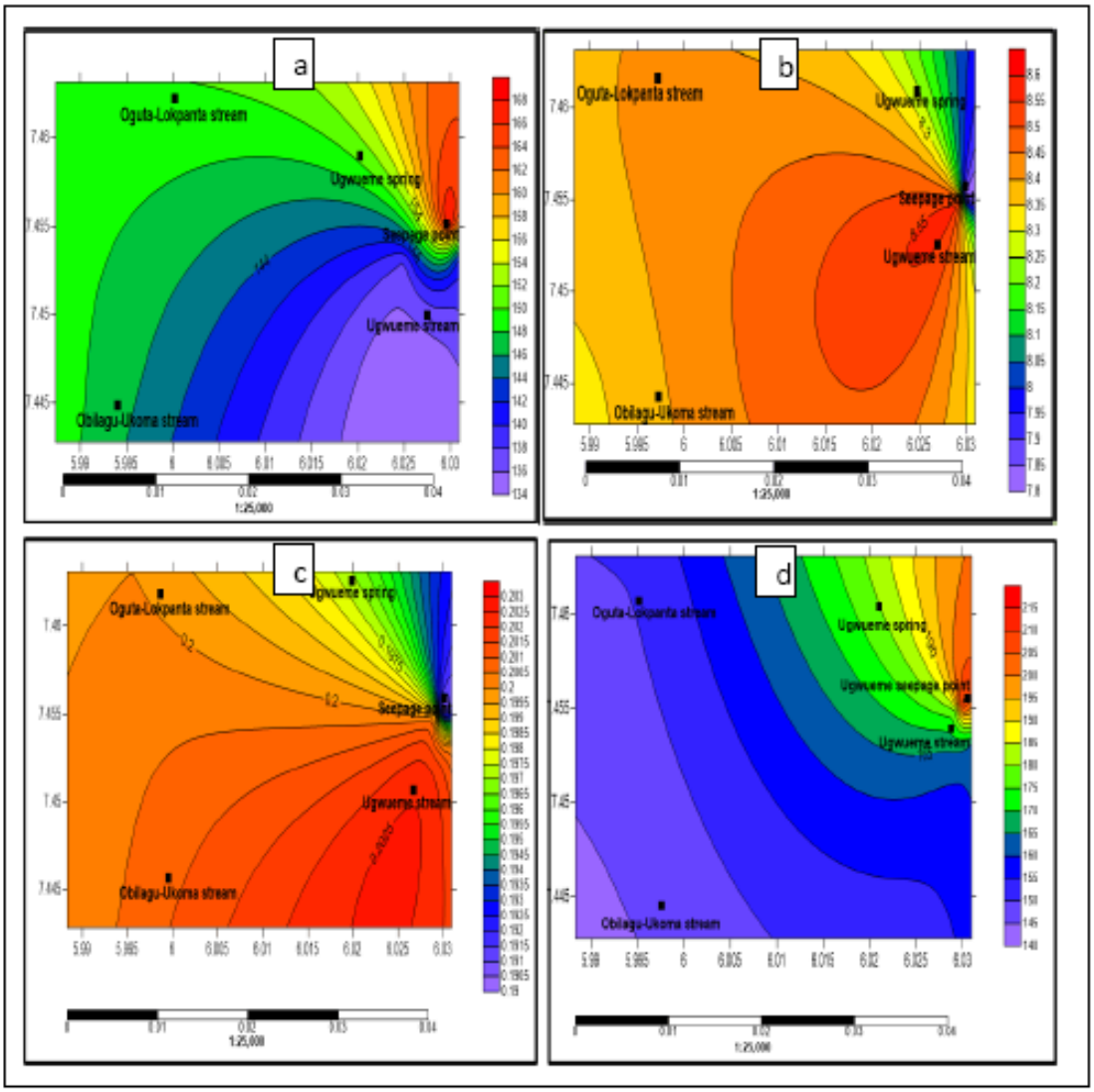

Fig 5. Spread map of (a) phenol (b) oranic chlorine (c) organic bromine (d) asphalthene

5. Conclusion

The above maps represent the interaction between sample locations and the organic contaminants. The enclosure of the map indicates a peak area from where contaminants migrate to other areas. As can be observed from the generated contour maps, the Ugwueme seepage point has most of the high concentration of all the tested hydrocarbon contaminants. Samples from the other locations; Oguta-Lokpanta, Ugwueme Stream and River Obilagu, contains organic parameters which range from trace amount to significantly high amounts. It varies in the concentration of hydrocarbon with respect to distance from seepage point and altitude. The hydrocarbon in Ugwueme stream channels is beyond the detection limit, hence affecting the biosphere through the water system, soil, and vegetation. It is recommended that further research should be conducted on the biochemical impact of this contamination on the indigene's health.

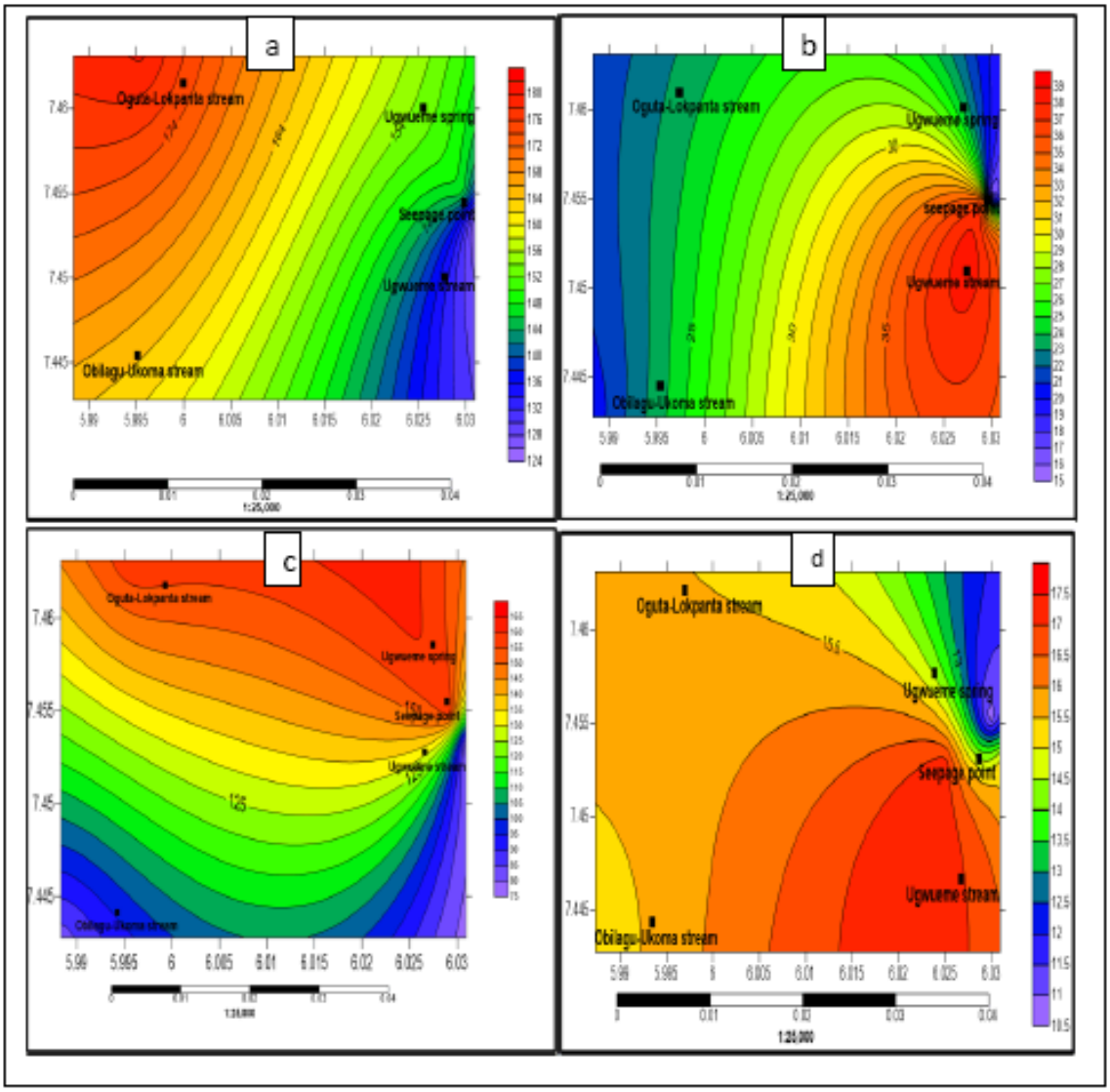

Fig 6. Spread map of (a) ethylene (b) benzene (c) tetramethylene (d) napthene

References

[1] Ozoko D, and Onyeabor C. Water Quality Assessment of Ugwueme surface and ground water system. International Journal of Science and Research, 2017;6(9): 833-838.

[2] Reyment RA. Aspects of the Geology of Nigeria. University of Ibadan Press 1965. P.48-60.

[3] Ekweozor CM, and Unomah GI. (1990). First discovery of oil shale in the Benue Trough, Nigeria. Fuel, 1990; 69(4): 502-508.

[4] Okeke FI, and Enoh MA. (2016). Analysing the effect of hydrocarbon seepage on vegetation in Ugwueme town, Awgu Local Government Area of Enugu State using Normalized Differencing Vegetation index (NDVI) threshold classification method. Int. J. multidisciplinary Research and Modern Education, 2016; 2(2): 446-454.

[5] Sonibare OO, Jacob DE, Ward CR, Foley SF. Mineral and trace elements composition of the Lokpanta oil shale in the Lower Benue Trough, Nigeri. Fuel, 2011; 90: 2843- 2849.

[6] National Population Commission of Nigeria (2006).

[7] Rain data (2015). Geography and meteorology department, Enugu State University of Science and Technology, Agbani, Enugu, Nigeria.

[8] Nwajide CS. Geology of Nigeria's Sedimentary Basin. C.S.S. Bookshops Limited, 2013. ISBN: 978-987-8410-67-4. Pp565.
[9] Miller L, and Houghton JA. The Micro- Kjeldahl Determination of the nitrogen content of amino acids and proteins. J. Biol. Chem., 1945; p.159; 373-383.
[10] Harvey D. Analytical Chemistry. MIT Press 1959: Cambridge, MA. p.355-409.
[11] Miller JN, Basic Statistical Methods for Analytical Chemistry, Part 2. Calibration and Regression Methods, A Review. Analyst, 1995:116 .
[12] World Health Organization (WHO), The world report: shaping the future, World Health Organization, 1211, Geneva 27, Switzerland (2003).
[13] Vincente JA, Peixoto F, Lopes ML, and Madeira VMC. Differential sensitivities of plant and animal mitochondria to the herbicide paraquat. Journal of biochemical and molecular toxicology, 2001; 15(6): 322-330.

To whom correspondence should be addressed: Dr. Kovo G. Akpomie, Department of Pure and Industrial Chemistry, University of Nigeria, Nsukka, Nigeria

Petroleum and Coal

Article **Open Access**

EXISTENCE AND UNIQUENESS OF SOLUTION FOR MOLECULAR DIFFUSION OF CO_2 IN CH_4 UNDER UNKNOWN BOUNDARY CONDITIONS IN ENHANCED GAS RECOVERY (EGR) PROCESS

Amirabbas Mohammadi[1], Abdullah Shidfar[1], Amir H. Mohammadi [2]

[1] School of Mathematics, Iran University of Science and Technology, Tehran, Iran
[2] Discipline of Chemical Engineering, School of Engineering, University of KwaZulu-Natal, Howard College Campus, King George V Avenue, Durban 4041, South Africa

Received April 30, 2018; Accepted June 27, 2018

Abstract

This study is intended to provide a one-dimensional inverse nonlinear problem to investigate molecular diffusion of CO_2 in CH_4 in a hydrocarbon reservoir. Generally, boundary fluxes at the top and the bottom of the reservoir are non-zero. Furthermore, it is not practically possible to identify the exact boundary conditions, therefore we are faced with an inverse problem which is discussed with two non-zero and unknown boundary conditions via the auxiliary problems. We will consider the case where the governing boundary conditions are defined as $f(u(0,t))$ and $f(u(1,t))$ so that u and f are unknown . We will provide the conditions for f where the desired problem has a unique solution. Assuming an over-specified data $u(0,t)=\psi(t)$ with several admissible conditions for ψ , we will prove the existence and uniqueness of solution (u^*, f^*) for the problem. In order to achieve this goal, we will demonstrate that a defined transfer T_ψ has a unique fixed point. Accordingly, we need to prove that T_ψ is a contraction. During this process, we will apply the other governing equations and functions such as Abel integral equation, Jacobi function, Volterra operators, Lipschitz function and Holder function on the discussed inverse problems.

Keywords: *Molecular Diffusion; Fick's first law; Fixed point; Contraction; Jacobi function; Volterra operator; Abel equation; Lipschitz function.*

1. Introduction

One of the most practical methods for EGR (Enhanced Gas Recovery) from a hydrocarbon reservoir, is CO_2 injection in the reservoir. In this method, high pressure CO_2 is injected in the reservoir, and the remaining hydrocarbon flows into the wellbore. About 80% (or more) of natural gas is methane (CH_4). Therefore a molecular diffusion between CO_2 and CH_4 can be introduced. At $t=0$ under the known temperature and pressure, the density of CO_2 is more than CH_4 , thus a vertical diffusion will occur between the gases. When the gas equilibrium is reached, the process will stop.

In this study, we assume that the reservoir is horizontal and uniform. Also, its upper half and lower half are respectively filled by pure methane and pure carbon dioxide. Uniformity of the reservoir means that the pressure and temperature are constant, so the gases have the same and fixed temperature.

Fick's first law will govern the behavior of each of the gases. On the other hand, we are faced with a vertical diffusion in the reservoir so the resulted diffusion equation will be one-dimensional nonlinear equation (ODE) which along with the governing boundary conditions will show a type of nonlinear inverse problems (NIP). In addition, it is not practically possible to identify the exact boundary conditions, thus this problem will be discussed with unknown

boundary conditions. In recent years, an important mathematically challenging and well-studied class of these problems is, to prove the existence and uniqueness of solution and investigate the unknown functions that appear in the partial differential equations. In this regard, one may find some studies in the literature which have been often carried out on heat conduction problems. For example, Rosch has investigated the identification of unknown boundary functions as optimal control problems [1-2]. Some researchers have employed the boundary element method to approximate the unknown boundary functions [3-4].

2. Mathematical formulation [5-6]

We consider that:

a) Attribute 1 is for CO_2 and attribute 2 is for CH_4.

b) l: Thickness of the reservoir

c) D_{12}: Effective diffusion coefficient of the composition of two gases.

d) ρ: Mass density of the composition of two gases.

e) ρ_i : Mass density of i^{th} the gas $i=1,2$

f) C_i: Concentration of i^{th} gas $i=1,2$

g) C : Concentration of the gas composition

h) J_i^*: Molar concentration of i^{th} gas $i=1,2$

i) z : Height

j) Δx_i : Mole fraction of i^{th} gas $i=1,2$

k) v_i: Speed of i^{th} gas $i=1,2$

l) N_i: Molar flux of i^{th} gas $i=1,2$

m) $\overline{V_i}$: Partial molar volume of i^{th} gas $i=1,2$

n) v^*: Molecular velocity

Generally, D_{12} is a function of temperature and pressure of the gas composition. When we ignore the changes in pressure and temperature and assume that the reservoir is uniform, we actually consider D_{12} is constant. We follow the problem assuming that D_{12} is constant.

As we know N_i and J_i^* are respectively defined as follows:

$$N_i = C_i v_i \qquad i=1,2 \qquad (1)$$

$$J_i^* = C_i(v_i - v^*) \qquad i=1,2 \qquad (2)$$

We put in the recent equation the following relation:

$$v^* = \frac{\sum_{j=1}^{2} C_j v_j}{C} \qquad (3)$$

And then, we have:

$$J_i^* = C_i v_i - \frac{C_i}{C}\sum_{j=1}^{2} C_j v_j \qquad i=1,2 \qquad (4)$$

Regarding $x_i = \frac{C_i}{C}$, $i = 1,2$ and (1):

$$J_i^* = N_i - x_i \sum_{k=1}^{2} N_k \qquad i = 1,2 \qquad (5)$$

Now, if ρ is constant (uniform mass density), Fick's first law will be defined according to the following equation:

$$J_i^* = -D_{12} \frac{\partial \rho_i}{\partial z} \qquad i = 1,2 \qquad (6)$$

In the case that ρ is not constant, the law will be stated as follow:

$$J_i^* = -CD_{12} \frac{\partial x_i}{\partial z} \qquad i = 1,2 \qquad (7)$$

In the more general case, we assume that ρ is not constant. According to equations (5) and (7):

$$N_i = x_i \left(N_1 + N_2\right) - CD_{12} \frac{\partial x_i}{\partial z} \qquad i = 1,2 \qquad (8)$$

In addition, the following equation is for N_i and $\bar{V}_i$:

$$\bar{V}_1 N_1 + \bar{V}_2 N_2 = 0 \qquad (9)$$

Using equations (8) and (9), we have:

$$N_1 = \frac{-CD_{12} \frac{\partial x_1}{\partial z}}{1 - x_1 \left(1 - \frac{\bar{V}_1}{\bar{V}_2}\right)} \qquad (10)$$

Similarly:

$$N_2 = \frac{-CD_{12} \frac{\partial x_2}{\partial z}}{1 - x_2 \left(1 - \frac{\bar{V}_2}{\bar{V}_1}\right)} \qquad (11)$$

If the concentration of each of the gases is shown as $C_i = C_i(z,t)$, $i = 1,2$, as the concentration of the gas composition is fixed, we can write

$$C_1(z,t) + C_2(z,t) = C. \qquad (12)$$

On the other hand $C_i = Cx_i$ so $x_1 + x_2 = 1$. Therefore, equations (10) and (11) can be written:

$$N_1 = \frac{-D_{12} \frac{\partial C_1}{\partial z}}{1 - x_1 \left(1 - \frac{\bar{V}_1}{\bar{V}_2}\right)} \quad \text{and} \quad N_2 = \frac{-D_{12} \frac{\partial C_2}{\partial z}}{x_1 + (1 - x_1) \frac{\bar{V}_2}{\bar{V}_1}} \qquad (13)$$

Regardless of chemical reactions, Molar balance equation would be:

$$\frac{\partial C_i}{\partial t} + \frac{\partial N_i}{\partial z} = 0 \qquad (14)$$

Substituting equation (13) in equation (14), we have:

$$\frac{\partial C_1}{\partial t}+\frac{\partial\left(\frac{-D_{12}\frac{\partial C_1}{\partial z}}{1-x_1\left(1-\frac{\bar{V}_1}{\bar{V}_2}\right)}\right)}{\partial z}=0 \quad \text{and} \quad \frac{\partial C_2}{\partial t}+\frac{\partial\left(\frac{-D_{12}\frac{\partial C_2}{\partial z}}{x_1+(1-x_1)\left(\frac{\bar{V}_2}{\bar{V}_1}\right)}\right)}{\partial z}=0 \tag{15}$$

As for the ideal gases, $\bar{V}_i$ is constant:

$$\bar{V}_i=\frac{RT}{P} \qquad i=1,2 \tag{16}$$

So (15) can be written as:

$$\frac{\partial C_i}{\partial t}+\frac{\partial\left(-D_{12}\frac{\partial C_i}{\partial z}\right)}{\partial z}=0 \qquad i=1,2 \tag{17}$$

Finally, we have the diffusion equation as follow:

$$\frac{\partial C_i}{\partial t}=D_{12}\frac{\partial^2 C_i}{\partial z^2} \qquad i=1,2 \tag{18}$$

Now, we consider boundary flows at the top and the bottom of the reservoir. In other words, we have the following boundary conditions (fluxes at the top and bottom of the reservoir is not zero):

$$\left.\frac{\partial C_i}{\partial z}\right|_{z=0}=g_{i0}(t) \quad \text{and} \quad \left.\frac{\partial C_i}{\partial z}\right|_{z=l}=g_{i1}(t) \quad i=1,2 \tag{19}$$

In real terms, $g_{i0}(t)$ and $g_{i1}(t)$ cannot be accurately identified. So, in this case, we are faced with an inverse problem with the boundary conditions. Assuming $\tilde{t}=\frac{D_{12}}{l}t$ and $\tilde{z}=\frac{1}{l}z$, we define $\tilde{C}_i$ so that $\tilde{C}_i(\tilde{z},\tilde{t})=\frac{l}{C}C_i(z,t)$. Now we can write:

$$\frac{\partial C_i}{\partial t}=\frac{CD_{12}}{l^2}\frac{\partial \tilde{C}_i}{\partial \tilde{t}} \quad \text{and} \quad \frac{\partial C_i}{\partial z}=\frac{C}{l}\frac{\partial \tilde{C}_i}{\partial \tilde{z}} \qquad i=1,2 \tag{20}$$

On the other hand:

$$\frac{\partial C_i}{\partial t}=\frac{CD_{12}}{l^2}\frac{\partial \tilde{C}_i}{\partial \tilde{t}}=\frac{1}{l}\frac{\partial}{\partial \tilde{z}}\left(D_{12}\frac{C}{l}\frac{\partial \tilde{C}_i}{\partial \tilde{z}}\right)=\frac{CD_{12}}{l^2}\frac{\partial^2 \tilde{C}_i}{\partial \tilde{z}^2} \qquad i=1,2 \tag{21}$$

Regarding equation(20) we can result:

$$\frac{\partial \tilde{C}_i}{\partial \tilde{t}}=\frac{\partial^2 \tilde{C}_i}{\partial \tilde{z}^2} \qquad i=1,2 \tag{22}$$

Also, the boundary conditions (19) will change as follows:

$$\left.\frac{\partial \tilde{C}_i}{\partial \tilde{z}}\right|_{\tilde{z}=0}=\tilde{g}_{i0}(\tilde{t}) \quad \text{and} \quad \left.\frac{\partial \tilde{C}_i}{\partial \tilde{z}}\right|_{\tilde{z}=1}=\tilde{g}_{i1}(\tilde{t}) \qquad i=1,2 \tag{23}$$

In an optimistic mode, we assume that:

$$\tilde{g}_{i0}(\tilde{t})=f(\tilde{C}_i(0,\tilde{t})) \quad \text{and} \quad \tilde{g}_{i1}(\tilde{t})=f(\tilde{C}_i(1,\tilde{t})) \qquad i=1,2 \tag{24}$$

where f is an unknown function. We provide the conditions in which, the problem has a unique solution.

3. Existence and uniqueness of the solution

Consider the following inverse problem:

$$\frac{\partial u}{\partial t}=\frac{\partial^2 u}{\partial x^2} \qquad 0<x<1 \qquad 0<t<T \tag{25}$$

$$u(x,0)=\varphi(x) \qquad 0\le x\le 1 \tag{26}$$

$$\frac{\partial u}{\partial x}(0,t)=g(t) \qquad 0\le t\le T \tag{27}$$

$$\frac{\partial u}{\partial x}(1,t)=h(t) \qquad 0\le t\le T \tag{28}$$

We consider the solution of this problem as $u=v+w$, where v and w are respectively the solutions of the following inverse problems as auxiliary problems.

$$\frac{\partial v}{\partial t}=\frac{\partial^2 v}{\partial x^2} \qquad 0<x<1 \qquad 0<t<T \tag{29}$$

$$v(x,0)=0 \qquad 0\le x\le 1 \tag{30}$$

$$\frac{\partial v}{\partial x}(0,t)=g(t) \qquad 0\le t\le T \tag{31}$$

$$\frac{\partial v}{\partial x}(1,t)=h(t) \qquad 0\le t\le T \tag{32}$$

And:

$$\frac{\partial w}{\partial t}=\frac{\partial^2 w}{\partial x^2} \qquad 0<x<1 \qquad 0<t<T \tag{33}$$

$$w(x,0)=\varphi(x) \qquad 0\le x\le 1 \tag{34}$$

$$\frac{\partial w}{\partial x}(0,t)=0 \qquad 0\le t\le T \tag{35}$$

$$\frac{\partial w}{\partial x}(1,t)=0 \qquad 0\le t\le T \tag{36}$$

Now, we discuss one of the basic properties of Jacobi function which will be used in this topic [7-9]. Jacobi function is defined as follows:

$$\theta(x,t)=\sum_{n=-\infty}^{+\infty}K(x+2n,t) \qquad x\in\Re \qquad t>0 \tag{37}$$

Or:

$$\theta(x,t)=K(x,t)+\sum_{n=1}^{+\infty}\left(K(x+2n,t)+K(x-2n,t)\right) \qquad x\in\Re \qquad t>0 \tag{38}$$

$$\theta(0,t)=K(0,t)+\sum_{n=1}^{+\infty}\left(K(2n,t)+K(-2n,t)\right)=K(0,t)+2\sum_{n=1}^{+\infty}K(2n,t) \qquad t>0 \tag{39}$$

If we define the function H so that $H(t)=\frac{1}{\sqrt{\pi t}}\sum_{n=1}^{+\infty}e^{-\frac{n^2}{t}}$ then:

$$\theta(0,t)=\frac{1}{\sqrt{4\pi t}}+H(t) \qquad t>0 \tag{40}$$

In this case, the function H is located in the set $C^{\infty}(0,\infty)$ such that:

$$H^n(0)=0 \qquad \forall n\in N \tag{41}$$

The following theorem is an important application of Jacobi function:

Theorem 1: Problem (29) to (32) has a solution as follow [8]:

$$v(x,t)=-2\int_0^t \theta(x,t-\eta)g(\eta)d\eta+2\int_0^t \theta(x-1,t-\eta)h(\eta)d\eta \tag{42}$$

Therefore, the solution of problem (25) to (28) will be:

$$u(x,t)=w(x,t)-2\int_0^t \theta(x,t-\eta)g(\eta)d\eta+2\int_0^t \theta(x-1,t-\eta)h(\eta)d\eta \tag{43}$$

And then for $x=0$:

$$u(0,t)=w(0,t)-2\int_0^t \theta(0,t-\eta)g(\eta)d\eta+2\int_0^t \theta(0-1,t-\eta)h(\eta)d\eta \tag{44}$$

Now we define:

$$S(t)=\frac{1}{2}\big(w(0,t)-u(0,t)\big)+\int_0^t \theta(-1,t-\eta)h(\eta)d\eta=\int_0^t \theta(0,t-\eta)g(\eta)d\eta \tag{45}$$

Equation (45) is an Abel integral equation. According to equation (40) we can write the recent equation as:

$$S(t)=\int_0^t\left(\frac{1}{\sqrt{4\pi(t-\eta)}}+H(t-\eta)\right)g(\eta)d\eta=\frac{1}{\sqrt{4\pi}}\int_0^t g(\eta)\frac{d\eta}{\sqrt{t-\eta}}+\int_0^t H(t-\eta)g(\eta)d\eta \tag{46}$$

If $S(t)$ is absolutely continuous and $S'(t)$ is bounded then, as equation (46) is an Abel integral equation it can be written as follow:

$$g(t)=\frac{2}{\sqrt{\pi}}\left(\frac{S(0)}{\sqrt{t}}+\int_0^t\frac{S'(\eta)}{\sqrt{t-\eta}}d\eta+\int_0^t E(t,\eta)g(\eta)d\eta\right) \tag{47}$$

where:

$$E(t,\eta)=\frac{1}{\sqrt{t-\eta}}+\int_\eta^t\frac{H'(t-\lambda)}{\sqrt{t-\lambda}}d\lambda \tag{48}$$

Now, Let us consider the case where functions g and h are defined as:

$$g(t)=f(u(0,t)) \qquad \text{and} \qquad h(t)=f(u(1,t)) \tag{49}$$

where the function f is unknown. For problem (25) to (28), over-specified data $u(0,t)=\psi(t)$ is considered so that function ψ is true in conditions (I) and (II):

(I) Function ψ in $[0,T]$ is absolutely differentiable and $\psi(0)=\varphi(0)$ also ψ is monotonic on $[0,T]$. Now, we write equation (45) as follow:

$$S(t)=\frac{1}{2}\big(w(0,t)-\psi(t)\big)+\int_0^t \theta(-1,t-\eta)\,f(u(1,\eta))d\eta \tag{50}$$

Based on equation(34), it is clear that:

$$S(0)=\frac{1}{2}\big(w(0,0)-\psi(0)\big)+\int_0^0 \theta(-1,-\eta)\,f(u(1,\eta))d\eta=0 \tag{51}$$

On the other hand:

$$S'(\eta)=\frac{1}{2}\big(w'(0,\eta)-\psi'(t)\big)+\int_0^\eta \theta'(-1,\lambda-\eta)\,f(u(1,\lambda))d\lambda \tag{52}$$

By substituting equations (52) and (51) in equation (47), we will have:

$$f(u(0,t)) = f(\psi(t)) = \frac{2}{\sqrt{\pi}}\int_0^t E(t,\eta) f(\psi(\eta))d\eta + \frac{1}{\sqrt{\pi}}\int_0^t \left\{ w'(0,\eta) - \psi'(t) + 2\int_0^\eta \theta'(-1,\lambda-\eta) f(u(1,\lambda))d\lambda \right\} \frac{d\eta}{\sqrt{t-\eta}} \quad (53)$$

The right side of the above equation is a nonlinear function of $f(t)$. Since the final term includes $f(u(1,t))$ and also $u(1,t)$ depends on f, therefore the value of u is depends on x, t and f. In other words $u(x,t) \equiv u(x,t;f)$. In addition, $u(x,t;f)$ should be located in the domain of f, in other words we consider the following condition:

(II) Regarding ψ is monotonic on $[0,T]$ then $\forall t \in [0,T]$, $u(1,t;f) \in [\psi(0),\psi(T)]$.

We write the left side of equation (53) as below:

$$fo\psi(t) = T_\psi[fo\psi](t) \quad (54)$$

Assuming $fo\psi = y$, we will have:

$$y(t) = T_\psi[y](t) \quad (55)$$

We mean to demonstrate T_ψ has a unique fixed point. In order to achieve this goal, we need to prove that T_ψ is a contraction. The following operators are defined:

$$d_1[f](t) = \frac{2}{\pi}\int_0^t E(t,\eta) f(\eta)d\eta \quad (56)$$

$$d_2[f](t) = \frac{2}{\pi}\int_0^t \theta'(-1,t-\eta) f(\eta)d\eta \quad (57)$$

$$a[f](t) = \int_0^t \frac{f(\eta)}{\sqrt{t-\eta}}d\eta \quad (58)$$

where d_1 and d_2 are Volterra linear operators and a is Abel linear operator. Also, function d_3 is defined as:

$$d_3(t) = \frac{1}{\pi} a[w'(0,t) - \psi'(t)] \quad (59)$$

With regards to the above definitions, equation (53) can be written as below:

$$y(t) = T_\psi[y](t) = d_1[y](t) + d_2(t) + a\big(d_2[T_\psi[y]]\big)(t) \quad (60)$$

To continue the discussion, we need some of the following lemmas. Before referring to the lemmas, we refer to the following definition.

Function f $x = x_0$ is a continuous Holder function of order α if there is a constant number such as r and a small sized neighborhood of x_0, so that for each x of this neighborhood we have:

$$\left| f(x) - f(x_0) \right| \le r\left| x - x_0 \right|^\alpha \quad (61)$$

The space of single-variable functions whose m^{th} derivative is a continuous Holder function of order $0 < \alpha \le 1$ on $[a,b]$ is shown by $C^{m+\alpha}[a,b]$. When $\alpha = 1$ we are faced with the continuity of Lipschitz . The space of single-variable continuous functions of Lipschitz on $[a,b]$ is shown by $lip[a,b]$. Also, the below relations respectively define a half-norm and a norm in this space:

$$|f|_{1\atop a\le x1\le x2\le b} = Sup\frac{|f(x_1)-f(x_2)|}{|x_1-x_2|} \quad (62)$$

$$\|f\|_1 = |f|_1 + \|f\|_\infty \quad (63)$$

The space of functions with a half-power fractional derivative on $[a,b]$ is shown by $H[a,b]$, and we define a half-norm in this space as follow:

$$|f|_{H\atop a\le x1\le x2\le b} = Sup\frac{|f(x_1)-f(x_2)|}{|x_1-x_2|^{\frac{1}{2}}} \quad (64)$$

Also, the below relation defines a norm in this space:

$$\|f\|_H = |f|_H + \|f\|_\infty \quad (65)$$

Lemma 1: If functions σ, h_1 and h_2 belong to space $lip[0,T]$, then there will be a constant number such as c so that $\|a[\sigma(h_1)]-a[\sigma(h_2)]\|_H \le c\|h_1-h_2\|_\infty$.

Proof: First, we define:

$$P(t) = a[\sigma(h_1)](t) - a[\sigma(h_2)](t) = a[\sigma(h_1)-\sigma(h_2)] \quad (66)$$

According to equation (58), we can write:

$$|P(t_1)-P(t_2)| = \left|\int_0^{t_1}\frac{1}{\sqrt{t_1-\tau}}[\sigma(h_1)(\tau)-\sigma(h_2)(\tau)]d\tau - \int_0^{t_2}\frac{1}{\sqrt{t_2-\tau}}[\sigma(h_1)(\tau)-\sigma(h_2)(\tau)]d\tau\right| \quad (67)$$

And then:

$$|P(t_1)-P(t_2)| \le \left|\int_0^{t_1}\frac{1}{\sqrt{t_1-\tau}}d\tau - \int_0^{t_2}\frac{1}{\sqrt{t_2-\tau}}d\tau\right|.\|\sigma(h_1)-\sigma(h_2)\|_\infty$$

$$= \left|2\sqrt{t_1}-2\sqrt{t_2}\right|.\|\sigma(h_1)-\sigma(h_2)\|_\infty$$

Or:

$$\frac{|P(t_1)-P(t_2)|}{|t_1-t_2|^{1/2}} \le 2\|\sigma(h_1)-\sigma(h_2)\|_\infty \quad (68)$$

On the other hand:

$$\|p\|_\infty \le \left|\int_0^{t}\frac{1}{\sqrt{t-\tau}}d\tau\right|.\|\sigma(h_1)-\sigma(h_2)\|_\infty = \left|2\sqrt{t}\right|.\|\sigma(h_1)-\sigma(h_2)\|_\infty$$

$$\le A\|\sigma(h_1)-\sigma(h_2)\|_\infty \quad (69)$$

According to equations (65), (68) and (69) we can write:

$$\|p\|_H = Sup\frac{|P(t_1)-P(t_2)|}{|t_1-t_2|^{1/2}} + \|p\|_\infty \le 2\|\sigma(h_1)-\sigma(h_2)\|_\infty + A\|\sigma(h_1)-\sigma(h_2)\|_\infty$$

$$= (2+A)\|\sigma(h_1)-\sigma(h_2)\|_\infty \quad (70)$$

σ is a continuous Lipschitz function, so:

$$\|\sigma(h_1)-\sigma(h_2)\|_\infty \le B\|h_1-h_2\|_\infty \quad (71)$$

Finally, from (70) and (71) we will have:

$$\|p\|_H \le c\|h_1-h_2\|_\infty \quad (72)$$

Lemma 2: We assume that f_1 and f_2 are Lipschitz functions .The following problem is considered:

$$\frac{\partial u^i}{\partial t}=\frac{\partial^2 u^i}{\partial x^2} \qquad 0<x<1 \qquad 0<t<T \qquad i=1,2 \tag{73}$$

$$u^i(x,0)=\varphi(x) \qquad 0\le x\le 1 \qquad i=1,2 \tag{74}$$

$$\frac{\partial u^i}{\partial x}(0,t)=f_i(u^i(0,t)) \qquad 0\le t\le T \tag{75}$$

$$\frac{\partial u^i}{\partial x}(1,t)=f_i(u^i(1,t)) \qquad 0\le t\le T \tag{76}$$

$$u^i(0,t)=\psi(x) \qquad 0\le x\le 1 \qquad i=1,2 \tag{77}$$

The solution of above problem is true in the following inequality:

$$\left\|u^{(1)}(1,t)-u^{(2)}(1,t)\right\|_H \le c\left\|f_1-f_2\right\|_\infty \tag{78}$$

where T is sufficiently small and constant c depends on T and Lipschitz norms of f_1 & f_2.

Proof: Function q is defined as below:

$$q(t)=u^{(1)}(1,t)-u^{(2)}(1,t)=\int_0^t L(t-\tau)\Big(f_1(u^{(1)}(1,\tau))-f_2(u^{(2)}(1,\tau))\Big)d\tau \tag{79}$$

where $L(T)$ is single kernel at coordinates origin. Assuming $0\le t_2<t_1\le T$, we write:

$$\begin{aligned}
q(t_1)-q(t_2)&=\int_0^{t_1} L(t_1-\tau)\Big(f_1(u^{(1)}(1,\tau))-f_2(u^{(2)}(1,\tau))\Big)d\tau\\
&\quad-\int_0^{t_2} L(t_2-\tau)\Big(f_1(u^{(1)}(1,\tau))-f_2(u^{(2)}(1,\tau))\Big)d\tau\\
&=\int_0^{t_2}\Big(L(t_1-\tau)-L(t_2-\tau)\Big)\Big(f_1(u^{(1)}(1,\tau))-f_1(u^{(2)}(1,\tau))\Big)d\tau\\
&\quad+\int_0^{t_2}\Big(L(t_1-\tau)-L(t_2-\tau)\Big)\Big(f_1(u^{(2)}(1,\tau))-f_2(u^{(2)}(1,\tau))\Big)d\tau\\
&\quad+\int_{t_2}^{t_1} L(t_1-\tau)\Big(f_1\big(u^{(1)}(1,\tau)\big)-f_1\big(u^{(2)}(1,\tau)\big)\Big)\,d\tau\\
&\quad+\int_{t_2}^{t_1} L(t_1-\tau)\Big(f_1(u^{(2)}(1,\tau))-f_2(u^{(2)}(1,\tau))\Big)d\tau=I_1+I_2+I_3+I_4
\end{aligned}$$

Now, we consider the recent integrals as follows:

$$\begin{aligned}
|I_1|&=\left|\int_0^{t_2}\Big(L(t_1-\tau)-L(t_2-\tau)\Big)\Big(f_1(u^{(1)}(1,\tau))-f_1(u^{(2)}(1,\tau))\Big)d\tau\right|\\
&\le\int_0^{t_2}\Big|L(t_1-\tau)-L(t_2-\tau)\Big|.\left\|f_1\right\|_1.\Big|u^{(1)}(1,\tau)-u^{(2)}(1,\tau)\Big|d\tau
\end{aligned}$$

$$\leq \int_{0}^{t_2}\int_{t_2}^{t_1}\frac{\partial L}{\partial s}(s-\tau).d\tau.\left\|f_1\right\|_1.\underset{0\leq t\leq T}{Sup}\left|u^{(1)}(1,t)-u^{(2)}(1,t)\right| \leq c_1\sqrt{t_1-t_2}.\left\|f_1\right\|_1.\underset{0\leq t\leq T}{Sup}\left|u^{(1)}(1,t)-u^{(2)}(1,t)\right|$$

$$\left|I_2\right| = \left|\int_{0}^{t_2}\Big(L(t_1-\tau)-L(t_2-\tau)\Big)\Big(f_1(u^{(2)}(1,\tau))-f_2(u^{(2)}(1,\tau))\Big)d\tau\right|$$

$$\leq \int_{0}^{t_2}\left|L(t_1-\tau)-L(t_2-\tau)\right|.\left|f_1(u^{(2)}(1,\tau))-f_2(u^{(2)}(1,\tau))\right|d\tau$$

$$\leq \int_{0}^{t_2}\int_{t_2}^{t_1}\frac{\partial L}{\partial s}(s-\tau)d\tau.\left\|f_1-f_2\right\|_\infty \leq c_2\sqrt{t_1-t_2}.\left\|f_1-f_2\right\|_\infty$$

$$\left|I_3\right| = \left|\int_{t_2}^{t_1}L(t_1-\tau)\Big(f_1(u^{(1)}(1,\tau))-f_1(u^{(2)}(1,\tau))\Big)d\tau\right|$$

$$\leq \int_{t_2}^{t_1}\left|L(t_1-\tau)\right|.\left\|f_1\right\|_1.\left|u^{(1)}(1,\tau)-u^{(2)}(1,\tau)\right|d\tau \leq c_3\sqrt{t_1-t_2}.\left\|f_1\right\|_1.\underset{0\leq t\leq T}{Sup}\left|u^{(1)}(1,t)-u^{(2)}(1,t)\right|$$

$$\left|I_4\right| = \left|\int_{t_2}^{t_1}L(t_1-\tau)\Big(f_1(u^{(2)}(1,\tau))-f_2(u^{(2)}(1,\tau))\Big)d\tau\right|$$

$$\leq \int_{t_2}^{t_1}\left|L(t_1-\tau)\right|.\left|f_1(u^{(2)}(1,\tau))-f_2(u^{(2)}(1,\tau))\right|d\tau \leq c_4\sqrt{t_1-t_2}.\left\|f_1-f_2\right\|_\infty$$

With respect to the recent relations:

$$\left|q(t_1)-q(t_2)\right| = \left|I_1+I_2+I_3+I_4\right| \leq \left|I_1\right|+\left|I_2\right|+\left|I_3\right|+\left|I_4\right|$$

$$\leq \sqrt{t_1-t_2}\left((c_1+c_3).\left\|f_1\right\|_1.\underset{0\leq t\leq T}{Sup}\left|u^{(1)}(1,t)-u^{(2)}(1,t)\right|+(c_2+c_4).\left\|f_1-f_2\right\|_\infty\right)$$

We can conclude:

$$\frac{\left|q(t_1)-q(t_2)\right|}{\left|t_1-t_2\right|^{\frac{1}{2}}} \leq \left((c_1+c_3).\left\|f_1\right\|_1.\left\|q\right\|_\infty+(c_2+c_4).\left\|f_1-f_2\right\|_\infty\right) \qquad (80)$$

If we define $c_5 = \max\left\{(c_1+c_3).\left\|f_1\right\|_1,(c_2+c_4)\right\}$ then, according to equation (64):

$$\underset{a\leq t_1\leq t_2\leq b}{\left|q\right|_H} = Sup\frac{\left|q(t_1)-q(t_2)\right|}{\left|t_1-t_2\right|^{\frac{1}{2}}} \leq c_5\left(\left\|q\right\|_\infty+\left\|f_1-f_2\right\|_\infty\right) \qquad (81)$$

On the other hand, regarding equation (64) we can conclude:

$$\left\|q\right\|_\infty \leq \sqrt{t}\left|q\right|_H \qquad (82)$$

Therefore:

$$\left\|q\right\|_H = \left|q\right|_H+\left\|q\right\|_\infty \leq \sqrt{t}\left|q\right|_H+\left|q\right|_H = (1+\sqrt{t})\left|q\right|_H$$

$$\le (1+\sqrt{t})c_5\left(\sqrt{t}|q|_H + \|f_1 - f_2\|_\infty\right) \le c_6\left(\sqrt{t}|q|_H + \|f_1 - f_2\|_\infty\right) \quad (83)$$

Eventually, we have: $\|q\|_H \le \frac{c_6}{1-c_6\sqrt{T}}\|f_1 - f_2\|_\infty$ (84)

As mentioned earlier, we mean to demonstrate that T_ψ is a contraction. We consider equation (60) and define y_1 and y_2 so that $y_1(r) = T_\psi[y_1](t) = f_1 o\psi(t)$, $y_2(r) = T_\psi[y_2](t) = f_2 o\psi(t)$. where f_1 and f_2 are true in lemma 2. Regarding equation (60) we can write:

$$\|T_\psi[y_1] - T_\psi[y_2]\|_H \le \|d_1[y_1] - d_1[y_2]\|_H + \|a(d_2[T_\psi[y_1]]) - a(d_2[T_\psi[y_2]])\|_H \quad (85)$$

In according to Lemma 1, the right side of the above relation can be written:

$$\|a(d_2[T_\psi[y_1]]) - a(d_2[T_\psi[y_2]])\|_H \le c\|T_\psi[y_1] - T_\psi[y_2]\|_H = c\|f_1(u^1(1,t)) - f_2(u^2(1,t))\|_\infty$$

$$\le c\|f_1(u^1(1,t)) - f_1(u^2(1,t))\|_\infty + c\|f_1(u^2(1,t)) - f_2(u^2(1,t))\|_\infty$$

$$\le c\|f_1\|_1\|u^1(1,t) - u^2(1,t)\|_\infty + c\|f_1 - f_2\|_\infty$$

$$\le c_0\left(\|u^1(1,t) - u^2(1,t)\|_\infty + \|f_1 - f_2\|_\infty\right) \quad (86)$$

where $c_0 = \max\{c, \|f_1\|_1\}$

Therefore, with regards to equation (86) we can write equation(85) as:

$$\|T_\psi[y_1] - T_\psi[y_2]\|_H \le c_0\left(\|u^1(1,t) - u^2(1,t)\|_\infty + \|f_1 - f_2\|_\infty\right) \quad (87)$$

On the other hand, according to equation (64) we can generally conclude that:

$$\|f\|_\infty \le \sqrt{t}|f|_H \le \sqrt{T}|f|_H \quad (88)$$

So:

$$\|T_\psi[y_1] - T_\psi[y_2]\|_H \le c_0\sqrt{T}\left(\|u^1(1,t) - u^2(1,t)\|_H + \|f_1 - f_2\|_H\right) \quad (89)$$

Now, regarding the recent relation and equation (84) we can write:

$$\|T_\psi[y_1] - T_\psi[y_2]\|_H \le c_0\sqrt{T}\left(\frac{c_6}{1-c_6\sqrt{T}}\|f_1 - f_2\|_\infty + \|f_1 - f_2\|_H\right)$$

$$\le c_0\sqrt{T}\left(\frac{c_6}{1-c_6\sqrt{T}}\sqrt{T}\|f_1 - f_2\|_H + \|f_1 - f_2\|_H\right)$$

$$\le c_0\sqrt{T}\left(\frac{c_6}{1-c_6\sqrt{T}}\sqrt{T} + 1\right)\|f_1 - f_2\|_H \quad (90)$$

Or:

$$\|T_\psi[y_1] - T_\psi[y_2]\|_H \le \frac{c'}{1-c'\sqrt{T}}\sqrt{T}\|f_1 - f_2\|_H \quad (91)$$

Therefore, for T which is small enough ($2c'\sqrt{T} < 1$), T_ψ is a contraction in space H. According to the principle of contraction Mapping, T_ψ has only and only a unique fixed point such as y^* and there is only and only one f^* corresponding to y^* s.t $y^* = f^* O\psi$. In other

words, if conditions (I) and (II) are established then problem (25) to (28) assuming equation(49) will has a pair of unique solution (u^*, f^*) in $[0,t^*]$ s.t $0 \le t^* \le T$.

4. Conclusion

The present study has shown that a molecular diffusion problem is arisen in a hydrocarbon reservoir, under the unknown boundary conditions as $f(u(0,t))$ and $f(u(1,t))$ (u and f are unknown) with considering an over-specified data as $u(0,t) = \psi(t)$ has a unique solution as (u^*, f^*) in $[0,T]$. In according to the below conditions, the problem can be extended on all the time:

1- we limit f to uniform Lipschitz functions.

2- f is limited to non-negative functions so that $f(0) = 0$, by applying the Maximum principle [10], u remains uniformly bounded.

It is very interesting to extend the discussion on the above problem when the temperature and pressure are not constant, e.g. when the reservoir is not uniform

References

[1] Rosch A. Identification of Nonlinear Heat Transfer Laws by Optimal Control. Numer. Funct. Anal. Optim., 1994; 15: 417–434.

[2] Rosch A. A Gauss-Newton Method for the Identification of Non-linear Heat Transfer Laws. Int. Ser. Numer. Math., 2002; 139: 217–230.

[3] Onyango TTM, Ingham DB, Lesnic D. Reconstruction of Boundary Condition Laws in Heat Conduction Using the Boundary Element Method. Comput. Math. Appl., 2009; 57: 153–168.

[4] Bialecki R, Divo E, Kassab AJ. Reconstruction of Time-Dependent Boundary Heat Flux by a BEM Based Inverse Algorithm. Eng. Anal. Bound. Elem., 2006; 30: 767–773.

[5] Skelland AHP. Diffusional Mass Transfer. John Wiley & Sons, New York, 1972.

[6] Tribal R. Mass Transfer Operations, Sixth Edition, McGraw-Hill, International Editions, Singapore, 1981.

[7] du Chateau P and Zachmann D. Partial Differential Equations. Schaum's Outlines, 1986.

[8] Cannon JR. The One-Dimensional Heat Equation, Addison–Wesley, Menlo Park, CA, 1984.

[9] Widdr DV. The Heat Equation, Academic Press, New York, 1975.

[10] Cannon JR and Lin Y. Determination of Parameters $p(t)$ in some Holder Classes for Semi-Linear Parabolic Equations. Inverse Problems, 1988; 4: 595-606.

To whom correspondence should be addressed: Prof. Amir H. Mohammadi, Discipline of Chemical Engineering, School of Engineering, University of KwaZulu-Natal, Howard College Campus, King George V Avenue, Durban 4041, South Africa, amir_h_mohammadi@yahoo.com

Petroleum and Coal

Article **Open Access**

EXISTENCE AND UNIQUENESS OF SOLUTION FOR LAYER DIFFUSION OF AN INCOMPRESSIBLE FLUID IN A HYDROCARBON RESERVOIR

Amirabbas Mohammadi[1], Abdullah Shidfar[1], Amir H. Mohammadi [2]

[1] School of Mathematics, Iran University of Science and Technology, Tehran, Iran
[2] Discipline of Chemical Engineering, School of Engineering, University of KwaZulu-Natal, Howard College Campus, King George V Avenue, Durban 4041, South Africa

Received April 30, 2018; Accepted June 27, 2018

Abstract

In the study of an incompressible fluid in a hydrocarbon reservoir, developing a reliable model to predict the fluid behavior in the reservoir, based on diffusion mechanism and some mathematical parameters is necessary. In the present study, we have tried to develop a nonlinear model of parabolic type to estimate some parameters such as volumetric capacity and diffusion coefficient of an incompressible fluid under layer diffusion in a homogeneous hydrocarbon reservoir. Initially for this type of fluid, Darcy's law is applied along with a continuity equation to create a nonlinear differential equation of parabolic type under boundary conditions. Via an auxiliary problem and based on Schauder fixed-point theorem and concepts of Banach spaces, we demonstrate the existence and uniqueness of solution for the aforementioned model. Afterward, we assume that the diffusion coefficient of the fluid is a polynomial function of degree n with unknown coefficients, accordingly a numerical algorithm is proposed for estimating the function as well as volumetric capacity of the fluid, so that the given error function becomes minimum.

Keywords: *Diffusion; Auxiliary problem; Banach space; Fixed point; Pre-compact set; Inverse problem.*

1. Introduction

Classical solutions for a nonlinear diffusion equation, have been catalogued for many important problems [1-2]. Furthermore, this type of equation with several admissible boundary conditions have been employed as inverse nonlinear problem in order to numerically analyze the problems arising from the oil and gas processes. This work has been motivated by a class of important problems caused by the reservoir processes, such as layer diffusion of incompressible fluid in a hydrocarbon reservoir. The diffusion equations of these problems can be characterized by parabolic differential equations along with the governing boundary conditions.

Determining unknown parameter in a parabolic differential equation has been previously treated by some authors [3-8]. Usually an over-specified data at the boundary $x = 0$ is applied in determining the unknown parameter. Such problems typically arise in oil and gas reservoirs [9-10].

As previously mentioned, in this work we consider a diffusion problem which occurs in a hydrocarbon reservoir. We assume that [11]:

1. The desired fluid is incompressible such as oil and water whose density does not change under the pressure change.
2. The problem is considered before well drilling and production operations.
3. Regarding (2), the incompressible fluid can be in layer diffusion in reservoir rock.

Darcy's law will govern the analysis of the fluid motion. It must be noted that we ignore the deposition of some materials such as asphaltene, so the reservoir rock can be considered completely homogeneous in terms of physical properties such as permeability and porosity. If

the volumetric capacity and the diffusion coefficient of the fluid, are respectively shown as u and a then, in the most applied problems, a will be a function of u and the governing partial differrential equation will be nonlinear. Considering the boundary conditions and by using an over-specified data at $x=0$, we will prove the existence and uniqueness of solution for this mathematical model in order to estimate the unknown parameters a and u which is impossible in most cases.

2. Mathematical formulation

As the hydrocarbon reservoir has been completely homogeneous, viscosity and porosity degree ϕ are constant. Also, volumetric capacity u is a function of time and place, also $0 \le u \le \phi$.

As mentioned earlier, the equation governs the fluid motion, is Darcy's law which along with the continuity equation are respectively as follows:

$$q = -a(u)grad(u) \qquad 0 \le u \le \phi \tag{1}$$

$$\frac{\partial u}{\partial t} + div(q) = 0 \tag{2}$$

q: volumetric flux of the fluid.

In particular, by combining them we will have a one-dimensional, nonlinear, parabolic equation as below:

$$\frac{\partial u}{\partial t} = div(a(u)\frac{\partial u}{\partial x}) \tag{3}$$

Supposing a time $T>0$ we define: $Q_T = \{(x,t) \in \Re^2 | 0<x<1, 0<t<T\}$

We assume that the volumetric flux of fluid (q) at the beginning and the end of the reservoir is known and respectively denoted by $g(t)$ and $h(t)$, then based on Darcy's law:

$$q(0,t) = -a(u(0,t))\frac{\partial}{\partial x}u(0,t) = g(t) \tag{4}$$

$$q(1,t) = -a(u(1,t))\frac{\partial}{\partial x}u(1,t) = h(t)$$

Assuming that the initial distribution of volumetric capacity is zero:

$$u(x,0) = 0 \qquad 0 \le x \le 1$$

So, we will have the following nonlinear inverse problem:

$$\frac{\partial u}{\partial t} = \frac{\partial}{\partial x}(a(u)\frac{\partial u}{\partial x}) \qquad 0<x<1 \qquad 0<t<T \tag{5}$$

$$u(x,0) = 0 \qquad 0 \le x \le 1 \tag{6}$$

$$-a(u(0,t))\frac{\partial}{\partial x}u(0,t) = g(t) \qquad 0 \le t \le T \tag{7}$$

$$-a(u(1,t))\frac{\partial}{\partial x}u(1,t) = h(t) \qquad 0 \le t \le T \tag{8}$$

As we will faced with many errors and problems during calculating diffusion coefficient a, so calculation and definition of a on Q_T is limited to the boundary of this area. Let us consider the following over-specified condition:

$$u(0,t) = f(t) \qquad 0 \le t \le T \tag{9}$$

3. Auxiliary problem

In this section, for the above problem we consider an auxiliary inverse problem. Assume that q at the bottom of the reservoir $(x=1)$ is zero. Therefore:

$$\frac{\partial u}{\partial t}=\frac{\partial}{\partial x}(a(u)\frac{\partial u}{\partial x}) \qquad 0<x<1 \qquad 0<t<T \qquad (10)$$

$$u(x,0)=0 \qquad 0\le x\le 1 \qquad (11)$$

$$-a(u(0,t))\frac{\partial}{\partial x}u(0,t)=g(t) \qquad 0\le t\le T \qquad (12)$$

$$\frac{\partial}{\partial x}u(1,t)=0 \qquad 0\le t\le T \qquad (13)$$

$$u(0,t)=f(t) \qquad 0\le t\le T \qquad (14)$$

Now, we assume that $0<a_0\le a(s)\le a_1$ and $s>0$ also a_0 and a_1 are constants. Consider the following transformation introduced for the first time by Cannon [12]:

$$C_a(s)=\int_0^s a(z)dz \qquad s\ge 0 \qquad (15)$$

Note that $C_a'(s)=a(s)\ge a_0>0$, therefore C_a is strictly increasing and invertible. Per solution $u(x,t)$ of the problem (10) to (14) we define $v(x,t)$:

$$v(x,t)=C_a(u(x,t))=\int_0^{u(x,t)} a(\delta)d\delta \qquad (16)$$

Then the auxiliary problem will be as follows:

$$\frac{\partial}{\partial t}v(x,t)=\hat{a}(v)\frac{\partial^2}{\partial x^2}v(x,t) \qquad 0<x<1 \qquad 0<t<T \qquad (17)$$

$$v(x,0)=0 \qquad 0\le x\le 1 \qquad (18)$$

$$\frac{\partial}{\partial x}v(0,t)=g(t) \qquad 0\le t\le T \qquad (19)$$

$$\frac{\partial}{\partial x}v(1,t)=0 \qquad 0\le t\le T \qquad (20)$$

$$v(0,t)=C_a(f(t))=\int_0^{f(t)} a(\delta)d\delta=F(t) \qquad 0\le t\le T \qquad (21)$$

where: $\hat{a}(v)=a(C_a^{-1}(v))$ (22)

It is clear that determining $\hat{a}(v)$ results in $a(u)$, also in according to equation (16) there is one-to-one correspondence between the original problem solution and the auxiliary problem solution.

4. Existence and uniqueness of solution for model

We consider the auxiliary problem (17) to (21) as well as the following hypothesis:

A. $v\in C^2(Q_T)$.

B. $\frac{\partial^2}{\partial x^2}v(0,t)\le M$ ، $\forall t\in[0,T]$ and $M>0$.

C. $\hat{a}\in C^{-1}[A,B]$ where $A=\min_{Q_T} v(x,t)$ and $B=\max_{Q_T} v(x,t)$.

D. $\forall s\in[A,B]$ $\hat{a}(s)>0$ ،and $\hat{a}$ is true on $[A,B]$ in Lipschitz condition.

E. $\hat{a}(s)$ in (17) to (21), is true.

F. $F, g \in C^1[0,T]$ *and* $F(0) = g(0) = 0$.

G. $F'(t), g'(t) > 0$ ، $\forall t \in [0,T]$.

Now we define:

$$\|u\|_{0,Q_T} = Sup_{Q_T} |v(x,t)| \tag{23}$$

$$R(v)_{\alpha,Q_T} = Sup_{(x_1,t_1),(x_2,t_2)\in Q_T} \frac{|v(x_1,t_1) - v(x_2,t_2)|}{\left(|x_1 - x_2|^2 + |t_1 - t_2|^2\right)^{\alpha/2}} \tag{24}$$

Also:

C^{α} Banach space of functions v ، continuous on Q_T.

$C^{1+\alpha}$ Banach space of functions v ، with continuous first partial derivatives on Q_T.

$C^{2+\alpha}$ Banach space of functions v ، with continuous second partial derivatives on Q_T.

Above spaces are respectively with the following norms:

$$\|v\|_{\alpha,Q_T} = \|v\|_{0,Q_T} + R(v)_{\alpha,Q_T} \tag{25}$$

$$\|v\|_{1+\alpha,Q_T} = \|v\|_{\alpha,Q_T} + \left\|\frac{\partial v}{\partial x}\right\|_{\alpha,Q_T} \tag{26}$$

$$\|v\|_{2+\alpha,Q_T} = \|v\|_{\alpha,Q_T} + \left\|\frac{\partial v}{\partial x}\right\|_{\alpha,Q_T} + \left\|\frac{\partial^2 v}{\partial x^2}\right\|_{\alpha,Q_T} + \left\|\frac{\partial v}{\partial t}\right\|_{\alpha,Q_T} \tag{27}$$

Now for $x = 0$ we have:

$$\frac{\partial}{\partial x} v(0,t) = \hat{a}(v(0,t)) \frac{\partial^2}{\partial x^2} v(0,t) \tag{28}$$

Regarding the condition (21):

$$F'(t) = \hat{a}(F(t)) \frac{\partial^2}{\partial x^2} v(0,t) \tag{29}$$

Now we set:

$s = F(t)$

As $F'(t) > 0$, so function F is invertible and can be written as:

$t = F^{-1}(s)$, $s \in [F(0), F(T)]$

Hence, according to equation (29) we have:

$$\hat{a}(s) = \left(\frac{F'(F^{-1}(s))}{\frac{\partial^2}{\partial x^2} v(0, F^{-1}(s))}\right) \tag{30}$$

Now, we consider the following required lemma:

Lemma: We assume that $(v, \hat{a})$ is a solution for problem (17) to (20). In this case, $v(x,t)$ is true for equation (21) if and only if $\hat{a}(v)$ is true in the condition (30):

Proof: As $(v, \hat{a})$ has been assumed as a solution for problem (17) to (20), so if $v(x,t)$ is true for (21), (according to the previous process) $\hat{a}(v)$ will be true for (30).Also, if $\hat{a}(v)$ is true for condition (30) and $v(x,t)$ is a solution for problem (17) to (20) then we must show that $v(0,t) = F(t)$.

By subtracting equation (29) from equation (28):

$$\frac{\partial}{\partial t}v(0,t)-F'(t)=\left(\hat{a}(v(0,t))-\hat{a}(F(t))\right)\frac{\partial^2}{\partial x^2}v(0,t) \quad (31)$$

Now we define the following function:

$$\tau(t)=v(0,t)-F(t) \quad (32)$$

So, we can write:

$$\left|\tau'(t)\right|=\left|\hat{a}(v(0,t))-\hat{a}(F(t))\right|\left|\frac{\partial^2}{\partial x^2}v(0,t)\right| \quad (33)$$

On the other hand, according to the assumption D, a positive number $k>1$ can be found:

$$\left|\hat{a}(v(0,t))-\hat{a}(F(t))\right|\le k\left|v(0,t)-F(t)\right| \quad (34)$$

So, we have:

$$\left|\tau'(t)\right|\le k\left|\tau(t)\right|\left|\frac{\partial^2}{\partial x^2}v(0,t)\right| \quad (35)$$

However, according to the assumptions D, E and the equation (29) we can conclude that:

$$\frac{\partial^2}{\partial x^2}v(0,t)>0$$

Therefore, equation (35) can be written:

$$\left|\tau'(t)\right|\le kM\left|\tau(t)\right|\le M\left|\tau(t)\right| \quad (36)$$

Or:

$$\tau'(t)\le M\left|\tau(t)\right|$$

By integrating the above inequality, we have:

$$\tau(t)\le\tau(0)M\int_0^t\left|\tau(z)\right|dz \quad (37)$$

According to Gronwall inequality, we conclude that:

$$\tau(t)\le\tau(0)e^{M\int_0^t\left|\tau(z)\right|dz} \quad (38)$$

But, regarding assumption F and equation (18), $\tau(0)=0$ so $\forall t\in[0,T]\ \tau(t)=0$, in other words

$\forall t\in[0,T]$, $v(0,t)=F(t)$.

We have shown that if $\hat{a}(v)$ is true in equation (30) then v is true in equation (17) to (21). Now, we consider the following problem:

$$\frac{\partial}{\partial t}v(x,t)=\left(\frac{F'(F^{-1}(\omega))}{\frac{\partial^2}{\partial x^2}\omega(0,F^{-1}(\omega))}\right)\frac{\partial^2}{\partial x^2}v(x,t) \quad \text{in } Q_T \quad (39)$$

$$v(x,0)=0 \qquad 0\le x\le 1 \quad (40)$$

$$\frac{\partial}{\partial x}v(0,t)=g(t) \qquad 0\le t\le T \quad (41)$$

$$\frac{\partial}{\partial x}v(1,t)=0 \qquad 0\le t\le T \quad (42)$$

$$v(0,t)=F(t) \qquad 0\le t\le T \quad (43)$$

where $\omega\in C_r$ with norms $\|\ \|_{1+\alpha,Q_T}$ and $\|\ \|_{1+\gamma,Q_T}$ that $0<\alpha<\delta<1$ and we show these norms by symbols $C_r^{1+\alpha}$ and $C_r^{1+\gamma}$. Also, $\omega\in C_r^{1+\alpha}$ is true in the following conditions:

1. $\|\omega\|_{1+\alpha,Q_T}$, $r>0$
2. $\omega(x,t)$ in conditions (40) to (43) is true.

Per $\omega \in C_r^{1+\alpha}$, problem (39) to (43) has a unique solution [13]. Now we consider transformation P so that $v = P\omega$ and $\omega \in C_r^{1+\alpha}$, also v is a solution for problem (39) to (43).

Theorem 1: Assume that $g(t)$ and $F(t)$ are true in F and G. Then per $\omega \in C_r^{1+\alpha}$, $v = P\omega$ has a fixed point.

Proof: First, we can mention the Schauder fixed-point theorem. According to this theorem, if Y is a subset of the Banach space X and S is a continuous function on Y and SY is located in Y and pre-compact, then S has a fixed point e.g. $\exists y_0 \in Y$ so that $Sy_0 = y_0$.

It must be noted, a set is a pre-compact set if and only if that is a subset of a compact set.

First, we show that $PC_r^{1+\alpha}$ is in $C_r^{1+\alpha}$, then θ function is defined as:

$$\theta = v - \psi \tag{44}$$

where $\psi \in C_r^{1+\alpha}$, so we have:

$$\psi(x,t) = v(x,t) \qquad \text{in } Q_T$$

Now we write:

$$\frac{\partial v}{\partial t} = \frac{\partial \theta}{\partial t} + \frac{\partial \psi}{\partial t}$$

$$\frac{\partial^2 v}{\partial x^2} = \frac{\partial^2 \theta}{\partial x^2} + \frac{\partial^2 \psi}{\partial x^2}$$

Therefore, according to equation (39) we have:

$$\frac{\partial \theta}{\partial t} - \left(\frac{F'(F^{-1}(\omega))}{\frac{\partial^2}{\partial x^2}\omega(0,F^{-1}(\omega))} \right) \frac{\partial^2 \theta}{\partial x^2} = -\frac{\partial \psi}{\partial t} + \left(\frac{F'(F^{-1}(\omega))}{\frac{\partial^2}{\partial x^2}\omega(0,F^{-1}(\omega))} \right) \frac{\partial^2 \omega}{\partial x^2} \qquad \text{in } Q_T \tag{45}$$

Also, it is clear that:

$$\theta(x,0) = 0 \qquad 0 \le x \le 1 \tag{46}$$

$$\theta(0,t) = 0 \qquad 0 \le t \le T \tag{47}$$

$$\theta(1,t) = 0 \qquad 0 \le t \le T \tag{48}$$

According to the theorem, there is a positive integer such as k that for $1 < \alpha$ the following inequality is true [14]:

$$\|\theta\|_{1+\alpha,Q_T} \le k \left\| \frac{\partial \psi}{\partial t} - \left(\frac{F'(F^{-1}(\omega))}{\frac{\partial^2}{\partial x^2}\omega(0,F^{-1}(\omega))} \right) \frac{\partial^2 \omega}{\partial x^2} \right\|_{0,Q_T} \tag{49}$$

Also, in definition of $C_r^{1+\alpha}$ we can choose r so that:

$$r \geq k\left\|\frac{\partial \psi}{\partial t}\right\|_{0,Q_T} + k\left\|\left(\frac{F'(F^{-1}(\omega))}{\frac{\partial^2}{\partial x^2}\omega(0,F^{-1}(\omega))}\right)\right\|_{0,Q_T}\left\|\frac{\partial^2 \psi}{\partial x^2}\right\|_{0,Q_T} + \|\psi\|_{0,Q_T} \quad (50)$$

Accordingly, we will have:

$$\|v\|_{1+\alpha,Q_T} \leq \|\theta\|_{1+\alpha,Q_T} + \|\psi\|_{1+\alpha,Q_T} \leq k\left\|\frac{\partial \psi}{\partial t}\right\|_{0,Q_T} + k\left\|\left(\frac{F'(F^{-1}(\omega))}{\frac{\partial^2}{\partial x^2}\omega(0,F^{-1}(\omega))}\right)\right\|_{0,Q_T}\left\|\frac{\partial^2 \psi}{\partial x^2}\right\|_{0,Q_T} + \|\psi\|_{1+\alpha,Q_T} \quad (51)$$

In other words, P transforms $C_r^{1+\alpha}$ to itself. Similarly, P transforms $C_r^{1+\gamma}$ to itself as well. Now, we can state the following theorem**:**

Theorem 2: Let D is a bounded set of $\Re^n$ space, also $C^{p+\alpha}$ is a set of functions with m^{th} order partial derivatives. These derivatives are locally continuous Holder functions. Also, we assume that $0<\alpha<\beta<1$ and $0 \leq p \leq q$. In this case, the bounded subset of $C^{q+\beta}$ is a pre-compact subset of $C^{q+\alpha}$ [15].

By definition, function f in $x=x_0$ is a continuous Holder function of order α, if there are a constant number such as r and a small sized neighborhood of x_0, so that for each x in this neighborhood we will have: $|f(x)-f(x_0)| \leq r|x-x_0|^{\alpha}$ [16].

The space of single-variable functions whose m^{th} derivative is a continuous Holder function of order $0<\alpha \leq 1$ on $[a,b]$, is shown by $C^{m+\alpha}[a,b]$.

In according to this theorem, $PC_r^{1+\gamma} \subseteq C_r^{1+\gamma}$ is a pre-compact subset of $C_r^{p+\alpha}$. At the present, we have to prove the continuity of P. So we put $v=\theta+v_m$ where $v=P\omega$ and $v_m=P\omega_m$ are solutions for problem (45) to (48). So it is clear that θ is true in the following equation:

$$\frac{\partial \theta}{\partial t} - \left(\frac{F'(F^{-1}(\omega_m))}{\frac{\partial^2}{\partial x^2}\omega_m(0,F^{-1}(\omega_m))}\right)\frac{\partial^2 \theta}{\partial x^2} = \left(\frac{F'(F^{-1}(\omega))}{\frac{\partial^2}{\partial x^2}\omega(0,F^{-1}(\omega))} - \frac{F'(F^{-1}(\omega_m))}{\frac{\partial^2}{\partial x^2}\omega_m(0,F^{-1}(\omega_m))}\right)\frac{\partial^2 v}{\partial x^2} \quad (52)$$

So, when $\|\omega_m-\omega\|_{1+\alpha,Q_T} \to 0$ we have:

$$\varepsilon_m = Sup_{Q_T}\left|\frac{F'(F^{-1}(\omega))}{\frac{\partial^2}{\partial x^2}\omega(0,F^{-1}(\omega))} - \frac{F'(F^{-1}(\omega_m))}{\frac{\partial^2}{\partial x^2}\omega_m(0,F^{-1}(\omega_m))}\right|\frac{\partial^2 v}{\partial x^2} \to 0 \quad (53)$$

On the other hand, according to the theorem [14]:

$$\|v\|_{1+\alpha,Q_T} = \|P\omega_m - P\omega\|_{1+\alpha,Q_T} \le c\varepsilon_m \to 0 \quad (54)$$

So when $\omega_m \to \omega$, we will have:

$$\|P\omega_m - P\omega\|_{1+\alpha,Q_T} \to 0 \quad (55)$$

In other words, $P\omega_m \to P\omega$ that means P is a continuous transformation. So using the Schauder fixed-point theorem we conclude that P has a fixed point.

5. A proposed numerical algorithm

With considering the problem (10) to (14) we can assume that the diffusion coefficient of $a(u)$ is a polynomial of degree n with unknown coefficients of $c_0,...,c_n$:

$$a(u) = c_0 + c_1 u + ... + c_n u^n \qquad n \in N \quad (56)$$

The aim is to find degree and unknown coefficients of the above polynomial for any time. The equation (10) is written in the form of differential as below:

$$\frac{1}{k}\Delta_t u_{i,j} = \frac{1}{2}\left\{\frac{\delta_x^2(a(u_{i,j})u_{i,j}) + \delta_x^2(a(u_{i,j+1})u_{i,j+1})}{h^2}\right\} \quad (57)$$

Now, according to equations (11) to (13) and assuming $\delta_t = 0.01$ for any time, we get the following nonlinear equations system:

$$-2a(u_1)u_1 + (2 + 2a(u_0))u_0 = 0 \qquad i = 0 \quad (58)$$

$$-a(u_{i-1})u_{i-1} + (2 + 2a(u_i))u_i - a(u_{i+1})u_{i+1} = 0 \qquad i = 1,...,9 \quad (59)$$

$$-2a(u_9)u_9 + (2 + 2a(u_{10}))u_{10} = 0 \qquad i = 10 \quad (60)$$

Now we can consider the following steps:

1. In the first stage, we assume that $a(u) = c_0$. According to the over-specified data (14), in the system of equations (58) and (60), $a(u)$ is known and c_0 as unknown , is inserted instead of $a(u_i)$ and then the values of c_0 and u_i for $i = 1,...,10$ will be calculated by solving a system with 11 equations and 11 unknowns. Now $a(u)$ is known, so the equations (10) to (13) can be solved for $0 \le t \le T$ and the minimum of function $J_1 = \int_0^T |u(0,t) - F(t)|^2 dt$ can be obtained.
2. In the second step, with regards to c_0 has been obtained at the first step, by assuming $a(u) = c_0 + c_1 u$, coefficient c_1 can be calculated by solving equations (58) to (60) and we calculate the minimum function $J_2 = \int_0^T |u(0,t) - F(t)|^2 dt$. If the value of J_2 is less than J_1, degree of the polynomial $a(u)$ will increase in the next step, otherwise we will stop this process.

6. Conclusion

The present work has put forward a nonlinear model which can be used to study the behaviour of an incompressible fluid in layer diffusion in a hydrocarbon reservoir. After proving the existence and uniqueness of solution for the problem, we have proposed a numerical algorithm in order to estimate the unknown parameters of the problem as described earlier. At the first, the mentioned steps in the algorithm, result in estimating the values of $a(u)$ at

time $t = 0.01$, afterward, we need to repeat the steps to obtain the diffusion coefficient rates at every time level .In these time levels, if the rates are the same then one of them is considered as the diffusion coefficient, otherwise we have to fit a curve to the obtained diffusion rates. This curve is the total diffusion rate. Eventually, it is very interesting to illustrate some numerical results for unknown parameters as a numerical experiment.

References

[1] Plaint M and Rundell W. An Inverse Problem for a Nonlinear Parabolic Equation. Comm. P.D.E., 1986.

[2] Haberman R. Elementary Applied Partial Differential Equations. Prentice Hall International Editions, Englewood Cliffs, New Jersey, 1987.

[3] du Chateau P and Rundell W. Unicity in an Inverse Problem for an Unknown Reaction term in a Reaction Diffusion Equation. J Differential Equation, 1985;59: 155-164.

[4] Cannon JR and du Chateau P. Determining Unknown Coefficient in a Nonlinear Heat Conduction Problem. SIAM J. Appl. Math., 1973; 24(3): 298-314.

[5] Shidfar A, Shahrezaee A and Garshasbi M. A Method for Solving an Inverse Biharmonic Problem. J. Math. Anal. Appl., 2005; 302: 457-462.

[6] Shidfar A, Karamali GR and Damirchi J. An Inverse Heat Conduction Problem with a Nonlinear Source Term. Nonlinear Analysis, Theory Methods & Applications, 2006; 65: 615-621.

[7] Cannon JR and Zachmann D. Parameter Determination in Parabolic Differential Equation from Over-Specified Boundary Data. Int. J. Eng. Sci.,1986; 20: 779-788.

[8] du Chateau P. Monotonicity and Uniqueness Results in Identifying and Unknown Coefficient in Nonlinear Diffusion Equation. SIAM J. APPL. Math., 1981; 41(2): 310-323.

[9] Peaceman DW. Numerical Simulation in Oil Reservoirs. Elsevier Scientific Publishing Company, Amesterdam, 1977.

[10] Tarek A. Reservoir Engineering Handbook, Gulf Professional Publishing, 4th Edition, 2010.

[11] M.R. Riazi, Familiarity with Oil and Gas Reservoirs Engineering, Scientific Publications, Sharif University of Technology, Tehran, Iran, 1995.

[12] Cannon JR. The One-Dimensional Heat Equation. Addison–Wesley, Menlo Park, CA, 1984.

[13] Sollonikov VA, Ladyzhenskaya OA and Uralceva NN. Linear and Quasi-Linear Equations of Parabolic type. AMS, Providence RI, 1986.

[14] Friedman A. Partial Differential Equations of Parabolic Type. Prentice Hall, Englewood Cliffs, NJ. Chapter 7 Theorem 4 (1964).

[15] Friedman A. Partial Differential Equations of Parabolic Type. Prentice Hall, Englewood Cliffs, NJ. Chapter 7 Theorem 1 (1964).

[16] Cannon JR and Lin Y. Determination of Parameters $p(t)$ in some Holder Classes for Semi-Linear Parabolic Equations. Inverse Problems, 1988;4: 595-606.

To whom correspondence should be addressed: Prof. Amir H. Mohammadi, Discipline of Chemical Engineering, School of Engineering, University of KwaZulu-Natal, Howard College Campus, King George V Avenue, Durban 4041, South Africa, amir_h_mohammadi@yahoo.com

Petroleum and Coal

Article **Open Access**

EVALUATING OF SBS POLYMER-MODIFIED BITUMEN EMULSION ON RECYCLED ASPHALT MIXTURE

Parham Hayati[1], Hasan Ziari[2], Sajad Rezaei[3]

[1] *Department of Civil Engineering, Islamic Azad University, Science and Research Branch, Tehran*
[2] *College of Civil Engineering, Iran University of Science & Technology, Tehran, Iran*
[3] *Department of Civil Engineering, Pooyesh Institute of Higher Education, Qom, Iran*

Received January 29, 2018; Accepted April 27, 2018

Abstract

In the base of researches Styrene Butadiene Styrene (SBS) copolymer is one of the best polymers for modifying the bitumen thermal properties. In this research, the effect of SBS with different percentage (0, 3, 4, and 5) on properties of the recycled asphalt mixture (100% RAP) with using Marshal and ITS tests is studied. In the base of experimented case studies such as the asphalt behavior modifying against the ambient the pavement stability increasing against perpetual deforming and the undercut of wheel path in high operational temperatures and consequently it is more stable against ambient temperature changings. It may be concluded that the adhesion of bitumen film to rock materials, the strength against the stresses and the stability against deforming in recycled samples including polymer-modified bitumen emulsion increases while their thermal sensitivity decreases.

Keywords: *Recycled Asphalt Mixture; Cold recycling; Bitumen Emulsion; Modified; SBS polymer.*

1. Introduction

Many types of research are annually conducted about the modification of bitumen behavior and the performance of asphalt mixtures using modifiers [1-2]. Among the high-consumption modifiers, styrene-butadiene-styrene copolymer is widely used [3]. Since this modifier is a copolymer block of polystyrene and poly butadiene, as the styrene block, and the butadiene block provide the resistance and flexibility, respectively, and the glass transition temperature of polystyrene is 100°C and poly butadiene is 90°C; Therefore, SBS can decrease the temperature sensitivity of the bitumen [4-5] and increase the resistance potential of asphalt mixtures against low temperature cracking, stripping, fatigue, and rutting [6-8].

The polymer-modified bitumen emulsions are produced by dispersing a polymeric phase as an internal phase in bitumen as external phase [9-10]. Although research on the effect of SBS on bitumen behavior and asphalt mix performance is widespread, investigations on the effect of this modifier in the emulsion bitumen are still limited in order to be used in recycled asphalt mixtures. Therefore, in this paper, the performance of the SBS additive in various percentages was analyzed for bitumen PG 64-16 or 60/70 bitumen as the most consumed bitumen in the production of recycled asphalt mixtures in Iran. For this purpose, the performance of the base bitumen and SBS bitumen compounds were evaluated based on softening point, penetration, ductility, elastic recovery, flash point, specific gravity, rotational viscosity and mass loss of RTFO and the performance of cold recycled asphalt mix modified with polymer bitumen emulsion was evaluated based on resistance and flow of Marshal and indirect tensile strength tests.

2. Method

2.1. Materials

The utilized materials in this research are pure bitumen with PG 64-16 (also called 60/70 bitumen) from Tehran Pasargad Oil Company, LG 501 SBS polymer from South Korea LG

Company, emulsifier to stabilize the emulsion production (STABIRAM 4582, CECA France), HCL acid with 35% purity and kerosene, and rock materials from reclaimed asphalt pavement (RAP) recovered by recycling machine from Imam Reza Highway East to West line in Tehran.

Table 1. Chemical composition of base bitumen, Physical and chemical properties of SBS, and Physical and chemical properties of emulsifier

Materials	The experiment	Method of experiment		Standard specification		Result
		AASHTO	ASTM	Max	Min	
bitumen	Specific gravity @25°C	T 228	D 70	1.10	1.00	1.026
	Penetration@25°C	T 49	D 5	70	60	65
	Softening point (Ring and Ball, °C	T 53	D 3398	56	49	50.3
	Ductility @25°C	T 51	D 113	-	100	+100
	Solubility in trichloroethylene	T 44	D 2042	-	99	99.8
	Flash points	T 48	D 92	-	250	312
	Kinematic viscosity in135°C(centiStoke)	T 201	D 2170	-	-	295
	C (poises) 60°C	T 202	D 2171	-	-	1705
	Absolut viscosity in TFOT (163°C -5hours)	T 179	D 1754	-	-	0.1
	Softening point) PI (Penetration@25°C	-	-	-	-	-0.127

SBS	Product name	Physical state	Colour	Density	Weight percent of styrene to total weight of polymer	Molecular structure
	LG 501	Solid	White	0.94	31	Linear

Emulsifier	Application	For producing shatterproof cationic emulsions in order to recovering and slurry sill. It should be solved in water in temperature between 40-50 centigrade and then neutralized with HCL to reach to appropriate PH.	
	Dosage (%)	0.4 - 1	
	PH	2 - 4	
	Composition	Quaternary Ammonium salt	
	Physical properties	Aspect@ 20°C	liquid
		Density @ 25°C	1.05
		Solid point	-13°C
		Flash point	40°C
		viscosity @20°C	40cP
	Storage	Stable at normal temperature and stored in closed containers protected from freezing.	
	Package	175 kg barrels	
	Safety precautions	It is not a dangerous material but it is better to wear glove, top coat and safety glasses when it is used.	

Table 2. The results of quality experiments on RAP

Experiment	Standard		Unit	Quality value in the base of standard	Result
	AASHTO	ASTM			
Abrasion by Los-Angeles in 500 rpm	T 96	C 131	%	Max 40	24
Materials weight decrease by sodium sulfate (salt cake)	T 104	C 88	%	Max 12	1.7
Percent of fracture in one front	-	D 5821	%	Min 50	89
Percent of fracture in two fronts	-	D 5821	%	Min 50	71
The maximum size	-	D 8	mm	Max 37.5	37.5
Sand equivalent	T 176	D 2419	%	Min 35	60
Absorption of water	T 84, 85	C 127, 128	%	Max 3	0.91

RAP was used instead of new rock materials to be representative of the real utilized mixture. They were characterized in the laboratory. The bitumen weight percentage was determined by extraction experiment equal to %4.9. The results of rock materials mixture's gradation by bitumen emulsion were consistent with continuous gradation D in bitumen institute method [11]. The properties of bitumen, polymer, and emulsifier are given in Table (1). The results of carried out quality experiments on RAP have been compared with standard values in Table (2).

2.2. Samples preparation

2.2.1. Samples preparation of SBS polymer-modified bitumen emulsion

The weight percent of effective materials in aqueous and bitumen phases were determined for producing stable cationic SBS polymer-modified bitumen emulsion, Table (3).

Table 3. Overall specifications of cationic SBS polymer-modified bitumen emulsion

	Phase of production	Phase percent	Effective materials	Specifications of effective materials	Weight percent
The weight percent of effective materials in SBS polymer-modified bitumen emulsion production with EMULAB device	Aqueous phase pH=2	40	Water	-	38.6
			Emulsifier	STABIRAM 4582 (CECA France)	1.2
			Acid	HCL %35 Purity	0.2
	Bitumen phase	60	Polymeric bitumen SBS= %3, %4, and %5	SBS polymer 60/70 bitumen	60

In the first step and in the bitumen phase, the polymeric bitumen is produced by shear stress of High Shear mixer by 4000 rpm for two hours in 175°C considering the compound formulation and the mixing trend of utilized materials in production of polymeric bitumen with different SBS percentages of 3, 4, and 5 percent of bitumen weight. In next step, aqueous phase (pH=2) containing water plus emulsifier (Quadrivalent Ammonium Salt) also (CECA France), STABIRAM 4582 with HCl (%35 Purity) were spilt in aqueous phase reservoir of EMULAB device at 50°C circulated by pump, then the resultant phase entered into colloidal meal at 90°C and while mead rate was to the maximum (8000 rpm), then the bitumen phase entered into meal, and finally the polymeric bitumen emulsion was extracted at 60–70°C.

2.2.2. Samples preparation of Recycled Asphalt Mixture

Samples of cold recycled asphalt mixture were prepared according to Marshal Method (ASTM D6927-15), Table (4).

Table 4. The governing conditions on samples preparation of recycled asphalt mixture using Marshal method

Project	Emulsion cold recycling	Temp of rock materials	25°C
The purpose of plan	Determination of SBS polymer effects on specifications of recovered asphalt mixture	Temp of bitumen	60°C
The place of sampling	Imam Reza multilane highway east to west	Temp of water	25°C
RAP percent at total weight of rock materials	100	Compression temp	60°C
Kind of bitumen	CSS	Treatment temp	60°C
Number of pulses on each side	50	Treatment time	6 hr

2.3. Experiments

The physical experiments including needle penetration in 25°C (ASTM D5), softening point (ASTM D36), ductility in 25°C (ASTM D113) and Elastic recovery in 25°C (ASTM D6084) was done on the base bitumen and SBS polymer-modified bitumen samples. Furthermore, to

examine the temperature susceptibility of the modified bitumen, needle penetration index (PI) [12] was used.

3. Results and discussion

3.1. The experimental study of polymeric bitumen samples' specifications with different SBS percentages

For studying the properties of produced polymeric bitumen samples with different percent of SBS, different experiments such as determination of penetration degree, softening point, elastic recovery, flash points, specific gravity, rotational viscosity, mass loss of RTFO, and needle penetration index were conducted on them. The results of these experiments for the base bitumen and SBS polymer-modified bitumen samples with different SBS percentages of 2, 3, 4, 5, and 6 percent of bitumen weight are presented in Table (5). As can be seen, the penetration degree of bitumen samples in 25°C decreases with the increase of polymer percentage and the bitumen becomes firmer. Also the softening point of bitumen samples, viscosity and PI increases with the increase of polymer. This fact shows the modification of bitumen behavior against ambient temperature changing, because it is possible to utilize this modified bitumen in a warmer zone or in a zone with heavier traffic. According to Table (5), given the fact that the maximum amount of SBS providing ductility equals 100 cm is a composite with SBS of 4 weight percent of bitumen.

Table 5. The results of performed experiments on base bitumen and SBS polymer-modified bitumen samples

Type of experiment		Method of experiment	Base bitumen	Polymeric asphalt results SBS 2%	SBS 3%	SBS 4%	SBS 5%	SBS 6%
Penetration @25°C		ASTM D5	65	56	54	48	43	42
Softening point, °C		ASTM D36	50.3	55.5	59.5	79.5	85	84.5
Ductility @25°C (cm)		ASTM D113	>100	>100	>100	>100	98	94
Elastic recovery in 25°C		ASTM D6084	16	37	50.5	62.5	66	67.5
PI		-	-0.127	0.090	0.259	0.790	0.852	0.835
Flash Points (°C)		ASTM D92	312	309	308	307	310	307
Specific Gravity (g/cm^3)		ASTM D70	1.026	1.007	1.005	1.007	1.005	1.002
Rotational viscosity (Pa.s)	120°C	ASTM D4402	0.667	0.858	1.11	1.761	2.136	2.714
	135°C		0.323	0.473	0.615	0.878	1.076	1.371
	150°C		0.162	0.259	0.328	0.473	0.565	0.758
	165°C		<0.100	0.149	0.191	0.267	0.33	0.413
	180°C		<0.100	<0.100	0.111	0.159	0.264	0.292
RTFO (Mass loss %)		AASHTO T240	0.07	0.23	0.24	0.22	0.25	0.27

3.2. Defining percentage of optimizing emulsion bitumen and that of optimizing humidity

Step A: a composite of RAP material with emulsion bitumen with adding filler of cement to optimizing %1.5 was considered. Alteration range of emulsion bitumen is from %0.5 to %4 with growth rate %0.5 to define optimizing emulsion bitumen percent. The mix humidity with material humidity %1 was calculated from the equation (2).

Equation (2) (Percent of humidity of rock material) + (water percentage of emulsion bitumen) = the water must be added

According to the results of Marshal test and specific weight of recycled samples and with controlling percentage of voids ranges between 9 to 14, that of optimizing emulsion bitumen equals %2.3, Table (6).

The step of B: a composite of emulsion and RAP material with adding an active filler of cement is considered and optimizing amount %1.5 in optimizing emulsion bitumen percentage (%2.3) is confirmed. Alteration range of mixture water is %2.5, %3.5, %4, and %4.5 according to the result of Marshal test and specific weight of recycled Sample and with controlling voids percent in ranges from 9 to 14, optimizing humidity percent is equal %3.5, Table (6).

Table 6. The Marshal results for (A) percent of optimizing emulsion bitumen and (B) percent of optimizing humidity

Steps	Emulsion bitumen (%)	Cement (%)	Water (%)	Real specific weight (g/cm³)	Max specific weight (g/cm³)	Void (%)	Marshal stability (kg)	Marshal Flow (mm)
A	0.5	1.5	2.8	1.967	2.261	13.00	1033	5.82
	1	1.5	2.6	2.005	2.273	11.80	1072	4.00
	1.5	1.5	2.4	2.038	2.298	11.30	1191	4.02
	2	1.5	2.2	2.071	2.325	10.90	1138	3.53
	2.5	1.5	2.0	2.089	2.339	10.70	1141	3.21
	3	1.5	1.8	2.080	2.313	10.05	1182	3.97
	3.5	1.5	1.6	2.067	2.299	10.10	931	4.00
	4	1.5	1.4	2.057	2.289	10.13	870	4.72
B	2.3	1.5	2.5	2.040	2.310	11.70	979	6.23
	2.3	1.5	3	2.068	2.325	11.06	1065	4.83
	2.3	1.5	3.5	2.085	2.331	10.54	1115	5.17
	2.3	1.5	4	2.073	2.321	10.68	1037	5.47

3.3. Defining percentage of optimizing SBS polymer-modified bitumen emulsion on recycled asphalt mixture

A composite of polymer emulsion bitumen with 0, 3, 4, and 5 percent of SBS in constant optimizing emulsion bitumen (%2.3) with RAP material with adding cement active filler (optimizing percentage= 1.5 and optimizing humidity percentage= 3.5) is considered to define percentage of optimizing polymer emulsion bitumen of recycled asphalt mixture samples. The comparisons and results of Marshal, ITS and Specific weight tests of recycled asphalt mixture samples are based on a various percentage of polymer emulsion bitumen as shown in Table (7) and Figure (1). According to this research, the marshal strength (resistance) increases as SBS polymer percentage increases. It is worth to be mentioned that as the SBS increases, the value of Marshal Resistance increases to %23.85. It is worth mentioning that the rate of Marshal Resistance is from %0 to %3 SBS, approximately %4, from %3 to %4 SBS, %17.73, and from %4 to %5 SBS increases to %1.16. Two above-mentioned cases represent that in equal conditions from the viewpoint of materials, the quantity and quality of active filler, moisture and constant optimum bitumen percentage, the quantity of consolidation against the stresses with the increase of SBS polymer percentage. With increasing percent of SBS, dry and saturation ITS and TSR of recycled samples increased.

Table 7. The effects comparison of SBS polymer-modified bitumen emulsion on recycled asphalt mixture

SBS (%)	0	3	4	5
Emulsion bitumen (%)	2.3	2.3	2.3	2.3
Cement (%)	1.5	1.5	1.5	1.5
Water (%)	3.5	3.5	3.5	3.5
Dry ITS (kPa)	278.8	288.7	294.9	295.1
Sat ITS (kPa)	182.4	192.1	202.9	206.8
TSR (%)	65.4	66.5	68.8	70.1
Real specific weight (g/cm³)	2.085	2.103	2.133	2.135
Max specific weight (g/cm³)	2.331	2.358	2.377	2.379
Void (%)	10.54	10.82	10.26	10.26
Marshal Stability (kg)	1115	1159.5	1365.1	1380.9
Marshal Flow (mm)	5.17	5.31	4.21	4.16

4. Conclusion

As seen in this research, with SBS percent increasing from 0 to 5 could be obtained that Marshal stability of recycled asphalt mixture samples has a positive increasing. With observing

dry and saturated tension resistance of recycled samples in different percentage of SBS, it can be concluded that increasing of this parameter have a direct relation to the increase of polymer percentage. With the increase of SBS polymer percentage, TSR in recycled asphalt mixture samples increases and this shows the increasing of wet resistance in recycled samples in comparison with not using polymer situation. Generally according to Marshal Stability, dry ITS, Sat. ITS, and TSR parameters, changes of these parameters from %4 to %5 SBS is insignificant, and the diagram turns into constants mode. So it can be concluded that with economic considerations and improvement of recycled asphalt mixture sample properties, %4 could be recommended as the optimum percent of SBS.

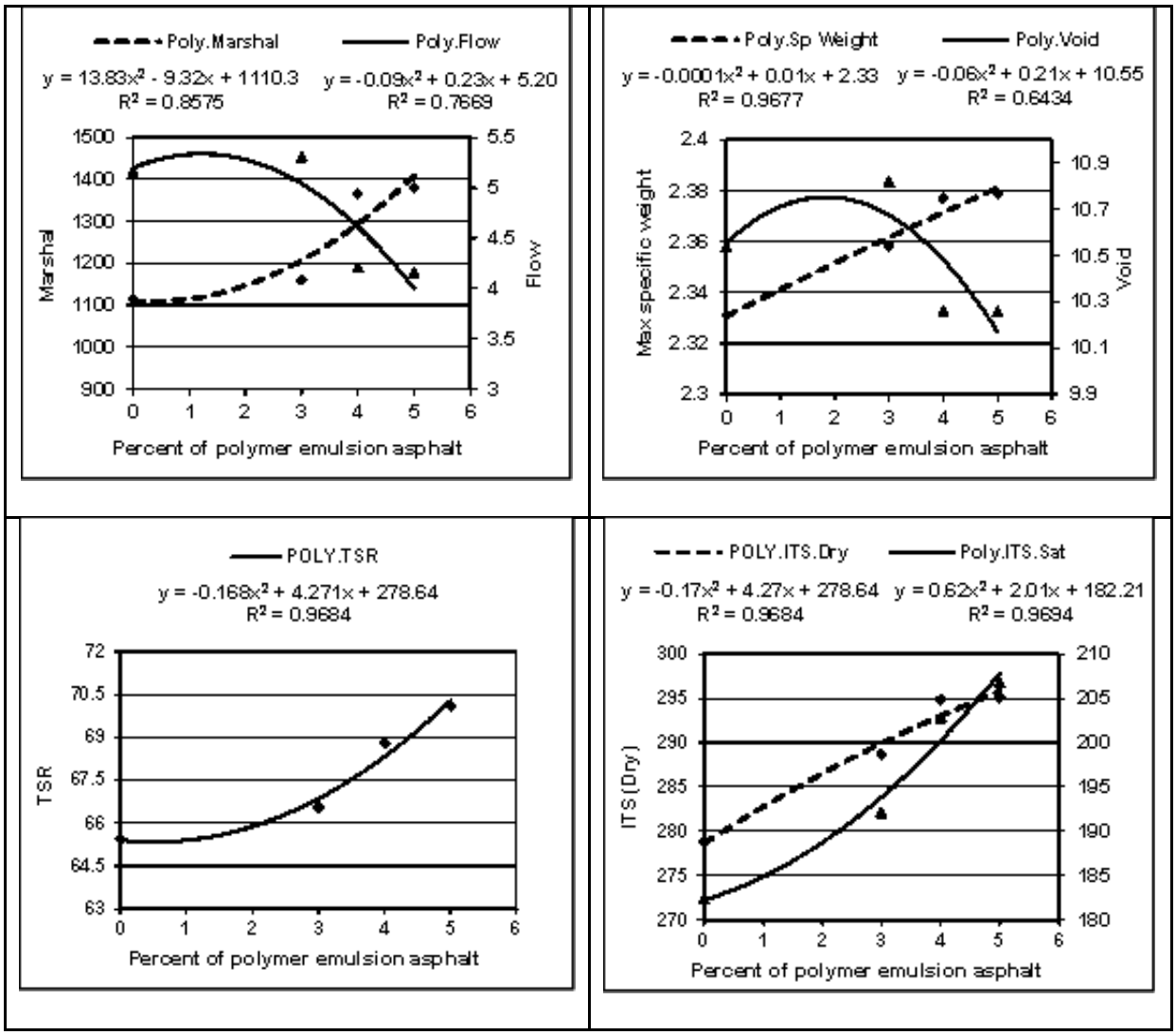

Figure 1. The diagrams of results of Marshal, ITS and specific weight tests of recycled asphalt mixture samples base on various percent of polymer emulsion bitumen

References

[1] Mundt DJ, Adams RC, & Marano KM. A historical review of additives and modifiers used in paving asphalt refining processes in the United States. Journal of occupational and environmental hygiene, 2009; 6(11): 705-713.

[2] Hrušková L, Peller A, & Daučík P. Evaluation of crumb rubber properties term of use as modifier for asphalt. Petroleum & Coal, 2016; 58(3): 349-358.

[3] Rezaei S, Khordehbinan M, Fakhrefatemi SMR, Ghanbari S, & Ghanbari M. The effect of nano-SiO2 and the styrene butadiene styrene polymer on the high-temperature performance of hot mix asphalt. Petroleum Science and Technology, 2017; 35(6): 553-560.
[4] Rezaei S, Ziari H, & Nowbakht S. (2016). Low temperature functional analysis of bitumen modified with composite of nano-SiO2 and styrene butadiene styrene polymer. Petroleum Science and Technology, 2016; 34(5): 415-421.
[5] Firoozifar SH, Alamdary YA, & Farzaneh O. Investigation of novel methods to improve the storage stability and low temperature susceptivity of polyethylene modified bitumens. Pet Coal, 2010; 52(2): 123-128.
[6] Bulatović VO, Rek V, & Marković KJ. Effect of polymer modifiers on the properties of bitumen. Journal of Elastomers and Plastics, 2014; 46(5): 448-469.
[7] Liang M, Liang P, Fan W, Qian C, Xin X, Shi J, & Nan G. (2015). Thermo-rheological behavior and compatibility of modified asphalt with various styrene–butadiene structures in SBS copolymers. Materials & Design, 2015; 88: 177-185.
[8] Karakas AS, Kuloglu N, Kok BV, & Yilmaz M. The evaluation of the field performance of the neat and SBS modified hot mixture asphalt. Construction and Building Materials, 2015; 98: 678-684.
[9] Chaverot P, & Demangeon F. (1995). U.S. Patent No. 5,382,612. Washington, DC: U.S. Patent and Trademark Office.
[10] Firoozifar SH, Foroutan S, & Foroutan S. The effect of pH and bituminous density on stabilization of bitumen-in-water emulsion. Pet Coal, 2010; 52(1): 31-34.
[11] Epps JA. Cold-recycled bituminous concrete using bituminous materials 1990:No. 160. Transportation Research Board.
[12] Galooyak SS, Dabir B, Nazarbeyg, AE, & Moeini A. (2010). Rheological properties and storage stability of bitumen/SBS/montmorillonite composites. Construction and Building Materials, 2010; 24(3): 300-307.

To whom correspondence should be addressed: Dr. Parham Hayati, Department of Civil Engineering, Islamic Azad University, Science and Research Branch, Tehran

Petroleum and Coal

Article **Open Access**

DEVELOPMENT OF A SMART DIGESTER FOR THE PRODUCTION OF BIOGAS

Ilesanmi A. Daniyan[1], Akporode K. Ahwin[1], Adeyemi A. Aderoba[1] and Lanre Daniyan[2]*

[1] *Department of Mechanical & Mechatronics Engineering, Afe Babalola University, Ado-Ekiti, Nigeria*
[2] *Department of Instrumentation, Centre for Basic Space Science, University of Nigeria, Nsukka, Nigeria*

Received April 30, 2018; Accepted June 27, 2018

Abstract

Due to the rising need for alternative sources of energy, as a result of the challenges of fossil fuel, studies must forge on to explore other viable sources of clean and renewable energy like biogas. Biogas is a combustible mixture of bio-methane, carbon (IV) oxide, and other trace gases. It is produced as a result of anaerobic digestion of organic matter. This work develops a small-scale biogas plant with a smart system that was used to enhance the study of biogas production at the Department of Mechanical and Mechatronics Engineering, Afe Babalola University Ado-Ekiti (ABUAD). The plant was designed using Autodesk Inventor and fabricated with Stainless steel due to its high resistance to biological corrosion. An Arduino Uno Microcontroller was also connected to a pressure, pH and temperature sensors to monitor the process parameters of the developed biogas plant. Results obtained to validate the direct relationship between organic loading rate and biogas production. It also showed the interaction between temperature and pressure, temperature and pH, pH and pressure. Optimization of the process parameters was carried out using the central composite design model and response surface methodology. Taking the biogas yield as the response of the designed experiment, the data obtained were statistically analysed to obtain a suitable model for optimization of biogas yield as a function of the process parameters. For a sample 24-hour period the optimum values of the process parameters for the optimum yield of biogas (23 litres) were found to be: Loading rate (0.75 kgVDM/m^3), temperature (25.34^{o}C), pH (7.04) and pressure (4.84 kPa). The work has been able to lay a foundation for studies on biogas production using sensors and continuous parameter monitoring. It has also laid a foundation for research work by developing a small scale biogas plant for experimental purposes.

Keywords: *anaerobic digestion; biogas; organic matter; smart system; renewable energy.*

1. Introduction

Biogas is a combustible mix of gases produced by the natural fermentation of wet biomass in an anaerobic process [1]. Biogas production technologies are highly beneficial to society as they transform waste into useful energy while reducing environmental pollution. Furthermore, the digestate (decomposed substrate) provides a source of potent fertilizer for improving plant yield. Biogas is a sustainable source of energy and can be explored to end the dependence on energy from fossil fuels.

The average human being produces about 1.2 kg of waste each day [2]. In all parts of the world, increasing production and improper management of organic waste is a major environmental problem [3]. Even more troubling, according to the World Energy Council [4], more than 80% of the world's energy need is currently being met from non-renewable energy sources. It is thus imperative for the engineering profession to develop waste-to-energy systems to help meet the energy demands of society. In domestic application, heat energy is required each day for warmth and cooking. This energy can be provided in a sustainable manner with the implementation of a waste-to-energy conversion system using anaerobic digestion of organic waste to yield biogas for cooking, space heating and even powering of combined heat and power (CHP) engines, and organic fertilizer for improving plant yield.

This work develops a small-scale biogas plant that converts food waste and animal excreta to biogas via anaerobic digestion. According to Ramatsa *et al.* [5], anaerobic digestion is a four-stage process brought about by the combined action of several species of bacteria. The first stage called hydrolysis where long chain substances like carbohydrates, proteins, and fats are broken down into smaller fragments such as simple sugars, glycerol, fatty acids and amino acids [6]. In the second stage called acidogenesis and acidification, fermentative microorganisms convert these smaller fragments into short chain fatty acids such as acetic acid, propionic acid, and butyric acid [7]. In the third stage of acetic acid formation (acetogenesis), the products of the previous stage are the starting substrates. With these products, lactic acid, alcohols, and glycerol, these substances are converted by acetogenic microorganism into acetic acid, hydrogen and CO_2. In the fourth and final stage, methane bacteria act on the acetic acid, hydrogen, and CO_2 to produce methane [7-8]. This biogas typically contains 50 - 70% of methane [9]. With the above process, it becomes evident that biogas production is a fairly complex process. According to Weise and Konig [9], without instrumentation and proper monitoring, biogas plants are often under-loaded i.e., the biomass feed rate (organic loading rate) are below required levels to make the process cost-effective. Thus, the biogas plant will also be incorporated with a monitoring system consisting of sensors and a microcontroller to continuously monitor the process parameters- pH, temperature and pressure and indicate plant malfunction.

The aim of this work is to develop and optimize a small-scale biogas plant with a smart system for use in small scale applications.

Since conventional biogas plants are not monitored, they are plagued with various challenges including the aforementioned under-loading of organic material (low organic loading rate) and overloading (excessive organic loading rate). Overloading slows down or stops the anaerobic digestion process and may cause a total system breakdown. Another considerable challenge that arises from lack of monitoring is diges-ter instability which arises as a result of unsuitable pH for biogas production. According to Weise and Konig [8], for the first and second stage of biogas production, the best pH is between 4.5 – 6.3. For the third and fourth stages where methane formation is evident, the optimal pH range is specified as 7.0 -7.7.

The anaerobic digestion process, however, self-regulates to achieve such a pH level, but it is common to have biogas plants fed with substrates that will make achieving this range difficult. This greatly increases the time needed for biogas production to commence. Furthermore, another challenge that arises from inadequate or non-existent biogas plant monitoring is poor production due to excessive temperature fluctuations or improper temperature range for various types of methanogenic bacteria. Methanogenic bacteria can either be psychrophilic (operating effectively between 12 to 24°C), mesophilic (operating optimally between 22-40°C) or thermophilic (thriving optimally between 50 – 60°C). All these points to a gap in cost-effective and easily accessible monitoring systems for biogas plants especially in the conventional pilot and small-scale biogas plants. With the recent national economic turbulence and a worldwide slump in oil prices, it has become evident that countries must look inward to renewable sources of wealth and energy that will be economical, socially and environmentally sustainable. According to Davidson [10], 'sustainable energy' is energy for 'sustainable development'. Hence, the development of this system that will minimize improper waste disposal in communities, while creating wealth from waste, reducing landfills and providing a potent organic fertilizer becomes not only attractive but needful. Since waste is generated on a daily basis in academic and industrial areas, the system becomes desirably sustainable to study the anaerobic digestion process continuously. The fertilizer output can then be used on farms to grow crops that will help meet the local nutritional needs of society. Incorporation of the monitoring system also becomes desirable in ensuring that the process is both safe and stable. The sensors can detect anomalies in operation, and warning alarms can be raised to prevent plant instability, accidents, and emergencies before they occur.

This research is limited to development of a small-scale biogas plant for studying biogas production using a variety of organic waste. The small-scale biogas plant is incorporated with a smart monitoring system that is limited to data acquisition and display.

Anaerobic digestion requires a vessel with an enclosed (i.e., air-tight) environment in which diverse microbial consortium which degrade organic material to generate biogas. When organic material including animal manure, agricultural residues, sewage sludge and food waste among others, undergo anaerobic digestion by the action of anaerobic bacteria, biogas is produced. According to Al Seadi *et al.* [3] and Friehe *et al.* [9], this gas mixture called biogas consists primarily of methane (50-75 % vol.) and carbon dioxide (25- 50 % vol.). Biogas also contains small quantities of hydrogen, hydrogen sulphide, ammonia and other trace gases. The composition of the gas is essentially determined by the substrate supplied, the fermentation (digestion) process and the technical design of the plant. According to Friehe *et al.* [9], monitoring biological processes is challenging. Despite this fact, however, a variety of options exist for monitoring of plants ranging from operating logs to fully automated data acquisition and control systems. In the small-scale application, however, complex systems are to be avoided due to cost implication.

According to Weise and Konig [8], to achieve optimal control of the biogas plant, detailed knowledge of key chemical and physical properties including temperature, pH, organic acid and fatty acid concentration, ammonium concentration and acid capacity. The sensors required for monitoring key process parameters including pH, pressure, and temperature will be studied subsequently. The process by which biogas is formed can be divided into four major steps as shown in Figure 1. These individual stages of decomposition (degradation) must be coordinated and harmonized with each other in the best way possible to ensure that the process completes smoothly without impediment or instability [9].

During the first stage, complex compounds of the starting material including carbohydrates, proteins, fats, and oils are broken down into simple organic compounds such as amino acids, sugars and fatty acids/glycerol. The hydrolytic bacteria involved in this stage releases enzymes that decompose the material by biochemical means.

During this acidification phase, the immediate products from hydrolysis are then further broken down by acid-forming (fermentative) bacteria to form lower fatty acids (acetic, propionic and butyric acid) alongside carbon dioxide and hydrogen. Also, small quantities of lactic acid and alcohols are also formed. The nature of products formed during this stage is influenced by the concentration of the intermediate hydrogen content.

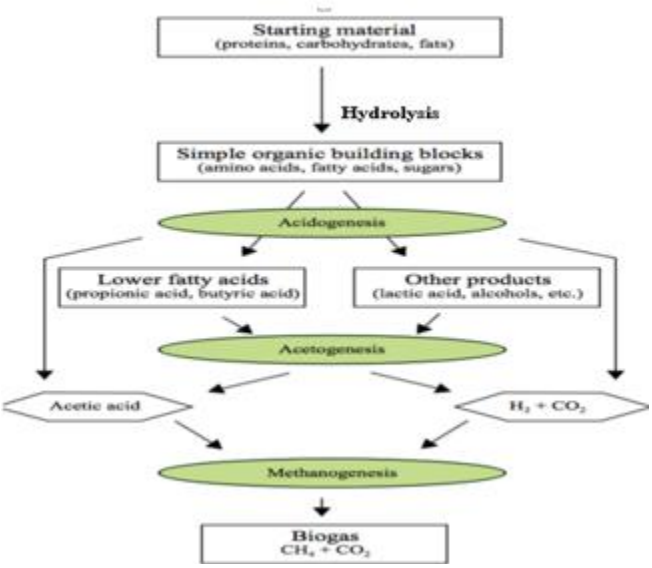

Figure 1. Schematic representation of anaerobic digestion *(Source: Friehe et al.* [9]*)*

In this stage, acetic acid forms. The products of the acidification phase (acidogenesis) are then converted by acetogenic bacteria into precursors of biogas (acetic acid, hydrogen, and carbon dioxide). The partial pressure of hydrogen is particularly important in this connection. Excessive partial pressure of hydrogen can prevent the conversion of the intermediate products of acidogenesis due to energy related reasons.

As a consequence of this excessive partial pressure, organic acids such as propionic acid, isobutyric acid, isovaleric acid and hexanoic acid accumulate and inhibit the formation of methane. For this reason, the hydrogen-forming (acetogenic) bacteria must co-exist in a close biotic community with the hydrogen-consuming methanogenic archaea, which consume hydrogen together with carbon dioxide during the formation of methane, thus ensuring an acceptable environment for the acetogenic bacteria.

This is the final stage of biogas generation. Acetic acid, hydrogen and carbon dioxide are converted into methane by strictly anaerobic methanogenic archaea. The hydrogenotrophic methanogens produce methane from hydrogen and carbon dioxide, whereas the acetoclastic methane-forming bacteria produce methane by acetic acid cleavage. At higher organic loading rates (usually obtainable in agricultural biogas plants), methane is formed primarily via the reaction pathway utilizing hydrogen, while it is only at relatively low organic loading rates that methane is formed via the reaction pathway involving the cleavage of acetic acid [11].

In an anaerobic digester or reactor, these four phases of anaerobic degradation take place simultaneously as a single-stage process. According to Vanek *et al.* [12], anaerobic digesters are open systems which means that diverse types of microbes can come in with the waste streams to circumvent the need to sterilize the inflow streams, and this eventually results in thousands of microbial species being present in a relatively stable consortium. This suggests that within the anaerobic digester, microbes comprise a food web, which means that a product from one microbe is the substrate (food) for another one.

According to Dobre *et al.* [13] and Friehe *et al.* [14], the following key factors affect the production of biogas via anaerobic digestion of organic waste. The hydraulic retention time (HRT) it is the mean range in which the substrate for anaerobic digestion process is retained in the digester, in contact with active bacterial mass. Substrates containing simple compounds are easily decomposed and require short HRT, while substrates containing complex compounds are harder decomposed and require a longer HRT. The retention time of the solids (SRT) is the measure of the biologic system capability to reach certain standards concerning the effluents and/or to maintain a satisfactory rate of pollutants biodegradation. SRT controls the microbial mass in the reactor in order to obtain a degree of waste stabilization.

Maintaining a high SRT translates to more stable running, better tolerance to toxic and shock loads and quick recovery after toxicity or instability. HRT is a key factor in the design process anaerobic digestion for digestible and hard complex organic pollutants, while SRT is the control parameter in the design process for readily digestible organic elements.

HRT is determined by the volume of the digester and the amount of substrate loaded per unit of time, according to the equation .1.

$$\mathrm{HRT} = \frac{V_d}{V_s}\ [\mathrm{days}], \qquad (1)$$

where: HRT is the hydraulic retention time [days]; V_d is the digester volume [m^3]; V_s is the amount of substrate loaded per time unit [m^3/s].

A short retention time determines a better flow rate of the raw material, but the low productivity of biogas.

In the production process of biogas, the pressure is of great significance. The experiments have shown that when hydrostatic pressure prevailing on the methanogenic bacteria increases over the range, 400 - 500 mm H_2O [13], biogas production ceases and is resumed when the hydrostatic pressure falls below that range. This is a critical component of the design work as it determines the height of fluid that the digester tank should operate with. For vertical digesters where the height can reach tens of meters, biogas is produced only up to maximum depth 4 – 5 m and the rest of the area occupied by the substrate does not produce biogas,

which is why it is necessary to periodically bring to surface the material under the limit of reaction, by the stirring continued. The negative impact of this factor can also be avoided by using a horizontal tank whose height is typically below 3.5 m.

In anaerobic digestion all biological processes are carried out at well-defined values of pH. The pH of the optimal hydrolytic stage is between 5 - 6, and for methane production (methanogenesis) stage, the optimal pH value varies between 6.5 – 8. If the pH value decreases below 6, methane production is strongly inhibited. In the hydrolytic stage, the acidogenic bacteria require a pH in the range 5.5 – 7.0, and in the final stages, methanogenic bacteria require a pH value ranging between 6.5 - 8.0.

A major limitation to the processing of organic substrates through the process of anaerobic digestion in a single phase is a lower value of pH in the reactor due to rapid acidification by the production of volatile fatty acids. This effect hinders and inhibits the activity of methanogenic bacteria. At digesters operating in a single phase with the full mixing of the substrate, the pH must meet the requirements of the populations of micro-organisms that coexist in the digester. The temperature of the reaction medium influences the pH value. While the temperature is increasing, the carbon dioxide solubility decrease; this is why in the case of thermophilic digesters the pH value is higher than in the mesophilic ones where the carbon dioxide will dissolve easier and will produce carbonic acid in reaction with the water, increasing the acidity. During the digestion process, the pH value may increase because of the ammonia presence resulted either by the protein degradation or by its presence in the charging flux. The size of organic particles to be digested affects the rate of anaerobic digestion and thus the overall rate of biogas production. The smaller the particle size, the faster the rate of anaerobic digestion due to increasing in surface area. This smaller particle size increases biogas generation rate and reduces the amount of residue thus reducing digestion time overall. Smaller particles also mean shorter settling time since particles can be suspended in the fluid for greater digestion [15].

To achieve steady and increased biogas production rate, the substrate to be digested and the anaerobic bacteria must have extensive contact. This contact can be achieved by proper mixing of the substrate in the digester tank. If there is insufficient mixing, layers of sediments begin to form in the digester tank, trapping bacteria beyond the reach of the undigested substrate [14]. Due to differences in density, these various substrates form layers with the majority of the bacterial mass settling at the bottom of the tank out of reach of the majority of the substrates to be decomposed.

Solids that can float then form a layer of scum at the top of the slurry making it difficult for gas to escape from lower levels. The result of these factors is a significantly lower biogas production rate. Thus, mixing is essential for proper biogas production. Excessive mixing must, however, be discouraged in biogas plants as the bacteria that help form acetic acid (during acidogenesis) and the archaea responsible for methanogenesis form a close biotic community that can be destroyed by excessive stirring. A compromise thus must be reached between stirring time and stirring intensity.

Other factors that affect biogas production include mixing ratio, inoculums, loading rate, nitrogen inhibition, C/N ratio, agitation, toxicity, solid concentration, seeding, metal cations, additives, etc.

A wide array of research work has been carried out on biogas production in Nigeria and in other parts of the world. Biogas production and science have steadily progressed in the last four decades. However there is much room for innovation and creative thinking. Otaraku and Ogedengbe [16] studied the effect of Sawdust concentration in the co-digestion of sawdust, cow dung, and water hyacinth. This was done over a period of 64 days, and it was observed that about 40% of Sawdust in the total solids yielded optimum biogas production. Increased Sawdust content lowered biogas productivity due to the high lignin content of the sawdust which is difficult to digest.

Yavini *et al.* [17] studied the mesophilic biogas production potential of Groundnut shell, Maize cobs, Rice straw, and Bagasse. It was observed that the inoculation of these agricultural

wastes with methanogenic bacteria sources such as cattle dung and poultry droppings had an important role and positive impact on biogas generation quantity. Rajendran *et al.* [18] gave an insightful overview into the various designs and operation of household biogas digesters, noting that moderate mixing is essential in biogas reactors as too much mixing stresses the microorganisms and too little mixing encourages foaming and even formation of scales.

Dahunsi and Oranusi [19]worked on co-digestion of food waste and human excreta for biogas production. They provided relevant data on the pH regime in the mesophillic temperature range for co-digestion of food waste and human excreta. The limitation of their research lies in the fact that temperature and pH were not continuously monitored but taken daily and weekly respectively. Ezeokoye and Okeke [20] worked on the design, construction, and performance evaluation of a Plastic Bio-digester and the Storage of Biogas. They Monitored parameters for biogas production from grains during batch digestion, but in their digesters, Practical digesters are mostly continuously fed, temperature monitored daily, pH monitored weekly. Dobre *et al.* [13] studied the overview of Main factors affecting biogas production. They highlighted lack of effective parameter monitoring to be a major cause of poor production and instability. Labatut and Gooch [21] monitored of anaerobic digestion process to optimize performance and prevent system failure. The work highlighted lack of process monitoring and operational management as a major cause of failure in most Biogas plants. They used analytical laboratories for onsite monitoring of large-scale plants which are too expensive for the domestic or small-scale application.

Despite the many benefits of biogas digesters, there are also a number of drawbacks that can make the implementation of this technology difficult. These difficulties include: Methanogens have many specific parameters, such as temperature and pH, this hinders widespread commercialization of anaerobic digesters [22]. The hydraulic retention time (HRT) poses a challenge, HRT which is the average time that the input slurry spends in the digester before it is removed, in tropical countries is 30 to 50 days, whereas in colder climates, it can be as long as 100 days, which requires a larger digester volume and raises costs [23]. While digesters can provide energy savings or even income to small-scale owners at farms—by way of selling electricity produced back to the power company—finding the right economies of scale possess yet another challenge. While biogas digesters do indeed offer a valuable way to reduce food waste and to capture energy that would otherwise be squandered, the actual potential of anaerobic digestion to produce a great deal of electricity is fairly limited. Even if the energy-producing capacity of biogas is small, given the waste-reducing benefits of anaerobic digestion, combined with its ability to slow climate change, pursuing policies to make digesters more common makes a great deal of sense. The main challenge is finding the right scale in order to make biogas digesters more economically feasible.

2. Materials and method

The biogas plant was designed as a continuously stirred reactor type (CSTR) due to its smaller footprint, ease of maintenance and improved gas production over the plug-flow mix type. A fixed-dome configuration was also selected over the floating-dome type due to its stability and relative ease of operation. A grinder was added to the digester vessel to reduce the particle size for improved biogas production. A stirrer system with an electric motor was also added to introduce substrate mixing that would boost biogas yield. The monitoring system was identified as a major improvement based on the limitations of other work and was implemented in the biogas plant.

The methodology employed for the design and construction is elucidated subsequently.

2.1. Materials

The following materials were used for the construction of a biogas plant:

i. Sparkless electric motor (1HP)
ii. Stainless steel type 316
iii. Stirrer

iv. Waste grinder
v. Hopper
vi. Valves and fittings
vii. Flashband sealing tape
viii. Arduino Uno Microcontroller
ix. pH Meter Kit
x. Pressure transducer sensor
xi. Temperature sensor
The part list of the developed small-scale biogas plant is presented in Table 1.

Table 1. Part list

S/N	Description	Quantity	Material	Remarks
1	Digestion tank	1	1 mm sheet metal	Stainless steel
2	Sparkless electric motor	1	Bought-out	0.35 kW
3	Stirrer	1	20 mm ø shaft	Stainless steel
4	Waste grinder	1	1 mm sheet metal for mesh. 125 mm diameter grater.	
5	Valves and fitting	2	Bought-out	½'' ball valve ½'' adapter ¾" socket ¾" X ½" bushing ¼'' gas outlet valve ½" T-fitting ½" PVC pipe
6	Flashband sealing tape	2	Bought-out	Aluminum faced, bitumen backed sealing tape
7	Arduino Uno	1	Bought-out	
8	pH Meter Kit		Bought-out	
9	Pressure transducer sensor	1	Bought-out	
10	Temperature sensor	1	Bought-out	

2.1. Digestion tank

The digestion tank is the main reactor chamber where anaerobic digestion takes place. The material for fabrication is selected as stainless steel due to its ability to combine high strength, good formability and good resistance to biological corrosion [24] that can result from the metabolic activity of anaerobic microorganisms. Painting with a chromium oxide based paint will also improve the surface thermal absorptivity from solar insolation. The following design calculations were evaluated for the overall reactor tank design.

i. The volume of the reaction tank

According to Bachmann [25], to ensure that micro-organisms have a balance between the time needed to breakdown waste substrates and the concentration or quantity of substrates available (to avoid overloading the micro-organisms and hence inhibiting biogas production), two factors must be considered in sizing of biogas plants. These include the organic loading rate (OLR) and the hydraulic retention time (HRT).

The formula for calculating the volume of digester tank is given by equation 2.

$$V_d = \frac{I_w \times DM \times VDM}{OLR} \quad (2)$$

where: V_d is the reactor volume [m^3]; I_w is the substrate input [kg/day]; DM is the dry matter content of the waste or total solids content expressed in %; VDM is the volatile dry matter content of the waste [% DM]; OLR is the theoretical organic loading rate [kgVDM/ m^3day]

OLR for a continuously stirred tank can be as high as 4 kgVDM/ m^3day [25]. Assuming maximum substrate input (I_w) is 1.4 kg/day of food waste from home kitchens (small-scale application). DM for food waste can be estimated at 20% and VDM as 85% [3,26]. Thus,

$$V_d = \frac{1.4 \times 0.2 \times 0.85}{4} \qquad V_d \approx 0.06\, m^3$$

ii. Tank dimensions

For minimal footprint and aesthetic consideration we take heuristics:

$h = 1.75d = 3.5r$ (3) but, $V_d = \pi r^2 h = .5\pi r^3$ (4)

Equating equations (3.2) and (3.3) $0.6 = 3.5\pi r^3$

Hence $r \approx 0.175\, m$ and $h \approx 0.61\, m$

According to Moss [27], the thickness of the tank is estimated from equation 5.

$$t = \frac{P.r}{SE - 0.6P} \quad (5)$$

where: t is the minimum thickness of the cylindrical reactor wall (mm); P is the maximum internal pressure (N/mm^2); r is the internal radius of the reactor tank (mm); S is the maximum allowable working stress of the component (N/mm^2); and E is the joint efficiency.

Anaerobic digestion is favored by near-atmospheric pressure condition, and anaerobic bacteria thrive best below 1.2 bar (120 kPa). Consequently, beyond the accepted range above, the anaerobic digestion process stalls and eventually biogas production ceases. Thus, the maximum pressure the tank should withstand should be within a safety limit of 1.2 bar. Using a Factor of Safety of 3, a maximum design pressure P calculated as 3.6 bar (360 kPa) is utilized. The internal radius of the tank, r is 0.175 m assuming a joint efficiency of the weld, E is 0.8. The maximum tensile strength of stainless steel is obtained as 520 MPa [28].

The permissible working stress is calculated as:

$$S = \frac{Maximum\ Tensile\ Strength}{FOS} = \frac{520MPa}{5} = 104\ MPa$$

$$t = \frac{360 \times 10^3 \times 0.175}{(104 \times 10^6 \times 0.8) - 0.6(600 \times 10^3)} = 0.000765\ m\ or\ 0.765\ mm$$

Thus, the thickness of plate was thus selected as 1 mm to the nearest mm.

iii. Baffle design

The digestion reaction tank (reactor tank) is equipped with baffles to prevent swirling and to induce turbulence required for mixing in the tank. According to James [29], the following heuristics apply: 3 to 4 baffles are sufficient for a cylindrical tank, and the geometry is shown in Figure 2.

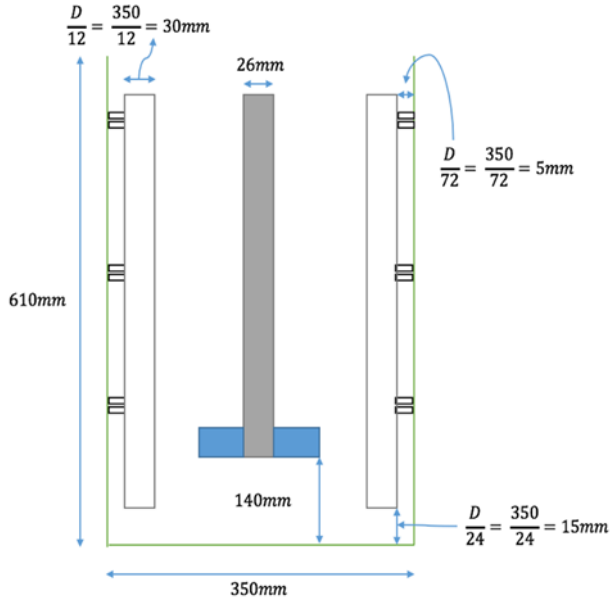

Figure 2. Baffle design for digester tank

The power requirement of the mixer was obtained using equation 6 according to Peters *et al.* [24].

$$P = \emptyset N_r^3 D_a^5 \rho \quad (6)$$

where: P is the power required for mixing (kW); $\emptyset$ is the power function; N_r is the impeller rotation per unit time (rps); D_a is the impeller diameter (m); ρ_s is the density of slurry to be mixed (kg/m^3)

The power function can be estimated from charts using the Reynolds number and impeller characteristics. The Reynolds number for the flow is given by equation 7.

$$Re = \frac{D_a^2 N_r \rho_s}{\mu} \quad (7)$$

The input waste is food waste of average density; $\rho_{fw} = 360$ kg/ m^3 [2] and water of density ρ_w= 1000kg/ m^3. With a mixture ratio 1:1, $c_{fw} = c_w$, the slurry density is given from equation 8.

$$\rho_s = \frac{\rho_w \cdot \rho_{fw(c_{fw} + c_w)}}{\rho_{fw} c_{fw} + \rho_w c_w} \quad (8)$$

$$\rho_s = \frac{1000 \times 360\ (2)}{360 + 1000} = 530\ \text{kg/}\ m^3$$

Slurry viscosity (μ) is approximately 650 cP or 0.65Ns/m^2 [29]. Assuming the impeller speed $N_r\ is\ 600\ rpm\ (10\ rps)$ and the diameter of impeller (D_{athe}) obtained from impeller sizing heuristics according to Peters *et al.* [24] is given as equation 9.

$$D_a = \frac{Tank\ Diameter\ (D_T)}{2.5} \quad (9)$$

$D_a = \frac{Tank\ Diameter\ (D_T)}{2.5} = \frac{350}{2.5} = 140\ mm$. Therefore, the Reynolds number is calculated from equation 7 as: $Re = \frac{0.14^2 \times 10 \times 530}{0.65} = 160$

Since Froude's number is not a factor (Re < 300), the relation between power function and the Reynolds number for a paddle mixer is shown in Figure A1 from Appendix A. Thus, the power function $\emptyset\ is\ 6$ as obtained from the chart for Reynolds number Re of 54.

Assuming $N_r = 600\ rpm = \frac{600}{60}\ rps = 10\ rps$, $D_a = 0.14\ m$, and $\rho_s = 530\ kg/m^3$.

Using equation 6, the power required for mixing is calculated as:

$P = 6 \times 10^3 \times 0.14^5 \times 530 = 171\ W$

With loading of 80%, the motor power required will thus be:

$P_m = \frac{171}{0.8} =$ 250 W (to the nearest standard). Using a safety factor of 2.5, $P_m = 250 \times 2.5 =$ 625 W

Due to availability, a **1 HP** (750 W) motor is selected.

2.2. Stirrer

The stirrer consists of paddle-type impeller blades with a vertical shaft subjected to twisting moment only.

i. The diameter of impeller (D_a)

According to Peters *et al.* [24] (2003), the diameter of imthe peller is obtained from impeller sizing heuristics as 140 mm by recalling equation 9.

$$D_a = \frac{Tank\ Diameter\ (D_T)}{2.5} \quad (Recall\ equation\ 9)$$

ii. Diameter of shaft

As the weight of the shaft is negligible and as the shaft is vertically oriented for mixing, it is subjected majorly to twisting moment. From Khurmi and Gupta [30], shafts may be designed on the basis of rigidity and strength. When subjected to twisting moment only, the following relation holds true:

$$\frac{T}{J} = \frac{\tau}{r} \quad (10)$$

with little mathematical consideration it can be shown that:

$$d^3 = \frac{16T}{\pi\tau} \quad (11)$$

where: T is the torque or twisting moment (Nm); τ is the allowable or permissible torsional shear stress (N/mm^2); J is the Polar moment of the shaft about its axis of rotation (mm^4); r is the radius of the shaft (mm); and d is the diameter of the shaft (mm).
The twisting moment T is calculated from equation 11 as

$$T = \frac{P}{2\pi N_r} \quad (12)$$

$$T = \frac{750}{2\pi \times 10} = 11.94\ Nm$$

The allowable shear stress for stainless steel can be obtained as $\tau = 0.18\sigma_u$ (13)
where: σ_u is the ultimate tensile strength given as 520 MPa [28].

$$\tau = 0.18 \times 520 = 93.6\ MPa$$

Thus, the diameter of shaft the the for the mixer is calculated as:

$$d^3 = \frac{16 \times 11.94}{\pi \times 93.6 \times 10^6} \qquad d = \mathbf{10\ mm}\ (nearest\ standard\ size)$$

Using a safety factor of 2, $d = \mathbf{20\ mm}\ (nearest\ standard\ size)$

2.3. Water crusher

Since food waste is to be used as a substrate, provision is made for the easy crushing of food remains including cooked food and spoiled fruits. The waste crusher will also aid in the particle size reduction of various grains and nuts that will be fed to the biogas reactor. The crusher consists of a roller with a shaft for power transmission. The power required to actuate the crusher depends on the torque needed to rotate the roller cylinder when loaded to maximum. As the digester will be loaded daily in batches of 1.4 kg; the force F on the crusher is given by equation 14.

$$F = m.g \quad (14)$$

$$F = 1.4 \times 9.81 = 13.74\ N$$

The torque T required is calculated from equation 15.

$$T = F.r \quad (15)$$

$$T = 13.74 \times 0.1 = 1.374\ Nm$$

Assuming a moderate speed of 40 rpm, hence the minimum power requirement for the crusher can be obtained as:

$$P = \frac{2\pi NT}{60} \qquad (Recall\ equation\ 12)$$

$$P = \frac{2\pi \times 40 \times 1.374}{60} = 5.8\ W$$

Hence, hand grinding was evaluated as an ecoeconomicaltion and thus selected.

2.4. Valves

Two ball valves are utilized for fluid control in the system. One ¾" valve serves as the drain or flush valve for emptying the contents of the tank after the design HRT is exceeded. A ¼" gas outlet valve serves for the feeding of gas to the plant outlet.

2.5. Flashband sealing tape

This is a self-adhesive, aluminum faced bitumen backed sealing tape. It is a quick, efficient and cost effective method of flashing, sealing and repair that produces lasting protection in all climates. It provides a watertight seal that improves over time [31].

2.6. Arduino Uno microcontroller

The Arduino Uno is a microcontroller board that provides a simple and modular way of interfacing the real world with the computer to handle basic processing tasks on a chip while working with hardware sensors. The Arduino Uno uses the ATmega328 chip that supports 14 digital pins that can be configured as either input or output and 6 analog inputs [32]. Table 2 shows the technical features of the Arduino Uno.

Table 2. Technical Specifications of the Arduino Uno

S/N	Item	Value	Remarks
1	Micro-controller	8-bit Atmel ATmega328p	1 mm sheet metal
2	Operational voltage	5V	Input range: 7-12V
3	Digital GPIO	14	6 capable of PWM
4	Analog IO	6	10-bit
5	Program memory	Flash 32kb, EEPROM 1kb	SRAM 2kb
6	Clock speed	16MHz	
7	USB	Type B socket	
8	Programmer	In-system firmware	USB-based
9	Serial communications	SPI, I2C	Software UART
10	Other	RTC, watchdog, interrupts	

The Arduino is programmed using the Arduino IDE with source code written in C.

2.7. Pressure transducer sensor

This measures the pressure of the gas with a carbon steel alloy sensor material. It has a working pressure range of 0-1.2 MPa. The normal working temperature range is 0-85°C and the response time is approximately 2 ms.

It consists of an elastic material that deforms under the application of pressure and an electrical element which detects the deformation and transmits it as changes in voltage.

2.8. pH Meter Kit

This is a kit that measures pH of a substance. It is specially designed for the Arduino and has an accuracy of $\pm 0.1\,pH$ (at 25°C). The kit has a range of 0 – 14pH. The kit consists of a pH sensor probe, a BNC connector and a pH 2.0 interface.

2.9. Temperature sensor

This takes temperature readings for the plant to aid process insights. It has a temperature range of -40°C - 80°C.

2.10. Construction of the biogas plant

The volume of digester constructed is 0.06 m^3. A 1 mm thick stainless steel sheet was used in the fabrication of the biogas reactor for the following reasons:

i. It has high resistance to biological corrosion which can arise due to anaerobic digestion process;
ii. It can withstand a wide range of temperatures and pressures.
iii. It also combines good strength with high formability.

In constructing the small-scale biogas plant, the following stages were undergone:

i. Construction of the cylindrical digester vessel of diameter 350 mm and height 610 mm;
ii. Construction of the grinding unit;
iii. The connection of the plant monitoring system circuit;
iv. Installation of the grinding unit on the digester vessel;
v. Installation of the electric motor;
vi. Installation of piping and fittings;
vii. Installation of plant monitoring circuit on digester vessel.

2.10.1. Construction of cylindrical vessel

The following steps are taken to construct the cylindrical biogas digester vessel:

i. The 1 mm stainless steel metal sheet was cut to size (1100 X 610 mm) using the Guillotine machine.
ii. The 1100 X 610 mm stainless steel sheet was rolled to shape using the metal rolling machine.

iii. The metal sheet was welded to form the cylindrical shape of the body plate.
iv. A separate stainless steel sheet was cut and welded into a conical shape for the bottom of the tank.
v. The circular metal plate of diameter 350 mm was marked out and cut as the top plate of the cylindrical vessel.
vi. Three stainless steel plates of dimension 94.5 X 580 mm were cut. These were rolled and welded into cylindrical baffles for the tank.
vii. The three cylindrical baffles were welded to the internal surface of the tank. Baffles at 90°, 180° and 270° relative to the circular top plate.
viii. The conical bottom plate was then welded to the cylindrical body plate.
ix. The stainless steel shaft was turned to 20 mm external diameter.
x. Two 140mm paddle impellers were welded to the stainless steel shaft.
xi. The mild steel square pipe was cut into three sections of length 300 mm These sections were then welded onto the cylinder as the vessel legs.
xii. A 20 mm bore was machined in the circular top plate for the stainless steel shaft.
xiii. The circular top plate was welded onto the cylindrical vessel and installation of a bearing assembly for the machined shaft.

2.10.2. Construction of the grinding unit

The following steps are taken to construct the grinding unit:

i. The side plates of the hopper were marked out with dimensions 70 X 65 mm for the square component and 130 X 70 X 110 mm for the trapezium component.
ii. The marked out shape was cut to specifications.
iii. The face plates of the hopper were marked out and cut with dimensions 90 X 65 mm for the square component and 175 X 90 X 110 mm for the trapezium component.
iv. The side plates were drilled to create a 25 mm bore for the shaft and cylindrical grinder mesh.
v. The cylindrical grinder mesh was developed with recommended 1.5 mm mesh basic size and 3mm clearance.
vi. The cylindrical mesh, shaft, and handle were assembled.
vii. The four plates (two side plates and two face plates) were welded together to obtain the hopper unit.

2.10.3. The connection of the biogas plant monitoring system circuit

The biogas plant monitoring system was connected on a breadboard for prototyping using the circuit diagram shown in Figure 3. Figure 3 show the connection of the ATmega328 chip on the Arduino Uno with the pH, pressure and temperature sensor.

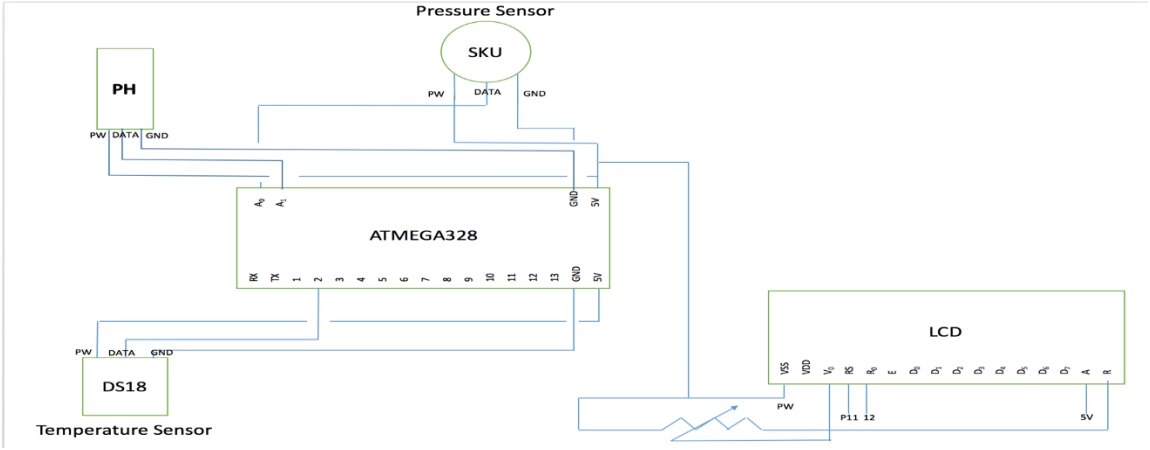

Figure 3. Monitoring system circuit with Arduino Uno microcontroller

2.11. Performance evaluation of the developed biogas reactor

This was done to evaluate the performance of the biogas plant in terms of effectiveness of the continuous monitoring system. Data were obtained from the pressure, pH and temperature sensors to determine their accuracy. The biogas yield is recorded to give daily and total biogas yield. The biogas yield is then evaluated with the pressure, pH and temperature variation per day.

2.12. Leak and integrity testing

After the electric motor, grinding unit and monitoring system are installed, the biogas plant is subjected to a leak and integrity test using the following steps:

i. Close all valves were closed and tighten all fitting joints.
ii. Introduce compressed air at a regulated pressure and inspect all fittings, valves, and joints for leakage.
iii. Mark out leaks if any.
iv. Tighten all joints and carry out final inspection on the entire plant.

2.13. Input Waste

The developed biogas plant was fed with 3.55 kg of food waste (comprising egg shells, cooked rice, pounded yam, etc.) and 11.45 kg of cassava waste water. The total input waste thus is about 15 kg.

2.14. Method

The waste material was gathered from the ABUAD Cafeteria 1 and the cassava waste water from a neighboring village close to the ABUAD community. The waste was prepared by removing foreign/non-organic materials and fed into the biogas plant and fed

The food waste material was fed by mixing with water in a ratio 1:1. The waste material is allowed to decompose for 7-14 days before biogas yield is evaluated. Immediately the waste was fed into the system, the biogas plant monitoring system was initiated to allow for data acquisition.

2.15. Determination of biogas yield

Biogas yield is determined using the water-displacement method. A known volume of water is used as a barrier and biogas is collected over it, and its volume is recorded daily. The correlation, prediction, modelling, and optimization of optimum process parameters and yield of biogas produced from food waste was done using the central composite design and response surface methodology.

The software employed was Design-Expert® (version 7) which is used for experiment design. A four-level-four factor central composite design model and response surface methodology were used to study the effect of independent variables such as organic loading rate (kgVDM/m^3), temperature (℃), pH and pressure (kPa) and on the biogas yield. The input process parameters varied and their range includes; organic loading rate (0.6-0.9 kgVDM/m^3); reaction temperature (24.27 – 26.42℃); pH (6.81-7.28) and pressure (4.20-5.48 kPa).

It is also used to investigate the quadratic cross effect of the four input process parameters earlier mentioned on biogas yield. Table 3 shows the input values for process parameters denoted as numeric factors over 4 levels. This generated a run of 30 experiments and the data obtained were statistically analyzed with the Design-Expert® software to get a suitable model for biogas yield (litres) as a function of the four independent variables.

The performance evaluation of the developed biogas plant was carried by introducing a total input waste of 15 kg. 3.55 kg of food waste material composing of 54% egg shells and 46% leftovers were sourced from the ABUAD Cafeteria. The food waste comprises egg shells, cooked rice, pounded yam, etc. 11.45 kg of cassava waste water was also fed into the plant.

3. Results and discussion

The developed biogas system with its associated expert system is shown in Figure 4.

Figure 4. Developed small-scale biogas plant

The system pressure, pH of the substrate and corresponding temperature variation were determined. The biogas yield per day for the given substrate was then obtained via collection over water as shown in Table 3.

Table 3. Methane yield per day

S/N	Time (days)	Weigh of input waste (kg)	Weight of consumed waste (kg)	Volume of methane generated (m^3)	Weight of methane generated (kg)	Amount of electricity generated (kWh)	Methane yield (%)
1	14	15	2.5	1.95	1.28	4.17	51.2
2	28	15	2.6	2.01	1.32	4.30	50.7
3	42	16	2.8	2.18	1.43	4.67	51.0
4	56	18	3.2	2.60	1.70	5.57	53.3
5	80	16	2.7	2.14	1.40	4.58	52.0
6	94	18	3.0	2.45	1.60	5.24	54.0

The volume of methane generated and the amount of electricity produced from 14-84 days is shown in Figure 5. High pressure favours the conversion of the substrate to methane gas. An optimum amount of 5.24 kWh of electricity was generated within 84 days which is sufficient for domestic applications.

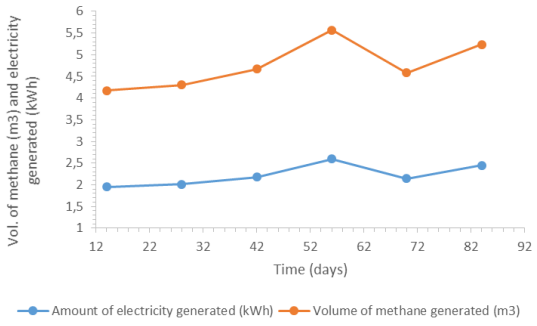

Figure 5. Volume of methane generated and amount of electricity produced

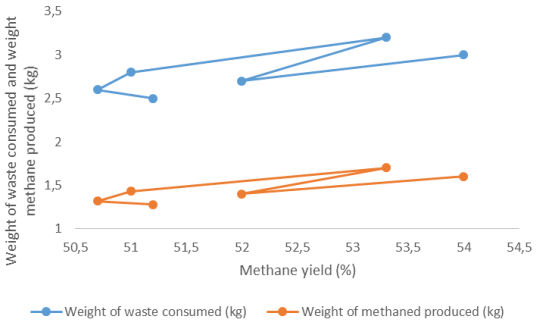

Figure 6. Methane yield for waste consumed and methane produced

Also, Figure 6 show the methane yield for the input waste consumed as well as the corresponding methane produced. The conversion efficiency of the consumed substrate to methane gas lies between 50-54%. This agrees with the findings of Banks [32] while evaluating the potential of anaerobic digestion to provide energy and soil amendment.

The summary of the designed experiment to predict biogas production in terms of study type using central composite as initial design and a quadratic design model was also given in Table 4.

Table 4. Numeric factors and levels

			S/N	Factor	Name	-alpha	+alpha
1.	A	Organic loading rate	kg/VDM/m^3	0.6	0.9	0.45	1.05
2.	B	Temperature	℃	24.27	26.42	23.195	27.495
3.	C	pH		6.81	7.28	6.575	7.515
4.	D	Pressure	kPa	4.20	5.48	3.56	6.12

The yield of the biogas from food waste was determined using equation 16.

$$Yield = \frac{Weight\ of\ biogas}{Weight\ of\ input\ waste} \times 100\% \qquad (16)$$

A predictive model for estimating the biogas yield in terms of the process parameters was obtained from Table 4 as given in equation 17.

$$Yield = 18.27 + 0.000 * A + 0.28 * B + 0.50 * C + 0.000 * D - 0.81 * A * B + 1.19 * A * C + 0.69 * A * D + 0.44 * B * C - 3.06 * B * D - 0.063 * C * D \qquad (17)$$

where: A denotes the organic loading rate (kgVDM/m^3); B is the temperature (℃); C is the pH and D is the pressure (kPa).

Figure 7 was a 3D response surface plot of the interaction effect loading rate and temperature when pH and pressure were held constant at 7.04 and 4.84 kPa respectively. The optimum yield of biogas was 23 litres. Increase in loading rate increases the temperature and increases the yield of the biogas.

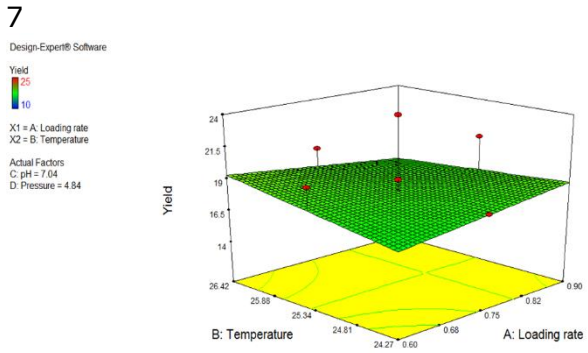

Figure 7. Effect of interaction of loading rate and temperature on biogas yield

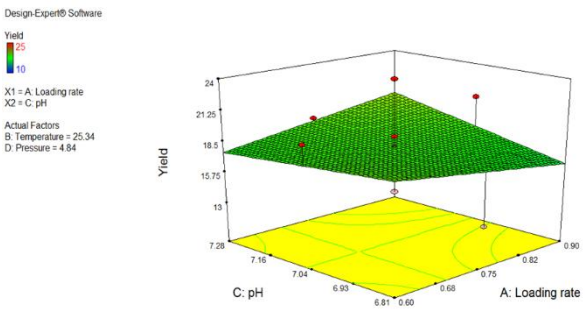

Figure 8. Effect of interaction of loading rate and pH on biogas yield

Figure 8 studies the interaction effect of loading rate and pH when temperature and pressure are held constant at 25.34°C and 4.84 kPa respectively. The optimum yield of biogas was 23 litres. Increase in loading rate increases the pH and increases the yield of the biogas up to the optimum yield point after which there is a sharp decrease in the yield with an increase in the loading rate and pH. This may be due to the fact that when the biogas is loaded beyond the optimum, the rate of decomposition decreases resulting in a decreased yield of the biogas.

Figure 9 is a 3D response surface plot of the interaction effect of the loading rate and pressure keeping temperature and pH constant at 25.34°C and 7.04 respectively. Increase in loading rate increases the pressure resulting in an optimum yield of biogas. Beyond the optimum yield of 23 litres, the yield of the biogas decreases with increase in loading rate and pressure.

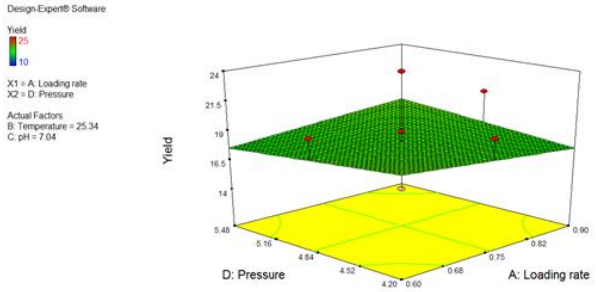

Figure 9. Effect of interaction of loading rate and pressure on biogas yield

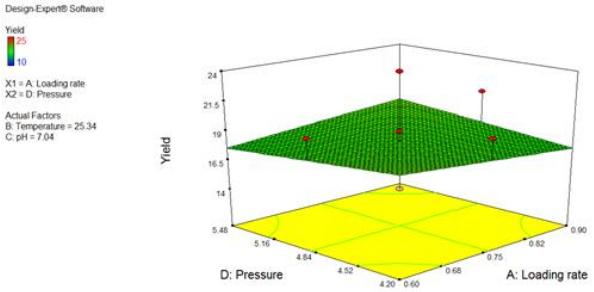

Figure 10. Effect of interaction of temperature and pH on biogas yield

Figure 10 was a 3D response surface plot of the interaction effect of temperature and pH when loading rate and pressure were held constant at 0.75 and 4.84 respectively. The value of pH is likely to be unaffected with an increase in temperature. Further increase in temperature beyond the optimum may kill the decomposition of anaerobic bacteria which will, in turn, slow down the rate of decomposition resulting in a decrease in the yield of the biogas.

Figure 11 is a 3D response surface plot of the interaction effect temperature and pressure on the yield of biogas when the loading rate and pH were held constant at 0.75 and 7.04 respectively. The interaction between the temperature and pressure was observed to be inversely proportional as an increase in temperature reduces the pressure and vice versa. The optimum yield of biogas was found to be 23 litres.

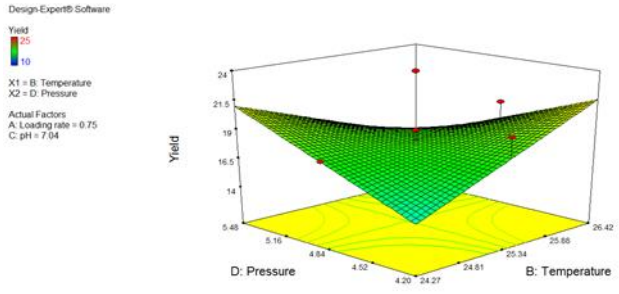

Figure 11. Effect of interaction of temperature and pressure on biogas yield

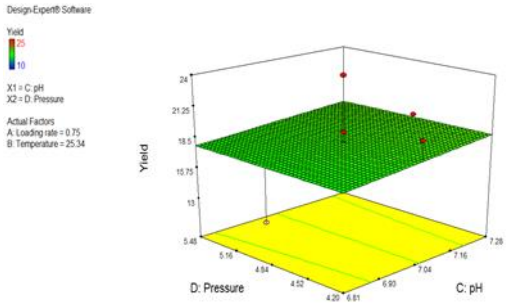

Figure 12. Effect of interaction of pH and pressure on biogas yield

Figure 12 is a 3D response surface plot of the interaction effect of pH and pressure on the yield of biogas. The variation in pH is unlikely to affect the pressure variation. Hence the optimum yield of biogas was found to be 23 litres.

From Figures 7-12, the optimum values of the process parameters for the optimum yield of biodiesel (23 litres) were found to be: loading rate (0.75 kgVDM/m^3), temperature (25.34^{o}C), pH (7.04) and pressure (4.84 kPa).

4. Conclusion, recommendations, and contribution to knowledge

4.1. Conclusion

The successful completion of this work featured the design a biogas plant for use in ABUAD for studying biogas production, fabrication of the designed biogas plant, incorporation of a relatively low-cost continuous parameter monitoring system for the small-scale biogas plant and evaluation and optimization of the developed biogas plant. The optimum conversion of substrate to methane gas was 54% which generated 5.24 kWh of electricity within 84 days.

4.2. Recommendations

The following recommendations will be pivotal to further work on the development of biogas plants with monitoring system:

i. A metering system should be added to measure the amount of biogas produced on the gas outlet line per day as water displacement method requires close human monitoring.
ii. A wireless module should be added to the system to make the system fully smart and communicate to as an 'Internet of Things' device.
iii. A non-conventional heating system e.g., passive solar heating using water and solar insolation should be considered to raise the temperature to the thermophilic range for faster biogas production.
iv. Implementation of a packaging system that will enhance the value of the produced fertilizer.

4.3. Contribution to knowledge

The work contributes to knowledge as follows:

i. Improvement in process control and monitoring with the use of sensors and a micro-controller.
ii. Incorporation of a low-cost monitoring system for the small-scale biogas plant.
iii. Provision of a design framework for small-scale biogas plant for laboratory and experimental purposes.

References

[1] Gerlach F, Grieb B and Zerger U. Sustainable Biogas Production: A handbook for Organic Farmers. Frankfurt: FiBL Projekte GmbH 2014. Available from: http://www.ecofys.com/files/files/ecofys-2014-sustaingas_handbook.pdf [Accessed 4 December 2016].

[2] Hoornweg D and Bhada-Tata P. What a Waste: A Global Review of Solid Waste Management. World Bank: Urban Development Series, Knowledge Papers 2012. [Online]. Available from: http://siteresources.worldbank.org/INTURBANDEVELOPMENT/Resources/336387-1334852610766/What_a_Waste2012_Final.pdf [Accessed: 25 November 2016].

[3] Al Seadi T, Rutz D, Prass, H, Kottner M, Finsterwalder T, Volk S and Janssen R. Biogas Handbook. Esbjerg: University of Southern Denmark 2008. [Online]. Available from: Lemvig Biogas. http://www.lemvigbiogas.com/download.htm [Accessed 25 November 2016].

[4] World Energy Council. World Energy Resources: 2013 Survey. London: World Energy Council. [Online]. Available from: https://www.worldenergy.org/wp-content/uploads/2013/09/Complete_WER_2013_Survey.pdf [Accessed: 25 November 2016].

[5] Ramatasa IM, Akinlabi ET, Madyna DM, and Huberts R. Design of the Bio-digester for Biogas Production: A Review. Proceedings of the World Congress on Engineering and Computer Science. Vol. II WCECS 2014 22-2, San Francisco USA. pp. 1-4.

[6] Sharma D, and Samar K. Frequently Asked Questions on Biogas Technology. Department of Renewable Energy Engineering. Maharana Pratap University of Agriculture and Technology 2016, Udaipur. pp. 1-62.

[7] Lahlou Y. Design of a Biogas Pilot Unit for Al Akhawayn University 2017. pp. 1-65.

[8] Wiese J, and Konig R. (2007). Monitoring of digesters in biogas plants. [Online]. Available from: https://uk.hach.com/asset-get.download.jsa?id=25593611187 [Accessed 2 March 2017].

[9] Friehe J, Weiland P and Schaffer A. Guide to Biogas: From Production to use. Fachagentur Nachwachsende Rohstoffe e.V. (FNR) 2010, Gülzow.

[10] Davidson O. Sustainable energy and climate change: African perspectives. In: Davidson O., Sparks D. (eds.) Developing energy solutions for climate change: South African research at EDRC. Cape Town: Energy and Development Research Centre 2002. pp. 145–152.

[11] Bauer, C., Korthals, M., Gronauer, A. & Lebuhn M (2008) Methanogens in biogas production from renewable resources - a novel molecular population analysis approach. Water Sci Technol 58: 1433–1439.

[13] Dobre P, Nicolae F and Matei F. Main factors affecting biogas production – an overview. Romainian Biotechnological Letters. 2014; 19(3), pp 9283 – 9296.

[14] Friehe J, Weiland P. and Schreiber A. Guide to Biogas. Fachagentur Nachwachsende Rohstoffe e.V. (FNR) 2012, Gulzow

[15] Perera KUC. Investigation of Operating Conditions for Optimum Biogas Production in Plug Flow Type Reactor. KTH Industrial Engineering and Management 2011, Stockholm, pp. 1-46

[16] Otaraku IJ, and Ogedengbe EV. (2013) Biogas Production from Sawdust Waste, Cow Dung and Water Hyacinth – Effect of Sawdust concentration, International Journal of Application or Innovation in Engineering & Management. 2013; 2(6): 91-93.
[17] Yavini TD, Taura WH, Mohammed N. and Namo JM. (2014). Comparative Study of Mesophillic Biogas Production Potential of Selected Agro-Wastes. The International Journal of Engineering and Science, 214; 3(2): 1-6.
[18] Dahunsi SO, and Oranusi US. (2013). Co-digestion of Food Waste and Human Excreta for Biogas Production, British Biotechnology Journal,2013; 3(4). 485-499.
[18] Rajendran K, Aslanzadeh S, and Taherzadeh MJ. (2012). Household Biogas Digesters – A Review. Energies, 2012; 5(1): 2911-2942.
[19] Ezekoye VA, and Okeke CE. (2006) Design, Construction, and Performance Evaluation of Plastic Biodigester and the Storage of Biogas. [Online]. Available from: http://www.akamaiuniversity.us/PJST7_2_176.pdf [Accessed 10 March 2017].
[20] Labatut RA, and Gooch CA. (2014) Monitoring of Anaerobic Digestion Process to Optimize Performance and Prevent System Failure. [Online]. Available from: https://ecommons.cornell.edu/bitstream/handle/1813/36531/21.Rodrigo.Labatut.pdf?sequence=1 [Accessed 9 March 2017].
[22] Chen Y, Cheng JJ, and Creamer KS. Inhibition of Anaerobic Process: A review. Bioresource Technology,2018; 99(10): 4044-4064.
[23] Yadvika S, Sreekrishnan TR, Kohli S, and Rana V. (2004) Enhancement of biogas production from solid substrates using different techniques – a review. Bioresource Technology, 2004; 95: 1-10.
[24] Peters MS, Timmerhaus KD, and West RF. Plant Design and Economics for Chemical Engineers. 5th ed. New York 2003: Elsevier.
[25] Bachmann N. Design and Engineering of Biogas Plants, in: Wellinger, A., Murphy, J., Baxter, D. (eds.) The biogas handbook: Science, production and applications. Cambridge 2013: Woodhead Publishing.
[26] SEAI: Sustainable Energy Authority Ireland. Energy in the Residential Sector: 2013 Report. September 2013. pp. 1-2.
[27] Moss DR. Pressure Vessel Design Manual: Illustrated procedures for solving major pressure vessel design problems. 3rd ed. Oxford 2004: Elsevier.
[28] James B. (2012). Mixing 101: Baffled by Baffles? How Baffle Configuration can Optimize Industrial Mixing. [Online]. Available from: http://www.dynamixinc.com/baffled-by-baffles[Accessed 11 March 2017].
[28] Wendt U. Materials Science and Engineering: Materials in Mechanical Engineering, in Grote, K., Antonsson, E. K. (eds.) Springer Handbook of Mechanical Engineering. New York 2009: Springer.
[29] ATS Rheosystems (2017). Viscosity Profile of Food Waste Slurry: Application Proof. [Online]. Available from: http://www.atsrheosystems.com/app_proofs/food/viscosity_profile_of_a_food_waste_slurry.pdf [Accessed 28 February 2017].
[30] Khurmi RS, and Gupta JK. A Textbook of Machine Design. New Delhi 2005: Eurasia Publishing House.
[31] Andek Corporation. (2015). Flashband. [Online]. Available from: http://www.andek.com/AProducts/flash.html [Accessed 14 April 2017].
[31] Goodwin S. Smart Home Automation with Linux and Raspberry Pi. 2nd Ed. New York 2013: Apress.
[32] Banks C. Optimising Anaerobic Digestion. University of Reading 2009, UK. pp. 1-39.

To whom correspondence should be addressed: Dr. I. A. Daniyan, Department of Mechanical and Mechatronics Engineering, Afe Babalola University Ado Ekiti